Springer Proceedings in Physics 265

Soumitra Sengupta · Samrat Dey · Saurya Das · Dhruba J. Saikia · Sudhakar Panda · Ramakrishna Podila *Editors*

Selected Progresses in Modern Physics

Proceedings of TiMP 2021

Springer

Springer Proceedings in Physics

Volume 265

Indexed by Scopus

The series Springer Proceedings in Physics, founded in 1984, is devoted to timely reports of state-of-the-art developments in physics and related sciences. Typically based on material presented at conferences, workshops and similar scientific meetings, volumes published in this series will constitute a comprehensive up-to-date source of reference on a field or subfield of relevance in contemporary physics. Proposals must include the following:

- name, place and date of the scientific meeting
- a link to the committees (local organization, international advisors etc.)
- scientific description of the meeting
- list of invited/plenary speakers
- an estimate of the planned proceedings book parameters (number of pages/articles, requested number of bulk copies, submission deadline).

Please contact:

For Americas and Europe: Dr. Zachary Evenson; zachary.evenson@springer.com
For Asia, Australia and New Zealand: Dr. Loyola DSilva; loyola.dsilva@springer.com

More information about this series at https://link.springer.com/bookseries/361

Soumitra Sengupta · Samrat Dey · Saurya Das ·
Dhruba J. Saikia · Sudhakar Panda ·
Ramakrishna Podila
Editors

Selected Progresses in Modern Physics

Proceedings of TiMP 2021

Springer

Editors
Soumitra Sengupta
Indian Association for the Cultivation of Science
Kolkata, India

Saurya Das
University of Lethbridge
Lethbridge, AB, Canada

Sudhakar Panda
National Institute of Science Education and Research
Bhubaneswar, Odisha, India

Samrat Dey
Pragjyotish College
Guwahati, Assam, India

Dhruba J. Saikia
University Centre for Astronomy and Astrophysics
Pune, Maharashtra, India

Ramakrishna Podila
Clemson University
Clemson, SC, USA

ISSN 0930-8989 ISSN 1867-4941 (electronic)
Springer Proceedings in Physics
ISBN 978-981-16-5140-3 ISBN 978-981-16-5141-0 (eBook)
https://doi.org/10.1007/978-981-16-5141-0

This Springer imprint is published by the registered company Springer Nature Singapore Pte Ltd.
The registered company address is: 152 Beach Road, #21-01/04 Gateway East, Singapore 189721, Singapore

Preface

The Springer International Conference on Trends in Modern Physics (TiMP) 2021, the third annual conference of the Physics Department of Assam Don Bosco University (ADBU), was organised from 26 to 27 February, 2021, by the department, in collaboration with Indian Association of Physics Teachers, after successfully organising TiMP 2019 and TiMP 2020. A large number of participants, from various universities, colleges and institutes of India and abroad, presented around hundred research papers in the event. Due to the restrictions imposed by the COVID-19 pandemic, the conference was held in hybrid mode, with half of the participants making their presentations online and the remaining half presenting offline, in person. The organisers of the conference made all possible efforts to ensure that every delegate is able to seamlessly access all the presentations, irrespective of whether the presenter or the presentation is online or offline. To this end, all the offline presentations were also streamed live via web-conferencing and all the posters were made available online. Selected papers of TiMP 2021 have found their place in the proceedings after going through the due processes of peer reviews.

It was a felt need by the department to hold yearly national conferences on TiMP, as in this region there were no such yearly conferences of physics, where young researchers can share their ideas and get suggestions and help from renowned academicians of the country and other parts of the world. It may be noted, in this context, that the Physics Department, ADBU, ever since its inception in 2018, has been working at different levels to popularise elementary as well as advanced physics though various other approaches, like symposiums, workshops, refresher course, etc. The TiMP conference series has not been confined to any specific branch of physics, but, practically, to all the major disciplines of physics with the following underlying philosophy. While it is true that each discipline of physics has become so highly specialised that it is not easily legible to a person of another discipline, we must remember that over the history of the development of modern science, physicists' contributions were not only across different branches of physics but also to various other fields of science. For example, Marie Curie, a physicist, won a Nobel Prize in chemistry, apart from a Nobel Prize in physics. James Watson who got the Nobel Prize for proposing the double helix structure of the DNA molecule was actually

inspired by physics Nobel Laureate Erwin Schrödinger's book, "What Is Life?". World Wide Web (WWW) was invented in a physics research institute, CERN. The first computer simulation was developed in nuclear physics. Physicists' contribution to mathematics can be exemplified by the development of calculus by Isaac Newton. Venki Ramakrishnan, a Ph.D. in physics, got the Nobel Prize for his studies of the structure and function of the ribosome which is important in the production of antibiotics. The list of physicists contributing to other fields of science is actually too long. Thus, it is evident that if people from physics can make so many contributions to additional domains of science outside the realm of physics, it is both productive and likely for them, even if they are from specific branches of physics, to contribute to and collaborate with other disciplines within physics. With that philosophy in mind, this multidisciplinary physics conference series was conceptualised and has been being implemented successfully.

We thank the convener of the international conference, Mr. Parag Bhattacharya, together with the co-conveners, Dr. Debajyoti Dutta and Dr. Ngangom Aomoa. We also express our gratitude to all the reviewers, Dr. Lalthakimi Zadeng, Dr. Yubaraj Sharma, Dr. Simanta Chutia, Prof. Sunandan Baruah, Dr. Sumita Kumari Sharma, Dr. Kaustubh Bhattacharyya, Dr. Shantu Saikia, Dr. Debajyoti Dutta, Dr. Ngangom Aomoa, Prof. Atri Deshamukhya, Dr. Subhankar Roy, Dr. Debasish Borah, Dr. Wandahun Longtrai Reenbohn, Dr. Rashi Borgohain, Prof. Pritam Deb, Dr. Pralay Kumar Karmakar, Dr. Ashok Kumar Jha, Dr. Umananda Dev Goswami, Dr. Hemen Kumar Kalita and Dr. Subhaditya Bhattacharya. Finally, we thank all the authors for their contributions in the proceedings.

Kolkata, India — Soumitra Sengupta
Guwahati, India — Samrat Dey
Lethbridge, Canada — Saurya Das
Pune, India — Dhruba J. Saikia
Bhubaneswar, India — Sudhakar Panda
Clemson, USA — Ramakrishna Podila

Contents

Contributors

S. Adhikari Department of Physics, University of Oslo, Oslo, Norway

Gazi Ameen Ahmed Department of Physics, Tezpur University, Napaam, Assam, India

S. Anciya PG and Research Department of Physics, The M. D. T. Hindu College, Tirunelveli, Tamil Nadu, India;
Manonmaniam Sundaranar University, Abishekapatti, Tirunelveli-12, Tamil Nadu, India

H. Bailung Dusty Plasma Laboratory, Physical Sciences Division, Institute of Advanced Study in Science and Technology (IASST), Guwahati, Assam, India

Kalyanjit Dutta Baruah State Cancer Institute, Gauhati Medical College, Guwahati, Assam, India

Dipankar Bhagabati State Cancer Institute, Gauhati Medical College, Guwahati, Assam, India

Ankita Bhagawati Department of Physics, Tezpur University, Tezpur, Assam, India

Chandrashekhar M. Bhambere Department of Physics, S. S. and L. S. Patkar-Varde College, Mumbai, Maharashtra, India

Ananya Bhattacharjee Department of Mathematics, Assam University Silchar, Silchar, Assam, India

Rangaraj Bhattacharjee State Cancer Institute, Gauhati Medical College, Guwahati, Assam, India

A. K. Bhunia Department of Physics, Government General Degree College at Gopiballavpur-II, Jhargram, Beliaberah, West Bengal, India

Rajib Biswas Applied Optics and Photonics Lab, Department Of Physics, Tezpur University, Tezpur, Assam, India

Kalpana Bora Physics Department, Gauhati University, Guwahati, Assam, India

Bichitra Bijay Boruah Tezpur University, Tezpur, Assam, India

Monojit Chakraborty Centre of Plasma Physics-Institute for Plasma Research, Tepesia Sonapur, Assam, Kamrup (M), India

Biprav Chetry Applied Photonics & Nano-Photonics Laboratory, Department of Physics, Tezpur University, Tezpur, Assam, India

Bidyut Chutia Dusty Plasma Laboratory, Physical Sciences Division, Institute of Advanced Study in Science and Technology (IASST), Guwahati, Assam, India

Simanta Chutia Department of Physics, St. Anthony's College, Shillong, India

Mrinal Kumar Das Department of Physics, Tezpur University, Tezpur, India; Department of Physics, Tezpur University, Napaam, Assam, India

Nipan Das Centre of Plasma Physics-Institute for Research, Sonapur, Assam, India

Pritam Das Department of Physics, Tezpur University, Napaam, Assam, India

Priyanka Das Applied Photonics & Nano-Photonics Laboratory, Department of Physics, Tezpur University, Tezpur, Assam, India

Saurya Das Theoretical Physics Group, Department of Physics and Astronomy and Quantum Alberta, University of Lethbridge, Lethbridge, AB, Canada

Upamanyu Das Rajiv Gandhi University, Doimukh, A.P, India

K. Deka Centre of Plasma Physics, Institute for Plasma Research, Sonapur, Kamrup(M), Assam, India

Kabita Deka Department of Physics, Tezpur University, Napaam, Assam, India

Paramita Deka Department of Physics, Gauhati University, Guwahati, Assam, India

Maibam Ricky Devi Department of Physics, Gauhati University, Guwahati, Assam, India

Samrat Dey Department of Physics, Assam Don Bosco University, Guwahati, Assam, India

Sangeeta Dey Cotton University, Guwahati, India

Zannatun Firdowzy Dey Department of Physics, Assam Don Bosco University, Sonapur, India

B. K. Duara Department of Radiology, Gauhati Medical College & Hospital, Guwahati, Assam, India

N. G. Durge Department of Physics, S. S. and L. S. Patkar-Varde College, Mumbai, Maharashtra, India

Debajyoti Dutta Department of Physics, Assam Don Bosco University, Sonapur, India

Suvangshu Dutta Dept. of Chemistry, D.R. College, Golaghat, Assam, India

Nayana Gautam Department of Physics, Tezpur University, Tezpur, India

J. P. Gewali Department of Physics, Lovely Professional University, Jalandhar, Punjab, India;
Department of Physics, Lovely Professional University, Phagwara, Punjab, India

Jeeban P. Gewali Department of Physics, School of Chemical Engineering and Physical Sciences, Lovely Professional University, Phagwara, Punjab, India

Sanjay Godara Department of Physics, MLV Government College, Bhilwara, Rajasthan, India

Bandana Gogoi Rajiv Gandhi University, Doimukh, A.P, India

Rupjyoti Gogoi Tezpur University, Napaam, Assam, India

Anirban Guha Department of Physics, Tripura University, Suryamaninagar, Tripura, India

Ansh Gupta Department of Physics, School of Chemical Engineering and Physical Sciences, Lovely Professional University, Phagwara, Punjab, India

Nilavjyoti Hazarika Physics Department, Gauhati University, Guwahati, Assam, India

Francis Iawphniaw Department of Physics, St.Anthony's College, Shillong, India; Department of Physics, Assam Don Bosco University, Guwahati, Assam, India

Yatendra S. Jain Department of Physics, North-Eastern Hill University, Shillong, India

B. Jaishy Department of Physics, Lovely Professional University, Phagwara, Punjab, India

B. M. Jyrwa Department of Physics, North Eastern Hill University, Umshing, Shillong, India

Jyotirmoy Kalita Department of Physics, Tripura University, Suryamaninagar, Tripura, India

Sachin Kaothekar Department of Physics, Mahakal Institute of Technology & Management, Ujjain, M.P, India

S. S. Kausik Centre of Plasma Physics, Institute for Plasma Research, Sonapur, Kamrup(M), Assam, India

Rukaiya Khatoon Tezpur University, Napaam, Assam, India

Anupam Kumar Department of Biotechnology, School of Bioengineering and Biosciences, Lovely Professional University, Phagwara, Punjab, India

Deepak Kumar Department of Chemistry, School of Chemical Engineering and Physical Sciences, Lovely Professional University, Phagwara, Punjab, India

Jugal Lahkar Department of Physics, Pragjyotish College, Guwahati, India

Soma Mandal Department of Physics, Government Girls' General Degree College, Kolkata, India

P. Arockia Michael Mercy PG & Research Department of Physics, Arul Anandar College, Karumathur, Madurai, India

A. K. Mishra Department of Physics, Vidyasagar University, Paschim Medinipur, Midnapore, West Bengal, India

Manoj Kumar Mishra Space Applications Centre, Indian Space Research Organization, Ahmedabad, India

Ranjeev Misra Inter-University Center for Astronomy and Astrophysics, Pune, India;
Inter-University Center for Astronomy and Astrophysics, Ganeshkhind Pune, India

R. Moulick Department of Physics, Rangapara College, Rangapara, Sonitpur, Assam, India

Biswajit Nath Silchar Medical College Hospital, Silchar, Assam, India

Pabitra Nath Applied Photonics & Nano-Photonics Laboratory, Department of Physics, Tezpur University, Tezpur, Assam, India

Ashamoni Neog Applied Optics and Photonics Lab, Department Of Physics, Tezpur University, Tezpur, Assam, India

Mahadev Patgiri Cotton University, Guwahati, India

R. Paul Centre of Plasma Physics, Institute for Plasma Research, Sonapur, Kamrup(M), Assam, India

Raj Prince Center for Theoretical Physics, Polish Academy of Sciences, Warsaw, Poland

A. Pyngrope Department of Physics, North-Eastern Hill University, Shillong, India

S. Jessie Jancy Rani PG and Research Department of Physics, The M.D.T. Hindu College, Tirunelveli, Tamil Nadu, India;
Manonmaniam Sundaranar University, Abishekapatti, Tirunelveli-12, Tamil Nadu, India

Jodie T. Ryngnga Department of Physics, North Eastern Hill University, Umshing, Shillong, India

S. Saha Department of Physics, Vidyasagar University, Paschim Medinipur, Midnapore, West Bengal, India

B. K. Saikia Centre of Plasma Physics, Institute for Plasma Research, Sonapur, Kamrup(M), Assam, India

Shantu Saikia Department of Physics, St.Anthony's College, Shillong, India

Jocelyn Sangma Centre of Plasma Physics-Institute for Plasma Research, Tepesia Sonapur, Assam, Kamrup (M), India

Lavina Sarma Tezpur University, Tezpur, Assam, India

A. Saxena Department of Physics, North-Eastern Hill University, Shillong, India

P. Selvarajan Department of Physics, Aditanar College of Arts and Science, Tiruchendur, Tamil Nadu, India;
Manonmaniam Sundaranar University, Abishekapatti, Tirunelveli-12, Tamil Nadu, India

Zahir Shah Inter-University Center for Astronomy and Astrophysics, Pune, India; Inter-University Center for Astronomy and Astrophysics, Ganeshkhind Pune, India

G. Sharma Centre of Plasma Physics, Institute for Plasma Research, Sonapur, Kamrup(M), Assam, India

Kuldeep Sharma State Cancer Institute, Gauhati Medical College, Guwahati, Assam, India

S. K. Sharma Dusty Plasma Laboratory, Physical Sciences Division, Institute of Advanced Study in Science and Technology (IASST), Guwahati, Assam, India

P. Sheron Department of Physics, Lovely Professional University, Phagwara, Punjab, India

M. Singh Department of Physics, Lovely Professional University, Jalandhar, Punjab, India

Madan Singh Department of Physics, M.N.S. Government College Bhiwani, Haryana, India

A. S. I. Joy Sinthiya PG and Research Department of Physics, The M.D.T. Hindu College, Tirunelveli, Tamil Nadu, India

R. Sree Devi Department of Physics, Aditanar College of Arts and Science, Tiruchendur, Tamil Nadu, India;
Manonmaniam Sundaranar University, Abishekapatti, Tirunelveli-12, Tamil Nadu, India

Dhanjit Talukdar Department of Physics, Pragjyotish College, Guwahati, India

A. Thakur Department of Physics, Lovely Professional University, Phagwara, Punjab, India

Ankush Thakur Department of Physics, School of Chemical Engineering and Physical Sciences, Lovely Professional University, Phagwara, Punjab, 144411 India

G. Jeeva Rani Thangam PG and Research Department of Physics, Pope's College, Thoothukudi, Tamil Nadu, India

K. S. Joseph Wilson PG & Research Department of Physics, Arul Anandar College, Karumathur, Madurai, India

Chapter 1
A Comparative Study of Experimental and Theoretical Z (*Compressibility Factor*) of Argon as a Typical Representative of Simple Fluids

Yatendra S. Jain and Simanta Chutia

Abstract Based on a theoretical analysis of compressibility factor, $Z = \frac{Z_c \rho_c}{\rho} \frac{P_r}{T_r}$ obtained from the basic definition of the compressibility factor of a fluid (Jain in J. Mol. Liq. 249:688–701, 2018; Jain in selected progress in modern physics, springer proceedings in physics 265, chapter 20, 2021) and its analysis for understanding the P_r dependence of Z at constant T_r, we calculate the Z values for Ar fluid (a typical representative of simple fluids) and compare with the corresponding experimental values. We note that $Z(P_r)$ of a low-density gas phase decreases/(increases) with P_r, if $T_r \leq 2.73$ (>2.73), corresponding to Boyle temperature $T_B = 2.73T_c$, while the same of the liquid or high-density gas phase (representing the incompressible state of the system) at a fixed T_r increases linearly with P_r. This not only demonstrates that the physical state of a low-density gas with particles moving, to a good approximation, like a free particle differs significantly from the state of a particle in liquid and high-density gas phase but also provides reasons for which a theory based on single-particle basis does not explain several experimental properties of the fluid including liquid to gas transition (L2GT) or gas to liquid transition (G2LT) and related properties and the microscopic basis of several empirical rules and principles of corresponding states.

Y. S. Jain
Department of Physics, North-Eastern Hill University, Shillong 793022, India

S. Chutia (✉)
Department of Physics, St. Anthony's College, Shillong 793001, India
e-mail: simanta@anthonys.ac.in

S. Sengupta et al. (eds.), *Selected Progresses in Modern Physics*, Springer Proceedings in Physics 265, https://doi.org/10.1007/978-981-16-5141-0_1

1.1 Introduction

Fluids are interesting many body physical systems, which have a long and rich history of theoretical and experimental investigations. Most of the theories of fluid are based on single-particle basis (SPB), which treats single particle as the basic unit for the theoretical framework. Despite its long history, theories based on SPB failed to explain several observations of great importance such as Guldberg rule [1], Trouton rule [2], principles of corresponding states [3], etc. A recently published microscopic theory of simple fluids [4] deviating from the SPB considered a pair of particle as the basic unit of the system (pair of particle basis (PPB)) and could explain many of the unexplained observations. This theory also provides a better understanding of the compressibility factor, Z, of a simple fluid and relates it to inter-particle potential $\left(V\left(r_{ij}\right)\right)$. In this work, we propose to use the compressibility relation available in ref. [4, 5] to unravel some of the aspects of gas to liquid phase transition. In the next section, we shall briefly discuss the theoretical basis of our works on the compressibility factor. We shall discuss our finding related to Argon, which is an example of simple fluid in Sect. 1.3 and conclude our study in Sect. 1.4.

1.2 Compressibility Factor, Z

Widely use the equation of state (EOS) of a real gas is the virial series expansion

$$\frac{PV}{RT} = Z = 1 + \frac{B_2}{V} + \frac{B_3}{V^2} + \ldots \tag{1.1}$$

where $B_2, B_3, \ldots$ are the second, third, … coefficients, respectively. To a good approximation for moderate P and T, a truncated relation

$$\frac{PV}{RT} = Z = 1 + \frac{B_2}{V} \tag{1.2}$$

is expected to give Z with reasonable accuracy. Higher order terms in the expansion provide higher accuracy in the value of Z. In this equation, Z is the term that depends on the interaction of the constituents, $V\left(r_{ij}\right)$, for which a real gas differs from an ideal gas. Evidently, Z is related directly or indirectly with the different principle of corresponding state (PCS), and a successful theory is expected to reveal its value.

The PPB theory [4] reveals that every fluid is a homogeneous mixture of two fluids: one composed of non-interacting quasi-particles and the other is composed of interacting quasi-particles. While the non-interacting quasi-particles are related to the centre of mass motion (K) of the PPB, the interacting quasi-particles are related to relative motion (q) of PPB. This theory also reveals that the behaviour of a fluid is controlled by equation of state (EOS)

$$P_{in}(q) + P_{in}(K) = P_{ex} + P_{coh} \tag{1.3}$$

where $P_{in}(q)$ and $P_{in}(K)$ are two components of internal pressure whereas P_{ex} and P_{coh} are, respectively, external and cohesive pressure. While P_{coh} is attractive in nature, $P_{in}(q)$ is in repulsive in nature. Due to non-interacting nature of K motion $P_{in}(K)$ is equivalent to P_{ex} of ideal gas (IG). One can re-write the equation of state as,

$$P_{ex} = P_{ex}^{IG} + P^R - P^A \tag{1.4}$$

The PPB theory also finds that

$$B_2 = BV_c\left(1 - \frac{sT_c}{T}\right) \tag{1.5}$$

with V_c and T_c are critical volume and temperature, respectively, and $B = 0.407$ and $s = 2.73$ are two parameters.

Use of B_2 in Eq. (1.2) gives

$$\frac{P_{ex}V}{RT} = Z = 1 + \frac{BV_c}{V}\left[1 - \frac{sT_c}{T}\right] = 1 + B\left[1 - \frac{sT_c}{T}\right]\frac{\rho}{\rho_c} \tag{1.6}$$

where ρ is the number density.

This relation gives us

$$P_{ex} = k_BT\rho + B\left[1 - \frac{sT_c}{T}\right]\frac{\rho}{\rho_c}k_BT\rho \tag{1.7}$$

Comparing it with Eq. (1.4), we get,

$$P_{ex}^{IG} = k_BT\rho,\ P^R = B\frac{\rho}{\rho_c}k_BT\rho, \text{and} P^A = B\frac{sT_c}{T}\frac{\rho}{\rho_c}k_BT\rho = \frac{Bs\rho}{\rho_c}k_BT_c\rho \tag{1.8}$$

The first relation of Eq. (1.8) represents ideal gas equation. The quantities P^R and P^A are expected to depend on repulsive and attractive components of potential $V^R(r_{ij})$ and $V^A(r_{ij})$, respectively, through B and s. We may use the effective kinetic energy expression of a real gas $E_N^{RG} = \frac{3}{2}P_{ex}V$ in Eq. (1.7) to find

$$E_N^{RG} = \frac{3}{2}k_BTN + (V^R - V^A) = N\left[\frac{3}{2}k_BT + (v^R - v^A)\right] \tag{1.9}$$

with

$$V^R = \frac{3}{2} V B \frac{\rho}{\rho_c} k_B T \rho = \left(\frac{3}{2} RT\right) \frac{B}{\rho_c} \rho$$
$$and \quad V^A = \frac{3}{2} V \frac{Bs\rho}{\rho_c} k_B T_c \rho = \left(\frac{3}{2} RT_c\right) \frac{Bs}{\rho_c} \rho \tag{1.10}$$

Equation (1.9) also gives

$$Z = 1 + \frac{2}{3} \frac{v^R - v^A}{k_B T} \tag{1.11}$$

This equation relates Z with $V(r_{ij})$ through v^R and v^A. It is well understood from Eq. (1.10) that repulsive component of the potential depends on $k_B T$ and ρ whereas attractive components of the potential depend on $k_B T_c$ and ρ. Evidently,

$$v^R \propto k_B T \rho \quad \text{or} \quad v^R = (3C/2) k_B T \rho$$
$$and \quad v^A \propto k_B T_c \rho \quad \text{or} \quad v^A = (3Ch/2) k_B T_c \rho \tag{1.12}$$

where $3C/2$ and $3Ch/2$ are proportionality constants having dimension of density inverse and to be determined by experimental results. Using Eq. (1.12) in (1.11) we find,

$$Z = 1 + C\rho_c \left(1 - \frac{hT_c}{T}\right) \frac{\rho}{\rho_c} \tag{1.13}$$

The PPB theory [4] further reveals that compressibility factor,

$$Z = \frac{V^{RG}}{V^{IG}} = \frac{Z_c \rho_c}{\rho} \frac{P_r}{T_r} \tag{1.14}$$

with V^{RG} and V^{IG} are the volume of real gas and ideal gas obtained under identical physical conditions, $P_r = P/P_c$ and $T_r = \frac{T}{T_c}$. Equation (1.14) can be used to find experimental Z of any real gas at a given pressure and temperature by using the experimental values of its ρ, ρ_c, Z_c, P_c and T_c.

1.3 Result and Discussion

One can use Eqs. (1.6), (1.11) or (1.13) to estimate the theoretical values Z at a given temperature and pressure. Pressure dependence of Z appears through density of the fluid, and an accurate pressure dependence relation for density would give direct pressure dependence of Z. While Z values obtained using Eq. (1.6) agree qualitatively with experimental values (Eq. (1.14)) at low-density gas phase, Z values

obtained using Eq. (1.11) are expected to agree more closely with the experimental values provided one includes all the contribution to the repulsive as well as attractive components of the potential. Interaction among the induced atomic dipoles is the major contributor to the attractive potential whereas overlapping of electronic charge distributions of atoms contributes to the repulsive potential. These contributions are usually expressed by Lennard–Jones potential. The quadrupole interaction, permanent dipole interaction or other kind of interactions may also contribute to the potential of the system. More accurate estimation of the potential is required to get accurate values of Z and any unknown nature of the interactions makes Eq. (1.11) less useful. In our present study, we prefer to use Eq. (1.13) to estimate the values of Z because the parameters C and h can be easily estimated from the experimental values. The foundation of Eq. (1.13) rests on Eq. (1.12), which is corroborated by experiments [3, 6]. Equation (1.12) also emphasizes that for better understanding of the system and accurate value of Z, one should separate different kind of inter particle interaction. Separation of repulsive and attractive potentials is also the need of Eq. (1.11).

In this study at different T_r values of C and h are chosen in such a way that $Z_{theo}(P_r)$ values agree with $Z_{exp}(P_r)$. We have used Eq. (1.14) to calculate $Z_{exp}(P_r)$ of Argon at different T_r with experimental values of ρ [7] and other entities, viz, $Z_c(= 0.292)$, $T_c(= 150.7\text{K})$, $P_C(= 48\text{atm})$, and $\rho_c\left(= 0.5308 \frac{g}{cc}\right)$, as reported in ref. [3]. We have depicted our findings in Fig. 1.1. We have found that $Z_{theo}(P_r)$ (see black solid lines in Fig. 1.1) agree with $Z_{exp}(P_r)$ (black dashed lines with Δ marks) only for low-density gas phase. We have also found that $Z_{exp}(P_r)$ values for high-density gas phase and nearly incompressible liquid phase have linear dependence on P_r. The linear dependence of $Z_{exp}(P_r)$ for both high-density gas phase and incompressible liquid phase can be expressed as

$$Z_{theo}(P_r) = m P_r + a \tag{1.15}$$

where m and a are two constants. This similarity suggests that more likely high-density gas phase becomes nearly incompressible like a liquid phase and impact of $V(r_{ij})$ in these states get saturated at the lowest P_r at which Z becomes linear in P_r. Values of C and h that make $Z_{theo}(P_r)$ agree with $Z_{exp}(P_r)$ are tabulated in Table 1.1 along with m and a of each line, which fits with linear dependence of $Z_{exp}(P_r)$ for different T_r. Linear dependence of $Z_{theo}(P_r)$ as represented by Eq. (1.15) is also depicted in Fig. 1.1 for each T_r (black dotted curves).

The parameters C in Eq. (1.13) and m and a in Eq. (1.15) depend upon temperature. Temperature dependence of these parameters is shown in Fig. 1.2. We observe that value of C decreases initially with temperature and then remains almost constant beyond the critical temperature. As density of the fluid/gas decreases with increasing temperature analysing Eq. (1.12), we find that temperature dependence of the repulsive as well as attractive components of the potential decrease beyond a certain temperature and at $T = T_B$ it becomes ideal gas.

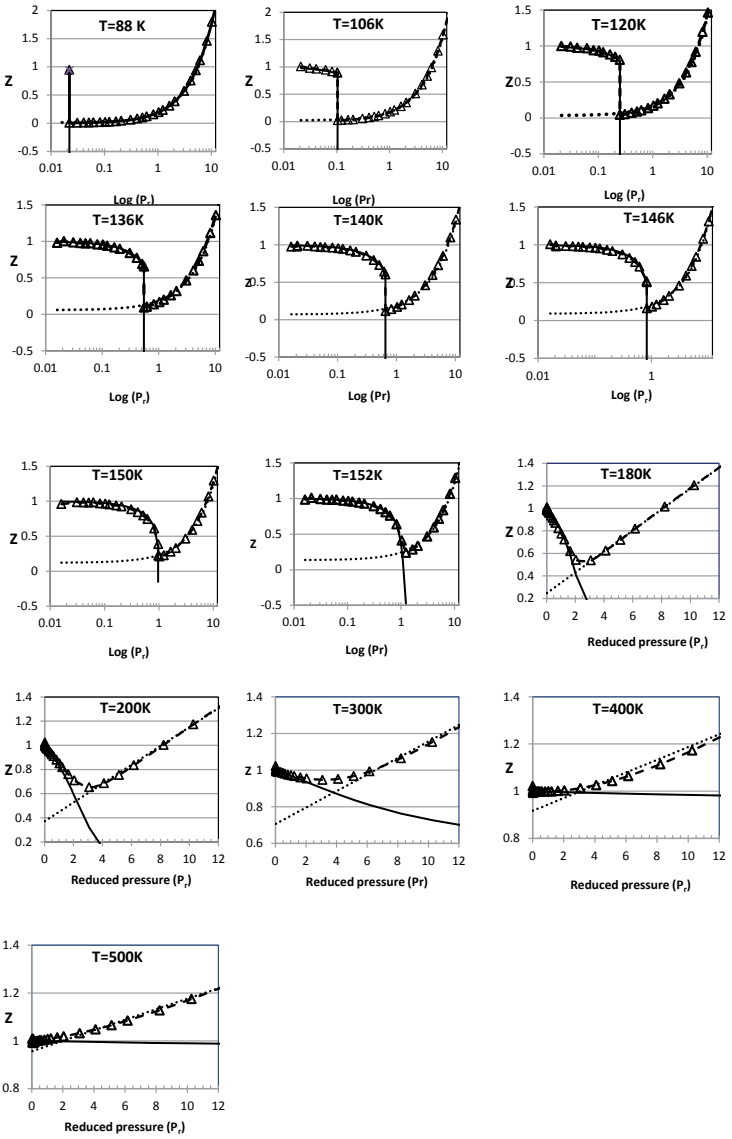

Fig. 1.1 $Z_{exp}(P_r)$ (dashed curves with Δ) and $Z_{Th}(P_r)$ (black solid and dotted curves) for Ar fluid for 88, 106, 120, 136, 140, 146, 150, 152, 180, 200, 300, 400, and 500 K. While the black solid curves obtained by using Eq. (1.13) represent low-density gas phase, the black dotted curves obtained by using Eq. (1.15) represent liquid phase or high-density gas phase. While for the clarity in depiction, we have used logarithmic scale for reduced pressure (log (P_r)) for coexisting gas and liquid phase at $T_r < 1$ as well as at $T_r \approx 1 (T = 152\text{K})$, linear scale for P_r is used for $T_r > 1$

Table 1.1 Values of C, m and a at different temperatures

T	T_r	C	m	a	T	T_r	C	m	A
88	0.58	3	0.174	0.010	152	1.01	0.9721	0.108	0.136
106	0.70	1.7198	0.150	0.021	180	1.19	0.9412	0.093	0.246
120	0.80	1.4001	0.137	0.033	200	1.33	0.8958	0.078	0.371
136	0.90	1.1856	0.125	0.058	300	1.99	0.8293	0.050	0.706
140	0.93	1.1286	0.121	0.069	400	2.65	0.7719	0.027	0.917
146	0.97	1.0716	0.117	0.090	500	3.32	0.6941	0.022	0.956
150	1.00	0.9749	0.110	0.123					

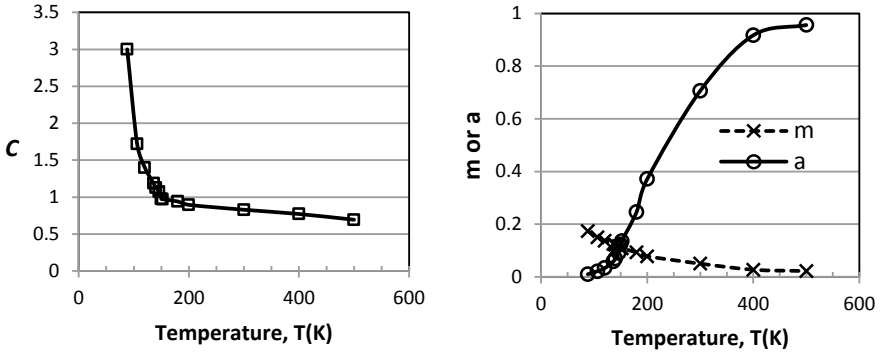

Fig. 1.2 Temperature dependence of *C* (used in Eq. (1.13)) and m and a (used in (15))

1.4 Conclusion

Compressibility factor, Z, is one of the most important parameters of a gas or fluid and a well-developed theory should account its microscopic origin. The PPB theory not only gives an account of the microscopic origin of Z but also provides a different way to estimate the values Z at different temperature and pressure. In this context, we may particularly mention that the basic equation of state represented by Eq. (1.4) provides a direct expression for Z based on the first principle. One can find value of Z by estimating repulsive and attractive potential experienced by different particles of the system. We have observed that the estimated value of Z based on the PPB theory matches closely with experimental value particularly at low-density gas or liquid phase. Though our current work is on Argon, same approach is valid for diverge many body systems with a suitable value of the different parameters. This work establishes that the PPB theory has the ability to explain the compressibility factor of different gases or fluids with desired clarity and simplicity.

References

1. C.M. Guldberg, Z. Phys. Chem. **5**, 374–380 (1890)
2. F. Trouton, On molecular latent heat. Phil. Mag. **18**, 54–57 (1984)
3. E.A. Guggenheim, The principle of corresponding states. J. Chem. Phys. **13**, 253–261 (1945)
4. Y.S. Jain, Microscopic theory of simple fluids. J. Mol. Liq. **249**, 688–701 (2018)
5. Y.S. Jain, Selected progress in modern physics, in *Springer Proceedings in Physics vol.* 265, *ed. by* S. Sengupta et al. (2021), Chapter 20
6. J.L. Finney, L.V. Woodcock, Renaissance of Bernal's random close packing and hypercritical line in the theory of liquids. J. Phys. Condens. Matter. **26**, 463102 (2014). https://doi.org/10.1088/0953-8984/26/46/463102
7. R.B. Stewart, R.T. Jacobsen, Thermodynamic properties of argon from the triple point to 1200 K with pressure to 1000 MPa. J. Phys. Chem. Ref. Data **18**, 639–798 (1989)

Chapter 2
A Theoretical Review to Analyze the Response Between the Radiographic Film and the Living Tissue in Terms of Energy Absorption

Dipankar Bhagabati, Rangaraj Bhattacharjee, Biswajit Nath, Kalyanjit Dutta Baruah, and B. K. Duara

Abstract The concept of this theoretical work has been boosted by the fact that different medium responds to ionizing radiation in different ways. In diagnostic radiology, patients are being exposed to X-rays. The emitting X-ray photons, from the patient's body, contains useful information regarding their internal organs. These X-ray photons are converted to light photons and decoded as optical density in the X-ray film. Similarly in radiotherapy, the concept of relative biological effectiveness (RBE) is the ratio of doses required by different types of radiation to produce the same level of effect in the living tissue as a function of linear energy transfer (LET). The optical density provides the information of how many light photons have been stopped by the X-ray film. This helps to differentiate between the soft tissue, air and bones based on the level of energy absorption in the patient's body. The linear energy transfer provides the information of the pattern generated by the deposition of radiant energy in biologic medium, which differentiates between the various types of radiation involved.

2.1 Introduction

Human beings are always curious to see the unseen. In the process of satisfying this fit of curiosity towards vision, many branches of physics were born and also led to many inventions such as telescope to see the distant objects, microscope to see the tiniest ones and accelerators, colliders to see the inside of an atom [1]. The act of seeing is basically viewing things as they are [1]. But the act of seeing the unseen can be categorized mainly in two forms. First, with the help of artificial aids, e.g.

D. Bhagabati · R. Bhattacharjee · K. D. Baruah
State Cancer Institute, Gauhati Medical College, Guwahati, Assam 781032, India

B. Nath
Department of Radiology, Silchar Medical College Hospital, Silchar, Assam 788014, India

B. K. Duara (✉)
Department of Radiology, Gauhati Medical College & Hospital, Guwahati, Assam 781032, India

S. Sengupta et al. (eds.), *Selected Progresses in Modern Physics*, Springer Proceedings in Physics 265, https://doi.org/10.1007/978-981-16-5141-0_2

telescope, microscope, magnifying glass, spectacles, etc., and second, by visualizing the effects of certain things like radiation [1]. The branch of radiology deals with the viewing of the internal body parts whereas radiotherapy is the branch of medicine especially dedicated to the treatment of cancer in which Relative Biological Effectiveness (RBE) and Linear Energy Transfer (LET) describe the effectiveness of the treatment. Many research work has been done on RBE and LET such as the identification of the ultimate RBE's relative position in terms of LET [2], the effect of high LET radiations on the reproductive system and foetal development [3], RBE variations in patients in case of cranio-spinal irradiation with proton beams [4], many physical and biological parameters show complex dependencies on RBE revealed from experimental investigations [5], the RBE–LET relationships are correlated with local energy deposition in small regions of the cells [6], the LET–RBE relationship of radiation-induced chromosome aberration and cell death [7], the dependence of the RBE for cell death on LET as per microdosimetric-kinetic theory [8] are the few to mention. Also, lots of research work has been done on the performance and characteristics of a radiographic film such as—the effect of film-screen combination on the speed of the film [9], the impact of image intensifying screens on the sharpness and sensitivity of X-ray films [10], the optical density versus dose sensitometric curves depicting the outcome of the various films sensitivity [11], the potential improvement in image quality by controlling the crossover without sacrificing process sensitivity [12], the film reciprocity effect on the patient exposure [13], the effect of numerous technical variables on image quality in screen-film radiography [14], to mention a few. This theoretical study in its own way is mainly dedicated towards the act of visualization in radiotherapy in terms of energy absorption. It is inspired mainly by two concepts, the "effects of interaction of various types of radiation with matter" and the "theory of everything", which assumes that, in this universe all things are connected to one another. This study also tries to correlate the effect of radiation in living as well as non-living objects, considering the various patterns of the effects of energy deposition based on well established phenomena.

2.2 Assumptions

1. Conventional film radiography is considered. Energy absorption in the X-ray film is given preference instead of human body. Exactly same type of film is considered and with constant exposure.
2. Dependence of RBE on radiation quality (LET) is considered. Other parameters like radiation dose, dose rate, biological system and endpoint on which RBE depends are kept constant. Here, living tissue is preferred over non-living things.

2.3 Methodology

The assumptions are made to show the analogous nature of the X-ray film and the living tissue in terms of energy deposition. X-ray film works on the concept of differential attenuation, which means that different tissues attenuate (absorb or scatter) X-ray differently and the radiographic film accentuates that difference and produces a visual pattern [15–18]. Conventional X-ray films contain silver bromide (AgBr) crystals as basic radiation sensor. These crystals are layered over a transparent plastic base [15–18]. The film is kept inside intensifying screens, which converts X-ray into visible light [15–18]. Thus, a film is not directly exposed by X-rays rather by visible light [15–18]. When the exposed film is developed it produces a grayscale pattern of the tissues [15–18]. Those tissues that absorb a high amount of X-rays appear as whitish while the less absorbing tissues take blackish colour [15–18]. A parameter called optical density (OD) controls the blackening of the film.

$$\mathrm{OD} = \log \frac{I_O}{I_t}$$

where, I_t is the intensity of light transmitted through the film, I_O is the incident light and log is the common logarithm (base 10) [15–18] (Figs. 2.1).

The speed of a film is the exposure required by a film to obtain a certain optical density. A film requiring less exposure to get a certain OD is called a fast film and

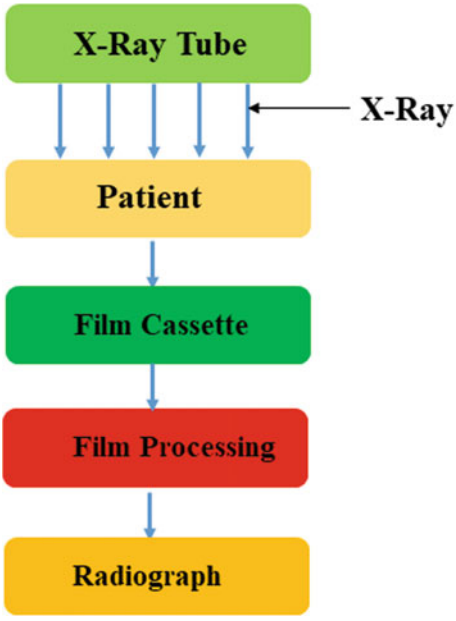

Fig. 2.1 A pictorial representation of X-ray imaging

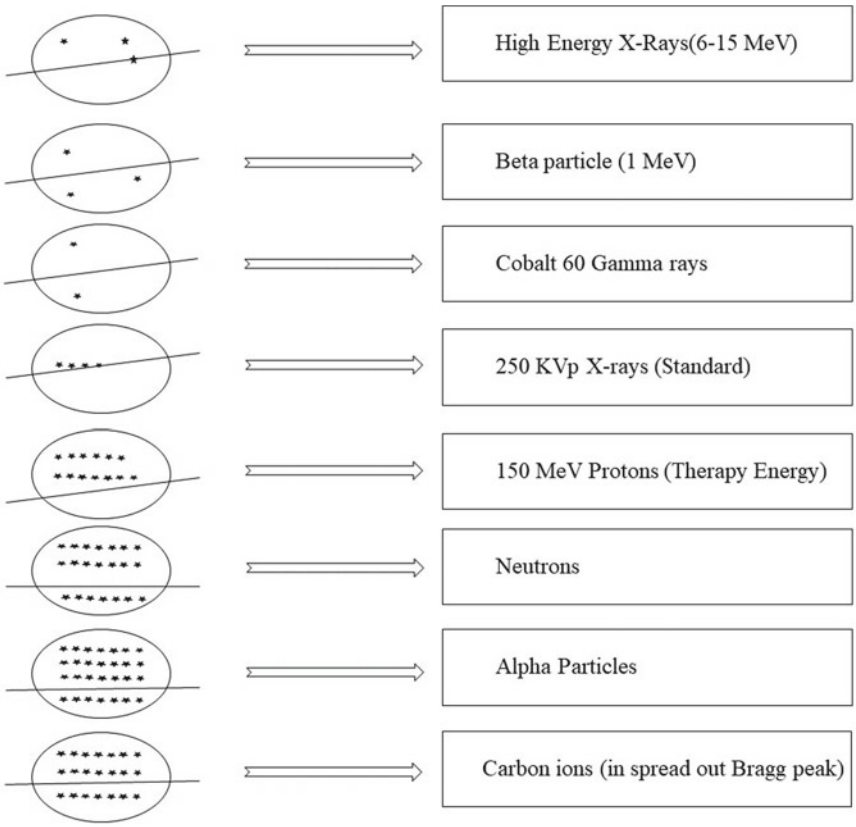

Fig. 2.2 A pictorial representation of various effects of different types of LET on living tissue, the circles represents the same hypothetical tissues and the stars depicts the effects of ionization caused by various types of radiation (Low and High LET radiations) on them.

the film requiring higher exposure for same OD is called a slow film. A film can enhance or destroy inherent information contained in an X-ray beam [15–18].

Relative biological effectiveness (RBE) is the ratio of the amount of radiation exposure of 250 kV X-ray required to cause a certain level of biological effect to the radiation dose required from another radiation to cause the same level of biological effect [19, 20] and gives the variation of RBE with the type of radiation [21]. The type of radiation can be classified in terms of linear energy transfer (LET) [20]. Linear energy transfer (LET) is defined as the amount of radiation energy transferred to the target tissue per unit path length travelled by the radiation beam [20]. The radiation that transfers more energy per unit length is termed as high LET radiation and the radiation that transfers less energy per unit path length is called low LET radiation [20]. Relative biological effectiveness (RBE), a parameter to show the radiation energy absorbed by tissue, depends on LET [20, 22, 23]. Thus, by looking at the radiation effect, the LET (type of radiation) can be predicted as shown in Fig. 2.2.

Also, the definition of RBE explains that it is a ratio of two LET's to get a certain radiation effect.

LET is directly proportional to the biological damage whereas optical density is directly proportional to the film blackening. Hence a resemblance can be drawn between the film and living tissue. The extent of black and white pattern (contrast) varies from film to film, so as; the variation of radiation damage varies from LET to LET. As, speed of a film is the comparison of two equal exposures to obtain a specific density, similarly, RBE is the ratio of two different LET's to obtain a certain level of biological effect. Thus, the film speed in radiology can be compared with RBE in radiotherapy. Though the phenomena are different but are having the same pattern. In radiology, the differential energy absorption by the body produces unique image for different organs, which helps to identify them. In radiotherapy, the identification of different organs can be done by observing organ sensitivity, that is, the extent of damage caused to the organs by energy absorption [24, 25].

2.4 Result and Discussion

The way optical density depends directly on film is similar to the way biological effect depends on LET. The variation of optical density in film can be considered as analogous to the radiation effect on living tissue. RBE is the ratio of two LETs to obtain a certain effect and closely resembles with speed of a film, where a comparison of two exposures was done to get an optical density of 1.

By looking at the optical density, internal structure of the human body through which the beam is passing can be predicted. Similarly, by looking at the effects of LET, which radiation has caused it, can be easily predicted. This satisfies the quest for vision in radiotherapy.

2.5 Conclusion

In radiology, X-ray comes out of the patient's body with useful information to produce a latent image on the X-ray film. This image is not visible until processed. Similarly, there are many latent concepts that can be brought to light by proper research. People mostly see what they have learned to see. In this study, an opportunity is taken to visualize an already existing phenomenon in a new way.

Acknowledgements We express our most sincere gratitude to the Director and Professor of Radiation Oncology, State Cancer Institute, Gauhati Medical College, Dr. B. C. Goswami, Superintendent, Dr. Devajit Choudhury, Professor of Radiation Oncology and HOD, Dr. N. K. Kalita, Associate Professor of Radiation Oncology, Dr. (Mrs.) Smriti Goswami for their continuous guidance and encouragement. We are thankful to Mrs. Ananya Bhattacharjee for her guidance and encouragement. We are also thankful to Mr. Mrigen Rabha, Intern Medical Physicist for his valuable cooperation.

References

1. R.W. Robert, L. Raphael, *Accelerators: Machines of Nuclear Physics* (Vakils, Feffer and Simons Pvt-Ltd, Bombay, 1967), pp. 17–34
2. B. Jones, M.A. Hill, The physical separation between the LET associated with the ultimate relative biological effect (RBE) and the maximum LET in a proton or ion beam. Biomed. Phys. Eng. Express **6**(5), 055001 (2020)
3. B. Wang, H. Yasuda, Relative biological effectiveness of high LET particles on the reproductive system and fetal development. Life **10**, 298 (2020)
4. K.S. Ytre-Hauge, L.F. Fjæra, E. Rørvik et al., Inter-patient variations in relative biological effectiveness for cranio-spinal irradiation with protons. Sci. Rep. **10**, 6212 (2020)
5. P. Colautti, G. Magrin, H. Palmans, M.A. Cortés-Giraldo, V. Conte, Characterizing radiation effectiveness in ion-beam therapy part II: microdosimetric detectors. Front. Phys. **8**, 550458 (2020)
6. G.W. Barendsen, The relationships between RBE and LET for different types of lethal damage in mammalian cells: biophysical and molecular mechanisms. J. Radiat. Res. **139**(3), 257–270 (1994)
7. T. Takatsuji, I. Yoshikawa, M.S. Sasaki, Generalized concept of the LET–RBE relationship of radiation-induced chromosome aberration and cell death. J. Radiat. Res. **40**(1), 59–69 (1999). https://doi.org/10.1269/jrr.40.59
8. R.B. Hawkins, A Microdosimetric-kinetic theory of the dependence of the RBE for cell death on LET. Med. Phys. **25**(7 Pt 1), 1157–1170 (1998)
9. E.R. Miller, Significance of speed and resolution characteristics of certain cassette-screen-film combinations. RSNA, Radiology **80**, 1 (1963)
10. W.F. Berg, A. Spühler, Sensitivity and sharpness of X-ray film exposed with intensifying screens. Jpn. J. Appl. Phys. **3**, 196 (1964)
11. O.A. Ojo, P.A. Oluwafisoye, C.O. Chime: Analysis of sensitometry in radiographic films using optical density measurement. EJMED Eur. J. Med. Health Sci. **2**, 4 (2020)
12. E.A. Butler, Evaluation of the image quality of an experimental lenticular film system for radiographic applications. Thesis, Rochester Institute of Technology, 1982
13. H. Fujita, S. Uchida, Reciprocity-Law Failure in Medical Screen-Film Systems and Its Effects on Patient Exposure and Image Quality, in *Springer Series in Optical Sciences*, vol. 31 (Springer, Berlin, Heidelberg, 1982)
14. A.G. Haus, Measures of screen-film performance. Radiographics **16**, 1165–1181 (1996)
15. D.R. Dance, S. Christofides, A.D.A. Maidment, I.D. McLean, K.H. Ng, *Diagnostic Radiology Physics: A Handbook for Teachers and Students* (International Atomic Energy Agency, Vienna, 2014), pp. 161–167
16. J.T. Bushberg, J.A. Seibert Jr., E.M. Meidholdt, J.M. Boone, *The Essential Physics of Medical Imaging*, 2nd edn. (Lippincott Williams and Wilkins, Philadelphia USA, 2002), pp. 157–163
17. T.S. Curry III, J.E. Dowdey Jr., R.C. Murry, *Christensen's Physics of Diagnostic Radiology*, 4th edn. (Williams & Wilkin, United States of America 1990), pp. 137–164
18. K. Thayalan, *Medical X-ray Film Processing*, 1st edn. (Jaypee Brothers Medical Publishers (P) LTD, New Delhi 2005), pp. 25–45
19. E.J. Hall, A.J. Giaccia, *Radiobiology for the Radiologist*, 7th edn. (Wolters Kluwer Lippincott Williams & Wilkins, Philadelphia USA, 2012), pp. 104–113
20. E.B. Podgorsak, *Radiation Oncology Physics: A Handbook for Teachers and Students* (International Atomic Energy Agency, Vienna, 2005), pp. 500–503
21. K. Ilicic, S.E. Combs, T.E. Schmid, New insights in the relative radiobiological effectiveness of proton irradiation. Radiat. Oncol. **13**, 6 (2018)
22. N. Hunter, C.R. Muirhead, Review of relative biological effectiveness dependence on linear energy transfer for low-LET radiations. J. Radiol. Prot. **29**(1), 5–21 (2009)
23. M. Ben Kacem, M.A. Benadjaoud, M. Dos Santos, F. Soysouvanh, V. Buard, G. Tarlet, B. Le Guen, A. François, O. Guipaud, F. Milliat, V. Paget, Variation of 4 MV X-ray dose rate strongly impacts biological response both in vitro and in vivo. Sci. Rep. **10**(1), 7021 (2020)

24. G.W. Barendsen, RBE for non-stochastic effects. Adv. Space Res. **12**(2–3), 385–392 (1992)
25. H. Paganetti, Significance and implementation of RBE variations in proton beam therapy. Technol. Cancer Res. Treat. **2**(5), 413–426 (2003)

Chapter 3
Biosynthesis, Characterization and Antibacterial Performance of Trimanganese Tetraoxide Nanoparticles Using *Azadirachta Indica* Leaf Extract

S. Jessie Jancy Rani, A. S. I. Joy Sinthiya, and G. Jeeva Rani Thangam

Abstract Nanoscale materials often present properties different from their bulk counterparts as their high surface to volume ratio results in the exponential increase of reactivity at the molecular level. Transition metal oxides are an intriguing class of materials due to their diverse structural choices and interesting physicochemical properties. In this respect, manganese oxides have a great potential because of their ability to adapt various oxidation states and particularly nanostructured hausmannite (Mn_3O_4) has efficacious application in the fields of pharmaceutical industries, catalysis, biosensors, high-density magnetic storage media, varistors etc. The present study reports the preparation of biosynthesized trimanganese tetraoxide nanoparticles by the reduction of potassium permanganate ($KMnO_4$) using Azadirachta Indica leaf extract at room temperature. The biosynthesized nanoparticles were characterized by X-ray diffraction, Fourier transform infrared spectroscopy, scanning electron microscopy, photoluminescence spectroscopy, ultraviolet radiation spectroscopy and vibrating sample magnetometry. Crystal phase identification of the nanoparticles was characterized by XRD analysis, and the formation of crystalline Mn_3O_4 has been confirmed. FTIR spectrum discloses the major functional groups and the chemical information present in the nanostructure. UV-Vis studies were performed to investigate the optical properties of the prepared samples. Morphological studies were carried out using SEM at various magnification levels. The magnetic properties of nanoparticles as a function of magnetic field were investigated using

S. J. J. Rani (✉)
PG and Research Department of Physics, The M.D.T. Hindu College, Tirunelveli, Tamil Nadu 627010, India

Manonmaniam Sundaranar University, Abishekapatti, Tirunelveli-12, Tamil Nadu, India

A. S. I. J. Sinthiya
PG and Research Department of Physics, The M.D.T. Hindu College, Tirunelveli, Tamil Nadu 627010, India

G. J. R. Thangam
PG and Research Department of Physics, Pope's College, Sawyerpuram, Thoothukudi, Tamil Nadu 628251, India

S. Sengupta et al. (eds.), *Selected Progresses in Modern Physics*, Springer Proceedings in Physics 265, https://doi.org/10.1007/978-981-16-5141-0_3

VSM. The Gel-Diffusion technique was used to test antibacterial activity against microorganisms.

3.1 Introduction

Nanotechnology is an escalating field of modern research involving structures, devices and systems in synthesis design, characterization, manufacturing and application by controlling shape and size at the nanometer scale [1]. For the past few years, the study of nanoparticles has gained tremendous interest because of their variation in physico-chemical, electronic and morphological properties. The quantum effects coupled with surface area effects make a beneficial impact on size-dependent properties of nanomaterials, and the physical and chemical properties of nanomaterials depend not only on their composition but also on the size and shape of particles. Nanoparticle synthesis can be performed by various methods such as physical, chemical and biological approaches [2]. Physical and chemical processes are commonly considered the best way to produce uniform particles with long-term stability, but they are costly and release hazardous materials to the atmosphere. Nanoparticle synthesis using the biosynthetic route is regarded as an eco-friendly process because the reducing and stabilizing agents used are either fungi, bacteria, yeast and plants themselves or their active component [3]. In order to successfully fulfil excessive needs and current market demand, plant-mediated biosynthesis is considered to be a suitable technology for the rapid production of metallic nanoparticles, resulting in a reduction in public health employment or hazardous material generation and easier to execute without requiring any special operating condition [4]. The plant-based synthesis of metal/metal oxide nanoparticles includes biologically active compounds such as alkaloids, phenols, flavonoids, ascorbic acid, citric acid, polyphenols and terpenes, which serve as metal salt-reducing agents. The functional properties of synthesized nanomaterials can be enhanced by the inclusion of biomolecules from medicinal plants [5]. Manganese oxide nanoparticles have been studied extensively, leading to the discovery of their utility in a variety of fields, including protein immobilisation [6], sensitive biosensors [7], electrochemical capacitors [8], lithium-ion batteries [9], synthesis of bioactive compounds [10], analysis of neuro-behaviour of rats [11], biometic catalysts [12] and metal adsorption [13]. Manganese oxide exists in many stoichiometric states such as MnO, MnO_2, Mn_3O_4, Mn_2O_3, with each oxide uniquely different in structure [14]. Also known as hausmannite, trimanganese tetraoxide (Mn_3O_4) is a technologically significant material with special physico-chemical properties that have been used in a number of academic research and industrial applications.

The antibacterial and antifungal activities of manganese oxide nanoparticles were documented using a method that used lemon extract and turmeric curcumin extract as a reduction and capping agent [15]. The green synthesis of manganese oxide nanoparticles from *Syzygium aromaticum*, i.e. clove extract (CE), has been reported to be used as a stabilizing and reducing agent, and the resulting nanoparticles have been

applied to p-nitrophenol (PNP) sensing agents [16]. In another analysis, nanoparticles of manganese dioxide were synthesized by the reduction of $KMnO_4$ using *Kalopanax pictus* leaf extract at room temperature and as an application, it was utilized for dye degradation for the first time [17].

A research analyzed *Shewanella* strains for their effectiveness in oxidizing manganese and found that the best oxidizer that could produce oxides at a rate of 20.3 mg/litre/day was *Shewanella lothica* strain PV-4 [18]. To enhance the prospects of eco-friendly approach, the current study is dedicated to the green synthesis of trimanganese tetraoxide nanoparticles using *Azadirachta Indica*, i.e. neem leaves, a member of *meliaceae* family. Neem is a medicinal plant known for its antifungal, antiviral and antibacterial properties. Terpenoids and flavanones are two key phytochemicals found in neem, which act as capping and reducing agents and also help to stabilize nanoparticles [19]. The protocol was analyzed for the effects of altering pH, temperature, initial $KMnO_4$ concentration and amount of neem leaves used for the process. The resulting particles were characterized through X-ray diffraction (XRD) study, UV-Vis spectroscopy, FTIR analysis, PL study, scanning electron microscopy (SEM), vibrating scanning magnetometry (VSM) study, and the antibacterial study was also screened.

3.2 Materials and Methods

Collection of Plant Extract

Azadirachta Indica leaves were collected in the local area, and the leaves were cleaned and washed with distilled water several times to remove dust and other contaminants, then dried at room temperature. The leaves were chopped, ground and the extract was filtered and stored for further use (Figs. 3.1 and 3.2).

Synthesis of Trimanganese Tetraoxide (Mn_3O_4) Nanoparticles

3.16068 g of $KMnO_4$ salt was dissolved in 100 ml of distilled water to make 0.2 M concentration. Then 15 ml of leaf extract was added to the above precursor, kept in the magnetic stirrer. The mixture was stirred for an hour at room temperature. The colour of the reaction mixture changed from purple to dark brown indirectly

Fig. 3.1 *Azadirachta Indica* leaves

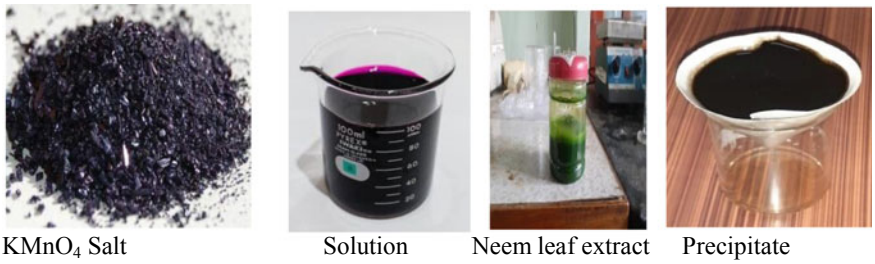

Fig. 3.2 Formation of Mn_3O_4 nanoparticles using biosynthesis method

indicating the formation of manganese oxide nanoparticles. The precipitate was then washed with distilled water and ethanol several times and filtered using Whatman No. 1 filter paper. The filtrate was placed in hot air oven at 80 °C for 8 hrs. Then the dried product was crushed using mortar to get nanopowder and annealed in muffle furnace at 400 °C for 2 hrs.

Instrumentation of Trimanganese Tetraoxide (Mn_3O_4) Nanoparticles

X-ray Diffraction Measurements

The biosynthesized trimanganese tetraoxide nanopowder was characterized by X-ray powder diffraction (x-pert PRO analytical diffractometer) using CuK_α as radiation source wavelength 1.5406 nm operated at 40 kV and current of 20 mA. The scanning was done in the region of 2θ from 20 to 80°.

UV-Vis Spectroscopy

UV-Vis spectra were recorded with T 90+ Spectrophotometer within the range 200–900 nm. The intensity of light reflected from a sample is measured and compared with the intensity of light reflected from reference material in UV-Vis spectrometer.

Fourier Transform Infrared Spectroscopy

Fourier transform infrared (FT-IR) spectra were recorded in transmission mode with a Thermo Nicolet 380 FTIR spectrometer. The nature of the chemical bonds formed was investigated by recording the spectra in the range 4500–500 cm^{-1}.

SEM Analysis

Surface morphology of the synthesized Mn_3O_4 nanoparticles was characterized by using JEOL Model JSM-6390 LV type Scanning Electron Microscope.

Photoluminescence Study

PL spectroscopy is a method for investigating nanoscale material. The light emitted by atoms or molecules that have absorbed photons is monitored in photoluminescence study.

VSM Measurements

VSM measurements were performed by using lakeshore, USA model 7407 Vibrating Sample Magnetometer.

Antibacterial Activity Study

Antibacterial study was carried out with the pathogenic bacteria such as *Staphylococcus aureus, Streptococcus and Klebsiella pneumoniae* in Smykon Biotech lab.

In a nutrient agar medium, the bacterial strains were cultured. The bacterial culture was incubated for a day at 37° centigrade. Antibiotics were used as positive control during antimicrobial activity studies. These were purchased from Himedia, Mumbai, India. Amikacin (10 micro gram) was used as the positive control. The bacterial strains were subcultured in nutrient agar medium (g/l), which contains the peptic digest of animal tissue 5, sodium chloride 5, beef extract 1.5, yeast extract 1.5 and agar 15. The selected bacterial isolates were cultured individually in the basal medium. The composition of basal medium consists of (g/l): glucose—0.5 g; yeast extract—0.1 g; peptone—0.25 g; KH_2PO_4—0.05 g; $MgSO_4$—0.01 g and NaCl—1.0 g. The medium pH was adjusted to 7.0 by using HCl/NaOH. Then the isolates were inoculated individually and incubated at 37 °C for 24 h. The bacterial growth was measured by monitoring the absorbance at 600 nm in a UV-Visible spectrophotometer.

3.3 Results and Discussion

Powder X-ray Diffraction Technique

The phase purity, structural identity and particle size of the annealed sample are determined by the XRD peaks shown in Fig. 3.3. The XRD analysis revealed the diffraction peaks that corresponded to the prepared nanoparticles BCC structure. Mn_3O_4 has a spinel structure with cubic close-packed oxide ions, Mn(II) occupying tetrahedral sites and Mn(III) occupying octahedral sites [20]. Intense peaks were observed at 32.527, 36.201, 44.592, 58.65, 60.09, 64.79° corresponding to (103), (211), (220), (321), (215) and (400) Bragg's reflection, respectively, and are in excellent agreement with the standard values of tetragonal hausmannite Mn_3O_4 structure (JCPDS. 89-4837). The crystal system was determined to be tetragonal with lattice parameter

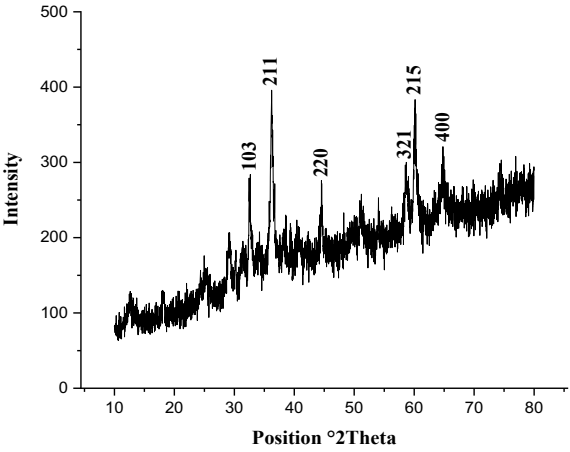

Fig. 3.3 XRD pattern of synthesized Mn_3O_4 nanoparticles

of 'a' value 5.763 A° and 'c' value 9.456 A°. The XRD pattern revealed some additional peaks, which may be due to the formation of crystalline compounds present in the plant extract [21]. The Debye-Scherer's formula $D = k\lambda/\beta\cos\theta$ [22] was used to determine the average size of the particle, where D represents grain size, k is an empirical constant ($k = 0.9$), λ is the X-ray wavelength of the CuK_α radiation. ($\lambda = 1.5406$ A°), β is the full width half maximum (FWHM) and θ is the diffracted angle, respectively. The average crystallite size of Mn_3O_4 nanoparticles was found to be about 25–30 nm.

UV-Visible Spectroscopy Study

The most commonly used method for investigating the optical properties of particles is UV-visible spectroscopy. The green synthesized Mn_3O_4 nanoparticles were characterized by UV-Vis spectroscopy by scanning them in the wavelength range of 200–900 nm. The formation of Mn_3O_4 nanoparticles when *Azadirachta Indica* leaf extract was added to potassium permanganate solution changed the colour of the solution from purple to dark brown. The excitation of surface plasmon vibrations with Mn_3O_4 nanoparticles causes these colour changes and it may be due to the interaction of conduction electrons of metal nanoparticles with incident photon [23, 24]. Figure 3.4 shows the UV-visible spectrum of synthesized Mn_3O_4 nanoparticles. The spectra showed important peak situated at 270 nm. The peak exhibited at this lower region may be due to the formation of nanoparticles aggregation. The energy band gap value of Mn_3O_4 nanoparticles was calculated as 4.59 eV using the formula $E_g = hc/\lambda$. The optical band gap was again calculated using Tauc's relation and was found to be 4.52 eV. The estimated band gap from the plot $(\alpha h\nu)^2$ versus $(h\nu)$ for Mn_3O_4 nanoparticles is shown in Fig. 3.5. The band gap energy is determined by extrapolating the straight line to the energy axis. In addition, the obtained E_g value was quite larger than the value reported for bulk Mn_3O_4 assigning to the quantum confinement effect [25]. Mn_3O_4 nanoparticles have a large optical band gap, making

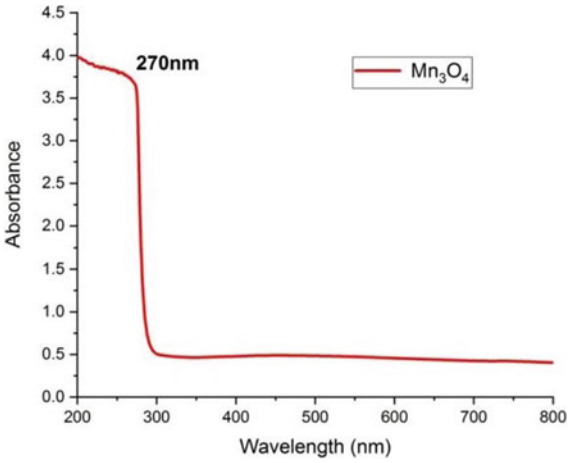

Fig. 3.4 UV-Vis spectroscopy of synthesized Mn_3O_4 nanoparticles

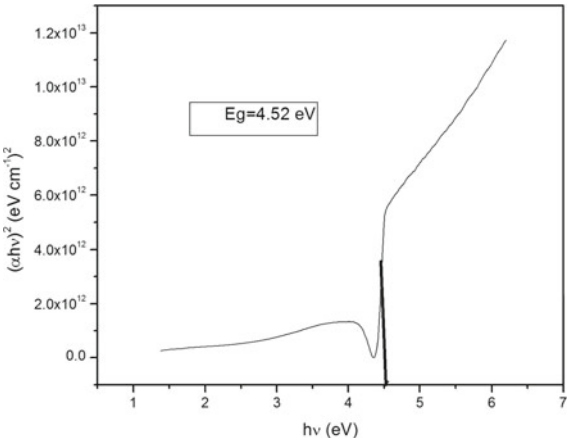

Fig. 3.5 Tauc's plot of synthesized Mn_3O_4 nanoparticles

them a viable candidate for use in Opto-electronics, including visible-light emitting devices.

Fourier Transform Infrared Spectroscopy

FTIR spectroscopy study was carried out to establish the purity and nature of Mn_3O_4 nanoparticles as synthesized by green synthesis method. The main functional groups and chemical information present in the hausmannite nanostructures were revealed by the FT-IR spectrum. Figure 3.6 shows the FT-IR spectrum of synthesized Mn_3O_4 nanoparticles in the range of 4500–500 cm^{-1}. From the data obtained, the peaks observed in the wave regions around 3406.24 cm^{-1} could be assigned with the stretching vibrations of hydrogen-bonded surface water molecules and hydroxyl groups. Additionally, the bands at 1625.63 and 1381.69 cm^{-1} correspond to the presence of a large number of residual hydroxyl groups, implying that traces of

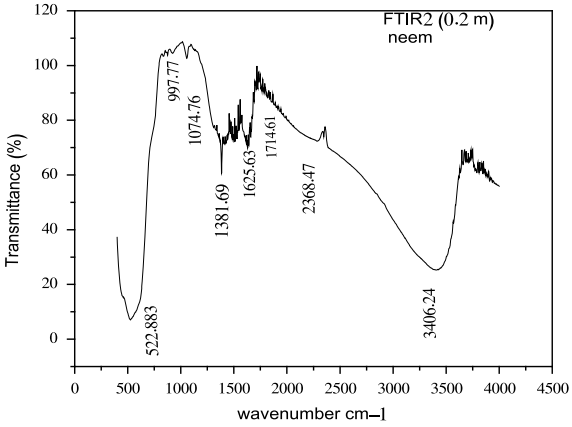

Fig. 3.6 FTIR spectrum of synthesized Mn_3O_4 nanoparticles

adsorbed water and carbonate ions present in the atmosphere are vibrating in the O–H mode within Mn atoms [26]. The band located at 522.883 cm^{-1} can be ascribed to the MnO vibrations of Mn_3O_4 nanopowder.

SEM Analysis

Morphology of synthesized Mn_3O_4 nanoparticles was characterized by SEM analysis. The SEM image of biofunctionalized nanoparticles with various magnifications is shown in Fig. 3.7. Due to the evolution of large amounts of gases during synthesis, product aggregation is composed of many irregular particles with a variety of pores and voids. The stability of nanoparticles is also represented by the SEM picture, which is mediated by the capping and stabilizing agents present in the extract [27]. The Mn_3O_4 nanoparticles formed can be considered to be moderately dispersed and slightly agglomerated. Polymorphic material morphology makes up the majority of the particles.

Photoluminescence Study

The photoluminescence spectroscopy is a contactless, non-destructive technique to explore the electronic structure of materials. The recombination of excited electrons and holes is primarily responsible for photoluminescence emission. The excitation and emission spectra of manganese oxide were usually recorded in the range of 260–450 nm. Figure 3.8 displays the photoluminescence (PL) emission spectrum of synthesized Mn_3O_4 nanostructures measured at room temperature with an excitation wavelength of 270 nm. PL emission peak at 760 nm was observed, which lies in red emission region. The intensity of the emission peak increases with annealing, while the band narrows with the removal of shoulder peaks. This behaviour can be explained by an increase in crystallinity and a reduction in oxygen vacancy caused by air during annealing. Thus, the non-radiative consolidation leads to the increase in the amount of free excitons and hence higher near band emission.

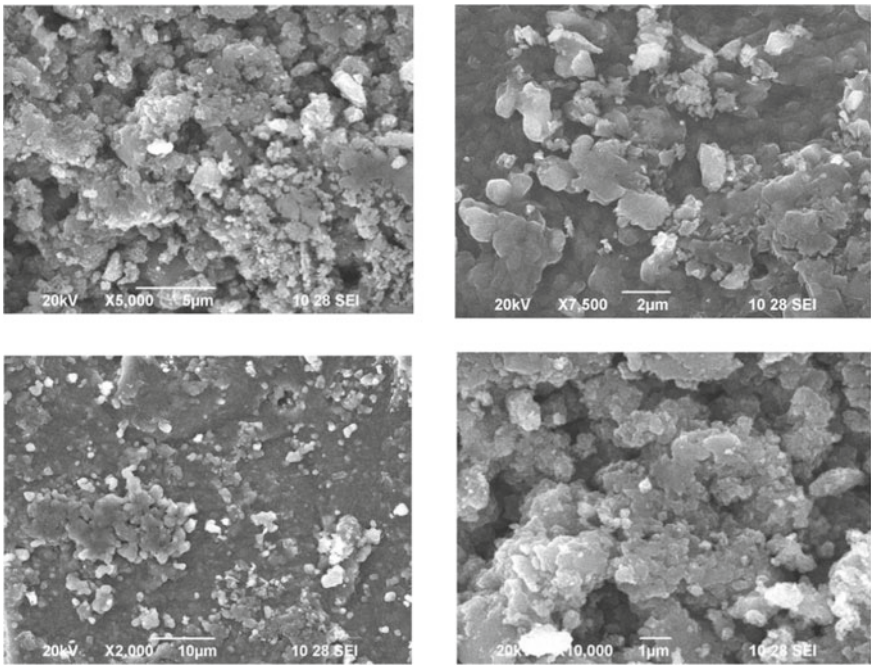

Fig. 3.7 SEM studies of synthesized Mn_3O_4 nanoparticles

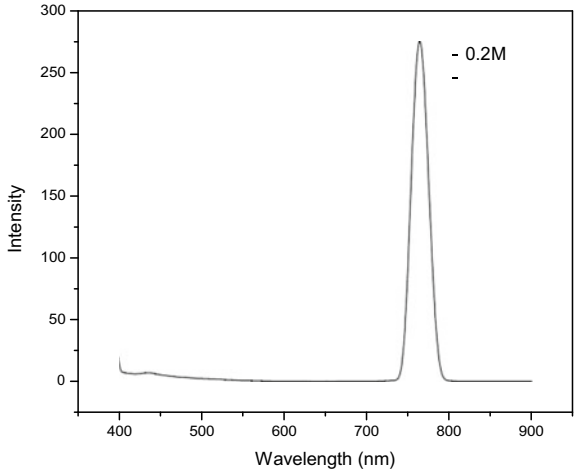

Fig. 3.8 Photoluminescence study of synthesized Mn_3O_4 nanoparticles

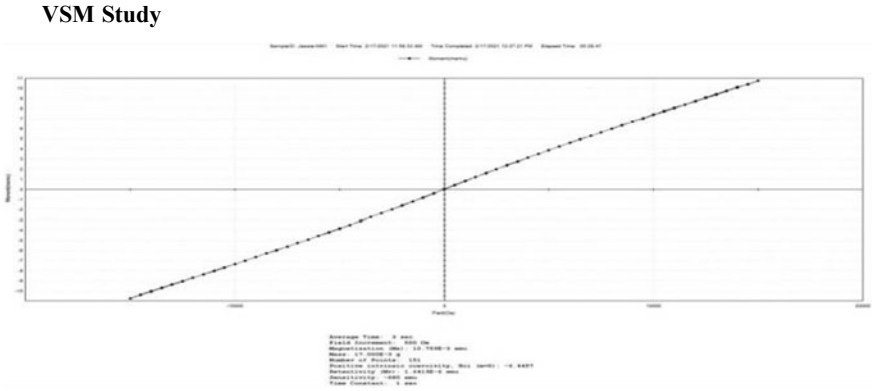

Fig. 3.9 VSM study of synthesized Mn_3O_4 nanoparticles

VSM Study

The magnetic behaviour of Mn_3O_4 nanoparticles was investigated by employing a vibrating sample magnetometer. Figure 3.9 shows the magnetization curve of a sample that shows linear behaviour in the range of applied field at room temperature between +15000 and −15000 Oe. The method of preparation, cation distribution, grain size, temperature, oxygen parameter and oxygen anion vacancies in lattices all influence the magnetic properties of nanoparticles [28]. The difference in the octahedral and tetrahedral lattice sites causes the magnetization of spinel materials. Mn_3O_4 nanoparticles exhibit paramagnetic behaviour at room temperature. The maximum magnetization (M_s) and coercivity (H_c) values for the synthesized sample were 10.759E-3 emu and 6.44357, respectively, with magnetic retentivity (M_r) value of 1.6419E-6 emu. When the particle size is small, the maximum anisotropy energy reaches the thermal energy, the hysteresis in single-domain ferrimagnetic particles disappears. The process of flipping of a single domain spin becomes uninhibited in this case [29]. This state of ferrimagnetism is called super paramagnetism as it does not show any hysteresis in its M–H behaviour and the magnetisation never gets saturated even at a very high applied field.

Antibacterial Screening

The pathogenic bacteria such as *Staphylococcus aureus*, *Streptococcus* and *Klebsiella pneumoniae* were used for antibacterial studies.

The sample well was created, and 20 microliters of sample were loaded into it. As a positive control, amikacin (10 microgram) was used. At 37 °C, all the plates were incubated for 24 hours. The zone inhibition's diameter was measured in millimetres (mm). The results were compared with those obtained with the standard drug Amikacin. The green synthesized Mn_3O_4 nanoparticles showed good antibacterial activity against *Streptococcus* bacteria. The inhibition zone diameter was 16 mm. It also had a mild antibacterial effect on *Klebsiella pneumoniae* and

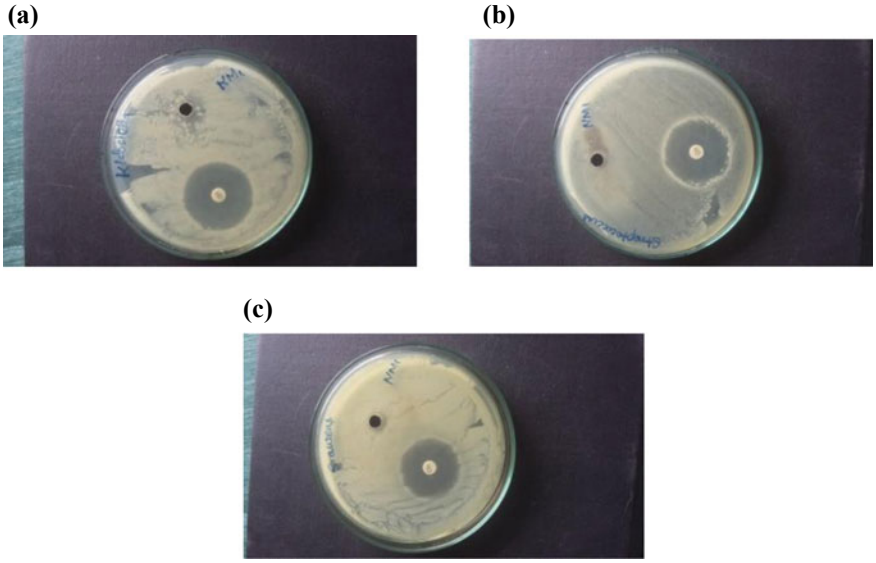

Fig. 3.10 Antibacterial activity of biosynthesized Mn_3O_4 nanoparticles against **a** *Klebsiella pneumonia* **b** *Streptococcus* **c** *Staphylococcus aureus*

Staphylococcus aureus. The inhibition zones were 9–10 mm in diameter, respectively. Moreover, Mn_3O_4 nanoparticles synthesized using *Azadirachta Indica* leaf extract showed significant antibacterial activity against *Streptococcus* bacteria compared with *Klebsiella pneumoniae* and *Staphylococcus aureus*. The activity of Mn_3O_4 nanoparticles against different bacteria is diagrammatically represented in Fig. 3.10.

	Zone of inhibition (mm)	
	Standard	Mn_3O_4 nanoparticles
Klebsiella pneumonia	30	9
Streptococcus	35	16
Staphylococcus aureus	30	10

3.4 Conclusion

The present work on the green process using *Azadirachta Indica* leaf extract is a simple, cost-effective and environmentally friendly alternative to traditional physical and chemical processes, with promising biomedical and pharmaceutical applications. Bioreduction was clearly observed due to the different plant metabolites present in the leaf extract. Structural and morphological properties of synthesized

nanoparticles were characterized. The XRD pattern clearly shows that the Mn_3O_4 nanoparticles formed have a tetragonal structure and are highly crystalline in nature and the particle size was in the range of 25–30 nm. The energy band gap value of the as-prepared nanoparticles estimated using Tauc plot was 4.52 eV. FTIR analysis of the green synthesised Mn_3O_4 particles confirms the various functional groups of the prepared sample. The VSM study elucidates that even at a very high applied magnetic field, magnetisation never got saturated. The maximum magnetisation obtained at 15 kOe is around 10.759E-3 emu. Biosynthesized Mn_3O_4 nanoparticles showed good antibacterial activity against Streptococcus bacteria with inhibition zone of 16 mm. The biosynthesis approach of Mn_3O_4 nanoparticles can be utilized in an implicit way in the light of novel innovations and contemporary inventions.

References

1. B.E. Naveena, S. Prakash, Biological synthesis of gold nanoparticles using marine algae Gracilaria corticata and its application as a potent antimicrobial and antioxidant agent. Asian. J. Pharm. Clin. Res. **6**, 179–182(2013)
2. B.M. Pradeep kumar, K. Sriram, R. Hari Krishna, T.H. Udayashankara, K.H. Shivaprasad, B.M. Nagabhushana, Synthesis, characterization of nano MnO_2 and its ad sorption characteristics over an azo dye. RRJM **2**(1) (2014)
3. P. Aggarwal, J.B. Hall, C.B. McLeland, M.A. Dobrovolskaia, S.E. McNeil, Nanoparticle interaction with plasma proteins as it relates to particle biodistribution, biocompatibility and therapeutic efficacy. Adv Drug Deliv Rev **61**(6), 428–437 (2009)
4. V. Makarov, A.J. Love, O.V. Sinitsyna, S.S. Makarova, I.V. Yaminsky, M.E. Taliansky, N.O. Kalinina, "Green" nanotechnologies: synthesis of metal nanoparticles using plants Acta Naturae **6**(1), 35–44 (2014)
5. K.S. Prasad, A. Batra, Green synthesis of MnO_2 nanorods using Phyllanthus amaranth plant extract and their fluorescence studies. Green Process. Synth **6**, 549–554 (2017)
6. Y. Lvov, B. Munge, O. Giraldo, I. Ichinnose, S.L. Suib, J.F. Rusling, Film of manganese oxide nanoparticles with polycations or myoglobin from alternate-layer adsorption. Langmuir. **16**, 8850–8857, (2000)
7. X.L. Luo, J.J. Xu,W. Zhao, H.Y. Chen, A novel glucose ENFET based on the special reactivity of MnO_2 nanoparticles. Biosens. Bioelectron. **19**, 1295–1300 (2004)
8. X. Mao-wen, B. Shu-Juan, Nanostructured MnO_2 for electrochemical capacitor, energy storage. Electrochim. Acta **55**(18), 5117–5122 (2010)
9. L. Xiaodi, C. Changzhong, Z. Yiyang, J. Bin, A review on the synthesis of manganese oxide nanomaterials and their applications on lithium-ion batteries. Hindawi Publishing Corporation. J. Nanomat. **2013**, 1–7 (2013)
10. G. Harichandran, P. Parameswari, D.S. Amalraj, P. Shanmugam, Preparation of MnO_2 nanoparticles and application in the synthesis of 2,2′-aryl methylene bis(3-hydroxy-5,5-dimethyl-2-cyclohexene-1-one). (IJIRSE) Int. J. Innov. Res. Sci. Eng. 443–447 (2014)
11. L. Tao, S. Tingting, L. Xiaobo, Z. Shuilin, Y. Lihong, P. Yuepu, Effects of nano-MnO_2 on dopaminergic neurons and the spatial learning capability of rats. Int. J. Environ. Res. Public Health **11**(8), 7918–7930 (2014)
12. M.N. Mohammad, R. Fahimeh, A. Eva-Mari, L. Choon-Hwan, I.A. Suleyman, Nano-sized manganese oxides as biomimetic catalysts for water oxidation in artificial photosynthesis: a review. J. R. Soc. Interface **9**, 2383–2395 (2012)
13. D. Van-Phuc, L. Ngoc-Chung, N. Ngoc-Tuan, Removal of copper (Ii) from aqueous solution by adsorption onto MnO_2 nanostructure: equilibrium and kinetic studies, in *The 4th Academic*

Conference on Natural Science for Young Scientists, Master & PhD. Students From Asean Countries, Publishing House for Science and Technology, 57–64 (2015)
14. J. Hou, Y. Li, L. Liu, L. Ren, X. Zhao, Effect of giant oxygen vacancy defects on the catalytic oxidation of OMS-2 nanorods. J. Mater. Chem. A **1**, 6736–6741 (2013)
15. M. Jayandran, M. Muhamed Haneefa, V. Balasubramanian, Synthesised manganese oxide nanoparticles by using lemon and turmeric curcumin extract as a reducing and capping agent. Synthesised particles are analyzed for their anti-bacterial and antifungal activities. J. Appl. Pharm. Sci. **5** (12), 105–110 (2015)
16. K. Vineet, S. Kulvinder, P. Shaily, K.M. Suyinder, Green synthesis of manganese oxide nanoparticles for the electrochemical sensing of p-nitrophenol. Int. Nano Lett. **7**, 123–131 (2017)
17. S. Moon, B. Salunke, B. Alkotaini, E. Sathiyamoorthi, B. Kim, Biological synthesis of manganese dioxide nanoparticles by Kalopanax pictus plant extract. IET Nanobiotechnol. **9**(4), 220–225 (2015)
18. M. Wright, S. Farooqui, A. White, A. Greene, Production of manganese oxide nanoparticles by Shewanella species. Appl. Environ. Microbiol. **82**(17), 5402–5409 (2016)
19. P. Banerjee, M. Satapathy, A. Mukhopahayay, P. Das, Leaf extract mediated green synthesis of silver nanoparticles from widely available Indian plants: synthesis, characterization, antimicrobial property and toxicity analysis. Bioresour. Bioprocess. **1**(1), 1–10 (2014)
20. H. Schmidbaur, Book review: chemistry of the elements. By N.N. Greenwood and A. Earnshaw. Angew. Chem. Int. Ed. Engl. **25**(2), 194–195 (1986)
21. L. Christensen, Biosynthesis of silver nanoparticles using Murraya koenigii (curry leaf): an investigation on the effect of broth concentration in reduction mechanism and particle size. Adv. Mater. Lett. **2**(6), 429–434 (2011)
22. H.P. Klug, L.E. Alexander, X-ray diffraction procedures for polycrystalline and amorphous materials, 2. Auflage. John Wiley & Sons, New York-Sydney-Toronto 1974, 966 Seiten, Preis: £ 18.55. Berichte der Bun sengesellschaft für physikalische Chemie **79**(6), 553–553 (1975)
23. S. Singh, R. Gopal, Synthesis of colloidal zinc oxide nanoparticles by pulsed laser ablation in aqueous media. Phys. E. **40**(4), 724–730 (2008)
24. G. Chen, M. Hong, B. Lan, Z. Wang, Y. Lu, T. Chong, A convenient way to prepare magnetic colloids by direct Nd:YAG laser ablation. Appl. Surf. Sci. **228**(1–4), 169–175 (2004)
25. H. Rahaman, S. Ghosh, Soft-templated synthesis of Mn_3O_4 microdandelions for the degradation of alizarin red under visible light irradiation. RSC Adv. **6**(6), 4531–4539 (2016)
26. D. Dubal, R. Holze, All-solid-state flexible thin film super capacitor based on Mn_3O_4 stacked nanosheets with gel electrolyte. Energy **51**, 407–412 (2013)
27. U. Suresh, K. Murugan, G. Benelli, M. Nicoletti, D. Barnard, C. Panneerselvam, P. Kumar, J. Subramaniam, D. Dinesh, B. Chandramohan, Tackling the growing threat of dengue: Phyllanthus niruri-mediated synthesis of silver nano particles and their mosquitocidal properties against the dengue vector Aedes ae gypti (Diptera: Culicidae). Parasitol. Res. **114**(4), 1551–1562 (2015)
28. N. Deraz, A. Abdeltawab, S. Al-Deyab, Preparation and characterization of bulk and alumina supported hausmannite nanoparticles. Asian J. Chem. **26**(7), 2120–2124 (2014)
29. T. Ozkaya, A. Baykal, H. Kavas, Y. Köseoğlu, M. Toprak, A novel synthetic route to Mn_3O_4 nanoparticles and their magnetic evaluation. Phys. B **403**(19–20), 3760–3764 (2008)

Chapter 4
Calculating CP Invariance Using Weak Basis Invariants in Hybrid Textures of Neutrino Mass Matrix

Madan Singh

Abstract In the present analysis, I have constructed the CP odd Weak Basis invariants (WB) at low energies, for Majorana neutrino mass matrix having a condition of two zeros and an equality between arbitrary non-zero elements in the flavour basis, where charged lepton mass matrix is diagonal. This particular form of neutrino mass matrix, also known as hybrid texture, is found to be viable with the current experimental data, as shown by S. Dev and D. Raj in their recent work. In this analysis, I compute the necessary and sufficient condition for leptonic CP invariance for each of the viable possibility of hybrid texture, and subsequently find some important implications regarding the leptonic CP properties.

4.1 Introduction

CP violation is considered as an important tool to explore the flavour sector [1–5] in the Standard Model (SM), and to probe the signals of New Physics (NP). As of now, Cabibbo–Kobayashi–Maskawa (CKM) [6] mechanism seems to be only way to understand CP violation in the SM. The picture is well supported by the precision measurements of $\sin 2\beta$ from the CP asymmetry in the decay, $B \to \psi K$, and also compatible with the global fits pertaining to the reconstruction of unitarity triangle, given by various well-known groups like Particle Data Group (PDG) [7], CKMfitter [8], UTfit [9] and HFAG [10]. In the quark sector, CP violation is contributed by an irremovable phase δ, which appears in CKM mixing matrix [6]. In contrast to the quark sector, SM does not allow the leptonic CP violation owing to the fact that neutrinos are massless. However, in the spirit of quark–lepton symmetry, it is natural to expect an entirely analogous mechanism to arise in the lepton sector, leading to leptonic CP violation. To this end, neutrino oscillation, [11–14], turns out to be the first experiment-based evidence, which indicates the leptonic CP violation, arising from the fact that neutrinos are massive and non-degenerate. This, in consequence, provides a window to explore the leptonic CP violation beyond the SM. The precision measurement of three neutrino mixing angles ($\theta_{12}, \theta_{23}, and \theta_{13}$) [15],

M. Singh (✉)
Department of Physics, M.N.S. Government College Bhiwani, Haryana 127021, India

S. Sengupta et al. (eds.), *Selected Progresses in Modern Physics*, Springer Proceedings in Physics 265, https://doi.org/10.1007/978-981-16-5141-0_4

further reinforces our prospects of finding CP violation in the ongoing and future experiments.

In contrast to the quark case, the parameterization of CP violation in the lepton sector is complicated by several factors. In particular, if the neutrinos are Majorana particles, then in comparison to the case of CKM matrix, the corresponding leptonic Pontecorvo–Maki–Nakagawa–Sakata (PMNS) mixing matrix has two additional phases apart from an analogous CKM phase δ.

The leptonic mixing matrix V can be given as in the standard parameterization [16, 17],

$$V = \begin{pmatrix} c_{12}c_{13} & s_{12}c_{13} & s_{13}e^{-i\delta} \\ -c_{12}s_{23}s_{13}e^{i\delta} - s_{12}c_{23} & -s_{12}s_{23}s_{13}e^{i\delta} + c_{12}c_{23} & s_{23}c_{13} \\ -c_{12}c_{23}s_{13}e^{i\delta} + s_{12}s_{23} & -s_{12}c_{23}s_{13}e^{i\delta} - c_{12}s_{23} & c_{23}c_{13} \end{pmatrix} \begin{pmatrix} 1 & 0 & 0 \\ 0 & e^{i\rho} & 0 \\ 0 & 0 & e^{i\sigma} \end{pmatrix},$$

where $c_{ij} = \cos\theta_{ij}$, $s_{ij} = \sin\theta_{ij}$ for $i, j = 1, 2, 3$, and δ (Dirac CP phase); ρ, σ (Majorana CP phases) are three CP-violating phases. The measurement of δ is expected in the experiments with superbeams and neutrino beams from neutrino factories or indirectly through the area of the unitarity triangles defined for the leptonic sector, while the Majorana-type CP phases may contribute to Lepton Number Violating (LNV) processes like neutrinoless double beta decay.

In the specific basis, where charged lepton mass matrix is diagonal, and assuming the neutrinos to be Majorana particles, neutrino mass matrix encodes all the information regarding the leptonic CP violation at low energy. To facilitate any specific predictions for the same, it is convenient to reduce the number of free parameters of mass matrix. To this end, several possibilities, for instance, some elements of neutrino mass matrix can be considered either zero or equal [18–21] or some cofactors of neutrino mass matrix to be either zero or equal [19, 22–24] have been found in the literature. Out of these, co-existence of texture zeros and an equal elements (or cofactors), also known as hybrid texture, is one of the most notable and abundantly studied. Not only they reduce the number of free parameters to an appreciable extent compare with texture zero but also can be naturally realized through flavor symmetry. In an addendum to this, Dev and Raj [25], have explored a new case of hybrid texture comprising two zero elements and an equality between the non-zero elements. This new possibility not only contains lesser number of free parameters compare to other hybrid textures but also has higher predictability.

Under the weak basis transformation, hybrid texture are not invariant similar to texture zeros implying that a given set of zeros and an equality, which appears in a certain Weak Basis (WB) may not be present or may appear in different entries in another WB, while leading to the same physics. In such a scenario, CP invariants are largely considered as an important tool to investigate the CP properties both in the quark and the leptonic sector. In the literature, special attention has been paid on invariants, owing to their suitability for the analysis of specific ansätze of neutrino mass matrix [26, 27] without even need of its diagonalization.

In the present analysis, I shall re-examine the WB invariants for the new possibility of hybrid texture comprising two zeros and an equality between the non-zero elements

in the flavoured basis, and find the CP conditions in lepton sector. The interest in the chosen model stems from the fact that an assumption of two zeros and an additional equality in the neutrino mass matrix reduces the number of free parameters to six. Hence, it is more predictive compare to the popular models with two texture zeros, one zero with a vanishing minor and other hybrid textures, respectively.

To investigate the leptonic CP properties, it is essential to find the WB invariants in terms of the Majorana neutrino mass matrix. To this end, I shall first define the WB invariants at low energy [28–30], which must be zero (non-zero) for CP invariance (violation) in leptonic sector. The invariant, which is sensitive to Dirac phase only, is given as

$$\mathrm{I1} = \mathrm{Tr}[\mathrm{m}_\nu \mathrm{m}_\nu^\dagger, \mathrm{m_l} \mathrm{m_l}^\dagger]^3, \tag{4.1}$$

where m_ν and $\mathrm{m_l}$ are Majorana neutrino mass matrix and charged lepton mass matrix, respectively. In the flavour basis, I1 reduces to

$$\mathrm{I1} = -6\mathrm{i}\Delta_{\mathrm{e}\mu}\Delta_{\mu\tau}\Delta_{\tau\mathrm{e}}\mathrm{Im}(\mathrm{h}_{12}\mathrm{h}_{23}\mathrm{h}_{31}),$$

where $\Delta_{\mathrm{ij}} = \mathrm{m_j^2} - \mathrm{m_i^2}$, ij run over the pairs, $e\mu$, $\mu\tau$, τe. The argument of the product, $\mathrm{h}_{12}\mathrm{h}_{23}\mathrm{h}_{31}$, is responsible for defining the CP properties for Dirac neutrinos. The quantity $\mathrm{h}(\equiv \mathrm{m}_\nu \mathrm{m}_\nu^\dagger)$, is a hermitian matrix, where

$$h_{ij} = \sum_{i,j=e,\mu,\tau}^{3} \sum_{a=e,\mu,\tau}^{3} m_{ia} m_{aj}^*$$

denotes the nine matrix elements. The invariant is sensitive to the Dirac-type CP phase δ, and hence depends on Lepton Number Conserving (LNC) process like neutrino oscillations. The vanishing of imaginary part of I1 implies $sin\delta = 0$, and thus leads to Dirac type CP invariance. The relationship between I1 and Jarlskog rephasing invariant, $\mathrm{J_{CP}}$ for lepton sector is established in [28]. The representation of $\mathrm{J_{CP}}$ in terms of $\sin\delta$ is found as

$$\mathrm{J_{CP}} = \frac{1}{8}\mathrm{s}_{2(12)}\mathrm{s}_{2(23)}\mathrm{s}_{2(13)}c_{13}\sin\delta, \tag{4.2}$$

where $\mathrm{s}_{2(\mathrm{ij})\equiv\sin 2\theta_{\mathrm{ij}}}$, i, j = 1, 2, 3.

Also $\mathrm{J_{CP}}$ is an 'invariant function' of mass matrices, and is related to the mass matrices as

$$\det \mathrm{C} = -2\mathrm{J_{CP}}\Delta_{\mathrm{e}\mu}\Delta_{\mu\tau}\Delta_{\tau\mathrm{e}}\Delta_{12}\Delta_{23}\Delta_{31}, \tag{4.3}$$

where $\mathrm{C} \equiv \mathrm{i}[\mathrm{m}_\nu \mathrm{m}_\nu^\dagger, \mathrm{m_l} \mathrm{m_l}^\dagger]$ and Δ_{12}, *etc.*, are analogue to the Δ_{ij} as defined earlier. The commutator C, is by definition, hermitian and traceless. Thus, eigen values are real. In fact, they are measurable, even though C itself is not a measurable. The

determination of any traceless 3×3 may be computed from trace of the third power of the matrix, i.e. $\det C = \frac{1}{3}\mathrm{Tr}(C^3)$, therefore, I have $\det C = -\frac{i}{3}\mathrm{Tr}[m_\nu m_\nu^\dagger, m_l m_l^\dagger]^3$, which is valid for any traceless 3×3 matrix. Therefore, from (4.3), I get

$$I_1 = -6iJ_{CP}\Delta_{e\mu}\Delta_{\mu\tau}\Delta_{\tau e}\Delta_{12}\Delta_{23}\Delta_{31}. \tag{4.4}$$

The above relation shows that I_1 is directly proportional to $sin\delta$.
Using (4.2, 4.4), I arrive at

$$J_{CP} = \frac{\mathrm{Im}(h_{12}h_{23}h_{31})}{\Delta_{sol}\Delta_{atm}^2}, \tag{4.5}$$

where $\Delta_{sol} \equiv \Delta_{12}$ and $\Delta_{atm} \equiv \Delta_{23} \simeq \Delta_{31}$ are solar and atmospheric neutrino mass squared differences, respectively.
The other two invariants, I2 and I3, are sensitive to both Dirac as well as Majorana-type CP phases. The invariant I2 is given as

$$I2 = \mathrm{Im}(\mathrm{Tr}[m_l m_l^\dagger m_\nu^* m_\nu m_\nu^* m_l^T m_l^* m_\nu]). \tag{4.6}$$

The above invariant was computed, for the first time, to derive the necessary and sufficient condition for CP invariance in the framework of two neutrinos [29]. In this framework, CP violation can occur only due to Majorana-type phase. In the flavoured basis, one can re-write I2 as a function of the elements of m_ν,

$$\begin{aligned} I2 = {} & m_e^4 m_{ee} H_{e1} + m_\mu^4 m_{\mu\mu} H_{\mu 2} + m_\tau^4 m_{\tau\tau} H_{\tau 3} \\ & + m_e^2 m_\mu^2 m_{e\mu}(H_{e2} + H_{\mu 1}) + m_\mu^2 m_\tau^2 m_{\mu\tau}(H_{\mu 3} + H_{\tau 2}) \\ & + m_e^2 m_\tau^2 m_{e\tau}(H_{e3} + H_{\tau 1}), \end{aligned} \tag{4.7}$$

where H is a complex matrix, and its elements are given as

$$H_{e1} = m_{ee}^* h_{ee} + m_{e\mu}^* h_{\mu e} + m_{e\tau}^* h_{\tau e},$$

$$H_{e2} = m_{ee}^* h_{e\mu} + m_{e\mu}^* h_{\mu\mu} + m_{e\tau}^* h_{\tau\mu},$$

$$H_{e3} = m_{ee}^* h_{e\tau} + m_{e\mu}^* h_{\mu\tau} + m_{e\tau}^* h_{\tau\tau},$$

$$H_{\mu 1} = m_{\mu e}^* h_{ee} + m_{\mu\mu}^* h_{\mu e} + m_{\mu\tau}^* h_{\tau e},$$

$$H_{\mu 2} = m_{\mu e}^* h_{e\mu} + m_{\mu\mu}^* h_{\mu\mu} + m_{\mu\tau}^* h_{\tau\mu},$$

$$H_{\mu 3} = m^*_{\mu e} h_{e\tau} + m^*_{\mu\mu} h_{\mu\tau} + m^*_{\mu\tau} h_{\tau\tau},$$

$$H_{\tau 1} = m^*_{\tau e} h_{ee} + m^*_{\tau\mu} h_{\mu e} + m^*_{\tau\tau} h_{\tau e},$$

$$H_{\tau 2} = m^*_{\tau e} h_{e\mu} + m^*_{\tau\mu} h_{\mu\mu} + m^*_{\tau\tau} h_{\tau\mu},$$

$$H_{\tau 3} = m^*_{\tau e} h_{e\tau} + m^*_{\tau\mu} h_{\mu\tau} + m^*_{\tau\tau} h_{\tau\tau}.$$

Substituting $m_\nu m_\nu^\dagger$ with $m_\nu (m_l m_l^\dagger)^* m_\nu^\dagger$ in (4.1), I_3 is found as

$$I3 \equiv \mathrm{Tr}[m_\nu m_l^T m_l^* m_\nu^\dagger, m_l m_l^\dagger]^3. \tag{4.8}$$

The computation of above invariant predicts CP violation for three or more generation of Majorana neutrinos even in the limit of complete neutrino mass degeneracy [29, 30].

In the flavour basis, I3 can be re-written as

$$I3 = -6i\Delta_{e\mu}\Delta_{\mu\tau}\Delta_{\tau e}\mathrm{Im}(h'_{12}h'_{23}h'_{31}),$$

where $\arg(h'_{12}h'_{23}h'_{31})$ is complex phase responsible for CP violation.
Similar to h, h' is also hermitian matrix, and its elements are given as

$$h'_{ij} = \sum_{x=e,\mu,\tau}^{3} m_x^2 \sum_{i,j=e,\mu,\tau}^{3} \sum_{a=e,\mu,\tau}^{3} m^*_{ia} m_{aj}$$

where m_e, m_μ and m_τ denote the electron, muon and tau neutrino, respectively.

Following the classification scheme of [25], all the eight experimentally viable possibilities have been encapsulated in Table 4.1. Among the viable cases, only five are found be independent ones. The ansatze corresponding to each pair, ($A1^{IV}$, $A2^{IV}$), ($A1^{V}$, $A2^{V}$) and ($A1^{VI}$, $A2^{VI}$), exhibit the similar phenomenological implications and are related *via* permutation symmetry. On the other hand, ansätze C^{II} and C^{IV} transform onto themselves independently.

The symmetry corresponds to the simultaneous exchange of 2–3 rows and 2–3 columns of m_ν. The corresponding permutation matrix can be given by

$$P_{23} = \begin{pmatrix} 1 & 0 & 0 \\ 0 & 0 & 1 \\ 0 & 1 & 0 \end{pmatrix}. \tag{4.9}$$

Table 4.1 The eight viable ansätze of Majorana neutrino mass matrices having two texture zeros and one equality

	IV	**V**	**VI**
Class A1	$\begin{pmatrix} 0 & 0 & e \\ & b & b \\ & & c \end{pmatrix}$	$\begin{pmatrix} 0 & 0 & e \\ & b & f \\ & & b \end{pmatrix}$	$\begin{pmatrix} 0 & 0 & e \\ & b & c \\ & & c \end{pmatrix}$
	IV	**V**	**VI**
Class A2	$\begin{pmatrix} 0 & d & 0 \\ & b & b \\ & & c \end{pmatrix}$	$\begin{pmatrix} 0 & d & 0 \\ & b & f \\ & & b \end{pmatrix}$	$\begin{pmatrix} 0 & d & 0 \\ & b & c \\ & & c \end{pmatrix}$
	II	**IV**	
Class C	$\begin{pmatrix} a & d & a \\ & 0 & f \\ & & 0 \end{pmatrix}$	$\begin{pmatrix} a & d & e \\ & 0 & e \\ & & 0 \end{pmatrix}$	

Using permutation symmetry, it is trivial to find the following relations among the neutrino oscillation parameters,

$$\theta_{12}^{\mathrm{X}} = \theta_{12}^{\mathrm{Y}}, \;\; \theta_{23}^{\mathrm{X}} = 90^\circ - \theta_{23}^{\mathrm{Y}}, \;\; \theta_{13}^{\mathrm{X}} = \theta_{13}^{\mathrm{Y}}, \;\; \delta^{\mathrm{X}} = \delta^{\mathrm{Y}} - 180^\circ, \tag{4.10}$$

where X and Y denote the pair of aforementioned ansätze related through a 2–3 permutation symmetry.

4.2 CP Invariance Condition for Viable Cases

In this section, I compute the WB invariants in terms of mass matrix elements for all the viable hybrid textures, and subsequently find the CP conditions corresponding to each ansätz.

Ansatz $(\mathrm{A1})^{\mathrm{IV}}$: Using (4.1), it is trivial to obtain

$$\mathrm{I1} = -6\mathrm{i}\Delta_{\mathrm{e}\mu}\Delta_{\mu\tau}\Delta_{\tau\mathrm{e}}|\mathrm{m}_{\mathrm{e}\tau}|^2|\mathrm{m}_{\mu\mu}|^2\mathrm{ImQ}_{(\mathrm{A1})^{\mathrm{IV}}}, \tag{4.11}$$

where $\mathrm{Q}_{(\mathrm{A1})^{\mathrm{IV}}} = \mathrm{m}_{\tau\tau}\mathrm{m}_{\mu\mu}^*$.
Using the above equation, $\mathrm{J_{CP}}$, which is a measurable neutrino oscillation parameter, can be given as

$$\mathrm{J_{CP}} = \frac{|\mathrm{m}_{\mathrm{e}\tau}|^2|\mathrm{m}_{\mu\mu}|^2\mathrm{ImQ}_{(\mathrm{A1})^{\mathrm{IV}}}}{\Delta_{\mathrm{sol}}\Delta_{\mathrm{atm}}^2}.$$

From the expression, it is convenient to directly compute J_{CP} from the elements of m_ν without even need to diagonalize the m_ν. Interestingly, condition $m_{\mu\mu} = m_{\tau\tau}$, leads to $J_{CP} = 0$ or equivalently sinδ=0. Hence, $m_{\mu\mu} = m_{\tau\tau}$ is essential to find the CP invariance relevant for LNC.
Using (4.7) and (4.8), the expressions for invariants I2 and I3, sensitive to both Dirac and Majorana phases, are found as

$$I2 = \Delta^2_{\mu\tau}|m_{\mu\mu}|^2 ImQ_{(A1)^{IV}} \tag{4.12}$$

and

$$I3 = -6i\Delta_{e\mu}\Delta_{\mu\tau}\Delta_{\tau e}m^2_\mu m^4_\tau |m_{e\tau}|^2|m_{\mu\mu}|^2 ImQ_{(A1)^{IV}}. \tag{4.13}$$

respectively. From the above discussion, it is clear that CP violation is possible if the phases associated with the elements $m_{\mu\mu}$ and $m_{\tau\tau}$ are not finely tuned.

More apparently, CP invariance condition is allowed for **ansatz** $(A1)^{IV}$ if and only if

$$\arg(m_{\mu\mu}) = \arg(m_{\tau\tau}). \tag{4.14}$$

Ansatz $(A1)^{V}$: Similarly, using (4.1), one can find I1 as

$$I1 = -6i\Delta_{e\mu}\Delta_{\mu\tau}\Delta_{\tau e}|m_{e\tau}|^2 ImQ_{(A1)^{V}}, \tag{4.15}$$

where, $Q_{(A1)^{V}} = m^2_{\mu\mu}(m^*_{\mu\tau})^2$.

The J_{CP}, can be found in terms of mass matrix elements as

$$J_{CP} = \frac{|m_{e\tau}|^2|m_{\mu\mu}|^2 ImQ_{(A1)^{IV}}}{\Delta_{sol}\Delta^2_{atm}}. \tag{4.16}$$

Therefore, condition $m_{\mu\mu} = m_{\mu\tau}$ implies $J_{CP} = 0$.

The other two invariants I2 and I3 can be derived using (4.7, 4.8)

$$I2 = \Delta^2_{\mu\tau}|m_{e\tau}|^2 ImQ_{(A1)^{V}} \tag{4.17}$$

and

$$I3 = -6i\Delta_{e\mu}\Delta_{\mu\tau}\Delta_{\tau e}m^2_\mu m^4_\tau |m_{e\tau}|^2 ImQ_{(A1)^{V}}. \tag{4.18}$$

The CP invariance condition can be found as

$$\arg(m_{\mu\mu}) = \arg(m_{\mu\tau}). \tag{4.19}$$

The mismatch between the elements $m_{\mu\mu}$ and $m_{\mu\tau}$ lead to CP violation in lepton sector.
Ansatz $(A1)^{VI}$: Using (4.1), it is found that

$$I1 = -6i\Delta_{e\mu}\Delta_{\mu\tau}\Delta_{\tau e}|m_{e\tau}|^2|m_{\tau\tau}|^2 ImQ_{(A1)^{VI}}, \tag{4.20}$$

where $Q_{(A1)^{VI}} = m_{\mu\mu}m^*_{\tau\tau}$.
Using (4.5), J_{CP} can be written as

$$J_{CP} = \frac{|m_{e\tau}|^2|m_{\tau\tau}|^2 ImQ_{(A1)^{IV}}}{\Delta_{sol}\Delta^2_{atm}}. \tag{4.21}$$

As found in ansätz $A1^{IV}$, (4.21) provides $J_{CP} = 0$ for $m_{\mu\mu} = m_{\tau\tau}$. In addition, phase relation for CP invariance is similar to ansätz $A1^{IV}$.
The other invariants I2 and I3 can be derived using (4.7) and (4.8),

$$I2 = \Delta^2_{\mu\tau}|m_{\tau\tau}|^2 ImQ_{(A1)^{VI}} \tag{4.22}$$

and

$$I3 = -6i\Delta_{e\mu}\Delta_{\mu\tau}\Delta_{\tau e}m^2_{\mu}m^4_{\tau}|m_{e\tau}|^2|m_{\tau\tau}|^2 ImQ_{(A1)^{VI}}. \tag{4.23}$$

Similarly, one can find the expressions for WB invariants for ansätze $A2^{IV}$, $A2^{V}$ and $A2^{VI}$ from $A1^{IV}$, $A1^{V}$ and $A1^{VI}$, respectively, by using the $\mu - \tau$ exchange permutation symmetry, as mentioned earlier.

The condition for CP invariance is similar for $A2^{IV}$ ($A2^{VI}$) as found for $A1^{IV}$ ($A1^{VI}$).

Ansatz C^{II}: The invariant I1 can be derived by using (4.1)

$$I1 = -6i\Delta_{e\mu}\Delta_{\mu\tau}\Delta_{\tau e}(|m_{e\mu}|^2 - |m_{e\tau}|^2)|m_{ee}|^2 ImQ_{C^{II}}, \tag{4.24}$$

where $Q_{C^{II}} \equiv m_{\mu\tau}m^*_{e\mu}$.
The Jarlskog rephasing invariant parameter J_{CP} can be written as

$$J_{CP} = \frac{(|m_{e\mu}|^2 - |m_{e\tau}|^2)|m_{ee}|^2 ImQ_{C^{II}}}{\Delta_{sol}\Delta^2_{atm}}. \tag{4.25}$$

From the above equation, it is explicit that $J_{CP} = 0$ might be due to $|m_{e\mu}| = |m_{e\tau}|$. Keeping in mind the texture zero condition for ansatz C^{II}, it can be inferred that Dirac

type CP symmetry is related to $\mu - \tau$ reflection symmetry (i.e. $m_{e\mu} = \pm m_{e\tau}, m_{\mu\mu} = m_{\tau\tau}$) [31, 32]. The other possibility for CP invariance arises if $m_{\mu\tau} = m_{e\mu}$ is considered.

Interestingly, it is found from the above equation that J_{CP} and $|m_{ee}|$ are strongly related to each other, i.e. $J_{CP} \propto |m_{ee}|^2$. This implies the parabolic relation between these experimentally measurable parameters, and further point out that the absence of neutrinoless double beta decay is related to $sin\delta = 0$ if other possibilities of CP invariance is relaxed.

The remaining invariants I2 and I3 can be written as

$$I2 = 2\Delta_{e\mu}\Delta_{\tau e}|m_{ee}|^2 ImQ_{C^{II}}, \tag{4.26}$$

and,

$$I3 = -6i\Delta_{e\mu}\Delta_{\mu\tau}\Delta_{\tau e}m_e^4(m_\mu^2|m_{e\mu}|^2 - m_\tau^2|m_{e\tau}|^2)|m_{ee}|^2 ImQ_{C^{II}}. \tag{4.27}$$

As already mentioned that CP invariants, I2 and I3, are sensitive to CP properties associated to Majorana nature of neutrinos. In the scenario of $\mu - \tau$ reflection symmetry, invariants I2 and I3 are non-zero and hence CP symmetry can be broken. This is contrary to the case of invariant I1, where CP symmetry can be preserved. Therefore, it can be stated that, for ansätz C^{II}, CP violation is attributed to only Majorana-type phases (ρ, σ) (and independent of Dirac-type phase δ), if $\mu - \tau$ reflection symmetry is assumed.

The CP invariance condition can be given as

$$arg(m_{\mu\tau}) = arg(m_{e\mu}). \tag{4.28}$$

Ansatz C^{IV}: Using (4.1), invariant I1 can be written as

$$I1 = -6i\Delta_{e\mu}\Delta_{\mu\tau}\Delta_{\tau e}(|m_{e\mu}|^2 - |m_{e\tau}|^2)|m_{e\tau}|^2 ImQ_{C^{IV}}, \tag{4.29}$$

where $Q_{C^{IV}} \equiv m_{ee}m_{e\mu}^*$.
The Jarlskog rephasing invariant can be written as

$$J_{CP} = \frac{(|m_{e\mu}|^2 - |m_{e\tau}|^2)|m_{e\tau}|^2 ImQ_{C^{IV}}}{\Delta_{sol}\Delta_{atm}^2}. \tag{4.30}$$

Again for $m_{ee} = m_{e\mu}$, $J_{CP} = 0$. Similar to ansätz C^{II}, $J_{CP} = 0$ can also hold if $\mu - \tau$ reflection symmetry is assumed.

The other invariants I2 and I3 can be written as

$$I2 = 2\Delta_{e\mu}\Delta_{\tau e}|m_{e\tau}|^2 ImQ_{C^{IV}} \tag{4.31}$$

and

$$I3 = -6i\Delta_{e\mu}\Delta_{\mu\tau}\Delta_{\tau e}m_e^4(m_\mu^2|m_{e\mu}|^2 - m_\tau^2|m_{e\tau}|^2)|m_{e\tau}|^2 ImQ_{C^{IV}}. \quad (4.32)$$

Similar arguments holds for the ansatz C^{IV} if $\mu - \tau$ reflection symmetry is considered, as discussed for ansatz C^{II}.

The CP invariance condition is given as

$$\arg(m_{ee}) = \arg(m_{e\mu}). \quad (4.33)$$

4.3 Summary and Conclusion

To summarize, I have constructed the three WB invariants in terms of neutrino mass matrix elements at low energy for hybrid textures of Majorana neutrinos with two texture zeros and an equality between the non-zero mass matrix elements in the flavour basis. From the above discussion, it is inferred that condition of either additional equality or texture zero in chosen ansatz automatically lead to CP invariance. This further implies that current hybrid texture model permits the maximum number of allowed choices of zeros and an equal elements, which contributes to CP violation. In addition, it is sufficient to assume one of the elements of mass matrix to be real, for the hybrid texture model to be CP invariant [(4.14), (4.19), (4.28) and (4.33)]. For illustration, if an element m_{ee} is considered real, or zero, which essentially implies that neutrinos are Dirac particle. The assumption simultaneously lead to vanishing imaginary part of $m_{e\mu}$, $m_{\mu\tau}$, $m_{\mu\mu}$ and $m_{\tau\tau}$, respectively [see (4.14), (4.19), (4.28),(4.33)]. Hence, the non-observation of neutrinoless beta decay in future experiments could imply that current hybrid texture is CP invariant.

The Dirac CP phase, which is sensitive to the CP violation in neutrino oscillation is contained in WB invariant I1, while invariants I2 and I3 are measures of Majorana-type CP phases, contribute to CP violation in neutrinoless double beta decay. However, it is explicit from the analysis, that all the three CP violating phases are not independent and there is only one physical phase in all the phenomenologically viable ansatze with two texture zeros and an equality between non-zero elements. However, Dirac and Majorana CP-type phases can not be distinguished in a concerned hybrid texture of Majorana mass matrix.

To conclude the discussion, I would like to point out that equalities derived in our analysis between the different neutrino mass matrix elements are found to have some profound connection with CP invariance pertaining to both LNC and LNV processes. Similar to the earlier analyses by Dev et al. [26, 27], it is maintained that there is only one physical phase which describes the CP properties in present model, while Dirac and Majorana phases can not be extracted without considering certain assumptions.

Conflicts of Interest The author declares that there are no conflicts of interest regarding the publication of this paper.

Acknowledgements The author would like to thank the Principal, M. N. S Government college, Bhiwani, for providing necessary facilities to work. Thanks to S. Dev and D. Raj for bringing forward the research work pertaining to new possibility of hybrid texture.

References

1. S.L. Glashow, Nucl. Phys. **22**, 597 (1961)
2. S. Weinberg, Phys. Rev. Lett. **19**, 1264 (1967)
3. A. Salam, *Proc. of the 8th Noble Symposium on Elementary Particle Theory, Relativistic Groups and Analyticity*, edited by N. Svartholm (1969)
4. H. Fritzsch, Gell-Mann and H. Leutwyler, Phys. Lett. B **4**, 365 (1973)
5. For excellent reviews on the Standard Model see, J.F. Dooghue, E. Golowich and B.R. Holstein, *Dynamics of the Standard Model* (Cambridge University Press, 1992)
6. N. Cabbibo, Phys. Rev. Lett. **10**, 531 (1963); M. Kobayashi and K. Maskawa, Prog. Theor. Phys. **B49**, 652 (1973)
7. M. Tanabashi et al. (Particle Data Group) Phys. Rev. D **98**, 030001 (2018), updated results available at http://pdg.lbl.gov/
8. J. Charles et al., CKM fitter Group, updated result available at http://www.ckmfitter.in2p3.fr/
9. A.J. Bevan et al. [Utfit Collaboration], JHEP **03**, 123 (2014), updated results available at http://www.utfit.org/
10. Y. Amhis et al., Heavy Flavor Averaging Group (HFAG), hep-ex/1207.1158 v2 (2013), updated results available at http://www.slac.stanford.edu/xorg/hfag/
11. R. Davis, Prog. Part. Nucl. Phys. **32**, 13 (1994); B.T. Cleveland et al., Astrophys. J. **496**, 505 (1998); S. Fukuda et al.,SuperKamiokande Collaboration, Phys. Rev. Lett. B **539**, 179 (2002); Q.R. Ahmad et al., SNO Collaboration Phys. Rev. Lett. **89**, 011301(2002); S.N. Ahmad et al., Phys. Rev. Lett. **92**, 181301 (2004)
12. Y. Fukuda et al., SuperKamiokande Collaboration, Phys. Rev. Lett. **81**, 1562 (1998); A. Surdo, MACRO Collaboration, Nucl. Phys. Proc. Suppl. **110**, 342 (2002); M. Sanchez, Soudan Collaboration, Phys. Rev. **D68**, 113004 (2003)
13. K. Eguchi et al., KamLAND Collaboration, Phys. Rev Lett. **90**, 021802 (2003); Phys. Rev. Lett. **94**, 081801 (2005)
14. M.H. Ahn et al., K2K Collaboration. Phy. Rev. Lett. **90**, 041801 (2003)
15. I. Esteban et al., JHEP **01**, 106 (2019). (arXiv: 1811.05487v1 [hep-ph])
16. H. Fritzsch, Z.Z. Xing, Phys. Lett. B **517** (2001) 363–368, arXiv: hepph/0103242
17. B. Pontecorvo, Zh. Eksp. Teor. Fiz. (JETP) **33**, 549 (1957); ibid. **34**, 257 (1958); ibid. **53**, 1717(1967); Z. Maki, M. Nakagawa, S. Sakata, Prog. Theor. Phys. **28**, 870 (1962)
18. P.H. Frampton, S.L. Glashow, D. Marfatia, Phys. Lett. B **536**, 79 (2002), hep-ph/0201008, Zhizhong Xing, Phys. Lett. B **530**, 159 (2002), hep-ph/0201151; J. Liao, D. Marfatia, K. Whisnant, arXiv:1311.2639 [hep-ph]; D. Meloni, A. Meroni, E. Peinado, Phys. Rev. D **89** (2014) 053009, arXiv:1401.3207 [hep-ph]; P. O. Ludl, W. Grimus, JHEP 07, 090 (2014), arXiv: 1406.3546 [hep-ph]
19. S. Dev, Radha Raman Gautam and Lal Singh, Phys. Rev. D **87**, 073011 (2013), arXiv: 1303.3092 [hep-ph]
20. J.-Y. Liu, S. Zhou, Phys. Rev. D **87**, 093010 (2013). (arXiv:1304.2334 [hep-ph])
21. S. Kaneko, H. Sawanaka, M. Tanimoto, JHEP **0508**, 073 (2005). (hep-ph/0504074)
22. L. Lavoura, Phys. Lett. B **609**, 317 (2005), hep-ph/0411232; E.I. Lashin, N. Chamoun, Phys. Rev. D **78**, 073002 (2008), arXiv:0708.2423 [hep-ph]; E.I. Lashin, N. Chamoun, Phys. Rev. D **80**, 093004 (2009), arXiv:0909.2669 [hep-ph]

23. J. Liao, D. Marfatia, K. Whisnant, JHEP **1409**, 013 (2014). (arXiv:1311.2639 [hep-ph])
24. Weijian Wang, Eur. Phys. J. C **73**, 2551 (2013). (arXiv:1306.3556 [hep-ph]; S. Dev, R.R. Gautam and Lal Singh, Phys. Rev. D 88, 033008 (2013), arXiv:1306.4281 [hep-ph])
25. S. Dev, D. Raj, Nucl. Phys. B **957**, 115081 (2020). (arXiv:2006.12019 [hep-ph])
26. S. Dev, S. Kumar, S. Verma, Phys. Rev. D **79**, 033011 (2009)
27. S. Dev, Shivani Gupta, R.R. Gautam. J. Phys. G **37**, 125003 (2010)
28. C. Jarlskog, Phys. Rev. Lett. **55**, 1039 (1985)
29. G.C. Branco, L. Lavoura, M.N. Rebelo, Phys. Lett. B **180**, 264 (1986)
30. G.C. Branco, M.N. Rabelo, J.I. Silva-Marcos Phys. Rev. Lett. **82**, 683 (1999)
31. P.F. Harrison, W.G. Scott, Phys. Lett. B **547**, 219 (2002). (arXiv: hep-ph/0210197)
32. W. Grimus, L. Lavoura, Phys. Lett. B **579**, 113 (2004). (arXiv: hep-ph/0305309)

Chapter 5
Characteristic Range of ^{238}U Ion in Polycarbonates

J. P. Gewali and M. Singh

Abstract Interaction of radiation with the matter has fascinated the researcher of different fields for many decades, and intensive studies have been done. It is found that they can withstand high temperatures and can easily discriminate the high energy radiation from background radiation. In this study, the stacks of Makrofol-E and CR-39 detector are irradiated with 16 meV/u ^{238}U ion. From the study, we could find that Makrofol-E and CR-39 detector (both of which are organic polymers, a product of carbon, hydrogen and oxygen, with variation in their composition and other parameters like density) shows almost the similar result for range and track length if irradiated with the same ion and with same energy. The detector has been irradiated at XO channel of UNILAC, GSI Dermstat Germany. The experimental data are compared with the theoretical data obtained from SRIM and DEDXT programs.

5.1 Introduction

It was Young [1] who first observed the tracks in LiF crystals. Heavy charged particle tracks in mica using electron microscope were observed by Silk and Barnes [2] in 1959. It was Fleischer, Price and Walker [3] in 1975 who did the pioneers work in the field of nuclear track detectors, which have a very broad scope in the modern world as it is very versatile due to its applications and accuracy. A couple of known solid-state nuclear detectors, for example, CR-39, cellulose nitrate, Lexan and ZnP-glass are very sensitive for the detection of heavy particles, because of their favorable properties like light weight, flexibility and their ability to discriminate against lightly ionizing particles. Also their properties to reveal the track of individual heavily ionizing particles by a simple etching technique give SSNTDs the advantage over other detectors [3, 4].

CR-39 ($\mathbf{C_{12}H_{18}0_7}$) or a poly allyl diglycol carbonate a highly sensitive SSNTDs detector where CR stands for Columbia Resin with its application in making of lenses was first discovered by Cartwright et al. [5]. This detector can detect charged

J. P. Gewali (✉) · M. Singh
Department of Physics, Lovely Professional University, Phagwara, Jalandhar, Punjab, India

S. Sengupta et al. (eds.), *Selected Progresses in Modern Physics*, Springer Proceedings in Physics 265, https://doi.org/10.1007/978-981-16-5141-0_5

particles from low-energy proton to relativistic uranium ions. Commercially, it is manufactured and marketed by Pittsburgh Plate Glass Company (PPG) of USA. CR-39 Detector of thickness 1500 μm is used in our study. Tarle et al. in 1981 [6] reported that for high Z nuclei, CR39 has a charge resolution superior to nuclear emulsions and ionization chambers of equivalent thickness. But it should be noted that the particle detection characteristics of CR-39 depend strongly on the etching and measuring procedures.

The shapes of tracks produced by heavy ions in Makrofol are needle-like with a slide spread toward their tail. They also offer a very convenient way of detecting heavy ions in the study of composition of heavy cosmic rays, heavy ions interaction, etc. Sheets of thickness ~400 μm are used in the present studies.

Both CR-39 and Makrofol nuclear track detectors have been successfully used as charged particle detectors. The nuclear track formation in polymer is a complex phenomenon and it totally depends on the charge and energy of incident ions. Here, we present our experimental outcomes on ranges of 16 meV/u ^{238}U in Makrofol-E foils and CR-39 as track detectors, respectively. Complex media like Makrofol-E and CR-39 have important applications in nuclear instrumentation. Therefore, it is desirous to study the range and stopping power of heavy energetic ions in these materials. In this section, we study the range of ^{238}U ions in different media. The results obtained are compared with the corresponding theoretical values in order to test the validity of our methodology and available theoretical data tables [4].

5.2 The Technique

The range and stopping power in complex media have been studied using the technique as explained in detail in the references [7–9]. In this technique, first, the detectors are calibrated at different ion energies by measuring its true track length experimentally. The detector itself is considered as both the target as well as the detector by considering a division into two segments. For comparison of the experimental data for range, two different theoretical predictions have been considered, these are (i) SRIM Programs by Ziegler [10] and (ii) DEDXT Programs by Mukherji and coworkers [11].

5.3 Result and Discussion

In this study, polycarbonates (Makrofol-E and CR-39) are used both as target and detector. We have found out the calibration curve from the incident ion energy and then using the target concept the energy loss curve is plotted. Using the energy loss curve, the range of ion is calculated in the detector.

For ^{238}U ion, incident on Makrofol-E calibration curve is shown in Fig. 5.1 where the variation of ion energy and its corresponding track length are depicted. Figure 5.2

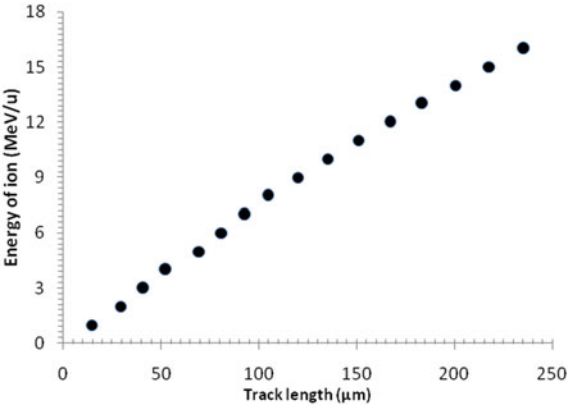

Fig. 5.1 Calibration curve 16.3 meV/u ^{238}U ion in Makrofol-E

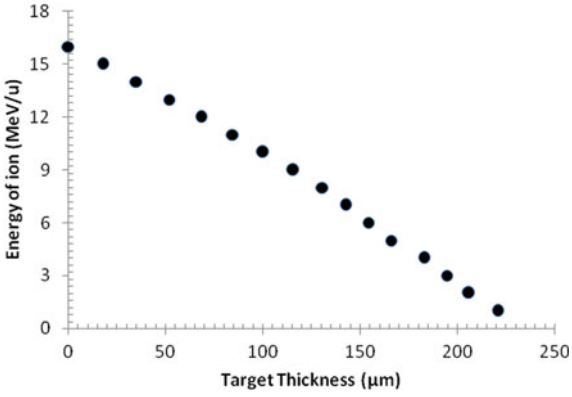

Fig. 5.2 Energy loss curve of ^{238}U ion in Makrofol-E as a target

shows the energy loss curve for ^{238}U in Makrofol-E, which is used as target. The mean range obtained from energy loss curve for 16.3 meV/u ^{238}U in Makrofol-E is equal to 230.8 $\pm$ 3.3 μm and is reported in Table 5.1. The range of ^{238}U in Makrofol-E is also obtained at several lower energies using energy loss curve and is given in Table 5.1 along with corresponding theoretical values from SRIM [10] and DEDXT [11]. The plot of range energy variation for ^{238}U in Makrofol-E is shown in Fig. 5.3 along with corresponding theoretical values from DEDXT [10] and SRIM [11]. Experimental range data follow much closer to the popular SRIM program as compared with that of the obscure DEDXT predictions.

The calibration curve for ^{238}U ion CR39 is represented in Fig. 5.4, which shows the variation of energy with track length. Variation of ^{238}U ion energy with CR39 target thickness also called the energy loss curve is represented in Fig. 5.5. The mean range obtained from energy loss curve for 15.4 meV/u ^{238}U in Cr-39 is equal to 219.4 $\pm$ 3.3 μm and is reported in Table 5.2. The range of ^{238}U in CR-39 is also obtained at several lower energies using energy loss curve and is given in Table 5.2 along with the corresponding theoretical values from SRIM [10] and DEDXT [11]. The

Table 5.1 Values of Makrofol-E target thickness, maximum etchable track length of ^{238}U in Makrofol-E detector, energy of the transmitted and absorbed energy and the ranges obtained in Makrofol-E, along with the corresponding theoretical values

Effective target thickness	Track length	Ion energy (MeV/u)		Range (μm)		
(μm)	(μm)	Transmitted	Absorbed	Experiment	DEDXT	SRIM
0.0	235.45 ± 1.1	16.3 ± 0.3	0	230.8 ± 3.3	274.21	264.52
17.7	217.78 ± 1.1	15.2 ± 0.3	1.1	213.13 ± 2.9	264.91	246.85
35.0	200.5 ± 1.3	14.2 ± 0.3	2.1	195.85 ± 2.8	246.68	229.57
51.8	183.61 ± 0.9	13.3 ± 0.3	3.0	178.96 ± 2.9	228.98	212.68
68.3	167.11 ± 1.3	12.4 ± 0.3	3.9	162.46 ± 3.0	211.78	196.18
84.5	150.99 ± 1.2	11.1 ± 0.3	5.2	146.34 ± 2.4	195.07	180.06
100.2	135.23 ± 0.8	10.2 ± 0.3	6.1	130.58 ± 2.6	178.95	164.3
115.6	119.81 ± 0.6	9.1 ± 0.3	7.2	115.16 ± 1.2	164.82	148.88
130.7	104.72 ± 0.5	8.1 ± 0.3	8.2	100.07 ± 1.1	151.01	133.79
142.6	92.85 ± 0.5	7.2 ± 0.3	9.1	88.20 ± 1.1	137.47	121.92
154.3	81.14 ± 0.4	6.3 ± 0.3	10.0	76.49 ± 1	124.12	110.21
165.9	69.57 ± 0.4	5.3 ± 0.3	11.0	64.92 ± 1.1	110.8	98.64
183.1	52.35 ± 0.4	4.1 ± 0.3	12.2	47.70 ± 1.5	97.22	81.42
194.6	40.88 ± 0.3	3.2 ± 0.3	13.1	36.23 ± 1.3	82.63	69.95
206.1	29.32 ± 0.3	2.1 ± 0.3	14.2	24.67 ± 0.9	65.11	58.39
221.0	14.47 ± 0.2	1.1 ± 0.3	15.2	9.82 ± 1.3	43.06	43.54

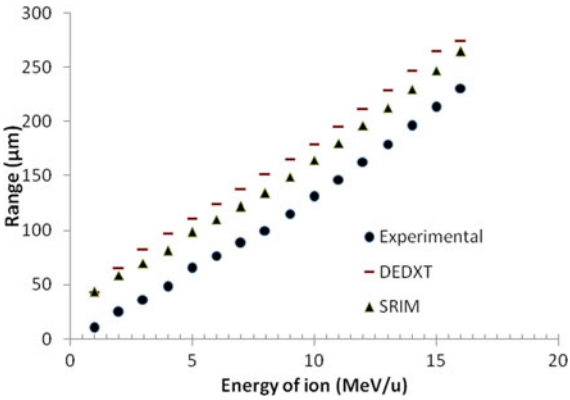

Fig. 5.3 Measured range energy data for ^{238}U in Makrofol-E along with the theoretical values

plot of range energy variation for ^{238}U in Cr-39 is shown in Fig. 5.6 along with the corresponding theoretical values from SRIM [10] and DEDXT [11]. Experimental range data follow much closer to the popular SRIM program as compared with that of the obscure DEDXT predictions.

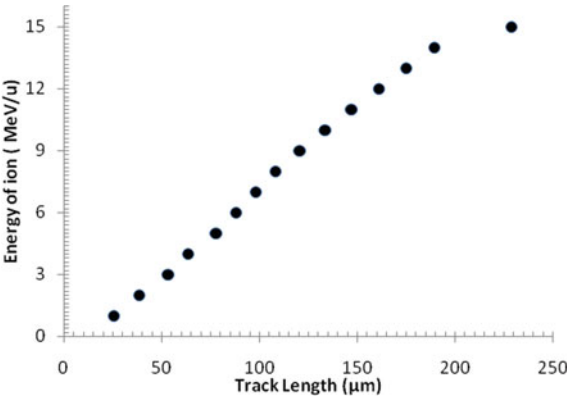

Fig. 5.4 Calibration curve of ^{238}U in CR-39

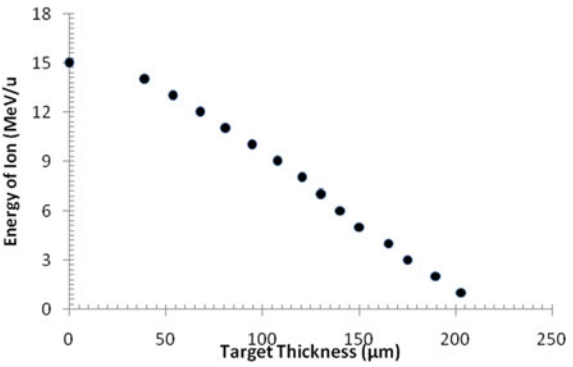

Fig. 5.5 Energy loss curve of ^{238}U in CR-39

5.4 Conclusion

Both Makrofol-E and CR-39 are polycarbonate detectors with carbon, hydrogen and oxygen as variable constituents. The same ion incident on the detector produces almost the similar track length and range with a little bit of deviation. Approximately, the same track length and range of ~215 μm are measured for both the studied detector incident with ion energy of ~15 meV/u. Thus, we can conclude that the behavior of both the detector is similar under studied conditions.

Table 5.2 Values of CR-39 target thickness, maximum etchable track length of ^{238}U in CR-39 detector, energy of the transmitted and absorbed energy, the ranges obtained in CR-39, along with the corresponding theoretical values

Effective target thickness (μm)	Track length (μm)	Ion energy (MeV/u)		Range (μm)		
		Transmitted	Absorbed	Experimental	DEDXT	SRIM
0.0	228.5 ± 1.2	15.4 ± 0.3	0	219.36 ± 2.3	228.78	210.8
39.3	189.18 ± 1.0	14.3 ± 0.3	1.1	180.04 ± 3.1	213.04	196.09
53.7	174.84 ± 0.9	13.1 ± 0.3	2.3	165.7 ± 2.8	197.75	181.75
67.7	160.83 ± 0.9	12.2 ± 0.3	3.2	151.69 ± 2.6	182.9	167.74
81.3	147.17 ± 1.0	11.2 ± 0.3	4.2	138.03 ± 2.8	168.47	154.08
94.7	133.81 ± 0.7	10.3 ± 0.3	5.1	124.67 ± 2.1	154.55	140.72
107.8	120.75 ± 0.5	9.3 ± 0.3	6.1	111.61 ± 1.7	142.34	127.66
120.6	107.95 ± 1.2	8.2 ± 0.3	7.2	98.81 ± 1.6	130.41	114.86
130.6	97.88 ± 0.9	7.4 ± 0.3	8.0	88.74 ± 1.4	118.72	104.79
140.6	87.92 ± 0.5	6.4 ± 0.3	9.0	78.78 ± 1.2	107.19	94.83
150.5	78.05 ± 0.7	5.3 ± 0.3	10.1	68.91 ± 1.2	95.69	84.96
165.2	63.33 ± 0.4	4.2 ± 0.3	11.2	54.19 ± 0.9	83.96	70.24
175.0	53.49 ± 0.6	3.2 ± 0.3	12.2	44.35 ± 0.8	71.36	60.4
190.0	38.53 ± 0.9	2.1 ± 0.3	13.3	29.39 ± 0.9	56.23	45.44
203.1	25.4 ± 0.4	1.2 ± 0.3	14.2	16.26 ± 1.1	37.19	32.31

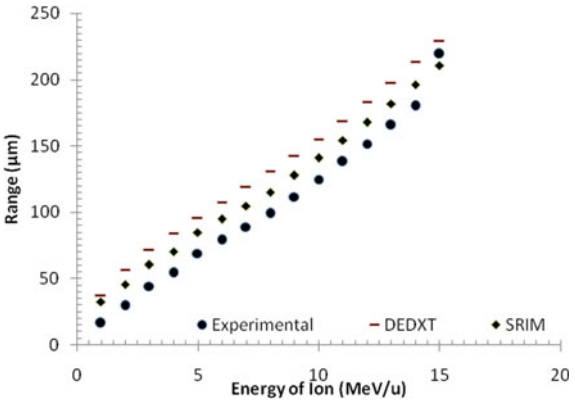

Fig. 5.6 Measured range energy data for ^{238}U in CR-39 along with the theoretical values

References

1. D.A. Young, Etching of radiation damage in lithium fluoride. Nature **182**, 375 (1958)
2. E.C.H. Silk, R.S. Barnes, Examination of fission fragment tracks with an electron microscope. Philos. Mag. **4**, 970 (1959)

3. R.L. Fleischer, P.B. Price, R.M. Walker, *Nuclear Tracks in Solids, Principles and Applications* (University of California Press, Berkeley, 1975)
4. J.P. Gewali, Studies on heavy ion electronic stopping power and thermal fading characteristics of nuclear tracks in solid state nuclear detectors, Ph.D. thesis, North-Eastern Hill University, Shillong, India, (2014)
5. B.G. Cartwright et al., Nucl. Instrum. Meth. **153**, 457 (1978)
6. G. Tarle, 17th Int. Cosmic Rays Conf. Paris **8**, 174 (1981)
7. J.P. Gewali et al., Eur. J. Mol. Clin. Med. **7**, 3493 (2020)
8. J.P. Gewali, A. Saxena, J. Phys. Conf. Ser. **1531**, 012040 (1999)
9. J.P. Gewali, B. Jaishy, A. Saxena, AIP Conf. Proc. **2050**, 020012 (2018)
10. J.F. Ziegler, M.D. Ziegler, J.P. Biersack, Nucl. Instrum. Methods Phys. Res. Sect. B **268**, 1818 (2010)
11. K.K. Dwivedi, Int. J. Radiat. Appl. Instrum Part D **15**, 345 (1998)

Chapter 6
Comparison of Protein Interaction with Different Shaped PbS Nanoparticles and Corona Formation

A. K. Mishra, A. K. Bhunia, and S. Saha

Abstract Different shaped PbS nanoparticles are synthesized at room temperature by using reagents, lead chloride ($PbCl_2$), sulfur powder (S), and sodium borohydride ($NaBH_4$), in the ethylenediamine medium. $NaBH_4$ has acted as a reducing agent, whereas ethylenediamine is used as a capping agent. The grown PbS nanoparticles are spherical (7 nm size) for the reagent ratio of $PbCl_2$, S, $NaBH_4$ as 1:1:1. and grown PbS nanoparticles are cubical shape (13 nm size) for the reagent ratio of $PbCl_2$, S, $NaBH_4$ as 1:1:3. The grown PbS nanoparticles are characterized structurally and optically. The interaction and formation of the bio-conjugate of bovine serum albumin with PbS nanomaterials are studied for biomedical application. The interaction, complexion process, and conformational changes of bovine serum albumin with PbS nanomaterials are quantified by the photophysical and structural study. PbS nanomaterials enable the aggregation of bovine serum albumin by the way of unfolding. The interaction and the bioconjugate formation of albumin with PbS nanoparticles are investigated using optical spectroscopy, TEM. UV–VIS–NIR shows the binding process that occurred between albumin and PbS samples.

6.1 Introduction

Now the recent trend of using nanotechnology increases more and more in the field of agriculture, biomedicine, packaging, cosmetics, and also in textiles. There are possibilities that these nanoparticles (NPs) are entering living organ cells through various natural processes like the food chain, respiration, etc. NPs are not used for biological imaging due to optical emission in the infrared region as many proteins strongly absorb visible light, so there is a limitation in the depth of penetration around few millimeters in the small wavelengths region. Another biological complex like

A. K. Mishra (✉) · S. Saha
Department of Physics, Vidyasagar University, Paschim Medinipur, Midnapore, West Bengal 721102, India

A. K. Bhunia
Department of Physics , Government General Degree College at Gopiballavpur-II , Jhargram, Beliaberah, West Bengal 721517, India

S. Sengupta et al. (eds.), *Selected Progresses in Modern Physics*, Springer Proceedings in Physics 265, https://doi.org/10.1007/978-981-16-5141-0_6

water and lipids strongly absorbs infrared light [1, 2]. PbS semiconducting NPs are an important IV–VI group due to their near-infrared (NIR) fluorescence property for bio-imaging applications. PbS semiconducting quantum dots with diameters between 3 and 6 nm show an emission wavelength in the NIR region. So PbS NPs have been projected as one of the best potential materials for application in various biomedical detection of animal studies [3]. Only 10–15 proteins may take part in protein corona formation from thousands of proteins in physiological conditions [4–8], that is, the exchange of soft corona proteins by hard corona proteins [9–11]. This hard protein corona helps the NPs in intracellular signaling due to longer life and also identifies the role of NPs in biological fluid [12]. This nano–bio interaction of different shaped PbS NPs is important in nanomedicine research due to physicochemical properties. The PbS NPs surface area surrounded by an assembly of proteins is known as protein corona and their complex is called the protein–PbS NPs complex. The protein corona formation process is playing a vital role in the functioning of PbS NPs in the biological system. The native structure of protein shows conformational change due to the interaction of PbS NPs with protein. This vibrant and driving process changes the functioning of protein for cellular interaction with PbS NPs [13, 14]. Yin et al. [15] evaluated the cytotoxic behavior of bared and protein-coated ZnO NPs against human hepatocellular carcinoma (HepG2) cells and they found that bare ZnO NPs at a concentration range of 20 mg L^{-1}–100 mg L^{-1} reduced the cell viability by 90–15%, whereas for protein-coated ZnO NPs, cell viability was reduced by only 5–15% even at 100 mg L^{-1} concentration. They proposed that the higher binding strength between protein and NPs prevented the generation of reactive oxygen species (ROS) due to which protein-coated ZnO NPs showed less cytotoxicity. Medina et al. [16] evaluated the role of protein concentration (BSA) on the NPs toxicity, protein adsorption, and NPs accumulation. They compared the intracellular uptake of gold nanorods coated with a cationic agent mercaptoundecyltrimethylammonium bromide (MUTAB-AuNRs) in MCF-7 cancer cells. They incubated the MUTAB-AuNRs directly in 10% fetal bovine serum (FBS) and compared it with MUTAB-AuNRs preincubated (1% BSA) with a low concentration of BSA (1%) and reported that preincubation in 1% BSA increased the intracellular uptake by three times. It could be due to the lower concentration of BSA (in comparison to physiological conditions), which has increased the entry of AuNRs into MCF-7 cancer cells. Luminescence correlation spectroscopy and UV–visible spectroscopy analysis suggested that the concentration of preincubation played an important role in the correlation decay and the agglomeration of NPs. Hence, diagnostics tests based on this corona analysis will become more efficient than the ordinary running biochemical test. So different techniques can be applied for the analysis of protein corona to get information on molecular consequence due to contact of PbS NPs. C. Vidaurre-Agut et al. [17] found that diagnostic tests which performed depending on proteomics analysis have more advantage than traditional biochemical tests. It is difficult to identify protein biomarkers which have a low molecular weight (MW) by standard mass spectrometer because these are normally at low concentrations and are masked by actual abundant resident proteins. They showed that mesoporous silica NPs were able to capture low MW protein comparatively better than the protein

corona (PC) adsorbed onto dense silica NPs from serum. They further investigated this effect using liquid chromatography − mass spectrometry (LC–MS) and thermogravimetric analysis (TGA) and compared the MW of the proteins in the coronas of mesoporous silica NPs with the same particle size but different pore diameters. They also examined the process by which two proteins, one small and one large, adsorb onto these mesoporous silica NPs to establish a theory of why the corona became enriched in low MW proteins. They developed a novel system for the diagnosis of prostate cancer and this was applied to LC − MS protein coronas from the serum of 22 cancer patients, identifying proteins specific to each patient group. They explained why low MW proteins predominate in the coronas of mesoporous silica NPs, and they illustrated the ability of this information to supplement more traditional diagnostic tests.

Experimental observation is carried out to understand the protein–PbS NPs complex for well-suited NPs with surface characterization for better biological application. The interaction of PbS NPs with bovine serum albumin (BSA) is studied and the bio-safety of exposed PbS NPs is determined. The "hard" and "soft" protein PbS NPs corona formation is represented by the interaction of PbS NPs with protein.

6.2 Experimental Section

The PbS NPs were synthesized by anhydrous lead chloride ($PbCl_2$) (99.999%), sulfur powder (99.999%), and an amount of sodium borohydride ($NaBH_4$) (99%). The ratio of a reagent was calculated assuming that all of the reagents are consumed but there is no excess of reagents in reaction completion. The ratio was calculated by the amount of mass multiplied by the molar mass of each reactant to the no of molecules required for each reactant per mole of reaction. In this method, $NaBH_4$ is used as a reducing agent to initiate the reaction between $PbCl_2$ and S at room temperature (25 C). Ethylenediamine (EDA) was used as a solvent. At first, an amount of 2.78 g $PbCl_2$ was dissolved in 50 ml of EDA. This solution was taken in a beaker and was stirred vigorously by using a magnetic stirrer. After 30 min, 0.32 g of sulfur was added to the above solution. Finally, 0.37 g and 1.11 g of $NaBH_4$ were added to two beakers, respectively, by taking the same amount of the above mixture to get grown PbS samples of different ratios. The solution was stirred for 4 h keeping the particular speed for all samples. The solution was turned into a black color. This was an indication of the formation of PbS NPs. The residue product of grown samples was washed with distilled water several times. Finally, the product samples were centrifuged and were kept for 2 weeks in a clean dry place at room temperature. The chemical reaction for PbS NPs preparation is given below

$$PbCl_2 = Pb^{+2} + 2Cl^-$$

$$NaBH_4 + 2Cl^- = NaCl + B_2H_6 + 2H + 2e^-$$

$$2H + S = H_2S$$

$$H_2S + Pb^{+2} + 2e^{-} = PbS + H_2$$

The grown PbS NPs were dispersed in deionized water by ultrasonication for 30 min. The PbS NPs concentration was varied from 0.01 mg/mL to 0.06 mg/mL. Now for the PbS–BSA-mixed solutions preparation, 0.1 mg/mL BSA is mixed with PbS NPs ranging from 0.01 to 0.06 mg/mL with proper ratio.

High-resolution Rigaku Mini Flex X-ray Diffractometer was used to get the X-ray diffraction (XRD) pattern of powder PbS nanosamples. Transmission electron microscopy (TEM) was done by JEOL-JEM-2100. The carbon-coated copper grid was taken and a solution sample of PbS NPs was dropped on it after properly disperse in distilled water medium and dried in the dust-free region. Scanning electron microscopy (SEM) image of powder PbS nanosamples obtained by JEOL-JSM 5800. Agilent Technologies Cary 5000 Series UV–VIS–NIR Spectrophotometer is used to obtain Optical absorption spectra of PbS nanosamples and conjugate solution with BSA immediately after ultrasonication concerning deionized water.

6.3 Result and Discussion

6.3.1 Absorption Study

The absorption spectra of tryptophan (TRY) of BSA with different concentrations of the different shaped PbS NPs and pure PbS NPs.

The absorption peak for TRY of BSA is seen at 280 nm in Fig. 6.1. This transition may correspond to π–π* transition of aromatic amino acid residues [18, 19].

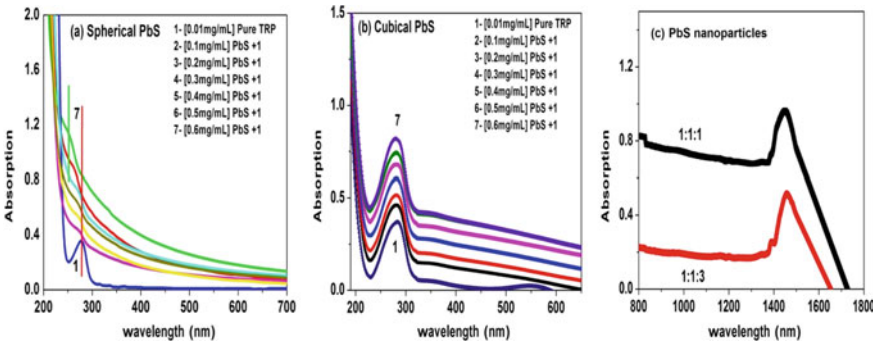

Fig. 6.1 Shows the absorption spectra of (a) tryptophan (TRY) of BSA with spherical PbS, (b) tryptophan (TRY) of BSA with cubical PbS, and (c) pure PbS NPs

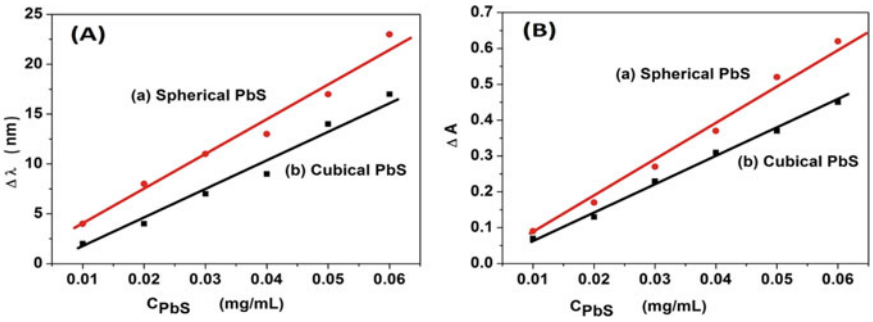

Fig. 6.2 Shows the plots of (A) C_{PbS} vs change in wavelength ($\Delta\lambda$) and (B) C_{PbS} vs change in absorbance (ΔA) for different shaped PbS NPs

The effect of binding of PbS NPs with concentrations ($C_{PbS} = 0.01$–0.06 mg/ml) with BSA ($C_{BSA} = 0.1$ mg/mL) is shown in Fig. 6.2.

These results show that the absorbance of TRY of BSA increases with the increment of C_{PbS} in Fig. 6.1. This intensity of absorbance of BSA gradually increases with C_{PbS}, due to the binding of BSA with PbS NPs and the formation of the ground state complex [20]. The absorption band of BSA is red-shifted gradually with an increment of C_{PbS}. This also confirms that PbS NPs interact with BSA through TRY and induces the conformational change of BSA [21]. The plots of C_{PbS} vs change in wavelength ($\Delta\lambda$) and C_{PbS} vs change in absorbance (ΔA) is shown in Fig. 6.2.

The plots of C_{PbS} vs change in wavelength ($\Delta\lambda$) are linear fit and C_{PbS} vs change in absorbance (ΔA) is shown that the interaction of BSA with PbS NPs increases with the increase of C_{PbS}.

In the equilibrium condition, the complex formation between PbS NPs and protein is given by the equation, where K_{app} is the apparent association constant.

$$K_{app}$$

$$\text{Tryptophan (Protein)} + \text{PbS nanoparticles} = \text{Protein.....PbS nanoparticles}$$

$$\text{Kapp} = \frac{[\text{Protein.....PbS nanoparticles}]}{[\text{Protein}][\text{PbS nanoparticles}]}$$

These K_{app} values are obtained using Benassi and Hildebrand method [19] and the equation is also given as

$$J_{obs} = (1 - \alpha)\, A_0 + \alpha\, A_c$$

Where A_{obs} is the value of absorbance of TRY (Protein) solution with different concentrations of PbS NPs and α is the degree of association between TRY (Protein)

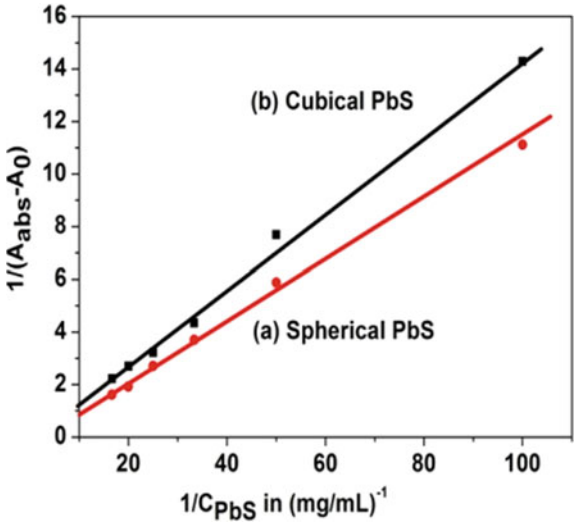

Fig. 6.3 Shows the plot of $\frac{1}{\text{Aobs}-\text{A0}}$ versus $1/C_{PbS}$ for different shaped PbS NPs

solution with PbS NPs. Here, A_0 and A_c are the absorbances of TRY (Protein) and complex of Protein and PbS NPs. This equation also can be written as

$$\frac{1}{\text{Aobs} - \text{A0}} = \frac{1}{\text{Ac} - \text{A0}} + \frac{1}{(\text{Ac} - \text{A0})\text{Kapp}[\text{CPbS}]}$$

Therefore, the plot of $\frac{1}{\text{Aobs}-\text{A0}}$ versus $1/C_{PbS}$ is linear fit with the slope $\frac{1}{(\text{Ac}-\text{A0})\text{Kapp}}$ and intercept to the axis is $\frac{1}{\text{Ac}-\text{A0}}$. From these data, K_{app} is also calculated.

The plot of $\frac{1}{\text{Aobs}-\text{A0}}$ versus $1/C_{PbS}$ for different shaped PbS NPs are shown in Fig. 6.3.

The absorption spectra show peaks at NIR and UV region for PbS NPs and BSA solution, respectively. The photoluminescence spectra of different shaped PbS NPs show emission in the NIR region. whereas the UV region for BSA protein [15].

PbS NPs come in contact with BSA and are surrounded by protein molecules. PbS NPs form a dynamic layer of proteins on the surface after getting associated with the BSA. Hence, *"NPs − protein corona"* is formed by this conjugated system[13, 22]. The change in absorbance intensity (ΔA) of BSA with $C_{BSA} = 0.1$ mg/mL is shown in Fig. 6.2(B) to detect the corona formation, and conformational changes of BSA are seen in the presence of PbS NPs. The change in absorbance intensity of BSA increases with PbS NP concentrations as well as decreases with the increase of PbS NP size.

It is confirmed from the exponential association mechanism that the "PbS NPs-BSA" corona formation starts just after incorporation of PbS NPs into BSA, whereas it is continued for a very long time to unfold the BSA. Hence, the BSA takes a long time to shield the PbS NPs surface with confirmation change and the BSA is unfolded [23–25]. The hard corona [22] is formed. The change of absorption intensity of BSA

(ΔA) in interaction with PbS NPs (C_{PbS} = 0.1 mg/mL to 0.6 mg/mL (Fig. 6.2(B)) shows a linear fit. The PbS NPs–BSA corona is formed at an inner layer of unfolded BSA using a slow exchange rate with free BSA (hard corona) whereas an outer layer of weakly bound BSA which follows linear kinetics and regarded as a faster exchange rate with free BSA (soft corona) [26–29].

6.3.2 XRD Study

The XRD pattern of the different shaped PbS NPs is shown in Fig. 6.4.

The X-Ray diffraction pattern is used to study the structural phase of the grown PbS NPs. The X-ray diffraction is taken with an angular range (2θ) from 20 to 80 degrees. The prominent diffraction peaks are (111), (2 00), (22 0), (311), (222), (400), (331), (420) correspond to pure face-centered cubic (FCC) phase (JCPDS # 05–0592) of the unit cell of PbS NPs. These planes are well matched with the standard crystal planes (111), (2 00), (22 0), (311), (222), (400), (331), (420) for diffraction angle 20–80° according to JCPDS no. 05–0592 [30, 31]. The highest intensity and sharp peak prove the well crystalline nature of grown PbS NPs. The size of PbS samples obtained from the Debye–Scherrer equation [31], D = 0.9 **λ** /(β COSθ), where D is particle size in nm**,** **λ** is the X-ray wavelength in nm, θ *is*, the diffraction angle in degrees, and β is the maximum peak width in half-height. The grown spherical PbS NPs are 7 nm in size and grown cubical shape PbS NPs are 13 nm in size.

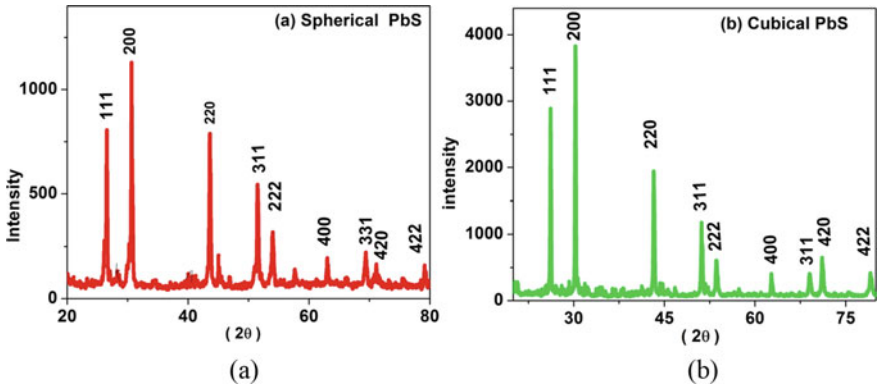

Fig. 6.4 Shows the XRD pictures of (a) spherical-shaped PbS NPs, (b) cubical PbS NPs

6.3.3 TEM Study

TEM pictures of spherical-shaped PbS NPs, corona formation with BSA, and SAED pattern are shown in Fig. 6.5.

There are shown in the figure the hard and soft corona structures formed by spherical-shaped PbS NPs under experimental conditions. The hard corona is represented by the inner blackish core. The *soft corona*" formation is represented by the outer fractal layer of BSA which is loosely bound with "*hard corona*". The hard coronas that almost spherical PbS NPs with a diameter of 260 nm are strongly attached to BSA. The image of a hard corona is shown by the arrow mark. This image represents that the core PbS NPs are fully covered with BSA along with a shell thickness of 7.5 nm which is matched with a dimension of BSA with 8 nm, calculated from protein data bank [6].

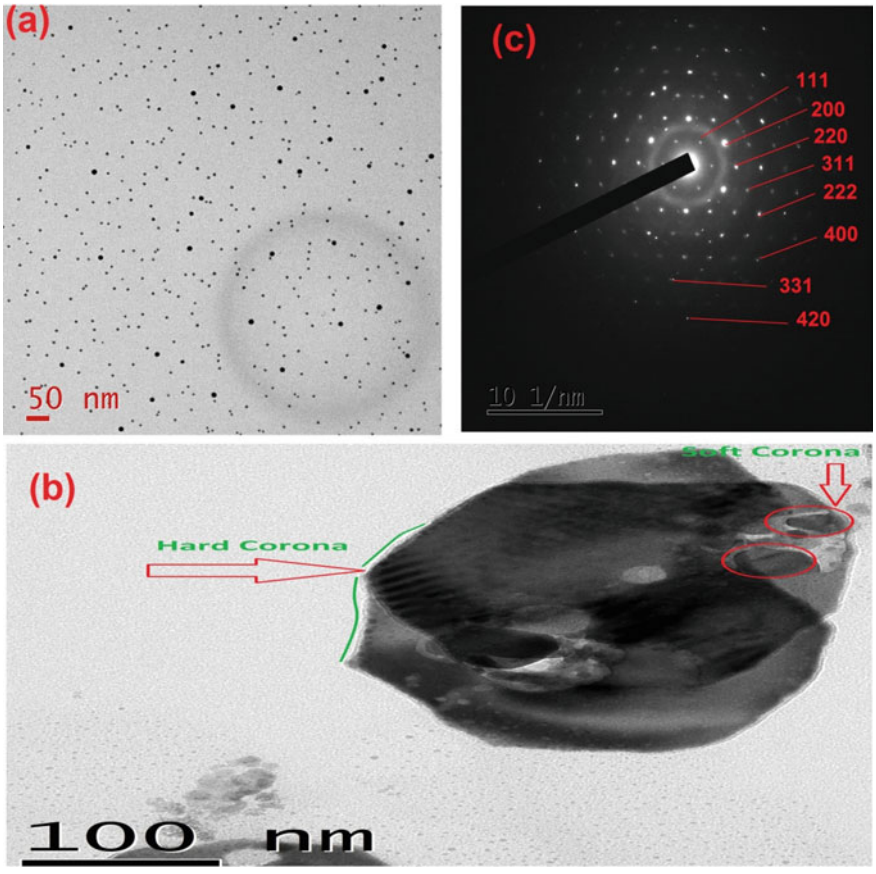

Fig. 6.5 Shows the TEM pictures of (a) spherical-shaped PbS NPs, (b) corona formation with BSA, and (c) SAED pattern

The SAED pattern of PbS NPs confirms the single crystalline nature. PbS samples have a face center cubic structure. The diffraction planes in the SAED pattern are equivalent to the diffraction planes of the XRD pattern.

TEM pictures of cubic-shaped PbS NPs, corona formation with BSA, and SAED pattern are shown in Fig. 6.6.

The TEM picture shows the formation of BSA–cubical PbS NPs hard and soft corona.

A large number of PbS NPs with a hard corona of BSA forms a "*colony*" with 280 nm × 290 nm dimensions. The soft corona also forms in this colony. The TEM picture supports the findings which are observed from absorption kinetics. The dimension of the BSA monomer matched with the shell thickness of BSA on the core of PbS NPs confirms the attachment of BSA with PbS NPs.

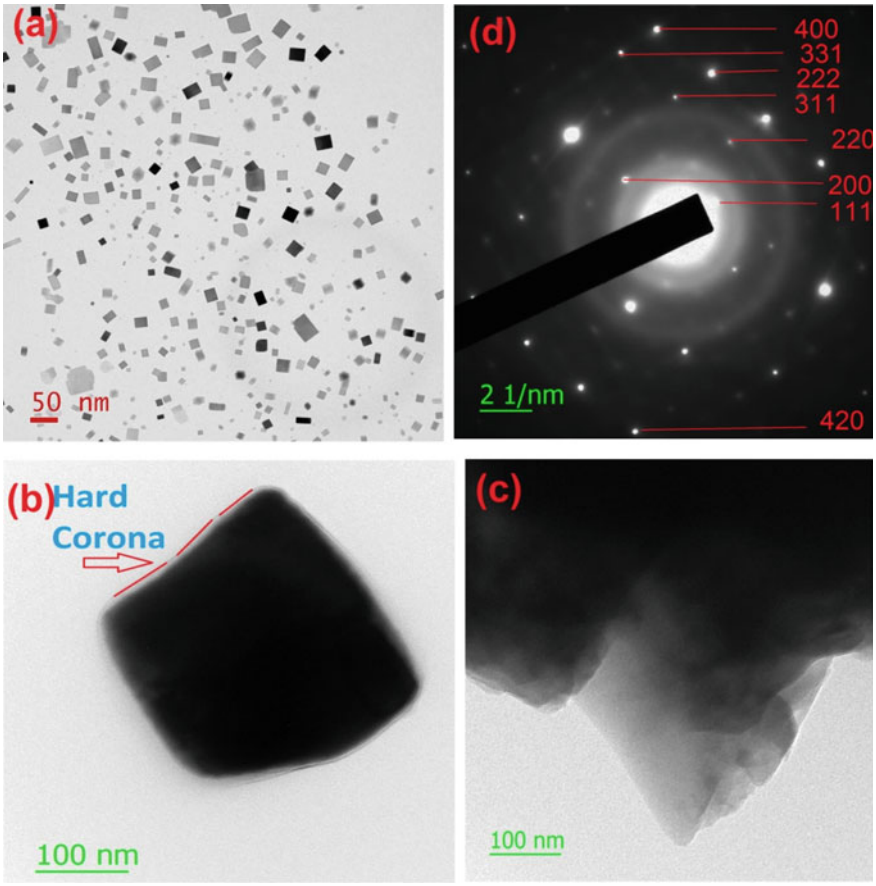

Fig. 6.6 Shows the TEM pictures of (a) cubic-shaped PbS NPs, (b, c) corona formation with BSA, and (d) SAED pattern

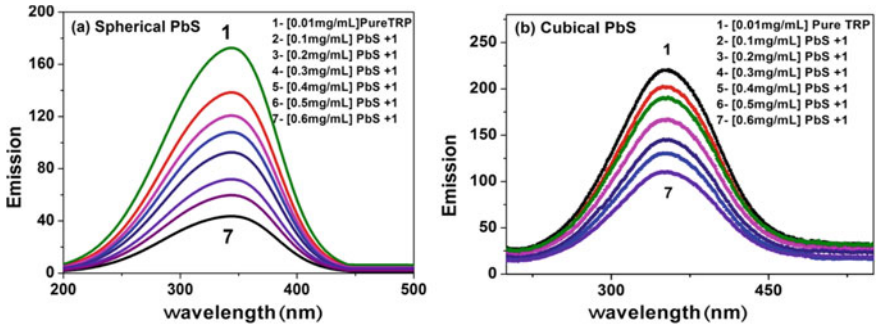

Fig. 6.7 Shows the emission spectra of tryptophan (TRY) of BSA with different concentrations of the (a) spherical PbS and (b) cubical PbS NPs

6.3.4 Emission Study

The emission spectra of TRY of BSA with different concentrations of the different shaped PbS NPs are shown in Fig. 6.7.

The PbS NPs–BSA-binding kinetics and conformational change of BSA are analyzed by fluorescence quenching measurements. The different concentrations of different shaped PbS NPs (C_{PbS} = 0.01–0.06 mg/mL) are added to BSA (C_{BSA} = 0.1 mg/mL) at room temperature and a change in the maximum intensity (I_{max}) of the fluorescence emission spectrum is observed. It is proved that the fluorescence quenching process has occurred. It also shows a maximum blue shift of about 5 nm is found with C_{PbS} = 0.06 mg/ml and C_{BSA} = 0.1 mg/mL due to hydrophobic interaction with PbS NPs. The binding of BSA with PbS NPs is analyzed by the popular Stern–Volmer equation [16].

$$\frac{F_0}{F} = K_{SV}[Q] + 1$$

F_0 and F are represented by the steady-state fluorescence intensities of fluorophore in the absence and presence of PbS NPs, respectively. K_{SV} is known as the Stern–Volmer quenching constant and [Q] represents the concentration of PbS NPs. The values of K_{SV} for different shaped PbS NPs are summarized in Table-1. The decrease of K_{SV} with increasing particle size signifies that the quenching mechanism of BSA is a dynamic quenching process in presence of PbS NPs and the strength of interaction increases with a decrease in particle size.

The plots of F_0/F versus $[Q(\mathrm{C_{PbS}})]$ and $ln\left[\frac{F_0-F}{F}\right]$ versus $ln[Q(\mathrm{CPbS}]$ for different shaped PbS NPs is shown in Fig. 6.8.

The binding constant K and the number of binding sites (n) between BSA and different shaped PbS NPs are calculated using the following equation [16]:

$$\ln\left[\frac{F_0 - F}{F}\right] = \ln K + nln[Q(CPbS)] \tag{6.1}$$

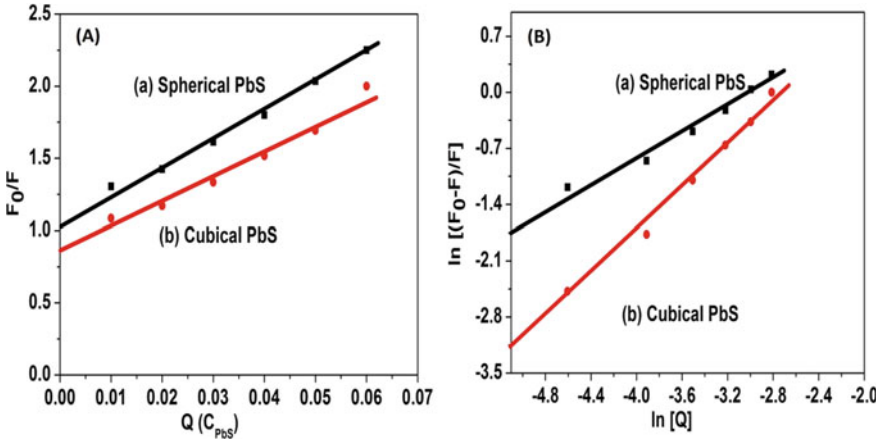

Fig. 6.8 Shows the plot of (A) F_0/F versus $Q(C_{PbS})$, and (B) $ln[\frac{F_0-F}{F}]$ versus $ln[Q(\text{CPbS}]$ for different shaped PbS NPs

Table 6.1 Comparison of parameters derived from bioconjugate analysis of BSA with PbS NPs

	K_{app}	K_{SV}	K	n
Spherical PbS NPs	7.9	19.9	23.6	1.28
Cubical PbS NPs	7.5	17.3	13.4	0.85

The plot of $ln\left[\frac{F_0-F}{F}\right]$ versus $ln[Q(C\text{PbS})]$ is a linear fit and the number of binding sites (n) is calculated from the slope of this graph.

The intercept of the straight line on the Y-axis determines the value of ln K.

The different characteristics values of bioconjugate analysis of BSA with different shaped PbS NPs are summarized in Table 6.1 and compared.

In favor of positive cooperative reaction, n > 1, reveals that once one protein molecule is bound to the NPs, its affinity for the NPs gradually increases in a super-linear fashion. However, in the case of a negative cooperative reaction, $n < 1$, the binding strength of the protein with the NPs becomes weaker as further proteins adsorb also for a non-cooperative reaction, $n = 1$ [17–22]. In the case of cubic PbS NPs, the negative cooperative reaction with BSA is found. However, for spherical PbS NPs, a positive cooperative reaction with BSA is found. Therefore, the affinity of BSA to the PbS NPs gradually increases in a superlinear fashion, which also supports the observation obtained from HRTEM images.

The interaction PbS NPs with TRY is studied to investigate the probable binding sites of BSA with PbS NPs. The value of n in case of interaction of PbS NPs with TRY for spherical PbS NPs almost matched with the PbS NPs–BSA complex. Therefore, TRY are the probable binding sites of BSA with PbS NPs as well as its affinity to PbS NPs increases with the decrease of NP size.

6.4 Conclusion

Simple chemically synthesized PbS NPs show the lowest energy excitonic band edge transition and emission in the NIR region. This formation of "*hard*" and "*soft*" corona is studied by the UV–VIS–NIR absorption along with TEM. The exponential association mechanism is followed for "PbS NPs-BSA" corona formation and corona formation starts immediately after incorporation of PbS NPs into BSA as well as the unfolding of BSA continues for a very long time. The enlarged image of a hard corona represents that the core PbS NPs are fully covered with BSA with a shell thickness of 7.5 nm, matched with a dimension of BSA (~8 nm). A large number of PbS NPs with a hard corona of BSA forms a " *colony*" with diameters in the range of 260 nm. The "*soft corona*" also grows on this colony. The fluorescence study reveals that the quenching of fluorescence BSA in presence of PbS NPs follows the dynamic quenching process and TRY is the major binding site. Nearest to spherical PbS NPs, the positive cooperative reaction between PbS NPs and BSA is found and the affinity of BSA to the PbS NPs gradually increases in a superlinear fashion.

Acknowledgements The authors would like to acknowledge the DST-FIST-sponsored Department of Physics, Vidyasagar University, for providing various instrumental facilities.

References

1. O. Khullar, J.V. Frangioni, M. Grinstaff, Y.L. Colson, Image-guided sentinel lymph node mapping and nanotechnology-based nodal treatment in lung cancer using invisible near-infrared fluorescence light. Thorac. Cardioid Surg. **21**, 309–315 (2009)
2. S. Cohen, S. Margel, Engineering of near IR fluorescent albumin nanoparticles for in vivo detection of colon cancer. J. Nanobiotechnology **10**, 36 (2012)
3. R.K. Joshi, H.K. Sehgal, Density of states near Fermi level in PbS nanoparticle films. Phys. E. **23**, 168–170 (2004)
4. E. Hellstrand, I. Lynch, A. Andersson, T. Drakenberg, B. Dahlbäck, K.A. Dawson, S. Linse, T. Cedervall, Complete high-density lipoproteins in nanoparticle corona. FEBS J. **276**, 3372 (2009)
5. S. Milani, F. Baldelli Bombelli, A. S. Pitek, K. A. Dawson, and J. Rädler, Reversible versus irreversible binding of transferrin to polystyrene nanoparticles: soft and hard corona. ACS Nano **6**, 2532 (2012).
6. E. Casals, T. Pfaller, A. Duschl, G.J. Oostingh, and V. Puntes, Time evolution of the nanoparticle protein corona. ACS Nano **4**, 3623 (2010).
7. J. Klein, Surface interactions with adsorbed macromolecules. J. Colloid Interface Sci. **111**, 305–313 (1986)
8. S.R. Saptarshi, A. Duschl, A.L. Lopata, Interaction of nanoparticles with proteins: relation to bio-reactisvity of the nanoparticle. J. Nanobiotechnol. **11**, 26 (2013)
9. T. Cedervall, I. Lynch, M. Foy, T. Berggård, S.C. Donnelly, G. Cagney, S. Linse, and K.A. Dawson, Effect of membrane charge density on the protein corona of cationic liposomes: interplay between cationic charge and surface area. Angew. Chem. Int.Ed. **119**, 5856 (2007).
10. D. Dell'Orco, M. Lundqvist, C. Oslakovic, T. Cedervall, and S. Linse, Modeling the time evolution of the nanoparticle-protein corona in a body fluid. PLoS One. **5**, e10949 (2010).

11. I. Lynch, T. Cedervall, M. Lundqvist, C. Cabaleiro-Lago, S. Linse, and K.A. Dawson, The nanoparticle-protein complex as a biological entity; a complex fluid and surface science challenge for the 21st century. Adv. Colloid Interface Sci. **167**, 134 (2007).
12. I. Lynch, K.A. Dawson, Protein-nanoparticle interactions. Nano Today **3**, 40 (2008)
13. I. Lynch, K.A. Dawson, and S. Linse, Detecting cryptic epitopes created by nanoparticles. Sci. Signal **327**, pe14 (2006).
14. F. Ding, S. Radic, R. Chen, P. Chen, N.K. Geitner, J.M. Brown, P.C. Ke, Direct observation of a single nanoparticle–ubiquitin corona formation. Nanoscale **5**, 9162 (2013)
15. H. Yin, R. Chen, P. Casey, P. Ke, T. Davis, C. Chen, Reducing the cytotoxicity of ZnO nanoparticles by a pre-formed protein corona in a supplemented cell culture medium. RSC Adv. **5**, 73963 (2015)
16. S. Dominguez-Medina, L. Kisley, L.J. Tauzin, A. Hoggard, B. Shuang, A.S.D.S. Indrasekara, S. Chen, L.Y. Wang, P.J. Derry, A. Liopo, Adsorption and unfolding of a single protein triggers nanoparticle aggregation. ACS Nano **10**, 2103 (2016)
17. C. Vidaurre-Agut, E. Rivero-Buceta, E. Romaní-Cubells, A.M. Clemments, C.D. Vera-, C.C. Landry, P. Botella, Protein corona over mesoporous silica nanoparticles: influence of the pore diameter on competitive adsorption and application to prostate cancer diagnostics. ACS Omega **4**(5), 8852–8861 (2019)
18. S. Dominguez-Medina, J. Blankenburg, J. Olson, C.F. Landes, S. Link, Adsorption of a protein monolayer via hydrophobic interactions prevents nanoparticle aggregation under harsh environmental conditions. ACS Sustain. Chem. Eng. **1**, 833 (2013)
19. P. Wang, X. Wang, L. Wang, X. Hou, W. Liu, and C. Chen, *In vitro* biomechanical properties, fluorescence imaging, surface-enhanced Raman spectroscopy, and photothermal therapy evaluation of luminescent functionalized $CaMoO_4$:Eu@Au hybrid nanorods on human lung adenocarcinoma epithelial cells. Sci. Technol. Adv. Mater. **16**, 034610 (2016).
20. W. Liu, J. Rose, S. Plantevin, M. Auffan, J.Y. Bottero, C. Vidaud, Protein corona formation for nanomaterials and proteins of a similar size: hard or soft corona. Nanoscale **5**, 1658 (2013)
21. R. Huang, R.P. Carney, K. Ikuma, F. Stellacci, B.L. Lau, Effects of surface compositional and structural heterogeneity on nanoparticle-protein interactions: different protein configurations. ACS Nano **8**, 5402 (2014)
22. W. Zhou, Y. Cao, D. Sui, W. Guan, C. Lu, J. Xie, Ultrastable BSA-capped gold nanoclusters with a polymer-like shielding layer against reactive oxygen species in living cells. Nanoscale **8**, 9614 (2016)
23. A.K. Mishra, A.K. Bhunia, S. Saha, Lead sulfide quantum dot–serum albumin bioconjugate: spectroscopic, microscopic investigation and photo-conducting current analysis. Appl. Phys. A **127**, 316 (2021)
24. A.K. Mishra, S. Saha, Photocatalytic activity of methylene blue in the presence of PbS nanoparticles and its comparison with bulk PbS. Int. J. Metall. & Mater. Sci. Eng. **10**(1), 13–20 (2020)
25. C. Louis-June, M.A. Andrade-Navarro, C. Perez-, Prediction of protein secondary structure from circular dichroism using theoretically derived spectra. Protein **80**, 374 (2012)
26. O.K. Abou-Zied, O.I. Al-, Characterization of subdomain IIA binding site of human serum albumin in its native, unfolded, and refolded states using small molecular probes. J. Am. Chem. Soc. **130**, 10793 (2008)
27. T. Chakraborty, I. Chakraborty, S.P. Moulik, S. Ghosh, Physicochemical and conformational studies on BSA-surfactant interaction in aqueous medium. Langmuir **25**, 3062 (2009)
28. I.R. Krauss, F. Sica, C.A. Mattia, A. Merlino, Physicochemical and conformational studies on BSA-surfactant interaction in aqueous medium. Int. J. Mol. Sci. **13**, 3782 (2012)
29. M. Carbonaro, P. Maselli, P. Dore, A. Nucara, Pulse foods: Processing, quality and nutraceutical applications. Food Chem. **108**, 361 (2008)
30. A.K. Mishra, S. Saha, Comparison of ethanol gas sensors based on PbS nanoparticles and bulk PbS. Int. J. Electrochem. Sci. **15**, 11594–11605 (2020)
31. A.K. Mishra, S. Saha, Growth and characterization of PbS nanoparticles using THF. J. Phys. Sci. **23**, 223–229 (2018)

Chapter 7
Dark Matter in Singlet Scalar, Inert Doublet and Mixed Scalar Dark Matter Models

Nilavjyoti Hazarika and Kalpana Bora

Abstract The presence of dark matter is an exciting and puzzling feature of our Universe. Although the presence of dark matter is strongly supported by many astrophysical and cosmological observations, there is no candidate of dark matter in the standard model (SM) of particle physics. Different extensions of the SM provide candidates of dark matter. In this work, we consider scalar extensions of SM—a singlet scalar (SSM), an inert scalar doublet (IDM) and a mixed scalar model (MSM) to explain the existence of dark matter. The SSM faces a large number of experimental and theoretical constraints, most notably from the results of direct detection experiments like XENON1T. The IDM on the other hand can be valid up to the Planck scale (M_{PL}). The MSM DM model is an admixture of SSM and IDM. In MSM, we consider mixing between the singlet and the CP-even component of inert doublet dark matter particles. The lightest neutral Higgs that comprises the CP-even component of inert doublet and the singlet scalar is considered to be the DM candidate. We find the parameter space, which is consistent with the constraints of relic density. The current limits from the XENON1T experiment are used to study the constraints on the parameter space of the models and match our theoretical results with the same.

Keywords Beyond standard model · Dark matter · XENON1T

7.1 Introduction

The quest to find the exact nature of dark matter (DM) is one of the unresolved problems in particle physics and cosmology. The presence of DM, non-zero neutrino masses and the baryon asymmetry in the universe indicate physics beyond SM. However, there is not any sign of new physics beyond the SM at the LHC. Therefore, we explore a few scenarios where the SM is extended by additional scalar fields. We consider three different extensions of SM—singlet scalar model (SSM), inert doublet model (IDM) and a mixed scalar model (MSM)—to study whether viable

N. Hazarika (✉) · K. Bora
Physics Department, Gauhati University, Guwahati781014, Assam, India
e-mail: nilavhazarika@gauhati.ac.in

S. Sengupta et al. (eds.), *Selected Progresses in Modern Physics*, Springer Proceedings in Physics 265, https://doi.org/10.1007/978-981-16-5141-0_7

candidates of these models satisfy correct relic abundance DM. One of the strongest constraints on a DM is that it must be able to account for the presently observed relic density of the universe $\Omega h^2 = 0.1199 \pm 0.0022$ (from PLANCK) [1].

The paper has been organized as follows. Sections 7.2, 7.3 and 7.4 discuss the SSM, IDM and a MSM. We find relic abundance of DM in all the three models and check their viability as a candidate of DM. We then conclude and discuss the results in Sect. 7.5.

7.2 Singlet Scalar Model

SSM is one of the extensions of the SM where the SM is extended by a real scalar singlet S [2]. An unbroken Z_2 symmetry ensures the stability of the scalar under which the singlet is odd while all other fields are even. The scalar singlet S can couple to SM particles, very weakly through SM Higgs. The model is characterized by three parameters—a dimensionless self-coupling and mass of the scalar particle, and dimensionless coupling of the scalar with the SM Higgs [3, 4]. The Lagrangian for SSM is

$$\mathscr{L}_S = \frac{1}{2}\partial^\mu S^\dagger \partial_\mu S + \frac{1}{2}m_0^2 S^2 + \frac{1}{2}\lambda_{hs} S^2 H^2 + \frac{1}{4}\lambda_s S^4 \tag{7.1}$$

where m_0 is the bare mass of singlet field, H is SM Higgs, λ_{hs} is coupling with Higgs and λ_s is self-coupling.

We perform standard relic density calculations for SSM and show how the present abundance restricts its parameter space. In order to calculate the relic density of the models, we use micrOMEGAs 4.3.5 [5]. In Fig. 7.1, we have shown the variation of DM relic with mass for the singlet scalar model. Here, we have taken the value of Higgs coupling with singlet as $\lambda = 0.1$. The Higgs mass is assumed to be $m_h = 125$ GeV. The noticeable feature from this figure is the suppression of the relic density

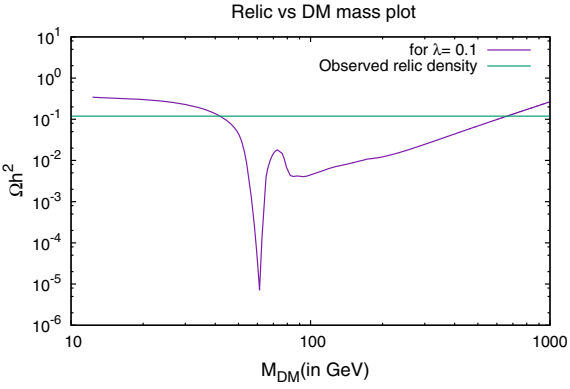

Fig. 7.1 Variation of relic density with mass for singlet scalar model

that takes place at the Higgs resonance, i.e., ($\frac{m_h}{2} \approx 62.5$ GeV). It is due to the reason that SSM DM candidate can annihilate through s-channel Higgs boson mediation into SM fermions and gauge bosons including Higgs.

7.3 Inert Doublet Model

The Inert Higgs Doublet model (IDM) in addition to the SM Higgs H contains an additional inert Higgs doublet ϕ [6]. This model has a Z_2 symmetry under which all the SM fields including H are even while ϕ is odd under Z_2, i.e., $\phi \rightarrow -\phi$. Further, it is assumed that Z_2 symmetry is not spontaneously broken, i.e., ϕ field does not develop vacuum expectation value (vev). These doublets can be parameterized as

$$H = \begin{pmatrix} 0 \\ \frac{1}{\sqrt{2}}(v+h) \end{pmatrix} \quad , \phi = \begin{pmatrix} H^+ \\ \frac{1}{\sqrt{2}}(H_0 + i A_0) \end{pmatrix} \tag{7.2}$$

The vev of the neutral component of the doublet H is denoted by v. The h state corresponds to the physical SM Higgs boson. The inert doublet consists of a neutral CP−even scalar H_0 having mass m_{H_0}, a pseudo-scalar A_0 having mass m_{A_0} and a pair of charged scalars $H^\pm$ having mass $m_{H^\pm}$. The IDM scalar potential V_{IDM} is given by

$$\begin{aligned} V_{IDM} = m_{11}^2(H^\dagger H) + m_{22}^2(\phi^\dagger\phi) + \lambda_1(H^\dagger H)^2 + \lambda_2(\phi^\dagger\phi)^2 + \\ \lambda_3(H^\dagger H)(\phi^\dagger\phi) + \lambda_4(H^\dagger\phi)(\phi^\dagger H) + \tfrac{\lambda_5}{2}[(H^\dagger\phi)^2 + h.c] \end{aligned} \tag{7.3}$$

Here, we have assumed $\Lambda_L = \lambda_3 + \lambda_4 + \lambda_5$ and $\Lambda_L^{'} = \lambda_3 + \lambda_4 - \lambda_5$. In Fig. 7.2, we have shown the variation of DM relic with mass for Inert doublet model considering the DM Higgs couplings $\lambda_L = 0.05$ and the quartic coupling $\lambda_2 = 0.1$ [7] and the mass splitting as $\Delta M = m_{A_0} - m_{H_0} = m_{H^\pm} - m_{H_0} = 50$ GeV. It is seen that there

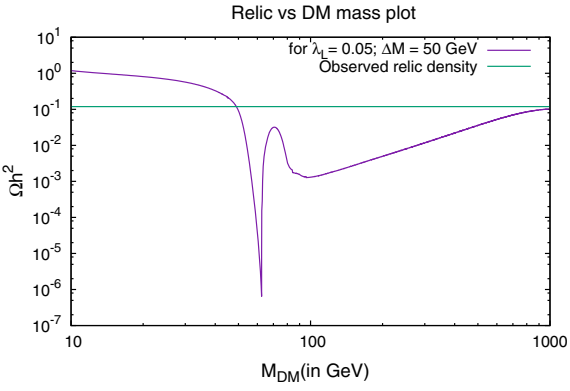

Fig. 7.2 Variation of relic density with mass for inert doublet model

exists a suppression of the relic density around the Higgs resonance $M_{DM} \simeq \frac{m_h}{2}$. This corresponds to the s-channel annihilation of DM into the SM fermions mediated by the Higgs boson h.

7.4 A Mixed Scalar DM Model

In the scalar singlet dark matter model, it has been observed that singlet mass abundance is around Higgs resonance—others ruled out from different bounds [8]. Similarly, in the inert doublet case the allowed mass region is the low mass region (below W mass) and above 550 GeV. Between the range 80–550 GeV, IDM doesn't satisfy relic. However, there is a possibility to satisfy relic in that range by combining SSM and IDM. In this context, we combine both SSM and IDM models as a mixed scalar DM model (MSM). In this model, both SSM and IDM transform under the same Z_2 symmetry. The combined scalar potential for the MSM will be then

$$\begin{aligned} V^{'} = & \mu_H^2(H^\dagger H) + \mu_I^2(\phi^\dagger\phi) + \mu_S^2(S^\dagger S) + \lambda_1(H^\dagger H)^2 + \lambda_2(\phi^\dagger\phi)^2 \\ & + \lambda_S(S^\dagger S)^2 + \lambda_3(H^\dagger H)(\phi^\dagger\phi) + \lambda_4(H^\dagger\phi)(\phi^\dagger H) + \tfrac{\lambda_5}{2}[(H^\dagger\phi)^2 + h.c] \\ & + \lambda_{HS}(S^\dagger S)(H^\dagger H) + \lambda_{\phi S}(S^\dagger S)(\phi^\dagger\phi) + \rho[(H^\dagger\phi)S + h.c] \end{aligned} \tag{7.4}$$

where μ_i, λ_j and ρ are coupling parameters.

By minimizing the potential in Eq.(7.4), we obtain the relation

$$\mu_H^2 = -\lambda_1 v^2 \tag{7.5}$$

and the mass terms for the SM Higgs, the charged scalar $H^\pm$ and pseudo-scalar A_0 can be obtained as

$$m_h^2 = 2\lambda_1 v^2 \tag{7.6}$$

$$m_{H^\pm}^2 = \mu_I^2 + \frac{\lambda_3}{2} v^2 \tag{7.7}$$

$$m_{A_0}^2 = \mu_I^2 + \Lambda_{345}^{'} v^2 \tag{7.8}$$

The term $\lambda_{\phi S}(S^\dagger S)(\phi^\dagger\phi)$ in Eq. (7.4) is responsible for the mixing of H_0 and S. We obtain a 2×2 mass matrix for the lightest neutral Z_2 odd scalar as

$$M = \begin{pmatrix} \mu_I^2 + \Lambda_{345} v^2 & \rho v \\ \rho v & 2\mu_S^2 + \lambda_{HS} v^2 \end{pmatrix} = \begin{pmatrix} m_{H_0}^2 & m_{H_0 S}^2 \\ m_{H_0 S}^2 & m_S^2 \end{pmatrix} \tag{7.9}$$

Here, $\Lambda_{345} = \frac{\lambda_3+\lambda_4+\lambda_5}{2}$ and $\Lambda_{345}^{'} = \frac{\lambda_3+\lambda_4-\lambda_5}{2}$.

The physical mass eigenstates can be defined as

$$\begin{aligned}\chi_1 &= H_0 \cos\theta + S \sin\theta \\ \chi_2 &= -H_0 \sin\theta + S \cos\theta\end{aligned} \tag{7.10}$$

The masses and mixing angle θ are found from the diagonalization process. Masses of the neutral physical scalars χ_1 and χ_2 are

$$\begin{aligned}m^2_{\chi_1} &= \frac{m^2_{H_0}+m^2_S}{2} - \frac{m^2_{H_0}-m^2_S}{2}\sqrt{1+\tan^2 2\theta}, \\ m^2_{\chi_2} &= \frac{m^2_{H_0}+m^2_S}{2} + \frac{m^2_{H_0}-m^2_S}{2}\sqrt{1+\tan^2 2\theta}\end{aligned} \tag{7.11}$$

$$\tan 2\theta = \frac{2m^2_{H_0 S}}{(m^2_{H_0} - m^2_S)} \tag{7.12}$$

The couplings in terms of the masses can be obtained as [1]

$$\begin{aligned}\lambda_1 &= \frac{m^2_h}{2v^2}, \\ \lambda_3 &= \frac{2(\Lambda_{345}v^2 + m^2_{H^\pm} - m^2_{\chi_1}c^2_\theta - m^2_{\chi_1}s^2_\theta)}{v^2}, \\ \lambda_4 &= \frac{m^2_{\chi_1}c^2_\theta + m^2_{\chi_2}s^2_\theta + m^2_{A_0} - 2m^2_{H^\pm}}{v^2}, \\ \lambda_5 &= \frac{m^2_{\chi_1}c^2_\theta + m^2_{\chi_2}s^2_\theta - m^2_{A_0}}{v^2}, \\ \mu^2_s &= \frac{m^2_{\chi_1}s^2_\theta + m^2_{\chi_2}c^2_\theta - \lambda_{HS}v^2}{2}, \\ \rho &= \frac{(m^2_{\chi_2} - m^2_{\chi_1})\sin 2\theta}{2v}, \\ \mu^2_I &= m^2_{\chi_1}c^2_\theta + m^2_{\chi_2}s^2_\theta - \Lambda_{345}v^2\end{aligned} \tag{7.13}$$

After mixing of the scalars, we consider one of the mixed states χ_1 as the lightest particle that would serve as the DM candidate. In Fig. 7.3, the variation of DM relic with mass for the mixed scalar DM model is shown for χ_1 as a DM candidate for $\Delta M = m_{\chi_2} - m_{\chi_1} = 20$ GeV. Here, the other parameters used are $\lambda_2 = 0.01$, $\lambda_S = \lambda_{HS} = \lambda_{\phi S} = 0.1$ and $\sin\theta = \cos\theta = 0.05$. In Fig. 7.4, the spin-independent cross section for χ_1 as a DM candidate is shown with varying Λ_{345}. The blue points shown in Fig. 7.4 satisfy relic density. It is seen that the mass of the mixed DM model DM candidate χ_1 lies within the 200–550 GeV range which lies in the allowed parameter space. This is due to mixing between the singlet and the CP-even component of inert doublet dark matter contributing to DM annihilation processes. This could be tested in higher sensitivity experiments like XENON1T in future.

[1] We have denoted $\cos\theta(\sin\theta)$ as $c_\theta(s_\theta)$ from now.

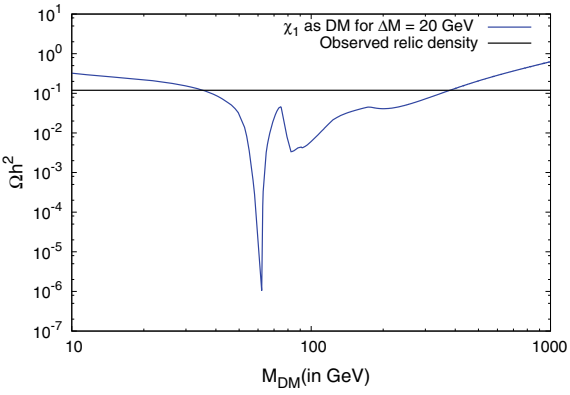

Fig. 7.3 Variation of relic density with DM mass for χ_1 with $\Delta M = 20$ GeV

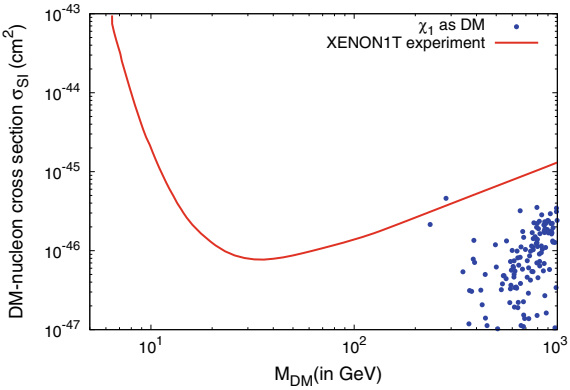

Fig. 7.4 Spin-independent cross section versus mass plot for χ_1 with varying Λ_{345}

7.5 Summary

In this study, we have considered scalar extensions of SM—Singlet scalar, inert doublet and mixed scalar dark matter models. The mixed scalar DM model which we had been considered can explain correct DM relic density in the intermediate range of 200–550 GeV. This is due to the DM annihilation process being affected by the mixing and co-annihilation effects. We conclude that in the present framework, the MSM provides a viable DM candidate with a mass range of 200–550 GeV. The DM candidates in this mass range could be probed in higher sensitivity experiments like XENON1T in future. Further detailed analysis is in progress and will be communicated to a Journal very soon.

Acknowledgements We thank Debasish Borah of IIT Guwahati for helpful discussions and suggestions. KB thanks Gauhati University for providing support to visit IIT Guwahati, during which a part of the work was done.

References

1. N. Aghanim et al. [Planck], Astron. Astrophys. **641** (2020), A1. https://doi.org/10.1051/0004-6361/201833880 arXiv:1807.06205 [astro-ph.CO]
2. V. Silveira, A. Zee, Phys. Lett. B **161**, 136–140 (1985). https://doi.org/10.1016/0370-2693(85)90624-0
3. J. McDonald, Phys. Rev. D **50**, 3637–3649 (1994)]. https://doi.org/10.1103/PhysRevD.50.3637 arXiv:hep-ph/0702143 [hep-ph]
4. C.P. Burgess, M. Pospelov, T. Ter Veldhuis, Nucl. Phys. B **619**, 709–728 (2001). https://doi.org/10.1016/S0550-3213(01)00513-2 arXiv:hep-ph/0011335 [hep-ph]
5. D. Barducci, G. Belanger, J. Bernon, F. Boudjema, J. Da Silva, S. Kraml, U. Laa, A. Pukhov, Comput. Phys. Commun. **222**, 327–338 (2018). https://doi.org/10.1016/j.cpc.2017.08.028 arXiv:1606.03834 [hep-ph]
6. A. Goudelis, B. Herrmann and O. Stål, JHEP **09**, 106 (2013). https://doi.org/10.1007/JHEP09(2013)106 arXiv:1303.3010 [hep-ph]
7. D. Borah and A. Gupta, Phys. Rev. D **96**(11), 115012 (2017). https://doi.org/10.1103/PhysRevD.96.115012 arXiv:1706.05034 [hep-ph]
8. A. Dutta Banik, D. Majumdar, Eur. Phys. J. C **74**(11), 3142 (2014). https://doi.org/10.1140/epjc/s10052-014-3142-6 arXiv:1404.5840 [hep-ph]

Chapter 8
Dependence of Particle Current and Diffusion on the System Parameters in a Model Under-damped Inhomogeneous Periodic Potential System

Francis Iawphniaw, Samrat Dey, and Shantu Saikia

Abstract In this work, we study the dynamics of a particle in a driven under-damped inhomogeneous periodic potential system. This forms an important field of study as it finds analogies in different physical and biological systems and hence helps to explain different natural processes. Particularly in the microscopic domain, particles in such a system undergo a directed transport even in the absence of any external bias utilizing the energy from the inherent random thermal fluctuations in the system. The resultant particle current is dependent on the various system parameters. The dynamics of the particles characterized by the particle current and the accompanying diffusion can be controlled and optimized by tuning the system parameters. This can have important technological applications. In this work, we study the dynamics of the particle in a model inhomogeneous system and show the dependence of particle current and diffusion on the system parameters.

8.1 Introduction

Systems at a finite temperature are subjected to random thermal fluctuations or noise. The energy scales of these fluctuations are small compared to the energy scales of the system. Hence in the macroscopic domain, these fluctuations cannot play a significant role in the system dynamics. But in the microscopic domain, the energy scales of these fluctuations are comparable to that of the system, and the effect of these fluctuations can no longer be neglected. In fact, many processes have been

F. Iawphniaw · S. Saikia (✉)
Department of Physics, St.Anthony's College, Shillong, India
e-mail: shantusaikia@anthonys.ac.in

F. Iawphniaw · S. Dey
Department of Physics, Assam Don Bosco University, Guwahati, Assam, India

S. Sengupta et al. (eds.), *Selected Progresses in Modern Physics*, Springer Proceedings in Physics 265, https://doi.org/10.1007/978-981-16-5141-0_8

found in different physical and biological systems which are due to these fluctuations. In these processes, the energy of these fluctuations is used constructively which is otherwise counterintuitive. Some of the phenomena and processes where noise plays a constructive role are stochastic resonance [1, 2], noise-enhanced stability of states [3], resonant activation [4], noise-enhanced transitions [5], noise-assisted energy transport [6], intracellular transport [7], ratchet effect [8] etc.

The dynamics of the particle in a periodic potential system in the presence of noise, as studied in this work, form an archetypal model in describing different processes and phenomena in a diverse physical and biological system. Ratchet effect [8] is one such phenomenon in which a system, driven away from equilibrium, utilizes the energy of the random fluctuations in the presence of an inherent asymmetry in the system, to generate particle current, in the absence of an obvious external bias. The ratchet effect plays an important role in explaining different processes like intracellular transport and Brownian motors [9], the motion of atoms on crystal surfaces [10], super-ionic conductors [11], cancer cell metastasis [12], ions movement through nano-pores [13] and the motion of vortices in superconductors [14]. The operation of naturally occurring Brownian motors led to the initial interest in the investigation of ratchets [9]. However, presently ratchets find applications in diverse fields [10, 11, 14]. Particularly, the possibility of fabricating nanodevices inspired by naturally occurring biological motors can have important technological applications [8].

Also, particle diffusion in a periodic potential system is an active field of research, both theoretically [16–19] and experimentally [20–23]. In any finite temperature system, particles undergo diffusion. This diffusion can be controlled by tuning the system parameters. The study of particle diffusion has important implications in varied fields like energy storage devices, microfluidics etc. [15 and references therein]. Also, the surface diffusion of particles can play a prominent role in different fields, like catalysis, microelectronics, biophysics etc.

The study of the phenomenon of ratchet effect and particle diffusion in an under-damped periodic potential system with space-dependent friction coefficient forms an important field of study as many systems encountered in nature are inhomogeneous. For example, motor protein experiences space-dependent friction when it moves along the periodic structure of microtubules [24], particles undergoing surface diffusion [25], in Josephson junctions, the periodically varying friction coefficient corresponds to the term present in interference between Cooper pair tunneling and quasi-particle tunneling [26], ad-atom motion on the surface of crystals [10] etc.

The study of particle dynamics in an inhomogeneous periodic potential system far from equilibrium has been an area of interest for research in the last few decades [27–46]. In such systems, particles experience non-uniform diffusion either due to a space-dependent temperature [27–29] or a space-dependent friction coefficient [30–46].

Particle transport in an under-damped inhomogeneous periodic potential system and its amplification is dependent on the different parameters of the system [34]. The particle also undergoes coherent motion at intermediate time regimes even in the presence of random fluctuations [36–38]. The time scale of this coherent motion regime can be regulated by regulating the different parameters of the system hinting

at possible technological applications. Multiple current reversals are observed in the same system in the deterministic regime [39]. The nature of the particle trajectories is critically dependent on the initial conditions. Hence with proper tuning of the system parameters, the ratchet effect can be optimized in this model system [40]. The model system also exhibits the phenomenon of stochastic resonance which is found to be dependent on the amount of damping in the system [43].

In the earlier works [41–45], the asymmetry in the system was due to only the space-dependent friction coefficient. Recently, it was shown that the addition of a slight asymmetry in the underlying periodic potential enhances the efficiency of transport [46].

Particle diffusion in an under-damped periodic potential system is also dependent on the system parameters and at times shows counterintuitive behavior. Particularly, the non-monotonic dependence of particle diffusion on temperature has generated interest with possible applications in different fields [48].

In the present work, studies on particle dynamics in the model under-damped inhomogeneous periodic potential system are presented. We study the dependence of particle current and diffusion on the system parameters.

8.2 Model

The motion of a particle of mass m in a periodic potential system can be described by the one-dimensional Langevin's equation given by

$$m\frac{d^2x}{d^2t} = -\gamma(x)\frac{dx}{dt} - \frac{\partial V(x)}{\partial x} + F(t) + \sqrt{\gamma(x)T}\xi(t) \tag{8.1}$$

where $\xi(t)$ are the random fluctuations satisfying the statistics $\xi(t) = 0$ and $\xi(t)\xi(t') = 2\delta(t-t')$. T represents the temperature of the system expressed in units of Boltzmann constant k_B. The underlying periodic potential is of the form $V(x) = -V_0(\sin(kx) + b\mathrm{Sin}(2kx))$, where b is the asymmetry parameter. $\gamma(x) = \gamma_0$ is the space-dependent friction coefficient having the same periodicity as that of the potential but with a phase difference ϕ with it (Fig. 8.1) and λ is the inhomogeneity parameter.

For simplicity, the equation is reduced to its dimensionless form by setting $m = 1, k = 1 and V_0 = 1$.

The dimensionless form of the above equation can be written as

$$\frac{d^2x}{d^2t} = -\gamma(x)\frac{dx}{dt} + \cos x + 2b\mathrm{Cos}2x + F(t) + \sqrt{\gamma(x)T}\xi(t) \tag{8.2}$$

In the dimensionless form too, $\xi(t)$ satisfies the same statistics as in Eq. 8.1.

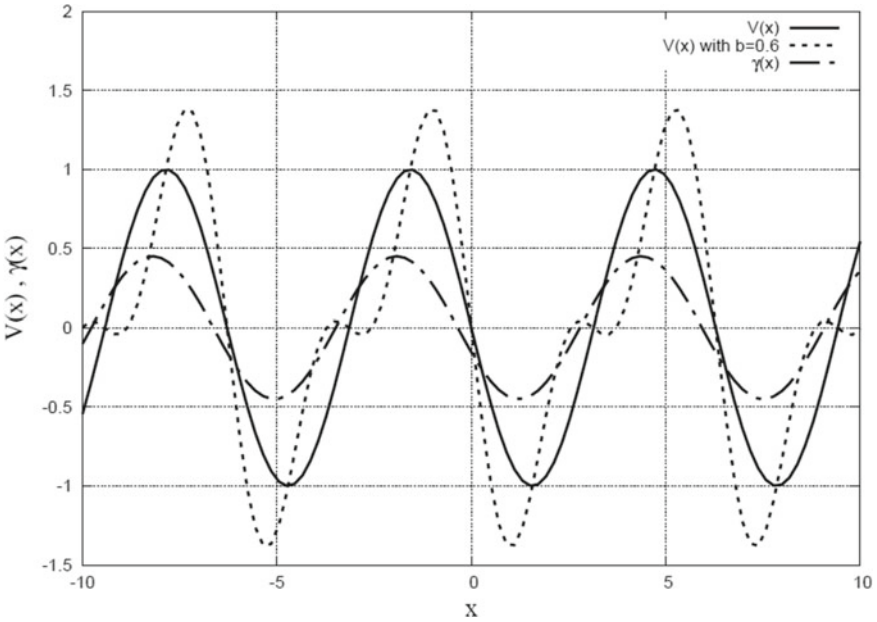

Fig. 8.1 Plot of potential V(x) (in the presence and absence of asymmetry) and friction coefficient $\gamma(x)$ with a phase difference of $\phi = 0.35$

The system is driven by an external periodic forcing of the form $F(t) = F_0 \cos(wt + \phi_0)$, which averages out to zero over a period of the forcing, thereby keeping the system unbiased.

8.3 Numerical Results

The dimensionless form of Langevin's equation (Eq. 8.2) is solved numerically using Heun's method which is a method of solving stochastic differential equations [47].

For a given initial condition, the particle is allowed to evolve over an effective time of about 10^5 and its trajectory is recorded. The resultant trajectory of the particle is sensitively dependent on the initial conditions. So, for different runs of the particle in the ensemble, the initial position is chosen from an evenly distributed grid between two successive maxima of the potential.

For physically relevant results, both time averaging (over a long time) and ensemble averaging (over different initial conditions) are done.

The mean velocity of the particle is defined as

$$V_{avg} = \lim_{t \to \infty} \frac{x(t)}{t}$$

Another quantity of interest is the diffusion coefficient of the particle which is defined as

$$D = \left(x^2(t) - x(t)^2\right)/2t$$

For this work, the system is allowed to evolve over effective times of $t = 10^5$ (100 periods of the external drive) and ensemble averaging $.\langle \ldots \rangle$ is done over an ensemble of 50 different initial conditions. Also, the values of the different parameters are $\gamma_0 = 0.12 : \lambda = 0.9; \phi = 0.35 and \phi_0 = 0.0$ unless otherwise stated.

Figure 8.2 shows plots of the particle trajectories for two different values of initial position x(0) in the system; other parameters remaining the same. It can be seen that a change in the initial conditions of the problem leads to totally different trajectories of the particle. Also, the particle exhibits two different states during its evolution—the locked state and the running state of motion. These are the result of a complex interplay of the stochastic nature and nonlinearity of particle motion. When inside a potential well, the particle experiences a finite barrier. This is achieved by keeping the amplitude of the external drive below a critical value where the barrier to particle motion disappears. The particles can escape from the well only in the presence of random fluctuations making the motion of the particles noise assisted. Once it escapes the particle will go to a running state where it will go over many potential periods only to be trapped again in a well of a potential where it will experience a period

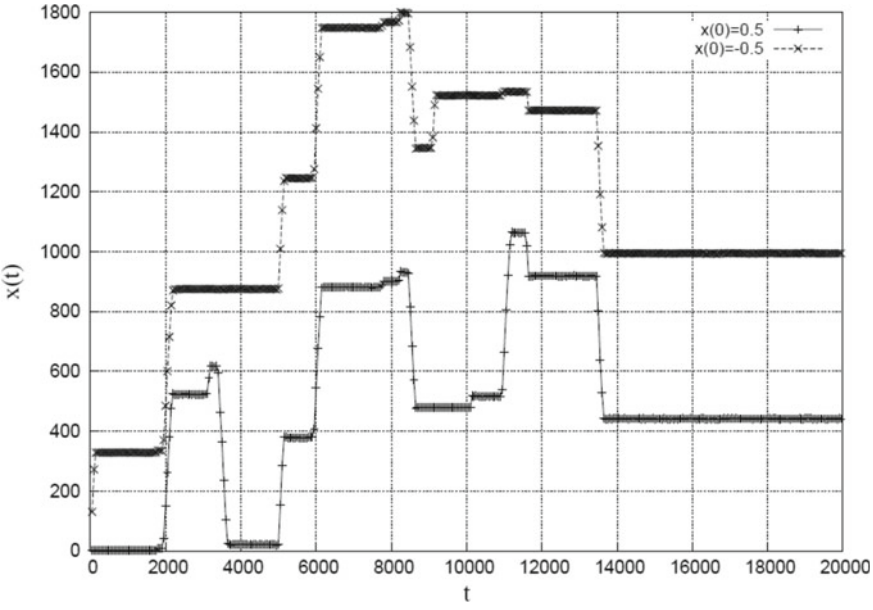

Fig. 8.2 Plot of particle trajectories for two different values of initial positions $x(0); T = 0.2; v(0) = 0; \gamma_0 = 0.12; \lambda = 0.9; \phi = 0.35; F_0 = 0$

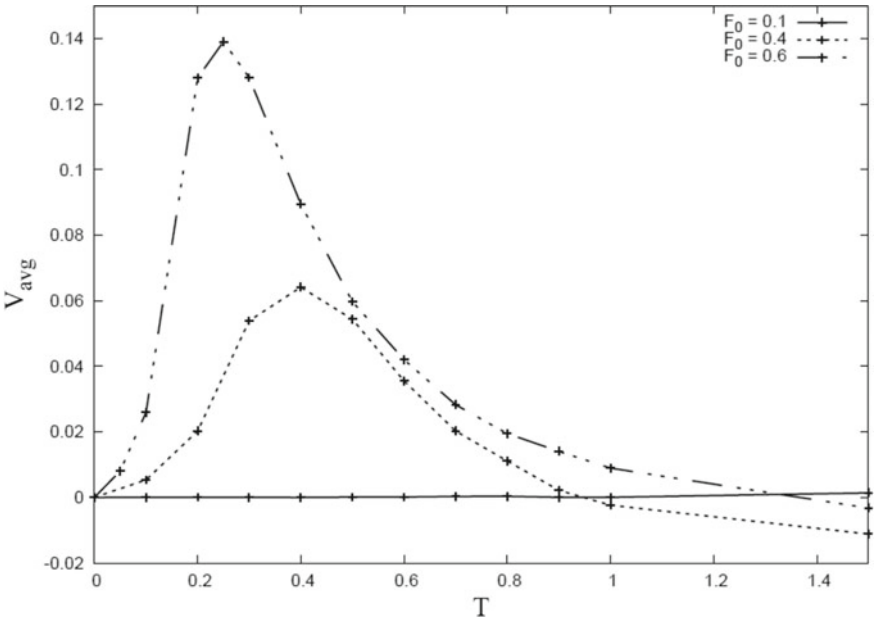

Fig. 8.3 Plot of the mean velocity V_{avg} versus temperature (T) for different value of $F_0 = 0.1,\ 0.4\&\,0.6 : \gamma_0 = 0.12 : \lambda = 0.9; \phi = 0.35$

of oscillatory motion locked in a single potential well. The duration of the locked and running state of motion of the particle is also stochastic in nature. Of course, it will be dependent on the parameters of the system like the temperature, damping, amplitude of external drive etc.

Figure 8.3 is a plot of the mean velocity of the particles as a function of temperature in the model under-damped inhomogeneous periodic potential system. The system when driven away from equilibrium by an external periodic drive exhibits substantial particle current for different sets of parameters. The directed particle transport is a result of the particles harnessing energy out of the random fluctuations in the presence of the asymmetry. The inherent asymmetry in the system skews the particle distribution around the potential minima. The particles get kicked around by the fluctuations in the potential minima. In each kick, there is a finite probability of the particle escaping from the well of the potential. On average, the particle has more probability of escaping in a particular direction because of the asymmetry in the system. The asymmetry, in this case, is either due to the space-dependent friction coefficient, a small asymmetry in the potential or a combination of both.

The nature of the variation of V_{avg} with temperature can be explained as follows. At very low temperatures the particles get very little energy from the fluctuations, as a result of which the number of escapes from the potential well is very less due to the finite potential barrier.

As temperature increases, the number of escapes increases leading to a higher particle current. However, when the temperature becomes high, the energy scales of the fluctuations become large. As a result, the effect of asymmetry on particle dynamics becomes negligible.

The particle current, therefore, exhibits a resonance—like behavior as a function of system temperature.

The particle current also depends on the amplitude of the external drive. For a particular value of temperature, the particle velocity is higher for a higher amplitude of drive. This is because at higher amplitudes, the probability of escape from a potential barrier is more. However, the amplitude of the external drive needs to be kept below the critical tilt at which the barrier to particle motion disappears. Otherwise, the effect of the random fluctuations and the small asymmetry becomes negligible.

Depending on the choice of parameters, the system exhibits current reversals. In the above figure, a current reversal can be seen as a function of temperature for $F_0 = 0.4$.

Also, in the range of temperatures from $T = 1$ to 1.2, $F_0 = 0.6$ shows particle current in the positive direction, whereas $F_0 = 0.4$ shows particle current in the negative direction. Though the plot shows just a signature of current reversals, with a proper choice of parameters, this reversal of particle current can be optimized and amplified.

Current reversals as a function of system parameters have important technological applications in particle separation techniques, and ratchet model systems are being used to understand and design particle separation devices [49].

Figure 8.4 shows the variation of diffusion coefficient with temperature for different amplitudes of the drive. The diffusion of particles in the system is clearly dependent on the parameters of the system like the temperature and amplitude of drive. This gives us the possibility of tuning the amount of diffusion of the particles by tuning the parameters of the system.

In the model system under our consideration, the space-dependent friction is a feeble cause of asymmetry. So, the effect of the introduction of a small asymmetry in the underlying periodic potential also was studied. Figure 8.5a and b shows the plot of V_{avg} and the diffusion coefficient D as a function of temperature—with a symmetric potential and with a small asymmetry introduced in the potential. It can be observed that with other parameters remaining the same, the introduction of a small asymmetry into the potential ($b = 0.05$) almost doubles the particle current V_{avg} (Fig. 8.5a). However, the diffusion coefficient remains almost the same (Fig. 8.5b). Thus, the introduction of a small asymmetry in the potential can substantially increase the effectiveness of particle transport without compromising on the coherency of transport.

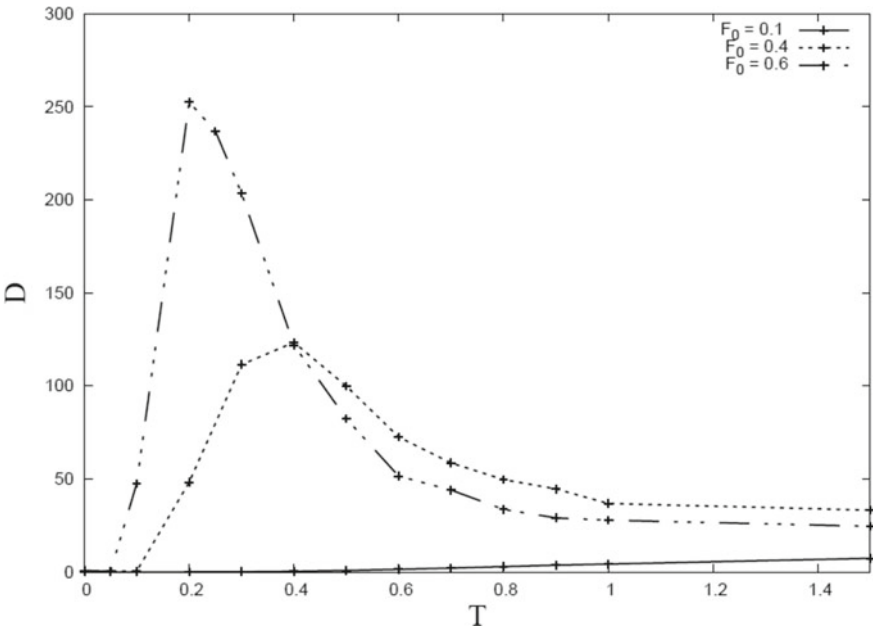

Fig. 8.4 Plot of diffusion coefficient (D) versus temperature (T) for different values of $F_0 = 0.1, 0.4\&0.6 : \gamma_0 = 0.12 : \lambda = 0.9; \phi = 0.35$

8.4 Conclusion

We have studied the particle dynamics in a periodic potential system with a space-dependent friction coefficient. Under the influence of thermal noise, the particles were shown to exhibit substantial particle current even without the presence of any external bias by harnessing energy from the random fluctuations. This demonstrates the capability of extracting constructive work from random fluctuations and can help in understanding different systems occurring in nature. Also, the possibility of controlling and optimizing the transport of particles by tuning the system parameters is demonstrated. This hints at possible technological applications in varied fields.

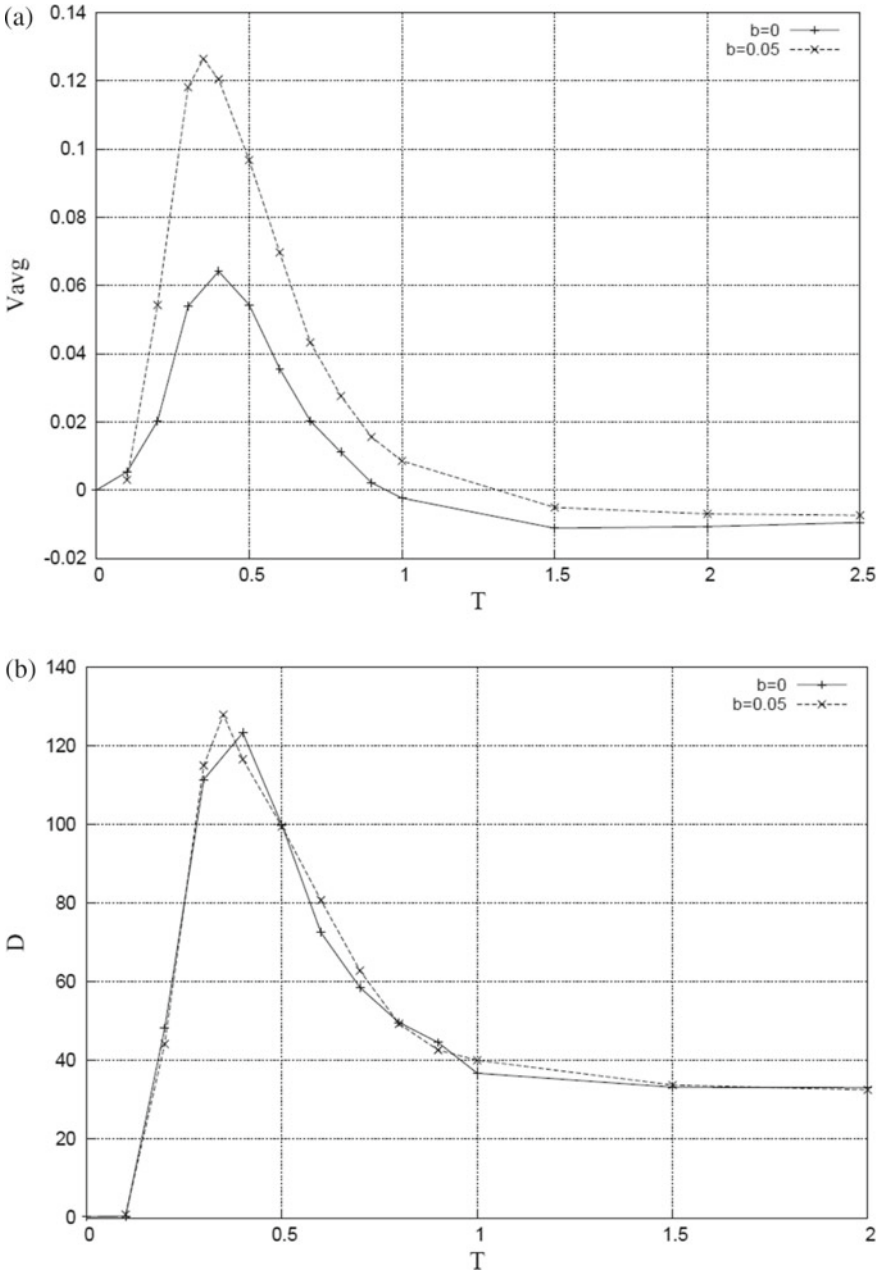

Fig. 8.5 (a) Plot of mean velocity V_{avg} versus temperature (T) for different values of b; $F_0 = 0.2$, $\gamma_0 = 0.12$, $\lambda = 0.9$; $\phi = 0.35$ (b) Plot of diffusion coefficient (D) versus temperature (T) for different values of b; $F_0 = 0.2$; $\gamma_0 = 0.12 : \lambda = 0.9$; $\phi = 0.35$

References

1. L. Gammaitoni, P. Hanggi, P. Jung, F. Marchesoni, Stochastic resonance. Rev Mod Phys. **70**, 223 (1988)
2. A. Simon, A. Lichaber, Escape and synchronization of a brownian particle. Phys. Rev. Lett. **68**, 3375 (1992)
3. R.N. Mantegna, B. Spagnolo, Noise enhanced stability in an unstable system. Phys. Rev. Lett. **76**, 563 (1996)
4. C.R. Doering, J.C. Gadoua, Resonant activation over a fluctuating barrier. Phys. Rev. Lett. **69**, 2318 (1992)
5. W. Horsthemke, R. Lefever, *Noise-Induced Transitions: Theory and Applications in Physics, Chemistry, and Biology* (Springer, Berlin, Heidelberg, New York, 1984)
6. R.D.J. Le on-Montiel, & J.P. Torres, Highly efficient noise-assisted energy transport in classical oscillator systems. Phys. Rev. Lett. **110**, 218101 (2013)
7. P.C. Bressloff, J.M. Newby, Stochastic models of intracellular transport. Rev. Mod. Phys. **85**, 135 (2013)
8. P. Reimann, Brownian motors: noisy transport far from equilibrium. Phys. Rep. **2002**(361), 57 (2002)
9. J.A. Spudich, How molecular motors work. Nature **372**, 515 (1994)
10. G. Wahnstrom, Diffusion of an adsorbed particle: theory and numerical results. Surf. Sci. **159**, 311 (1985)
11. P. Fulde, L. Piternero, W.R. Schneider, S. Strassler, Problem of brownian motion in a periodic potential. Phys. Rev. Lett. **35**, 1776 (1975)
12. G. Mahmud et al., Directing cell motions on micropatterned ratchets. Nature Phys. **5**, 606 (2009)
13. R. Karnik et al., Rectification of ionic current in a nanofluidic diode. Nano Lett. **7**, 547 (2007)
14. I. Zapata, R. Bartussek, F. Sols, P. Hanggi, Voltage rectification by a SQUID ratchet. Phys. Rev. Lett. **77**, 2992 (1996)
15. M.M. Millonas, M.I. Dykman, Transport and current reversal in stochastically driven ratchets. Phys. Lett. A **185**, 65 (1994)
16. P. Hanggi, & F. Marchesoni, Introduction: 100 years of brownian motion. Chaos, **15**, 026101 (2005)
17. J. Spiechowicz, J. Luczka, & L. Machura, Efficiency of transport in periodic potentials: dichotomous noise contra deterministic force. J. Stat. Mech. **2016**, 054038 (2016)
18. B. Lindner, & I.M. Sokolov, Giant diffusion of underdamped particles in a biased periodic potential. Phys. Rev. E. **93**, 042106 (2016)
19. K. Lindenberg, J.M. Sancho, A.M. Lacasta, & I.M. Sokolov, Dispersionless transport in a washboard potential. Phys. Rev. Lett. **98**, 020602 (2007)
20. J. Spiechowicz, & J. Luczka, Diffusion anomalies in ac-driven brownian ratchets. Phys. Rev. E. **91**, 062104 (2015)
21. S.H. Lee, & D.G. Grier, giant colloidal diffusivity on corrugated optical vortices. Phys. Rev. Lett. **96**, 190601 (2006)
22. M. Evstigneev, O. Zvyagolskaya, S. Bleil, R. Eichhorn, C. Bechinger, & P. Reimann, Diffusion of colloidal particles in a tilted periodic potential: Theory versus experiment. Phys. Rev. E. **77**, 041107 (2008)
23. R. Hayashi, K. Sasaki, S. Nakamura, S. Kudo, Y. Inoue, H. Noji, & K. Hayashi, Giant acceleration of diffusion observed in a single-molecule experiment on F1-ATPase. Phys. Rev. Lett. **114**, 248101 (2015)
24. R.H. Luchsinger, Transport in nonequilibrium systems with position-dependent mobility. Phys. Rev. E **62**, 272 (2000)
25. L.P. Faucheux, A.J. Libchaber, Confined brownian motion. Phys. Rev. E **49**, 5158 (1994)
26. C.M. Falco, Phase-space of a driven, damped pendulum (Josephson weak link). Am. J. Phys. **44**, 733 (1976)

27. G. Wahnstrom, Diffusion of an adsorbed particle: theory and numerical results. Surf. Sci. **159**, 311 (1985)
28. R.J. Landauer, Motion out of noisy states. Stat. Phys. **53**, 233
29. M. Buttiker, Transport as a consequence of state-dependent diffusion. Z. Phys. B **68**, 161 (1987)
30. Y.M. Blanter, & M. Buttiker, Rectification of fluctuations in an underdamped ratchet. Phys. Rev. Lett. **81**, 4040 (1988)
31. D. Dan, & A.M. Jayannavar, Giant diffusion and coherent transport in tilted periodic inhomogeneous systems. Phy. Rev. E **66**, 041106 (2002)
32. D. Dan, M.C. Mahato, A.M. Jayannavar, Mobility and stochastic resonance in spatially inhomogeneous systems. Phys. Rev. E **60**, 6421 (2000)
33. M.C. Mahato, & A.M. Jayannavar, Multiple current reversals in forced inhomogeneous ratchets. Phys. Rev. E **63**, 056307 (2001)
34. R. Krishnan, M.C. Mahato, & A.M. Jayannavar, Brownian rectifiers in the presence of temporally asymmetric unbiased forces. Phys. Rev. E **70**, 021102 (2004)
35. M.C. Mahato, A.M. Jayannavar, Enhancement of mobility by periodically modulating the slanting slope of a washboard potential. Phys. A **318**, 154 (2003)
36. W.L. Reenbohn et al., Motional dispersions and ratchet effect in inertial systems. Pramana Jour. of Phys. **71**(2), 297–306 (2008)
37. W.L. Reenbohn, & M.C. Mahato, Net particle current in an adiabatically driven unbiased inhomogeneous inertial system in a periodic potential. J. Stat. Mech.: Theory Exp. P03011 (2009)
38. S. Saikia, & M.C. Mahato, Dispersionless motion and ratchet effect in a square-wave-driven inertial periodic potential system. J. Phys.: Condens. Matter **21**, 175409 (2009)
39. S. Saikia, & M.C. Mahato, Dispersionless motion in a periodically rocked periodic potential. Phys. Rev. E **80**, 082102 (2009)
40. S. Saikia, M.C. Mahato, Deterministic inhomogeneous inertia ratchets. Phys. A **389**, 4052 (2010)
41. D. Kharkongor et al., Inertial frictional ratchets and their load bearing efficiencies. J. Stat. Mech. 033209 (2018)
42. S. Saikia, A.M. Jayannavar, & M.C. Mahato, Stochastic resonance in periodic potentials. Phys. Rev. E **83**, 061121 (2011)
43. W.L. Reenbohn, & M.C. Mahato, Relative stability of dynamical states and stochastic resonance in a sinusoidal potential. Phys. Rev. E **88**, 032143 (2013)
44. S. Saikia, The role of damping on stochastic resonance in a periodic potential. Phys. A **416**, 411 (2014)
45. W.L. Reenbohn, & M.C. Mahato, Dynamical states, stochastic resonance, and ratchet effect in a biharmonically driven sinusoidal potential. Phys. Rev. E **91**, 052151 (2015)
46. D. Kharkongor, W.L. Reenbohn, & M.C. Mahato, Particle dynamics in a symmetrically driven underdamped inhomogeneous periodic potential system. Phys. Rev. E **94**, 022148 (2016)
47. S. Saikia, Ratchet effect in an underdamped periodic potential and its characterisation. Phys. A **468**, 219 (2016)
48. R. Mannella, 'A gentle introduction to the integration of stochastic differential equation', in *Stochastic Processes in Physics, Chemistry and Biology*, vol. 557, ed. by J.A. Freund & T. Poschel, Lecture Notes in Physics, (Springer, Berlin, 2000), P. 353
49. J. Spiechowicz, & J. Łuczka, Diffusion in a biased washboard potential revisited. Phys. Rev. E **101**, 032123 (2020)

Chapter 9
Development of Agro-waste Based Nanosized Cellulose

Suvangshu Dutta

Abstract Buckles of Nahar seeds available in North East India, which becomes agro-waste after the utilization of the seeds, were collected. Dewaxing by Soxhlet extraction and alkali treatment of the buckles at 80 ± 2 °C followed by bleaching removed the non-cellulosic components. The whitened bleached fibers were then subjected to sulfuric acid (60 wt%) hydrolysis at 42 ± 2 °C for 60, 90, and 120 min, respectively, followed by sonication to obtain the nanosized cellulose. The formation of nanosized celluloses was confirmed by XRD, FTIR, TGA, and FE-SEM techniques. The study showed a diameter of maximum 30 nm and length 210 nm with high crystallinity for the isolated nanosized cellulose samples. The study concludes that the nanosized cellulose derived from nahar-based agro-waste of North Eastern India, with renewable potential, have tremendous scopes to be utilized as very good reinforcing agents for production of eco-friendly nanobiomaterials. This may, in fact, be a great initiative for reducing environmental pollution.

9.1 Introduction

Cellulose is an evergreen versatile biopolymer existing in the planet earth. Famous French chemist Anselme Payen isolated it from plant resources for the first time and elucidated its chemical composition (C:H:O = 1.2:2:1). Cellulose never exists alone in nature, hemicellulose, lignin, and some other waxy materials are always being its partners in the plant resources. Cellulose is a homopolymer of large molecular weight, β-D-glucopyranose units being the monomers associated via β-1,4-glycosidic linkages [19] (Fig. 9.1). The microfibrils are associated with each other in an ordered manner to form the cellulose fiber. The degree of crystallinity of cellulose depends upon the extent of systematic aggregation of the microfibrils. Parts of cellulose fibrils, however, lacks such systematic aggregation and is therefore called amorphous. The unique mechanical features of most of the natural fibers are largely due to its crystalline cellulose content. Cellulose is the core ingredient of common natural fibers

S. Dutta (✉)
Dept. of Chemistry, D.R. College, Golaghat, Assam, India

S. Sengupta et al. (eds.), *Selected Progresses in Modern Physics*, Springer Proceedings in Physics 265, https://doi.org/10.1007/978-981-16-5141-0_9

like jute, cotton, sisal, hemp, pond hyacinth, coconut, mango seeds, luffa cylindrica, sugarcane bagasse, and pine apple wastes [2, 12, 13, 21]. Algae, tunicates, and some bacteria are also found to synthesize cellulose naturally [9]. Statistical analysis of most of the lignocellulosic agro-wastes shows that ca. 35–50% by mass is cellulose, ca. 20–35% is hemicelluloses, and ca. 5–30% is lignin [26]. Nanosized cellulose (NC) are the ones having at least one dimension in the nanometer range (1 nm = 10^{-9} m). Research and development initiatives for conversion of cellulose-based agro-wastes into cellulose nanostructures are continuously growing [16]. This is understandable as nanofibrillation of cellulose makes it equipped with certain unique and inimitable properties such as (i) low density, (ii) low cost, (iii) biocompatibility, (iv) well-defined size and morphology, (v) controlled surface chemistry, (vi) high specific strength, (vii) high modulus. Further, nanosized cellulose can well improve the biopolymer characteristics by getting involved therein as nanofiller to form nanocomposites. The resulting nanocomposites are expected to possess better mechanical strength, toughness, elongation, thermal resistance, barrier properties, biodegradability, and optical properties as compared to the virgin biopolymer. This leads the scientific community to focus on the ever-growing research field of development of nanocomposites from agro-waste-based renewable resources.

Cellulose is biodegradable. An important enzyme known as "cellulase" (produced by fungi and bacteria) can hydrolyze cellulose or in fact depolymerizes it into fundamental sugar, glucose units [22, 24], leaving no toxic element to the earth. Tailor-made cellulase with specific properties have been isolated from agro-waste cum renewable resources. Production of fermentable sugars by this type of hydrolysis may also lead to the formation of the green "bioethanol" [20].

The North Eastern Region of India is known for its vast forest, mineral, agricultural, and horticultural resources. Existing literature indicates the development of nanosized cellulose from a lot of natural resources [16], however, exploration of many potential resources from North Eastern region, particularly, the waste generated from the plant resources is still awaited. The agro-waste cum buckles of nahar plant (*Mesua ferrea* L.) seeds of the region is of no use after extraction of the oil for polymer synthesis [3, 5, 6]. This chapter emphasizes on the production of nanosized celluloses (NC) from nahar seed buckles, the relatively new unexplored agro-waste cum renewable resources of North East India. The high cellulose content of plant fibers inspire to develop NC [8] from these resources. NCs were developed by alkali treatment, bleaching, and acid hydrolysis techniques followed by sonication. Physical, chemical, morphological, and thermal characterization of the nanosized celluloses is done by standard techniques like FTIR, XRD, TGA, SEM, and TEM. The concept of reinforcement of nanosized cellulose (NC) into biopolymers will open new research directions and bio-economic opportunities. The end products are expected to have the potential to replace the existing conventional non-environment responsive polymers. This will unravel the issue of environmental degradation arising from polymeric materials to a considerable extent and will sustain our living planet in favor of the imminent generations for long times to come.

9.2 Materials and Methods

9.2.1 Materials

The agro-waste cum buckles of nahar plant were collected from Padumoni village area of Golaghat district of Assam, India. Selected healthy buckles were washed with distilled water repeatedly, dried, and stored in airtight containers for further use. Sodium hydroxide, Acetone, Toluene, Sulfuric acid (98%), acetic acid, and $NaClO_2$ were supplied by Merck, India.

9.2.2 Extraction of Nanosized Cellulose

The stored buckles of nahar seeds were dewaxed using a Soxhlet apparatus with mixture of toluene and acetone as the solvent system. Dewaxed buckles were then dried in a vacuum oven at 60 ± 5 °C for 3 h. The well-dried biomass was crushed and grounded gently into small particles. The grounded fiber was dried in the vacuum oven at 50 °C overnight which was then treated with 2% NaOH solution at 80 ± 2 °C followed by 1.5% $NaClO_2$ treatment. Each treatment was done for 1 h, and the process was repeated four times with repeated washes using deionized water in order to avoid excess unwanted chemicals as well as to achieve a neutral pH. The bleached whitened fibers were then hydrolyzed using 60 wt% sulfuric acid under strong stirring conditions of 10,000 rpm, at 42 ± 2 °C for 30, 60, and 90 min, keeping fiber/acid ratio at 1:10 (g/ml). Immediately following the hydrolysis, the suspensions were diluted ten times with ice cold water to cease the hydrolysis reaction. The solutions were then centrifuged vigorously for 15 min at 15,000 rpm to eliminate the acid residues. This process of vigorous stirring was continued until the supernatant became turbid, i.e., becoming a colloidal suspension. The solutions were dialyzed with deionized water for 72 h until the pH reaches the range of ca. 6.5–7.5. Afterwards, the suspension was dispersed by using a probe ultrasonicator for 1 min. In this way, all the three suspensions of 30, 60, and 90 min were prepared. Finally, all the suspensions were stored in a refrigerator at 4 ℃. A few drops of chloroform were added to the suspensions to avoid fungal growth. All the samples were dried properly under vacuum conditions at the time of characterization [15, 17].

9.3 Results and Discussion

9.3.1 FTIR Characterization

To have a clear idea about the stepwise changes during nanosized cellulose (NC) formation, the samples were coded into three types. The crude cellulose sample (raw nahar seed buckle) was labeled as Bu, the sample after alkali treatment and bleaching (done for removal of hemicelluloses and lignin part) was labeled as BuB, whereas the sample of nanosized cellulose fibers obtained after 90 min of acid hydrolysis was labeled as BuS.

The FTIR spectrum of crude cellulose fibers (Bu) and nanosized fibers (BuS) was recorded in the wavenumber range of 4000–400 cm^{-1}. The peaks observed at ca. 3400 and 2960 cm^{-1} are due to –OH and –CH stretching vibrations, respectively. The prominent peak observed at ca. 1742 cm^{-1} in the crude fiber, Bu, was certainly due to the carbonyl component of either the acetyl and uronic ester groups of the hemicelluloses or the ester linkage of carboxylic acid group of the ferulic and *p*-coumaric acids of lignin or hemicelluloses [4]. Interestingly, this peak disappeared or decreased considerably in intensity in BuS (the nanosized cellulose). This clearly suggests that after bleaching and hydrolysis, the unwanted lignin and hemicelluloses have been separated considerably. Again, the peak at ca. 1512 cm^{-1} was observed in the original crude fiber (Bu) indicating the C = C stretching of aromatic rings of lignin. However, in BuS, it disappeared due to the partial removal of lignin. The original fiber has a peak at ca. 1635 cm^{-1} representing the adsorbed water, and this peak was decreased in BuS which again supports the fact of removal of hemicelluloses. In the FTIR spectrum of BuS, the peaks observed at ca. 1058 and 896 cm^{-1} were attributed to C–O stretching and C–H rocking vibration, respectively, of characteristic cellulose structure [1] (Fig. 9.2).

9.3.2 X-Ray Diffraction (XRD) Study

X-Ray diffraction study of the samples Bu, BuB, and BuS have been done in order to predict the structural and chemical change after each step of treatment. Although cellulosic fibers consist of three main components as discussed earlier, only the α-cellulose component is responsible for the crystalline nature, while lignin is amorphous in nature. The cellulose fibers are always surrounded by the non-cellulosic hemicelluloses and lignin template. The increase in the desirable crystalline cellulose part may only be achieved by the removal of the hemicelluloses and lignin during the chemical treatments like alkali treatment, bleaching, etc. The diffractograms with

a prominent peak at $2\theta = 22.5^0$ and a shoulder in the region $2\theta = 15–16^0$ are indicative of the presence of celluloses [25]. XRD patterns of all the samples indicated that during the alkaline treatment, bleaching, acid hydrolysis as well as ultrasonic treatments, the unique crystalline structure of cellulose did not change.

The crystallinity index (C.I.) is generally calculated from Segal equation,

$$\text{C.I.} = [(I_{200} - I_{am}) / I_{200}] \times 100$$

where I_{200} is the diffraction intensity at $2\theta = 22.5^0$ (height of the 200 peak representing crystalline material) and I_{am} is the diffraction intensity close to $2\theta = 18^0$ (the minimum between the 200 and 110 peaks representing amorphous material) in the treated samples of cellulose [25]. The C.I. measured for the samples BuA (Alkali treated Buckles), BuB (Bleached Buckles) and BuS (Sulphuric acid hydrolysed Buckles, i.e., nanosized fibers) were found to be 48.2. 57.9 and 63.3 respectively. The acid hydrolysed nanosized cellulose fibers (BuS) show strong crystalline nature which is attributed to its higher diffraction intensity at $2\theta = 22.5^0$. The higher peak intensity of the bleached or even higher in acid treated fibers indicates the complete removal of noncellulosic parts, the noncellulosic part has been removed specially after acid hydrolysis and also due to the dissolution of the lignin during high speed centrifugation and ultrasonication. Some additional peaks were also observed giving rise to new crystalline regions [23]. High crystallinity of the nahar agro-waste based nanosized cellulose may play great role in reinforcement of polymer nano-composites as crystallinity is responsible for obtaining highly stiff materials.

9.3.3 Morphological Study

The change of fiber surface after the formation of nanosized cellulose is shown in Fig. 9.3. As shown in the figure, the SEM images of the raw nahar seed buckles (Bu) presented a microstructure with irregularity and presence of some starch granules. The SEM analysis of the fiber after alkaline treatment and bleaching (BuB) indicated that these chemical treatments changed the structure considerably resulting in a ribbonlike structure (BuB). The treatment with NaOH and acidified $NaClO_2$ caused delignification by breaking down the non-cellulosic phenolic compounds of the chromophoric group present in lignin, and finally helps in obtaining the whitened cellulose fiber [10, 14].

The size of the nanosized cellulose (BuS) varies from 200 ± 10 nm [Fig. 9.3(c)] in length and about 30 ± 5 nm in width.

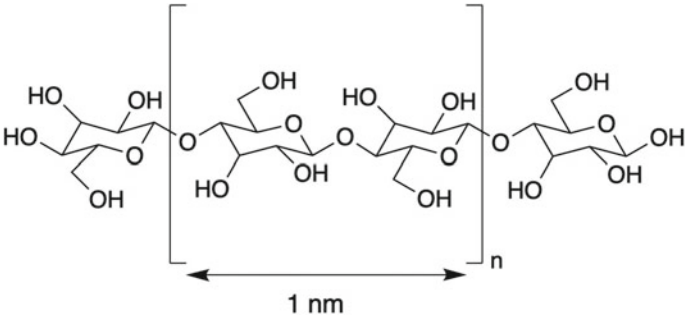

Fig. 9.1 Chemical structure of nanosized cellulose

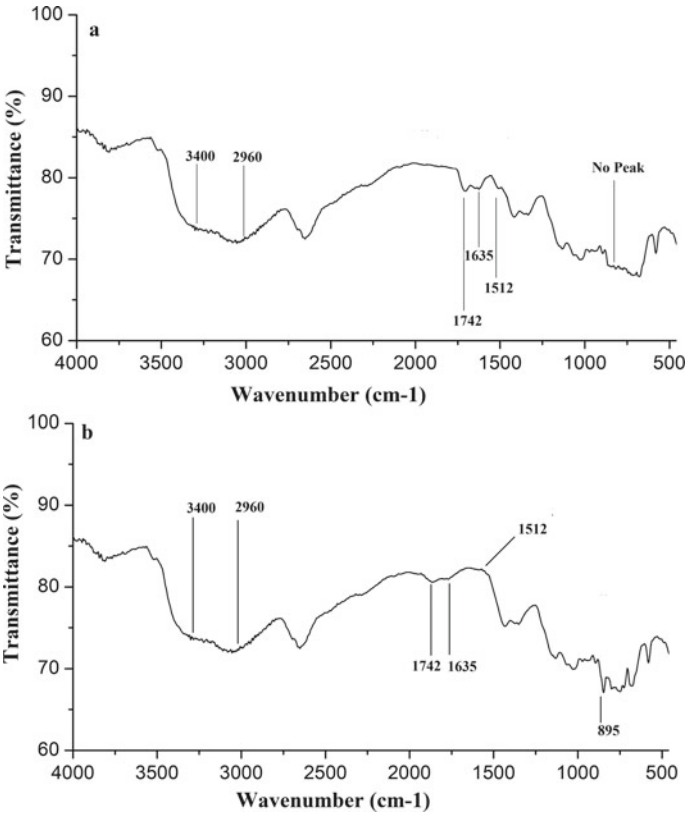

Fig. 9.2 FTIR spectra of (a) Crude cellulose, Bu and (b) nanosized cellulose, BuS

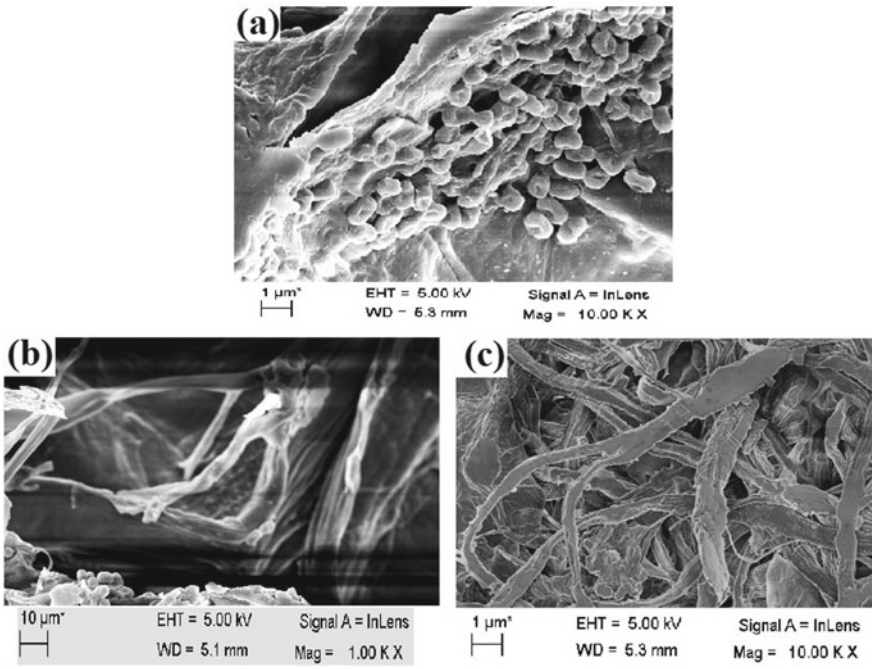

Fig. 9.3 FE-SEM Micrographs of (a) Bu, (b) BuB, and (c) BuS

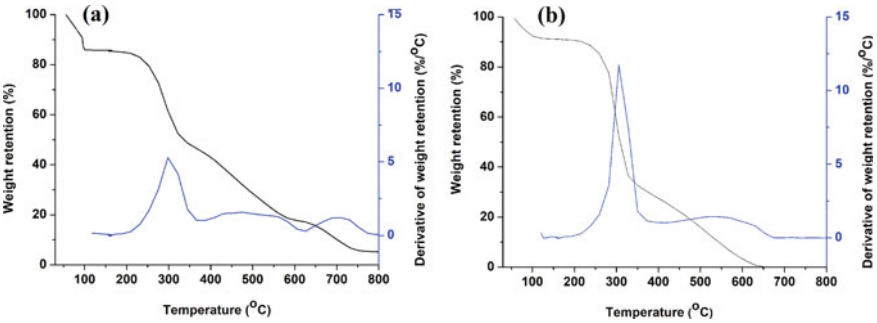

Fig. 9.4 TGA and DTG Curves for (a) Crude cellulose, Bu and (b) nanosized cellulose, BuS

9.3.4 Thermogravimetric Analysis (TGA)

The thermogravimetric analysis (TGA) of the nanosized cellulose (BuS, obtained after 90 min acid hydrolysis) showed comparably higher thermal resistance as compared to the ones obtained from contemporary resources. On going from Bu to BuS, the thermal stability is found to be considerably increased in a stepwise manner. DTG curves show the most sharp peak for nanosized cellulose (BuS) [Fig. 9.4(b)].

This may be due to the high cellulose content and perfection in homogeneity of the crystalline structure arising from acid hydrolysis [7]. These results clearly evidenced the superior thermal stability of nanosized cellulose (BuS) as compared to the raw nahar buckle fibers (Bu).

The initial degradation of all the samples in the region of 25° to 120 °C with a weight loss of 14% is due to elimination of the moisture content of the fiber and initial thermal degradation. The second major degradation step was initiated at ca. 230° due to breakage of glycosidic linkages due to thermal depolymerization of hemicelluloses [18]. The initial degradation temperature for Bu, BuA, BuB, and BuS was found to be initiated at 230.2, 237.5, 256.2, and 272.1 °C, respectively. Cellulose degradation started at around 312 °C in the case of Bu, and at around 342 °C in the case of BuS (evident from DTG curve, Fig. 9.4) and continued upto 410 °C. The final minor degradation was observed after 420 °C which is due to the decomposition of the thermally resistant aromatic lignin and other waxy residues [11]. The degradation temperatures were found to be well above for the acid hydrolyzed sample (BuS) as compared to that for the alkali-treated (BuA) or bleached sample (BuB). Thus, nahar agro-waste-based nanosized cellulose (BuS) could find myriads of application in the field of high temperature processed nanocomposites.

9.4 Conclusion

Nanosized cellulose was isolated from the agro-waste (buckles of nahar seeds) via. a chemo-mechanical treatment (alkali refining, bleaching, acid hydrolysis followed by homogenization via. centrifugation and sonication technique). Such nanocellulose can also be isolated by enzymatic and/or microbial hydrolysis. However, the present work utilized sulfuric acid hydrolysis technique as the preferred method due to the formation of sulfate charges on the surface which disallows aggregration and therefore helps in stabilizing the colloidal suspension.

The FTIR spectroscopic study confirmed the removal of non-cellulosic lignin and hemicelluloses after dewaxing by soxhlet extraction, alkali treatment, and bleaching processes. The increase in crystallinity was reflected in XRD analysis. The morphological study confirmed the formation of nanosized cellulose as expected. The study concludes that the nanosized celluloses derived from nahar-based agro-waste with high aspect ratio and thermostability have tremendous scopes to be utilized as fillers in high performance sustainable nanocomposites. Further, the production of nanosized cellulose from this underutilized agro-waste has commercial application potential in the field of biodegradable composite materials. The study concludes that the nanosized cellulose derived from nahar-based agro-waste of North Eastern India have tremendous scopes to be utilized as effective reinforcing agents for production of eco-friendly biomaterials. This may, in fact, be a great initiative for saving the planet earth from environmental pollution.

Acknowledgements The author greatly acknowledges University Grants Commission (UGC) for its financial through MRP Grant (No. F.5-2015-16(MRP/NERO)/505). Authority and Biotech Hub of D.R. College, Tezpur University, and NEIST, Jorhat are greatly acknowledged for their helps during various analysis of the samples.

References

1. K. Abe, H. Yano, Comparison of the characteristics of cellulose microfibril aggregates isolated from fiber and parenchyma cells of Moso bamboo (Phyllostachys pubescens). Cellulose **17**(2), 271–277 (2010)
2. M.A. Azizi Samir, F. Alloin, A. Dufresne, Review of recent research into cellulosic whiskers, their properties and their application in nanocomposite field. Biomacromolecules **6**(2), 612–626 (2005)
3. S. Chanda, K. Rakholiya, J. Parekh, Indian medicinal herb: Antimicrobial efficacy of Mesua ferrea L. seed extracted in different solvents against infection causing pathogenic strains. J. Acute Disease **13**, 277–281 (2013)
4. W. Chen, H. Yu, Y. Liu, Y. Hai, M. Zhang, P. Chen, Isolation and characterization of cellulose nanofibers from four plant cellulose fibers using a chemical-ultrasonic process. Cellulose **18**, 433–442 (2011)
5. S. Dutta, R.R. Devi, Cellulose nanofibers from agro-wastes of north east india for nanocomposite and bioenergy applications, in *Substrate analysis for effective biofuels production*, ed. by N. Srivastava, M. Srivastava, P.K. Mishra, V.K. Gupta (Springer, Singapore, 2020), pp. 149–172
6. S. Dutta, N. Karak, *Novel Biodegradable Polyurethanes Derived from a Sustainable Resource* (Lambert Academic Publishing, Germany, 2012)
7. I.S. Ghahafarrokhi, F. Khodaiyan, M. Mousavi, H. Yousefi, Preparation and characterization of nanocellulose from beer industrial residues using acid hydrolysis/ultrasound. Fib. Polym. **16**(3), 529–536 (2015)
8. V.K. Guna, M. Ilangovan, M.G. Anantha Prasad, N. Reddy, Water hyacinth: a unique source for sustainable materials and products. ACS Sus. Chem. Eng. **5**, 4478–4490 (2017)
9. M.A. Henrique, H.A. Silvério, W.P. Flauzino Neto, D. Pasquini, Valorization of an agro-industrial waste, mango seed, by the extraction and characterization of its cellulose nanocrystals. J. Environ. Manag. **121**, 202–209 (2013)
10. N. Johar, I. Ahmad, A. Dufresne, Extraction, preparation and characterization of cellulose fibres and nanocrystals from rice husk. Ind. Crop. Prod. **37**, 93–99 (2012)
11. P Khawas, SC Deka, Isolation and characterization of cellulose nanofibers from culinary banana peel using high-intensity ultrasonication combined with chemical treatment. Carbohydrate Polym. **137**, 608–616 (2016)
12. A. Kumar, V. Choudhary, N.K. Bhardwaj, Characterization of cellulose nanocrystals produced by acid hydrolysis from sugarcane as agro-waste. J. Mater. Phys. Chem. **2**, 1–8 (2014)
13. J.I. Moran, V.A. Alvarez, V.P. Cyras, A. Vazquez, Extraction of cellulose and preparation of nanocellulose from sisal fibers. Cellulose **15**, 149–159 (2008)
14. W.P.F. Neto, H.A. Silvérioa, N.O. Dantas, D. Pasquini, Extraction and characterization of cellulose nanocrystals from agroindustrial residue–Soy hulls. Ind. Crop. Prod. **42**, 480–488 (2013)
15. M. Nogi, S. Iwamoto, A.N. Nakagaito, H. Yano, Optically transparent nanofiber paper (2009)
16. V. Prasad, A.K. Bharimalla, S.P. Deshmukh, N. Vigneshwaran, P.G. Patil, Nanocellulose-polymer composites for applications in food packaging: current status, future prospects and challenges. Polym.-Plastics Technol. Eng. **56**(8), 805–823 (2017)

17. R.M.D. Santos, W.P. Flauzino Neto, H.A. Silve´rio, D.F. Martins, N.O. Dantas, D. Pasquini, Cellulose nanocrystals from pineapple leaf, a new approach for the reuse of this agrowaste. Ind. Crop. Prod. **50**, 707–714 (2013)
18. N. Saravanan, P.S. Sampath, T.A. Sukantha, Extraction and characterization of new cellulose fiber from the agrowaste of lagenaria siceraria (Bottle Guard) plant. J. Adv. Chem. **12**, 4382–4388 (2016)
19. H.A. Silvério, W.P. Flauzino Neto, N.O. Dantas, D. Pasquini, Extraction and characterization of cellulose nanocrystals from corncob for application as reinforcing agent in nanocomposites. Ind. Crops Prod. **44**, 427–436 (2013)
20. R.R. Singhania, J.K. Saini, R. Saini, M. Adsul, A. Mathur, R. Gupta, D.K. Tuli, Bioethanol production from wheat straw via enzymatic route employing Penicillium janthinellum cellulases. Bioresour. Technol. **169**, 490–495 (2014)
21. A. Sonia, K. Priya Dasan, Chemical, morphology and thermal evaluation of cellulose microfibers obtained from Hibiscus sabdariffa. Carbohydrate Polym. **92**(1), 668–674 (2013)
22. N. Srivastava, M. Srivastava, P.K. Mishra, V.K. Gupta, G. Molina, S. Rodriguez-Couto, A. Manikanta, P.W. Ramteke, Applications of fungal cellulases in biofuel production: advances and limitations. Renew. Sustain. Energy Rev. **82**, 2379–2386 (2018)
23. T. Theivasanthia, A.F.L. Christmab, A.J. Toyinc, C.B. Subash, G.R. Ravichandran, Synthesis and characterization of cotton fiber-based nanocellulose. Int. J. Biol. Macromol. **109**, 832–836 (2018)
24. S.P. Thota, P.K. Badiya, S. Yerram, P.V. Vadlani, M. Pandey, N.R. Golakoti, S.K. Belliraj, R.B. Dandamudi, S.S. Ramamurthy, Macro-micro fungal cultures synergy for innovative cellulase enzymes production and biomass structural analyses. Renew. Energy **103**, 766–773 (2017)
25. A. Thygesen, J. Oddershede, H. Lilholt, A.B. Thomsen, K. Stahl, On the determination of crystallinity and cellulose content in plant fibres. Cellulose **12**, 563–576 (2005)
26. H. Zabeda, J.N. Sahu, A.N. Boyce, G. Faruq, Fuel ethanol production from lignocellulosic biomass: an overview on feedstocks and technological approaches. Renew. Sustain. Energy Rev. **66**, 751–774 (2016)

Chapter 10
Distribution of X-Ray Flux: RXTE-PCA Observation of Cygnus X-1

Kabita Deka, Zahir Shah, Ranjeev Misra, and Gazi Ameen Ahmed

Abstract In this work, we have studied the long term flux distribution of Cygnus X-1 using the RXTE-PCA (Proportional Counter Array) data. Cygnus X-1 is known to have two (or three!) spectral states named "low/hard", "intermediate", and "high/soft". The source shows variability on different time-scales ranging from seconds to months. It is important to understand the high energy behaviour of the accretion disk of compact sources and the multiplicative processes which emanate in the acceretion disk. Analysis of a large number of pointed observations by a more sensitive instrument like the RXTE/PCA will provide significantly better information. Here, we observed that both the component, i.e., hard and soft, are better represented by a log-normal distribution.

10.1 Introduction

Cygnus X-1 is one of the most important Galactic Black hole binaries.This binary system consists of the 09.7 Iab type super giant HDE226868 and a Black hole orbiting around with a period of 5.6 days and the mass of the compact object is 21.2 ± 2.2 $M_{\odot}$ [1, 2]. Cygnus X-1 is a persistent and primary source which has been studied widely to understand the accretion and ejection processes and their links in Black Hole Binaries. The X-ray emission of Cygnus X-1 shows aperiodic Strong flickering type variability at time scales from milliseconds to years and falls into one of the two distinct states, named "low/hard" and "high/soft" [4]. Accreting galactic black hole binaries (BHBs) show two main spectral states : a soft state with a thermal X-ray spectrum dominated by an accretion disk and a hard state with a power law spectrum with a photon index $\Gamma \sim 1.7$ [5]. The source often undergoes state transitions between

K. Deka (✉) · G. A. Ahmed
Department of Physics, Tezpur University, Napaam 784028, Assam, India

Z. Shah · R. Misra
Inter-University Center for Astronomy and Astrophysics,
PB No.4, Ganeshkhind, Pune 411007, India

S. Sengupta et al. (eds.), *Selected Progresses in Modern Physics*, Springer Proceedings in Physics 265, https://doi.org/10.1007/978-981-16-5141-0_10

the two spectral states which make it a suitable source for studies of intermediate state [3]. It is significantly interesting to understand the high energy nature of the accretions disk of compact sources and the multiplicative processes which emanate in the accretion disk.

To understand the variability processes, we have studied flux distribution of the source. In our previous work, the study of the flux distribution of Cygnus X-1 using the RXTE/ASM (Rossi X-Ray Timing Explorer/ All Sky Monitor) had been made to understand the both spectral states of Cygnus X-1. It is found that log-normal is the better fitted distribution for hard state and gaussian for soft state. However, analysis of a large number of pointed observations by a more sensitive instrument like the RXTE/PCA will provide significantly better information than the sky monitor data. The Rossi X-ray Timing Explorer (RXTE) was launched on December 30, 1995, from NASA's Kennedy Space Center.The Proportional Counter Array (PCA) aboard the Rossi X-ray Timing Explorer (RXTE) consists of 5 large area proportional counter units (PCUs) designed to perform observations of bright X-ray sources with high timing and modest spectral resolution [6].

10.2 Methodology

10.2.1 Data Selection

We have considered the archival pointed RXTE observations of Cygnus X-1 made during the RXTE lifetime (MJD 50164 to MJD 55338). The "stdprod" directory of a typical ObsId(P10066/10066-01-01-00/stdprod) contains a collection of files including lightcurves (xpObsId_M2B.lc, 16 s source, background, and net light curves in 5 bands: a,b,c,d,e where a = 2–9 keV, b = 2–4 keV, c = 4–9 keV, d = 9–20 keV and e = 20–40 keV). We have collected all the light curves corresponding to the energy range b = 2–4 keV and c = 4–9 keV. Using these lightcurves, we find out the informations about observation time, count rate (flux points). In this work, we have considered those PCA observations for b band (2-4keV) and c band(4-9keV) which are not adjectly similar but next to ASM Dwell observations corresponding to the energy band B(3–5 keV) and C band(5–12 keV), respectively.

10.2.2 Histogram Fitting

Since Cygnus X-1 shows at least two distinct spectral states, to characterize the probability distribution, we would require two (or three) probability distribution function. We have created normalized histograms of PCA b and c band such that each bin in the histogram contained equal number of flux points. We define two probability density functions (PDF) as

$$l(x) = \frac{1}{\sqrt{2\pi}\sigma_l x} \exp\left(\frac{-[log(x) - \mu_l]^2}{2{\sigma_l}^2}\right) \tag{10.1}$$

$$g(x) = \frac{1}{\sigma_g\sqrt{2\pi}} \exp\left(\frac{-[x - \mu_g]^2}{2{\sigma_g}^2}\right) \tag{10.2}$$

Equation 10.1 results in a log-normal fit with μ_l and σ_l as the centroid and width of corresponding logarithm flux distribution, while Eq. 10.2 results in a Gaussian/normal fit with μ_g and σ_g as the centroid and width of corresponding normal distribution. The resultant histogram obtained for the RXTE-PCA (b-band and c-band) light curves are shown in Figs. 10.1 and 10.3. We used different combinations like log-normal-Gaussian (Eqs. 10.1 and 10.2), log-normal-log-normal (Eqs. 10.1 and 10.1), given below, to fit the normalised histograms the log-normal-gaussian PDF is given by (Fig. 10.2)

$$\begin{aligned} D(x) &= l(x) + g(x) \\ &= \frac{f_h}{\sqrt{2\pi}\sigma_l x} \exp\left(\frac{-[\log(x) - \mu_l]^2}{2{\sigma_l}^2}\right) \\ &\quad + \frac{1 - f_h}{\sigma_g\sqrt{2\pi}} \exp\left(\frac{-[x - \mu_g]^2}{2{\sigma_g}^2}\right) \end{aligned} \tag{10.3}$$

where μ_l and μ_g are the centroids of the logarithm flux distributions with widths σ_l and σ_g, respectively, f_h is fraction of time the source is in Hard state. The histogarms are shown in the following Sect. 10.3. Boroson et al. had used 3% systematic error to analize the light curve of Cygnus X-1 based on Crab pulsar measurements [7], hence we have also used a 3% systematics to obtain a better χ^2_{red}. In Table 10.1, we have summed up the best fit parameter values collected by using different double PDF. The χ^2_{red} obtained suggest that the PCA b and c band histograms are better fitted with double log-normal PDF as shown in Figs. 10.1 and 10.3.

10.3 Results and Discussion

We have analyzed the long term flux of Cygnus X-1 using pointed observation from RXTE/PCA in two energy bands. We have fitted the distributions using the combination of log-normal and Gaussian distribution. It is observed that, for the both bands, the components Hard and Soft are better represented by a log-normal distribution. It can be seen that $\chi^2_{\rm red}$ obtained in b band fitting is greater than 1. As the energy range of b band is 2–4 keV, so the flux from this band may be affected by the variable absorption. Log-normal distribution indicates that the X-ray variability of the source could be due to a multiplicative process. Stochastic propagation model

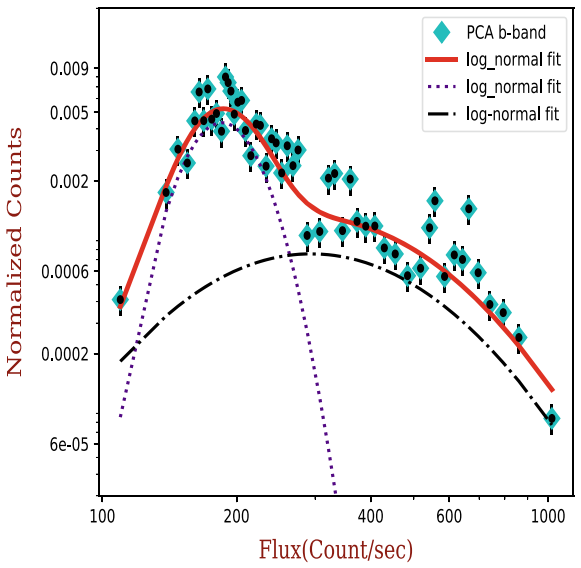

Fig. 10.1 Histogram of the long-term X-ray flux distribution of Cygnus X-1 PCA b band (green diamond points). The solid curve shown are the best fitted double-log-normal PDF. Dotted and dashed dotted curves are the individual log-normal components

Table 10.1 Best fit parameter values of the double PDF fitted to the flux histograms of PCA b and c Band Col:-1: Combination of functions , 2–9: Best fit values of μ_1,σ_1,μ_2, σ_2 , 10: Normalization fraction and 11: χ^2_{red}(Degrees of freedom)

PCA	b band					
PDF	μ_1	σ_1	μ_2	σ_2	f_h	χ^2_{red}(dof)
Log & Log	191.90±1.91	0.18±0.02	412.89±28.90	0.58±0.04	0.38±0.05	2.60(46)
Log & Gauss	191.95±3.81	0.52±0.07	434.41±3.33	36.42.81±3.89	0.58 ±0.06	2.70(46)
PCA	c band					
PDF	μ_1	σ_1	μ_2	σ_2	f_h	χ^2_{red}(dof)
Log & Log	453.02±9.06	0.19±0.05	629.87±94.48	0.32±0.04	0.44±0.02	1.19(31)
Log & Gauss	443.02±53.16	0.31±0.05	612.03±11.38	70.55±20.53	0.65 ±0.23	1.31(31)

suggests that perturbations at different time and radii of the accretion disk can have multiplicative effect on the inner disk which leads to X-ray variablity of the source [8]. Another potential possibilities for the observation of log-normal flux distribution could be related to the Gaussian variability of spectral index [9] or emission from large number of randomly oriented mini-jets [10] (Fig. 10.4).

The study of flux distribution of other persistent sources (Neutron star Binary) will also be a prominant one, which can also be done by using repeated and unbiased pointed observations from monitoring instruments.

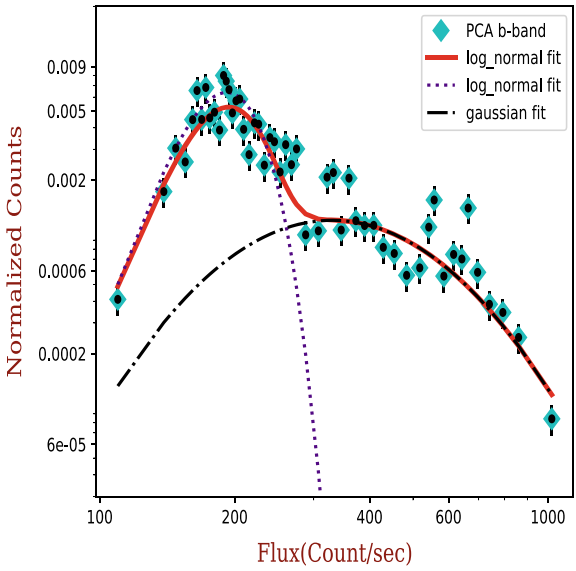

Fig. 10.2 Histogram of the long-term X-ray flux distribution of Cygnus X-1 b band(green diamond points). The solid curve shown are the best fitted log-normal-Gaussian PDF. Dotted curves are the individual log-normal and Gaussian components

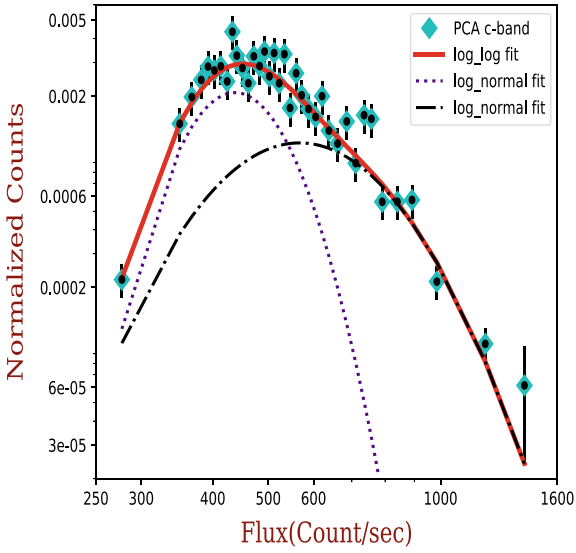

Fig. 10.3 Histogram of the long-term X-ray flux distribution of Cygnus X-1 PCA c band (green diamond points). The solid curve shown are the best fitted double-log-normal PDF. Dotted and dashed dotted curves are the individual log-normal components

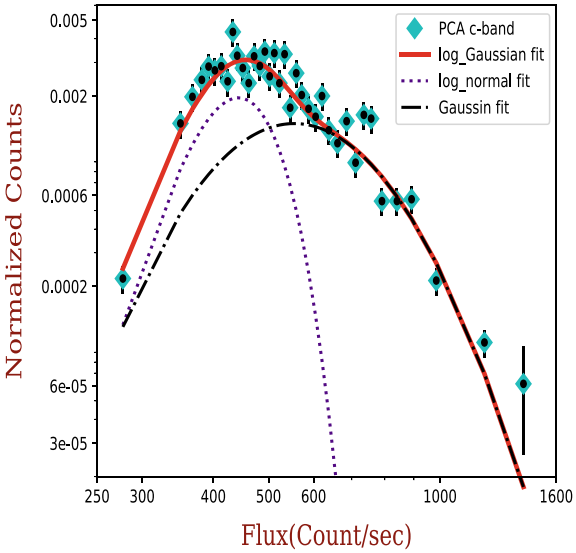

Fig. 10.4 Histogram of the long-term X-ray flux distribution of Cygnus X-1 c band (green diamond points). The solid curve shown are the best fitted log-normal-Gaussian PDF. Dotted curves are the individual log-normal and Gaussian components

References

1. J.C.A. Miller-Jones, A. Bahramian, J.A. Orosz, I. Mandel, L. Gou, T.J. Maccarone, C.J. Neijssel, X. Zhao, J. Ziółkowski, M.J. Reid, P. Uttley, X. Zheng, D.-Y. Byun, R. Dodson, V. Grinberg, T. Jung, J.-S. Kim, B. Marcote, S. Markoff, M.J. Rioja, A.P. Rushton, D.M. Russell, G.R. Sivakoff, A.J. Tetarenko, V. Tudose, J. Wilms, Cygnus x–1 contains a 21–solar mass black hole—implications for massive star winds. Science **371**(6533), 1046–1049, 2021. ISSN 0036-8075
2. A. Herrero, R.P. Kudritzki, R. Gabler, J.M. Vilchez, A. Gabler, Fundamental parameters of galactic luminous OB stars. II. A spectroscopic analysis of HDE 226868 and the mass of Cygnus X-1. aap, **297**, 556 (1995)
3. K. Pottschmidt, J. Wilms, M.A. Nowak, G.G. Pooley, T. Gleissner, W.A. Heindl, D.M. Smith, R. Remillard, R. Staubert, Long term variability of Cygnus X-1. I. X-ray spectral-temporal correlations in the hard state. AAP **407**, 1039–1058 (2003)
4. E.P. Liang, P.L. Nolan, Cygnus X-1 revisited. SSR **38**, 353–384 (1984)
5. V. Grinberg, N. Hell, K. Pottschmidt, M. Böck, M.A. Nowak, J. Rodriguez, A. Bodaghee, M. Cadolle Bel, G.L. Case, M. Hanke, M. Kühnel, S.B. Markoff, G.G. Pooley, R.E. Rothschild, J.A. Tomsick, C.A. Wilson-Hodge, J. Wilms, Long term variability of Cygnus X-1. V. State definitions with all sky monitors. AAP **554**, A88 (2013)
6. K. Jahoda, J.H. Swank, A.B. Giles, M.J. Stark, T. trohmayer, W. Zhang, E.H. Morgan, *In-orbit performance and calibration of the Rossi X-ray Timing Explorer (RXTE) Proportional Counter Array (PCA), volume 2808 of Society of Photo-Optical Instrumentation Engineers (SPIE) Conference Series*, pp. 59–70 (1996)
7. B. Boroson, S.D. Vrtilek, X-ray Variations at the orbital period from Cygnus X-1 in the high/soft state. APJ **710**(1), 197–206 (2010)
8. Y.E. Lyubarskii, Flicker noise in accretion discs. MNRAS **292**, 679 (1997)

9. A. Sinha, R. Khatoon, R. Misra, S. Sahayanathan, R. Mandal, N. Bhatt, N. The flux distribution of individual blazars as a key to understand the dynamics of particle acceleration. MNRAS **480**(1), L116–L120 (2018)
10. J. Biteau, B. Giebels, The minijets-in-a-jet statistical model and the rms-flux correlation. AAP, **548**, A123 (2012)

Chapter 11
Establishing a Mathematical and Radiological Relation Between the Malignant Tumour Inside the Body and the Outer Body Surface of the Patient

Kuldeep Sharma, Ananya Bhattacharjee, Rangaraj Bhattacharjee, Biswajit Nath, Kalyanjit Dutta Baruah, and Dipankar Bhagabati

Abstract This is an assumption-based study that intends to create a mathematical map of the routine procedure of simulation in radiotherapy. CT Simulator uses X-rays to provide precise radiological localization of the malignant tumour inside the patient's body. In radiotherapy, lead markers are used during the simulation, which serve as reference points for localization of the tumour on the body surface. The most vital aspect of radiotherapy is to match up the malignant tumour in the patient's body with the surface of the body. This radiological relation can also be shown mathematically with the help of Euclidean space and Euclidean geometry, taking into account three basic assumptions, thereby easing the use of Cartesian coordinate system. What is accomplished in the process is an algebraic and geometric correlation**.**

11.1 Introduction

Radiotherapy is the use of ionizing radiation to treat cancer [1]. In radiotherapy, treatment planning plays a vital role. It is a process where the optimal treatment parameters are determined in accordance with the location of the malignant tumour. The first step in the treatment procedure is simulation which is to locate the tumour and its spread. To give a mathematical interpretation to the above treatment procedure, Euclidean space and Euclidean geometry have been considered in this study. This is because of two reasons: first, simulation is a well-established protocol in radiotherapy, but a fresh mathematical recapitulation is attempted to visualize it in a new abstract

K. Sharma · R. Bhattacharjee (✉) · K. D. Baruah · D. Bhagabati
State Cancer Institute, Gauhati Medical College, Guwahati, Assam 781032, India

A. Bhattacharjee
Department of Mathematics, Assam University Silchar, Silchar, Assam 788011, India

B. Nath
Silchar Medical College Hospital, Silchar, Assam 788014, India

S. Sengupta et al. (eds.), *Selected Progresses in Modern Physics*, Springer Proceedings in Physics 265, https://doi.org/10.1007/978-981-16-5141-0_11

perspective. Secondly, in recent times, many researchers have dealt with the concept of Euclidean space in different fields like computational analysis [2], discrete analysis [3], algorithm to calculate shortest distance with obstacle [4], to mention a few. So, in this study, the concept of Euclidean space and geometry has been applied in the field of radiotherapy to locate the malignant tumour, thus adding another dimension to this field of study.

11.2 The Routine Procedure of CT Simulation

A routine procedure is followed in order to locate the malignant tumour. This is accomplished in a CT Simulator. After placing the patient on the CT couch, three micropore tapes, one anterior and two bilateral are fixed on the body or over the immobilization device (Mould), then by using the fixed horizontal and vertical lasers, marking is done over the micropore with a permanent marker. Now, lead markers are placed over one anterior and two bilateral markings in the patient's body or in the mould as reference. Images are produced by the differential attenuation of the X-ray photons in the patient's body. These images are then transferred to the Monaco Treatment Planning System. After importing the CT images using the 'Import new data' option, they are converted in terms of electron density which is available in the import tool. Using the Contouring option in the Monaco TPS, patient, target and organs at risk are drawn. After that, a treatment plan is developed by using the various options in 'Planning' option available in the Monaco software. An isocentre is defined while planning in the CT images which represent the entire coverage of the volume or area to be treated. Monaco TPS facilitates the marking of the isocentre using the 'tool' option and then selecting the 'Interest points and Marker' option. Here, by using the mouse, isocentre is marked, then by choosing the 'Plan Option' bar and by going to 'Scan and Setup Reference', the lead markers in the CT image are matched with the axes available in the Monaco TPS system. After that, by choosing the 'marked isocenter' in the Scan and Setup Reference tool and by locking all the data, a 'Scan Setup Reference Document' is generated. In this document, all coordinates are displayed using internal coordinate values as per the Monaco TPS. From the Scan Setup Reference Document, Scan reference coordinates and Setup reference (here the selected point is the Isocentre) coordinates are obtained. The Isocentre defined in the CT image of the patient had to be marked in the outer body surface of the patient in order to treat them. Monaco TPS facilitates to obtain this by subtracting the Scan reference value from the Setup Reference value. Thus, the Monaco software generated coordinate (X, Y, Z) is obtained which is called Shift. Shift = (Setup Reference − Scan Reference). Let, Shift X: A cm, Shift Y: B cm and Shift Z: C cm. These shift values explain how much the patient had to be shifted in the X, Y and Z direction from the lead markers to obtain the exact position of the Isocentre in the outer body surface of the patient. Monaco TPS also provides the information regarding the way in which the patient has to be shifted to get the exact Isocentre location. The patient is placed on the couch with the immobilization

Table 11.1 Shifting procedure of the patient in the therapy machine couch for supine position

Serial no	Axes direction	Direction in which the patient to be shifted	Direction in which the couch to be shifted	Machine axis-new value obtained from the shift value
1	X-direction	Right	Left	Value to be added
2	X-direction	Left	Right	Value to be Subtracted
3	Y-direction	Inferior	Superior	Value to be added
4	Y-direction	Superior	Inferior	Value to be Subtracted
5	Z-direction	Anterior	Posterior	Value to be Subtracted
6	Z-direction	Posterior	Interior	Value to be added

device or mould as per treatment protocol. Wall-mounted fixed lasers in the treatment room are matched with the lead markers on the patient's body. When this is done, a coordinate value is displayed in the machine-mounted computer display in the treatment room, say the values be D, E and F. The shift values A, B and C are fed into the treatment machine computer which in turn generates new coordinate. And as per the new coordinate values, the couch is moved accordingly to set the exact position of the Isocentre. Example: When the patient is being moved in the right side, then the couch should be moved in the left direction. The shift value to be added, $D + A = P$ (the new coordinate value, already mentioned above). Similarly, when the patient is being moved in the left side, then the couch should be moved in the right. Then the shift value to be subtracted, $D - A = P$. Table 11.1 demonstrates the shifting of the patient in the therapy machine couch. As the patient cannot be moved in the treatment table (couch), the couch is shifted to get the accurate position. Now, the patient is ready for the treatment.

11.3 Assumptions

Spaces have been differently classified based on the different perspective of analysis like Metric spaces, Vector spaces, topological spaces, to mention a few [5]. The foremost among them is Euclidean space. Euclidean space is the fundamental space or the three-dimensional space, where originally the Euclidean geometry is studied [5]. Euclidean space is specifically used for the pattern study of different shapes in the physical universe. The core of Euclidean space consists of points and their properties which defines them.

If one considers the principle of radiotherapy, it aims to give maximum dose to the tumour and minimum dose to the normal tissue. For optimum accuracy in destroying the tumour, the prescribed dose is delivered in such a way that the central ray of the radiation beam strikes a representative point, called isocentre. Depending on the

organ at risk, sometimes, it is needed to shift the isocentre from the tumour to its peripheral or neighbouring region to obtain optimal dose distribution.

Considering the above premises, three assumptions are made in order to conduct this study.

(1) The patient is considered as Euclidean Space.
(2) The tumour is considered as Euclidean geometry in the Euclidean space.
(3) The isocentre, which sometimes does not coincide with the tumour, can also be considered as Euclidean geometry in the Euclidean space.

In this study, patient is considered as the three-dimensional space whose X, Y, Z axes are drawn according to the lead markers placed on patient's body, and the point of intersection of the axes becomes the origin. The prime objective of treatment planning is to locate and destroy the malignant tumour in the patient's body. As the patient's body is considered as Euclidean space, without the loss of generality, the malignant tumour can be considered as Euclidean geometry.

11.4 Experimental Procedure for Assumption-Based Manual Study

A slab phantom is used instead of actual patient. After placing the phantom on the CT couch, three micropore tapes, one on anterior and two on lateral sides are fixed on the slab phantom. Then, by using the wall-mounted fixed horizontal and vertical lasers, marking is done over the micropore with a permanent marker as shown in Fig. 11.1.

Now lead markers are placed, one over the anterior and two over the bilateral markings in the slab phantom. Images are produced and transferred to the Monaco Treatment Planning System. After importing and converting the CT images in terms

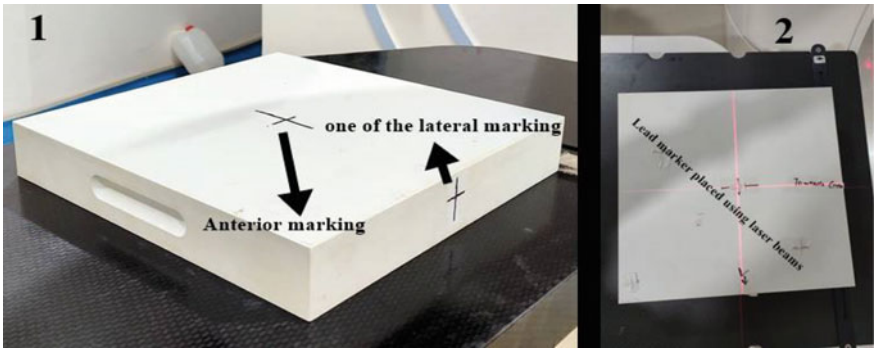

Fig. 11.1 The representation of the markings on the slab phantom is shown in 1 and placing of lead markers using wall-mounted laser beams in 2 at SCI, GMC, Assam

of electron density using the 'Import new data' option, target is drawn using the Contouring option in the Monaco TPS. Five different treatment plans are developed with five different targets by using the various options in 'Planning' option available in the Monaco software. Five different isocentre are defined for each plan to obtain five different sets of shift values. The remaining procedure is same as the routine procedure mentioned above resulting in five different Monaco TPS-generated shift values. For the assumption-based manual study, the lead markers in the CT image are matched with the axes available in the Monaco TPS system using the 'Plan Option' and 'Scan and Setup Reference' tool bars. Here, by using the 'tool' option and 'measure' option, a manual measurement of the shift is obtained considering the lead markers as origin, which nearly matches with the system-generated values verified by the second experiment using Laser Alignment test tool described below. The Monaco TPS-generated shift values and the assumption-based manual shift values are given in Table 11.2. Prior to the main experiment, the orthogonality of the field size is checked. A very simple technique is used for this. A square field size is opened in the therapy machine over a white plain paper. The edge of the field is marked with a compass. Then, based on the compass marking, a square field is drawn on the paper. Placing a protractor on each of the edges of the field, the orthogonality is confirmed geometrically as shown in Fig. 11.2.

Another simple experiment is performed to assist the main experiment using a Laser Alignment Test Tool (LATT). This test tool has a flat panel with defined axes

Table 11.2 Comparison between Monaco TPS-generated shift and assumption-based manual shift in slab phantom

Plan serial no	Monaco TPS-generated shift value (cm)	Manually generated shift value (cm)	Deviation (mm)	Remark
1	X = 13.11	X = 13.0	1.10	Under tolerance
	Y = 3.00	Y = 3.00	0.00	Under tolerance
	Z = 0.06	Z = 0.00	0.60	Under tolerance
2	X = 4.56	X = 4.50	0.60	Under tolerance
	Y = 8.10	Y = 8.00	1.00	Under tolerance
	Z = 9.51	Z = 9.50	0.10	Under tolerance
3	X = 9.25	X = 9.30	0.50	Under tolerance
	Y = 3.00	Y = 3.00	0.00	Under tolerance
	Z = 0.00	Z = 0.00	0.00	Under tolerance
4	X = 0.97	X = 1.00	0.30	Under tolerance
	Y = 2.56	Y = 2.50	0.60	Under tolerance
	Z = 0.26	Z = 0.30	0.40	Under tolerance
5	X = 7.94	X = 8.00	0.60	Under tolerance
	Y = 0.00	Y = 0.00	0.00	Under tolerance
	Z = 0.28	Z = 0.30	0.20	Under tolerance

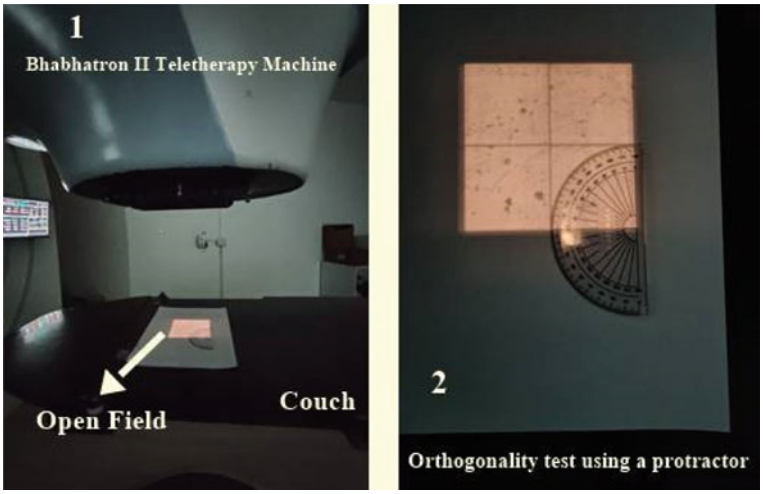

Fig. 11.2 The procedure for orthogonality test in the Bhabhatron II teletherapy machine at SCI, GMC, Assam

which are considered as same as the lead markers. In this test tool, a micropore is fixed in the horizontal axis of the flat panel, and using a ruler, the value of X-coordinate (obtained manually) is plotted. In the same way, Y and Z directions are also marked. Now, by moving the couch as per movement protocol given in Table 11.1, all the marked dots coincides perfectly with the laser beams as shown in Fig. 11.3.

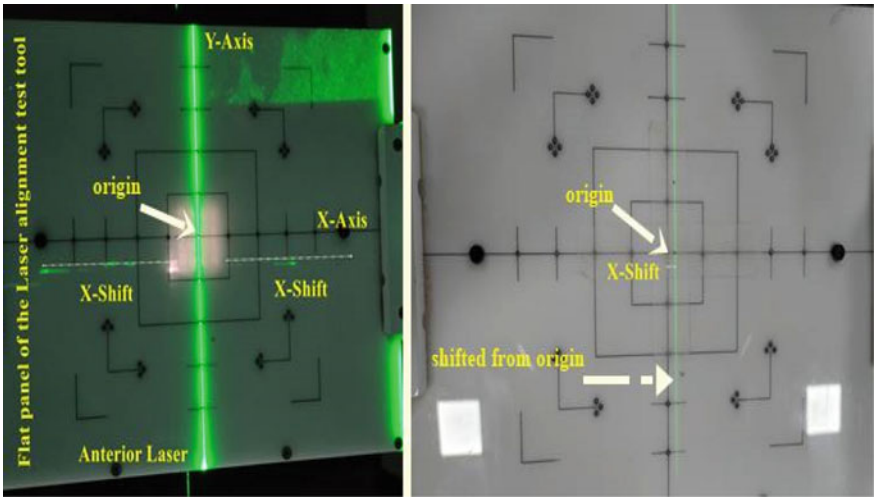

Fig. 11.3 The procedure for X-shift in laser alignment test tool performed at the Bhabhatron II teletherapy machine at SCI, GMC, Assam

The main experiment involves the placing of the slab phantom in the couch of the therapy machine. Laser beams are matched with the CT markings, and based on the Monaco TPS shift data along with the couch movement protocol given in Table 11.1 and by following the routine procedure, shifts are performed and isocentre is defined. Thus, the slab phantom (the virtual patient) is ready for the treatment. Now, with the same placement, shift is performed using a ruler. The intersection point of the laser beams and the CT markings is considered as the Origin. By placing a ruler along x, y and z axes, shifting is performed which approximately matches with the shift data positions obtained earlier from Monaco TPS (shown in Table 11.2). Graphical comparative study of two data is shown in Figs. 11.4, 11.5 and 11.6.

This experiment is performed on slab phantom whose surface is plain and not irregular, but in real situation, patients surface are irregular in shape. So, in order to create a real situation, same procedure is followed by using ten different Head and Neck moulds as shown in Fig. 11.7. Table 11.3 shows the difference between the Monaco TPS-generated shift and assumption-based manual shift for Head and Neck

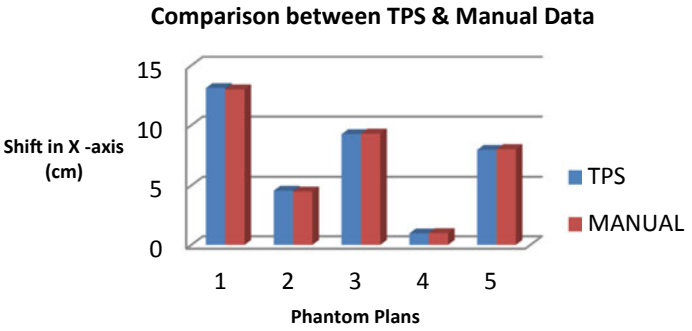

Fig. 11.4 A graphical comparison between the Monaco TPS-generated shift and the assumption-based manual shift in X-axis performed using slab phantom

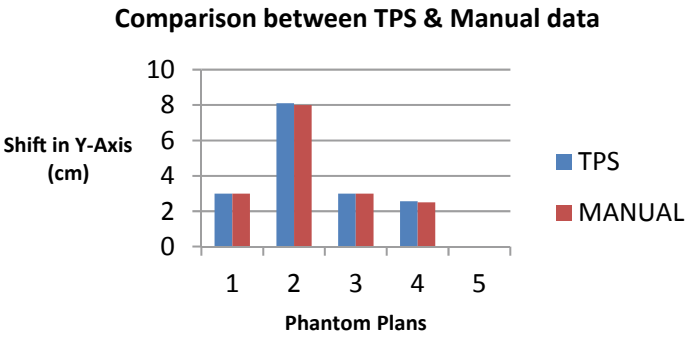

Fig. 11.5 A graphical comparison between the Monaco TPS-generated shift and the assumption-based manual shift in Y-axis performed using slab phantom

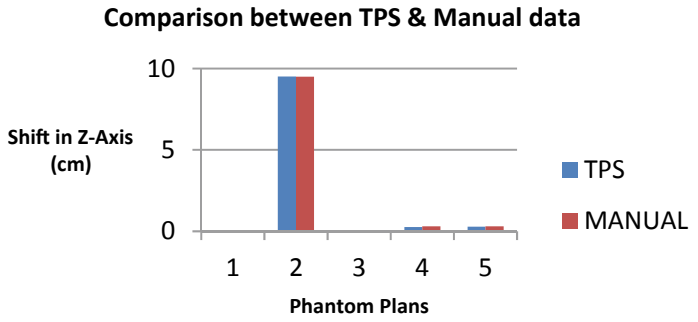

Fig. 11.6 A graphical comparison between the Monaco TPS-generated shift and the assumption-based manual shift in Z-axis performed using slab phantom

Fig. 11.7 The assumption-based manual shift procedure in X, Y and Z axes using head and neck mould at SCI, GMC, Assam

moulds. Graphical comparative study of the two data is shown in Figs. 11.8, 11.9 and 11.10. Schematic representations of the two procedures are shown in Fig. 11.11.

11.5 Result and Discussions

The results of the experimentation clearly shows that the value obtained by the Monaco TPS-generated shift and assumption-based manual shift is nearly same, thus validating the assumption and consequently proving that the research has been proceeded in the direction as expected. It has been seen that the difference between the

Table 11.3 Comparison between Monaco TPS-generated shift and assumption-based manual shift in head and neck mould

Serial no	Monaco TPS-generated shift value (cm)	Manually generated shift value (cm)	Deviation (mm)	Remark
1	X = 0.10	X = 0.00	1.00	Under tolerance
	Y = 1.00	Y = 1.10	1.00	Under tolerance
	Z = 2.21	Z = 2.30	0.90	Under tolerance
2	X = 0.83	X = 0.60	2.30	Under tolerance
	Y = 1.50	Y = 1.70	2.00	Under tolerance
	Z = 2.28	Z = 2.20	0.80	Under tolerance
3	X = 0.55	X = 0.70	1.50	Under tolerance
	Y = 3.50	Y = 3.70	2.00	Under tolerance
	Z = 0.86	Z = 1.00	1.40	Under tolerance
4	X = 2.91	X = 2.70	2.10	Under tolerance
	Y = 0.00	Y = 0.00	0.00	Under tolerance
	Z = 0.56	Z = 0.70	1.40	Under tolerance
5	X = 0.00	X = 0.00	0.00	Under tolerance
	Y = 6.00	Y = 5.90	1.00	Under tolerance
	Z = 1.46	Z = 1.70	2.40	Under tolerance
6	X = 0.17	X = 0.00	1.70	Under tolerance
	Y = 3.29	Y = 3.50	2.10	Under tolerance
	Z = 0.85	Z = 1.00	1.50	Under tolerance
7	X = 1.17	X = 1.40	2.30	Under tolerance
	Y = 2.00	Y = 2.30	3.00	Under tolerance
	Z = 0.29	Z = 0.30	0.10	Under tolerance
8	X = 0.08	X = 0.00	0.80	Under tolerance
	Y = 1.00	Y = 1.20	2.00	Under tolerance
	Z = 2.12	Z = 2.00	1.20	Under tolerance
9	X = 0.03	X = 0.00	0.30	Under tolerance
	Y = 0.50	Y = 0.50	0.00	Under tolerance
	Z = 0.45	Z = 0.50	0.50	Under tolerance
10	X = 0.15	X = 0.00	1.50	Under tolerance
	Y = 3.50	Y = 3.70	2.00	Under tolerance
	Z = 2.04	Z = 2.00	0.40	Under tolerance

Monaco TPS-generated shift and assumption-based manual shift is slightly higher in case of Head and Neck mould as compared to slab phantom. The variation in reading is mainly due to the surface irregularities of the mould, thickness of the marking because of the use of permanent marker and also sometimes on the performer. The

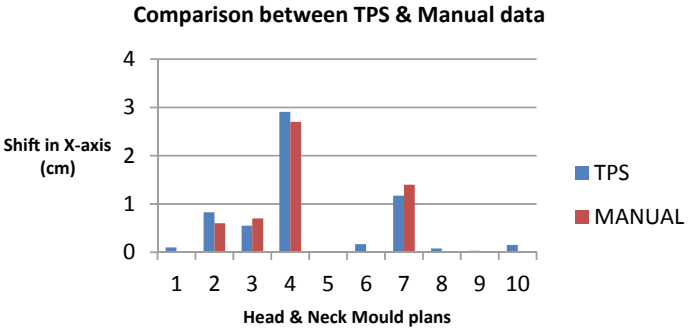

Fig. 11.8 A graphical comparison between the Monaco TPS-generated shift and the assumption-based manual shift in X-axis performed using head and neck mould

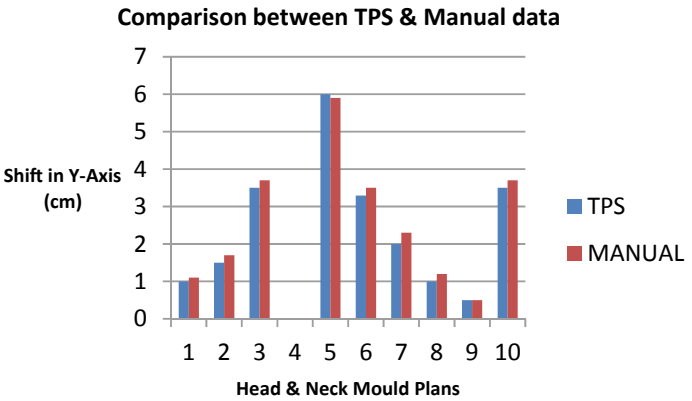

Fig. 11.9 A graphical comparison between the Monaco TPS-generated shift and the assumption-based manual shift in Y-axis performed using head and neck mould

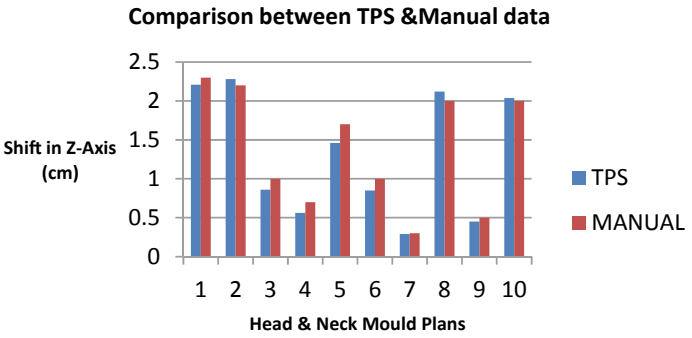

Fig. 11.10 A graphical comparison between the Monaco TPS-generated shift and the assumption-based manual shift in Z-axis performed using head and neck mould

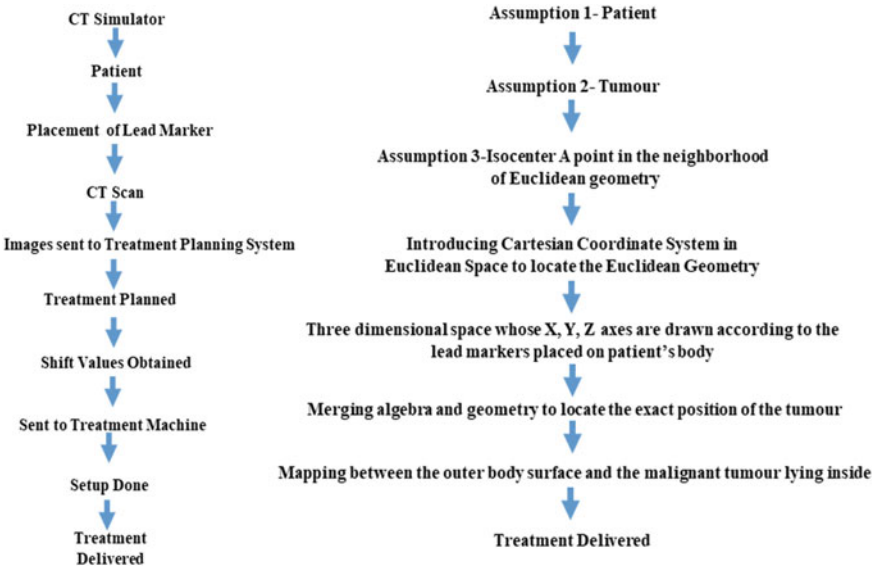

Fig. 11.11 A stepwise representation of the entire routine treatment procedure on left and mathematical assumption-based manual study procedure on right

manual mathematical method can be an alternative to machine-mounted computer display in radiotherapy.

11.6 Conclusion

A mathematical mapping has been established between the radiological version of the malignant tumour inside the body and its location at the surface of the body. The entire routine procedure of simulation in radiotherapy has been described mathematically with the help of three assumptions. The concept of Euclidean space and Euclidean geometry is coordinated by introducing a relatable Cartesian coordinate system, thus, merging algebra and geometry to locate the exact position of the tumour. It may be considered novel because first, it uses Euclidean space and analytical geometry to establish the relation between the positions of the tumour inside the body to its surface in an abstract manner, and secondly, it can be a handy alternative in radiotherapy. This stance thus, opens up a huge scope for further research elaboration, which may lead to the development of newer treatment technique.

Acknowledgements We express our most sincere gratitude to the Director and Professor of Radiation Oncology, State Cancer Institute, Gauhati Medical College, Assam, Dr. B. C. Goswami, Superintendent, Dr. Devajit Choudhury, Professor of Radiation Oncology and HOD, Dr. N. K. Kalita, Associate Professor of Radiation Oncology, Dr. (Mrs.) Smriti Goswami for their guidance and continuous support. We also express our most sincere gratitude to Mrs. Kalyani Chowdhury, PGT

English, K. V. Masimpur, Silchar, Assam, for her guidance and encouragement. We are thankful to Mr. Mrigen Rabha, Intern Medical Physicist for his valuable cooperation.

References

1. L.K. Singh, *Advances in Nuclear Physics and Condensed Matter*, 1st edn. (EBH Publishers, India 2020), pp. 1–11
2. J. Tiwari, M. Pande, Euclidean space and their functional application for computation analysis. Int. J. Adv. Technol. Eng. Explor. **6**, 194–199 (2019)
3. M. Fampa, Insight into the computation of Steiner minimal trees in Euclidean space of general dimension. Discret. Appl. Math. (2019)
4. Z. Shao, Q. Ma, X. Liu, J. Ma, An algorithm for shortest raster distance in Euclidean space with obstacles, in *19th International Conference on Geoinformatics* (IEEE, Shanghai, China, 2011), pp. 1–4
5. Euclidean space landing page, https://en.wikipedia.org/wiki/Euclidean_space#CITEREFBerger1987. Accessed 23 March 2021

Chapter 12
Exploring Invisible Neutrino Decay at Long-Baseline Experiments

Zannatun Firdowzy Dey and Debajyoti Dutta

Abstract Neutrino decay is one of the popular new physics scenarios in the neutrino sector. There are three active neutrinos, and they can decay into lighter active neutrino state and boson(s), or they can decay into a sterile fermion and boson(s). In visible neutrino decay, neutrinos decay into final active states and boson(s) and these are visible to the detectors. These scenarios are highly constrained. On the other hand, if the active neutrinos decay to some final sterile state, these are invisible to the neutrino detectors. Here in this work, we aim to study the possibility of invisible neutrino decay scenarios in long-baseline experiments. Previous studies show that by combining neutrino oscillation experiments it is possible to improve the constraints in invisible neutrino decay. We, here in this work, have measured the bounds on the invisible decay parameters at DUNE and NOνA experiments. We have also combined the two experiments to see the effect of the combination in improving the bounds on invisible neutrino decay.

12.1 Introduction

The neutrino oscillation phenomenon is responsible for the mass of neutrinos. Neutrinos have six oscillation parameters—three mixing angles ($\theta_{12}, \theta_{13}, \theta_{23}$), two mass squared differences ($\Delta m^2_{21}, \Delta m^2_{31}$) and the CP violating phase δ_{cp}. From the previous studies, it can be observed that the parameters $\theta_{12}, \theta_{13}, \Delta m^2_{21}$ and the absolute value of Δm^2_{31} have been measured to an excellent precision by the oscillation experiments. Among the six oscillation parameters, Δm^2_{21} and θ_{12} have been measured precisely from solar neutrino experiments [1] and kamland [2]. The measurement of Δm^2_{32} and θ_{23} has been given by Atmospheric experiments [3]. The reactor experiments DayaBay [4], Double CHOOZ [5] and RENO [6] are also able to determine the value of θ_{13}. The unknown parameters in the neutrino oscillation sector are (i) the neutrino mass ordering, i.e., whether $m_3 > m_2 > m_1$ denotes normal hierarchy

Z. F. Dey (✉) · D. Dutta
Department of Physics, Assam Don Bosco University, Sonapur 782402, India
e-mail: debajyoti.dutta@dbuniversity.ac.in

S. Sengupta et al. (eds.), *Selected Progresses in Modern Physics*, Springer Proceedings in Physics 265, https://doi.org/10.1007/978-981-16-5141-0_12

(NH) or if $m_3 < m_2 < m_1$ leading to inverted ordering (IH), (ii) the measurement of the octant of θ_{23} and (iii) the precise measurement of CP phase-δ_{cp}. There are many presently running experiments like T2K [7] and NOvA [8, 9] which can give some indications of these unknown quantities of neutrino experiments. However, no clear conclusion has been found yet. There are also many experiments which are planned for the near future with the aim of determining the unknown parameters of neutrino oscillation physics. Examples of such experiments are DUNE [10], T2HK/T2HKK [11, 12], ESSnuSB [13], JUNO [14], INO [15], PINGU [16], KM3NeT-ORCA [17], etc. Neutrino oscillation phenomena proved that neutrinos are massive, which lead us to the physics beyond the standard model. So, if there is a new physics beyond SM, then that can give modification to the oscillation probabilities in these experiments. Invisible neutrino decay is one such new physics idea.

The idea of invisible neutrino decay is such that a heavy neutrino state decays into a light sterile state, which is invisible. Invisible neutrino decay can happen for both Dirac and Majorana neutrinos. Theoretically, if neutrinos are Dirac, then there is a coupling between neutrinos and a light scalar boson [18]. For this, the decay channel can be written as $\nu_j \rightarrow \bar{\nu}_{iR} + \chi$, where $\bar{\nu}_{iR}$ is a right- handed singlet and χ is an iso singlet scalar. On the other hand, in the case of Majorana particles a neutrino can couple with a majoron J and a sterile neutrino ν_s for which the channel can be written as $\nu_j \rightarrow \nu_s + J$. Neutrinos can also decay to another visible state. For this type of decay, the channel can be written as $\nu_j \rightarrow \bar{\nu}_i + J$ or $\nu_j \rightarrow \nu_i + J$. References [19, 20] discuss the visible neutrino decay in the context of long-baseline experiments.

Generally, all the three neutrino states ν_1, ν_2 and ν_3 can decay into invisible states. The first idea of neutrino decay was proposed in order to explain the solar neutrino problem [21]. Later, neutrino oscillation with decay solutions was studied assuming ν_2 to be the unstable state and obtained bound on life time τ_2. The bound obtained from solar data is $\frac{\tau_2}{m_2} > 7.2 \times 10^{-4}$ s/eV at 99% CL [22]. The decay due to ν_2 is constrained from solar neutrino data and the decay due to ν_1 and ν_2 state is bound from supernova SN1987A [23] data. From a high- resolution multiton xenon detector, bound can also be put on τ_1 and τ_2. In Ref. [24], authors have shown that, in case of invisible decay, such detectors can give very strong bounds $\frac{\tau_1}{m_1} \geq 3 \times 10^{-2}$ s/eV and $\frac{\tau_2}{m_2} \geq 8 \times 10^{-3}$ s/eV at 2σ level using solar neutrinos. Decay due to ν_s state can be observed in the present and future atmospheric, accelerator and reactor experiments. One can see Ref. [25] for the study of invisible neutrino decay in ongoing atmospheric neutrino experiment Super-Kamiokande and the future atmospheric neutrino experiment INO. References [26–28] discuss the work on invisible neutrino decay in the accelerator experiments.

The invisible decay of the mass eigenstates ν_1 and ν_2 are strongly constrained as the mixing between ν_1 and ν_2 with ν_e state is large. The remaining possibility is the decay of ν_3 into some fourth neutrino startle which is sterile in nature. The bound on the ν_3 mostly comes from atmospheric and long-baseline experiments. In Ref. [29], the global analysis of the full atmospheric data from Super-Kamiokande together with long-baseline K2K and MINOS has been done to study the interplay of neutrino oscillation with invisible neutrino decay. The bound obtained in this analysis

is $\frac{\tau_3}{m_3} \geq 2.9 \times 10^{-10}$ s/eV at 90% CL. Again, the combined analysis of MINOS and T2K reported the constraint as $\frac{\tau_3}{m_3} \geq 2.8 \times 10^{-12}$ s/eV at 90% CL [30].

In this work, we study the scenario of invisible neutrino decay in two long-baseline experiments at Fermilab, i.e., DUNE and NOvA. Using the simulated data of the DUNE and NOvA experiments, we probe the constraints on $\frac{\tau_3}{m_3}$ assuming the ν_3 state as the unstable state. We have also combined both the experiments to see if the bounds can be improved by the combinations.

The paper is organised as follows: In Sect. 12.2, we have explained the theory of the model. In Sect. 12.3, we present the experimental and simulation details to be used in this work. The results have been presented in Sect. 12.4. Finally, we conclude in Sect. 12.5.

12.2 Theory of Invisible Neutrino Decay

We assume that the third mass eigenstate is unstable and decays into a sterile neutrino and a scalar singlet ($\nu_3 \rightarrow \bar{\nu_4} + J$) with life time τ_3. In this situation, we can write the mass and flavour bases by the following unitary relation

$$\begin{pmatrix} \nu_\alpha \\ \nu_s \end{pmatrix} = \begin{pmatrix} U & 0 \\ 0 & 1 \end{pmatrix} \begin{pmatrix} \nu_i \\ \nu_4 \end{pmatrix} \tag{12.1}$$

where U is the standard Pontecorvo–Maki–Nakagawa–Sakata (PMNS) matrix describing the standard three neutrino oscillations, $\alpha \rightarrow \nu_e, \nu_\mu, \nu_\tau$ and $i = 1, 2, 3$. We assume that the decay eigenstates and the mass eigenstates are the same. Under these assumptions, we can write the neutrino evolution in the presence of matter in the following way:

$$i\frac{d}{dx}\nu_f = \frac{1}{2E}[U\widetilde{H}U^\dagger + A]\nu_f. \tag{12.2}$$

where

$$\widetilde{H} = \begin{pmatrix} 0 & 0 & 0 \\ 0 & \Delta m^2_{21} & 0 \\ 0 & 0 & \Delta m^2_{31} - \frac{im_3}{\tau_3} \end{pmatrix}, \tag{12.3}$$

and

$$A = 2\sqrt{2}G_F n_e E. \tag{12.4}$$

Here, A is the matter potential due to neutrino electron scattering, G_F is the Fermi coupling constant, E is the energy and n_e is the density of electron. We consider $\alpha = \frac{\tau_3}{m_3}$ as the decay rate of m_3 state. The probability of getting a neutrino from an initial ν_a state to ν_b state can be written as

$$P_{ab} = | < \nu_b | \nu_a > |^2 \tag{12.5}$$

where a, b represent the flavour states e, μ, τ.

The effect of the decay comes as the $\exp(-\alpha L/E)$ factor in the probability expression. So an experiment is sensitive to the values of α, where $\alpha \sim E/L$.

12.3 Experimental and Simulation Details

In this section, we describe the experimental details used in our analysis.

12.3.1 DUNE

Deep underground neutrino experiment (DUNE) is an international experiment for neutrino science and proton decay. DUNE will consist of two neutrino detectors: Near detector—It will record the particle interactions near the source of the beam (at Fermi accelerator laboratory in Batavia, Illinois). The source of the beam will consist of an 80–120 GeV proton which will give the neutrino beam eventually; Far detector—It will be installed more than a kilometre underground at the Sandford underground research laboratory in South Dakota-1300 km downstream of the source.

12.3.2 NOvA

The NuMI Off-axis ν_e Appearance (NOvA) experiment uses a neutrino beam from the Fermilab NuMI (neutrino at the main injector). The source power is 10^{21} pot yr^{-1} corresponding to a target power of 1.21 MW. The NOvA experiment consists of two detectors: A 300 metric ton near detector at Fermilab and a 14 metric kiloton far detector in Minnesota, just south of US–Canada border. The neutrino flux are first measured at the near detector and then detected at the far detector situated 810 km away near Ash River, Minnesota, at an off-axis angle. The off-axis location of the far detector gives a narrow energy spectrum at the far detector with a peak near 2GeV.

We have used the GLoBES [31] package to simulate the DUNE and NOvA experiments. For DUNE, our simulations are for a runtime of 5+5 years both in neutrino and antineutrino modes. For NOvA simulations, we have considered exposure of 3 years each for both neutrinos and antineutrinos and hence a total exposure of 6 years. We have modified the probability code of the GLoBES for the calculation of probability in the presence of invisible neutrino decay. We have used $\theta_{12} = 34.8°$, $\theta_{13} = 8.5°$, $\Delta m^2_{21} = 7.54 \times 10^{-5} eV$, $\Delta m^2_{31} = 2.52 \times 10^{-3} eV$ and $\delta_{cp} = -90°$ for generating the simulated data.

12.4 Results and Discussions

Here in this section, we have presented the sensitivity of DUNE and NOvA experiments in the presence of invisible neutrino decay. First, we have shown how the neutrino oscillation probabilities change in the presence of invisible neutrino decay in the $\nu_\mu \to \nu_e$ and $\nu_\mu \to \nu_\mu$ channels. Then we have presented the χ^2 analysis with and without assuming invisible neutrino decay in data.

12.4.1 Probability at DUNE and NOvA Experiments

Here, we have compared the standard 3 flavour oscillation probabilities with the probabilities in the presence of invisible neutrino decay. Figure 12.1 gives the neutrino oscillation probability plots as a function of energy. We present the neutrino oscillation probability plots for appearance and disappearance channels. The left panels of Fig. 12.1 show the probabilities for the appearance channel while the right panels show the probabilities for the disappearance channel. The top panels show the probabilities for DUNE experiment, while the bottom panels show the probability curves for the NOvA experiment.

The red solid lines in all the panels represent the standard 3 flavour oscillation probability. To understand the effect of invisible decay in the neutrino oscillation probabilities, we have considered three values of the decay parameters; the blue lines are for $\alpha = 1.2 \times 10^{-11}$ s/eV, green lines are for $\alpha = 2.36 \times 10^{-11}$ s/eV and the pink lines are for $\alpha = 4.36 \times 10^{-11}$ s/eV, respectively. We have shown the probabilities for two values of $\theta_{23}(\theta_{23} = 48.3^\circ$ and $\theta_{23} = 41.7^\circ)$, i.e., we have shown the results for the true values of θ_{23} in both the octants.

From the probability plots, it is observed that the effect of invisible neutrino decay is significant at the oscillation maxima for both the experiments. The appearance probability is somehow larger in the higher octant compared to the lower octant both in the presence and absence of the neutrino decay. However, in the disappearance channel, the effect of the octant is not much significant. But still, the presence of invisible neutrino decay can also be realised in the disappearance channel.

12.4.2 χ^2 Analysis

Here in Fig. 12.2, we have shown the sensitivities of different experiments to constrain the decay parameter α. The red solid lines in the plots are obtained from the DUNE experiment, blue lines are obtained from NovA experiment and green lines are obtained from the combination of DUNE and NOvA experiments.

In the top panel, we assume that nature does not permit neutrinos to decay and hence we have simulated the invisible neutrino decay in the theory only. On the other

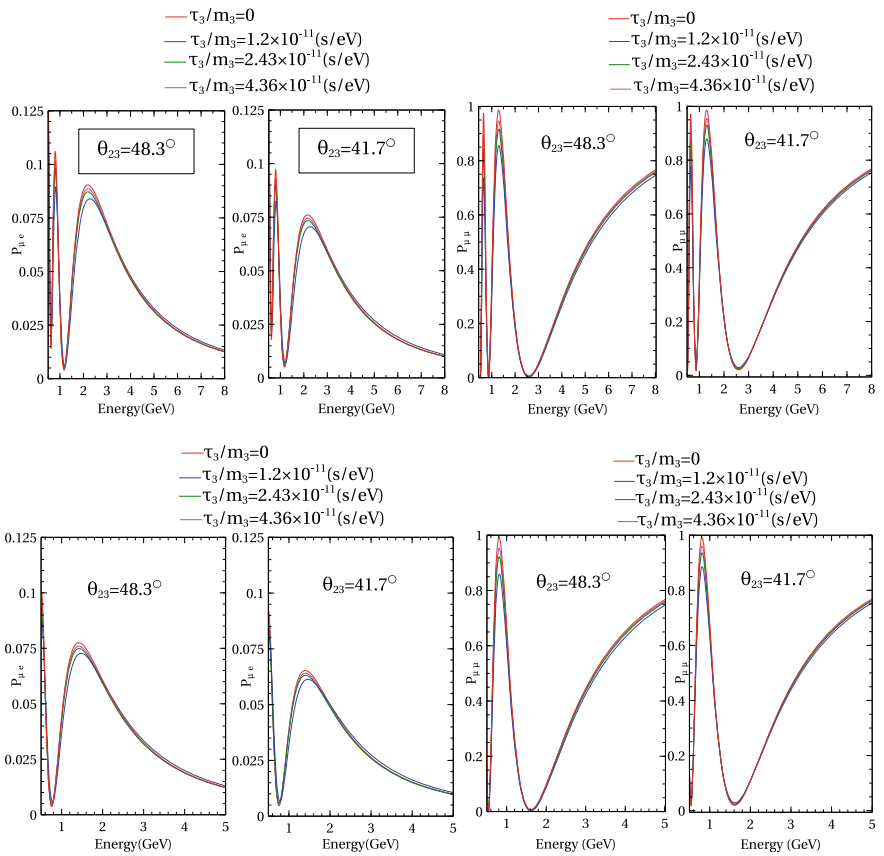

Fig. 12.1 The appearance (left panels) and disappearance (right panels) channels of neutrino probabilities for both DUNE (Top panels) and NOvA (Bottom panels) experiments as a function of neutrino energy

hand, in the lower panel, we have shown the sensitivity of the two experiments to measure invisible neutrino decay if nature has some neutrino states which can decay.

It can be seen from the top panel that (no decay in data) at 3σ CL for $\theta_{23} = 41.7°$, DUNE could constrain all $\alpha > 2.69 \times 10^{-11}$ s/eV while NOvA could constrain all $\alpha > 3.16 \times 10^{-12}$ s/eV. The combination of DUNE+NOvA could constrain all $\alpha > 2.95 \times 10^{-11}$ s/eV at 3σ CL. We have also observed the same for $\theta_{23} = 48.3°$, and we can see that for $\theta_{23} = 48.3°$ DUNE could constrain all $\alpha > 3.12 \times 10^{-11}$ s/eV, NOvA could constrain all $\alpha > 3.47 \times 10^{-12}$ s/eV and the combination can constrain all $\alpha > 3.12 \times 10^{-11}$ s/eV. It is observed that the effect of combining the two long baseline experiments is not significantly changing the results compared to the sensitivity of DUNE. So the combined result obtained in this analysis is an improvement over Ref [30] where a combined analysis of T2K and MINOS had been carried out.

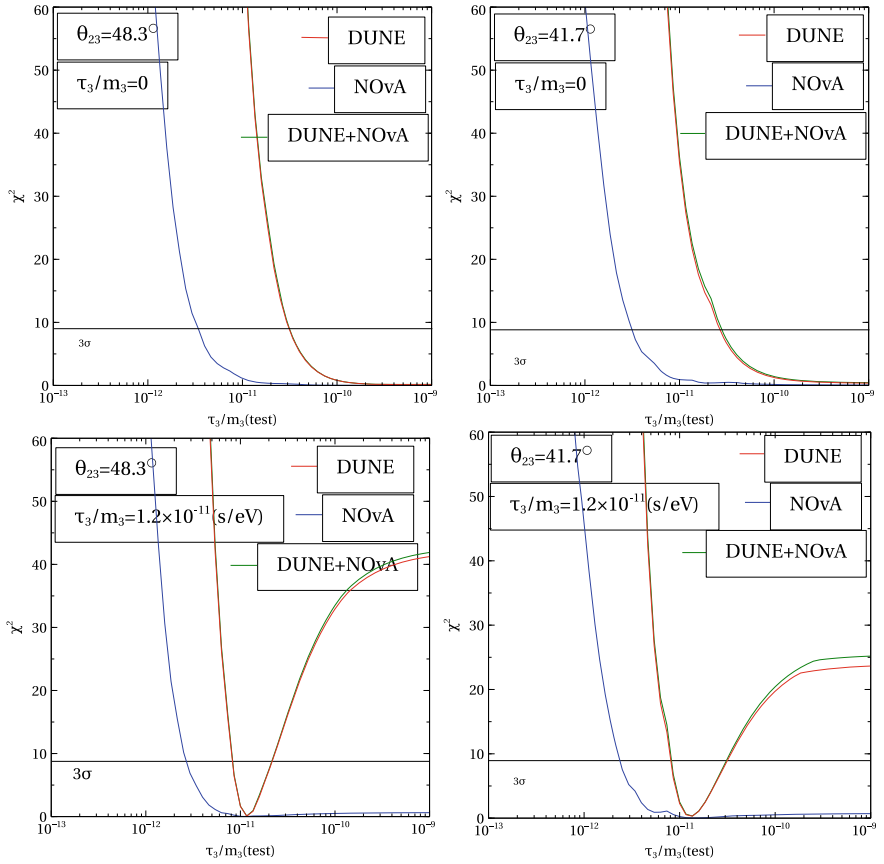

Fig. 12.2 The χ^2 as a function of α for DUNE, NOvA and DUNE+NOvA experiments

It is observed from the bottom panel where we have assumed decay both in the data and theory that DUNE has much better precision than NOvA at 3σ CL, and it can precisely measure α in the range 3.17×10^{-11} s/eV$> \alpha > 8.27 \times 10^{-12}$ s/eV for the given true value of $\alpha = 1.2 \times 10^{-11} s/eV$ when the atmospheric mixing angle is in the lower octant, i.e., $\theta_{23} = 41.7°$, whereas for the same value of α and θ_{23}, NOvA can constrain all $\alpha > 2.36 \times 10^{-12}$ s/eV at 3σ CL. The combination, on the other hand, can constrain all 3.17×10^{-11} s/eV$> \alpha > 8.27 \times 10^{-12}$ s/eV at 3σ CL.

Similarly for the same value of α and true $\theta_{23} = 48.3°$, we have seen the constraints for three sets of experiments. We can see that at 3σ CL, DUNE could constrain all 2.23×10^{-11} s/eV$> \alpha > 8.33 \times 10^{-12}$ s/eV while NOvA could constrain all $\alpha > 2.7 \times 10^{-12}$ s/eV. The combination of DUNE+NOvA can constrain all 2.23×10^{-11} s/eV$> \alpha > 8.33 \times 10^{-12}$ s/eV 3σ CL.

12.5 Summary and Conclusion

We have analysed the DUNE and NOvA data for invisible neutrino decay. We have assumed a case where ν_3 is unstable and it decays into some sterile state. We have used the modified GLoBES [32] for simulating the DUNE and NOvA experiments. We have shown the probabilities for DUNE and NOvA experiments both for appearance and disappearance channels. We have considered three different values ($\alpha = 1.2 \times 10^{-11}$ s/eV, $\alpha = 2.36 \times 10^{-11}$ s/eV and $\alpha = 4.36 \times 10^{-11}$ s/eV) of decay parameters in our simulation to calculate the probabilities. We have also checked how DUNE, NOvA and DUNE+NOvA experiments can put a bound on decay parameters. We have shown the sensitivity of DUNE, NOvA and DUNE+NOvA experiments by considering $\alpha = 1.2 \times 10^{-11} s/eV$.

As seen from Fig. 12.2 (top panel), DUNE rules out all $\frac{\tau_3}{m_3} > 2.69 \times 10^{-11}$ s/eV (approx) at 3σ CL and around 1.2×10^{-11} s/eV (approx) at 5σ CL if θ_{23} is in the lower octant. The sensitivity of DUNE lies in the range 3.17×10^{-11}s/eV$> \alpha > 8.27 \times 10^{-12}$ s/eV if nature allows ν_3 to decay and can have the value around 1.2×10^{-11} s/eV. However, if θ_{23} is in the lower octant (top panel), NOvA can constrain all $\alpha > 3.16 \times 10^{-12}$s/eV at 3σ CL for no decay case.

We have measured the constraints on the decay parameters by combining NOvA and DUNE experiments. It is observed that DUNE has much better ability to constrain invisible neutrino decay as compared to NOvA. However, the combination of both the experiments is not significantly improving the constraints.

References

1. Q.R. Ahmad et al., SNO. Phys. Rev. Lett. **89**, 011301 (2002). (nucl-ex/0204008)
2. A. Gando et al. (KamLAND), Phys. Rev. D **83**, 052002 (2011), 1009.4771
3. Y. Fukuda et al., Super-Kamiokande. Phys. Rev. Lett. **81**, 1562 (1998). (hep-ex/9807003)
4. F. P. An et al. (Daya Bay), Phys. Rev. Lett. **108**, 171803 (2012), 1203.1669
5. Y. Abe et al. (Double Chooz), Phys. Rev. Lett. **108**, 131801 (2012), 1112.6353
6. J. K. Ahn et al. (RENO), Phys. Rev. Lett. **108**, 191802 (2012), 1204.0626
7. K. Abe et al. (T2K), Phys. Rev. Lett. **118**, 151801 (2017), 1701.00432
8. P. Adamson et al. (NOvA), Phys. Rev. Lett. **116**, 151806 (2016), 1601.05022
9. P. Adamson et al. (NOvA) (2017), 1703.03328
10. DUNE collaboration, Long-Baseline Neutrino Facility (LBNF) and Deep Underground Neutrino Experiment (DUNE): Conceptual Design Report, Volume 2: The Physics Program for DUNE at LBNF, 1512.06148
11. Hyper-Kamiokande Proto-collaboration, Physics potential of a long-baseline neutrino oscillation experiment using a J-PARC neutrino beam and Hyper-Kamiokande, PTEP 2015 (2015) 053C02 [1502.05199]
12. Hyper-Kamiokande collaboration, Physics potentials with the second Hyper-Kamiokande detector in Korea, PTEP 2018 (2018) 063C01 [1611.06118]
13. ESSnuSB collaboration, A very intense neutrino super beam experiment for leptonic CP violation discovery based on the European spallation source linac, Nucl. Phys. B **885** (2014) 127 [1309.7022]
14. JUNO collaboration, Neutrino Physics with JUNO, J. Phys. G **43** (2016) 030401 [1507.05613]

15. I.C.A.L. Collaboration, S. Ahmed et al., Physics potential of the ICAL detector at the India-based Neutrino Observatory (INO). Pramana **88**, 79 (2017). ([arXiv:1505.07380])
16. IceCube PINGU collaboration, Letter of Intent: The Precision IceCube Next Generation Upgrade (PINGU), 1401.2046
17. KM3NeT collaboration, The KM3NeT deep-sea neutrino telescope, Nucl. Instrum. Meth. A **766** (2014) 83 [1408.1392]
18. M. Lindner, T. Ohlsson, W. Winter, A combined treatment of neutrino decay and neutrino oscillations. Nucl. Phys. B **607**, 326 (2001). ([hep-ph/0103170])
19. C. Kim, W. Lam, Some remarks on neutrino decay via a Nambu-Goldstone boson. Mod. Phys. Lett. A **5**, 297 (1990)
20. A. Acker, A. Joshipura, S. Pakvasa, A Neutrino decay model, solar anti-neutrinos and atmospheric neutrinos. Phys. Lett. B **285**, 371 (1992)
21. J. N. Bahcall, N. Cabibbo, and A. Yahil, Phys. Rev. Lett. **28**, 316 (1972), [285(1972)]
22. R. Picoreti, M.M. Guzzo, P.C. de Holanda, O.L.G. Peres, Neutrino Decay and Solar Neutrino Seasonal Effect. Phys. Lett. B **761**, 70 (2016). ([arXiv:1506.08158] [INSPIRE])
23. Kamiokande-II Collaboration, K. Hirata et al., Observation of a neutrino burst from the supernova SN1987A, Phys. Rev. Lett. **58** (1987) 1490
24. G.-Y. Huang and S. Zhou, Constraining Neutrino Lifetimes and Magnetic Moments via Solar Neutrinos in the Large Xenon Detectors, JCAP **02** (2019) 024 [1810.03877]
25. Super-Kamiokande Collaboration, J. Hosaka et al., Three flavor neutrino oscillation analysis of atmospheric neutrinos in Super-Kamiokande, Phys. Rev. D **74** (2006) 032002, [hep-ex/0604011]
26. S. Choubey, D. Dutta, D. Pramanik, Invisible neutrino decay in the light of NOvA and T2K data. JHEP **08**, 141 (2018). ([arXiv:1805.01848])
27. S. Choubey, S. Goswami, D. Pramanik, A study of invisible neutrino decay at DUNE and its effects on θ_{23} measurement. JHEP **02**, 055 (2018). ([arXiv:1705.05820])
28. J. Tang, T.-C. Wang, Y. Zhang, Invisible neutrino decays at the MOMENT experiment. JHEP **04**, 004 (2019). ([arXiv:1811.05623])
29. M. C. Gonzalez-Garcia, and Michele Maltoni, Status of Oscillation plus Decay of Atmospheric and Long-Baseline Neutrinos, Phys. Lett. B **663**, 405–409, (2008) [arXiv:0802.3699v2]
30. R. A. Gomes[a,b], A. L. G. Gomes[a], and O. L. G. Peres[c,d], Constraints on neutrino decay lifetime using long-baseline charged and neutral current data, Phys. Lett. B **740** (2015) 345, [arXiv:1407.5640]
31. P. Huber, M. Lindner, W. Winter, Simulation of long-baseline neutrino oscillation experiments with GLoBES (General Long Baseline Experiment Simulator). Comput. Phys. Commun. **167**, 195 (2005). ([hep-ph/0407333])
32. P. Huber, J. Kopp, M. Lindner, M. Rolinec, and W. Winter, New features in the simulation of neutrino oscillation experiments with GLoBES 3.0: General Long Baseline Experiment Simulator, Comput. Phys. Commun. **177** (2007) 432, [hep-ph/0701187]

Chapter 13
Flux Distribution Study of Mkn 421 with SPOL, RXTE and Fermi-LAT Telescopes

Rukaiya Khatoon, Zahir Shah, Raj Prince, Ranjeev Misra, and Rupjyoti Gogoi

Abstract We analyse the long-term γ-ray data (2008–2019) for blazar Mkn 421 using Fermi-LAT. The contemporaneous optical (2008–2018) and X-ray (1996–2012) data obtained by SPOL and RXTE observatories are also used. We apply the condition of $\mathbb{R} = \overline{\sigma_{err}^2}/\sigma^2$ is applied on the observed light curves to get the statistically significant light curves. We present here the flux distribution study of the selected light curves using the Anderson–Darling (AD) test and histogram fitting methods. The optical flux resembles lognormal distribution, which is consistent with the AD test result. However, γ-ray and X-ray flux distributions are neither normal nor lognormal by AD test, and their flux histograms show double hump structures. The two peaks in the flux histograms can be fitted with double lognormal probability distribution functions. We report the correlation between the simultaneous light curves using the DCF method. The significant correlation observed between γ-ray and optical light curves with zero time lag suggests that the emissions are co-spatial and a similar emission mechanism is responsible for them. Further, the optical and γ-ray spectrum that lies before the synchrotron-peak and Compton-peak suggest that the low-energy electron distributions are responsible for these emissions. However, the inconsistency in their flux distributions is possibly associated with the gaps in the optical light curve.

13.1 Introduction

Blazars are the radio-loud active galactic nuclei (AGN) with relativistic jets oriented close to the observer line of sight [1]. Blazars are further classified into two

R. Khatoon (✉) · R. Gogoi
Tezpur University, Napaam 784028, Assam, India

Z. Shah · R. Misra
Inter-University Center for Astronomy and Astrophysics, Post Bag 4, Ganeshkhind Pune 411007, India

R. Prince
Center for Theoretical Physics, Polish Academy of Sciences, Al.Lotnikov 32/46, 02-668, Warsaw, Poland

S. Sengupta et al. (eds.), *Selected Progresses in Modern Physics*, Springer Proceedings in Physics 265, https://doi.org/10.1007/978-981-16-5141-0_13

subclasses, namely, BL-Lac objects and Flat Spectrum Radio Quasars (FSRQs). The classification is based on the presence or absence of the emission/absorption line features in the optical spectrum like FSRQs show strong emission lines, whereas for BL-Lacs, the emission lines are faint. One of the distinct properties of blazars is their rapid flux variability across the entire electromagnetic spectrum on timescales ranging from years down to minutes. The cause of the variability is still not well understood, however, long-term flux distribution study of blazars can hint about the underlying particle acceleration and diffusion processes.

Mkn 421, located at a redshift of 0.031 is the first detected TeV blazar. This is the BL-Lac type object with the peak of the synchrotron spectrum lies in the X-ray regime. The source is highly variable across the entire wavebands from radio to TeV and at all timescales [2–4]. This is a widely studied BL-Lac object across the entire electromagnetic spectrum. The flux distribution studies of Mkn 421 have shown single as well as double lognormal in different energy bands. A study of long-term data (2009–2015) collected from various instruments has clearly detected the lognormal behavior at different energy bands [5]. The bi-lognormal profile has also been revealed in X-ray energy band [6]. Recently, a detailed flux distribution study of Mkn 421 during its historically low state between 2015–2016 suggests a possibility of both Gaussian and lognormal at the wavebands ranging from VHE gamma-rays to the radio at 37 GHz.

The source has been monitored in γ-ray by Fermi-LAT, and its optical counterpart has been observed by the SPOL telescope at the Steward Observatory. Along with these observations, we selected the X-ray data using RXTE-Proportional Counter Array (PCA). In case of pointing instruments, Target of Opportunity may bias the observations towards high flux states, and therefore, the flux distribution study may not be reliable. Therefore, to reduce the effects being introduced by the bias, we binned the light curves by clubbing the flux points from 2 days to 10 days. Further, the uncertainties in the light curves due to the measurement errors have been taken care of in the analysis. The flux distribution study using multiband observations has been performed previously by other authors [5–7], however; we present here the updated light curves, which are further analyzed to get the statistically significant flux light curves. The final light curves were then used to perform the distribution study and the correlation study, respectively. The paper is assembled as follows: in Sects. 13.2 and 13.3, we describe about the data analysis and the light curve selection procedures. In Sects. 13.4 and 13.5, we present the flux distribution study and the correlation study of the selected light curves. Finally, in Sect. 13.6, we discuss the results.

13.2 Multiwaveband Observations

We present the multiwaveband flux light curves for the source Mkn 421 based on the observations from Fermi-LAT, RXTE, and SPOL telescopes.

13.2.1 Fermi-LAT Data Analysis

The Large Area Telescope (LAT) on board the Fermi satellite is a pair conversion telescope with a field of view ∼2.4sr and an effective area ∼8000 cm^2/GeV photon. It is sensitive to photon energy with a range from 20 MeV to more than 300 GeV. The observation mode of Fermi-LAT is a monitoring mode, which scans the entire sky every 3 h. The source Mkn 421 has been monitored continuously by Fermi-LAT in γ-ray, since August 2008. We consider the γ-ray data for the selected source during the period from 2008 to 2019 (MJD 54688–58624). The data were then analyzed with the help of the maximum likelihood method (gtlike) and the standard Fermi Science Tools[1] (version v10r0p5). The analysis was carried out in the energy range from 100 to 300 GeV, with a region of interest (ROI) of 10 degrees centering the source position. We estimated the photon flux with the detection significance of $\sqrt{TS} \approx 3\sigma$.

13.2.2 RXTE

The Rossi X-ray Timing Explorer (RXTE) provides a systematically analyzed flux and index light curves for the AGN source for a long duration from 1996 to 2012. It consists of two co-aligned instruments: one is the Proportional Counter Array (PCA, 2–60 keV) and another is the High-Energy X-ray Timing Experiment (HEXTE, 15–250 keV). We consider the 2–10 keV long-term flux light curves for the selected source for the duration from 1996 January to 2012 January. The data is publicly available on the webpage.[2] The light curve is unevenly sampled since observations for different periods had been proposed for different scientific goals.

13.2.3 SPOL

The SPOL is a ground-based imaging telescope at the Steward Observatory situated at the University of Arizona. It monitors the gamma-ray sources, especially blazars in the optical V and R bands. It also has the capability to measure the polarization and the position angle from the optical emission. The source Mkn 421 has been monitored as a part of the Fermi multiband support program. We have downloaded the optical R-band and V-band data (from 2008 to 2018), which is publicly available on the SPOL webpage.[3]

[1] https://fermi.gsfc.nasa.gov/ssc/data/analysis/documentation/.

[2] https://cass.ucsd.edu/rxteagn/.

[3] http://james.as.arizona.edupsmith/Fermi/.

13.3 Lightcurve Selection

To select the light curves with good significance, we define the significance fraction as, $\mathbb{R} = \overline{\sigma_{err}^2}/\sigma^2$, where $\overline{\sigma_{err}^2}$ and σ^2 are the mean square error and the variance of flux distribution, respectively. The light curve with less uncertainty, i.e., with $\mathbb{R} < 0.2$, will be used for further studies. The condition of $\mathbb{R}$ is not satisfied with the selected unbinned light curves for all the wavebands. Therefore, we binned the flux light curves such that the combined the flux points range from 2 days to a maximum of 10 days. We also ensure that the number of data points (N) in the binned lightcurve should be >100. After applying these conditions, we are restricted to 10 days binned γ-ray light curve, 2 days binned X-ray, and optical light curves. These binned light curves have been used throughout the studies. The binned light curves are presented in Fig. 13.1, and $\mathbb{R}$ and N values are reported in Table 13.1.

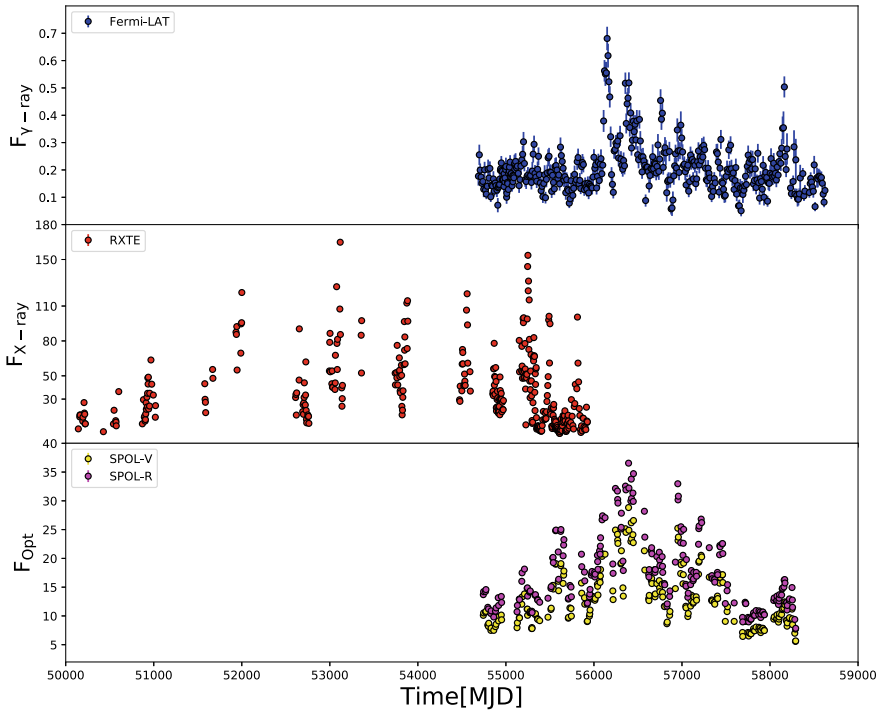

Fig. 13.1 Multiwaveband flux light curves. Panel 1: Fermi-LAT flux in 10^{-6} ph cm^{-2} s^{-1}, panel 2: RXTE-PCA flux in 10^{-11} erg cm^{-2} s^{-1}, panel 3: Optical flux in 10^{-11} erg cm^{-2} s^{-1}

Table 13.1 Significance fraction "$\mathbb{R}$" values of normal fluxes and the AD test results for the normal and lognormal fluxes of the gamma-ray, X-ray, and optical R-band light curves (see Fig. 13.1) for the source Mkn 421

Facility	No. of data points	$\mathbb{R} = \frac{\overline{\sigma_{err}^2}}{\sigma^2}$	Normal (Flux)AD(p-value)	Lognormal (Flux)AD(p-value)
Fermi (10d binned)	421	0.12	13.94(3.7×10^{-24})	1.76(1.65×10^{-4})
RXTE (2d binned)	360	2.72×10^{-5}	11.74(3.7×10^{-24})	3.79(1.77×10^{-9})
SPOL band-V (2d binned)	227	1.81×10^{-3}	5.19(7.13×10^{-13})	1.03(0.04)

13.4 Distribution Study

Blazars being a variable source, their fluxes vary significantly and the flux distribution study can provide hints causing such variations. Their long-term flux distribution in various energies has been studied recently by various authors [5–8]. Typically, when the flux variation are stochastic and linear, one would obtain a Gaussian distribution of fluxes with the width of the distribution determining the flux variation. However, if the stochastic flux variation is non-linear, one would obtain a Gaussian distribution in logarithmic flux values and this is commonly referred as lognormal distribution. In such case, the flux distribution can be expressed as

$$f(x) = \frac{1}{\sigma\sqrt{2\pi}} \frac{1}{x} \exp\left[\frac{-(\log x - \mu)^2}{2\sigma^2}\right] \tag{13.1}$$

where, σ is the standard deviation and μ is the mean flux. Non-linearity expressed by a lognormal flux distributions suggests, the underlying process responsible for the flux variation to be a multiplicative one [9].

Lognormal flux distributions are often found in galactic and extragalactic sources, like X-ray binaries, gamma-ray bursts, and AGNs, at different timescales ranging from sub-second to days [9, 10]. Among blazars, such lognormal behavior is seen across the electromagnetic spectrum for many BL-Lac objects and FSRQs [2, 5–8, 12]. In addition to the single lognormal, double lognormal distributions have also been obtained at different wavebands [6, 7, 12]. The lognormal behavior of these astrophysical sources is usually interpreted as due to fluctuations in accretion disk and thereby propagating into the jets. However, [13] showed that a linear Gaussian perturbation in the particle acceleration timescale can reproduce such lognormal distribution in the flux.

13.4.1 AD Test

Several studies of blazar flux distribution show an asymmetric trend in the flux light curves. The Anderson-Darling (AD) test is a useful statistical tool to check the normality of the data. The null hypothesis probability value (p-value) of the AD test is such that p-value >0.01 would indicate the normal distribution, otherwise it would indicate the deviation from the normality. The p-value for the 10d binned γ-ray lightcurve suggests that the fluxes are neither Gaussian nor lognormal distributed. Similar results have been found for the 2d binned X-ray lightcurve. However, p-value for the 2d binned optical lightcurve indicates a lognormal flux distribution.

13.4.2 Flux Histogram

Further, we construct the histogram of the log of flux with the selected light curves. The optical light curve which shows a single peak in the histogram is fitted with the lognormal PDF (see Eq. 13.1), while the γ-ray and X-ray light curves show two hump structures in their flux histograms. Subsequently, we fitted the histograms with the double lognormal PDF. The histogram plots are shown in Fig. 13.2 and the best fit parameter values are given in Table 13.2.

13.5 Correlation Study: DCF Method

The Discrete Correlation Function (DCF) method was presented by Edelson and Krolik [14] to search for the correlations and the possible time delays between two different light curves. We apply the DCF method to study the correlation between the selected light curves.

The RXTE observation provides the data up to MJD-55925 (see Fig. 13.1), therefore, to check the possible correlation between the X-ray lightcurve with the γ-ray/optical bands, we consider the simultaneous data of γ-ray/optical, with the X-ray one.

1. **Correlation between γ-ray and optical bands**: The γ-ray and R-band optical light curves have a 10-years long overlap (2008–2018) (MJD 54743–58291), as shown in Fig. 13.1. The DCF correlation between γ-ray and optical light curves suggests a moderate correlation of 58% with zero time lag.
2. **Correlation between γ-ray and X-ray bands**: The γ-ray and X-ray light curves have a 3-year long overlap (2009–2012) (MJD 54832–55930), as shown in Fig. 13.1. We observed a weak correlation of 38% with zero time lag.

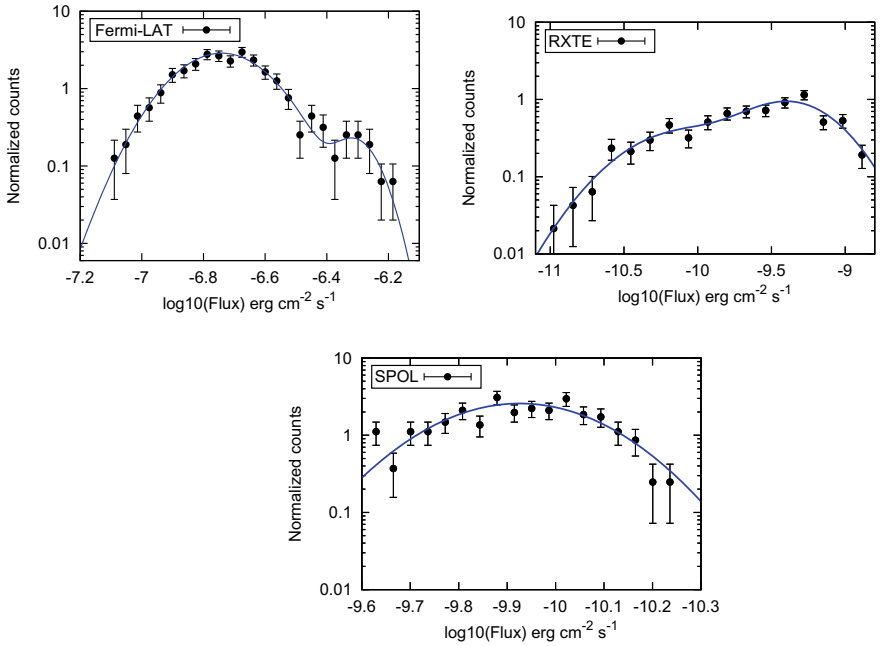

Fig. 13.2 Histograms of the logarithm of fluxes at different wavebands

Table 13.2 Best fit parameter values of the double lognormal PDF fitted to the logarithm of gamma-ray and X-ray flux histograms, and lognormal PDF fitted to the logarithm of optical flux histogram

	μ_1	σ_1	μ_2	σ_2	a	dof	χ^2/dof
Fermi(10d)	-6.31 ± 0.02	0.06 ± 0.02	-6.74 ± 0.005	0.13 ± 0.004	0.82 ± 0.09	20	0.76
RXTE(2d)	-9.37 ± 0.11	0.29 ± 0.06	-10.09 ± 0.33	0.37 ± 0.19	0.36 ± 0.28	13	1.14
SPOL-V(2d)	-9.92 ± 0.02	0.18 ± 0.02	–	–	–	16	0.9

3. **Correlation between X-ray and optical bands**: The X-ray and R-band optical light curves have a 3-year long overlap (MJD 54831–55926) as shown in Fig. 13.1. The DCF correlation result suggests that there is no correlation between the X-ray and optical bands (Fig. 13.3).

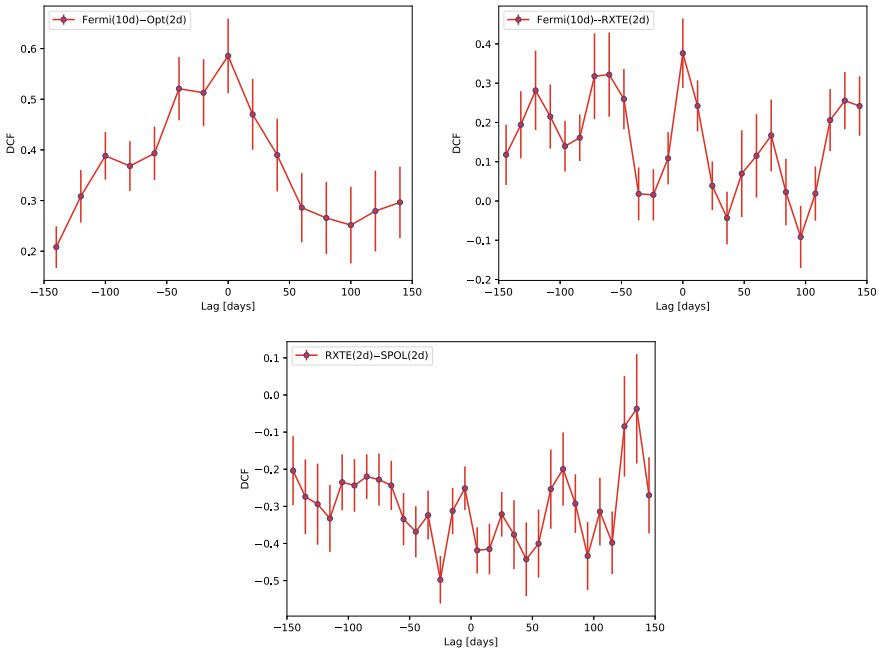

Fig. 13.3 The DCF plots between various wavebands

13.6 Discussion

We perform the AD test and histogram fitting on the selected light curves to characterize their flux distributions. The AD test statistic results suggest that the flux distribution of optical lightcurve is consistent with the lognormal distribution and the histogram is fitted well with the lognormal PDF. While the flux distribution for γ-ray and X-ray light curves are not consistent with either Gaussian or lognormal distribution as suggested by the AD test. Moreover, their flux histograms show two peaks and are consistently fitted with the double lognormal PDFs. Previously, [5] showed that the γ-ray flux observed by Fermi-LAT over a period of 2009–2015, preferred the single lognormal distribution. However, in this study, we have used updated data till 2019, and possibly the extended data included an additional peak in the flux histogram. Furthermore, The double lognormal flux distributions in γ-ray and X-ray have been found previously by [6, 7, 12].

Further, we study the correlation between the simultaneous light curves using the DCF method. The correlation with zero time lag between the γ-ray and optical bands suggests the emissions in both the bands may have a similar origin [5]. In case of HBL source like Mkn 421, the optical and γ-ray emissions fall before the break energy of the synchrotron and Compton spectrum, hence the emissions are mainly due to the low-energy end of the electron distributions. Therefore, they may have similar

feature in their light curves and hence flux histograms. However, the optical ligtcurve shows single lognormal distribution, while the γ-ray has bi-lognormal distribution. The possible reason behind this is that the optical lightcurve has gaps because of the pointing observations, and therefore, it might have removed the possible second peak from the distribution.

Acknowledgements RK and RG would like to thank CSIR, New Delhi (03(1412)/17/EMR-II), for financial support.

References

1. C.M. Urry, P. Padovani, Unified schemes for radio-loud active galactic nuclei. PASP **107**, 803 (1995)
2. A. Shukla, V.R. Chitnis, P.R. Vishwanath et al., Multiwavelength study of the TeV blazar Mrk 421 during a giant flare. Astron. Astrophys. **541**, A140 (2012)
3. A. Sinha, A. Shukla, R. Misra et al., Underlying particle spectrum of Mkn 421 during the huge X-ray flare in April 2013. Astron. Astrophys. **580**, A100 (2015)
4. V.A. Acciari, E. Aliu, T. Aune et al., Simultaneous multiwavelength observations of Markarian 421 during outburst. Astrophys. J. **703**, 169 (2009)
5. A. Sinha, A. Shukla, L. Saha et al., Long-term study of Mkn 421 with the HAGAR array of telescopes. Astron. Astrophys. **591**, A83 (2016)
6. R. Khatoon, Z. Shah, R. Misra et al., Study of long-term flux and photon index distributions of Blazars using RXTE observations. Mon. Not. R. Astron. Soc. **491**, 1934 (2020)
7. Z. Shah, N. Mankuzhiyil, A. Sinha et al., Log-normal flux distribution of bright Fermi Blazars. Res. Astron. Astrophys. **18**, 141 (2018)
8. R. Prince, R. Khatoon, C.S. Stalin, Broad-band study of OQ 334 during its flaring state. Mon. Not. R. Astron. Soc. **502**, 5245 (2021)
9. P. Uttley, I.M. McHardy, S. Vaughan, Non-linear X-ray variability in X-ray binaries and active galaxies. Mon. Not. R. Astron. Soc. **359**, 345 (2005)
10. B. Giebels, B. Degrange, Lognormal variability in BL Lacertae. Astron. Astrophys. **503**, 797 (2009)
11. J. Chevalier, M.A. Kastendieck, F.M. Rieger et al., 34th International Cosmic Ray Conference (ICRC2015), p. 829 (2015)
12. P. Kushwaha, S. Chandra, R. Misra et al., Evidence for two lognormal states in multi-wavelength flux variation of FSRQ PKS 1510–089. Astrophys. J. Lett. **822**, 13 (2016)
13. A. Sinha, R. Khatoon, R. Misra et al., The flux distribution of individual Blazars as a key to understand the dynamics of particle acceleration. Mon. Not. Royal Astron. Soc. Lett. **480**, 116 (2018)
14. R.A. Edelson, J.H. Krolik, The discrete correlation function: a new method for analyzing unevenly sampled variability data. Astrophys. J. **333**, 646 (1988)

Chapter 14
Growth, Structural, Optical, Thermal and Mechanical Studies of a Novel Nickel Sulphate Admixtured Sulphamic Acid Single Crystals for Optical Applications

S. Anciya, A. S. I. Joy Sinthiya, P. Selvarajan, and R. Sree Devi

Abstract A novel good quality crystal of nickel sulphate-doped sulphamic acid (NSSA) has been grown by slow evaporation solution growth technique at room temperature. The single crystal XRD analysis confirms that the grown sample belongs to monoclinic system with the space group of P_{21}/C. UV-Vis studies reveal that the crystals have the good optical transmission in the whole visible region. Photoluminescence spectra for the NSSA crystals were recorded using fluorescent spectrophotometer. EDAX analysis confirms that (Ni) ion is incorporated in the harvested crystal. The surface analysis is carried out using a scanning electron microscope (SEM) which shows that the surface has fine morphology with microcrystal. Thermogravimetric analysis measure the dehydration temperature of the nickel sulphate-doped sulphamic acid crystal, which is found to be about 130 °C. Vickers hardness analysis validate that these crystals have good mechanical strength.

14.1 Introduction

Bulk single crystals are the backbone of the modern technological devices [1]. The search of new organic, inorganic and semi organic nonlinear materials which have potential applications in photonics, optoelectronics, optical communication, optical image processing is increased in recent times. Sulphamic acid and its derivatives have wide industrial applications [2]. It is a strong inorganic acid that exhibits zwitterion form while mixing it with water [3, 4]. Due to the rapid growth of laser diode industries, the influence of metal ions on the single crystals is currently receiving

S. Anciya (✉) · A. S. I. J. Sinthiya
PG and Research Department of Physics, The M. D. T. Hindu College, Tirunelveli, Tamil Nadu 627010, India

P. Selvarajan · R. Sree Devi
Department of Physics, Aditanar College of Arts and Science, Tiruchendur, Tamil Nadu 628216, India

S. Anciya · A. S. I. J. Sinthiya · P. Selvarajan · R. Sree Devi
Manonmaniam Sundaranar University, Abishekapatti, Tirunelveli-12, Tamil Nadu, India

S. Sengupta et al. (eds.), *Selected Progresses in Modern Physics*, Springer Proceedings in Physics 265, https://doi.org/10.1007/978-981-16-5141-0_14

a great interest. In recent past, efforts have been made to understand the inclusion of inorganic metal ions, which changes the growth rate and the physical properties of single crystals. Doping of divalent metals can alter the optical activity which makes it a promising candidate for optoelectronic application [5, 6]. Hence, in the present work, the growth and characterization of nickel-incorporated sulphamic acid single crystals by SEST method is reported. The crystalline perfection, structural, optical and thermal behaviour of the grown crystal were revealed by single crystal X-ray diffraction, UV-Vis-NIR, TG/DTA, photoluminescence, SEM-EDS and microhardness studies.

14.2 Experimental Details

14.2.1 Experimental Procedure

In order to grow (NS:SA) crystals, the high purity (99%) Analar grade sulphamic acid (H_2NSO_3H), and nickel sulphate ($NiSO_4$) were taken in equimolar ratio in 100 ml of deionized water, in a glass beaker and stirred by magnetic stirrer for 2 hrs to obtain saturated solution at room temperature. This solution was filtered using filter paper to get clear solution and kept for growth in a dust-free place at room temperature. In a period of 40 days' time, a good quality, transparent crystal, with dimension of about $10 \times 10 \times 11$ mm^3, was harvested. The grown crystals are shown in Fig. 14.1.

Fig. 14.1 As grown NS:SA single crystal

Table 14.1 Lattice parameters of pure SA and NS:SA single crystals

Parameter	Pure SA	NS:SA
a Å	8.100	6.2205
b Å	8.049	12.4408
c Å	9.220	9.1644
V $Å^3$	604.8	678.49

14.2.2 Characterization Techniques

SCXRD analysis is done by BRUKER KAPPA APEX II of the grown crystal. The energy dispersive X-ray (EDX) analysis spectrum was recorded using Jeol 6390LA/OXFORD XMX N, accelerating voltage varied from 0.5 to 30 kV. Thermal behaviour of grown crystal is calculated between 3 and 75 °C in nitrogen atmosphere at a heating rate of 2 °C/min using HITACHI-STA7300 thermal analysis system. Optical properties in the visible wavelength range of 190–1100 nm were studied using Lamda 35 UV-Vis-NIR Spectrophotometer by dissolving the crystals in double distilled water. Microhardness of the pure and nickel sulphate-doped SA was determined using Shimadzu HMV-2T with a Vickers diamond indenter attached with an optical microscope. The Photoluminescence (PL) Spectrum study of NSSA crystal was captured with the Perkin Elmer LS 45 photo spectrometer in the range between 200 and 900 nm with an excitation wavelength of 395 nm.

14.3 Results and Discussion

14.3.1 Single Crystal X-ray Diffraction

The crystal structure system and the lattice parameters of the as grown NS:SA single crystal were identified by using the Bruker Kappa Apex II X-ray diffractometer. The observed lattice parameters and volume are given in Table 14.1. While analysing the data given in the table, it can be seen that in nickel sulphate-doped crystal, the values of 'a', 'b' and 'c' are different, indicating that it crystallizes in monoclinic structure with space group P_{21}/C, whereas the pure SA crystal is orthorhombic [7]. This clearly indicates that the metal ion inside the crystal lattice has some effect on the structural parameters.

14.3.2 Energy-Dispersive X-ray Spectroscopy

The elemental composition of the sample can be described, based on the energy difference of the two shells and of the atomic structure of the compound, which is

Table 14.2 Elemental composition of NS:SA crystal

Element	Weight%	Atomic%
O	11.84	18.54
C	57.64	67.8
S	14.53	8.53
Ni	15.99	5.13

influenced by the energy of emitted X-rays from the sample. The existence of the nickel (Ni) ions in the crystalline lattice was confirmed by the EDAX analysis. The amount of Nickel (Ni), Sulphur (S), Oxygen (O) and carbon (C) present in the grown sample is listed in Table 14.2.

14.3.3 UV-Vis-NIR Spectroscopy

The optical studies are essential for identifying the practical application of the crystals in the field of optics. The optical transmission spectrum gives valuable information about the structure of the molecule, because the absorption of UV and visible light involves promotion of electrons in σ and π orbits from the ground state to a higher energy state [8]. Transmittance of the grown crystals is examined from 190 to 1100 nm using lambda 35 UV-Vis-NIR spectrometer. The transmittance spectrum of NS:SA single crystal has a good transmission and the lower cut off wavelength is 200 nm, whereas the lower cut off wavelength of pure SA crystal is 270 nm. The recorded absorption spectrum is shown in Fig. 14.2a. The grown crystal sample shows less absorption, near 394 nm because of the presence of Ni^{2+} ion that shows the molar absorptivity in the IR wavelength range of 375–395 nm. It is clear from the figure that the grown crystals are having significant transparency (i.e. 98% for NSSA crystals) in the entire tested range and could be useful for various optical devices. The direct band gap energy (Eg) of the NS:SA crystals is found at 6.1 eV as shown in Fig. 14.2b, which is relatively closer to that of pure sulphamic acid crystals [9].

14.3.4 Thermal Analysis

TGA measures the changes in weight with temperature which can be due to changes in the sample composition and thermal stability [10, 11]. Thermal analysis informs the maximum temperature with which a material can be utilized for practical applications [12, 13]. The NS:SA compound was subjected to thermogravimetric and differential thermal analyses using HITACHI-STA7300 thermal analysis system in nitrogen and oxygen atmosphere between 3 and 75 °C at a heating rate of 20 °C/min. TGA/DTG spectrum of NS:SA is shown in Fig. 14.3. Initial weight of the sample used for investigation is 15.157 mg. It is observed that there is no weight loss in the sample

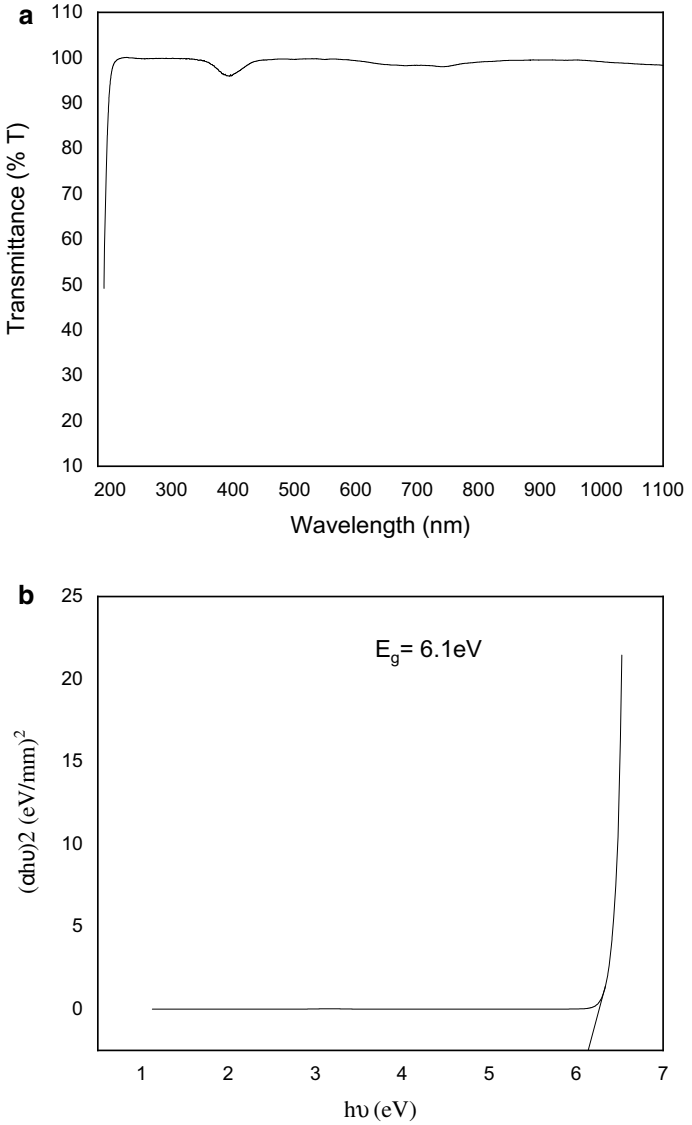

Fig. 14.2 **a** UV-Vis-NIR spectrum of NS:SA single crystal. **b** Plot of photon energy versus $(\alpha h\upsilon)^2$ for NS:SA single crystal

upto 100 °C. The major weight loss of about 63% is found in the temperature range from 100 to 126 °C. The next stage between 162 and 176 °C with a weight loss of 6%. The third stage of weight loss is about 6% in a range of temperature between 313 and 368 °C. It is noticed that the decomposition gets completed at a temperature of 434 °C for the grown crystal. From the sharpness of the peak, the purity and high

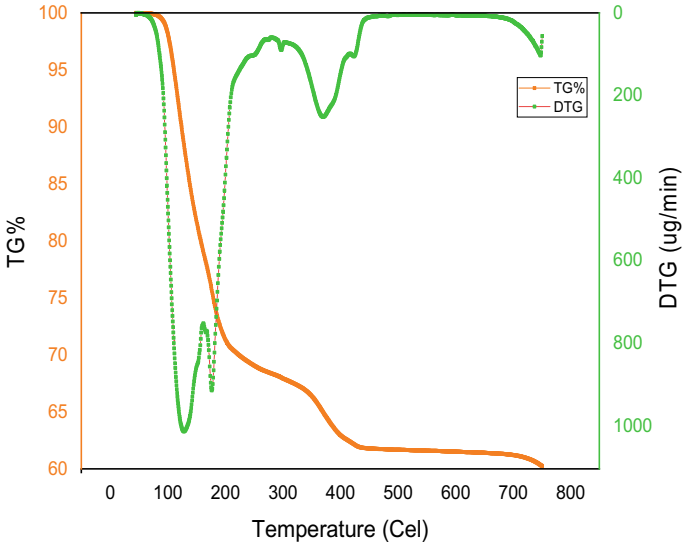

Fig. 14.3 TG-DTG thermograms of NS:SA

degree of crystallinity of the grown crystal can be confirmed. The endothermic peaks of DTG coincide well with the decomposition in the TGA trace. From the analysis, it is observed that the presence of sulphamic acid improves the thermal stability of nickel sulphate (the melting point of nickel sulphate is 53 °C) in the NS:SA sample.

14.3.5 Surface Morphology of the Grown Crystals

The influence of the dopants on the surface morphology of grown NS:SA single crystals was studied by scanning electron microscope. Figure 14.4a, b shows the SEM micrographs of the pure and grown sample. The surface quality of the pure SA crystal is relatively smooth when compared with that of the nickel sulphate-doped crystals, which is in good accordance with the reported values [14]. From the SEM image, it is observed that the sample has crystalline morphology.

14.3.6 Microhardness Studies

The resistance of a material to the motion and displacement of dislocations, deformations or defects under an applied stress is measured by the hardness of the crystal. The ratio of the applied load to the projected area indentation gives the hardness. High purity and good quality crystals are known to have the minimum hardness

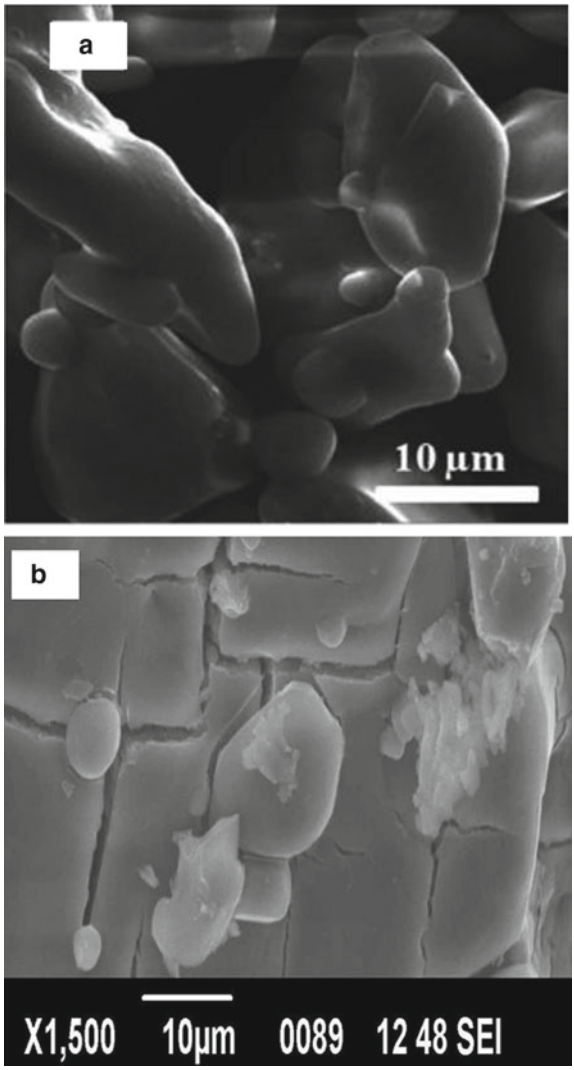

Fig. 14.4 **a** and **b** SEM images of pure and grown crystal

[15]. The Vickers microhardness of the samples was measured using the Shimadzu model HMV-2T microhardness tester. Loads of magnitude varying from 25 to 100 g is applied for a fixed interval of time over a well-polished grown crystal. The Vickers Microhardness number HV is calculated using the relation **HV = 1.8544*P/d² kg/mm²,** where P is the applied load in kg and d is the average diagonal length of the indentation in mm. A graph is plotted between Hardness number (HV) and applied load (P) and is shown in Fig. 14.5a. For NSSA crystals, there is an increase in hardness with load which is due to the work hardening of the surface layer [16]. This proves that these crystals exhibit Reverse Indentation Size Effect (RISE). Meyer's

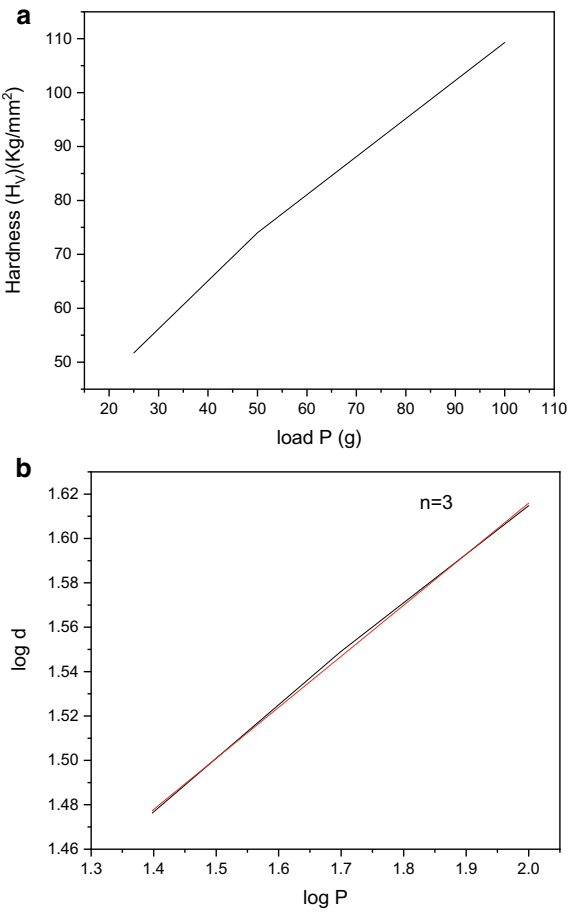

Fig. 14.5 **a** Variation of HV with load P. **b** Plot of log p versus log d

index was estimated by Meyer's equation: $P = k_1.d^n$ where k_1 is a constant and n is the work hardening coefficient that could be determined from the slope of the straight line, plotting of a curve between log p and log d in Fig. 14.5b. According to Onitsch concept [17], for hard material, Meyer's index number lies between 1 and 1.6, and for soft materials, it is greater than 1.6. The grown material belongs to soft category since the value of 'n' is equal to 3. Hardness parameters like yield strength and elastic stiffness constant (C11) were calculated in Table 14.3, which gives the

Table 14.3 Yield strength and elastic stiffness constant of NS:SA single crystals

Load (gram)	σ y (MPa)	C11 (Pa)
25	18.09	$19.3*10^{14}$
50	24.75	$33.4*10^{14}$
100	31.26	$50.3*10^{14}$

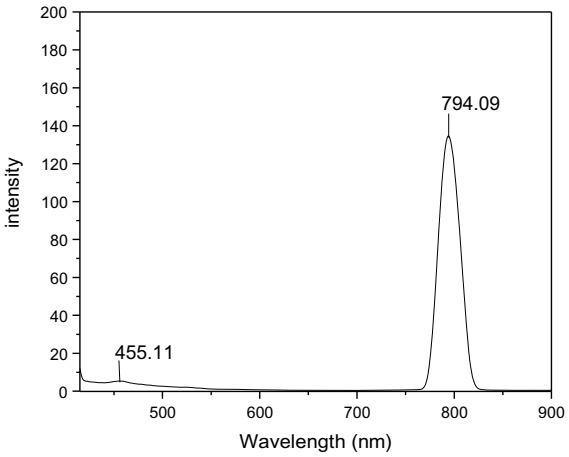

Fig. 14.6 Photoluminescence spectrum of NS:SA single crystal

information about the nature of relationship among the interatomic bonding strength in crystal lattice [18].

14.3.7 Photoluminescence

Photoluminescence spectroscopy is one of the effective tools to provide relatively direct information about the physical properties of materials at the molecular level, including shallow and deep level defects and band gap states. The photoluminescence (PL) spectrum of nickel sulphate-doped sulphamic acid at room temperature is shown in Fig. 14.6. PL spectrum was recorded in the range of 200–900 nm. Under the excitation wavelength of the 395 nm, the samples exhibit an excellent luminescence. The two emission peaks at 455–795 nm are due to the transitions within the electron configuration. The observed sharp emission peak at 795 nm suggests that NSSA single crystals are the promising material for red light emission.

14.4 Conclusion

An efficient inorganic nonlinear optical single crystals of $NiSO_4$-doped sulphamic acid in equimolar ratio were grown using the slow evaporation solution growth technique. Single crystal X-ray diffraction studies confirm that the grown crystal belongs to a monoclinic system. The presence of the Nickel (Ni) ion in the crystal lattice is confirmed using energy dispersive X-ray analysis (EDAX). The optical transparency of the grown sample has been revealed by UV-Vis-NIR study and its cutoff wavelength was found to be 200 nm. The band gap is determined to be 6.1 eV. From DSA

study, the melting point of NSSA is found to be at 12 °C. Morphological observations through SEM analysis indicate that the pure sample possess relatively smooth surfaces comparing with NSSA, and also it is clear that the obtained sample has mild cracks but free from major defects. The Vickers microhardness test confirms that the grown crystals are of soft material type. In the photoluminescence studies, the strongest peak at 794.09 nm shows the characteristic red emission due to the presence of the Nickel (Ni) ions.

Acknowledgement The authors are thankful to ACIC St. Joseph's College, Trichy, India for the UV-Vis-NIR, Microhardness and Photoluminescence studies, and Cochin University, STIC, Kerala, India for providing SCXRD, SEM-EDX, Thermal analysis facilities.

References

1. G. Bhagavannarayana, S. Parthiban, S. Meenakshisundaram, An interesting correlation between crystalline perfection and second harmonic generation efficiency on KCl-and oxalic acid-doped ADP crystals. Cryst. Growth Des. **8**(2), 446–451 (2008)
2. R. Sass, A neutron diffraction study on the crystal structure of sulfamic acid. Acta Crystallogr. **13**(4), 320–324 (1960)
3. F. Kanda, A. King, The crystal structure of sulfamic acid[1]. J. Am. Chem. Soc. **73**(5), 2315–2319 (1951)
4. M. Senthil Pandian, U. Charoen In, P. Ramasamy, P. Manyum, M. Lenin, N. Balamurugan, Unidirectional growth of sulphamic acid single crystal and its quality analysis using etching, microhardness, HRXRD, UV-visible and thermogravimetric-differential thermal characterizations. J. Cryst. Growth **312**(3), 397–401 (2010)
5. K. Anand, G. Vinitha, S. Gautam, K. Chae, R. Mohan, K. Asokan, T. Ravindran, R. Jayavel, Enhancement of third-order nonlinear optical properties of HMTA stabilized pure and doped ZnS nanoparticles and their electronic structures. J. Nonlinear Opt. Phys. Mater. **27**(02), 1850016 (2018)
6. F. Abrinaei, N. Molahasani, Effects of Mn doping on the structural, linear, and nonlinear optical properties of ZnO nanoparticles. J. Opt. Soc. Am. B **35**(8), 2015 (2018)
7. B. Kannan, P. Seshadri, P. Murugakoothan, K. Llangovan, Growth and characterisation of gadolinium doped sulphamic acid single crystal. Int. J. Chem. Tech. Res. **6**(2), 1168–1173 (2014)
8. N. Prabavathi, L. Jayanthi, K. Sudha, Growth and characterization of an inorganic material: pure and hydrochloric acid doped sulphamic acid single crystal. Chem. Sci. Lett. **5**(19), 272–278 (2016)
9. J. Arumugam, M. Selvapandiyan, Senthilkumar Chandran, M. Srinivasan, P. Ramasamy, Effect of $MgSO_4$ on sulphamic acid single crystals and their structural, optical, mechanical, thermal and third order nonlinear optical studies. Mater. Chem. Phys. **242**, 122479 (2020)
10. S. Gunasekaran, G. Anand, S. Kumaresan, S. Kalainathan, Mechanical, dielectric and thermal analysis of semi-organic NLO materials. Adv. Appl. Sci. Res. **2**(3), 550–557 (2011)
11. A.S.I. Joy Sinthiya, P. Selvarajan, Studies of L-asparagine crystals admixtured with ammonium chloride (LAAC) grown by solution method. Indian J. Appl. Res. **3**(9), 521–523 (2011)
12. T. Bruno, P. Svoronos, *Hand Book of Basic Tables for Chemical Analysis-Second Edition* (CRC Press, U. S., 1989)
13. A. Ruby, S. Alfred Cecil Raj, Growth, spectral, optical, thermal and mechanical properties of thiourea doped trisglycine zinc chloride nonlinear optical crystal. IJSRP **3**(3), 1–5 (2013)

14. R. Ramesh Babu, R. Ramesh, R. Gopalakrishnan, K. Ramamurthi, G. Bhagavannarayana, Growth, structural, spectral, mechanical and optical properties of pure and metal ions doped sulphamic acid single crystals. Spectrochim. Acta Part A Mol. Biomol. Spectrosc. **76**(5), 470–475 (2010)
15. F. Meng, M. Lu, Z. Yang, H. Zeng, Thermal and crystallographic properties of a new NLO material, urea-(d) tartaric acid single crystal. Mater. Lett. **33**(5–6), 265–268 (1998)
16. V. Siva shankar, R. Sankar, R. Siddheswaran, R. Jayavel, P. Murugakoothan, Growth and characterization of tetra l-lysine alanine mono hydrochloride dihydrate (TLAMHCl), a new semiorganic nonlinear optical single crystal. Mater. Chem. Phys. **109**(1), 119–124 (2008)
17. K. Senthilkumar, S. Moorthy Babu, B. Kumar, G. Bhagavannarayana, Effect of rare earth ions on the properties of glycine phosphite single crystals. J. Cryst. Growth **362**, 343–348 (2013)
18. R. Dhas, J. Benet Charles, F. Gnanam, Growth and microhardness studies on $NH_4Sb_3F_{10}$ single crystals. J. Cryst. Growth **137**(1–2), 295–298 (1994)

Chapter 15
Impact of Multi-Nucleon Effects on Neutrino Scattering Cross Section and Events at Near and Far Detectors of NOνA Experiment

Paramita Deka and Kalpana Bora

Abstract Nuclear effects in neutrino interactions are one of the major sources of systematic uncertainties in the neutrino beam oscillation experiments. Our present understanding of these effects is still insufficient. Another source of uncertainty is the energy dependence of neutrino oscillation probability which is a nontrivial function of the true incoming neutrino energy. The NUMI Off-Axis ν_e Appearance (NOνA), a long-baseline neutrino oscillation experiment, is designed to measure $\nu_e(\bar{\nu}_e)$ appearance probability and $\nu_\mu(\bar{\nu}_\mu)$ disappearance probability at Fermilab's NUMI (Neutrinos at the Main Injector) beam. In this work, we use the kinematic method of reconstruction of the incoming neutrino energy, both at the ND and FD, and investigate the role of Multi-Nucleon (MN) effects on neutrino nucleus scattering cross section and event distribution at ND and FD of NOνA.

15.1 Introduction

In the ongoing long-baseline neutrino oscillation experiments (T2K [1], NOνA [2]), one of the most complicated issues is the correct modelling of neutrino-nucleus interactions. One important systematic uncertainty comes from the description of nucleon correlations in the initial state which may induce two-particle two-hole (2p-2h) states in the final state. This leads to a bias in the reconstruction of neutrino energy as we have insufficient knowledge of the size of the 2p-2h interaction cross section compared to 1p-1h (quasielastic interactions) contributions. Since most of the modern detectors are made of heavy target nuclei, a large amount of uncertainty comes from these nuclear effects. This systematic uncertainty is one of the biggest uncertainties in the neutrino oscillation experiments. In this paper, we focus on the

P. Deka (✉) · K. Bora
Department of Physics, Gauhati University, Guwahati, Assam, India
e-mail: deka.paramita@gmail.com

S. Sengupta et al. (eds.), *Selected Progresses in Modern Physics*, Springer Proceedings in Physics 265, https://doi.org/10.1007/978-981-16-5141-0_15

behaviour of nuclear effects in neutrino cross section and event distributions as a function of reconstructed energy in NOνA experiment.

The NuMI Off-Axis ν_e Appearance or NOνA is a long-baseline neutrino experiment which is designed to measure muon neutrino (ν_μ) disappearance probability $P(\nu_\mu(\bar{\nu}_\mu) \rightarrow \nu_\mu(\bar{\nu}_\mu))$ and electron neutrino (ν_e) appearance probability $P(\nu_\mu(\bar{\nu}_\mu) \rightarrow \nu_e(\bar{\nu}_e))$. The experiment consists of two functionally and identically segmented, tracking calorimetric detectors—Near Detector (ND) and Far Detector (FD)—to observe neutrino oscillations. NOνA uses high intensity neutrino beam from the collision of 120 GeV protons coming from Fermilab's Neutrinos at the Main Injector (NuMI) facility. The 3.8 m $\times$ 3.8 m $\times$ 12.8 m ND has mass about 0.3 kiloton and it is placed 105 m underground, 1 km from NuMI beam at Fermilab, mainly used to measure unoscillated neutrino beam. The 15 m $\times$ 15 m $\times$ 60 m 14 kiloton FD is located near Ash River, Minnesota at 810 km from the NuMI target, which measures the oscillated beam. Both the detectors are placed 14.6 mrad off-axis from the centre of the NuMI beam to provide a narrow beam neutrino flux peaked at around $\sim 2\ GeV$ and to enhance the sensitivity to ν_μ disappearance and ν_e appearance. From these oscillation measurements, NOνA is expected to determine the mass hierarchy and leptonic CP-violating phase δ_{CP} and resolve the octant of θ_{23} mixing angle.

15.1.1 Multi-nucleon Effect

When a neutrino interacts with the nucleons inside the nucleus exchanging a W boson, it is absorbed by nucleons which results in the knock out of two-particle and two-hole pairs (2p-2h) through an exchange of a meson. There is also a possibility of knocking out three-particle three-hole pairs producing 3p-3h in the final state, which in general can be termed as np-nh or multi-nucleon excitation. These multi-nucleon events have a dominant contribution from 2p-2h processes. The Meson Exchange Current (MEC) or 2p-2h events mostly occur in the energy region between QE and resonance production. The term MEC refers to the correlation in the initial state nucleons as they are exchanging a pion. This process contributes significantly to the neutrino-nucleus scattering and its contribution can be observed in the cross section plot in Fig. 15.1. The Random Phase Approximation (RPA) is a non-perturbative method and has been developed to incorporate the effects of long-range nucleon-nucleon correlations. This method is used to describe the complexity of many body interactions.

15.1.2 Oscillation Analysis

In this work, we consider only the disappearance $\nu_\mu \rightarrow \nu_\mu$ channel for the analysis of neutrino oscillation. In this oscillation channel, the significant background contribution comes from neutral current events which are wrongly identified as CC events. In

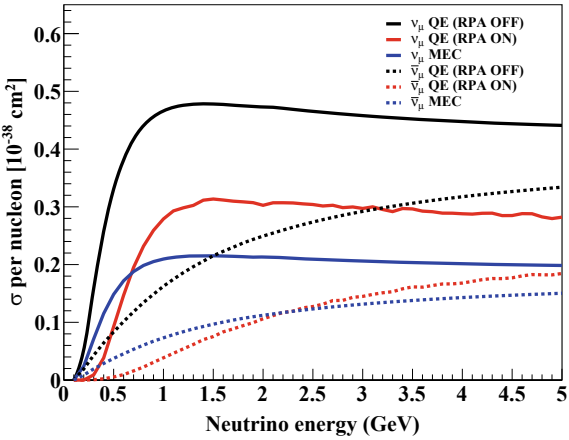

Fig. 15.1 The ν-Carbon (solid lines) and $\bar{\nu}$-Carbon (dashed lines) integrated cross section as a function of the true $\nu_\mu(\bar{\nu}_\mu)$ neutrino energy for different charged-current processes. The black line is for QE (RPA OFF), red for QE with RPA suppression (RPA ON) and blue for MEC interactions

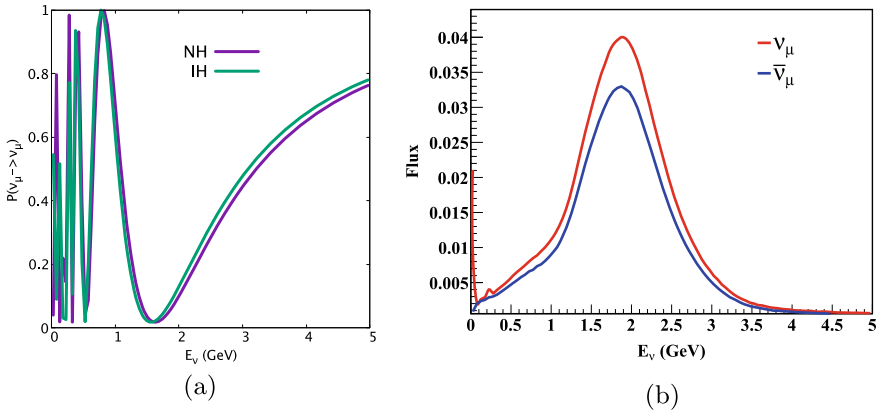

Fig. 15.2 **a** The three flavour $\nu_\mu \rightarrow \nu_\mu$ disappearance or survival probability for both NH and IH. **b** NOνA ND neutrino and antineutrino flux as a function of neutrino energy used in our work

general, this contribution is considered to be very low; therefore, in our analysis, we have neglected it. The relevant oscillation probability for NOνA for disappearance channel can be expressed as

$$P(\nu_\mu \rightarrow \nu_\mu) = 1 - \sin^2 2\theta_{23} \sin^2 \Delta_{32} + 4 \sin^2 \theta_{23} \sin^2_{13} \cos^2 2\theta_{23} \sin^2 \Delta_{32} \quad (15.1)$$

where $\Delta_{ij} = \frac{\Delta m_{ij} L}{4E}$ and shown in Fig. 15.2a. The true values of the oscillation parameters used in our analysis are taken from the recent global fit data [3].

For reconstruction of neutrino energy, we consider the kinematic method which is based on the assumptions that the beam particle interacts with a single neutron at

rest with a constant binding energy and that no other nucleons are knocked out from the nucleus and depends upon the angle and momentum of the outgoing lepton.

15.2 Simulation and Experimental Details

In this work, we have presented an analysis based on simulation using GENIE (v2_12_8) [4] neutrino event generator. Neutrino experiments use their own event generators with in-build models tuned on experimental data to produce events at the detectors. These event generators work as a bridge between the experimental and theoretical physicist. In GENIE, Quasielastic scattering (QE) is modelled using the Llewellyn-Smith model [5] and this model is considered as the default model. In QE interactions, the Relativistic Fermi Gas model (RFG) is used to describe the nuclear effects in the QE region, which is based on a simple independent particle model known as Fermi Gas model. In GENIE, the RFG model is based on the model suggested by Bodek and Ritchie [6]. For Resonance (RES), GENIE uses the Rein-Sehgal model [7] while for Deep Inelastic Scattering(DIS) interactions, the Bodek and Yang model is used [8]. We have tuned GENIE's description of QE interactions to include the Nieves model [9] based on the RPA effect for simulation. For modelling 2p-2h interaction, GENIE implements the 'empirical' model.

We have generated 1 million charged current ν_μ events at ND. The $\nu(\bar{\nu})$ flux used in our analysis is shown in Fig. 15.1b. The signal spectra ν_μ at FD is based on the observed spectra of ν_μ candidate events in the ND. This technique is known as the 'extrapolation' technique [2].

15.3 Results and Discussion

The $\nu_\mu(\bar{\nu}_\mu)$-Carbon interaction cross section is shown in Fig. 15.1 which includes the QE, RES ($\Delta(1232)$ resonance production only), 2p-2h/MEC and DIS interactions. Due to the RPA effect, we observe a significant suppression in QE cross section both in ν_μ and $\bar{\nu}_\mu$ mode. The RPA effect decreases strongly as the neutrino energy increases. In Fig. 15.3, we have plotted ND events as a function of neutrino reconstruction energy. The event distribution for all the interactions peaks around 2 GeV where the neutrino flux also peaks. There is also a decrease in event number with RPA effect than QE without RPA as the event is the convolution of neutrino flux and cross section. In Figs. 15.4 and 15.5, we have shown the extrapolated event distribution at FD for both neutrino and antineutrino mode for both Normal Hierarchy (NH) and Inverted Hierarchy (IH). In the FD event, we observe two peaks in the distribution which is in accordance with the oscillation probability.

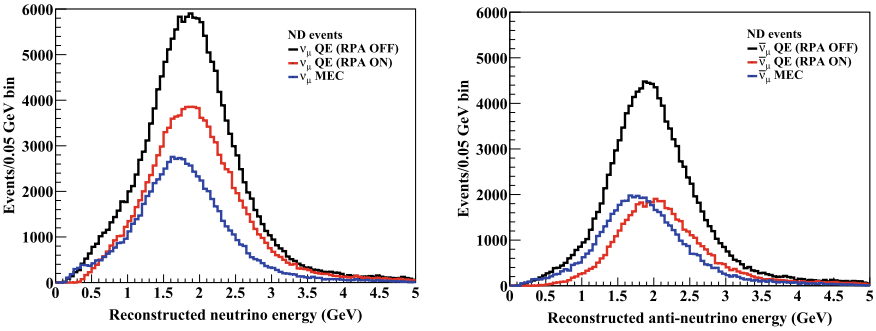

(a) ND ν_μ events (b) ND $\bar{\nu}_\mu$ events

Fig. 15.3 Events versus reconstructed ν_μ-energy for both neutrino (left) and antineutrino (right). Events are shown for three different interactions: QE without RPA (black line), QE with RPA (red line) and MEC (blue line)

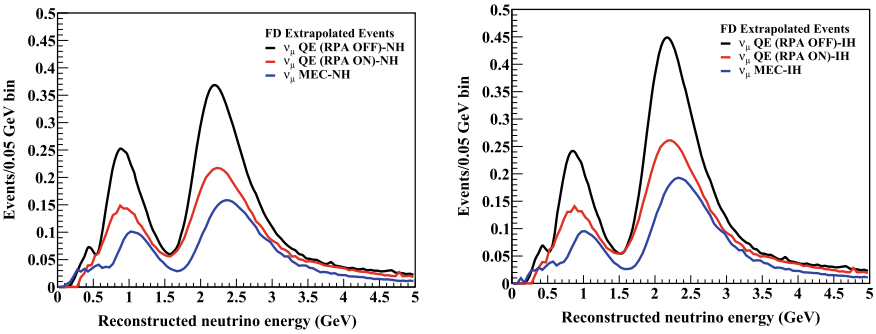

(a) FD ν_μ events (NH) (b) FD ν_μ events (IH)

Fig. 15.4 Left and right panel shows extrapolated FD events as a function of reconstructed ν_μ energy for both NH and IH. The colour scheme is same as described in Fig. 15.3 caption

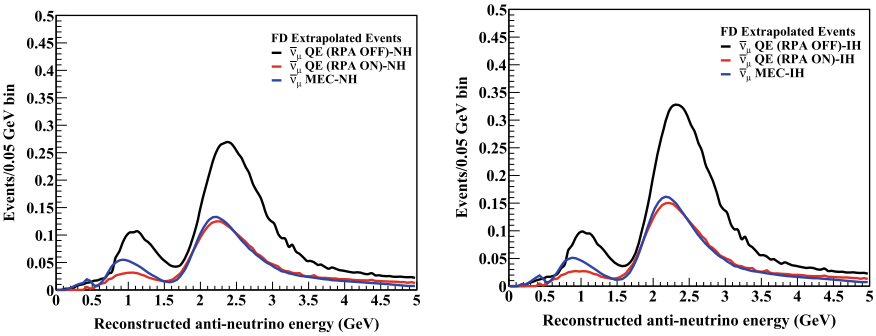

(a) FD $\bar{\nu}_\mu$ events (NH) (b) FD $\bar{\nu}_\mu$ events (IH)

Fig. 15.5 Left and right panel shows extrapolated FD events as a function of reconstructed $\bar{\nu}_\mu$ energy for both NH and IH. The colour scheme is same as described in Fig. 15.3 caption

15.4 Summary

To summarise, in this work, we studied the effects of multi-nucleon interactions on neutrino scattering cross section and events at ND and FD, at the NOνA experiment of Fermilab, USA, and found that they are significant, as is evident from our results in Figs. 15.1, 15.3, 15.4 and 15.5. So, they must be included in the neutrino oscillation parameter analysis, which might have an important effect on the sensitivity analysis. This work is in progress and will be communicated very soon.

Acknowledgements KB thanks DST-SERB, Govt. of India, for the support through her major project EMR/2014/000296, during which a part of this work was done. We thank Dr. Neelakshi Sarma and Jaydip Singh for helpful discussions and suggestions.

References

1. K. Abe et al. [T2K], Phys. Rev. D **96**(9), 092006 (2017) [erratum: Phys. Rev. D **98**(1), 019902 (2018)] https://doi.org/10.1103/PhysRevD.96.092006, arXiv:1707.01048 [hep-ex]
2. M.A. Acero et al. [NOvA], Phys. Rev. Lett. **123**(15), 151803 (2019) https://doi.org/10.1103/PhysRevLett.123.151803, arXiv:1906.04907 [hep-ex]
3. P.F. de Salas, D.V. Forero, S. Gariazzo, P. Martínez-Miravé, O. Mena, C.A. Ternes, M. Tórtola, J.W.F. Valle, JHEP **02**, 071 (2021). https://doi.org/10.1007/JHEP02(2021)071, arXiv:2006.11237 [hep-ph]
4. C. Andreopoulos, A. Bell, D. Bhattacharya, F. Cavanna, J. Dobson, S. Dytman, H. Gallagher, P. Guzowski, R. Hatcher, P. Kehayias, et al. Nucl. Instrum. Meth. A **614**, 87–104 (2010) https://doi.org/10.1016/j.nima.2009.12.009, arXiv:0905.2517 [hep-ph]
5. C.H. Llewellyn Smith, Phys. Rept. **3**, 261–379 (1972) https://doi.org/10.1016/0370-1573(72)90010-5
6. A. Bodek, J.L. Ritchie, Phys. Rev. D **24**, 1400 (1981). https://doi.org/10.1103/PhysRevD.24.1400
7. D. Rein, L.M. Sehgal, Annals Phys. **133**, 79–153 (1981). https://doi.org/10.1016/0003-4916(81)90242-6
8. A. Bodek, U.K. Yang, J. Phys. G **29**, 1899–1906 (2003) https://doi.org/10.1088/0954-3899/29/8/369, arXiv:hep-ex/0210024 [hep-ex]
9. J. Nieves, I. Ruiz Simo, M.J. Vicente Vacas, Phys. Lett. B **707**, 72–75 (2012) https://doi.org/10.1016/j.physletb.2011.11.061, arXiv:1106.5374 [hep-ph]

Chapter 16
Impact of Texture Zeros of Neutrino Mass Matrix on Dark Matter Phenomenology

Nayana Gautam and Mrinal Kumar Das

Abstract We study an inverse seesaw ISS (2,3) framework to explain neutrino phenomenology and dark matter simultaneously with one zero textures of neutrino mass matrix. ISS (2,3) is obtained by the addition of two right-handed neutrinos and three gauge singlets sterile fermions to the standard model. The model is more predictive because of presence of less number of right-handed neutrinos than the conventional inverse seesaw. Moreover, texture zeros in the structures of the mass matrices reduce the free parameters. We extensively study the effect of different textures of neutrino mass matrix on sterile neutrino dark matter phenomenology. Based on different properties of the dark matter, we verify the viability of different one zero textures of the light neutrino mass matrix.

16.1 Introduction

Neutrino mass and mixing, ordering of the neutrino mass, Dirac CP phase, dark matter and baryon asymmetry of universe (BAU) are major reasons to expect physics beyond standard model (BSM). Different BSM frameworks are available in literature which can account for such issues. Inverse seesaw is one of the most promising mechanisms as the neutrino mass generation takes place at lower scale than the conventional seesaw. Here, we study an inverse seesaw framework where two right-handed neutrinos and three sterile fermions are added to the standard model particle content. The most attractive feature of the model lies in the fact that besides explaining neutrino mass, it can lead to a sterile neutrino in keV scale which can account for a viable dark matter candidate. We consider the possibility of one zero at certain position of the neutrino mass matrix. In the framework of ISS (2,3), there are three phenomenologically viable one zero textures of neutrino mass matrix. We have stud-

N. Gautam (✉) · M. K. Das
Department of Physics, Tezpur University, Tezpur 784028, India
e-mail: nayana@tezu.ernet.in

M. K. Das
e-mail: mkdas@tezu.ernet.in

S. Sengupta et al. (eds.), *Selected Progresses in Modern Physics*, Springer Proceedings in Physics 265, https://doi.org/10.1007/978-981-16-5141-0_16

ied dark matter phenomenology in all the three textures. Then we have implemented cosmological bounds on the parameters and have confirmed the viability of different textures.

The paper is planned as follows. In Sect. 16.2, we describe the neutrino mass and dark matter production within the framework of ISS (2,3). Section 16.3 is the brief discussion on different one zero textures of neutrino mass matrix. We discuss the results of the numerical analysis in Sect. 16.4. Finally, we conclude in Sect. 16.5.

16.2 Neutrino Mass and Dark Matter Production

In ISS(2,3), the standard model is extended by the sequential addition of RH neutrinos and SM singlet fermions s_i [1, 2]

$$L = -\frac{1}{2} n_L^T C M n_L + h.c \tag{16.1}$$

The mass matrix in the basis $n_L = (\nu_L, N_R, s)$ can be written as,

$$M = \begin{pmatrix} 0 & M_d & 0 \\ M_d^T & 0 & M_N \\ 0 & M_N^T & \mu \end{pmatrix} \tag{16.2}$$

We obtain the light active neutrino mass in this framework as

$$m_\nu \approx M_d d M_d^T \tag{16.3}$$

where d is a 2×2 matrix given by

$$M_H^{-1} = \begin{pmatrix} d_{2\times 2} & \cdots \\ \cdots & \cdots \end{pmatrix} with\ M_H = \begin{pmatrix} 0 & M_N \\ M_N^T & \mu \end{pmatrix} \tag{16.4}$$

Apart from the light active neutrinos, the model naturally leads to a sterile neutrino dark matter (DM). To study DM phenomenology, one needs to consider three main aspects: relic abundance, stability and structure formation. The relic abundance of the proposed dark matter can be expressed as [1]

$$\Omega_{DM} h^2 = 1.1 \times 10^7 \sum C_\alpha(m_s) |\mathcal{U}_{\alpha s}|^2 \left(\frac{m_s}{keV}\right)^2, \alpha = e, \mu, \tau \tag{16.5}$$

$C_\alpha(m_s)$can be determined numerically and are found to be of order 0.5.

To ensure the stability of dark matter, we calculate the decay rate of the lightest sterile neutrino in the process $N \longrightarrow \nu + \gamma$ which is given by [4],

$$\Gamma = 1.38 \times 10^{-32} \left(\frac{sin^2 2\theta}{10^{-10}} \right) \left(\frac{m_s}{keV} \right)^5 s^{-1}. \tag{16.6}$$

where $sin^2 2\theta = 4 \sum_\alpha |\mathcal{U}_{\alpha s}|^2$ with $\alpha = e, \mu, \tau$.

16.3 Different One Zero Textures of Neutrino Mass Matrix in ISS(2,3)

The one zero textures of the neutrino mass matrix allowed in the framework of ISS (2, 3) are

$$a = \begin{pmatrix} \times & 0 & \times \\ 0 & \times & \times \\ \times & \times & \times \end{pmatrix}, \; b = \begin{pmatrix} \times & \times & \times \\ \times & \times & 0 \\ \times & 0 & \times \end{pmatrix}, \; c = \begin{pmatrix} \times & \times & 0 \\ \times & \times & \times \\ 0 & \times & \times \end{pmatrix}. \tag{16.7}$$

For class a ,

$$M_D = \begin{pmatrix} 0 & b \\ c & 0 \\ e & h \end{pmatrix}, \; \mu = \begin{pmatrix} p & 0 & 0 \\ 0 & p & 0 \\ 0 & 0 & p \end{pmatrix}, \; M_N = \begin{pmatrix} f & 0 & 0 \\ 0 & g & 0 \end{pmatrix}. \tag{16.8}$$

For class b ,

$$M_D = \begin{pmatrix} a & b \\ c & 0 \\ 0 & h \end{pmatrix}, \; \mu = \begin{pmatrix} p & 0 & 0 \\ 0 & p & 0 \\ 0 & 0 & p \end{pmatrix}, \; M_N = \begin{pmatrix} f & 0 & 0 \\ 0 & g & 0 \end{pmatrix}. \tag{16.9}$$

For class c ,

$$M_D = \begin{pmatrix} 0 & b \\ c & d \\ e & 0 \end{pmatrix}, \; \mu = \begin{pmatrix} p & 0 & 0 \\ 0 & p & 0 \\ 0 & 0 & p \end{pmatrix}, \; M_N = \begin{pmatrix} f & 0 & 0 \\ 0 & g & 0 \end{pmatrix}. \tag{16.10}$$

In all the cases, we have considered maximal possible zeros in M and μ. Different zero textures of M_D are taken to get the one zero textures of the neutrino mass matrix.

16.4 Numerical Analysis and Results

The light neutrino mass matrix can be diagonalised with the unitary PMNS matrix [5] as follows:

$$m_\nu = U_{PMNS} m_\nu^{diag} U_{PMNS}^T \tag{16.11}$$

Again, the active-sterile mixing can be obtained by the numerical diagonalisation of the full 8×8 mass matrix using $\mathcal{U}$

$$\mathcal{U}^T M \mathcal{U} = M^{diag} = diag(m_1, m_2 ....m_8) \tag{16.12}$$

In the framework of ISS (2, 3), the lightest neutrino mass is found to be zero. We evaluate the model parameters in all the textures by comparing the neutrino mass matrix arising from the model with the one which is parametrised by the available 3σ global fit data [3]. After evaluating the model parameters, we calculate the mass of the sterile neutrino dark matter m_{DM} as well as DM-active mixing using Eq. 16.12 and the parameter space for all the categories are shown in Fig. 16.1. Again, with the mass and mixing of the dark matter, we evaluate the decay rates of the sterile DM and relic abundance in the above categories which are represented in Figs. 16.2 and 16.3, respectively. We have also implemented the cosmological X-ray bound [4] and XQ-100 Lyman-α which is also compatible with SDSS-I + UVES data [6] bound on sterile neutrino dark matter.

From Figs. 16.1 and 16.2, it is evident that a wide range of parameter space is allowed by cosmology data. However, the texture A2 can account for only 15% of the total DM abundance for the allowed mass region as can be seen from Fig. 16.3.

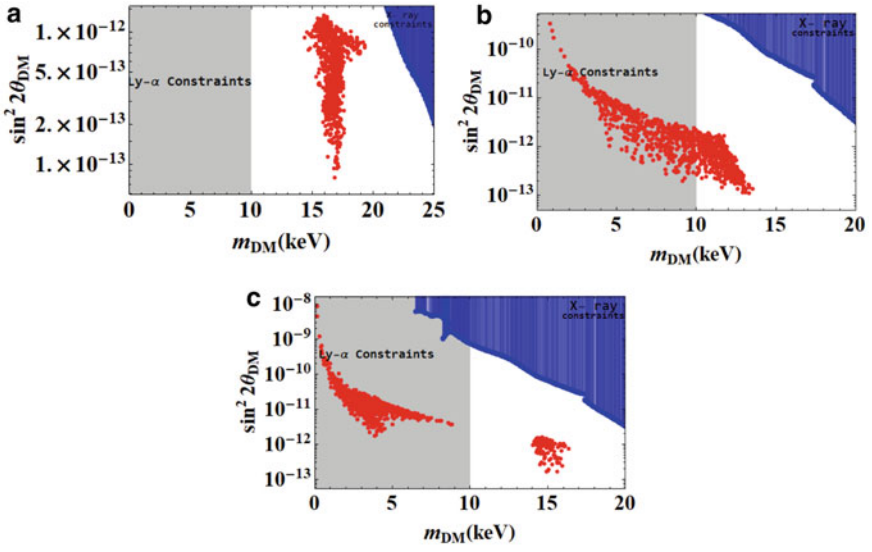

Fig. 16.1 DM-active mixing as a function of the mass of the DM in different textures

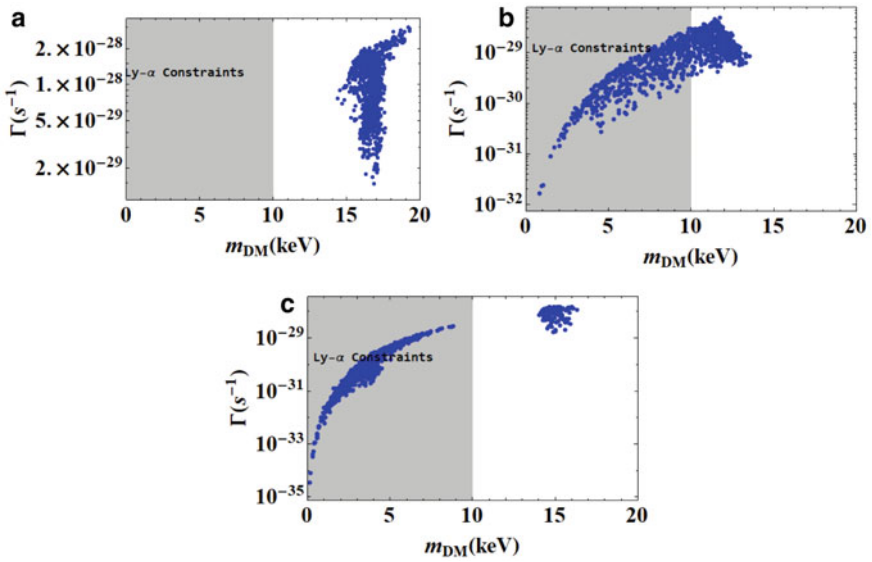

Fig. 16.2 Decay rate (in s^{-1})of the lightest sterile neutrino as a function of DM mass in different textures

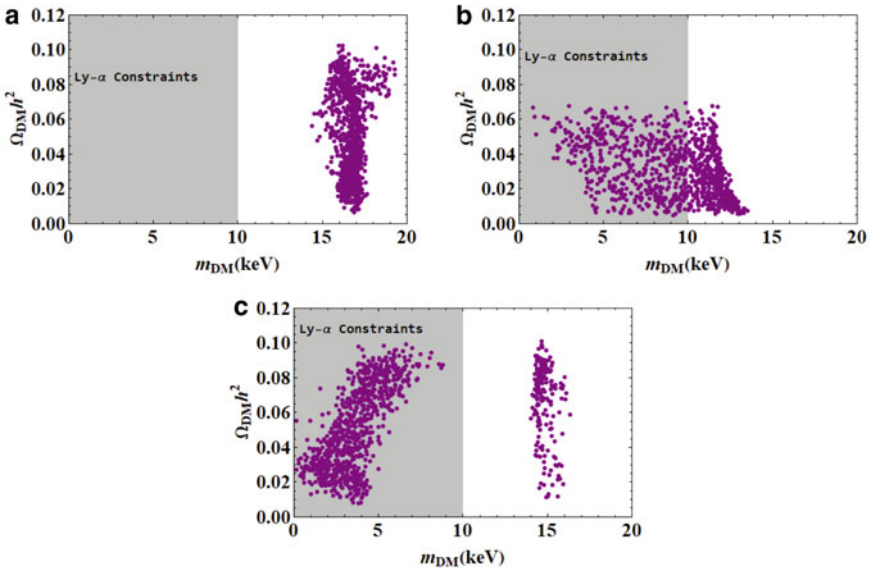

Fig. 16.3 Predictions of different textures on relic abundance of sterile neutrino dark matter

16.5 Summary and Conclusion

We have conducted our study in the framework of ISS(2,3) which leads to three light active neutrino states, two pseudo-Dirac states and an additional sterile state in keV range. We have explored the scenario with only two right-handed neutrinos and one texture zero of neutrino mass matrix and their impacts on sterile neutrino dark matter phenomenology. We have calculated dark matter mass, DM-active mixing and decay rate of the proposed particle and have obtained the mass-mixing parameter space within the range predicted by cosmology for the three textures. However, it has been observed that one particular texture leads to a very small relic abundance of dark matter. Thus, we may conclude that only two $1-0$ textures in the framework of ISS $(2, 3)$ are suitable for explaining dark matter as well as neutrino phenomenology.

Acknowledgements NG would like to acknowledge Department of Science and Technology (DST),India(grant DST/INSPIRE Fellowship/2016/IF160994) for the financial assistantship.

References

1. A. Abada, G. Arcadi, M. Lucente, Dark matter in the minimal Inverse Seesaw mechanism. J. Cosmol. Astropart. Phys. **2014**(10), 001 (2014). https://doi.org/10.1088/1475-7516/2014/10/001
2. N. Gautam, M.K. Das, Phenomenology of keV scale sterile neutrino dark matter with S4 flavor symmetry. JHEP **01**, 098 (2020). https://doi.org/10.1007/JHEP01(2020)098
3. I. Esteban, M. Gonzalez-Garcia, M. Maltoni et al., The fate of hints: updated global analysis of three-flavor neutrino oscillations. J. High Energy Phys. **2020**, 178 (2020). https://doi.org/10.1007/JHEP09(2020)178
4. K.C.Y. Ng et al., New constraints on sterile neutrino dark matter from NuSTAR M31 observations. Phys. Rev. D **99**, 083005 (2019). https://doi.org/10.1103/PhysRevD.99.083005
5. C. Giganti, S. Lavignac, M. Zito, Neutrino oscillations: the rise of the PMNS paradigm. Prog. Part Nucl. Phys. 98 (2018). https://doi.org/10.1016/j.ppnp.2017.10.001
6. J. Baur, N. Palanque-Delabrouille, C. Yeche, A. Boyarsky, O. Ruchayskiy, É. Armengaud, J. Lesgourgues, Constraints from Ly-α forests on non-thermal dark matter including resonantly-produced sterile neutrinos. JCAP **12**, 013 (2017). https://doi.org/10.1088/1475-7516/2017/12/013

Chapter 17
Improved Potential Approach and Masses of Heavy Flavour Mesons

Dhanjit Talukdar and Jugal Lahkar

Abstract Potential models in Quantum Chromo Dynamics (QCD) showed tremendous success in explaining the static properties of heavy flavour mesons. The most extensively used potential is the linear plus coulomb Cornell potential throughout the years. In the present work, we consider a new potential as reported recently by Hassanabadi et al., for $Q\bar{Q}$ system and applied quantum mechanical variational scheme to estimate the masses of a few heavy flavour mesons. We have made a detailed comparison with the results of different other approaches in this arena and also with experimental results.

PACS 03.65.Ge · 12.39.Pn · 14.40.n

17.1 Introduction

Quantum Chromodynamics (QCD) [1]—the theory of strong interactions has two important aspects: (1) Perturbative and (2) non-perturbative. While perturbative approach deals with processes involving high momentum transfer like deep inelastic scattering(DIS) and hard scatterings at LHC, the non-perturbative approach(NPQCD) deals with low momentum transfer processes like hadron masses, decay constants and form factor of hadrons. The most sophisticated approach in NPQCD is lattice QCD, which involves numerical computation with high-power computers. A less ambitious approach is the analytical study of the NPQCD with potential models, where the known property of hadron like confinement is imposed through suitable confinement parameter "b". As early as 1975, De Rujula Georgi and Glashow [2] applied a familiar effective potential of Quantum Electrodynamics (QED) to the quark physics. It is to be noted that the potential is a notion of non-relativistic quantum mechanics, not of relativistic quantum field theory where one visualizes the interaction as arising from the exchange of quanta. However, for slowly moving particles, it is nothing more than the three-dimensional Fourier transform of the lowest order covariant matrix element. This potential is called Fermi-Breit potential [3] and

D. Talukdar (✉) · J. Lahkar
Department of Physics, Pragjyotish College, Guwahati 781009, India

S. Sengupta et al. (eds.), *Selected Progresses in Modern Physics*, Springer Proceedings in Physics 265, https://doi.org/10.1007/978-981-16-5141-0_17

has terms more singular than r^2. It was not exactly solvable. This work was improved by Godfrey and Isgur [4] by adding smearing fractions to remove the singularities, but at the cost of additional parameters.

In the potential model approach, the quark anti-quark interaction potential plays a dominant role in the estimation of static and dynamic properties of mesons. In this regard, the most successful is the Coulomb plus Linear Cornell potential. Here, we mention some of such potentials:

(1) Martin potential:$V(r) = A + Br^{\alpha}$ [5],
(2) Song and Lin potential:$V(r) = Ar^{\frac{1}{2}} + Br^{-\frac{1}{2}}$ [6],
(3) Cornell potential: $V(r) = -\frac{4\alpha_s}{3r} + br + C$ [7],
(4) Logarithmic potential: $V(r) = A + Blnr$ [8],
(5) Richardson potential: $V(r) = Ar - \frac{B}{rln\frac{1}{\Lambda r}}$ [9].

Very recently,a new $Q\bar{Q}$ potential is reported by Hassanabadi et al. [14] as, $V(r) = -\frac{4\alpha_s}{3r} + br + \frac{c}{r^2} + k_0 e^{-\frac{\beta^2 r^2}{2}}$,where, α_s is the strong coupling constant,b is the standard confinement parameter and c, k_0, β are parameters of the potential listed in Table 17.1. Then, they used this potential to estimate some static properties of heavy flavour mesons using Dalgarno's perturbation theory [10].

However, while using perturbation theory we have to choose one part of the potential as parent and other as perturbation. However, such approach is fraught with inherent limitation: there are intermediate range of inter quark separation where both parts of the potential are equally effective and preference of one above the other as parent or perturbation makes no sense. Hence, it will be of topical interest to explore alternative methods where such divide is not necessary. It is, therefore, instructive to go back to the traditional variational method and see if a proper trial wave function can effectively generate the effect of the potential without assuming such division of the potential.

Application of variational method in Heavy quark physics was first started by Hwang et al. [11] using the linear cum coulomb potential, which was later successfully applied by Rai et al. [12]. Also, the variational method is applied to heavy flavour physics by Vega and Flores using super-symmetric potential [13]. We applied the variational scheme with linear plus Coulomb potential in [21] with reasonable theoretical success. Therefore, in this work, we consider the potential suggested in

Table 17.1 Values of the parameters used in our model [14]

Parameter	Value
b	0.183 GeV^2
α_s	0.39(c-scale),0.22(b-scale)
β	0.8 GeV
k_0	0.23 GeV
c	0.03 GeV^{-1}

[14] and applied variational method to estimate the masses of a few heavy flavour mesons and compare with previous results.

The manuscript is arranged as follows: Sect. 17.1 is the introduction, Sect. 17.2 is devoted to formalism and in Sect. 17.3 we summarize the results and conclusion.

17.2 Formalism

Let us consider a Gaussian trial wave function as [11]

$$\psi(r) = (\frac{\alpha}{\sqrt{\pi}})^{\frac{3}{2}} e^{-\frac{\alpha^2 r^2}{2}} \tag{17.1}$$

where, α is the variational parameter. Now, we consider the $Q\bar{Q}$ potential as [14]

$$V(r) = -\frac{4\alpha_s}{3r} + br + \frac{c}{r^2} + k_0 \exp(-\frac{\beta^2 r^2}{2}) \tag{17.2}$$

where α_s is the strong coupling constant and b is the standard confinement parameter ($b \sim 0.183 GeV^2$) and the other parameters are listed in Table 17.1. The potential given in Eq. (17.2) is plotted and compared with standard Cornell potential in Fig. 17.1. It can be seen that for small r the behaviour of the potentials is totally opposite, but for large r they show almost same behaviour.

Now, following Quantum mechanical variational scheme, the ground state energy is given by

$$E(\alpha) = \langle \psi | H | \psi \rangle \tag{17.3}$$

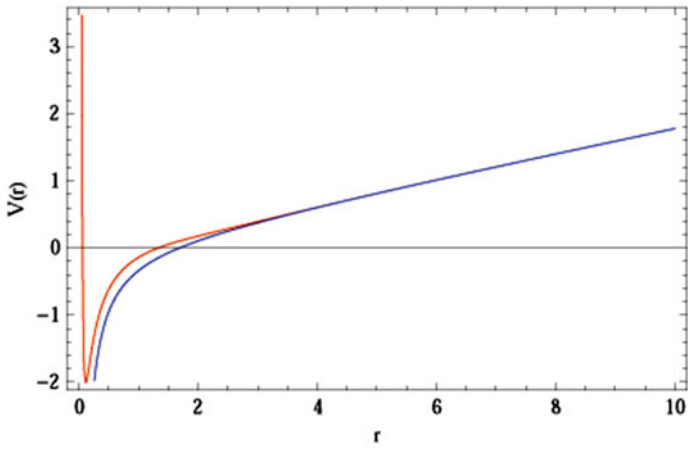

Fig. 17.1 Cornell potential(blue) versus Hassanabadi potential(red)(r in GeV^{-1},V in GeV)

Now, using the trial wave function, we obtain the expectation values of each term in the Hamiltonian

$$< -\frac{\nabla^2}{2\mu} >= -\frac{3\mu^2\alpha^2}{4} \tag{17.4}$$

$$< \frac{-4\alpha_s}{3r} >= -\frac{2\mu^3\alpha A}{\sqrt{\pi}} \tag{17.5}$$

$$< br >= \frac{2b\mu^3}{\sqrt{\pi}\alpha} \tag{17.6}$$

$$< \frac{c}{r^2} >= 2c\beta^2 \tag{17.7}$$

$$< k_0 e^{-\frac{\beta^2 r^2}{2}} >= \frac{\alpha^2}{\alpha^2 + 0.48} \tag{17.8}$$

Therefore, adding all the three equations above, we get

$$E(\alpha) = -\frac{3\mu^2\alpha^2}{4} - \frac{2\mu^3\alpha A}{\sqrt{\pi}} + \frac{2b\mu^3}{\sqrt{\pi}\alpha} + 2c\beta^2 + \frac{\alpha^2}{\alpha^2 + 0.48} \tag{17.9}$$

where, $A = \frac{4\alpha_s}{3}$. Now, by minimizing $E(\alpha)$ with respect to α, we can find the variational parameter α for different heavy flavoured mesons as

$$\frac{dE(\alpha)}{d\alpha} = 0 \tag{17.10}$$

at $\alpha = \bar{\alpha}$.

$$\bar{\alpha}^3[1.5\mu^2 - 4b - (\frac{0.96k_0}{\bar{\alpha}^2 + 0.48}^2)] + \frac{2\mu^3 A\bar{\alpha}^2}{\sqrt{\pi}} + \frac{2\mu^3 b}{\sqrt{\pi}} = 0 \tag{17.11}$$

Solving this equation in Mathematica, we get the variational parameter for different heavy flavour mesons as given in Table 17.2.

17.2.1 Masses of Heavy Flavour Mesons

The masses of Pseudo-scalar/vector mesons can be computed from the following relation [15, 16]:

$$M_{P/v} = M + m + \triangle E \tag{17.12}$$

Here, M and m are the masses of Heavy quark/anti-quark and light quark/anti-quark, respectively. The energy shift of mass splitting due to spin interaction in the perturbation theory is given by [15, 16]

$$\triangle E = \frac{32\pi\alpha_s}{9Mm} S_Q.S_{\bar{Q}} |\ \psi(0)\ |^2 \tag{17.13}$$

For pseudo-scalar mesons, $S_Q.S_{\bar{Q}} = -\frac{3}{4}$, therefore, pseudo-scalar meson masses can be expressed as

$$M_P = M + m - \frac{8\pi\alpha_s}{3Mm} |\ \psi(0)\ |^2 \tag{17.14}$$

Similarly, for vector mesons, $S_Q.S_{\bar{Q}} = \frac{1}{4}$, so

$$M_V = M + m + \frac{8\pi\alpha_s}{9Mm} |\ \psi(0)\ |^2 \tag{17.15}$$

This particular aspect was overlooked in references [17, 18].

17.2.2 Results

17.2.3 Masses of Heavy Flavour Mesons

Now substituting WFO in Eq. (17.15), we calculate the masses of a few heavy flavoured pseudo-scalar mesons which are shown in Table 17.3. The input parameters are $m_{u/d} = 0.336Gev$, $m_b = 4.95GeV$, $m_c = 1.55GeV$, $m_s = 0.483GeV$ and $b = 0.183GeV^2$, also we take $\alpha_s = 0.39$ for C-scale and $\alpha_s = 0.22$ for b-scale [17]. Also, in Table 17.3, comparison with previous models and experimental values is done. Again, the computed masses for a few vector heavy flavour mesons is shown in Table 17.4.

Table 17.2 Variational parameter for different Heavy Flavour mesons

Mesons	α'
$D(c\bar{u}/\bar{c}d)$	0.172
$D(c\bar{s})$	0.1418
$B(u\bar{b}/d\bar{b})$	0.2048
$B_s(s\bar{b})$	0.369
$B(\bar{b}c)$	0.2867
$\eta_c(\bar{c}c)$	0.318
$\eta_b(\bar{b}b)$	0.318

Table 17.3 Masses of heavy flavour pseudo-scalar mesons (in GeV)

Mesons	M_P(our)	M_P [12]	M_P (t das) [17]	M_P(Lattice) [19]	M_P(Experimental Mass) [20]
$D(c\bar{u}/cd)$	1.880	2.080	2.378	1.885	1.869 ± 0.0016
$D(c\bar{s})$	2.03	2.154	2.5	1.969	1.968 ± 0.0033
$B(u\bar{b}/d\bar{b})$	5.284	5.519	5.798	5.28	5.279 ± 0.0017
$B_s(s\bar{b})$	5.426	5.6	5.902	5.366	5.366 ± 0.0024
$B(\bar{b}c)$	6.47		6.5	6.278	6.277 ± 0.006
$J/\psi(\bar{c}c)$	3.09				3.096 ± 0.011
$\gamma(\bar{b}b)$	9.89				9.46 ± 0.26

Table 17.4 Masses of heavy flavour vector mesons

Meson	M_V(GeV)	Exp.Mass(GeV) [20]
$D(c\bar{u}/cd)$	2.007	2.006 ± 0.0016
$D_s(c\bar{s})$	2.112	2.106 ± 0.0033
$B(u\bar{b}/d\bar{b})$	5.2862	5.324 ± 0.0017
$B_s(s\bar{b})$	5.416	5.415 ± 0.0024

It can be seen that compared to the previous models [14, 17, 18] which were based on perturbative approach, variational method provide good analogy between the theoretically calculated mass of heavy flavoured mesons and their experimental values. Specifically, for D meson, our results are very close to the experimental values compared to Rai et al. [12], where variational scheme is applied in momentum space with power law potential. Similarly, our results for heavy heavy mesons ($c\bar{c}$, $b\bar{b}$) are also in excellent agreement with experimental data. Also, our results conforms well with the results of more advanced approaches like Lattice QCD [19].

Also, from Table 17.4, it is clear that the computed masses of vector heavy flavour mesons are in good agreement with the experimental data. Specifically, the masses for D, D_s, B_s mesons obtained from our results are almost same as the experimental findings.

17.3 Conclusion

In this work, we consider a new $Q\bar{Q}$ potential as suggested recently by Hassanabadi et al. [14], and apply quantum mechanical variational scheme to calculate the masses of a few heavy flavour mesons. The variational method is quite cumbersome as it is difficult to choose an appropriate trial wave function in terms of unknown parameter which is later optimized to estimate the parameter. At this juncture, we follow the previous works with Cornell potential [11] and power law potential [12], where it is

established that the Gaussian wave function is the best choice to explore static and dynamic properties of heavy flavour mesons.

We have also compared our results with different models, as well as with those of more advanced approaches like lattice QCD. Comparison shows our results conform well with the results of above mentioned approaches and also with experimental data. Phenomenologically, variational method with Gaussian wave function with the potential as given in Eq. (17.2) provides a simple way to investigate the static properties of heavy flavour mesons. This encourages for further application of the approach to estimate different properties of heavy flavour mesons which is presently under study.

Incorporation of relativistic effects in the light quark of heavy flavour mesons may improve the results, which is a limitation of present work and there is scope of further study.

References

1. L.I. Schiff, *Quantum Mechanics* 3rd edn. (McGRAW-Hill book company, 1985)
2. A. De Rujula, H. Georgi, S.L. Glashow, Phy. Rev. D **A2**, 14 (1975)
3. J.J. Sakurai, *The Advanced Quantum Mechanics* (1971), p. 258
4. S. Godfrey, Isgur, Phys. Rev. D **32**, 189 (1985)
5. A. Martin, Phys. Lett. B **93**, 338 (1980)
6. X. Song, H. Lin, Z. Phys. C **34**, 223 (1987)
7. E. Eichten et al., Phys. Rev. D **21**, 203 (1980)
8. C. Quigg, J.L. Rosner, Phys. Lett. B **71**, 153 (1977)
9. J.L. Richardson, Phys. Lett. B **82**, 272 (1979)
10. A. Dalgarno, *Stationary Perturbation Theory in Quantum Theory, I Elements*, ed. by D.R. Bates (Academic, NewYork, 1961)
11. D.S. Hwang et al., Phys. Rev. D **53**, 4951 (1996)
12. A.K. Rai, R.H. Parmar, P.C. Vinodkumar, J. Phys. G: Nucl. Part Phys. **28**, 2275 (2002)
13. A. Vega, J. Flores, Pramana. J. Phys. **87**, 73 (2016). https://doi.org/10.1007/s12043-016-1278-7
14. M. Moazami, H. Hassanabadi, S. Zarrinkamar, Few-Body Syst. **59**, 100 (2018). https://doi.org/10.1007/s00601-018-1422-7
15. D. Griffiths, *Introduction to Elementary Particles* (John Wiley and Sons, New York, 1987), p. 158
16. K.K. Pathak, D.K. Choudhury, Chin. Phys. Lett. **28**, 101201 (2011)
17. T. Das, D.K. Choudhury, Int. J. Mod. Phys. A (2016). https://doi.org/10.1142/S0217751X1650189X
18. S. Roy, D.K. Choudhury, Can. J. Phys. **94**, 1282 (2016). https://doi.org/10.1139/cjp-2015-0549
19. R.J. Dowdall et al., HPQCD Collab. arXiv:hep-lat/1207.5149v1
20. C. Patrignani, Particle Data Group. Chin. Phys. C **40**, 100001 (2016)
21. J. Lahkar, D.K. Choudhury, B.J. Hazarika, Commun. Theo. Phy. **71**, 49–55 (2019)

Chapter 18
keV Sterile Neutrino Mass Model and Related Phenomenology

Pritam Das and Mrinal Kumar Das

Abstract We study a model of keV scale sterile neutrino within the framework of a minimal extended seesaw and check its effect on neutrinoless double beta decay ($\nu\beta\beta$) study. This framework is based on A_4 flavour symmetry and the discrete $Z_4 \times Z_3$ symmetry to stabilize the model and construct desired mass matrices for neutrino mass. We use a non-trivial Dirac mass matrix with broken $\mu - \tau$ symmetry to generate the leptonic mixing. A non-degenerate mass structure for right-handed neutrinos is considered to verify the observed baryon asymmetry of the universe via the mechanism of thermal leptogenesis.

18.1 Introduction

In this work, we have considered a sterile neutrino flavour with mass in the keV range under minimal extended seesaw (MES) [1], where an additional fermion singlet (sterile neutrino) is added along with three RH neutrinos. A sterile neutrino can affect the electron energy spectrum in tritium β-decays, and we have studied the influence of a keV scale sterile neutrino in the effective mass spectrum. Typically, sterile neutrinos with mass (0.4–50) keV are considered WIMP particles since they are relatively slow and much heavier than active neutrinos. In fact, to successfully observe $0\nu\beta\beta$, the upper bound for sterile neutrino mass should be 18.5 keV. Hence, we have chosen a mass range for the keV regime sterile neutrino within (1–18.5) keV. The study of keV sterile neutrino as a dark matter candidate has skipped in this study and can be found in [2]. It is well know that our universe is matter-dominated, and there is an asymmetry in the baryon number that is observed. Baryogenesis is a process that explains the scenario of baryon asymmetry of the universe (BAU). Numerical definition for baryon asymmetry at current date reads as, $Y_{\Delta B}\left(\equiv \frac{n_B - n_{\overline{B}}}{s}\right) = (8.75 \pm 0.23) \times 10^{-11}$[3]. The SM does not have enough ingredients (Shakarov conditions) to explain this

P. Das (✉) · M. K. Das
Department of Physics, Tezpur University, Napaam 784028, Assam, India
e-mail: pritam@tezu.ernet.in

M. K. Das
e-mail: mkdas@tezu.ernet.in

S. Sengupta et al. (eds.), *Selected Progresses in Modern Physics*, Springer Proceedings in Physics 265, https://doi.org/10.1007/978-981-16-5141-0_18

Table 18.1 Particle content and their charge assignments under SU(2), A_4 and $Z_4 \times Z_3$ groups for NH mode

Particles	l	e_R	μ_R	τ_R	H_1	H_2	ζ	φ	ξ	ξ'	ν_{R1}	ν_{R2}	ν_{R3}	S	χ
SU(2)	2	1	1	1	2	2	1	1	1	1	1	1	1	1	1
A_4	3	1	$1''$	$1'$	1	1	3	3	1	$1'$	1	$1'$	1	$1''$	$1'$
Z_4	1	1	1	1	1	i	1	i	1	-1	1	$-$i	-1	i	$-$i
Z_3	1	1	1	1	1	1	1	1	1	1	1	1	1	ω^2	ω

asymmetry. Hence, we have to go beyond the SM framework to explain baryogenesis. Several popular mechanisms explain baryogenesis, and thermal leptogenesis is one of the most convenient and economical ways. In thermal leptogenesis, the decay of the lightest right-handed (RH) neutrino to a lepton doublet and a Higgs doublet produces sufficient lepton asymmetry, which is then converted into baryon asymmetry. Here, we have attempted to verify baryogenesis produced via the mechanism of thermal leptogenesis within our model, and finally correlate baryogenesis and $0\nu\beta\beta$ under the same framework.

18.2 Model Framework

Apart from the type-I seesaw particle content, few extra flavons are added to construct the model. Two triplets $\zeta and \varphi$ and two singlets ξ and ξ' are added to produce broken flavour symmetry. Besides the SM Higgs H_1, we have also introduced additional Higgs doublets (H_2) to make the model work. Non-desirable interactions were restricted using extra Z_4 and Z_3 charges to the fields. To accommodate sterile neutrino into the framework, we add a chiral gauge singlet S, which interacts with the RH neutrino ν_{R1} via A_4 singlet ($1'$) flavon χ to give rise to sterile mixing matrix. We used dimension-5 operators for Dirac neutrino mass generation. The particle content with $A_4 \times Z_4 \times Z_3$ charge assignment under NH are shown in the Table 18.1. In lepton sector, the leading order invariant Yukawa Lagrangian is given by,

$$\begin{aligned}\mathcal{L} \supset\ & \tfrac{y_2}{\Lambda}(\bar{l}\tilde{H}_1\zeta)_1\nu_{R1} + \tfrac{y_2}{\Lambda}(\bar{l}\tilde{H}_1\varphi)_{1''}\nu_{R2} + \tfrac{y_3}{\Lambda}(\bar{l}\tilde{H}_2\varphi)_1\nu_{R3} \\ & \tfrac{y_1}{\Lambda}(\bar{l}\tilde{H}_1\zeta')_1\nu_{R1} + \tfrac{y_1}{\Lambda}(\bar{l}\tilde{H}_1\varphi')_{1''}\nu_{R2} + \tfrac{y_1}{\Lambda}(\bar{l}\tilde{H}_2\varphi')_1\nu_{R3} \\ & + \tfrac{1}{2}\lambda_1\xi\overline{\nu_{R1}^c}\nu_{R1} + \tfrac{1}{2}\lambda_2\xi'\overline{\nu_{R2}^c}\nu_{R2} + \tfrac{1}{2}\lambda_3\xi\overline{\nu_{R3}^c}\nu_{R3} + \tfrac{1}{2}\rho\chi\overline{S^c}\nu_{R1}.\end{aligned} \tag{18.1}$$

In this Lagrangian, various Yukawa couplings are represented by y_i, λ_i (for $i = 1, 2, 3$) and ρ for respective interactions. Λ is the cut-off scale of the theory, which is around the GUT scale. The scalar flavons involved in the Lagrangian acquire VEV along $\langle\zeta\rangle = (v, 0, 0)$, $\langle\varphi\rangle = (v, v, v)$, $\langle\xi\rangle = \langle\xi'\rangle = v$ and $\langle\chi\rangle = v_\chi$ by breaking the flavour symmetry, while $\langle H_i\rangle (i = 1, 2)$ get VEV (v_i) by breaking EWSB at electroweak scale. We have added a perturbation to the Dirac mass matrix to break the trivial

$\mu - \tau$ symmetry in the light neutrino mass matrix so that we can get non-zero reactor mixing angle.[1] The Lagrangian for the perturbative matrix is given by the second line of Eq. (18.1). New $SU(2)$ singlet flavon fields (ζ' and φ') are considered and supposed to take $A_4 \times Z_4 \times Z_3$ charges as same as ζ and φ respectively. After breaking flavour symmetry, they acquire VEV along $\langle\zeta'\rangle = (v_p, 0, 0)$ and $\langle\varphi'\rangle = (0, v_p, 0)$ directions, giving rise to the M_P matrix.

18.2.1 Neutrino Mass and Mixing Angles

Minimal extended seesaw(MES) is realized in this work to construct active and sterile masses. Under MES framework, the active and sterile masses are realized as follows:

$$m_\nu \simeq M_D M_R^{-1} M_S^T (M_S M_R^{-1} M_S^T)^{-1} M_S (M_R^{-1})^T M_D^T - M_D M_R^{-1} M_D^T, \tag{18.2}$$

$$m_s \simeq -M_S M_R^{-1} M_S^T. \tag{18.3}$$

The mass scale of M_S being slightly higher than the M_D scale, which is near to the EW scale, while M_R is around 10^{13} GeV.

A fixed non-degenerate values for the right-handed neutrino mass parameters as $R_1 = 5 \times 10^{12}$ GeV, $R_2 = 10^{13}$ GeV and $R_3 = 5 \times 10^{13}$ GeV are assigned in such a fashion that they can demonstrate favourable thermal leptogenesis without effecting the neutrino parameters. The mass matrix generated from Eq. (18.2) gives rise to complex parameters due to the presence of Dirac and the Majorana phases. As the leptonic CP phases are still unknown, we vary them within their allowed 3σ ranges $(0, 2\pi)$. Since we have included one extra generation of neutrino along with the active neutrinos in our model, thus the final neutrino mixing matrix for the active-sterile mixing takes 4×4 form as

$$V \simeq \begin{pmatrix} (1 - \frac{1}{2} W W^\dagger) U_{PMNS} & W \\ -W^\dagger U_{PMNS} & 1 - \frac{1}{2} W^\dagger W \end{pmatrix}, \tag{18.4}$$

here, U is the unitary PMNS matrix and $W = M_D M_R^{-1} M_S^T (M_S M_R^{-1} M_S^T)^{-1}$ is a 3×1 matrix governed by the strength of the active-sterile mixing, i.e., the ratio $\frac{\mathcal{O}(M_D)}{\mathcal{O}(M_S)}$. Using MES, the mass matrices obtained for active neutrinos and active-sterile mixing elements are shown in Table 18.2. Respective interaction terms from the Lagrangian 18.1 are parametrized as D_1, D_2, R_1, R_2, R_3, P and G to minimize the complexity. We have solved the model parameters of the active mass matrix using current global fit 3σ values for the light neutrino parameters and carried out our analysis accordingly.

[1] When the $m_{\mu\mu}$ and $m_{\tau\tau}$ positions in the light neutrino mass matrix are same, one cannot achieve non-zero reactor mixing angle (θ_{13}). Recently, it was found that the reactor mixing angle have non-zero value, $\theta_{13} = 8.5^\circ \pm 0.2^\circ$.

Table 18.2 The active and sterile neutrino mass matrices and corresponding Dirac (M_D), Majorana(M_R) and sterile(M_S) mass matrices for NH and IH mode. The active-sterile mixing matrices (W) and sterile mass for NH and IH mass pattern are also shown in respective columns

Matrices	Mass structures
Normal Heirarchy $M_R = \begin{pmatrix} R_1 & 0 & 0 \\ 0 & R_2 & 0 \\ 0 & 0 & R_3 \end{pmatrix}$ $M_D = \begin{pmatrix} D_1 & D_1 & D_2+P \\ 0 & D_1+P & D_2 \\ P & D_1 & D_2 \end{pmatrix}$ $M_S = \begin{pmatrix} G & 0 & 0 \end{pmatrix}$	$-m_\nu = \begin{pmatrix} \frac{D_1^2}{R_2}+\frac{(D_2+P)^2}{R_3} & \frac{D_1(D_1+P)}{R_2}+\frac{D_2(D_2+P)}{R_3} & \frac{D_1^2}{R_2}+\frac{D_2(D_2+P)}{R_3} \\ \frac{D_1(D_1+P)}{R_2}+\frac{D_2(D_2+P)}{R_3} & \frac{(D_1+P)^2}{R_2}+\frac{D_2^2}{R_3} & \frac{D_1(D_1+P)}{R_2}+\frac{D_2^2}{R_3} \\ \frac{D_1^2}{R_2}+\frac{D_2(D_2+P)}{R_3} & \frac{D_1(D_1+P)}{R_2}+\frac{D_2^2}{R_3} & \frac{D_1^2}{R_2}+\frac{D_2^2}{R_3} \end{pmatrix}$ $m_S \simeq \frac{G^2}{\lambda_1 v}$ $W = \begin{pmatrix} \frac{D_1}{G} \\ 0 \\ \frac{P}{G} \end{pmatrix}$
Inverted Hierarchy $M_R = \begin{pmatrix} R_1 & 0 & 0 \\ 0 & R_2 & 0 \\ 0 & 0 & R_3 \end{pmatrix}$ $M_D = \begin{pmatrix} D_1 & -D_1 & D_2+P \\ 0 & -D_1+P & D_2 \\ P & 2D_1 & D_2 \end{pmatrix}$ $M_S = \begin{pmatrix} G & 0 & 0 \end{pmatrix}$	$\begin{pmatrix} \frac{D_1^2}{R_2}+\frac{(D_2+P)^2}{R_3} & \frac{D_1(D_1-P)}{R_2}+\frac{D_2(D_2+P)}{R_3} & \frac{-2D_1^2}{R_2}+\frac{D_2(D_2+P)}{R_3} \\ \frac{D_1(D_1-P)}{R_2}+\frac{D_2(D_2+P)}{R_3} & \frac{(D_1-P)^2}{R_2}+\frac{D_2^2}{R_3} & \frac{-2D_1(D_1-P)}{R_2}+\frac{D_2^2}{R_3} \\ -\frac{2D_1^2}{R_2}+\frac{D_2(D_2+P)}{R_3} & -\frac{2D_1(D_1-P)}{R_2}+\frac{D_2^2}{R_3} & \frac{4D_1^2}{R_2}+\frac{D_2^2}{R_3} \end{pmatrix}$ $m_S \simeq \frac{G^2}{\lambda_1 v}$ $W = \begin{pmatrix} \frac{D_1}{G} \\ 0 \\ \frac{P}{G} \end{pmatrix}$

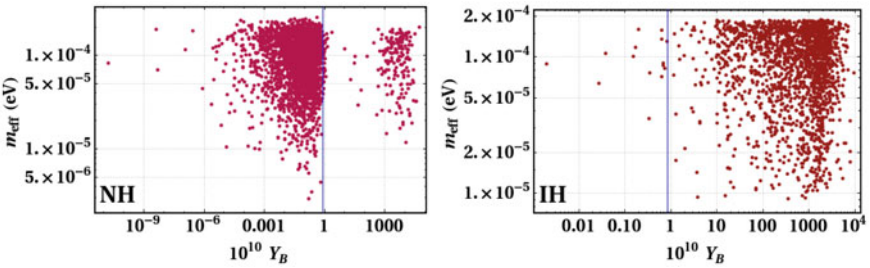

Fig. 18.1 Correlation between baryogenesis and $0\nu\beta\beta$ for both normal and inverted hierarchy mass pattern in presence of a single generation of keV sterile neutrino. The vertical blue line represents the current BAU value, $Y_B = (8.7 \pm 0.06) \times 10^{-11}$

18.2.2 Baryogenesis and $0\nu\beta\beta$

We have considered a hierarchical mass pattern for RH neutrinos, among which the lightest will decay to Higgs and lepton. This decay would produce sufficient lepton asymmetry to give rise to the observed baryon asymmetry of the universe. We have used the parametrization from [3], where the working formula of baryon asymmetry produced is given by

$$Y_B = ck\frac{\epsilon_{11}}{g_*}. \tag{18.5}$$

The quantities involved in this Eq. 18.5 can be found in [3, 4].

The baryon asymmetry of the universe can be calculated from Eq. (18.5) followed by the evaluation of lepton asymmetry. The Yukawa matrix is constructed from the solved model parameters D_1, D_2 and P, which is analogous to the 3×3 Dirac mass matrix.

As we have considered only one sterile state, hence the effective electron neutrinos mass is modified as [1]

$$m_{eff}^{3+1} = m_{eff}^{3_\nu} + m_4|\theta_S|^2, \tag{18.6}$$

where, $|\theta_S|$ is obtained from the first element of the W matrix and m_4 is constrained within [1–18.5] keV satisfying both $0\nu\beta\beta$ and DM phenomenology under MES framework simultaneously.

In Fig. 18.1, we have plotted baryogenesis values obtained from our model along X-axis and effective mass from $0\nu\beta\beta$ along Y-axis for both normal and inverted hierarchy mass pattern. These results correlated both these observables, and NH mass pattern shows more promising results compared to the IH pattern.

18.3 Conclusion

In this study, we have checked the viability of keV sterile neutrino giving an observable effect in $0\nu\beta\beta$ and baryogenesis via the mechanism of thermal leptogenesis. We have used A_4 based flavour model with discrete $Z_4 \times Z_3$ to construct desired Yukawa coupling matrices. A singlet gauge fermion S is considered, which couples with the right-handed neutrino. The Dirac neutrino mass matrix, M_D, is modified using a matrix, M_P, which is generated via the same fashion as M_D to make the active mass matrix $\mu - \tau$ asymmetric.

In conclusion, we have found that sterile neutrino has an observable effect in $0\nu\beta\beta$ study. Under MES, it is possible to correlated baryogenesis and $0\nu\beta\beta$ for both the mass ordering. However, NH mass pattern becomes more favourable than IH pattern in the correlation study.

Acknowledgements The research work of P.D. and M.K.D. is supported by the Department of Science and Technology, Government of India under the project grant EMR/2017/001436.

References

1. J. Barry, W. Rodejohann, H. Zhang, JHEP **07**, 091 (2011). https://doi.org/10.1007/JHEP07(2011)091, arXiv:1105.3911 [hep-ph]
2. P. Das, M.K. Das, Int. J. Mod. Phys. A **35**(22), 2050125 (2020). https://doi.org/10.1142/S0217751X20501250, arXiv:1908.08417 [hep-ph]
3. S. Davidson, E. Nardi, Y. Nir, Phys. Rept. **466** (2008), 105–177 https://doi.org/10.1016/j.physrep.2008.06.002, arXiv:0802.2962 [hep-ph]
4. P. Das, M.K. Das, N. Khan, JHEP **03**, 018 (2020). https://doi.org/10.1007/JHEP03(2020)018, arXiv:1911.07243 [hep-ph]

Chapter 19
Lee-Wave Clouds in Martian Atmosphere: A Study Based on the Images Captured by Mars Color Camera (MCC)

Jyotirmoy Kalita, Manoj Kumar Mishra, and Anirban Guha

Abstract Atmospheric internal gravity wave cloud, commonly known as lee-wave cloud, used to form over the north-eastern slope of Ascraeus Mons and the eastern slope of Tharsis Tholus in Mars. Mars Color Camera (MCC) captured ~ 30 images of such cloud structure during Martian years 33 and 34. In the present analysis, we objectify our focus on the atmospheric parameter related to the captured lee-wave events, and we interpret our results physically with other instrument data viz. MCS-MRO, MARCI. We estimated the reflectance at TOA, cloud's wavelength, wind velocity, formation height, formation temperature, nature of the cloud particle, the effective radius of the particle, and other atmospheric parameters related to the lee-wave events. Estimated maximum reflectance of 0.75 in the blue channel implies water ice particles in the cloud portion. The wavelength of the lee-wave cloud varies from 27 ± 2 to 39 ± 3 km implying a wind speed range from 32 ± 3 to 54 ± 7 m/sec at the height of 25 ± 2 to 37 ± 5 km from the surface of Mars. We used the Global Circulation Model (GCM) model to validate our initial findings. Further, the estimated AOD value variations from 0.8 to 2.4 for the blue channel implies the contribution of water ice particles in the increment of AOD over the Martian volcano. The effective radius of the water ice particle is found to be 3.2 μm based on the MCS-MRO analyzed data. The scale height of AOD varies from 3 to 6.5 km over Ascraeus Mons, and Tharsis Tholus indicates the presence of a non-homogeneous mixture of air and airborne particle near the lee side of Ascraeus Mons. The present study illustrates a Spatio-Temporal distribution of lee-wave cloud during solar longitude 70 to 140° with variation in 160 to 190 K formation temperature.

J. Kalita · A. Guha (✉)
Department of Physics, Tripura University, Suryamaninagar, Tripura 799022, India

J. Kalita
e-mail: jyotirmoy.physics@tripurauniv.in

M. K. Mishra
Space Applications Centre, Indian Space Research Organization, Ahmedabad 380053, India
e-mail: manoj8187@sac.isro.gov.in

S. Sengupta et al. (eds.), *Selected Progresses in Modern Physics*, Springer Proceedings in Physics 265, https://doi.org/10.1007/978-981-16-5141-0_19

19.1 Introduction

Vertical deflection of the wind by the topographic obstacle results in a horizontal wave-like pattern in the cloud that appears at the lee side of the high topographic ridge. Clouds are aligned orthogonal to the prevailing wind and form a divergent pattern due to the adiabatic cooling at the wave's crest [1–3]. The scientific community has been observing these kinds of events since mariner-9 times [4, 3, 5, 6, 7, 8, 9, 10]. In our observation, we considered Ascraeus Mons and Tharsis Tholus as our prime obstacle, over where lee-wave cloud was captured by MCC. According to the previous study, the object may vary in size, and depending on the size, the cloud may extant up to 1000 km downstream from the topographic ridge [11, 10, 12, 13, 14]. During the Mariner era, lee-wave clouds have been studied based on the sinusoidal deformation in laminar flow and varying brightness. Variation in the brightness is due to the concentration in the cloud's local condensate and scattering properties.

Mariner-9 shows an extension for the lee-wave cloud of 300 km with an average wavelength of ~ 40 km [15]. The mid-latitude and polar region lee-wave cloud may become extant up to 400 km with an average wavelength ~ 50 km [1]. We estimated the deviation of the lee-wave cloud based on the wind thrust on the laminar flow in the atmosphere using MCD-GCM [15]. Lee-wave clouds usually appear during Ls = 60° to Ls = 195°, become sharp during Ls = 170° to Ls = 195°, and disappear after Ls = 20°. Seasonal variation says that the lee-wave cloud appears during late summer and forms until late winter [3]. Physical parameters like wavelength, propagation characteristics of lee-wave clouds depend on the temperature, wind profiles of the atmosphere, and the pressure gradient. Hence, investigation regarding the lee-wave cloud helps us predict atmospheric characteristics and atmosphere dynamics [16, 1].

Moreover, spatial variation of lee-wave cloud helps us predict the Martian atmosphere's seasonal characteristics. MCC onboard Mangalyaan captured so many images of lee-wave cloud, and we did consider the image data as our primary source for our study. Martian volcanoes and high ridge play a significant role in atmosphere dynamics [3]. With the analysis of this characteristic of the lee-wave cloud, we may report the local atmospheric condition over the Martian volcano. We may note how westerlies and northerlies (high wind speed) affect the cloud condensate and drives the cloud stake over the lee side of the volcanoes [1].

Moreover, we may determine the surface and top of the atmosphere temperature from this study. Surface temperature and radiative forcing contribute to the atmospheric circulation process and result in convictions, driving the cloud steak up to 50 km [16, 4]. Also, the Headley circulation process is affected by the atmospheric parameters estimated in this study [4]. Also, atmospheric stability can be estimated from the trapped lee-wave cloud [1]. We tried to report the parameters to understand the atmospheric condition over the Martian volcanoes like Ascraeus Mons and Tharsis Tholus. Since the images are of RGB Bayer pattern, it allows us to distinguish between the ice clouds (High reflectance at TOA in the blue channel) and dust clouds (High reflectance at TOA in the Red channel). Since the observation is under visible wavelength range and direct observation is difficult to report whether the observed

cloud is water ice or carbon dioxide crystal. In our study, we consider GCM-MCD, MRO-MCS, and MARCI data to validate our observation.

19.2 Methodology

19.2.1 Wavelength Calculation

We converted the raw images available in the database into true-color images. Using Gaussian filter and Savitzky-Golay filters, we reduced the noise of the image reflectivity from the surface of Mars. We used GIMP (https://www.gimp.org/) to enhance the contrast of images. For 8 bit images, the DN number varies from 1 to 255 for the entire channel. For our present study, we converted the DN numbers to respective radiance value as follows [17, 18]:

$$Radiance_{\lambda} = \frac{Radiance_{\max_{\lambda}} - Radiance_{\min_{\lambda}}}{QCAL_{\max_{\lambda}} - QCAL_{\min_{\lambda}}} * (QCAL - QCAL_{\min}) + Radiance_{\min_{\lambda}} \tag{19.1}$$

where radiance $_{\lambda}$ is the pixel value as radiance, QCAL is the digital number associated with each pixel. Radiance (MIN_{λ}) = spectral radiance scales to QCALMIN Radiance (MAX_{λ}) = spectral radiance scales to QCALMAX, QCALMIN = the minimum quantized calibrated pixel value (typically = 1) QCALMAX = the maximum quantized calibrated pixel value (typically = 255). These radiance values have been converted into reflectance value as,

$$\rho_{\lambda} = \pi * L_{\lambda} * \frac{d^2}{ESUN_{\lambda}} * \cos\theta \tag{19.2}$$

In the above equation, ρ_{λ} = Planetary reflectance, L_{λ} = Radiance (from DN number), d = Mars–Sun distance in astronomical units, $ESUN_{\lambda}$ = mean solar exoatmospheric irradiances. θs = solar zenith angle. We may see the Ascraeus Mons raster map projected on the MOLA hillside color map in Fig. 19.1. We developed the required software algorithms using MATLAB to extract detailed information of the images captured by MCC.

The first MATLAB algorithm produces a reflectance plot as a function of the horizontal distance from the evolution point of the cloud. A series of uneven ripples in Fig. 19.2 indicates the sinusoidal structure of the cloud. The red plot presents the filtered data. The significant peaks with maximum reflectivity in the plot represent the trough of the wave. The wavelength of the Lee-wave cloud can be measured as the distance between the two troughs. We used the pixel counting method to estimate the distance [19, 20, 8]. Pixel counting method is given as,

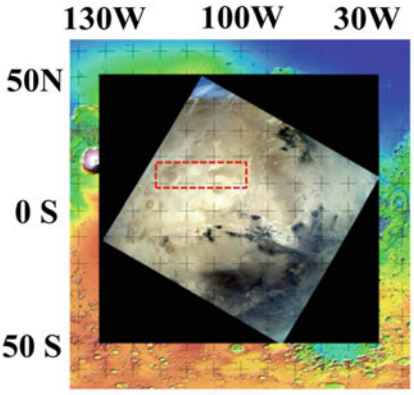

Fig. 19.1 Position of the Ascraeus Mons and Tharsis Tholus based on the MOLA topography map. We projected the MCC image over the base MOLA color hillside map using ARC-GIS

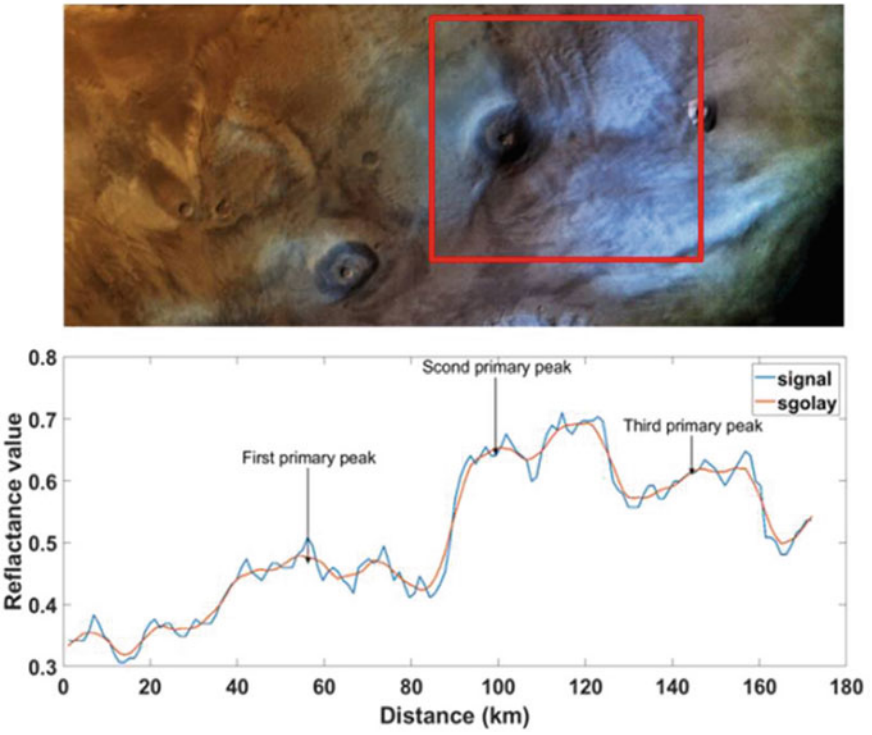

Fig. 19.2 Position of the cloud near Ascraeus Mons and Tharsis Tholus, captured by MCC https://mrbrowse.issdc.gov.in/MOMLTA/login.xhtml. We prepared a reflectance plot to show the wave structure of the cloud portion through a transact along 14° N. The reflectance is varying as a function of distance for the cloud portion [18]

Wavelength of the cloud = (no of pixel counted from one trough to another through of the wave) X (spatial pixel resolution at the center of the image) + other error

Our second algorithm works based on the zenith angles associated with each pixel of the image plane. Zenith angle is not the same for each pixel in an image associated with the instrument. So, we need to correct the angle values to change the spatial pixel resolution for each pixel in the image plane. In MCC captured images, spatial pixel resolution is defined and estimated on the center of the image plane. If the numbers of pixels in the image are (a, b) in (x, y) direction, then the spatial pixel resolution is defined for the center pixel coordinates at (a/2, b/2). Incorporation of angle correction for the spatial pixel resolution (m, n) at any given coordinate (i, j) can be expressed as,

$$(m, n) = (a/2, b/2) * (1/\cos(zenith\_angle\_at\_(i, j))) \tag{19.3}$$

We estimated the direction of the lee-wave cloud from the MCC geometry file. We considered the direction of the intersecting lines to be perpendicular to the lee-wave steak for maximum accuracy of $\pm$ 1° with the line of propagation. Error estimation regarding the wavelength calculation is based on the parameters responsible for forming the lee-wave cloud. In Fig. 19.1, red arrow indicates the direction of the cloud. We encountered a shift of maximum reflectance value in the red curve from actual data in the blue curve in Fig. 19.2 due to a low pass filter. It may cause an error in the maximum reflectance. Also, we encountered angle NAN values in the Grid file, which have been extrapolated using MATLAB software. Considering both cases, the total estimated error comes around $\pm$ 2.6 km.

Necessary Corrections: MCC was not in an exact nadir position while capturing the lee-wave cloud. Hence, lens angle is not 90° for the cloud. So, we corrected the data by imposing the angle.grid file available in the dataset and Pythagoras geometry. Nadir spatial pixel resolution is given for the center of the image. Hence, we corrected the data before applying the pixel to the distance conversion algorithm. Also, the transact was taken along a fixed longitude. Accordingly, we converted the reflectance plot as per the varying lat/long value.

19.2.2 Wind Speed Calculation

We have estimated the wind speed based on the atmospheric internal gravity wave calculation. The velocity of the wind is perturbed as, ($\bar{u}$ + u, w) after meeting the high ridge or an obstacle. Also, density and pressure value for each point is perturbed due to air mass movement. Ganna Valeriyivna Portyankina demonstrated a mathematical formulation in her Ph.D. to calculate the wavelength of the cloud using the wind speed value. The same has been adopted for our work in modified form. According to the concerned literature, the wavelength of the lee-wave cloud is given by [21],

$$LW(\lambda) = 2\pi u c_s / g\sqrt{\gamma - 1 - \gamma^2 * u^2/4c^2} \tag{19.4}$$

where u = wind speed, g = acceleration due to gravity on Mars (3.69 m/s^2), LW (λ) = wavelength, = Cp/Cv (1.3055), and cs = sound speed for mars ~ (226 m/s) [15].

Utilizing Eq. 19.4, we may estimate the horizontal wind speed that drives the cloud parcel along the north-eastern slope of the high ridge topography of Mars. The speed of light is very high compared to the wind's speed, and hence (such that $u^2/c^2 \approx 10^{-3}$), the third term inside the square root will vanish. We may rearrange the equation as follows [22],

$$u = gLW(\lambda)\sqrt{(\gamma - 1)}/2\pi c_s \tag{19.5}$$

Since specific heat capacity changes with temperature, wind speed will vary for every event [23]. Considering the error in wavelength and case of specific heat capacity, we estimated the total error in the calculation of wind speed is ± 9.67 m/s. In our present work, the estimated wind speed is a bit higher for the Martian atmosphere according to previous wind speed estimates and model results [24–26].

19.2.2.1 Shape of the Cloud: Effect of W-E and S–N Wind

We observed a total of 25 events over Martian years 33 and 34. The shape of the cloud is more or less similar for every event following the propagating direction along the lee side of the high ridge topography. We presented a plot of W-E vs. S–N wind, along the crest of the wave cloud and at the height of 35 km. From the plot, we may see that the W-E wind is much stronger than the S–N wind. Combination of both the component contributes the cloud parcel to follow the north-eastern direction. At the trough, the wind speed is relatively higher, which we have estimated based on the wavelength of the cloud as mentioned in the previous section of this manuscript.

19.2.3 Cloud Height Calculation

With the help of the temperature gradient and vertical wind speed value, we may estimate the approximate height of the cloud [27]. We used General Circulation Model (GCM) based on MCD to estimate the temperature gradient value. Mars Climate Database V5.3 in association with GCM can predict most of the parameters (http://wwwmars.lmd.jussieu.fr/mcd_python/). We have calculated the Scorer parameter to estimate the height of the cloud. The Scorer parameter [m-1] was used to validate the development of gravity waves in the atmosphere. It combines the Brunt-Väisälä frequency with characteristics of the vertical wind profile and maybe calculated as follows [4, 2, 28, 29, 3]:

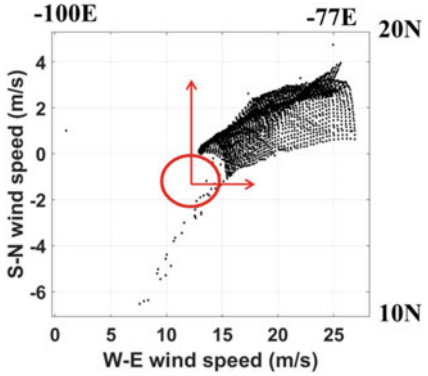

Fig. 19.3 We may see the wind direction at the crest position during the formation of the lee-wave cloud. Plot data based on the MCD-GCM http://www-mars.lmd.jussieu.fr/mcd_python/. We may clearly see how wind is distributed to carry the water ice parcel over the north-eastern slope of Ascraeus Mons. Red circle indicate the Ascraeus Mons and red arrow illustrate the direction of the wind

$$SP^2(z) = \frac{B^2(z)}{U^2(z)} \tag{19.6}$$

where B = B (z) is the Brunt-Väisälä frequency, and U = U (z) is the vertical profile of the horizontal wind. Both the parameters are determined using GCM based on MCD [28]. When SP^2 (z) decreases strongly concerning the atmospheric height, conditions are favorable for trapped lee waves. At higher levels, the Scorer parameter often shows values of about 0.5/km, and the value rarely exceeding 1/km. In the figure, we may see a decrement between 25 and 30 km which supports the required Scorer parameter value and the favorable condition for the formation of lee waves (Fig 19.4).

However, when SP2 (z) is nearly constant with height, it indicates a favorable condition for vertically propagating mountain waves or lee-wave cloud. We compare our calculated wind speed with GCM to first validate our findings than to see the more accurate height of the lee-wave cloud [29].

Figure 19.4 demonstrates a plot based on the wind profile and scorer parameter profile for a particular time as a function of atmospheric height. Thus, we may estimate the tentative size of the Lee-wave clouds [25]. Also, we validate our findings with MCS-MRO data for more accuracy regarding the height of the cloud. S R Lewis et al. forwarded their findings regarding MCD-GCM with an error bar of $\pm$ 5% in the calculation of temperature, pressure, and other atmospheric parameters [30, 23, 26]. If we consider that error, the height of the lee-wave cloud will vary from 30 $\pm$ 3 km to 35 $\pm$ 4.2 km. Our estimation regarding the wind speed also satisfies that particular height with a low margin of error depending on the findings of previous literature [30, 23, 26].

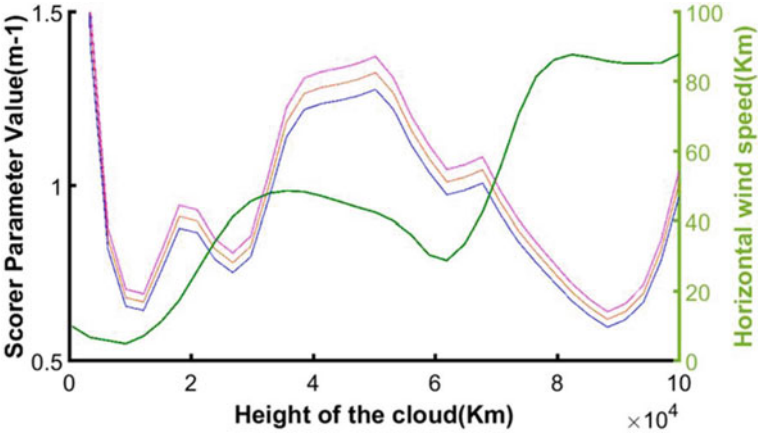

Fig. 19.4 Scorer parameter vs. Altitude vs. Normalized Horizontal wind speed for the observed events to see the exact height and type of the lee-wave cloud. Estimated height of the cloud is 30 to 35 km [18]

19.2.4 Estimation of Atmospheric Parameters

19.2.4.1 Calculation for TOA with the Help of MCC Radiance Value

We estimated the reflectance value at the top of the atmosphere (TOA) by converting the MCC visible bands radiance data (Lλ) to the top of the atmosphere reflectance values (I/Fλ) [17]. The reflectance values at the top of the atmosphere in our case can be estimated as follows:

$$I/F_{\lambda} = \pi * L_{\lambda}/F_{(0,\lambda)} \cos(i) \cos(\theta) \tag{19.7}$$

where L_{λ}, i, and θ_0 are referred to as the spectral radiance observed by MCC for each pixel, the incidence angle, and the solar zenith angle for the same pixel coordinate. Fλ refers to the corrected incoming solar incidence flux per unit area of the surface at the top of the atmosphere [17]. MCC broadband is available with a spectral width of ~ 0.2 μm. Integrated incoming solar flux F(0,λ) used in the calculation of TOA for each band is estimated using the spectral response function of the corresponding band as shown in Fig. 19.5 [17]. In Fig. 19.5, we may observe the normalized count representations for the red, blue, and green channels. We may find out the values of the spectral response function (F_{λ}) by using the solar constant S and the normalized count.

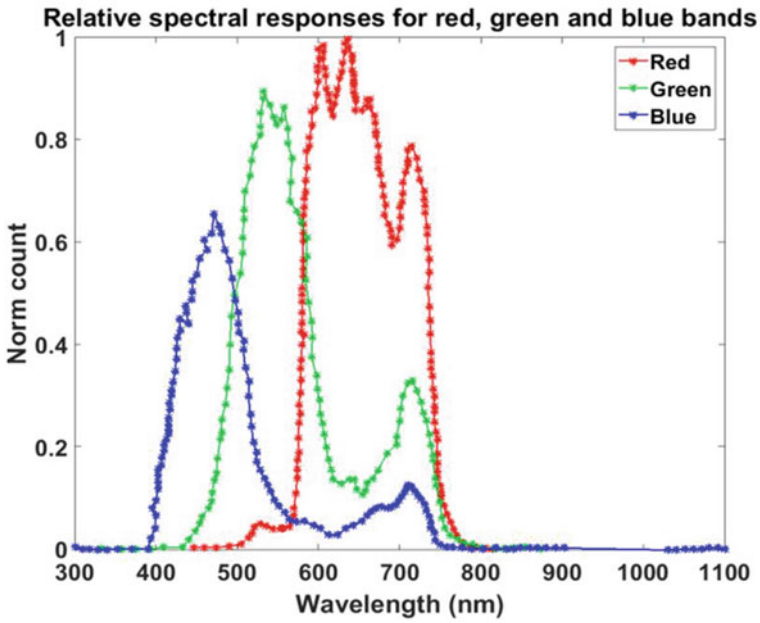

Fig. 19.5 Spectral response as a function of Norm count for each band for Mars Color Camera (MCC) [17, 18]

19.2.4.2 Calculation for Angstrom Exponent (A)

Angstrom exponent is defined as the parameter that decided the mode of the particle. Depending upon the observation wavelength, we may predict whether the observed particle is a coarse- or fine-mode. The relation between α and TOA can be expressed as follows:

$$(\lambda_1/\lambda_2)^{-\alpha} = (I/F)_{\lambda_1}/(I/F)_{\lambda_2} \tag{19.8}$$

where λ1 and λ2 are the wavelengths for red and blue color bands in our study, selecting these two particular bands is that the red color has maximum scattering through the atmosphere. In contrast, blue has minimum dispersion because of the short wavelength [17, 31]. If α is greater than 1, the particle's effective radius is less than the wavelength (fine-mode). In contrast, if α is less than 1, the particle's effective radius is greater than the corresponding wavelength value (coarse-mode) [31].

19.2.4.3 Calculation for AOD (T)

In the previous works, the authors calculated the AOD values by contrast variation for the images captured by Viking [32] and HRSC [33, 34]. We followed the same to estimate the AOD for our observed images. We know that the contrast and the clarification of remote sensing images depend on the atmospheric deposition of water ice and dust particles. An increment in the AOD makes the surface less visible for observation. Hence, the reflectance at the top of the atmosphere decreases for the observation. Hoekzema et al. [33] described the stereo image method based on the comparison of the contrasts in two HRSC stereo images for estimation of atmospheric optical depth over volcano Pavonis Mons [33] and Valles Marineris [32]. The stereo method adopted in our present work is briefly described as follows:

Let us consider $\mu 1$ and $\mu 2$ are the emission angles for two stereo images captured by MCC. If $\mu 1$ is greater than $\mu 2$, then in association with $\mu 1$ has a longer path length through the atmosphere, and hence, it will show a solid atmospheric contribution in the decrement in contrast as compared to image with emission angle $\mu 2$. We may use this difference in comparison to estimate atmospheric optical depth [35].

Let us consider the inward radiation to be O (i; j) for the observed image, where indices i, j refer to pixel number for a two-dimensional image. Let R (i; j) represent the upward reflection by the surface in the direction of pixel i; j for the observed image. If we observed the image in an atmosphere with a minor condition, then O (i; j) and R (i; j) would be equal. However, in the atmosphere on a planet, totally reflected radiation R (i; j) will not reach the camera because of scattering in the atmosphere during its way up through the atmosphere.

Therefore, the fraction of R (i; j) that reaches to Camera can be written as R (i; j) exp ($-\tau/\mu$). Here 'r' represent the atmospheric optical depth (AOD). In fact, airborne dust particles scatter only a tiny fraction of incident radiation back to the space. However, dust haze, water ice, and high altitude cloud haze of small particles significantly backscatter the incident radiation [36, 37]. We included the fraction of inbound backscattered radiation and outbound forward scattered radiation by the airborne aerosols contributing to the radiation data collected by the Camera by B (i; j). Therefore, the radiation at the top of the atmosphere observed by the Camera on board an Orbiter is given by,

$$O(i, j) = R(i, j) \exp(-\tau/\mu_2) + B(i, j) \tag{19.9}$$

Since B will not show large variation over an observed area, hence, we may convert the above equation as,

$$contrast(O_1) = (contrast(R_1(i, j) \exp(-\tau/\mu_1) \tag{19.10}$$

$$contrast(O_2) = (contrast(R_2(i, j) \exp(-\tau/\mu_2) \tag{19.11}$$

For a Lambertian surface, R1 = R2 for a perfect camera. Therefore, when MCC captures two images with almost similar phase angles, then Lambertian approximation is acceptable even with different emission angles. This approximation again considered that the contrast of S1 and S2 would be very similar over a given region while O1 and O2 will be different. In our present study, the phase angle varies from 42.86 to 44.69° for the stereo images. Now, if we use Lambertian approximation in Eq. (19.9), we will get,

$$contrast(O_1) = \exp(-\tau/\mu_1)(contrast(R_1)\} \tag{19.12}$$

$$contrast(O_2) = \exp(-\tau/\mu_2)(contrast(R_2)\} \tag{19.13}$$

Now AOD can be given as,

$$\tau = [\mu_1\mu_2/\mu_1 - \mu_2]\log\{(contrast(O_1)/ < O_1 >)/(contrast(O_2)/ < O_2 >)\} \tag{19.14}$$

Thus, we may estimate the AOD from two stereo images captured by a camera.

19.2.4.4 Calculation of the Temperature (K)

We know that the power radiated by a black body concerning the temperature variation, that phenomenon was described by the Stefan–Boltzmann law. Stefan–Boltzmann law states that the total energy radiated per unit surface area of a black body across all wavelengths per unit time is directly proportional to the fourth power of the thermodynamic temperature T of the back body. The radiance value ($Wm^{-2}\theta^{-1}$) for a black body can be formulated as follows [38]:

$$\begin{aligned} L &= (\sigma/\pi) * T^4 \\ => P &= \sigma A T^4 \end{aligned} \tag{19.15}$$

We have estimated albedo value from the MCC images, and that can be used, and hence can modify the above equation as follows:

$$=> T = (1-a)^{1/4}\frac{279}{r^{1/2}}K \tag{19.16}$$

where L is the radiance value, σ is Stephen's constant = 5.670367(13) × 10 − 8 $W{\cdot}m^{-2}{\cdot}K^{-4}$, where "T" is the temperature, "a" denotes albedo value, r is the distance between mars and sun in the atmospheric unit. We took an approach to calculate the albedo value from the direct solar insolation value and the image radiance value. We have verified our findings with the Mars SWIR Albedo map prepared in Ramdayal Singh et al. with an error bar of ± 0.05. Estimated temperature varies

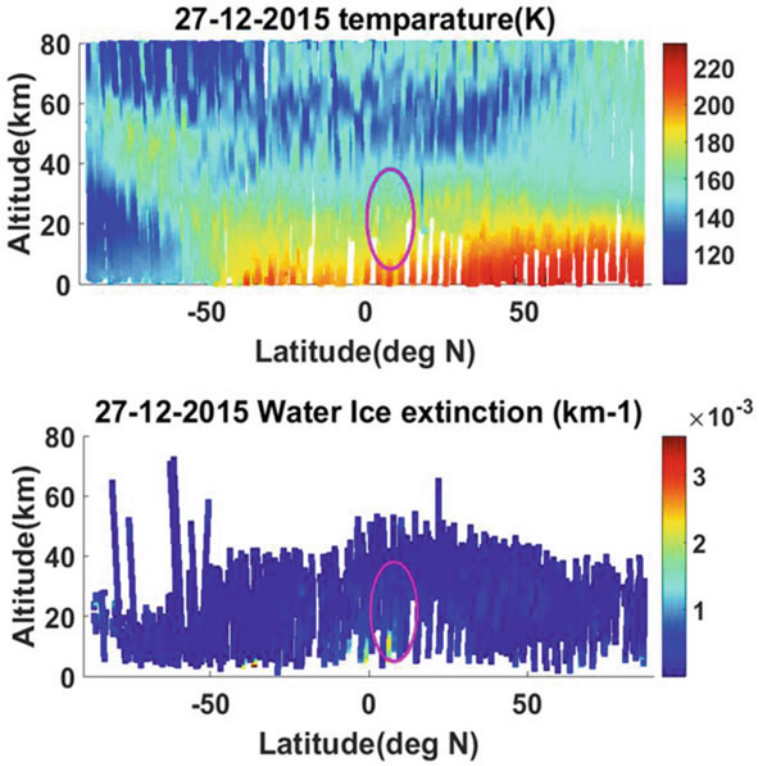

Fig. 19.6 We may see the water extinction color plot. Pink circle indicates the presence of water ice cloud for the same event captured by MCC on 27 Dec 2015 along with exact latitude value. Temperature color map based on the MRO-MCS data. Pink circle indicates the studied area and showing some temperature profile that follow the constrain set in Guha et al., [39] and hence verified our findings regarding the calculation of CBL height

from 160 ± 3 K to 180 ± 4 K (Figs. 19.6). Further, we have re-verified our result with the GCM model and MCS observed temperature and weather report data (Figs. 19.7, 19.8). Please refer to Fig. 19.9 of Kalita et al [18] .

19.2.4.5 MCS/MARCI Data Analysis and Observations

MRO observe Martian limb, nadir, and off-nadir in nine broadband channels to detect dust, temperature, and condensates [40, 41] since September 24, 2006 (LS = 111°, MY 28). We may extract vertical profiles of temperature (K), dust extinction (km-1; at 463 cm − 1 wavenumber), and water ice extinction (km-1; at 843 cm-1 wavenumbers) through the limb observations with a moderate (5 km) vertical resolution from the surface to ~ 80 km altitude through MRO observation [41]. The uncertainty in extinction usually varies from $10 - 5$ to $10 - 6$ km − 1 for MRO dust

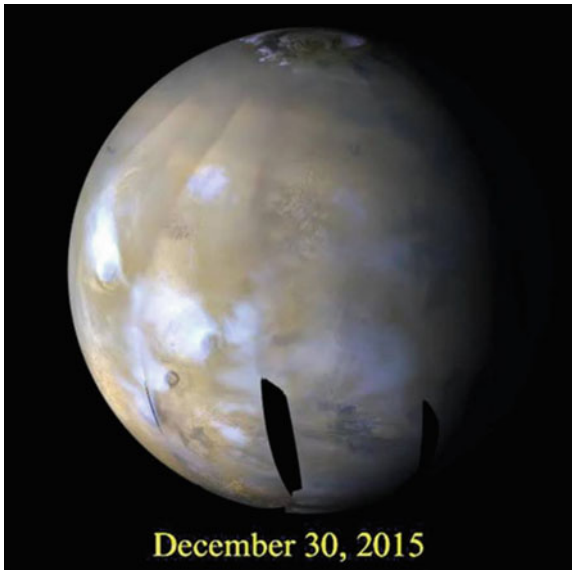

Fig. 19.7 We may see the lee-wave cloud in Marci images also correspondence with MCC event that we observed in our present work. http://www.msss.com/msss_images/2016/01/06/

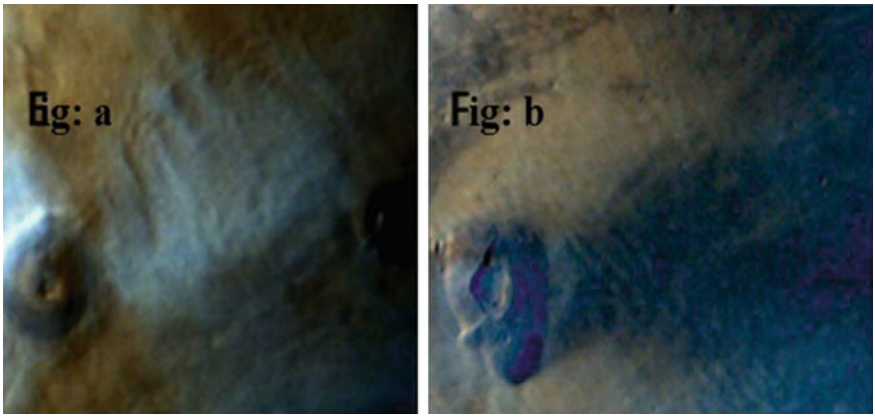

Fig. 19.8 We may see the lee-wave cloud near Ascraeus Mons and Tharsis Tholus during 11/04/2016 and 04/01/2018. Fig. a) We may see the clear ripple of the lee-wave cloud; b) Ripples are less distinct due to high wind flow over the Tharsis Tholus region (westerlies)

observational data [42], whereas the uncertainty in the altitude data varies as $\pm$ 1 km [12, 13, 40, 41]. We used MCS DDR data for MY 33–34 in our present work, available in NASA-PDS. Vertically integrated dust extinction is available in a .tab file inside MCS observational DDR data product. We may use the water ice extinction data to analyze the total observed water ice opacity. Eventually, MCS retrievals in dusty conditions do not extend to the surface with maximum atmospheric mass [43]. So, the vertically integrated dust opacity is calculated by assuming a well-mixed profile

using the lowest retired point. We adopted the density-scaled opacity approach given in [39] to examine the variability in atmospheric parameters. The profile forwarded by [26] cannot estimate the vertical dust distribution at certain latitudes and seasons. Moreover, density-scaled opacity helps understand a particular dust profile's radiative and dynamic importance [39].

From the temperature data, we found that temperature in the cloud region is ~ 180 K.

Radius of the Particle

We followed the Mie theory to calculate the radius of the particle. First, we calculate the density-scaled opacity derived from MCS dust extinction and water ice extinction data. We used the data to estimate the mixing ratio of dust and water ice particle, then using the Mie theory, we calculated the effective radius of the particle as follows:

$$mixing\ ratio(q) = \frac{4\rho_D(d_z\tau)r_{eff}}{3Q_{ext}\rho} \tag{19.17}$$

The value of Qext is 0.35, which can be obtained from the Mie theory described by [41], reff is the effective radius of a dust particle, and density is obtained from MCS data using the ideal gas equation. ρ_D is the retrieved density that has the value of 3000 kg m-3. The effective radius of the dust particle varies from 0.40 to 3.2 μm. The mixing ratio is considered from the MCD-GCM for that particular event.

MARCI Daily Weather Report

To become more rigid with the findings, we consulted MARCI daily weather reports and global images associated with the cloud events captured by MCC. During Ls 200 to 260, regional dust storms and dust lifting process have been reported by MARCI. During the Martian non-dust storm season, the appearance of water ice cloud is reported in MARCI daily weather report.

Report Aphelion cloud-belt spread as Solstices came. The regional storm swept over plains northward Tempe. Dust unfurled East–West sporadic storms passed "top" equatorial lands http://www.msss.com/msss_images/2016/01/06/.

Results and Discussions

In our present work, we considered all the images captured by MCC, having evidence of the presence of the Lee-wave clouds in the Martian Atmosphere. In Fig. 19.9, we may see the lee-wave cloud near Ascraeus Mon and Tharsis Tholus. We illustrate the reflectance plot in Fig. 19.2 for lee-wave cloud images along latitude 13° N. Forget et al. [44] illustrate their work regarding the global climate models during periods of high obliquity (>45◦), which shows a strong westerly wind across Tharsis. This strong wind carried the parcel equatorward from the polar caps through the Tharsis region. As soon as the air encountered the steep slopes of the high ridge of Ascraeus

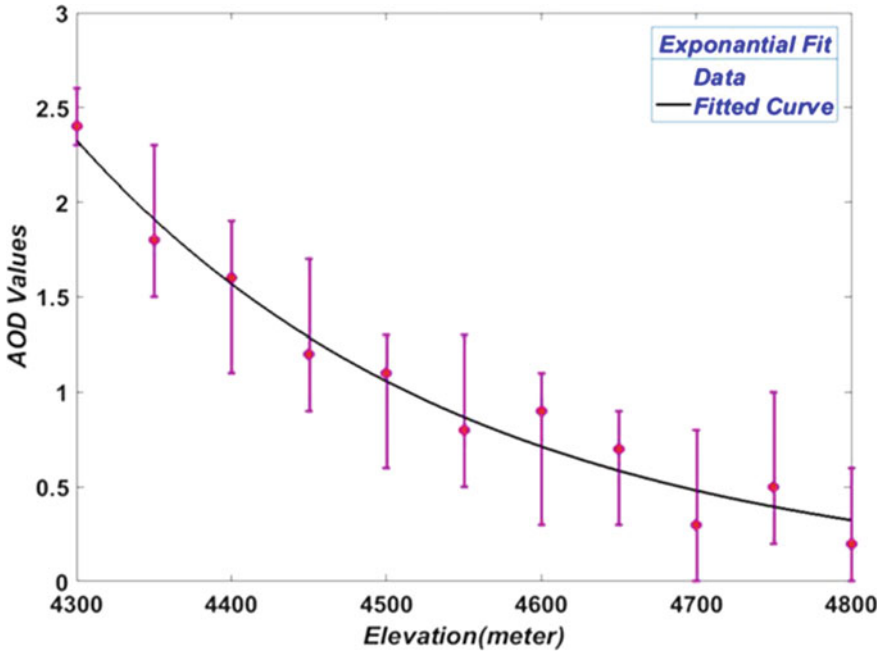

Fig. 19.9 We may see the AOD values are varying as a function of altitude. We fitted the data exponentially to evaluate the scale height of the AOD as a function of altitude

Mons and Tharsis Montes, instantly the parcel rose up and hence cooled adiabatically, resulting in the precipitation on the western flanks of the volcanoes [26, 7]. In Table 19.1, we have tabulated all the starting locations of lee-wave cloud events.

We have considered 35 events for 7 days. Each day contains five stereo images. The estimated wavelength for the lee-wave cloud on 27 November is 31.2 km with an average wind speed of nearly 45.29 m/s at the height of 30 km from the surface of Mars. We have also computed the wavelength and the average wind speed values for the other events, respectively, on 18 December, 27 December, and 30 December 2015, 11 April 2016, 13 October 2017, and 04 January 2018. The estimated wavelength varies from 27 $\pm$ 3 to 39 $\pm$ 3 km, and the wind speed ranges from 32 $\pm$ 9 to 54.25 $\pm$ 9 m/s for the observed events. We may see all results in the table regarding the wavelength, wind speed, and the height of the Lee-wave cloud. In our observation, the height of the cloud varies from 25 to 37 km. As we mentioned earlier, to estimate the height of the cloud, we considered the scorer parameter value, and for that, we have consulted MCD-based GCM predictions. In Fig. 19.4, we may see how the scorer parameter decreases from 1.0 and 0.5 within the height limit of 27 to 30 km. After calculating the height, we validated our results with MCS-MRO data. We found that the scorer parameter application effectively determines the height of the trapped lee-wave cloud.

Table 19.1 Computed values of wavelength, wind speed, and height of the lee-wave clouds

Sl. no	Name of the image [a]	Orbit no	lat./lon	Spatial pixel resolution (m/pixel)[b]	Wave-length (km)	Wind speed (m/s) [c]	Approximate height of the cloud as per GCM model (km)
1	MCC_MRD_2015 1127T060758768_D_D32.IMG	179	15 °N/ −102 °E	1688	31.2	45.29	30
2	MCC_MRD_2015 1230T004401330_D_D32.IMG	191	15 °N/ −102 °E	1383	27.7	43.3	28
3	MCC_MRD_2015 1227T005201328_D_D32.IMG	190	14 °N/ −101 °E	2467	29.8	46.51	28
4	MCC_MRD_2015 1218T193408097_D_D32.IMG	187	15 °N/ −101 °E	2591	31.4	45.67	30.2
5	MCC_MRD_20160411T225813687_D_D18.IMG	230	15 °N/ −102 °E	1210	25.6	36	24
6	MCC_MRD_20171013T160604035_D_D32.IMG	000	16 °N/ −102 °E	3509.0	32.2	46.90	30
7	MCC_MRD_20180104T182317141_D_D32.IMG	463	16 °N/ −102 °E	789	25.6	40.90	29

[a] The image name refers to the year, day of the year, and time of capture. Name of the image in the format like MCC_MRD_YYYYMMDD T TT: TT: TT ID_D_D32.IMG suggests YYYY (year), MM (month), DD (date) TT (hour): TT (minute): TT(second) of the image.
[b] Spatial resolution of the image (pixel/meter).
[c] Wind speed which is responsible for the vertical deflection of the wind and the formation of the Lee-wave clouds.

Atmospheric properties of the planet may be predicted from TOA values, since the TOA value depends on the incoming solar flux and backscattered radiation. Therefore, we first estimated the reflectance values at the top of the atmosphere for the entire visible bands. For example, on 18 December 2015, reflectance values at the top of the atmosphere are 0.31, 0.26, and 0.20 for blue, green, and red bands. We analyzed the MOLA_DEM using ARC-GIS to estimate the elevation profile. We also calculated the Angstrom Exponent (α) values to predict the nature of the Lee-wave cloud particles and reported α value vary from 0.9 to 2.3 accordingly. Our findings indicate that the cloud may contain both fine-mode as well as coarse-mode particles. It is to be mentioned that the cloud portion shows maximum reflectance in the blue channel indicating the presence of water ice particles. We consulted GCM to collect the water ice mixing ratio during the observed period to calculate the effective radius of the particles present in the cloud. The effective radius of the dust particle varies from 0.16 to 1.33 μm, while the water ice particle radius varies from 0.6 to 3.2 μm.

MCC has captured the entire lee-wave cloud images during northern summer Ls = 60 ˚ to Ls = 90 (longest distance between the Sun and Mars). Dust haze also can be observed during the mentioned period [45, 17, 10, 12]. In our present work, we evaluated the optical depth as a function of altitude [46]. The optical depth or optical thickness can be defined as the natural logarithmic ratio of incident to transmitted radiant power when the beam passes through a material or the atmosphere. We reported that the optical depth values vary from 0.5 to 2.2 for the red channel. In contrast, the blue channel ranges from 0.9 to 2.01 with an error of ± 0.2 using the stereo image processing method.

The scale height, f (Z) = 1.8676 *exp (−0.524*Z) is for red channel and f (Z) = 1.2676 *exp (−0.344*Z) is for blue channel as demonstrated in Fig. 19.9. Computed scale height varies from 3 to 5 km. Pressure scale height is given by H(z) = RT/gM, where R, T, g, and M refer to ideal gas constant, temperature, Martian gravity, and molecular weight, respectively. Pressure scale height is found in 8.6–10.1 km based on the Lewis et al [23]. Though the red channel scale height of AOD is slightly higher than the blue channel AOD, both the values are highly different from the estimated pressure scale height value. Previous literature showed that the scale height of AOD is comparable to the pressure scale height of the Martian atmosphere. They argued the presence of heterogeneous mixture near mountain region due to the mismatch of pressure scale height and scale height of AOD, where usually lee-wave clouds are formed [5, 47, 48, 6].

Table 19.2 illustrates the formation temperature of the cloud based on the Stephen–Boltzmann law. Estimated temperature varies from 180 to 190 K. We may see an albedo map based on the MSM and MCC in Fig. 19.9 Kalita et al., where albedo value ranges from 0.8 to 1.0 for the lee-wave cloud. In contrast, temperature varies from 170 to 180 K at the height of 28 km. We cross-verified our results with GCM and MRO-MCS and verified that the estimated temperature at the altitude of 28 km falls within 1% of error. We also confirmed water ice cloud variability during solar longitude 73 to 136° using MARCI daily weather report and MARCI global images. The season approaching 85 clouds used to disappear and reappeared at Ls 110 to Ls 136. The reason for this variability is concluded as dust storms [45, 9, 11]. We

Table 19.2 The effective radius of the dust particles and the formation temperature of the Lee-wave clouds in the Martian atmosphere

Sl. no	Orbit no	Effective radius of the dust particle (n m)	Albedo value for the cloud region	Estimated temperature value (K)	MCD Temperature value (K)
1	27.11.2015	160	0.7	176	179
2	30.12.2015	330	0.8	182	180
3	27.12.2015	270	0.7	171	181
4	18.12.2015	240	0.9	182	178
5	11.04.2016	250	0.6	165	160
6	13.10.2017	360	0.8	179	175
7	04.01.2018	310	0.9	185	190

validate our findings using MCS-MRO data analyzed for water ice extinction and temperature. We reported a particular height for the lee-wave cloud, depending on the frequency value, temperature lapse rate, and scorer parameter. As we can see, the scorer parameter curves intersect the attitude curve in two particular points, and we considered only the first one and reported that the height is 30 km. To be more concertize about our finding, we consulted MCS-MRO data, and from the figure, we may see that there is no data for water ice extinction above the height of 70 km. Also, at an altitude of 30 to 35 km, we may see the water ice cloud's clear presence and the same coordinate. From this observed data, we validate our findings within 2% of error regarding the height of the cloud. Secondly, we have calculated the temperature using Stephen Boltzmann's law and verified our results with MCD-GCM. An observed data for that particular period will give more accuracy regarding our findings. So, we analyzed the MCS temperature data, and it provides a temperature with a value within 1.5% of our estimated value.

19.3 Conclusion

During non-dust storm season, a tropical cloud used to appear in the Martian atmosphere. These water ice clouds are carrying significant importance in seasonal variation. MCC captured these water ice content lee-wave clouds near the slope of the high ridge of Ascraeus Mons and Tharsis Tholus. We reported the cloud as a water ice cloud with an effective radius of 1.2 to 3.2 μm. The clouds are spreading over a large area of 100 km2, and the cloud parcel contains both coarse-mode and fine-mode particles. Due to high wind flow and adiabatic changes in the atmosphere, the cloud parcel reached a height of 35 km from the mean surface of Mars. The scorer parameter value for these wave clouds varying from 0.5 to 1.0 indicates trapped lee-wave characteristics with a reported wavelength of 27 to 39 km and a wind shear of ~ 55 m/s. Due to the high deposition of water ice in the atmosphere, AOD increases to

2.1. Most of the radiation is reflected at the top of the atmosphere. The scale height of AOD was 3 to 6 km, which is not the same as the pressure scale height for the observed period, indicating a heterogeneous mixture. Due to the adiabatic variation in the atmosphere, the cloud parcel passes through different temperature levels and condensates at ~ 190 K. We verified our estimated temperature and height of the cloud with MCD-GCM and MRO-MCS. Also, we consulted MARCI daily weather report and MARCI-DGM to more concretize our findings.

Acknowledgements The authors are also thankful for the MCC data product team members for providing access to the required data for the present analysis (https://mrbrowse.issdc.gov.in/MOMLTA/) and the Indian Space Research Organization (ISRO) for funding the project with fund reference ISRO/SSPO/MOM-AO/2016–2019. A special thanks to Dr. Satadru Bhattacharya, Planetary Sciences Division, and Space Applications Centre (ISRO) for his constant support. An acknowledgment is due to the Department of Science and Technology for a supporting fund to the Department of Physics, Tripura University through DST-FIST fund reference SR/FST/PSI-191/2014 and University Grants Commission SAP fund reference F.530/23/DRS-I/2018(SAP-I).

References

1. S.E. Wood, C.D. Catling, C.S. Rafkin, E.A. Ginder, C.G. Peacock, in *Proceeding of the Sixth International Conference on Mars, July 20 25 2003, Pasadena California,* abstract no.**3283** (2003)
2. M.G. Tomasko, J. Geophys. Res. **104,** (E4) 8987 (1999)
3. H. Wang, *Ph.D. thesis* (2004)
4. D.R. Durran, *Meteorological Monograph,* vol. 23**,** 45 (1990)
5. R. Kahn, R. Goody, B.J. Pollack, J. Geophys. Res. **84**, 5833 (1984)
6. J.A. Coakley, Elsevier Science Ltd, 1914 (2003)
7. S.J. Kadisha, J.W. Heada, R.L. Parsonsb, D.R. Marcha, Icarus. **197**, 84 (2008)
8. J.A. Pirraglia, Icarus. **7**, 517 (1976)
9. C.B. Leovy, R.W. Zurek, J. Atmos. Sci. (1973)
10. G.A. Briggs, JGR, **82**, 4121 (1977)
11. F. Montmessin, JGR planets, (2004)
12. G.A. Briggs, C.B. Leovy, Bull. Amer. Met. Soc. **55**, 278 (1974)
13. A.O. Pickersgill, G.E. Hunt, JGR **84**, 8317 (1984)
14. S.C.R. Rafkin, Icarus. **151**, 228 (2001)
15. R.L. Wildey, *Nature,* **249** (1974)
16. P.S. Ray, *Springer,* **272** (1986)
17. M.K. Mishra, P. Chauhan, R. Singh, S.M. Moorthi, S.S. Sarkar Icarus. **265**, 84 (2016)
18. J. Kalita, M.K. Mishra, A. Guha, Indian J. Phys. (2021)
19. K. Ohnuki, S. Yoshida, M. Ohta, M. Shimizu, S. Mochizuki, M. Nishioka, K. Fukuda, M. Ishizaki, E. Hirakawa, T. Andou, Int. J. Cardiol. (2006)
20. K. Nithyakalyani, R. Kalpana, S. Sudhakar, N. Vigneswaran, Biosciences Biotechnology Research Asia, **12**, 677 (2015)
21. R. Singh, P. Chauhan, in *Proceeding of the 49th Lunar and Planetary Science Conference 2018* (*LPI Contrib. No.* **2083**), (2018)
22. G.V. Portyankina, *Dissertation Gottingen,* (2005)
23. S.R. Lewis, M. Collins, P.L. Read, F. Forget, J. Geophys. Research–Planets (1999)
24. M.A. Mischna, J.F. Bell, P.B. James, D.D. Crisp, Geophys. Res. Lett. **25,** 611 (1998)
25. J.R. Murphy, C.B. Leovy, J. Geophys. Res. **95**, 57 (1990)

26. F. Forget, F. Hourdin, R. Fournier, C. Hourdin, O. Talagrand, M. Collins, S.R. Lewis, P.L. Read, J.P. Huot, Geophys. Res. **104,** 155 (1999)
27. W.J. Markiewick, J. Geophys. Res. **104,** (E4) 9009 (1999)
28. R.S. Quart and J Roy *Meteor. Soc.* **75** 41 (1949)
29. P.S. Ray (ed.), *Mesoscale Meteorology and Forecasting,* (1986)
30. A.S.K. Kumar, P. Chauhan, Curr. Sci. **107**(7), 1096 (2015)
31. K. Soni, S. Singh, T. Bano, R.S. Tanwar, S. Nath, Aerosol Sci. Technol. **45**, 148 (2011)
32. T.E. Thorpe, J. Geophys. Res. (1979)
33. M.N. Hoekzema, in *Proceeding of the Seventh International Conference on Mars, LPI Contributions No,* **1353**, 3154 (2007)
34. M.N. Hoekzema, Earth Planet. Sci. Lett. **294**, 534 (2010)
35. J. Appelbaum, D.J. Flood, NASA Tech. Memo. **102299**, 33 (1989)
36. J.W. Markiewicz, J. Geophys. Res.**104,** (E4) 9009 (1999)
37. G.M. Tomasko, J. Geophys. Res. **104**, (E4) 8987 (1999)
38. M.C. Lopresto, N. Hagoort, Phys. Teach. **49**, 113 (2011)
39. B.K. Guha, J. Panda, P. Chauhan, Icarus. (2018)
40. D.J. McCleese, J. Geophys. Res. **112** (2007)
41. J. Kleinböhl, Geophys. Res. **114**, E10006 (2009)
42. J.L. Benson, D.M. Kass, A. Kleinböhl, D.J. McCleese, J.T. Schofield, F.W. Taylor, J. Geophys. Res. **115**(E12) (2010)
43. N.G. Heavens, J. Geophys. Res. (2011)
44. F. Forget, R. Haberle, F. Montmessin, Levrard, Benjamin, Head, James, Science (New York, N.Y.), **311** (2006)
45. J.L. Benson, B.P. Bonev, B.P. James, J.K. Shan, Icarus. **165,** 34 (2006)
46. M.K. Mishra, Lunar Planet. Sci. 46. Contribution no. **1995** (2015)
47. D. Grassi, Planet. Space Sci. **55**, 1346 (2007)
48. M.T. Lemmon, *Spirit and opportunity science,* vol. **306**, 1756 (2004)

Chapter 20
Microscopic Foundation of Some Empirical Rules and $Z(P_r)$ of a Simple Fluid

Yatendra S. Jain

Abstract In this paper, we use our recently reported microscopic theory of simple fluids (Jain in J. Mol. Liquids, 249:688–701, 2018) to explain how high energy particles present as a solute weaken the liquid structure, facilitate the formation of bubbles and trigger liquid to gas transformation (L2GT). The average kinetic energy of these particles is concluded to fall $\approx 3k_BT_c/2$ and this fact helps in finding the temperature (T) dependence of their number density. This explains the detailed microscopic origin of Guldberg rule, triple point temperature $T_t \approx 0.52T_c$, Trouton rule and ideal gas (IG) behaviour of the gas at Boyle temperature (T_B). Analyzing our mathematical relation $Z = Z_c\rho_c P_r/\rho T_r$ derived from the basic definition of compressibility factor Z of a fluid. It explains why $Z(P_r)$ of a low-density gas decreases linearly with an increase in P_r, while the same for high-density incompressible gas and liquid states increases linearly with P_r and vaporisation of a liquid is a basic property of gas-liquid interface (GLI). It is discovered that $Z^{inv} = 1/Z$ is directly related to two terms representing interparticle attraction and repulsion and this fact can greatly simplify the evaluation of Z for any simple fluid. Particles in the liquid state are concluded to make a macroscopically large molecule with solid like incompressible structure having vanishingly small shear forces. A new useful form of the equation of state of a real gas is also discovered.

20.1 Introduction

Recently, we reported a microscopic theory of simple fluids [1] developed by using pair of particle basis (PPB) which identifies each particle as a part or a representative of pair of particles. It obviously differs from all other theories developed by other scientists [2] by using single particle basis (SPB) which recognizes each particle as a free particle. While PPB theory can treat the two body central potential ($V(r_{ij})$) exactly, SPB theories use different methods which treat it only approxi-

Y. S. Jain (✉)
Department of Physics, North-Eastern Hill University, Shillong 793022, India

S. Sengupta et al. (eds.), *Selected Progresses in Modern Physics*, Springer Proceedings in Physics 265, https://doi.org/10.1007/978-981-16-5141-0_20

mately. The merit of our theory lies in the fact that it answers several questions of great importance not answered by SPB theories. This refers to the questions related to the microscopic mechanism of liquid to gas transition (L2GT) and gas to liquid transition (G2LT) [1, 3, 4], several important empirical rules followed by simple fluids and the explicit relation of $V(r_{ij})$ with compressibility factor (Z) appearing in the well known equation of state (EOS), $PV = ZRT$. In this paper, we unravel the detailed microscopic reasons for the observation of some of the important empirical rules such as Guldberg rule [5], Trouton rule [6], etc. In addition, we analyze $Z(P_r)$ in relation to its dependence on $P_r = P/P_c$ for a given $T_r = T/T_c$. We also find an important fact that $V(r_{ij})$ are more directly related to $Z^{\text{inv}}(= 1/Z)$ than Z. While, Z^{inv} and $V(r_{ij})$ are related through two simple terms representing the impacts of attractive and repulsive components of $V(r_{ij})$, Z is known to represent an expansion series with terms having different powers of ρ which poses a problem for its non converging nature. The study provides enough reasons to believe that the liquid state represents a macroscopically large molecule with solid like incompressible structure having vanishingly small shear forces which allow its particles to flow.

20.2 Microscopic Foundations of Important Empirical Rules and IG Behaviour of a Real Gas

20.2.1 Guldberg Rule

In our earlier paper [1], we unravelled the microscopic basis of Guldberg rule ($T_b^1/T_c = 2/3$ with T_b^1 being the boiling point of the liquid at 1 atm pressure) by using a simple scientific logic. However, in this article, we explain its foundation by using necessary mathematical relations. Accordingly, we combine $\mathrm{v} = \mathrm{V}/N$ (*volume per particle*) and theoretical $Z_c = 0.2962$ [1], with

$$P_{\text{coh}}\mathrm{V} = (N - N^*)k_BT = (1 - Z)Nk_BT \tag{20.1}$$

followed from [1]. Here P_{coh} is cohesive pressure and $N^* = ZN$ is the number of free particles, while $N - N^*$ particles are fully controlled by P_{coh}. Accordingly, we have

$$P_{\text{coh}}^{T_c} = \frac{(1 - Z_c)Nk_BT_c}{\mathrm{V}_c} = \frac{0.7036k_BT_c}{\mathrm{v}_c} = 0.7036k_BT_c\rho_c. \tag{20.2}$$

at $T = T_c$. Similarly, for the liquid phase at $T < T_c$, we also have

$$P_{\text{coh}}^{T_b} = \frac{(1 - Z_l^{T_b})Nk_BT_b}{\mathrm{V}_l^{T_b}} \approx \frac{(1 - Z_l^{T_b})k_BT_b}{\mathrm{v}_l^{T_b}} = \left(1 - Z_l^{T_b}\right)k_BT_b\rho_l^{T_b}, \tag{20.3}$$

which represents $P_{\rm coh}$ at an arbitrary boiling point T_b. Using this relation with our theoretical result [1] that the liquid phase at temperatures as low as T_b^1 has $Z_l^{T_b} \approx 0$ (corroborated by the experimental value), we find

$$P_{\rm coh}^{T_b^1} = (1 - Z_l^{T_b^1}) k_B T_b^1 \rho_l^{T_b^1} = k_B T_b^1 \rho_l^{T_b^1}, \tag{20.4}$$

Combining, (20.2) and (20.4) with $F^b = 3(1 - Z)$, *-the number of degrees of freedom* (DOF) *of a particle controlled by* P_{coh} [1], we find following F^b, respectively, due to $P_{\rm coh}^{T=T_c}$ and $P_{\rm coh}^{T=T_b^1}$.

$$F^b(T = T_c) = 3(1 - Z_c) = 2.1108 \quad \text{and} \quad F^b(T = T_b^1) = 3(1 - Z_l^{T_b^1}) \approx 3. \tag{20.5}$$

The fact, that these numbers match closely with corresponding numbers "2 and 3" adopted to explain the Guldberg rule, underlines the accuracy of our argument [1]. However, to add more to this account, we examine the boiling process and formation of a bubble for their role in the onset of L2GT in Appendix 20.5. Accordingly, we find that a liquid becomes critical for L2GT at a T_b when a small amount of GIB (*gas in bubbles*) assumes a state of $\epsilon_{GIB} > C\epsilon_{GLI}$ (see Appendix 20.5 for notations) by crossing the state of

$$\epsilon_{GIB} = \mathrm{C}\epsilon_{GLI} \quad \equiv \text{to} \quad F_{\rm evap} = F_{\rm cond} \tag{20.6}$$

representing the state of equilibrium (*cf.*, (20.5.4)), where rate of evaporation of liquid particles equals rate of condensation of gas particles. Here $F_{\rm evap}$ is a force which induces a liquid particle to evaporate, while $F_{\rm cond}$ is an opposite force which makes a gas particle to condense. We assume that ϵ_{GLI} includes the impact of P_r which also opposes the evaporation of a liquid particle from GLI. To reveal possible aspects of L2GT from (20.6), we note the following points.

(a) As shown in [1], PPB concludes that each particle has two motions (q and K). Notably, q-motion represents relative motion of two particles having equal and opposite momenta (q, -q) with respect to their centre of mass (CM) which moves with momentum K in the laboratory frame. Since the share of q-motion in the KE (=$3k_BT/2$) of a particle is 2 times the share of K-motion [1], 3 components of $\mathbf{q}$ [q_x, q_y and q_z] and three similar components of $\mathbf{K}$ have an energy impact 9 times that of a single $\mathbf{K}_i$ (with $i = x/y/z$) which implies that each particle has 9 *apparent degrees of freedom* (ADOF) which are controlled by the increasing impact of $F_{\rm cond} \equiv P_{\rm coh}$ in process of cooling. For example, as indicated by (20.5), $F_{\rm cond}$ controls about 4.2216 ADOF (representing 2.1108 components of $\mathbf{q}$) at $T = T_c$ and 6 ADOF (representing all the 3 $\mathbf{q}_i$) at all T_b where $Z_l^{T_b}$ has negligibly small value.

(b) Since $V(r_{ij})$ appears only in the equation of q-motions, $F_{\rm cond}$ first achieves direct control over 6 ADOF of 3 $\mathbf{q}_i$. The remaining 3 ADOF of K-motion are controlled indirectly at a latter stages of cooling.

(c) As GIB is a gas of $T = T_c$, ϵ_{GIB} in (20.6) equals $3k_BT_c/2$ and further since 9 ADOF of a particle have $3k_BT/2$ KE (i.e., a single ADOF has $k_BT/6$ KE), $|\epsilon_{GLI}|$ appearing in same equation can be expressed as $|\epsilon_{GLI}| = \gamma(k_BT_\gamma/6)$ by assuming that F_{cond} (originating from this energy) controls γ ADOF at $T = T_\gamma$. When these values of ϵ_{GIB} and $|\epsilon_{GLI}|$ are combined with (20.6) by using (20.5.2, 20.5.3 and 20.5.4 of Appendix 20.5), we have (i) $3k_BT_c/2 = C\gamma(k_BT_\gamma/6)$ for any T_γ between T_t and T_c and (ii) $3k_BT_c/2 = 4.2216C(k_BT_c/6)$ at $T = T_c$, since F_{cond} at T_c controls γ =4.2216 ADOF (*cf.*, point-**(a)** above). This renders

$$\frac{T_\gamma}{T_c} = \frac{4.2216}{\gamma}, \tag{20.7}$$

a very useful relation, to determine T_b^1/T_c and T_t/T_c since related γ can be easily fixed. We note that each particle in the solid phase at $T = 0$ has only small amplitude oscillatory motion (zero point motion) around its location as a manifestation of its q-motion. The K-motion of each particle appears as collective oscillatory motions known as phonons at non-zero T. The fact that phonon energy is decided by inter-particle forces, indicates that all the 9 ADOF of each particle in a solid phase remain under control of the cohesive forces. However, when the liquid melts at its melting point, the cohesive forces ease out their control on a minimum of 1 ADOF related to K-motions necessary for the liquid like behaviour. No easing out of any ADOF of q-motion is expected before all the 3 ADOF of K-motions are eased out since interactions appear in the equation of q-motion and not in that of K-motion. This implies that a maximum of two ADOF of K-motion remain under the control of cohesive forces indicating that γ related to T_t can be $\leq$8. On the other hand, since a liquid particle at the GLI can diffuse along the $x-$ and $y-$ directions in the plane of GLI but not along the $z-$direction ($\perp$ to GLI), it is clear that a minimum of 1 ADOF of K-motion remains under the control of cohesive forces with rise in T from T_t to T_b^1. Evidently, the minimum value of γ related to T_b^1 is 7. Accordingly, the maximum value of T_b^1/T_c and minimum value of T_t/T_c are found to be

$$\frac{T_b^1}{T_c} = \frac{4.2216}{7} = 0.603 \quad and \quad \frac{T_t}{T_c} = \frac{4.2216}{8} = 0.528 \tag{20.8}$$

The fact, that these results agree closely with corresponding experimental values falling, respectively, around 0.58 and 0.555 [7], proves their accuracy. Notably, the former also supports the Guldberg rule because 0.603 is not far from 0.667 (anticipated from the rule); this is, particularly important since the Guldberg rule is largely derived from the experimental value of T_b^1/T_c for liquids composed of molecules having a large number of atoms whose rotational motions can make observable impact on T_b^1/T_c. It may be noted that such molecules are likely to lose energy of their linear motion in favour of their rotational motion causing a reduction in their force to blow up the bubble or rupture the GLI. As a result, T_b^1/T_c is expected to be higher than 0.603 (20.8) and it can be as high as 0.7036 resulting from $\gamma = 6$.

In order to provide a complete understanding of possible values of T_b/T_c, we also add following points.

(a) T_b^1/T_c has special relation with the general behaviour of simple fluids because our atmosphere is basically composed of *viz.*, N_2 (78%), O_2 (21%), Ar (0.93%) and CO_2 (0.04%) and they all represent a simple fluid. Obviously, T_b^1/T_c for these fluids, (found to fall, respectively, around 0.613, 0.583, 0.580 and 0.640), indicate that 1 atm pressure represent their intrinsic vapour pressure at their T_b^1. Consequently, all simple fluids having non-polar structure with few atoms per molecule should have $T_b^1/T_c \approx 0.604$ (the average of four T_b^1/T_c mentioned above). Since this value neither differs significantly from 0.667, underlined by Guldberg rule [5], nor from $T_s = T_b/T_c = 0.58$, emphasized by Guggenheim [7], it is not surprising that most simple fluids are found to have T_b^1/T_c between 0.58–0.67.

(b) Boiling of a liquid at T_b^1 is also unique for the point of experimental requirement, since making a liquid boil at $T_b < T_b^1$ [or at $T_b > T_b^1$] needs an extra arrangement to achieve corresponding P_{ex} (*externally applied pressure*) < 1 atm [or $P_{ex} > 1$ atm]. Notably, $P_{ex}(< 1$ atm) is achieved by putting the liquid under the suction force of a vacuum pump which weakens the liquid structure (in particular the GLI) and promotes boiling at $T_b < T_b^1$. Similarly, $P_{ex}(> 1$ atm) is achieved by putting the liquid in a closed container which allows control over the increasing P_{ex} to get the desired P_{ex}. The increased P_{ex} adds necessary strength to GLI against its disintegration due to increased n_{GIB} in the liquid. Accordingly, we can have any T_b between T_b^1 and T_c.

(c) $T/T_c = 0.469$ obtained by using $\gamma = 9$ in (20.7) refers to a situation where each particle is bound by cohesive forces in respect of its all the 9 ADOF and such a state represents a perfect solid which does not have its sublimation. This implies that sublimation of solid phase of a simple fluid is possible between T_t and $T_r = 0.469$ only.

20.2.2 Trouton Rule About Heat of Vaporisation, $\Delta_{vap}H^{T_b^1}$

The statement of Trouton's empirical rule $\Delta_{\text{vap}}H^{T_b^1} \approx 9RT_b^1$ was slightly modified by Guggenheim [7] by using a more accurate analysis of experimentally observed $\Delta_{\text{vap}}H^T$. Accordingly, simple fluids more consistently follow

$$\Delta_{vap}H^{T_s} \approx 9RT_s \tag{20.9}$$

at $T_s = 0.58T_c$, not at T_b^1. We revisit our earlier account [1] of this rule to provide alternative account with greater degree of clarity of reasons. We note that $\Delta_{\text{vap}}H^{T_s}$ represents the energy required to move N particles from their collectively bound

liquid state to gaseous state having vanishingly small binding. This, can, therefore, be evaluated by using

$$P_{ex}\mathrm{V} = ZRT \tag{20.10}$$

with a fact that a simple fluid at its T_B behaves like an IG defined by (20.10) with $Z = 1$ and the same in its l-phase at a low boiling point such as $T_s = 0.58T_c$ can be defined by (20.10) with $Z^l = Z^l_{T_s} \approx 0$. Accordingly, we have

$$E^{IG}_{T_B} = \frac{3}{2}RT_B \quad \text{and} \quad E^l_{T_s} = \frac{3}{2}Z^l_{T_s}RT_s \approx 0, \tag{20.11}$$

and

$$\Delta_{\text{vap}}H^{T_s} = [E^{IG}_{T_B} - E^l_{T_s}] + \epsilon_s \tag{20.12}$$

where $E^{IG}_{T_B}$ and $E^l_{T_s}$ represent the thermal energy of particles assumed to, respectively, have IG state at T_B and l-state at T_s, while ϵ_s expressed as

$$\epsilon_s \approx \frac{3}{2}Nk_BT_s = \frac{3}{2}RT_s \tag{20.13}$$

represents the energy of inter-particle correlations present in the liquid phase. Using these relations with $T_B = 2.73T_c = 4.706T_s$, as concluded in [1], we easily have

$$\Delta_{\text{vap}}H^{T_s} = \frac{3}{2}RT_B - 0 + \frac{3}{2}RT_s = 7.05RT_s + 1.5RT_s = 8.55RT_s. \tag{20.14}$$

We also find $\Delta_{\text{vap}}H^{T_s}$ by using another alternative of these steps and the following relation which needs evaluation of $[\mathrm{V}_g/\mathrm{V}_l]$ representing the ratio of $N-$particle volumes in their g- and l-phases at $T = T_s$. Accordingly, we have

$$\Delta_{\text{vap}}H^{T_s} = (E^{IG}_{T_s} - E^l_{T_s}) + RT_s \ln\left[\frac{\mathrm{V}^{T_s}_g}{\mathrm{V}^{T_s}_l}\right] + \epsilon_s \tag{20.15}$$

which renders

$$\Delta_{\text{vap}}H^{T_s} = \left(\frac{3}{2}RT_s - 0\right) + RT_s \ln\left[\frac{\mathrm{V}^{T_s}_g}{\mathrm{V}^{T_s}_l}\right] + \frac{3}{2}RT_s = 1.5RT_s + 5.547RT_s + 1.5RT_s = 8.547RT_s. \tag{20.16}$$

since we easily have $\mathrm{V}^{T_s}_g/\mathrm{V}^{T_s}_l \approx 256.52$ by using: (i) $Z \approx 1.0$ and $P_{ex} = P_c/50$ [7] (for the gas at $T = T_s$), and (ii) $Z_c = 0.2962$, $P_{ex} = P_c$ and $\mathrm{V} = \mathrm{V}_c$ (for the gas at $T = T_c$) with $\mathrm{V}_l = \mathrm{V}_c/2.62$ (obtainable from ρ_l/ρ_c relation (*cf.*, (6.1)-of-[7]); one can also find $\mathrm{V}^{T_s}_g/\mathrm{V}^{T_s}_l \approx 256.52$ by using similar information for T_B in place of T_c.

The fact that $\Delta_{vap}H^{T_s} = 8.55RT_s$ (20.14 and 20.16) agrees closely with its experimental value $\approx 9RT_s$ observed for a large number of simple fluids [7], underlines the accuracy of our account of the Trouton rule in its modified statement.

20.2.3 IG Behaviour at T_B

In our earlier paper [1], we used a qualitative argument to identify the cause of IG behaviour of a RG at $T = T_B$ with the balance of forces originating from $V^R(r_{ij})$ and $V^A(r_{ij})$. Here we find how exactly a fluid sustains this balance. Using $B_2(T)$ ((Eqn. 20.6) reported in [1]) in the standard expression for Z, we have

$$Z = 1 + \frac{B_2(T)}{\mathrm{V}} = 1 + \frac{B\mathrm{V}_c}{\mathrm{V}}\left[1 - \frac{sT_c}{T}\right] = 1 + B\left[1 - \frac{sT_c}{T}\right]\frac{\rho}{\rho_c}. \tag{20.17}$$

with $B \approx 0.407$ and $s \approx 2.73$ as concluded in [1]. Combining this relation with (20.10) and using $\rho = N/\mathrm{V}$, we get

$$P_{ex} = k_BT\rho + B\frac{\rho}{\rho_c}\left[1 - \frac{sT_c}{T}\right]k_BT\rho = {P_{ex}}^{IG} + (P^R - P^A). \tag{20.18}$$

with

$${P_{ex}}^{IG} = k_BT\rho, \qquad P^R = B\frac{\rho}{\rho_c}[k_BT\rho] \qquad P^A = \frac{Bs\rho}{\rho_c}[k_BT_c\rho] \tag{20.19}$$

where P^R and P^A are expected to depend, respectively, on $V^R(r_{ij})$ and $V^A(r_{ij})$ [with superscripts R and A indicating repulsive and attractive parts of $V(r_{ij})$ through

$$B \propto \sum_j V^R(r_{ij})\ (= V^R) \qquad \text{and} \qquad s \propto \sum_j V^A(r_{ij})\ (= V^A), \tag{20.20}$$

Notably, as indicated by (20.19), P^R representing $V(r_{ij})$] through (equated normally to the *hard core* (HC) repulsion $V_{HC}(r)$) depends linearly on T and this agrees with what is noted in [3]. On the other hand, P^A representing $V^A(r_{ij})$ rightly remains constant for a given V. Naturally, with change in T, a RG kept in a container of fixed V is expected to have

$$P^R = P^A \tag{20.21}$$

at $T = T_B$ defined by

$$T_B = sT_c \approx 2.73T_c. \tag{20.22}$$

Analyzing this result in combination with (20.19), it becomes clear that, a *RG* (*independent of its* ρ) assumes $P^R = P^A$ only at $T_B \approx 2.73T_c$. However, this inference,

based on (20.17), does not include higher order terms (such as third, fourth, …) of the Virial series expansion written in terms of ρ as

$$P_{ex} = RT\rho[1 + B_2\rho + B_3\rho^2 + ...], \tag{20.23}$$

although these terms are not expected to be negligible since (20.23) assumes poor convergence with increasing ρ. We may now recast (20.18) for the effective KE ($E_N^{RG} = 3P_{ex}\mathrm{V}/2$) of the RG to find

$$E_N^{RG} = 1.5RT + V^R - V^A = N(1.5k_BT + v^R - v^A). \tag{20.24}$$

with

$$V^R = \frac{B\rho}{\rho_c}(1.5RT) \qquad \text{and} \qquad V^A = \frac{Bs\rho}{\rho_c}(1.5RT_c), \tag{20.25}$$

which are, respectively, related to $V^R(r_{ij})$ and $V(r_{ij})$ through B and s ((20.20). Using (20.22, 20.24 and 20.25), we have

$$V^R = V^A, \tag{20.26}$$

at $T = T_B$. Equation (20.26) not only shows that V^R, representing the $+ve$ energy of each particle at T_B, gets neutralized by V^A, representing its $-ve$ energy, but also demonstrates its similarity with (20.21) which represents a balance of repulsive and attractive forces, experienced by each particle in the fluid at T_B. Naturally, it underlines the need of re-analyzing the role of interparticle forces in determining Z (where $P_r = P_{ex}/P_c$ and $T_r = T/T_c$) as discussed in the following section.

20.3 Compressibility Factor Z

20.3.1 Relation with P_r, T_r and $V(r_{ij})$

Since P^R (20.19) and V^R (20.24) for a given ρ, depend linearly on T, and P^A and V^A remain independent of T, contributions of $V^R(r_{ij})$ and $V^A(r_{ij})$ to Z have to be evaluated from $\sum_j V^R(r_{ij})$ and $\sum_j V^A(r_{ij})$ as separate terms, not by using their sum, $\sum_j(V^R(r_{ij}) - V^A(r_{ij}))$ as a single term. This important fact helps in finding Z, - the most significant factor required to find different properties of a fluid under different physical conditions. To this effect, we recast our theoretical relation for Z (equation 20.27 of [1]) as

$$Z = \frac{Z_c\rho_c}{\rho}\frac{P_r}{T_r}, \tag{20.27}$$

obtained by using its basic definition

$$Z = \frac{\mathrm{V}^{RG}}{\mathrm{V}^{IG}}, \tag{20.28}$$

with V^{RG} and V^{IG} being the volumes of RG and IG obtained *under identical physical conditions*. Obviously, (20.27) can be used to find experimental Z of any RG by using the experimental values of its ρ, ρ_c, Z_c, P_c and T_c.

However, combining (20.10) and (20.24) and $P_{ex} = 2E_N^{RG}/3\mathrm{V}$, we find

$$Z = 1 + \frac{2(v^R - v^A)}{3k_B T} \quad \text{with} \quad v^R = V^R/N \text{ and } v^A = V^A/N \tag{20.29}$$

which relates Z with $V(r_{ij})$ through v^R and v^A without using any approximation, provided V^R and V^A are evaluated by using all possible interactions a particle has with other particles in the system. We now assume that

$$v^R \propto k_B T\rho \text{ or } v^R = (3C/2)k_B T\rho \quad \text{and} \quad v^A \propto k_B T_c\rho \text{ or } v^A = (3Ch/2)k_B T_c\rho, \tag{20.30}$$

where C and h are proportionality constants. The assumption follows from the fact that each particle keeps its neighbouring particles at a distance d through a repulsive force generated by its collisional motion whose energy depends on T, while v^A, responsible for the collective binding energy of a particle in the fluid, can be expressed in terms of $k_B T_c$. (20.29) and (20.30) render

$$Z = 1 + C\left(1 - \frac{hT_c}{T}\right)\rho = 1 + C\rho_c\left(1 - \frac{hT_c}{T}\right)\frac{\rho}{\rho_c} \tag{20.31}$$

which reveals the details of how Z depends on $V^R(r_{ij})$ and $V^A(r_{ij})$. The fact that (20.31) agrees exactly with (20.17) (with $B = C\rho_c$ and $s = h$) implies that 2nd term of Virial series expansion accounts for the entire contribution of two body central potential to Z, while 3rd, 4th, ... terms should explain the contribution of non-central potential and other factors. Since the basis of (20.31) lies with (20.30) which is corroborated by experiments [3, 7], it appears that the interparticle forces of different nature should be separated to evaluate their contributions for a better understanding of any fluid. To this effect, one may find that a comparative study of $Z_{\text{exp}}(P_r)$ (experimental $Z(P_r)$) and $Z_{\text{theo}}(P_r)$ (theoretical $Z(P_r)$) calculated by using (20.31) for a typical representative of simple fluids such as Argon fluid (as reported by Jain and Chutia [8]) provides reasonably satisfying correlations of ρ/ρ_c, C and h with interparticle attraction and repulsion. However, we note that (20.29) and (20.31) assume that the pressure equivalent of potential energy (PE) can be obtained by using 2(PE)/3V in a manner we find pressure due to kinetic energy (KE) by using 2(KE)/3V, although the former can be identified to have some problem for its exact validity because the nature PE differs that of KE. While KE depends on T, PE has involved dependence on V. Interestingly, good correlations can still be expected if the physical conditions of the system are such that PE contributions are smaller than those of KE. We address this point again in Sect. 20.3.3.

20.3.2 Analysis of the Basic Relation for Z at a Fixed T_r

To analyze Z from its basic expression (20.27) for a fixed T_r, we find that g-phase $Z(= Z_g)$ can be expressed as

$$Z_g = A\frac{P_r}{\rho_g^{T_r}} \qquad with \quad A = \frac{Z_c\rho_c}{T_r} \quad \text{a constant}, \tag{20.32}$$

Assuming that ρ_g changes with P_r through,

$$\rho_g^{T_r} = \eta(P_r)P_r, \tag{20.33}$$

we can write (20.32) as

$$Z_g = A\frac{P_r}{\eta(P_r)P_r} = A\frac{1}{\eta(P_r)} \tag{20.34}$$

Similarly, for the l-phase which shows very small deviation from its $P_r = 0$ density $(\rho_o^{T_r})$ under increased P_r, we have

$$\rho_l^{T_r} = \rho_o^{T_r} + \eta(P_r)P_r, \tag{20.35}$$

with $\rho_o^{T_r} >> \eta(P_r)P_r$ which renders

$$Z_l = A\frac{P_r}{\rho_l} = A\frac{P_r}{\rho_o^{T_r} + \eta(P_r)P_r} \tag{20.36}$$

To analyze the nature of $\eta(P_r)$ for both phases, we use experimentally observed P_r- dependence of Z_g and Z_l and note the following:

(i) Since (20.34) can agree with the experimental observation of decrease in Z_g with P_r falling below $P_r < P_r^*$ (identified as a pressure above which Z_g has a linear increase with P_r), if $\eta(P_r)$ is expressed as

$$\eta(P_r) = \eta_o + \eta_1 P_r \qquad with \quad \eta_o > \eta_1 P_r \tag{20.37}$$

where η_o and η_1 are two independent constants which can determined by fitting the experimentally observed Z_g in

$$Z_g = A\frac{1}{(\eta_o + \eta_1 P_r)} \approx \frac{A}{\eta_o}\left(1 - \frac{\eta_1}{\eta_o}P_r + ...\right). \tag{20.38}$$

If Z_g is observed to decrease with P_r faster than linear decrease (20.38), one can use (20.34) with

$$\eta(P_r) = \eta_o + \eta_1 P_r + \eta_2 P_r^2, \tag{20.39}$$

by considering $\eta_o > \eta_1 P_r > \eta_2 P_r^2$. This renders

$$Z_g \approx \frac{A}{\eta_o}\left(1 - \frac{\eta_1}{\eta_o}P_r - \frac{\eta_2}{\eta_o}P_r^2 + ...\right). \tag{20.40}$$

which agrees with experimentally observed Z_g indicating a linear decrease of Z_g if $P_r < 1$ and non-linear decrease in Z_g if $P_r \geq 1$.

(ii) The fact that Z_l (20.36) exhibits a linear increase with P_r, shows that $\eta(P_r)P_r$ in (20.35) is $<< \rho_l^{T_b}$ and we have

$$Z_l = A\frac{P_r}{\rho_o^{T_b}} \tag{20.41}$$

where T_b refers to the boiling point related to a given $T_r = T_b/T_c$. This relation not only explains the linear increase of Z_l, but also emphasizes that the l-phase represents a nearly incompressible fluid.

(iii) The linear increase of Z_g at higher $P_r (> P_r^*)$ can, obviously, be described by a relation similar to (20.41) which describes similar dependence of Z_l. Accordingly, we have

$$Z_g = A\frac{P_r}{\rho_o^{T_r}} \tag{20.42}$$

where $\rho_o^{T_r}$ can be identified, to a good approximation, as the minimum density for which the g-phase behaves like an incompressible fluid and starts showing a linear rise in Z with increase in P_r

This analysis clearly indicates that higher density g-phase and l-phase, having observable similarity in respect of their $Z(P_r)$, differ significantly from low-density g-phase. This explains why Virial series expansion for high ρ (independent of their gas/liquid state) has poor convergence and why should be careful in using any perception of a low-density gas in accounting for the properties of a liquid and high density gas.

20.3.3 Significance of $Z^{inv} = 1/Z$

We may now use

$$\mathrm{V}^{IG} = \frac{RT}{P_{ex}} \quad \text{and} \quad \mathrm{V}^{RG} = \frac{RT}{P_{ex} + P_{coh} - P_{corr}}, \tag{20.43}$$

with P_{corr} identified as the pressure representing repulsive interaction combined with the energy of relative motion which obviously depends on T, we have

$$Z^{\text{inv}} = \frac{\mathrm{V}^{IG}}{\mathrm{V}^{RG}} = \frac{P_{ex} + (P_{\text{coh}} - P_{\text{corr}})}{P_{ex}} = \frac{P_r + (P_{r/\text{coh}} - P_{r/\text{corr}})}{P_r} \tag{20.44}$$

with $P_{r/\text{coh}} = P_{\text{coh}}/P_c$ and $P_{r/\text{corr}} = P_{\text{corr}}/P_c$ and

$$\frac{P_{r/\text{coh}}}{P_r} = \frac{a'T_c\rho}{\rho_c} \quad \text{and} \quad \frac{P_{r/\text{corr}}}{P_r} = \frac{b'T\rho}{\rho_c}. \tag{20.45}$$

where a' and b' are proportionality constants which obviously depend, respectively, on average value of V_o and the parameters of repulsive part of $V(r_{ij})$. Followed from Eqs. (20.44) and (20.45), we have

$$Z^{\text{inv}} = 1 + (a'T_c - b'T)\frac{\rho}{\rho_c} \tag{20.46}$$

which renders

$$Z = \left[1 + (a'T_c - b'T)\frac{\rho}{\rho_c}\right]^{-1} = 1 - (a'T_c - b'T)\frac{\rho}{\rho_c} + (a'T_c - b'T)^2\frac{\rho^2}{\rho_c^2} + \ldots \tag{20.47}$$

This not only agrees with the well known fact that Z has a power series expansion in terms of ρ/ρ_c with each term having zero value at single $T = T_B$, but also underlines the accuracy of (20.46) for finding Z. Notably (20.47) should converge if the second term in [....] is < 1 and this is observed when the impact of interactions has only small deviations from the state of $Z = 1$ observed at $T = T_B$. This explains why (20.31) should be expected to have good agreement with experiments [8] if pressure equivalent of PE is much smaller than that of KE of the system, *viz.* for the fluid at $T \approx T_B$ or that of low density. Notably, this analysis identifies

$$[P_{ex} + P_{\text{coh}} - P_{\text{corr}}]\,\mathrm{V}^{RG} = RT, \tag{20.48}$$

as an EOS of a RG where P_{coh} and P_{corr} are directly linked to the parameters of $V^A(r_{ij})$ and $V^A(r_{ij})$ through a' and b' (20.45 and 20.46). It is obvious that the information useful for understanding the properties of any simple fluid would emerge if (20.46) is analyzed for a large number of simple fluids to find a' and b' as a function of P_r and T_r and a' and b' are found to be independent of a simple fluid in question. Naturally, this achievement will help in concluding the microscopic foundation of $P_{ex}\mathrm{V} = ZRT$. To this effect, one may find that this analysis finds (20.48) as an improved form of the EOS we concluded as equations (20.5) and (20.6) reported in [1]. We hope this point would have better clarity with our future studies related to the criticality of a fluid at $T < T_c$ and other aspects.

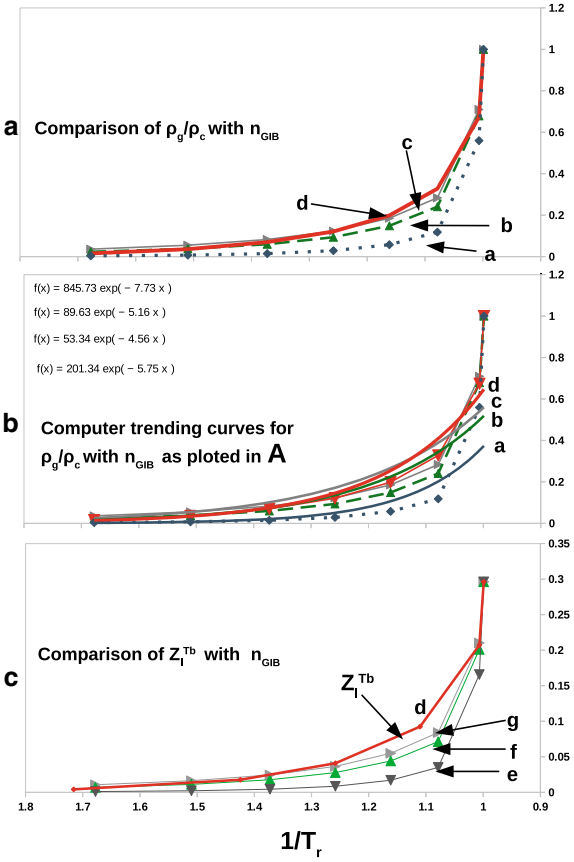

Fig. 20.1 **a** Plots of three different sets of n_{GIB}/Z_cN as function of $1/T_r$) for Ar fluid ((20.5.1) (Curve-**a**, **b** and **c**) and their comparison with experimental ρ_g/ρ_c (*cf.*, Curve-d) of Ar Fluid, **b** Comparison of trending curves as obtained through computer software [curves -**a**, **b**, **c** and **d** corresponding to similar curves ploted in (**a**), and **c** Comparison of three sets of $Z_l^{T_b}$ (Curves-**e**, **f**, and **g**) with experimental $Z_l^{T_b}$ (Curve **d** red colour) for Ar fluid. (For more details, See Text)

20.3.4 n_{GIB}, ρ_g/ρ_c, Z_l and Related Aspects

As concluded in Appendix 20.5, the l-phase has uncondensed higher energy gas like particles (identified as GIB particles) whose number n_{GIB} (20.5.1) decreases exponentially with decrease in T_r. Interestingly, since this dependence seems to match with T_r dependence of ρ_g/ρ_c and Z_l, we decided to examine its accuracy. To this effect, we used (20.5.1) and $V_o(T)^{\text{cal}}$ (calculated $V_o(T)$ for Argon (Ar) fluid [9]) to obtain three different sets of n_{GIB}/Z_cN for $V_o(T) = V_o(T)^{\text{cal}}$, $V_o(T) = 0.667V_o(T)^{\text{cal}}$ and $V_o(T) = 0.59V_o(T)^{\text{cal}}$.; $V_o(T)$ being depth of potential seen by a particle well below the GLI. We plot these sets of n_{GIB}/Z_cN in Fig.(20.1A) as Curves-**a**, **b** and **c** and compare them with a plot of ρ_g/ρ_c (Curve-**d**) for Ar fluid from [10]. This clearly indicates that $\rho_g/\rho_c(1/T_r)$ (Curve-**d**) agrees more closely with Curves-**b** and **c** and it is evident that interparticle forces seen by particles at the GLI really play an important

role in deciding the ρ_g/ρ_c of the g-phase coexisting with l-phase at different $T < T_c$ since only such particles are expected to have a $V_o(T)$ falling around $0.6V_o(T)^{\text{cal}}$.

Comparison of the trending curves (*cf.* Curves-**a**, **b** and **c** (Fig. 20.1b) representing the three sets of $n_{GIB}/Z_cN(1/T_r)$ with similar curve for $\rho_g/\rho_c(1/T_r)$ (*cf.*, Curve-**d**, Fig. 20.1b) also confirms that, to a good approximation, $\rho_g/\rho_c(1/T_r)$ matches more closely with Curves-**b** and **c** in comparison to Curve-**a**). These curves were obtained by using the computer software (LibreOffice Calc).

Changing (20.5.1) to get $Z_l = n_{GIB}/N$ of the liquid phase by using $Z_c = 0.2962$ [1], we plotted all the three sets of Z corresponding to $V_o(T)^{\text{cal}}$, $0.667V_o(T)^{\text{cal}}$ and $0.59V_o(T)^{\text{cal}}$ (*cf.*, Curves **e**, **f** and **g**, (Fig. 20.1(C)) to compare with experimental values of $Z_l^{T_b}$ (Curve **d**, Fig. 20.1C). Once again we find that $Z_l^{T_b}$ values are more close to Curves **f** and **g** in comparison to Curve **e**, Fig. 20.1c) and this underlines the role of surface particles at the GLI in controlling the criticality of a liquid for L2GT or G2LT. We plan to analyze these results at desired length in a separate paper.

20.4 Conclusion

Based on our theory [1], we conclude detailed microscopic account of Guldberg rule, Trouton rule, etc., and the ideal gas behaviour of a real gas at T_B. We reveal that vaporisation of liquid is a basic property of the gas-liquid interface and $Z^{\text{inv}} = 1/Z$ is more explicitly related to $V(r_{ij})$ though two simple terms are representing its repulsive and attractive components: $V^R(r_{ij})$ and $V^A(r_{ij})$. It is emphasized that the Z^{inv} should be used to find Z to have a better understanding of different properties of a simple fluid. We urge that large scale efforts are made by interested researchers to correlate Z^{inv} (20.46) with parameters of interparticle attraction and repulsion and quantities like V_o (depth of potential seen by a particle) for a large number of simple fluids. To this effect, one needs simple computer program [9] and relevant density data as reported for some systems in [10]. This will help in finding the links of a' and b' (20.46) (rendering Z values in agreement with experiments) with $V(r_{ij})$; notably unravelling these links stands as an important goal of a microscopic theory of simple fluids which focuses on the well known EOS, $PV = ZRT$. The facts that ρ_l (liquid phase density) matches closely with ρ_s (solid phase density) and Z_l for a given T_r has a linear increase with P_r, make it amply clear that a pure liquid state represents a macroscopically large molecule with solid like incompressible structure having vanishingly small shear forces which allow its particles to flow or shift from their positions by shifting other particles. However, a real state of liquid has a small fraction of particles in microscopic bubbles which not only weaken this macroscopic molecule, but also serve as a source of its critical break down at a boiling point. As a result, the liquid is transformed into gas with each particle moving as a free particle. In our next paper, we hope to report how the new form of the equation of state (20.48) would help in having a better description of a real gas.

Appendices

20.5 Microscopic Picture of Boiling Process and Its Implication

(1) The boiling process can be identified with the formation of bubbles, triggered by *uncondensed* gas particles of higher KE present in the liquid. These particles make what can be known as the *gas in bubbles* (GIB).

(2) The state of GIB can be identified with the state of the gas at $T = T_c$ for the simple reason that the latter remains in the gaseous state under every possible P_{ex} and, as concluded in [1], P_{coh} operating internally in the liquid is identical in its operations to P_{ex}. The use of, $P_{ex}\text{V} = ZNk_BT$ and $N^* = ZN$ as the number of particles which behave like free particles, for $T \leq T_c$ situations reveals that particles counting Z_cN (or a little less) make the gas phase and the remaining ones, $(1 - Z_c)N$ (or a little more) make the liquid phase when the two phases get separated on cooling the fluid to T_c^- (a T just below T_c). With $Z_c = 0.2962$ [1], it is clear that about 30% particles make gas phase, while about 70% particles make liquid phase just at T_c^-. However, the segregation of two phases at this T is not total; some microscopic liquid drops stay in the gas phase and some gas particles stay in the liquid phase as GIB. Assuming that number of GIB particles n_{GIB} at $T = T_c$ count Z_cN and they retain an average $\text{KE} = 1.5k_BT_c$ at all $T \leq T_c$, we easily have,

$$n_{GIB} = Z_cN \exp\left(-\frac{V_o(T) - V_o(T_c))}{k_BT}\right). \tag{20.5.1}$$

where $V_o(T)$ is the depth of potential seen by a GIB particle. Followed from (20.5.1), one may find that n_{GIB} changes exponentially with the change in T from a reasonably high value at Ts close to T_c to a negligibly small value at T_t.

(3) A bubble serves as a defect in the liquid structure and facilitates seeding of new bubbles and increase in n_{GIB} with rise in liquid T. The liquid structure loses its strength and reaches a state of its criticality for the onset of the *liquid to gas transition* (L2GT) at T_b^* and related $P_{ex} = P_{ex}^*$. The entire heat supplied to the liquid works for transforming its particles in to GIB particles which leave the *gas-liquid interface* (GLI) with bursting of bubbles and the liquid keeps boiling without any rise in T beyond T_b^*.

(4) Since the liquid assumes the state of non-critical equilibrium as soon as its T drops to T_b^{*-} (a T just below T_b), we focus on the mechanism which makes such a sharp change possible. It is obvious that n_{GIB} increases with rise in T and reverse

happens on its fall. Accordingly, a liquid at every T has a kind of dynamic equilibrium in which the rate of vaporisation (transformation liquid particles into gas) equals the rate of condensation (transformation of gas particles into liquid particles), while the former dominates the latter with the rise in T and reverse happens with a fall in T. This also means that heating accelerates the seeding of new bubbles and increase of n_{GIB} in existing bubbles but the cooling does the opposite.

(5) Surface tension (σ_s) of a liquid is one of the several parameters (e.g., T_r, P_r, $\rho_l - \rho_g$, *etc.*) which control the stability of a bubble and this can be noted from σ_s becoming zero when the liquid reaches at its boiling point. We note that σ_s is related to ϵ_{GLI} (*the average binding energy of a particle at the* GLI) which serves as the origin of a force (F_{cond}) which tries to condense gas particles and opposes the force (F_{evap}) which facilitates evaporation by bursting the bubble and allowing GIB particles escape the liquid through GLI. Notably, as F_{evap} is related to the average KE (ϵ_{GIB}) of GIB particles, we can have

$$F_{\text{cond}} \propto \epsilon_{GLI} \quad \text{or} \quad F_{\text{cond}} = \text{C}'\epsilon_{GLI} \tag{20.5.2}$$

and

$$F_{\text{evap}} \propto \epsilon_{GIB} \quad \text{or} \quad F_{\text{evap}} = \text{C}''\epsilon_{GIB} \tag{20.5.3}$$

These relations render

$$\frac{F_{\text{evap}}}{F_{\text{cond}}} = (1/\text{C})\frac{\epsilon_{GIB}}{\epsilon_{GLI}} \tag{20.5.4}$$

with $\text{C} = \text{C}'/\text{C}''$. Since $\epsilon_{GIB} = 3k_BT_c/2$ has a fixed value, this relation indicates that its comparison with ϵ_{GLI} can help us unravel some important aspects of evaporation, condensation, and criticality of a liquid such as T_b^1/T_c and T_t/T_c, etc., as shown in Sect. 20.2.1.

References

1. Y.S. Jain, Microscopic theory of simple fluids. J. Mol. Liq. **249**, 688–701 (2018). https://doi.org/10.1016/j.molliq.2017.11.010
2. Y.S. Jain, See different papers cited in [1]
3. J.L. Finney, L.V. Woodcock, Renaissance of Bernal's random close packing and hypercritical line in the theory of liquids. J. Phys.: Condens. Matter **26**, 463102 (2014) (19pp). https://doi.org/10.1088/0953-8984/26/46/463102
4. A. Parola, D. Pini, L. Reatto, Liquid-vapor transition from a microscopic theory: beyond the Maxwell construction. Phys. Rev. Lett. **100**, 165704 (2008). PhysRevLett.100.165704
5. C.M. Guldberg, Z. Phys. Chem. **5**, 374–380 (1890)
6. F. Trouton, On molecular latent heat. Phil. Mag. **18**, 54–57 (1984). https://doi.org/10.1080/14786448408627563
7. E.A. Guggenheim, The principle of corresponding states. J. Chem. Phys. **13**, 253–261 (1945). https://doi.org/10.1063/1.1724033

8. Y.S. Jain, S. Chutia, A comparative study of experimental and theoretical Z (compressibility factor) of argon as a typical representative of simple fluids, Chapter 1 of this book.
9. S. Chutia, Y.S. Jain, Calculation of the depth of potential ($V_o(T)$) and related aspects for fluid Argon (to be published)
10. H.M. Roder, Liquid densities of Oxygen, Nitrogen, Argon and Para-hydrogen, NBS Technical Note 361 (Revised) Metric Supplement—1974, US Department of Commerce/National Bureau of Standards. Cryogenics Division, Institute for Basic Standards, U S National Bureau of Standards Boulder, Colorado 80302

Chapter 21
Moisture Content Study of Soil Found in Sung Valley, Meghalaya

Jodie T. Ryngnga and B. M. Jyrwa

Abstract In this work, the moisture content of the clayey soil found in Sung Valley at West Jaiñtia Hills District in Meghalaya is studied. The soil samples from the valley are collected up to a depth of 10 feet from the surface and its moisture content is measured using the gravimetric method. From the measured data, it is observed that the moisture content from 0–10 feet varies from 20–48%. However, in the region of interest (7–8.5 feet), from where most of the soil is extracted for manufacturing process, the moisture content is 25–33%, the average of which is 29%. This observed moisture content influences the mechanical properties of the soil in the region.

21.1 Introduction

The soil moisture content is an integral part of the soil composition and exists in three forms viz., gravitational moisture, capillary moisture and hygroscopic moisture. Gravitational moisture is defined as the free moisture that moves through the soil due to the force of gravity. Normally, gravitational moisture drains out of the soil in 2–3 days after the rainfall. Capillary moisture is the moisture present in the micropores of the soil and is held within the soil due to cohesion and adhesion against the force of gravity. This moisture is responsible for all the physical, chemical and biological interactions between the soil and the environment. Hygroscopic moisture forms a very thin film around the surface of the soil particles. Since, it is not held in the pores of the soil, but is on the surface of these particles, it is very difficult to remove them due to the presence of strong forces of adhesion [1].

Soil moisture content information is needed for studies in various disciplines, such as hydrology, soil science, ecology, meteorology and agronomy [2]. Mechanical properties of the soil, namely, weight, consistency, viscosity, compatibility, cracking, swelling, shrinkage and density are dependent on the soil moisture content [3]. Soil moisture also influences the physical and chemical properties of the soil, such as

J. T. Ryngnga (✉) · B. M. Jyrwa
Department of Physics, North Eastern Hill University, Umshing, Shillong 793022, India

S. Sengupta et al. (eds.), *Selected Progresses in Modern Physics*, Springer Proceedings in Physics 265, https://doi.org/10.1007/978-981-16-5141-0_21

conductivity [3], radon and thoron concentration [4], dielectric property [5], qualitative and quantitative elemental composition of the soil [6]. It has been reported that the soil moisture content is also strongly related to soil strength which influences its mechanical resistance and bulk density [7, 8]. In those works, it is shown that with increase in soil moisture content, the mechanical resistance and bulk density of the soil decreases.

A number of techniques have been developed for measuring soil moisture content like alcohol burning method [9], neutron scattering method [10], remote sensing method [11] and dielectric techniques like time domain reflectometry, frequency domain reflectometry and capacitance detection [12, 13]. However, these techniques are quite intricate, expensive and sensitive. Alternatively, a conventional measuring method for determining the moisture content is the gravimetric method. Gravimetric method is technically non-destructive, incurs minimal error and requires simple instrumentation to measure the moisture content [14].

In this work, the variation of moisture content with depth for the clayey soil found in the Sung Valley of Meghalaya is studied using gravimetric method. Such characteristic study of the soil will enable us to establish the correlation between soil moisture content and the observed features of the soil for exploring useful applications.

21.2 Material and Methods

21.2.1 Study Area

The soil samples under study are collected from the Sung Valley. Sung Valley is located in West Jaiñtia Hills District of Meghalaya in India at 25°36' N of latitude and 92°07' E of longitude. It is also called the 'Rice bowl' of Meghalaya. The Sung Valley has an abundance of a unique type of blackish clayey soil that is predominantly found at a depth of 6–10 ft from the surface. This soil has been used for making potteries by the local tribe for household utilities and religious purposes since time immemorial. It is observed that the manufactured potteries are significantly heavy, sturdy and durable. Such physical feature of the potteries is attributed to the soil composition that influence the soil strength. In order to investigate the soil composition, a total of 20 samples are collected and its moisture content is investigated.

21.2.2 Sampling and Measurement

The soil samples are collected from the valley up to a depth of 10 feet from the surface at 1 feet interval during the month of January. After extracting the soil samples, they are packed in airtight containers to avoid atmospheric exposure. Each container is labelled with respect to its depth in feet. Soil moisture content is then measured

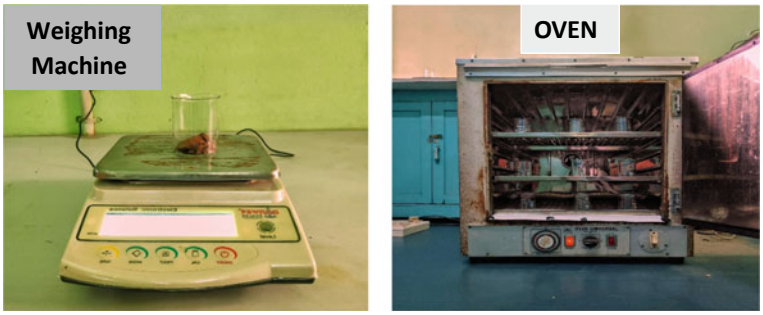

Fig. 21.1 Images of the experimental setup utilized for determining the percentage of soil moisture

using the gravimetric method. The gravimetric method incurs minimal instrumental error and offers accurate measurement as the possible sources of error can be readily checked by precise weighing of the samples. The method involves a series of steps to determine the moisture content. Firstly, each raw sample is weighed using an electronic weighing machine. Subsequently, the sample is dried in an oven at 105 °C for 24 h until the specimen has attained a constant weight which ensures that the water content from the soil is removed. The final mass of the dry soil is then recorded. Images of the experimental setup implemented for the study is shown in Fig. 21.1. The percentage of soil water content is evaluated by taking the ratio of the weight of the raw samples to the weight of the oven-dried sample multiplied by 100.

It is determined using the following formula [15]:

$$\text{Moisture Content } (\%) = \frac{Lossofmoisture(m_2 - m_1)g}{massofovendriedsample(m_3 - m_{1)}g} \times 100$$

where, m_1 = mass of the empty moisture can.
m_2 = mass of moisture can + moisture soil.
m_3 = mass of moisture can + oven-dry soil.

21.3 Results and Discussions

The measured experimental data of variation of soil moisture content in percentage with respect to soil depth is represented in Fig. 21.2. It is observed that the distribution of moisture content from 0–10 feet varies from 20–48%. In the depth of 7–8.5 feet, from where most of the soil is extracted by the locals for manufacturing process, the moisture content varies over 25–33% with an average value of 29%. The moisture content is lowest at 8.5 feet where its value is 25.6%.

It is widely reported that the moisture content of clayey soil ranges over 20–40% with an average of 30% [16]. On comparing this with the experimental results

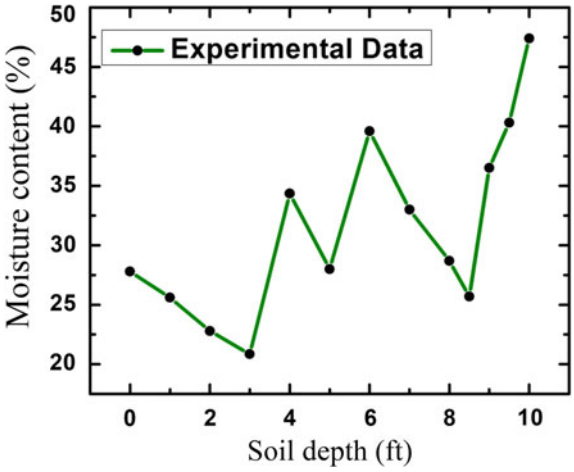

Fig. 21.2 Plot of variation of moisture content with soil depth

obtained for the soil in the region of interest, it is found that the moisture content is lesser than the world average moisture content of clayey soil. Thus, such moisture value has a definite impact on the hardness of the clayey soil that is observed to have considerable mechanical resistance. Consequently, it is inferred that the bulk density of the soil is significant due to its clayey nature and observed moisture content [17]. This influences the sturdiness and heaviness of the products manufactured using the clayey soil. Furthermore, the elemental composition of the soil is expected to vary with depth due to variation in moisture content.

References

1. S.U. Susha Lekshmi, D.N. Singh, M.S. Baghini, A critical review of soil moisture measurement. Meas. J. Int. Meas. Confed. **54**, 92 (2014)
2. I.A. Lunt, S.S. Hubbard, Y. Rubin, Soil moisture content estimation using ground-penetrating radar reflection data. J. Hydrol. **307**, 254 (2005)
3. H.-Y. Fang, J.L. Daniels, Introductory Geotechnical Engineering, Introd. Geotech. Eng. (2006)
4. K.P. Strong, D.M. Levins, Effect of moisture content on radon emanation from uranium ore and tailings. Health Phys. **42**, 27 (1982)
5. E.T. Selig, S. Mansukhani, Relationship of soil moisture to the dielectric property. ASCE J. Geotech. Eng. Div. **101**, 755 (1975)
6. C.L. Dyer, P.M. Kopittke, A.R. Sheldon, N.W. Menzies, Influence of soil moisture content on soil solution composition. Soil Sci. Soc. Am. J. **72**, 355 (2008)
7. J. Letey, *Relationship Between Soil Physical Properties and Crop Production*, vol. **1** (1958), pp. 277–294
8. C.J. Gerard, P. Sexton, G. Shaw, Physical factors influencing soil strength and root growth 1. Agron. J. **74**, 875 (1982)
9. X. Liang, F. Hu, Discussion on the application of alcohol combustion method in the determination of soil moisture content, in *IOP Conference Series: Earth and Environmental Science*, vol. 525 (IOP Publishing Ltd, 2020)

10. E.H. Waters, G.F. Moss, Estimation of moisture content by neutron scattering: effect of sample density and composition [4]. Nature
11. B.P. Mohanty, M.H. Cosh, V. Lakshmi, C. Montzka, Soil moisture remote sensing: state-of-the-science. Vadose Zone J. **16**, (2017). https://doi.org/10.2136/vzj2016.10.0105
12. B.F. Schwartz, M.E. Schreiber, T. Yan, Quantifying field-scale soil moisture using electrical resistivity imaging. J. Hydrol. **362**, 234 (2008)
13. O.H. Jacobsen, P. Schjønning, A laboratory calibration of time domain reflectometry for soil water measurement including effects of bulk density and texture. J. Hydrol. **151**, 147 (1993)
14. J.D. Cooper, *Gravimetric Method, in Soil Water Measurement,* (John Wiley & Sons, Ltd, 2016), pp. 26–42
15. S.K. Maiti, *Handbook of Methods in Environmental Studies*, vol. 2 (Air, noise, soil and over burden analysis) (2003)
16. M.J. Brandt, K.M. Johnson, A.J. Elphinston, D.D. Ratnayaka, Hydrology and surface supplies (2017)
17. C.W. Smith, M.A. Johnston, S. Lorentz, The effect of soil compaction and soil physical properties on the mechanical resistance of South African forestry soils. Geoderma **78**, 93 (1997)

Chapter 22
Neutrinoless Double Beta Decay in a Flavor Symmetric Scotogenic Model

Lavina Sarma, Bichitra Bijay Boruah, and Mrinal Kumar Das

Abstract We have studied the scotogenic model proposed by Ernest Ma, wherein the Standard Model is extended by three singlet right-handed neutrinos and a scalar doublet. This model proposes that the light neutrinos acquire a non-zero mass at a one-loop level. We have done a $A_4 \times Z_4$ realization of the scotogenic model in this framework. This model results in the production of non-zero θ_{13} by the assumption of a non-degeneracy in the right-handed neutrino masses. We have further studied the $0\nu\beta\beta$ in the model by the consideration of constraints from neutrino oscillation data and KamLAND-Zen limit.

22.1 Scotogenic Model

Scotogenic model is an extension of the inert Higgs doublet model (IHDM), and the IHDM is nothing but a minimal extension of the SM by a Higgs field which is a doublet under $SU(2)_L$ gauge symmetry with hypercharge $Y = 1$ and a built-in discrete Z_2 symmetry. In this model, three neutral singlet fermions N_i with $i = 1, 2, 3$ are added in order to generate neutrino masses and assign them with a discrete Z_2 symmetry. Here, N_i is odd under Z_2 symmetry, whereas the SM fields remain Z_2 even +[1, 2]. Symbolic transformation of the particles under Z_2 symmetry is given by

$$N_i \longrightarrow -N_i, \ \eta \longrightarrow -\eta, \ \Phi \longrightarrow \Phi, \ \Psi \longrightarrow \Psi, \tag{22.1}$$

where η is the inert Higgs doublet, Φ is the SM Higgs doublet and Ψ denotes the SM fermions.

We have no Dirac mass term with ν and N_i, however, a similar Yukawa-like coupling involving η is allowed. Nevertheless, the scalar cannot get a VEV. The neutrino mass can be generated through a one-loop mechanism, which is based on the exchange of η particle and a heavy neutrino. The Lagrangian involving the newly added field is

L. Sarma (✉) · B. B. Boruah · M. K. Das
Tezpur University, Tezpur 784028, Assam, India
e-mail: lavina@tezu.ernet.in

S. Sengupta et al. (eds.), *Selected Progresses in Modern Physics*, Springer Proceedings in Physics 265, https://doi.org/10.1007/978-981-16-5141-0_22

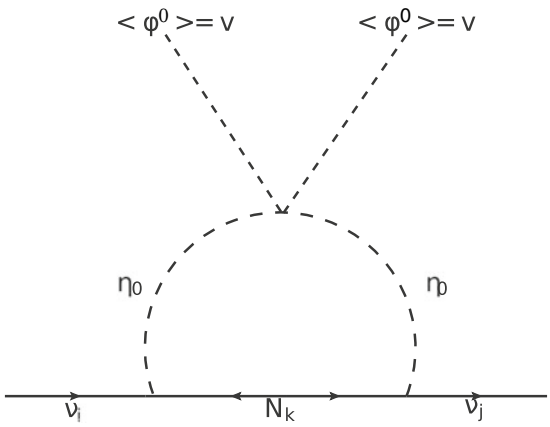

Fig. 22.1 One-loop contribution of neutrino mass generation with the exchange of right-handed neutrino N_i and the scalar η_0

$$\mathcal{L} \supset \frac{1}{2}(M_N)_{ij} N_i N_j + Y_{ij} \bar{L} \tilde{\eta} N_j + h.c \tag{22.2}$$

where the first term is the Majorana mass term for the neutrino singlet and the second term is the Yukawa interactions of the lepton. The new potential on addition of the new inert scalar doublet is

$$V_{\text{Scalar}} = m_1^2 \Phi^+ \Phi + m_2^2 \eta^+ \eta + \frac{1}{2}\lambda_1 (\Phi^+ \Phi)^2 + \frac{1}{2}\lambda_2 (\eta^+ \eta)^2 + \lambda_3 (\Phi^+ \Phi)(\eta^+ \eta) + \lambda_4 (\Phi^+ \eta)(\eta^+ \Phi) + \frac{1}{2}\lambda_5 [(\Phi^+ \eta)^2 + h.c.]. \tag{22.3}$$

The neutrino mass matrix arising from the radiative mass model is given by

$$M_{ij}^{\nu} = \sum_k \frac{Y_{ik} Y_{jk}}{16\pi^2} M_{N_k} \left[\frac{m_{\eta_R^0}^2}{m_{\eta_R^0}^2 - M_{N_k}^2} \, ln \frac{m_{\eta_R^0}^2}{M_{N_k}^2} - \frac{m_{\eta_I^0}^2}{m_{\eta_I^0}^2 - M_{N_k}} \, ln \frac{m_{\eta_I^0}^2}{M_{N_k}} \right] \tag{22.4}$$

where M_k represents the mass eigenvalue of the mass eigenstate N_k of the neutral singlet fermion N_k in the internal line with indices j=1,2,3 running over the three neutrino generation with three copies of N_k and Y is the Yukawa coupling matrix.

22.2 Flavor Symmetric Scotogenic Model

We have done a $A_4 \times Z_4$ [3, 4] realization of the scotogenic model in this work so as to incorporate various phenomenologies. We have basically studied the neutrino mass generation and neutrinoless double beta decay within this model. Thereby,

making it viable for ongoing as well as future sensitivity experiments. The charged leptonic Lagrangian is given by [6]

$$\mathcal{L}_l = \frac{y_e}{\Lambda}(\bar{l_L}\phi\chi_T)l_{R_1} + \frac{y_\mu}{\Lambda}(\bar{l_L}\phi\chi_T)l_{R_2} + \frac{y_\tau}{\Lambda}(\bar{l_L}\phi\chi_T)l_{R_3}. \tag{22.5}$$

Here, y_e, y_μ and y_τ are the coupling constants and Λ is the cut-off scale. The effective Lagrangian for the Dirac mass term is as follows:

$$\mathcal{L}_D = \frac{\eta}{\Lambda}[Y^{'} l_{L_i} N_i \chi_S + Y^{''} l_{L_i} N_i \chi]. \tag{22.6}$$

We also have the additional right-handed neutral fermions which are expressed by the Lagrangian:

$$\mathcal{L}_{\mathcal{M}_\mathcal{N}} = Y_N \omega N_i N_j \tag{22.7}$$

where i, j = 1,2,3 are the indices running over the three generations of neutrinos. Now, with the consideration of the vev allignment of the flavons such as $< \chi_T >= v_T(1,0,0), < \chi_S >= v_S(1,1,1), < \chi >= \mathrm{u}$ and $< \omega >= \mathrm{v}$, we have the charged leptonic mass matrix (M_l), Yukawa coupling matrix (Y) and RHN mass matrix (M_N) as follows:

$$M_l = \frac{v_T < \phi >}{\Lambda} \begin{pmatrix} y_e & 0 & 0 \\ 0 & y_\mu & 0 \\ 0 & 0 & y_\tau \end{pmatrix} \tag{22.8}$$

$$Y = \begin{pmatrix} 2a+b & -a & -a \\ -a & 2a & b-a \\ -a & b-a & 2a \end{pmatrix} \tag{22.9}$$

$$M_N = \begin{pmatrix} M & 0 & 0 \\ 0 & 0 & M \\ 0 & M & 0 \end{pmatrix} \tag{22.10}$$

where $a = Y^{'}\frac{v_S}{\Lambda}$ and $b = Y^{''}\frac{u}{\Lambda}$ are the model parameters and $M = Y_N \mathrm{v}$ is the degenerate RHN mass. Now, in order to make the RHN mass matrix a diagonal one, we need to go to a different basis. Thus, this change in basis further imposes a change in the Yukawa coupling matrix which now takes the form:

$$Y = \begin{pmatrix} -a & -a & 2a+b \\ b-a & 2a & -a \\ 2a & b-a & -a \end{pmatrix}. \tag{22.11}$$

Within this model, a loop contribution factor $\mathrm{r_i}$ is addressed via the relation $r_i \propto \frac{1}{M_{N_i}}$[3]. Thus, the final neutrino mass matrix obtained by the above considerations turns out to be a $\mu - \tau$ symmetric one. In order to break the $\mu - \tau$ symmetry without

introducing any extra flavon or perturbation, we require to assume the condition $r_1 \neq r_2 \neq r_3$. This further results in the non-degeneracy of the RHN masses. Therefore, we arrive at a neutrino mass matrix of the form:

$$M_\nu = \begin{pmatrix} m_{11} & m_{12} & m_{13} \\ m_{12} & m_{22} & m_{23} \\ m_{13} & m_{23} & m_{33} \end{pmatrix}. \tag{22.12}$$

22.3 Analysis and Results

We finally solve the model parameters using the UPMNS matrix, further generating the Yukawa coupling matrix. With the help of the coupling matrix, we obtain the active neutrino mass matrix which can be further implemented to calculate the effective mass of the neutrinos. A significant technique to measure the effective mass of the neutrinos is the $0\nu\beta\beta$. We measure the effective neutrino mass $|m_{\beta\beta}|$ expressed by the formula,

$$m_{fifi}| = \sum_{k=1}^{3} m_k U_{ek}^2 \tag{22.13}$$

where U_{ek}^2 are the elements of the neutrino mixing matrix with k holding up the generation index. The above expression can be further expressed as

$$|m_{\beta\beta}| = |m_1 U_{ee}^2 + m_2 U_{e\nu}^2 + m_3 U_{e\tau}^2|. \tag{22.14}$$

Some of the important experiments in relation to the measurement of the effective mass are KamLAND-Zen, KATRIN, GERDA, etc. We use the constraint coming from the KamLAND-Zen [5] experiment which sets an upper limit on the effective mass to be $m_{\beta\beta} < 0.11$ eV. From Fig. 22.2, we can say that the effective mass of active neutrinos that we have obtained abides by the upper limit given by the KamLAND-Zen experiment for both NH and IH. Also, it is seen that the lightest neutrino mass is of sub eV which further implies the summation of the neutrinos to obey the Planck limit, viz., $\sum_{k=1,2,3} m_k < 0.11$ eV. As we have numerically solved the model parameters, we show a contour plot depicting a co-relation between them w.r.t the effective mass of the neutrinos. Thus, from Fig. 22.3, it can be concluded that almost the entire range of model parameters falls in the allowed region for both NH and IH.

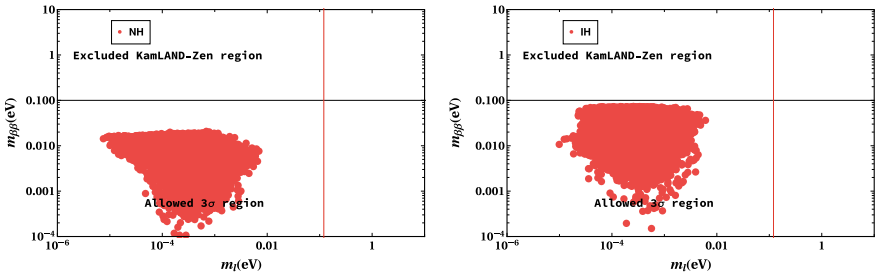

Fig. 22.2 Lightest active neutrino mass as a function of effective mass ($m_{\beta\beta}$) for NH/IH. The horizontal (black) line depicts the upper bound on the effective mass ($m_{\beta\beta}(eV) \sim 0.1(eV)$) of light neutrinos obtained from KamLAND-Zen experiment

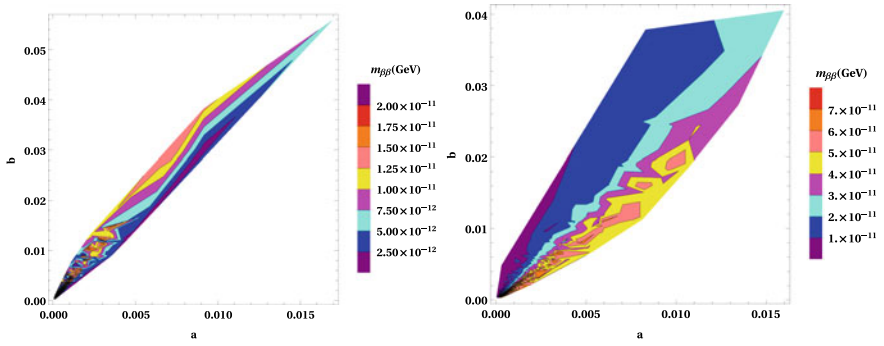

Fig. 22.3 Contour plot showing variation between the model parameters a and b w.r.t. the effective mass of neutrinos. The left panel is for NH and the right one is for IH

22.4 Conclusion

In this work, we have shown an assumption on how we can break the $\mu - \tau$ symmetry without the consideration of extra flavons. This further helps in taking a non-degenerate RHN masses, which can be also used to study low-scale vanilla leptogenesis in the scotogenic model. However, we have limited our analysis to neutrinoless double beta decay in our flavor symmetric scotogenic model. Along with it, we have also constrained the model parameters w.r.t. the effective neutrino mass. From Figs. 22.2 and 22.3, it can be firmly concluded that the model is viable in light of the experiments undertaken to measure the effective neutrino mass. Also, it is in agreement with the ongoing as well as future sensitivity of various experiments.

References

1. E. Ma, Verifiable radiative seesaw mechanism of neutrino mass and dark matter. Phys. Rev. D **73**, 077301 (2006). https://doi.org/10.1103/PhysRevD.73.077301
2. D. Borah, P.S.B. Dev, A. Kumar, TeV scale leptogenesis, inflaton dark matter and neutrino mass in a scotogenic model. Phys. Rev. D **99**, 055012 (2019). https://doi.org/10.1103/PhysRevD.99.055012
3. S. Pramanick, Scotogenic S_3 symmetric generation of realistic neutrino mixing. Phys. Rev. D **100**, 9 (2019). https://doi.org/10.1103/PhysRevD.100.035009
4. K.S. Babu, S. Pakvasa, Neutrino Masses and Family Symmetry. Phys. Lett. B **172**, 360–362 (1986). https://doi.org/10.1016/0370-2693(86)90270-4
5. A. Li, A Bayesian approach to neutrinoless double beta decay analysis in KamLAND-Zen. J. Phys. Conf. Ser. **1468** (2020). https://doi.org/10.1088/1742-6596/1468/1/012201
6. B.B. Boruah, L. Sarma, K.M. Das, Lepton flavor violation and leptogenesis in discrete flavor symmetric scotogenic model (2021). arXiv:2103.05295

Chapter 23
Novel Design of Multi-Band Double U Slotted Microstrip Patch Antenna with DGS for Satellite and Radar Applications

P. Arockia Michael Mercy and K. S. Joseph Wilson

Abstract A compact multi-band double U slotted microstrip patch antenna is sketched and investigated to accomplish X-band satellite applications like military, weather monitoring, etc., fixed-satellite service in Ku-band and K-band radar applications. The suggested antenna configuration is made up of a reduced novel double U-shaped slot having two triangular-shaped slots and four rectangular slots cutting in the bottom of the patch with defected ground structure (DGS) for achieving size reduction, high radiation efficiency, bandwidth enhancement, and multi-bands. It resonates at 8.6935, 12.53, 15.70, 18.41, and 19.02 GHz with enhanced bandwidths of 0.6 GHz (9.6453–10.1048 GHz), 1.055 GHz (9.8789–9.6252 GHz), 1.7336 GHz (10.0206–10.0880 GHz), 2.412 GHz (9.9892–10.3217 GHz), a gain of 3, 4.86, 5.3, 5.87 and 5.81 dB, and radiation efficiency of 93, 83, 82, 89, and 84%, respectively. This efficiently designed antenna is most suitable for the X-band range of 8–12 GHz, the Ku-band range of 12–18 GHz, and the K-band range of 18–27 GHz applications.

23.1 Introduction

The extensive manipulation of wireless communication systems is becoming greater in the time-being extraverted day-to-day life. The execution of lightweight, economical, low-posture antennas that is extremely fused with other communication systems is immensely necessary [1, 2]. Multi-band resonant frequency microstrip antennas have grown as a potent aspirant to the current and imminent Ku-band satellite communication devices caused by the escalation of feasible implementations emerging in a unique device and space restrictions [3]. For the effect in the dual and multi-band application, microstrip patch antennas [MPAs] are configured and achieved the successive benefits of inexpensive, lightweight, and facile investiture. It is deliberated by a partial ground structure to obtain indispensable radiation parameters and hence to bring down the microstrip patch cross-polarized radiation [4]. Many research

P. A. M. Mercy (✉) · K. S. J. Wilson
PG & Research Department of Physics, Arul Anandar College, Karumathur, Madurai 625514, India

S. Sengupta et al. (eds.), *Selected Progresses in Modern Physics*, Springer Proceedings in Physics 265, https://doi.org/10.1007/978-981-16-5141-0_23

have been carried out in each career, both as a manufacturing and as an educational related with ultra-wideband [UWB] devices. The probable merits of UWB devices are considerably portable, small potential consumption, powerless spectral density, enhanced radiation power, the rapid data communication rate, and economical and broadband frequency [5].

Mostly, a significant defect correlated with the natural microstrip antennas is a single band with narrow bandwidth, which is being with them [6]. For attenuating the deficiency of microstrip antenna overall of studies have been done by configuring it to function for a multi-band extending the operating bandwidth. A quite number of researchers have taken notice of this objective on the growth of antennas that put forward over and above a resonant frequency in keeping with the implementation essential upon a sole unit. Several techniques comprise of loading shorting wall or shoring pin at various placements [7], establishing stub [8, 9], interposing parasitic constituent further in radiating element or ground structure [10, 11], manufacturing additional film as superimposed [12], making use of metamaterials [13] are exhibited. The accomplishment of an antenna is upgraded by the introduction of the different slots upon the patch, thereby compositing a radiating surface. It is crucial to make a mindful resolution to snip off of slots and cuts on the patch [14]. Furthermore, several researchers recommended the slot making of diverse dimensions, constitution, form, and configuration upon the radiating component to bring in additional operating resonant frequency ranges [15]. Although the foresaid microstrip patch antennas [MPAs] further be the owner of an intricate configuration or compound cuttings above the patch. Also, some outline occurrences require a haphazard measurable form for the patch as well as for the slot cuttings. Consequently, the configuration and manufacture technique of the antennas turn out most troublesome even it may be in some cases. Furthermore, in accordance with the design intricacies and substrate materials utilized, the MPAs besides might be in possession of noticeably further down gain, insufficient bandwidth, deficient of more than one band operation also expensive. In this work, to overcome some demerits of the above consideration and analysis, to enhance the radiation efficiency and hence to broaden up the application band range, double U slotted with triangular, rectangular slot microstrip patch antenna is designed with the partial ground which causes size reduction and multi-band frequencies. So this configuration is feasible for Direct Broadcasting Satellite systems, Global Positioning System, and several mobile applications [16, 18].

23.2 Antenna Layout and Configuration

The conception of printed circuit technology is the greatest achievement of the MPA in the late twentieth century. Ordinarily, most of the antenna's patch takes square shape, rectangular shape, dipole shape, triangular shape, elliptical shape, or circular shape. Here, we consider a rectangular microstrip patch for our analysis and it is shown in Fig. 23.1. It is known that the attainable dielectric constants for the substrate are $2.2 \leq \varepsilon r \geq 12$. The thickness of substrates presumes a crucial role in

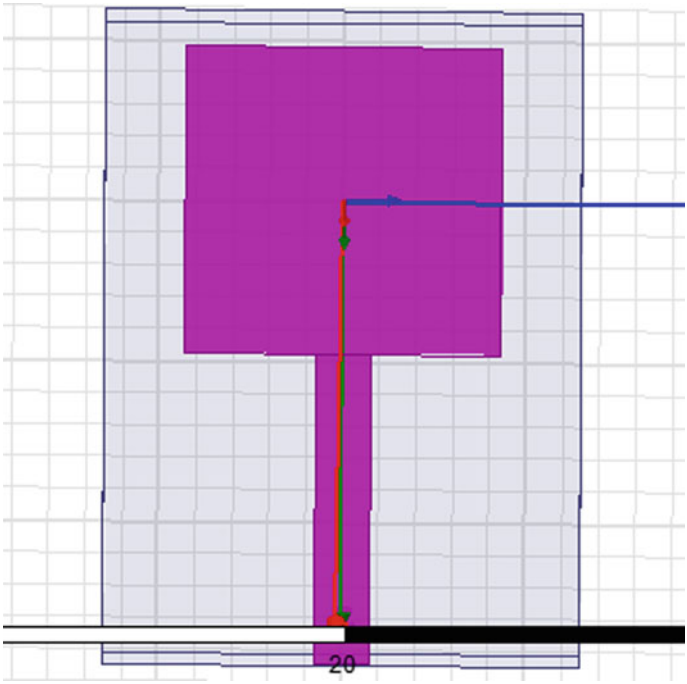

Fig. 23.1 Proposed rectangular microstrip patch

MPA that imputes at the range of $0.03 \leq L \geq 0.05$ cm utilized as a ground structure [17]. Appropriate substrate conformation and working frequency are the foremost aspects in constructing the microstrip antenna. In this work, a frequency of 8.5 GHz is preferred as the working frequency, which is in the X-band region [18].

The proposed antenna's patch takes the form of a rectangule mounted on the commercially cheapest dielectric material FR4 as a substrate which holds ε_r=4.4 having dimensions of 40 × 26 mm. The feed line is being in possession of 3 mm width and 19.2 mm length. The feed-line is situated in the midpoint of the patch. Size reduction may be an essential demand in the communication field. So the double U slots with two triangular slots and four rectangular slots are embedded in the patch to minimize the return loss and hence to maximize the radiation efficiency and for size reduction. The compact microstrip antenna with slots and its final configuration are shown in Figs. 23.2 and 23.3.

The defective ground structure is utilized because it aids to obtain broadband for the preferred resonant frequency as suggested by a few investigators [19, 20]. A defected ground plane of length Lg=12.12 mm and Wg=19.27 mm is configured on the backside of the substrate for achieving multi-band characteristics. It brings down the surface currents and makes the antenna resonate at multi-bands. This creation of partial ground may influence the matching of input impedance by the interchange of capacitance and inductance and hence the endmost determination

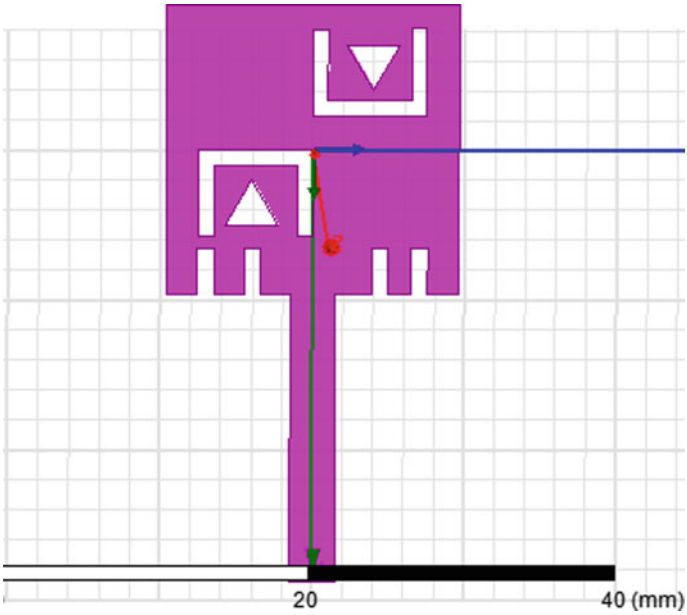

Fig. 23.2 Proposed antenna with slots

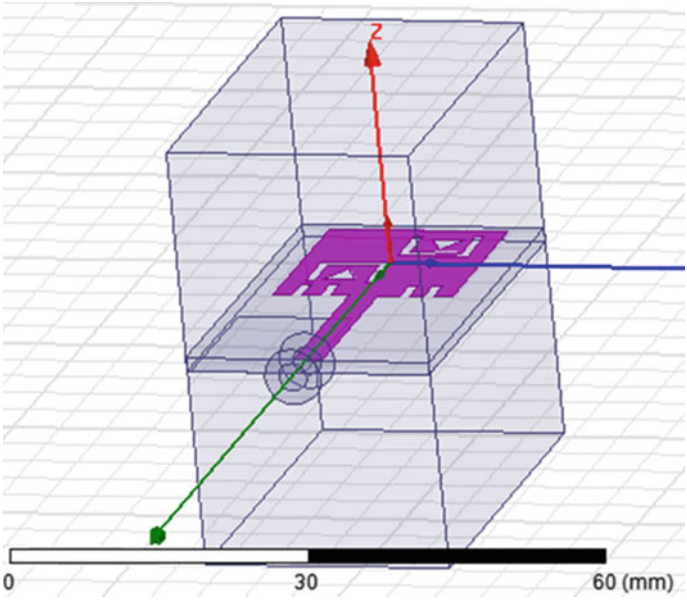

Fig. 23.3 Proposed antenna structure

may be connected with the bandwidth. It is beneficial to extend the normal working band by synchronizing those variables. The simulation was performed by HFSS Software 13.0.

The configuration of the antenna with partial ground is demonstrated in Fig. 23.4.

The optimized measurements of the recommended antenna are displayed below in Table 23.1.

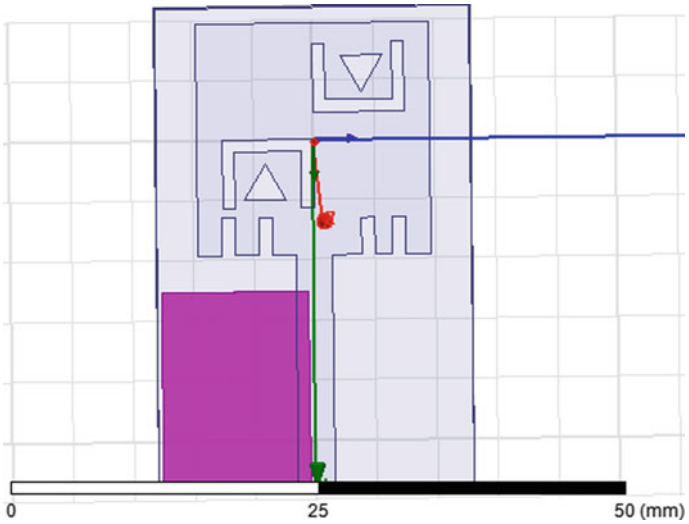

Fig. 23.4 The proposed antenna with partial ground

Table. 23.1: Geometry of recommended MPA

S. No.	Parameters	Measurements (mm)
1	Substrate length($L_{s)}$	40
2	Substrate width($W_{s)}$	26
3	Patch length ($L_{p)}$	19.3
4	Patch width ($W_{p)}$	19.27
5	Ground length($L_{g)}$	16.2
6	Ground width ($W_{g)}$	12.12
7	Substrate height H	1.43
8	Feedline width ($W_{f)}$	3
9	Feedline length ($L_{f)}$	19.2

23.3 Result and Discussions

The recommended MPA's characteristics are analyzed and simulated by the HFSS 13.0 Software. The S_{11} parameter, VSWR, gain, directivity, radiation efficiency, and radiation pattern are analyzed for the designed MPA. The simulation is carried out at the frequency range of 5–20 GHz because this range covers the X-band, Ku-band, and K-band applications specified by IEEE**.**

23.3.1 S_{11} of the Recommended Antenna

The correlation among the input and output ports of an electrical system is described by S11. The determination of characteristics with reference to impedance match between the transmission and the receiving end is computed by the S_{11} parameter. Figure 23.5 exhibits simulated reflection coefficient (S11) characteristics of the currently designed MPA. S11 has to be below −10 dB. The maximum negative values of S_{11} parameter is realized by the recommended design are −22.34, −32.94, −25.49, −20.43, and −20 dB at the achieved five resonant frequencies of 8.69, 12.53, 15.70, 18.41, and 19.02 GHz, respectively. The corresponding moderate bandwidths are predicted as 610MHz (9.3125–10.1048GHz), 1.055GHz (9.8789–9.6252GHz), 1.733GHz(10.0206–10.0880 GHz), and 2.412 GHz(9.9892–10.3217 GHz), respectively.

23.3.2 VSWR of the Proposed Antenna

The defensible value of VSWR is less than two. Figure 23.6 exhibits the VSWR of the recommended MPA. In this simulation work, we obtained the best results of

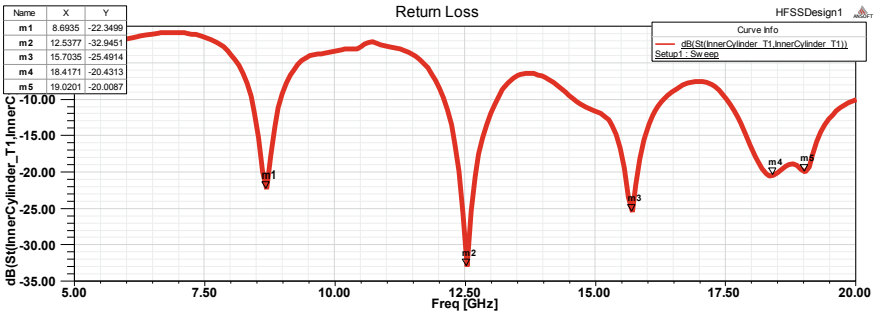

Fig. 23.5 S_{11} Parameter of recommended MPA

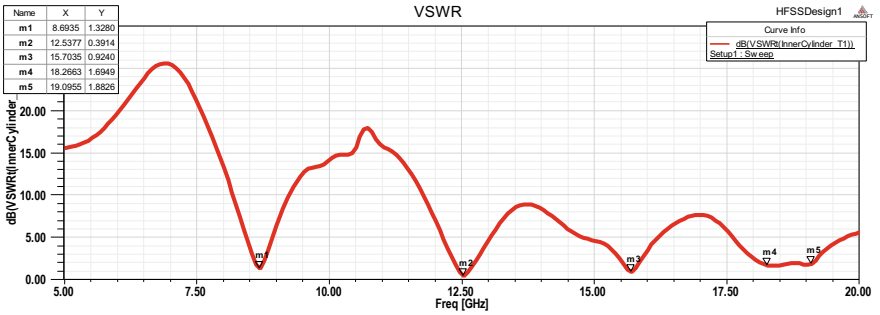

Fig. 23.6 VSWR of recommended MPA

VSWR which are 1.32, 0.39, 0.92, 1.69, and 1.88 at the resonant frequencies of 8.69, 12.53, 15.70, 18.26, and 1.88 GHz, respectively.

23.3.3 Gain of the Proposed Antenna

The amount of power transmission in the direction to an isotropic region is indicated by the parameter of gain. The gain curves for various resonant frequencies are shown in Fig. 23.7 a–e. The proposed microstrip antenna achieves the gain of 3, 4.86, 5.30, 5.87, and 5.81 dB at the frequency range of 8.69, 12.53, 15.70, 18.41, and 19.02 GHz, respectively.

23.3.4 Directivity of the Proposed Antenna

The directivity curves at diverse resonant frequencies are illustrated from Fig 23.8a–e. The recommended MPA achieves the better directivity of 3.23, 5.82, 6.42, 6.53, and 6.89 dB at the obtained resonant frequencies of 8.69, 12.53, 15.70, 18.41, and 19.02 GHz, respectively.

23.3.5 Radiation Pattern of the Recommended MPA

The radiation pattern is one of the antenna character criteria that specifies the directionality of the power radiation toward the antenna. Figure 23.9a–e exhibits the radiation pattern of the recommended MPA.

In order to validate the characteristics of the suggested MPA, two triangular slots inside the double U slots and four rectangular slots are engraved on the patch with the partial ground and are analyzed using HFSS Software 13.0. From Table. 23.2,

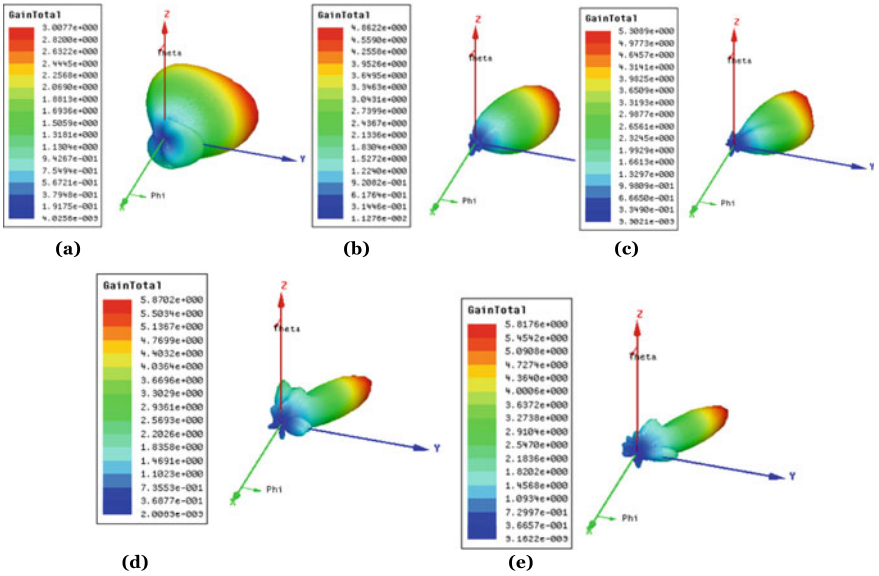

Fig. 23.7 Gain curve of the proposed MPA, (a) at 8.69 GHz, (b) at 12.53 GHz, (c) at 15.70 GHz, (d) at 18.41 GHz, and (e) at 19.02 GHz

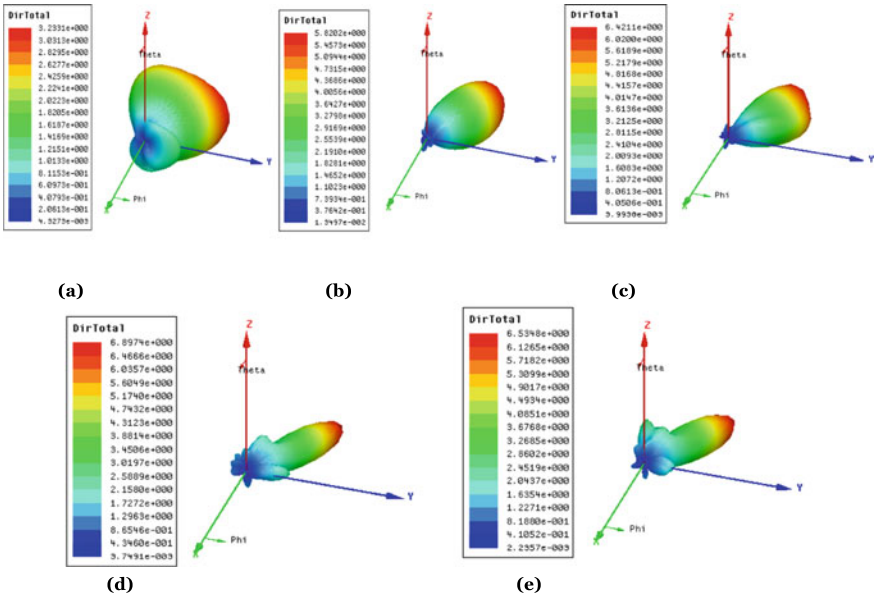

Fig. 23.8 Directivity curve of the proposed MPA, (a) at 8.69 GHz, (b) at 12.53 GHz, (c) at 15.70 GHz, (d) at 18.41 GHz, and (e) at 19.02 GHz

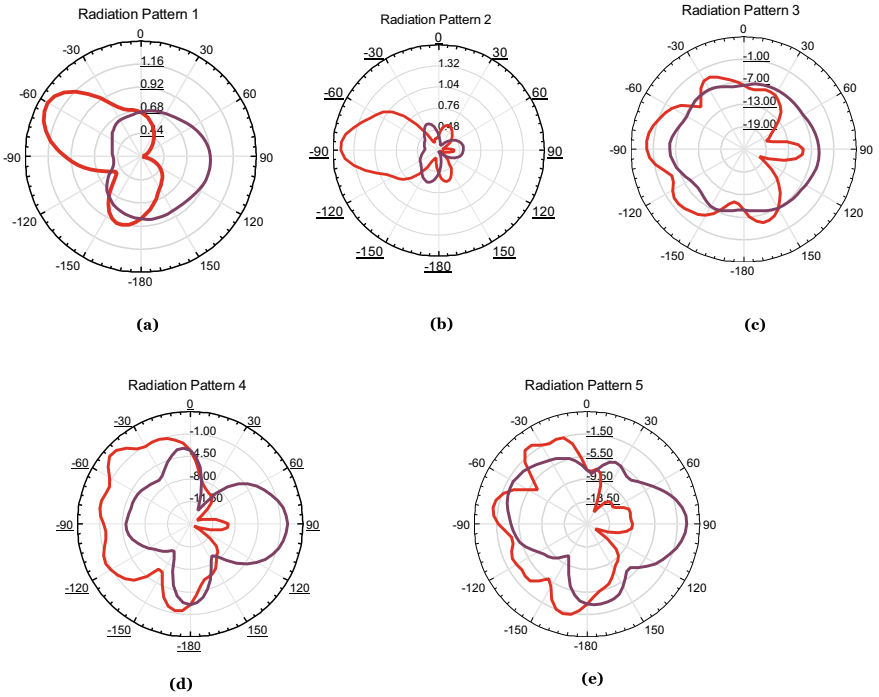

Fig. 23.9 Radiation of the proposed MPA, (a) at 8.69 GHz, (b) at 12.53 GHz, (c) at 15.70 GHz, (d) at 18.41 GHz, and (e) at 19.02 GHz

Table. 23.2 Performance of suggested microstrip patch antenna

S. No.	F_r(GHz)	S_{11}(dB)	Gain (dB)	Directivity (dB)	Bandwidth (GHz)	RE (%)
1	8.69	−22.34	3	3.23	0.61	93
2	12.53	−32.94	4.86	5.82		83
3	15.70	−25.49	5.30	6.42	1.05	82
4	18.41	−20.43	5.87	6.53	1.733	89
5	19.02	−20	5.81	6.89	2.412	84

we come to know that the performance of the proposed antenna has achieved multi-band frequencies, better gain performance, higher radiation efficiency, enhanced bandwidth, and lesser reflection coefficient over an operating band of 5 GHz–20GH. This novel design covers the application range of X-band, Ku-band, and K-band with five resonant frequencies of 8.69, 12.53, 15.70, 18.41, and 19.02 GHz having the highest gain of 5.81 dB at 19.02 GHz, enhanced radiation efficiency of 93% which is recorded at 8.69 GHz, better bandwidth of 2.412 GHz that is suitable for the applications of radar altimeter, security and military systems, and other modern wireless communication.

23.4 Conclusion

The research article emphasizes a treaty double U-shaped MPA for X-band, Ku-band, and K-band radar and satellite applications with high radiation efficiency, low return loss, enhanced bandwidth, and better gain as well as for size and cost reduction. By the introduction of double U slots, with two triangular slots inside the double U slots and four rectangular slots on the bottom of the patch, the ultra-wideband proficiency is executed in our design, and also the multi-band characteristics are attained by using partial ground mounted on the back of the substrate. Final results confirm that utilizing slots upon the patch and making defects above the ground structure are crucial factors to increase the radiation efficiency, enhance the bandwidth and bring down the return loss with the multi-band resonant frequencies. The proposed MPA resonates five multi-bands possessing a minimum S_{11} parameter of −32.94 dB at 12.53 GHz, having a maximum bandwidth of 2.412 GHz, high gain of 5.87 dB at 18.41, high directivity of 6.89 dB at 19.02 GHz, and higher radiation efficiency of 93% at 8.69 GHz. Presented results demonstrated that the recommended design could be more suited to radar and satellite communication implementations.

References

1. M.R. Ahsan, M.H. Ullah, M.T. Islam, Slot loaded rectangular patch antenna for dual-band operations on glass-reinforced epoxy laminated inexpensive substrate. J. Comput. Electron. **13**, 989–995 (2014)
2. J.D. Zhang, L. Zhu, Q.S. Wu, N.W. Liu, W. Wu, A compact microstrip-fed patch antenna with enhanced bandwidth and harmonic suppression. IEEE Trans. Antennas Propag. **64**(12), 5030–5037 (2016)
3. R. Kumar, Gurpreet Singh Saini, and Daljeet Singh, compact tri-band patch antenna for Ku band applications. Prog. Electromagn. Res. C **103**, 45–58 (2020)
4. A. Singh, R.M. Mehra, V.K. Pandey, Design and optimization of microstrip patch antenna for UWB applications using moth–flame optimization algorithm. Wirel. Pers. Commun. **112**, 2485–2502 (2020)
5. C. Singh, G. Kumawat, A compact rectangular ultra-wideband microstrip patch antenna with double band notch feature at Wi-Max and WLAN. Wirel. Pers. Commun. **114**, 2063–2077 (2020)
6. D.M. Pozar, Microstrip antennas. IEEE Proc. **80**(1), 79 (1992)
7. P. Callaghan et al., Dual-band pin-patch antenna for Wi-Fi applications. IEEE Antennas Wirel. Propag. Lett. **7**, 757 (2008)
8. K.F. Lee et al., Theory and experiment on microstrip patch antennas with shorting walls. IEEE Proc.-Microw. Antennas Propag. **147**(6), 521 (2000)
9. J.R. Panda et al., A printed 2.4 GHz/5.8 GHz dual-band monopole antenna with a protruding stub in the ground plane for WLAN and RFID applications. Prog. Electromagn. Res. PIER. 425 (2011)
10. X.L. Ma et al., A novel dual narrow band-notched CPW-Fed UWB slot antenna with parasitic strips. Appl. Comput. Electromagn. Soc. J. **27**(7), 581 (2012)
11. M.T. Islam et al., Triple band-notched planar UWB antenna using parasitic strips. Prog. Electromagn. Res. PIER. **129**, 161 (2012)
12. G.M. Yang et.al., Loading effects of self-biased magnetic films on patch antennas with substrate/superstrate sandwich structure. IET Microw Antennas Propag. **4**(9), 1172 (2010)

13. K.L. Sheeja et al., Compact tri-band metamaterial antenna for wireless applications. Appl. Comput. Electromagn. Soc. J. **27**(11), 947 (2012)
14. R. Thangjam, K. Bhattacharyya, Design and analysis of slotted microstrip patch antenna- a review. J. Telecommun. Study. **4**, (2018)
15. M.H. Ullah et al., Printed prototype of a wideband S-shape microstrip patch antenna for Ku/K band applications. Appl. Comput. Electromagn. Soc. J. **28**(4), 307 (2013)
16. S.C. Gao, L.W. Li, M.S. Leong, T.-S. Yeo, Analysis of a H-shaped patch antenna by using the FDTD method. Prog. Electromagn. Res. PIER **34**, 165–187 (2001)
17. R. Soni, R. Gupta, D. Sen, Efficient design of micro strip patch antenna for the ultra wideband (UWB) Applications. Int. J. Recent. Technol. Eng. (IJRTE). **8,** (2020)
18. R. Mishra, R.G. Mishra, R.K. Chaurasia, A.K. Shrivastava, Design and analysis of microstrip patch antenna for wireless communication. Int. J. Innov. Technol. Explor. Eng. (IJITEE)**. 8**, 2278–3075 (2019)
19. M. Chakraborty, B. Rana, P.P. Sarkar, A. Das, Design and analysis of a compact rectangular microstrip antenna with slots using defective ground structure. Procedia Technol. **4**, 411–416 (2012)
20. M.K. Khandelwal, B.K. Kanaujia, S. Kumar, Defected ground structure: fundamentals, analysis, and applications in modern wireless trends. Int. J. Antennas Propag. **2017,** 2018527 (2017)

Chapter 24
Observation and Characterization of Cyclic Particle Growth Process in rf Discharge of Ar-C_2H_2 Gas Mixture

Bidyut Chutia, S. K. Sharma, and H. Bailung

Abstract The in situ growth of nanometer-sized particles in a reactive gas discharge has been studied in a newly developed experimental setup. A repetition of the growth process of carbonaceous dust particles up to 4 cycles has been observed in the capacitively coupled rf discharge of Argon (Ar) and Acetylene (C_2H_2) mixture when the C_2H_2 flow is kept on for 80 min. The observed periodicity in the growth process has been confirmed by measuring the discharge parameters and the scattered light intensity from the particle cloud.

24.1 Introduction

Particle growth in low-temperature and low-pressure plasmas is a very well-known phenomenon that occurs in various technological (semiconductor fabrication) and astrophysical (star formation) environments [1–5]. In laboratory environments, particles of nanometer size can be easily grown either by using reactive gas discharge of silane (SiH_4) [6], hydrocarbon [3] (C_2H_2, CH_4, etc.), or by sputtering electrodes or coated surfaces [7]. The in situ grown nanoparticles get charged negatively by collecting plasma species and become a component of the plasma and take part in the plasma charge equilibrium. Hence, they can strongly affect the plasma density and discharge characteristics of the medium. As a result of this, a decrease in electron density and increase in electron temperature can be seen with high number density of nanoparticles. Growth of nanoparticles in reactive plasma has a cyclic nature which is observed in case of reactive plasmas very often [8]. Such cyclic growth process is well-studied in the case of silane plasmas compared to hydrocarbon plasmas.

In this work, cyclic growth phenomenon of carbonaceous nanoparticles in Ar-C_2H_2 discharge is studied in detail using the laser light scattering (LLS) method and discharge characteristics measurement. It is to be noted that, in most of the cases, the sophisticated technique of the third harmonic of discharge current signal [8 9] is measured to study cyclic growth. In this work, we have showed that the

B. Chutia (✉) · S. K. Sharma · H. Bailung
Dusty Plasma Laboratory, Physical Sciences Division, Institute of Advanced Study in Science and Technology (IASST), Paschim Boragaon, Guwahati, Assam 781035, India

S. Sengupta et al. (eds.), *Selected Progresses in Modern Physics*, Springer Proceedings in Physics 265, https://doi.org/10.1007/978-981-16-5141-0_24

simple measurement of rms values of discharge voltage and current also provides the information of cyclic growth of nanoparticles in reactive plasmas.

24.2 Experimental Setup and Procedure

The experiment is performed in a newly developed setup in which fine dust particles of nanometer size are grown from rf discharge of the Ar-C_2H_2 mixture. The schematic diagram of the experimental setup is shown in Fig. 24.1. The table-top experimental device consists of a vertically mounted cylindrical quartz tube of length 50 cm with an outer diameter of 6 cm. The chamber is equipped with two vacuum-sealed stainless-steel (SS) flanges at both ends. The upper flange is equipped with a feedthrough probe insertion and a gas inlet. The chamber is evacuated using a rotary pump to a base pressure of 0.001 mbar, and it is measured using a capacitance manometer. Both the rotary pump and the pressure gauge are connected through the bottom flange which is electrically grounded. The Ar gas is injected into the chamber through a mass flow

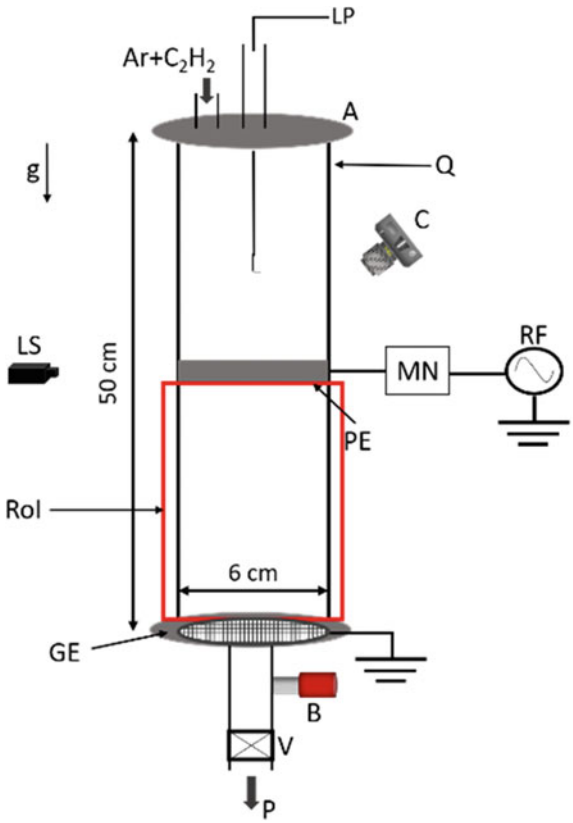

Fig. 24.1 Schematic diagram of the experimental setup (nDuPlEx). LP: Langmuir Probe; A: Stainless Steel Flange; Q: Quartz Tube; C: Camera; MN: Matching Network; RF: Radio Frequency power supply; PE: Powered Electrode; B: Baratron capacitance manometer; V: Angle Valve; P: Rotary Pump; GE: Grounded Electrode; RoI: Region of Interest; LS: Laser Source; g: acceleration due to gravity

controller (Alicat Scientific MC-100 sccm) at a controlled flow rate of 2–10 sccm through which a working pressure of 0.01–0.23 mbar is achieved. To produce the plasma, rf power (13.56 MHz) 1–10 W is applied. The powered electrode consists of a circular aluminium strip placed on the outer surface of the middle portion of the quartz tube. A stainless-steel mesh grid is placed inside the tube at the bottom which acts as the grounded grid electrode. The top and bottom flanges are also electrically grounded.

24.3 Results and Discussions

The discharge parameters such as rf voltage and current signals of pristine Ar plasma are measured using a voltage and a current probe, respectively, in Ar plasma for different rf power values and neutral pressure. The signals are recorded in a digital storage oscilloscope. A typical example of instantaneous voltage and current signals recorded at a fixed rf power of 1 W and Ar pressure of 0.17 mbar is shown in Fig. 24.2(a). The rms values of the discharge current (I_{rms}) and voltage (V_{rms}) are then obtained from the recorded signals and are plotted in Fig. 24.2(b) and (c), respectively, as a function of rf power and neutral pressure. It is found that I_{rms} increases with the increase in rf power at a fixed pressure. This is due to the increased ionization collision in the medium. On the other hand, a slight decrease in the I_{rms} value is observed with increased pressure at the higher power end. This happens due to the increased electron-neutral collision with pressure. The measured V_{rms} also shows a similar trend of variation with power and pressure as that of Irms. The V_{rms} value increases with rf power (1–19) W and is found to be in the range 85–310 V for the present neutral pressure range of 0.13–0.20 mbar. It is also noted that the discharge voltage signal lags behind the current signal with a phase shift, which is found to be in the range ~ 83–86° for the present variation range of rf power and pressure.

Cyclic nature of the particle growth process is observed in the experiment when the Ar-C_2H_2 discharge is kept on for a longer period of time (more than 10 min). Typical images of dust cloud recorded between 2 and 20 min of Ar-C_2H_2 discharge at an interval of 2 min are shown in Fig. 24.3. The rf power is 1 W, and Ar and C_2H_2 flow rates are 6 and 2 sccm, respectively. The total pressure inside the chamber is 0.20 mbar. The cloud becomes detectable by the laser light scattering within a few tens of seconds of ignition of the discharge. Gradually, the nanoparticle cloud fills up the whole chamber (vertical extension ~ 40 cm, radial extension ~ 5 cm) with two dust voids just above and below the powered electrode. The spontaneous generation of dust void is a very common phenomenon in case of nanodusty plasma. From 8 min onwards, a spontaneously excited dust density wave (DDW) appears in the cloud propagating from the powered electrode to the bottom. At 12 min, the void gets filled up by the particles, and the spontaneous DDW keeps propagating throughout the cloud. At 14 min, the particle cloud is found to be relatively less dense, indicating the loss of particles.

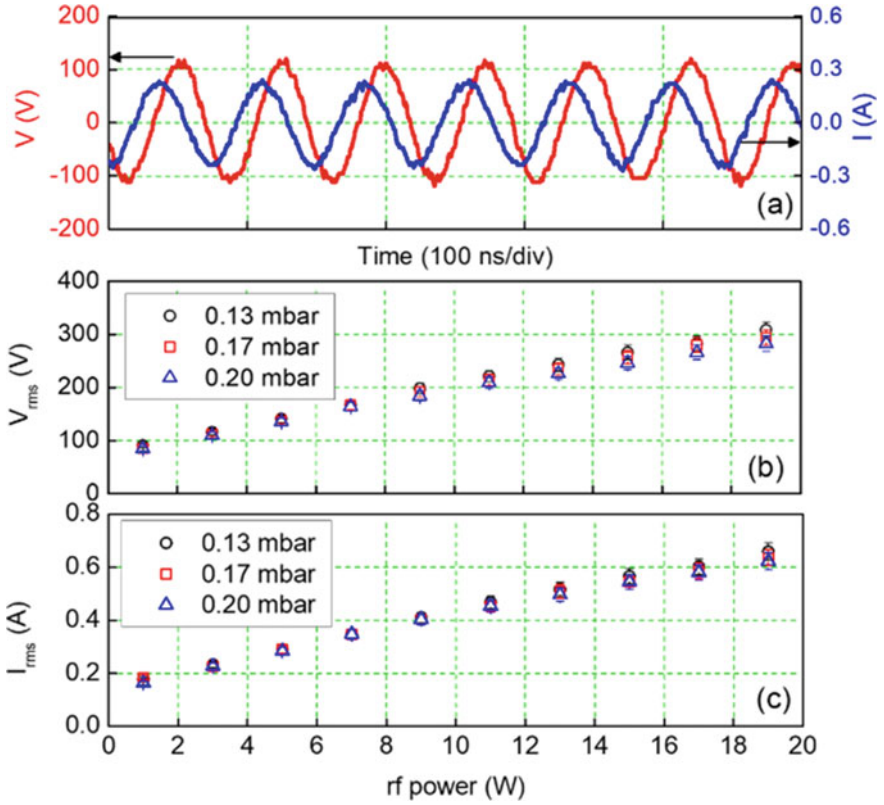

Fig. 24.2 (a) Typical instantaneous discharge voltage (V) and current (I) signals for rf power 1 W, Ar pressure 0.17 mbar. The rms values of (b) discharge voltage and (c) current signals as a function of applied rf power for different pressure values

Here, we noticed that the particles gradually fall down and are lost in the process. After a few minutes (16 min), the upper region becomes empty and only a section of the particle cloud is seen at the bottom. A new set of particles (second cycle) start to form which is visible at 18 and 20 min. Both the first and second batches of particles are found to be separated by a sharp boundary which is indicated by the yellow arrow mark in the figure. The growth of the second batch of particle clouds (along with the vertically extended central void) observed at 18 and 20 min is similar to that observed for the first batch of particles at 2 and 4 min, respectively, indicating a repetition of the particle growth process. The whole process keeps repeating continuously until the C_2H_2 flow is stopped. The observed repetition of growth process has been confirmed by performing the experiment several times and the periodicity (for the first cycle) is found to be around ~ (19 ± 3) min.

The temporal variation of V_{rms} of the discharge voltage signal and I_{rms} of the discharge current signal is shown in Fig. 24.4 for four cycles of growth. In the first cycle of particle growth, the V_{rms} starts to increase rapidly from 58 V (mean value)

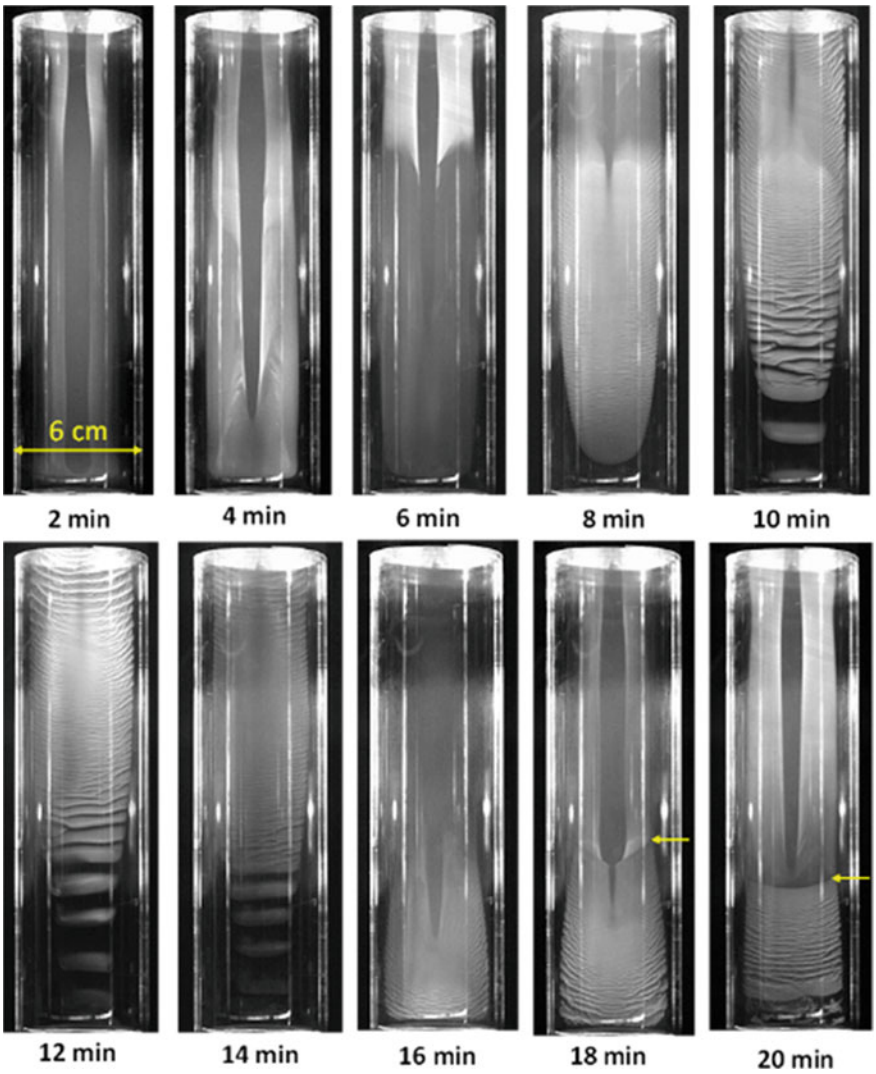

Fig. 24.3 Typical snapshots of dust cloud at different time intervals of discharge with C_2H_2 flow ON condition for a long period of time. The rf power is 1 W, Ar flow rate is 6 sccm, C_2H_2 flow rate is 2 sccm and total pressure is 0.20 mbar. The yellow arrow marks (at 18 and 20 min images) represent the separation between the first and second batches of particle clouds

to a peak value of 103 V during 0–6 min and then comes back to the mean value (during 6–22 min). The second growth cycle starts with a similar pattern as the first cycle, however, the peak value of V_{rms} (82.7 V) is smaller in this case. The temporal width of the second cycle is 18 min. The successive cycles, from the second cycle onwards, behave identically over time. The I_{rms}, initially, falls from 31.1 to 24 mA

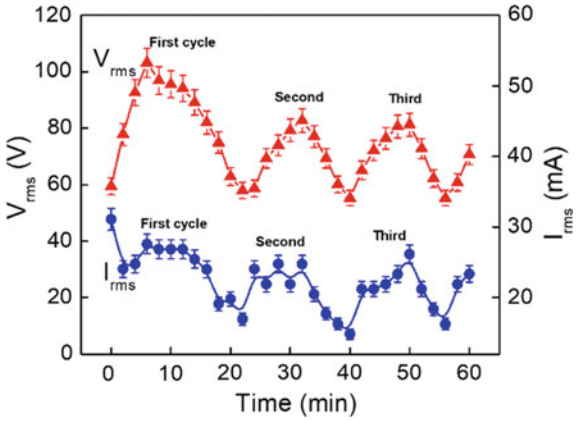

Fig. 24.4 Temporal variation of V_{rms} and I_{rms} during the cyclic growth of nanoparticles

for 2–4 min and then rises to 27.6 mA and saturates at that value from 6 to 12 min. Then it decreases to 16.9 mA at 22 min and the first cycle completes. From the second cycle onwards, a similar variation is observed for I_{rms}.

The variation of intensity of the transmitted and scattered light during the growth process is shown in Fig. 24.5 (a) and (b), respectively. For the first cycle, the transmitted light decreases slowly and reaches a minimum arbitrary value at 8 min, and it almost remains constant for up to 16 min. Then it starts to rise and reaches a peak value at 22 min, and again the whole process repeats over and over again as long as the reactive gas flow is kept on. The scattered intensity rises to a maximum value (0–8 min) and then comes back to the initial level (8–25 min) and successive cycles behave similarly over time. A time delay of ~ 2 min in the temporal variation of scattered light intensity compared to that of V_{rms} is observed probably due to longer resident time of nanodust cloud. On the other hand, the reduction in the peak value of

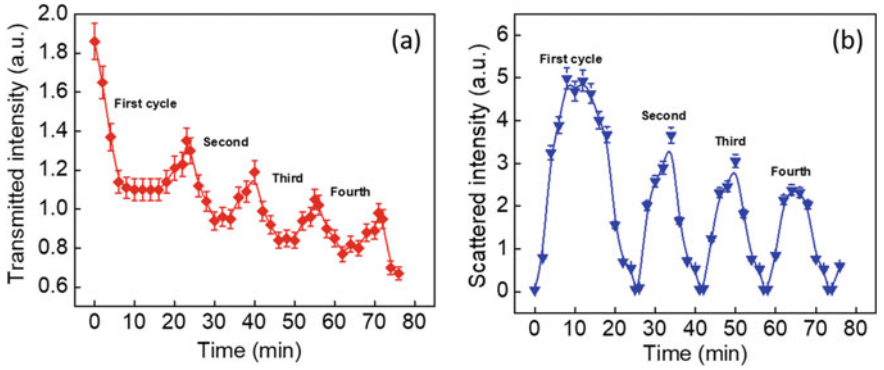

Fig. 24.5 Temporal variation of (a) transmitted and (b) scattered light intensity during cyclic growth for 4 cycles

the scattered light intensity in successive cycles is attributed primarily to the thickness of the coating on the inner wall of the quartz tube. The rf power and gas flow rates are kept unaltered throughout the experiment. So, the periodic variation of the V_{rms} and scattered light intensity indicate that the cyclic growth process is a reliable source of nanodust particles.

24.4 Conclusion

The cyclic growth process of carbonaceous nanoparticles in Ar-C_2H_2 discharge is studied in detail using laser light scattering method, discharge voltage and current signal measurement, laser extinction method, etc. All the methods showed a correlation among each other which confirms the cyclic growth phenomena. The evolution of the nanoparticle cloud can be clearly seen from snapshots which show the clear separation between old and new generations of particles. It has been noted from the measured discharge voltage and current signal data during the growth process that the growth of nanoparticles has a tremendous impact on the plasma discharge.

Acknowledgements One of the authors (SKS) would like to thank DST, Govt. of India, for supporting the work under the Women Scientist (WOS-A) project scheme. Another author (B.C.) would like to thank DST, Govt. of India, for financial support under INSPIRE fellowship. The authors would like to thank Prarthana Gogoi for assistance during experiments. The authors would also like to thank Tonuj Deka and Yoshiko Bailung for valuable suggestions and discussions.

References

1. A. Melzer, *Introduction to Colloidal (Dusty) Plasmas* (Institut Fur Physik Ernst-Moritz-Arndt-Universitat Greifswald, Greifswald, 2005)
2. P.K. Shukla, A.A. Mamun, *Introduction to Dusty Plasma P K Shukla* (IOP Publishing Ltd., Bristol and Philadelphia, 2002)
3. L. Boufendi, A. Bouchoule, Plasma Sources Sci. Technol. **11**, A211 (2002)
4. A. Bouchoule, *Dusty Plasmas: Physics, Chemistry, and Technological Impacts in Plasma Processing* (John Wiley & Sons Ltd., Chichester, 1999)
5. J. Berndt, E. Kovačević, I. Stefanović, O. Stepanović, S.H. Hong, L. Boufendi, J. Winter, Contrib. Plasma Phys. **49**, 107 (2009)
6. M. Mikikian, L. Boufendi, A. Bouchoule, H.M. Thomas, G.E. Morfill, A.P. Nefedov, V.E. Fortov, New J. Phys. **5**, 19 (2003)
7. C. Dominique, C. Arnas, J. Appl. Phys. **101**, 123304 (2007)
8. M. Cavarroc, M. Mikikian, Y. Tessier, L. Boufendi, Phys. Rev. Lett. **100**, 045001 (2008)
9. M. Cavarroc, M. Mikikian, Y. Tessier, L. Boufendi, Phys. Plasmas. **15**, 103704 (2008)

Chapter 25
Optical Study of Liquid Dispersed Few-Layered WS_2 Nanosheets

Ashamoni Neog and Rajib Biswas

Abstract Bulk WS_2 nanosheets were exfoliated using solvo-sonication method with isopropanol (IPA) and water mixture in order to obtain few layered WS_2 nanosheets. The micrographs obtained from scanning electron microscope and Raman spectra of the exfoliated WS_2 sheets drop-casted on glass substrate confirmed the formation of few layered sheets. Prominent absorption peaks A and B of the nanosheets were observed at wavelengths ~ 629.5 nm and ~ 526.5 nm, respectively, which correspond to direct excitonic absorptions. A gradual redshift in all the prominent absorption peaks were observed, with time. Characteristic absorption peaks were observed to be stable only for 4–5 days followed by decrease in intensities and reddening of absorption peaks. The redshift of peak A implies the restacking of the WS_2 nanosheets with time.

25.1 Introduction

Liquid phase exfoliation is a highly appreciated method for production of atomically thin structures of two-dimensional (2D) transition metal dichalcogenides (TMDCs). Defect-free nanosheets and high yield can be achieved with these methods. By doing liquid cascade centrifugation, monolayer enriched dispersion can also be achieved [1]. Again by mixing low boiling point solvents as well as surfactants, high yield exfoliations can be carried out [2, 3]. One of the most potential 2D TMDC material is Tungsten disulfide (WS_2). The importance of the WS_2 nanosheets lies in the application of atomic scale device fabrication [4], sensing [5, 6], photocatalytic application [7], etc. Though, several synthesis methods have already been devised for exfoliation of WS_2 nanosheets [8], the stability of nanosheets in liquid is still under investigation. Therefore in the present work, time lapsed optical analysis of the liquid dispersed nanosheets has been carried out.

A. Neog · R. Biswas (✉)
Applied Optics and Photonics Lab, Department Of Physics, Tezpur University, Tezpur, Assam, India
e-mail: rajib@tezu.ernet.in

S. Sengupta et al. (eds.), *Selected Progresses in Modern Physics*, Springer Proceedings in Physics 265, https://doi.org/10.1007/978-981-16-5141-0_25

25.2 Experimental

25.2.1 Exfoliation of WS_2

The bulk WS_2 (batch No-1645254–100 g, particle size ~ 2 μm) purchased from Sisco Research Laboratories Pvt. Ltd (SRL) was made to undergo liquid exfoliation. As suggested by A. Sajedi-Moghaddam et al. [2], the liquid exfoliation was carried out in a mixture of water and 2-propanol (water:2-propanol = 80:20). However, unlike A. Sajedi-Moghaddam et.al., the exfoliation was carried out in a bath sonicator of output power 100 W and for 6 h. The concentration of WS_2 in the solvent was about 1.6 mg/ml. Then, the exfoliated samples were centrifuged for 1 hour with 2500 rpm and the supernatant was taken for further assessment.

25.2.2 Characterization of WS_2

Unique molecular vibrational analysis of exfoliated WS_2 sheets was carried out with the help of Raman Spectroscopic analysis. The instrument used for this purpose was RENISHAW (model—Basis Series). The laser source used in the spectrometer was Ar^+ at wavelength 514 nm. Optical absorption properties of exfoliated WS_2 sheets were studied with the help of UV–Vis spectrophotometer (Shimadzu 2450). Scanning Electron Microscope (SEM) by JEOL was used to capture the SEM micrograph of WS_2 nanosheets.

25.2.3 Preparation of WS_2 Thin Films

In order to obtain the thin films of the exfoliated nanosheets, the as-dispersed WS_2 nanosheets were drop-casted on glass slides (Blue Star microslides) which were polished with 7000 grit sandpaper and cleaned with acetone in a bath sonicator. Then the slides were dried in hot air oven at 65ºC to get rid of the solvent part and then kept for further assessment.

25.3 Results and Discussions

25.3.1 SEM Micrograph of Exfoliated WS_2 Sheets

In $2H_c$-WS_2, Tungsten atoms are coordinated with six Sulfur atoms in trigonal prismatic molecular bonding geometry and form an entity of a layer. There are two such

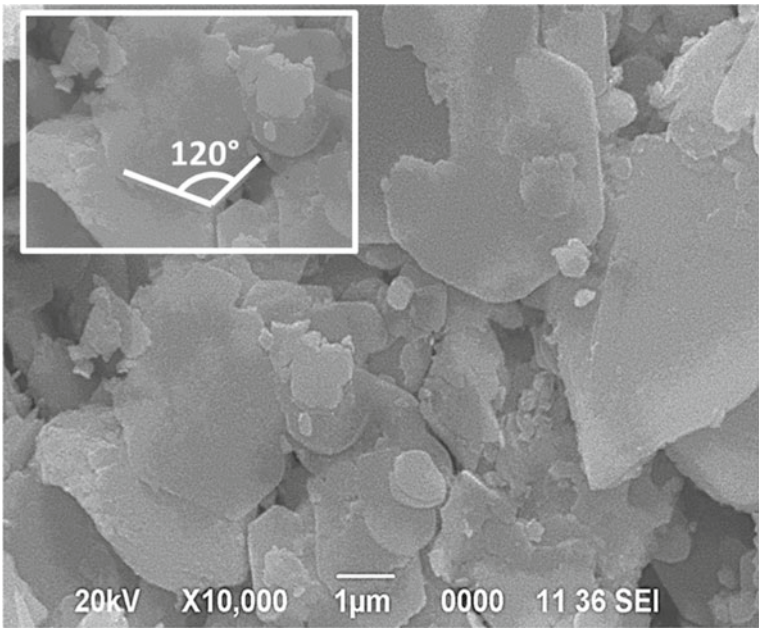

Fig. 25.1 SEM micrograph of WS_2 nanosheets

layers in the unit cell of this material and have hexagonal symmetry [9]. SEM micrograph (Fig. 25.1) of WS_2 nanosheets shows the hexagonal symmetry (inset) of the WS_2 sheets [10].

25.3.2 Raman Spectra of WS_2 Thin Films

Figure 25.2 shows Raman spectra of the WS_2 thin films. The prominent peaks of the exfoliated sheets were at 354.13 cm^{-1} and 424.39 cm^{-1}, which correspond to 2LA(M) and A_{1g} (Γ) optical modes, respectively. The I_{2LA}/I_{A1g} (Intensity ratio) is calculated out to be 0.8 which implies that the thin films were of nano dimension [11, 12].

25.3.3 UV–Vis Spectra of Exfoliated Nanosheets

Alike fluorescence spectroscopy [13, 14], UV–Vis spectroscopy is one of the most exploited techniques to analyze the underlying physics of a material in consideration. In case of 2D transition metal dichalcogenides, position of the peaks in the UV–Vis spectra can convey information about the size of the nanostructure [1, 15]. In the

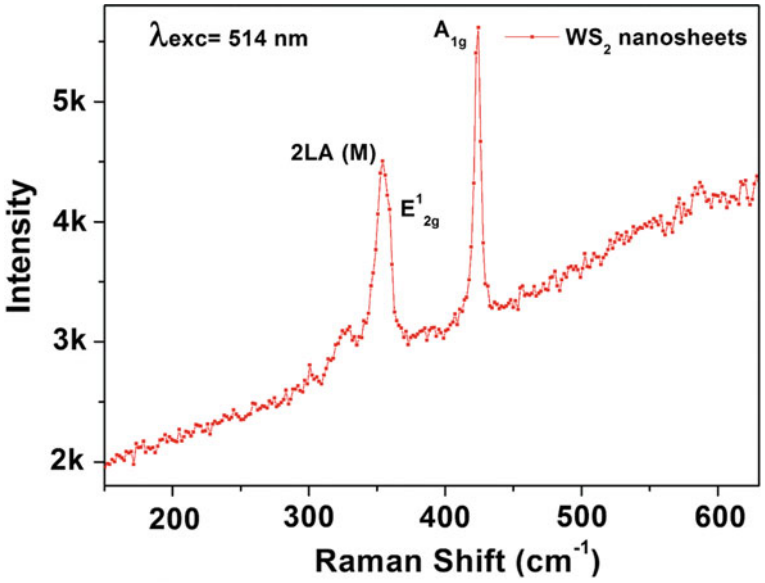

Fig. 25.2 Raman Spectra of water–IPA exfoliated WS_2 nanosheets drop-casted on glass substrate

present investigation, the absorption spectra of the exfoliated, liquid dispersed WS_2 nanosheets were taken on the date of its synthesis and also on several dates after the date of its synthesis in order to study the change in the intensity and peak positions of the absorption peaks. Figure 25.3 shows the UV–Vis spectroscopy of water–IPA exfoliated WS_2 nanosheets on 1st, 21st, 33rd, 34th, 36th, 36th, and 39th day of its synthesis. The peaks A and B correspond to direct band gap transition at k point [16–18]. The energy difference between A and B peaks are attributed to the measure of strength of spin–orbit interaction [19]. Peak C corresponds to optical transition between the densities of states peaks in the valence band and conduction band [20]. It is evident from the graph that with time, the peaks eventually red shifted followed by decrease in intensity. It was observed that the graphs for 33rd, 34th, and 36th day overlapped, and on 39th day, the intensity of the absorption peaks dropped followed by reddening of the peaks. Here, the wavelength corresponding to A excitonic peak increases from 629 nm (on 1st day) to 632 nm (on 36th day). These observations suggest that WS_2 nanosheets dispersed in water–IPA environment can retain similar optical behavior only for 4–5 days. According to several reports [1, 15, 21, 22], the optical properties of the transition metal dichalcogenides depends on their thickness. As number of layers increases, the energy corresponding to A excitonic absorption decreases. Therefore, reddening of the peak A with time (in the present study), implies increase in the average number of the layers in the dispersed nanosheets, which suggest that as time passes, the van der Waals bonded WS_2 nanosheets try to restack. Therefore, it is clear from the study that dispersion of nanosheets in water–IPA solution is not stable for a longer period of time.

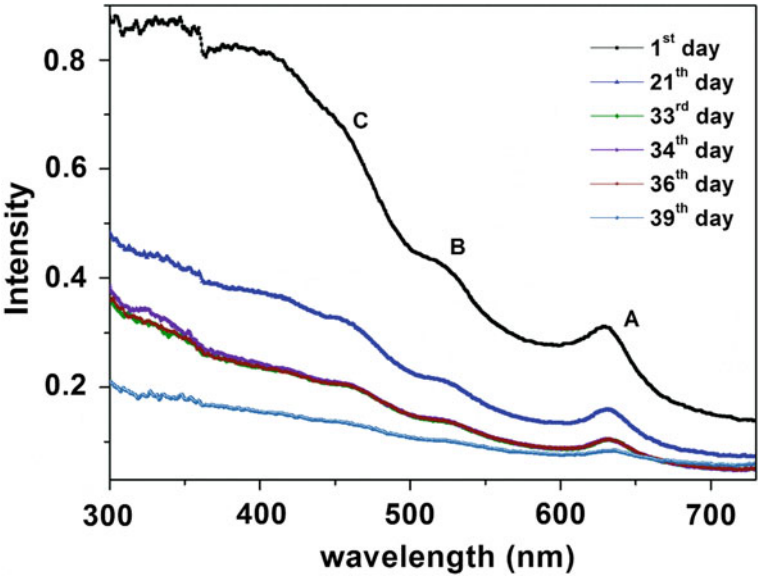

Fig. 25.3 UV–Vis spectroscopy of water–IPA exfoliated WS_2 nanosheets in 1st, 21st, 33rd, 34th, 36th, 39th day

25.4 Conclusion

WS_2 nanosheets were exfoliated in water–IPA solution and time dependent optical analysis was carried out. It was observed that, with time, the nanosheets restack in the solution itself, which implies that though the process gives good absorption peaks, the above synthesis process is not suitable to prepare stock solution of liquid dispersed WS_2 nanosheets. The average thickness of the nanosheets remains same only for 4–5 days in this process. However, thin films of WS_2 nanosheets prepared on glass substrate showed satisfactory Raman Spectra with distinct excitonic peaks.

Acknowledgements The authors are thankful to Department of Physics for providing UV–Vis spectrophotometer (Shimadzu 2450), centrifuge, oven, and cooling facilities. Author A.N acknowledges the funding from Research and Innovation Grant, Tezpur University. We are thankful to SAIC, Tezpur University for providing the XRD and Raman facilities. Author A.N acknowledges Tezpur University for institutional fellowship.

References

1. C. Backes, B.M. Szydłowska, A. Harvey, S. Yuan, V. Vega-Mayoral, B.R. Davies, P.L. Zhao, D. Hanlon, E.J. Santos, M.I. Katsnelson, W.J. Blau, Production of highly monolayer enriched dispersions of liquid-exfoliated nanosheets by liquid cascade centrifugation. ACS Nano **10**(1), 1589–1601 (2016)
2. A. Sajedi-Moghaddam, E. Saievar-Iranizad, High-yield exfoliation of tungsten disulphide nanosheets by rational mixing of low-boiling-point solvents. Mater. Res. Express. **5**(1), 015045 (2018)
3. R.J. Smith, P.J. King, M. Lotya, C. Wirtz, U. Khan, S. De, A. O'Neill, G.S. Duesberg, J.C. Grunlan, G. Moriarty, J. Chen, Large-scale exfoliation of inorganic layered compounds in aqueous surfactant solutions. Adv. Mater. **23**(34), 3944–3948 (2011)
4. N. Perea-López, A.L. Elías, A. Berkdemir, A. Castro-Beltran, H.R. Gutiérrez, S. Feng, R. Lv, T. Hayashi, F. López-Urías, S. Ghosh, B. Muchharla, Photosensor device based on few-layered WS_2 films. Adv. Funct. Mater. **23**(44), 5511–5517 (2013)
5. T. Järvinen, G.S. Lorite, J. Peräntie, G. Toth, S. Saarakkala, V.K. Virtanen, K. Kordas, WS_2 and MoS_2 thin film gas sensors with high response to NH_3 in air at low temperature. Nanotechnology. **30**(40), 405501 (2019)
6. A. Neog, S. Deb, R. Biswas, Atypical electrical behavior of few layered WS_2 nanosheets based platform subject to heavy metal ion treatment. Mater. Lett. **268**, 127597 (2020)
7. W. Ashraf, T. Fatima, K. Srivastava, M. Khanuja, Superior photocatalytic activity of tungsten disulfide nanostructures: role of morphology and defects. Appl. Nanosci. **9**(7), 1515–1529 (2019)
8. J.N. Coleman, M. Lotya, A. O'Neill, S.D. Bergin, P.J. King, U. Khan, K. Young, A. Gaucher, S. De, R.J. Smith, I.V. Shvets, Two-dimensional nanosheets produced by liquid exfoliation of layered materials. Science **331**(6017), 568–571 (2011)
9. M. Chhowalla, H.S. Shin, G. Eda, L.J. Li, K.P. Loh, H. Zhang, The chemistry of two-dimensional layered transition metal dichalcogenide nanosheets. Nat. Chem. **5**, 263–275 (2013)
10. Y. Sang, Z. Zhao, M. Zhao, P. Hao, Y. Leng, H. Liu, From UV to near-infrared, WS2 nanosheet: a novel photocatalyst for full solar light spectrum photodegradation. Adv. Mater. **27**(2), 363–369 (2015)
11. A. Berkdemir, H.R. Gutiérrez, A.R. Botello, N. Perea-López, A.L. Elías, C.I. Chia, B. Wang, V.H. Crespi, F. López-Urías, J.C. Charlier, H. Terrones, Identification of individual and few layers of WS2 using Raman spectroscopy. Sci. Rep. **3**(1), 1–8 (2013)
12. Y. Li, X. Li, T. Yu, G. Yang, H. Chen, C. Zhang, Q. Feng, J. Ma, W. Liu, H. Xu, Y. Liu, Accurate identification of layer number for few-layer WS_2 and WSe_2 via spectroscopic study. Nanotechnology. **29**(12), 124001 (2018)
13. C. Cong, J. Shang, Y. Wang, T. Yu, Optical properties of 2D semiconductor WS_2. Adv. Opt. Mater. **6**(1), 1700767 (2018)
14. H.G. Ji, P. Solís-Fernández, U. Erkılıç, H. Ago, Stacking orientation-dependent photoluminescence pathways in artificially stacked bilayer WS_2 nanosheets grown by chemical vapor deposition: implications for spintronics and valleytronics. ACS Appl. Nano Mater. **4**(4), 3717–3724 (2021)
15. T.P. Nguyen, W. Sohn, J.H. Oh, H.W. Jang, S.Y. Kim, Size-dependent properties of two-dimensional MoS2 and WS2. J. Phys. Chem. C **120**(18), 10078–10085 (2016)
16. W. Zhao, Z. Ghorannevis, L. Chu, M. Toh, C. Kloc, P.H. Tan, G. Eda, Evolution of electronic structure in atomically thin sheets of WS2 and WSe2. ACS Nano **7**(1), 791–797 (2013)
17. A.R. Beal, J.C. Knights, W.Y. Liang, Transmission spectra of some transition metal dichalcogenides. II. Group VIA: trigonal prismatic coordination. J. Phys. C: Solid State Phys. **5**, 3540 (1972)
18. R.A. Bromley, R.B. Murray, A.D. Yoffe, The band structures of some transition metal dichalcogenides. III. Group VIA: trigonal prism materials. J. Phys. C: Solid State Phys. **5**, 759 (1972)

19. A. Ramasubramaniam, Large excitonic effects in monolayers of molybdenum and tungsten dichalcogenides. Phys. Rev. B **86**, 115409 (2012)
20. L.F. Mattheis, Band structures of transition-metal-dichalcogenide layer compounds. Phys. Rev. B **8**, 3719–3740 (1973)
21. Y. Niu, S. Gonzalez-Abad, R. Frisenda, P. Marauhn, M. Drüppel, P. Gant, R. Schmidt, N.S. Taghavi, D. Barcons, A.J. Molina-Mendoza, S.M. De Vasconcellos, Thickness-dependent differential reflectance spectra of monolayer and few-layer MoS_2, $MoSe_2$, WS_2 and WSe_2. Nanomaterials. **8**(9), 725 (2018)
22. K. Synnatschke, P.A. Cieslik, A. Harvey, A. Castellanos-Gomez, T. Tian, C.J. Shih, A. Chernikov, E.J. Santos, J.N. Coleman, C. Backes, Length-and thickness-dependent optical response of liquid-exfoliated transition metal dichalcogenides. Chem. Mater. **31**(24), 10049–10062 (2019)

Chapter 26
Our Universe: The Known, Unknown, and Some Speculations

Saurya Das

Abstract Our Universe is simple at scales larger than a few hundred megaparsecs: it is smooth, homogeneous, isotropic, spatially flat, and expanding at an accelerating rate, following the laws of general relativity. Yet it presents a number of unresolved problems. These include the origin and fate of our Universe, nature of its main constituents—dark matter and dark energy, and the mechanism behind its high degree of homogeneity, isotropy, and flatness. I will briefly describe the success and failures of some of the theories which try to address these and will also present some new ideas which attempt to explain the above.

I would like to start by thanking the organizers for this very well-organized conference, especially during the pandemic! The following is a short summary of a talk of the same title which I have given at the conference.

It can be argued that the Universe becomes simpler as one goes to smaller and smaller length scales. For example, the description of biological systems at say, a length scale of 1 meter, is arguably more complex than the description of atoms at about 10^{-10} m, and in fact, quarks and leptons at about 10^{-19} m. It is expected that at the smallest length scale that can be constructed out of the fundamental constants of nature, namely, the Planck scale $\ell_{Pl} = \sqrt{G\hbar/c^3} \simeq 10^{-35}$ m, the fundamental spacetime structure is quite simple, namely, a vacuum, possibly accompanied by quantum fluctuations, which can be estimated by a successful theory of Quantum Gravity, on its completion.

It is interesting to note that apparently as one goes up length scales, the description of the physical Universe also gets progressively simpler. For example, as one goes up from the planetary to the galactic, super-galactic, and finally the cosmological length scales, the description in terms of gases and other elements give way to the much simpler description in terms of a set of perfect fluids. The equation of state of one such perfect fluid is given by $p = w\,\rho$, where p and ρ are the pressure and density respectively, w is a constant and a total of 3 such fluids, namely, non-relativistic visible

S. Das (✉)
Theoretical Physics Group, Department of Physics and Astronomy and Quantum Alberta, University of Lethbridge, 4401 University Drive, Lethbridge, AB T1K 3M4, Canada
e-mail: saurya.das@uleth.ca

S. Sengupta et al. (eds.), *Selected Progresses in Modern Physics*, Springer Proceedings in Physics 265, https://doi.org/10.1007/978-981-16-5141-0_26

and Dark Matter (DM) with $w = 0$, a cosmological constant or alternatively, Dark Energy (DE) with $w = -1$ or $w \simeq -1$, and a negligible amount of radiation (in the present epoch) with $w = 1/3$. Furthermore, the matter distribution is homogeneous and isotropic in the co-moving frame, which implies, purely from mathematical considerations [1] that the metric describing the Universe at large distances can be written in the following form, in the so-called co-moving coordinates

$$ds^2 = c^2 dt^2 - a^2(t) \left(\frac{dr^2}{1 - \kappa r^2} + r^2 (d\theta^2 + \sin^2 \theta d\phi^2) \right). \tag{26.1}$$

The above, known as the Friedmann-Lemaitre-Robertson-Walker (FLRW) metric, describes the geometry of a 3-dimensional flat space ($\kappa = 0$), sphere ($\kappa = 1$) or one of constant negative curvature ($\kappa = -1$), together with a time-dependent scale factor $a(t)$ which determines the distance between two objects, e.g., two galaxies, at large length scales.

The dynamics governing the scale factor $a(t)$ is given by the Einstein equations and the equation of continuity for the perfect fluid

$$H^2 \equiv \left(\frac{\dot{a}}{a}\right)^2 = \frac{8\pi G\rho}{3} + \frac{\Lambda c^2}{3} - \frac{\kappa c^2}{a^2}, \tag{26.2}$$

$$\frac{\ddot{a}}{a} = -\frac{4\pi G}{3} \left(\rho + \frac{3p}{c^2} \right) \tag{26.3}$$

$$\dot{\rho} + 3H(\rho + p) = 0. \tag{26.4}$$

Of the above three equations, any two can be taken to be independent, and the third is derivable from them. One also defines the following useful quantities

$$\text{Red-shift } z = \frac{a}{a_0} - 1\,, \tag{26.5}$$

$$\text{Change of } \lambda \text{ and } \nu \quad \lambda = \lambda_0 (1 + z),\ \nu = \frac{\nu_0}{1+z} \tag{26.6}$$

$$\text{Velocities } v \propto \frac{da}{dt} = \frac{\dot{a}}{a} d = H d \propto H(1 + z) \tag{26.7}$$

$$\text{Horizon } L = \frac{1}{H} \approx 10^{26}\, m \tag{26.8}$$

$$\text{Temperature } T = \frac{T_0}{a} = T_0 (1 + z)\,, \tag{26.9}$$

where the subscript 0 refers to the present epoch. Therefore in an expanding Universe, $z > 0$, $\lambda > \lambda_0$ and $H > 0$, while for a contracting phase $z < 0$, $\lambda < \lambda_0$ and $H < 0$. Solving Eqs. (26.2–26.4), one obtains for the (dimensionless) density parameters for the various sources of matter/energy as follows

$$\text{Radiation } \Omega_R = \Omega_R^{(0)} \left(\frac{a_0}{a}\right)^4 \tag{26.10}$$

$$\text{Matter } \Omega_M = \Omega_M^{(0)} \left(\frac{a_0}{a}\right)^3 \tag{26.11}$$

$$\text{Cosmological constant } \Omega_\Lambda = \Omega_\Lambda^{(0)}\,, \tag{26.12}$$

and in general $\Omega_i = \Omega_i^0 \left(\frac{a_0}{a}\right)^{3(1+w_i)} = \Omega_i^{(0)} \ (1+z)^{3(1+w_i)}$. In the above, the $\Omega_i = \rho_i/\rho_c$, where ρ_i is the density of species i, $\rho_c = 3H^2/8\pi G$ the *critical density*, the superscript 0 refers to the present epoch and for a spatially flat Universe, to which we will restrict ourselves henceforth, and it follows from Eq. (26.2) that at any epoch one has $\sum_i \Omega_i = 1$. Next, using the Friedmann equations one can derive an expression for the 'luminosity distance' $d_L \equiv \sqrt{L_s/4\pi F}$, where L is the absolute luminosity of any source and F the flux seen by the observer, as a function of the red-shift and the densities of the various matter/energy components in the present epoch

$$d_L(\Omega_i, z) = \frac{1+z}{H_0} \int_0^z \frac{dz}{\sqrt{\sum_i \Omega_i \ (1+z)^{3(1+w_i)}}} \ . \tag{26.13}$$

The remarkable fact is that it was shown beyond reasonable doubt by the Supernovae 1A luminosity distance vs. red-shift observations, that the best fit curve is given by the following parameters $\Omega_R^{(0)} \approx 0$, $\Omega_M^{(0)} = 0.25$, $\Omega_\Lambda^{(0)} = 0.70$ and out of the cold matter density. This implies that about 95% of our Universe's contents is practically unknown, although there are a number of proposed viable candidates. The Nobel prize in physics (2011) was awarded for the above fundamental result [2, 3].

Let us list below the other important unanswered questions of our Universe and its evolution.

- Cosmic Microwave Background Radiation (CMBR)

  At about red-shift $z = 1100$, or 400, 000 years after the presumptive Big-Bang singularity, the electrons and photons in the dense hot soup of our Universe decoupled from each other, and the free photons have been traveling ever since, influenced only by the expansion of the Universe. This is known as the Cosmic Microwave Background Radiation (CMBR). Remarkably, the spectrum of the radiation is that of a black body, with temperature given by $T(a) = 2.7/a$ K. Therefore the CMBR is 2.7 K at the present epoch [4, 5]. While this radiation is clear evidence for an expanding Universe, what remains a mystery is its observed incredible homogeneity and isotropy, about 1 part in 10^5. The time from the Big-Bang is just not enough for information to be communicated from one end of the Universe to the other and equilibrium to set in throughout the observed sky. In fact, points in the sky separated by only about a few degrees should be in thermal equilibrium at this epoch, and not the full 4π steradians of solid angle, an observed! This is also known as the horizon problem in cosmology [1].

- Dark Matter

  As mentioned earlier, about 25% of the matter content of our Universe is invisible, although it exists [6, 7]! A number of DM candidates have been proposed, although there has not been any direct or indirect evidence in favor of any. Among the more popular candidates are axions, supersymmetric particles, and the so-called weakly interacting massive particles or WIMPS and there are other exotic candidates as well [8].

- Dark Energy

  Arguably, the most natural candidate for DE is the sum of vacuum energy densities of quantum fields [9]. The problem with this idea that if one tries to estimate the zero-point of even a single quantum field, e.g., a scalar field, given by the momentum integral [10]

$$\rho_\Lambda = \int_0^{k_{\max}} dk\, k^2 \sqrt{k^2 + m^2} \approx k_{\max}^4, \tag{26.14}$$

  where $k_{\max}$ is the ultraviolet. Although one can take $k_{\max} \to \infty$, thereby giving an infinite vacuum energy density, one should in reality, equate it to a physical scale up to which one trusts the theory. For example, if we choose $k_{\max} = E_{EW} \approx TeV$, the electroweak energy scale, or $k_{\max} = E_{Pl} \approx 10^{16}\, TeV$, the Planck energy scale, the ratio of the vacuum energy density E_{vac} to the cosmological constant Λ goes as $\mathcal{O}(10^{50} - 10^{124})$, which is clearly an unacceptable discrepancy.

- Spatially flat Universe

  As mentioned earlier, large-scale homogeneity and isotropy require that the spatial sections of the Universe (at any given time t) to be either flat or a three-dimensional sphere with positive constant curvature or a three-dimensional saddle with negative constant curvature. Out of these, the Universe seemingly chooses the first option. Although it may be argued that with a probability of $1/3$, this is not too bad, the problem is that spatial flatness of one part in 10^5 at the current epoch (as observed) implies flatness in progressively earlier epochs at an incredible level of accuracy, of one part in 10^N, with $N \gg 1$. While this cannot be ruled out, it suggests a Universe on the knife-edge early on, with a tremendous fine tuning, which is undesirable and needs a better understanding. This is known as the flatness problem.

- The initial singularity

  An expanding Universe means a tiny scale factor in early epochs and in principle $a = 0$ at $t = 0$. Matter densities and spacetime curvatures become infinite at that point and the theory of gravity itself along with its predictive power (general relativity, the Friedmann equations) breaks down. Again, while this remains a possibility, other beginnings of the Universe or its remaining everlasting cannot be ruled out.

Proposed solutions and some speculations

- Inflation

  The paradigm of inflation aims to solve the homogeneity, isotropy and flatness problems in one stroke, by proposing that the Universe underwent a rapid phase of exponential expansion soon after the Big-Bang, thereby 'flattening' out any curvature (making it spatially flat) and causally connecting its far reaches, thereby

solving the horizon and flatness problems in one stroke [11–14]. Inflation does come with a number of potential problems however [15].

- Quantum Friedmann equation

The quantum Raychaudhuri equation, formulated by replacing classical geodesics with quantal trajectories, gives rise to the quantum corrected Friedmann equation as follows

$$\frac{\ddot{a}}{a} = -\frac{4\pi G}{3}(\rho + 3p) + \frac{\hbar^2}{3m^2} h^{ab} \left(\frac{\Box\mathcal{R}}{\mathcal{R}}\right)_{;a;b} \tag{26.15}$$

$$\equiv -\frac{4\pi G}{3}(\rho + 3p) + \frac{\Lambda_Q}{3}\,, \tag{26.16}$$

where $\Psi = \mathcal{R}e^{iS}$, with $\mathcal{R}$ and S being real functions, is the wavefunction of a 'quantum fluid' stretching across cosmological length scales. Next, if one makes a simple assumption, namely, that there is an abundance of light bosons in our Universe with mass $m < 6\,eV/c^2$, then it can be shown that the critical temperature of the bosons T_c always exceeds the ambient temperature of the Universe (e.g., the CMBR temperature). This means that a Bose-Einstein condensate (BEC) of the bosons will form in the early Universe, with the wavefunction Ψ. This can be a viable source of DM. Furthermore, a physically motivated wavefunction which respects spatial homogeneity, isotropy and the dilution of DM as $1/a^3$, given by $\Psi = \frac{R_0}{a^{3/2}}\, e^{-r^2/\sigma^2} \equiv \mathcal{R}(x)$ where $\sigma^2 = \frac{2\hbar}{m(4\pi G\rho_c/3)^{1/2}}$ and gives from Eq. (26.16),

$$\Lambda_Q = \frac{\hbar^2}{m^2} h^{ab} \left(\frac{\Box\mathcal{R}}{\mathcal{R}}\right)_{;a;b} = 8\,\pi G\rho_c \tag{26.17}$$

$$\rho_\Lambda \quad = \frac{\Lambda}{4\pi G} = 2\,\rho_c \approx \rho_{DM}\,. \tag{26.18}$$

In other words, a positive cosmological constant of approximately the right magnitude emerges for the BEC with the above wavefunction. The explanation for its positivity, smallness, and approximate equality with DM is easily explainable in this picture. It is positive because being the quantum potential, it must have the opposite signature of the attractive, classical gravitational potential, which induces it. In fact, there exists a rigorous but not such well-known result that (classical potential)=- (classical potential) for stationary states. The last result also implies its smallness and equality with DM density. Of course, the above idea is still speculative and its proof would depend on observable predictions that it can make. Some of the predictions are the existence and abundance of light bosons with an estimated mass at about $m \approx 10^{-30}\ eV/c^2$, a change of the cosmological constant in the far past and far future and further corrections to measurable quantities when one includes the excited states of the BEC [16–19].

To conclude, we have summarized here some of the recent observations in cosmology, the inferences that one can draw from them, the problems that remain unanswered and some proposals and speculations that attempt to resolve them. One can perhaps be optimistic that at least some of them will be better understood in the near future.

Acknowledgements I thank the organizers of the conference for their kind invitation to give a talk. This work was supported by the Natural Sciences and Engineering Research Council of Canada.

References

1. S. Weinberg, Cosmology, Oxford (2008)
2. S. Perlmutter et al., Astrophysical J. **517**(2), 565 (1999). [arXiv:astro-ph/9812133]
3. A.G. Riess et al., Astron. J. **116**, 1009 (1998). ([arXiv:astro-ph/9805201])
4. A.A. Penzias, R.W. Wilson, The Astrophys. J. **142**(1), 419–421 (1965)
5. P.J.E. Peebles, *Principles of Physical Cosmology*. Princeton University Press (1993)
6. F. Zwicky, *Publications of the Astronomical Society of the Pacific*, vol. 73, no. 434, p. 314
7. V. Rubin, W. Ford, W. Kent Jr., The Astrophys. J. **159**, 379–403 (1970)
8. J.L. Feng, Ann. Rev. Astron. Astrophys. **48**, 495 (2010)
9. E.J. Copeland, M. Sami, M. Tsujikawa, Int. J. Mod. Phys. D **15**, 1753–1936 (2006)
10. S. Weinberg, Rev. Mod. Phys. **61**, 1 (1989)
11. A. Guth, *The Inflationary Universe: The Quest for a New Theory of Cosmic Origins* (Basic Books, 1997)
12. A.A. Starobinsky, J. Exp. Theor. Phys. Lett. **30**, 682 (1979)
13. A. Linde, Phys. Lett. B **108**(6), 389–393 (1982)
14. D. Baumann, TASI Lectures on Inflation, arXiv:0907.5424
15. J. Earman, J. Mosterin, Philos. Sci. **66**(1), 1–49 (1999)
16. S. Das, Phys. Rev. D **89**, 084068 (2014). [arXiv:1311.6539]
17. S. Das, R.K. Bhaduri, Class. Quant. Grav. **32**, 105003 (2015). arXiv1411.0753
18. S. Das, S. Sharma, S. Sur, arXiv:2102.03032
19. S. Das, Int. J. Mod. Phys. **29**(14), 2043013 (2020). arXiv:2005.08071

Chapter 27
Phenomenological Study of Neutrino Mass Matrices with One Vanishing Minor and Zero Sum of Mass Eigenvalues with Majorana Phases

Sangeeta Dey and Mahadev Patgiri

Abstract In this work we have carried out a phenomenological texture study of neutrino mass matrix having one vanishing minor and zero sum of the neutrino mass eigenvalues. Out of six possible cases of a neutrino mass matrix with one vanishing minor, we have studied only two cases, i.e., $C_{11} = 0$ and $C_{12} = 0$ by imposing the zero trace condition in flavor state basis. It is found that case $C_{11} = 0$ is allowed for both Normal Hierarchy (NH) and Inverted Hierarchy (IH) while $C_{12} = 0$ is allowed only for NH. Here we have investigated the allowed ranges of Majorana and Dirac CP-phases for the cases.

27.1 Introduction

A number of neutrino oscillation experiments carried out since last few decades have confirmed the neutrino oscillations, i.e., flipping from one kind of flavors to another takes place during their transit. These phenomena of neutrino oscillations can be understood if neutrinos are massive and mix themselves. To formulate such dynamics, the three-generation neutrinos are represented by a complex (3×3) symmetric Majorana neutrino mass matrix M_ν. Since this leptonic sector is not completely known, so one is allowed to construct the matrix M_ν in a number of different forms consisting of free parameters. It is expected that the Nature will choose a particular texture of M_ν and may be in the minimal form. The origin of such texture may be explored in model building. In the first place, the textures should be phenomenologically consistent with the current neutrino data as well as have minimum number of free parameters. In order to proceed in this direction, investigations have been carried out by undertaking various ansatzes in literature, viz., vanishing minor [1], zero textures [2], hybrid textures [3]. These phenomenological studies pave out the way to explore the underlying symmetry of the successful textures.

S. Dey (✉) · M. Patgiri
Cotton University, Guwahati, India

S. Sengupta et al. (eds.), *Selected Progresses in Modern Physics*, Springer Proceedings in Physics 265, https://doi.org/10.1007/978-981-16-5141-0_27

In the present work we intend to explore the texture of neutrino mass matrices with two ansatzes: (1) one vanishing minor [1, 4] and (2) zero sum of neutrino mass eigenvalues [5, 6]. The primary motivations of considering these two ansatzes on neutrino mass matrix are the following: (a) the more attractive way of obtaining the light left-handed neutrino mass matrices is the framework of seesaw models beyond standard model of particle physics: $M_\nu = -M_D M_R^{-1} M_D^T$. The Dirac mass matrix M_D and heavy right-handed Majorana mass matrix M_R are more fundamental than M_ν, and any vanishing minor or texture zero in M_ν is a result of zeros in M_D and M_R that propagate via seesaw formula. The zeros in M_D and M_R represent underlying flavor symmetry that may be realized by the discrete symmetry group Z_N. Again Z_N is a subgroup of $U(1)$ Abelian gauge group, thus giving a strong theoretical foundation in this approach. (b) The absolute mass scale can be directly measured in non-oscillation experiments, viz., neutrinoless double beta decay, tritium beta decay endpoint spectrum, etc., whereas the oscillation experiments measure the mass squared differences of neutrinos known as solar and atmospheric mass splittings. But Black et al. showed in their paper [5] that the zero sum of eigenvalues condition enables one to calculate the absolute masses of neutrinos in normal hierarchy (NH) or in inverted hierarchy (IH) mass pattern from current neutrino data from oscillation experiments and in conjunction the form of neutrino mass matrix becomes simpler.

In symmetric (3×3) neutrino mass matrix M_ν, there are 6 possible textures having one vanishing minor. We restrict the present study to vanishing minors $C_{11} = 0$ and $C_{12} = 0$ as representative cases only for limited space for this paper. Viabilities of such textures are analyzed on the basis of 3σ values of mass squared differences Δm_{ij}^2, mixing angles θ_{ij} and constraints on Dirac phase δ.

The paper is organized as follows: In Sect. 27.2, we have shown the formalism used to form the Majorana mass matrix and obtain some useful relation of neutrino mass ratios and majorana phases with Dirac CP-phases imposing one vanishing minor and vanishing sum of neutrino mass eigenvalues in the neutrino mass matrix. In Sect. 27.3, we have done the numerical analysis and finally we have concluded in Sect. 27.4.

27.2 Formalism

There are six textures of neutrino mass matrices with one vanishing minor of which we have studied only two following textures, i.e., $C_{11} = 0$ and $C_{12} = 0$:

$$C_{11} = 0, m_{22}m_{33} - m_{23}m_{32} = 0 \tag{27.1}$$

$$C_{12} = 0, m_{21}m_{33} - m_{23}m_{31} = 0. \tag{27.2}$$

Here C_{ij} denote the cofactor of 3×3 m_{ij} neutrino mass matrix. We may express the neutrino mass matix M_ν as

$$M_\nu = V \begin{pmatrix} m_1 & 0 & 0 \\ 0 & m_2 & 0 \\ 0 & 0 & m_3 \end{pmatrix} V^T \tag{27.3}$$

where V is PMNS matrix which may be parametrized as $V = U P_\nu$ [7] on diagonal charged lepton mass matrix

$$U = \begin{pmatrix} c_{12}c_{13} & c_{13}s_{12} & s_{13}e^{-i\delta} \\ -s_{12}c_{23} - c_{12}s_{13}s_{23}e^{i\delta} & c_{12}c_{23} - s_{12}s_{13}s_{23}e^{i\delta} & c_{13}s_{23} \\ s_{23}s_{12} - c_{12}c_{23}s_{13}e^{i\delta} & -c_{12}s_{23} - c_{23}s_{12}s_{13}e^{i\delta} & c_{13}c_{23} \end{pmatrix} \tag{27.4}$$

where $P_\nu = diag(1, e^{i\alpha}, e^{i(\beta+\delta)})$ with α and β being the Majorana CP-phases and δ the Dirac CP phase. Thus the neutrino mass matrix may be expressed as

$$M_\nu = U \begin{pmatrix} \lambda_1 & 0 & 0 \\ 0 & \lambda_2 & 0 \\ 0 & 0 & \lambda_3 \end{pmatrix} U^T \tag{27.5}$$

where $\lambda_1 = m_1, \lambda_2 = m_2 e^{2i\alpha}, \lambda_3 = m_3 e^{2i(\beta+\delta)}$. Now using Eq. (27.5) we can express any element of the neutrino mass matrix M_ν as

$$M_{ab} = \sum_{i=1}^{3} U_{ai} U_{bi} \lambda_i. \tag{27.6}$$

Therefore the condition for one vanishing minor of any element of neutrino mass matrix can be given by

$$C_{mn} = (-1)^{m+n}(M_{\nu(ab)} M_{\nu(cd)} - M_{\nu(ef)} M_{\nu(gh)}) = 0. \tag{27.7}$$

Solving Eq. (27.7) we get

$$m_1 m_2 e^{i\alpha} A_3 + m_2 m_3 e^{i(\alpha+\beta+\delta)} A_1 + m_3 m_1 e^{i(\beta+\delta)} A_2 = 0 \tag{27.8}$$

where

$$A_i = (U_{pj} U_{qj} U_{rk} U_{sk} - U_{tj} U_{uj} U_{vk} U_{wk}) + (j \longleftrightarrow k) \tag{27.9}$$

here (i, j, k) is a cyclic permutation of (1,2,3). Therefore the two constraint equations are

$$\lambda_1 \lambda_2 A_3 + \lambda_2 \lambda_3 A_1 + \lambda_3 \lambda_1 A_2 = 0 \tag{27.10}$$

$$\lambda_1 + \lambda_2 + \lambda_3 = 0. \tag{27.11}$$

Solving Eqs. (27.10) and (27.11) we get the following ratios

$$\frac{m_1}{m_2}e^{-2i\alpha} = \frac{(A_3 - A_1 - A_2) \pm \sqrt{(A_3 - A_1 - A_2)^2 - 4A_1A_2}}{2A_2} \tag{27.12}$$

$$\frac{m_1}{m_3}e^{-2i\beta} = \frac{(A_2 - A_1 - A_3) \pm \sqrt{(A_2 - A_1 - A_3)^2 - 4A_1A_3}}{2A_3}e^{2i\delta}. \tag{27.13}$$

The ratios of the magnitude of the neutrino masses are given by

$$\rho = \left|\frac{m_1}{m_2}e^{-2i\alpha}\right|, \sigma = \left|\frac{m_1}{m_3}e^{-2i\beta}\right|. \tag{27.14}$$

Now ρ and σ are related to each other with the ratio of solar and atmospheric mass squared difference R_ν where

$$R_\nu = \frac{\delta m^2}{\Delta m^2} = \frac{2\sigma^2(1-\rho^2)}{2\rho^2 - \sigma^2(1+\rho^2)} \tag{27.15}$$

where the three neutrino masses are given by $m_1 = \sqrt{\frac{\delta m^2 \rho^2}{1-\rho^2}}$, $m_2 = \frac{m_1}{\rho}$ and $m_3 = \frac{m_1}{\sigma}$, where $\delta m^2 = m_2^2 - m_1^2$ and $\Delta m^2 = |m_3^2 - \frac{1}{2}(m_1^2 + m_2^2)|$. For NH we have $R_\nu = \frac{\sigma^2(1-\rho^2)}{\rho^2}$ and for IH $R_\nu = \frac{2(1-\rho^2)}{1+\rho^2}$.

The measure of CP violation, i.e., Jarkslog invariant [8]

$$J_{CP} = s_{12}c_{12}s_{23}c_{23}s_{13}c_{21}^3 \sin\delta.$$

27.2.1 Case $C_{11} = 0$

From Eq. (27.9) we arrive at the values of A_1,A_2 and A_3

$$A_1 = c_{12}^2c_{13}^2,\ A_2 = s_{12}^2c_{13}^2,\ A_3 = s_{13}^2e^{2i\delta}. \tag{27.16}$$

Using Eq. (27.16) in Eqs. (27.12) and (27.13) and considering terms upto order of s_{13}^2, we get

$$\frac{m_1}{m_2}e^{-2i\alpha} = \pm\left(\frac{s_{13}^2e^{2i\delta} \mp c_{13}^2\cos 2\theta_{12}}{c_{13}^2\cos 2\theta_{12}}\right) \tag{27.17}$$

$$\frac{m_1}{m_3}e^{-2i\beta} = \frac{-\cos 2\theta_{12}e^{2i\delta} - e^{2i\delta}}{2\cos 2\theta_{12}};\ \frac{-2c_{13}^2\cos^2 2\theta_{12} - s_{13}^2\cos 2\theta_{12}e^{2i\delta} + s_{13}^2e^{2i\delta}}{2s_{13}^2\cos 2\theta_{12}} \tag{27.18}$$

Equations (27.17) and (27.18) lead to the following expressions

$$\alpha = \mp\frac{1}{2}\tan^{-1}\frac{s_{13}^2 \sin 2\delta}{c_{13}^2 \cos 2\theta_{12} \pm s_{13}^2 sin2\delta} \tag{27.19}$$

$$\beta = \frac{-1}{2}\tan^{-1}\frac{\cos 2\theta_{12}\sin 2\delta + \sin 2\delta}{\cos 2\theta_{12}\cos 2\delta + \cos 2\delta} \tag{27.20}$$

$$\beta = \frac{-1}{2}\tan^{-1}\frac{\cos 2\theta_{12}\sin 2\delta - \sin 2\delta}{2\cot^2 2\theta_{13}\cos^2 2\theta_{12} + \cos 2\theta_{12}\cos 2\delta - \cos 2\delta} \tag{27.21}$$

27.2.2 Case $C_{12} = 0$

For case $C_{12} = 0$ we have the values of A_1,A_2 and A_3 as

$$A_1 = c_{12}s_{12}c_{23}c_{13} + c_{12}^2 c_{13}s_{13}s_{23}e^{-i\delta} \tag{27.22}$$

$$A_2 = -c_{12}s_{12}c_{23}c_{13} + s_{12}^2 s_{23}s_{13}c_{13}e^{-i\delta},\ A_3 = s_{23}s_{13}c_{13}e^{i\delta}. \tag{27.23}$$

Using Eqs. (27.22) and (27.23) in Eqs. (27.12) and (27.13) and considering term upto the order of s_{13}^2 we have

$$\frac{m_1}{m_2}e^{-2i\alpha} = \frac{4c_{12}c_{23}c_{12}s_{23}s_{13}(e^{i\delta} - e^{-i\delta} \pm \cos 2\theta_{12}e^{-i\delta}) \pm s_{23}^2 s_{13}^2(2 + e^{2i\delta} + \cos^2 2\theta_{12}e^{-2i\delta})}{\pm 4c_{12}s_{12}c_{23}(2c_{12}s_{12}c_{23} + s_{23}s_{13}\cos 2\theta_{12}e^{-i\delta})} \tag{27.24}$$
$$8c_{12}s_{12}c_{23}(-c_{12}s_{12}c_{23} + s_{12}^2 s_{23}s_{13}e^{-i\delta})$$

$$\frac{m_1}{m_3}e^{-2i\beta} = \frac{8c_{12}^2 s_{12}^2 c_{23}^2 - 4c_{12}s_{12}c_{23}s_{23}s_{13}(e^{i\delta} - \cos 2\theta_{12}e^{-i\delta}) \mp 8c_{12}^2 s_{12}^2 c_{23}^2 \mp 4c_{12}s_{12}s_{13}c_{23}s_{23}\cos 2\theta_{12}e^{-2i\delta}}{\mp s_{23}^2 s_{13}^2(2 + e^{2i\delta} + \cos^2 2\theta_{12}e^{-2i\delta})}. \tag{27.25}$$
$$8s_{23}s_{13}c_{12}s_{12}c_{23}e^{-i\delta}$$

On calculating α and β from Eqs. (27.22) and (27.23) we have

$$\alpha = \frac{1}{2}\tan^{-1}\frac{s_{23}s_{13}(\pm 4c_{12}s_{12}c_{23}\sin\delta(2s_{12}^2 + \cos 2\theta_{12}) - s_{23}s_{13}\sin 2\delta(4s_{12}^2\sin 2\delta \pm \sin^2 2\theta_{12}))}{4s_{23}s_{13}c_{12}s_{12}c_{23}\cos\delta(2 \mp \cos 2\theta_{12} \pm 2s_{12}^2) \mp 8c_{12}^2 s_{12}^2 c_{23}^2} \tag{27.26}$$
$$\pm s_{23}^2 s_{13}^2(4s_{12}^2\cos 2\theta_{12} - (2 + \cos 2\delta \mp \cos^2 2\theta_{12}\cos 2\delta \pm 8s_{12}^2\cos^2\delta))$$

$$\beta = \frac{-1}{2}\tan^{-1}\frac{s_{23}s_{13}(2\sin\delta + \sin 3\delta - \cos^2 2\theta_{12}\sin\delta) + 4c_{12}s_{12}c_{23}\sin 2\delta}{s_{23}s_{13}(2\cos\delta + \cos 3\delta + \cos^2 2\theta_{12}\cos\delta) + 4c_{12}s_{12}c_{23}\cos 2\delta} \tag{27.27}$$

$$\beta = \frac{-1}{2}\tan^{-1}\frac{4s_{23}s_{13}c_{12}s_{12}c_{23}\sin 2\delta + s_{23}^2 s_{13}^2(\cos^2 2\theta_{12}\sin\delta - 2\sin\delta - \sin 3\delta) - 16c_{12}^2 s_{12}^2 c_{23}^2\sin\delta}{4s_{23}s_{13}c_{12}s_{12}c_{23}(\cos 2\delta - 2\cos 2\theta_{12}) - s_{23}^2 s_{13}^2(2\cos\delta + \cos^2 2\theta_{12}\cos\delta + \cos 2\delta) - 16c_{12}^2 s_{12}^2 c_{23}^2\cos\delta}. \tag{27.28}$$

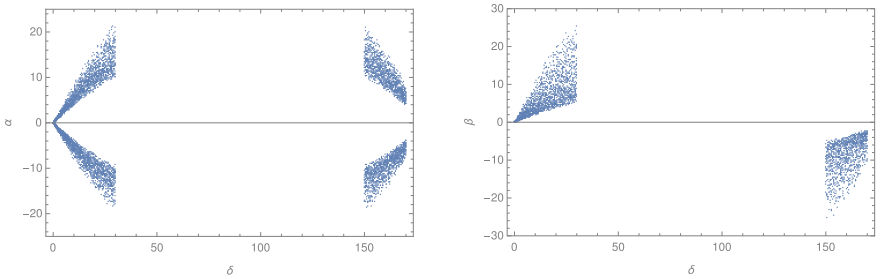

Fig. 27.1 Scatter plot for Majorana versus Dirac CP Phase for case $C_{11} = 0$ for NH, where δ is constrained in the range (5°, 30°) and (150°, 170°)

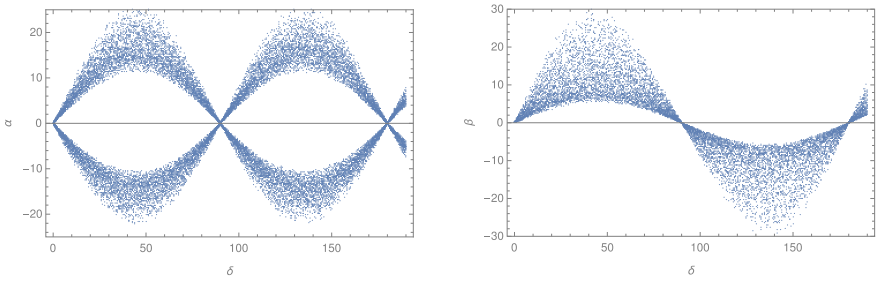

Fig. 27.2 Scatter plot for Majorana versus Dirac CP Phase for case $C_{11} = 0$ for IH, where the range of δ = (0°,190°)

27.3 Numerical Analysis and Discussion

From plots of J_{cp} (not presented here) for both the cases it is found that it is consistent with the experimental data at 3σ confidence level when the Dirac CP phase (δ) is constrained in the range (0°, 190°) for both case $C_{11} = 0$ and $C_{12} = 0$.

27.3.1 Case $C_{11} = 0$

From the scatter plot of R_ν (not presented here) it is found that it remains consistent with the experimental data in the 3σ range when δ is further constrained in the range (5^o, 30^o) and (150^o, 170^o) for NH and (0^o, 190^o) for IH. On plotting the graph for Majorana CP-phases(α,β) for the allowed ranges of Dirac CP phase (δ) for case $C_{11} = 0$ we get the following scatter plot.

From the Fig. 27.1 we find that for NH α lies in the range (−20°, 20°) and β lies within (−25°, −1°) and (0, 25°). While from Fig. 27.2 we observe that for IH both α and β lies within the range (−30°, 30°).

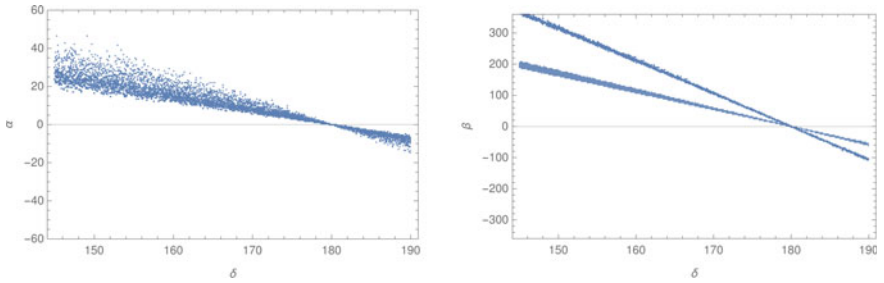

Fig. 27.3 Scatter plot for Majorana versus Dirac CP Phase for case $C_{12} = 0$ for NH, where δ is constrained in the range (145°, 190°)

27.3.2 Case $C_{12} = 0$

From R_ν plot (not presented here) for NH for case $C_{12} = 0$ it is found that it remains consistent with the experimental data at 3σ confidence level when δ is constrained in the range (145^o, 190^o). While for IH R_ν is inconsistent with the experimental data for all values of δ. Therefore this case is allowed only for NH. Now we plot Majorana versus Dirac CP phase for the allowed range of δ for NH (Fig. 27.3).

From the scatter plot we find that for NH, Majorana phase α is constrained within the range $(-15°, 45°)$ while β lies within $(-100°, 360°)$.

27.4 Conclusion

We have investigated CP-phases (δ, α, β) for neutrino mass matrices with one vanishing minor and vanishing sum of neutrino mass eigenvalues. In Case $C_{11} = 0$, based on the allowed ranges of values of J_{CP} and R_ν, Dirac CP-phases δ have been found to be constrained to the range (5°, 30°) and (150°, 170°) for NH, and (0°,190°) for IH. Such allowed ranges of δ has led to the constrained Majorana phases α to the range $(-20°, 20°)$, and β to the ranges $(-25°, -1°)$ and $(0°, 25°)$ for NH. Both α and β for IH lie in the same range $(-30°, 30°)$. In Case $C_{12} = 0$, following the similar procedure, we have found δ constrained to the range (145°, 190°) for NH, while for IH δ is forbidden. For NH the ranges of Majorana phases α and β have been constrained to $(-15°, 45°)$ and $(-100°, 360°)$, respectively.

References

1. S. Dev et al., Neutrino mass matrices with a texture zero and a vanishing minor. Phys. Rev. D **81**(5), 053010 (2010)
2. L. Lavoura, Phys. Lett. **B609**, 317 (2005); E.I. Lashin, N. Chamoun, Phys. Rev. **D80**, 093004 (2009); S. Dev,S. Gupta, R.R. Gautam, Mod. Phys. Lett. **A26**, 501 (2011)

3. S. Kaneko, H. Sawanaka, M. Tanimoto, J. High Energy Phys. **08**, 073 (2005)
4. X.-G. He, A. Zee, Neutrino masses with a “zero sum" condition:m 1+ m 2+ m 3= 0. Phys. Rev. D **68**(3), 037302 (2003)
5. D. Black et al., Complementary Ansatz for the neutrino mass matrix. Phys. Rev. D **62**(7), 073015 (2000)
6. M. Singh, The texture one-zero neutrino mass matrix with vanishing trace, in *Advances in High Energy Physics*, vol. 2018 (2018)
7. W. Wang, Neutrino mass textures with one vanishing minor and two equal cofactors. The Eur. Phys. J. C **73**(9), 1–8 (2013)
8. C. Jarlskog, Commutator of the quark mass matrices in the standard electroweak model and a measure of maximal CP nonconservation. Phys. Rev. Lett. **55**(10), 1039 (1985)

Chapter 28
Programmable Electro-Mechanical Dust Dispenser for Dusty Plasma Experimental Device

Nipan Das, S. S. Kausik, and B. K. Saikia

Abstract An electro-mechanical dust dispenser has been designed and developed for dropping dust into the plasma produced in dusty plasma experimental setup. Mechanical setup of the dust dispenser has been developed and fabricated in the laboratory. The frequency of vibration and amplitude of the developed dust dispenser can be controlled electronically to ensure precise and accurate density of dust in dusty plasma experiments. Drive circuits have been developed and integrated in the system that enable voltage and frequency control of the dispenser. Control signals are generated by LabVIEW software and applied to the inputs of drive circuit. A provision for predefined time interval for dust dropping time is also incorporated in the LabVIEW program. The dust dispenser has been calibrated for dust density using laser beam and photodiode arrangement.

28.1 Introduction

A plasma containing suspended dust particles of micron or submicron size, known as dusty plasma, is encountered in space plasmas [1], the mesosphere of the earth [2] and specifically designed laboratory experiments [1]. Study of dusty plasma is interesting because of the presence of dust particles alters the property of plasma significantly and can be used for development of other experimental devices such as negative hydrogen ion source reported in ref. [3]. At Centre of Plasma Physics Institute of Plasma Research (CPP-IPR), there are dusty plasma devices where various experiments are being conducted. In the same laboratory there is a sophisticated and complicated experimental device, where most of the instruments and subsystems are operated remotely from a PXI based data acquisition and control system (DAQ&C). In such a case, it becomes necessary to design and develop a dust dispenser which can also be controlled remotely from the same centralized computer with required level of precession and accuracy. Therefore, an electro-mechanical dust dispenser is designed, developed and fabricated. Graphical user interface (GUI) to control the

N. Das · S. S. Kausik (✉) · B. K. Saikia
Centre of Plasma Physics-Institute for Research, Sonapur, Assam 782402, India

S. Sengupta et al. (eds.), *Selected Progresses in Modern Physics*, Springer Proceedings in Physics 265, https://doi.org/10.1007/978-981-16-5141-0_28

dust dispenser is also developed. Finally, the dust dispenser is calibrated and the whole system is integrated for its full functionality. This paper reports details of the design, development, fabrication and calibration.

28.2 Brief Description of Dusty Plasma Experimental Device and PXI Based Data Acquisition and Control System

The experimental device has mainly three sections—Plasma generation chamber, dust dropping unit and dust collection chamber. A schematic diagram of the experimental device is shown in Fig. 28.1.

Hydrogen plasma is produced by thermionic emission technique in the plasma generation chamber at a working pressure of ~ 5×10^{-4} mbar. Produced plasma is confined by a magnetic cusp arrangement. Tungsten dust particles of size 1–5 microns are dropped from the top of the dust dispenser unit and allowed it to fall into the plasma. The developed dust dispenser will be used in basic experiments in

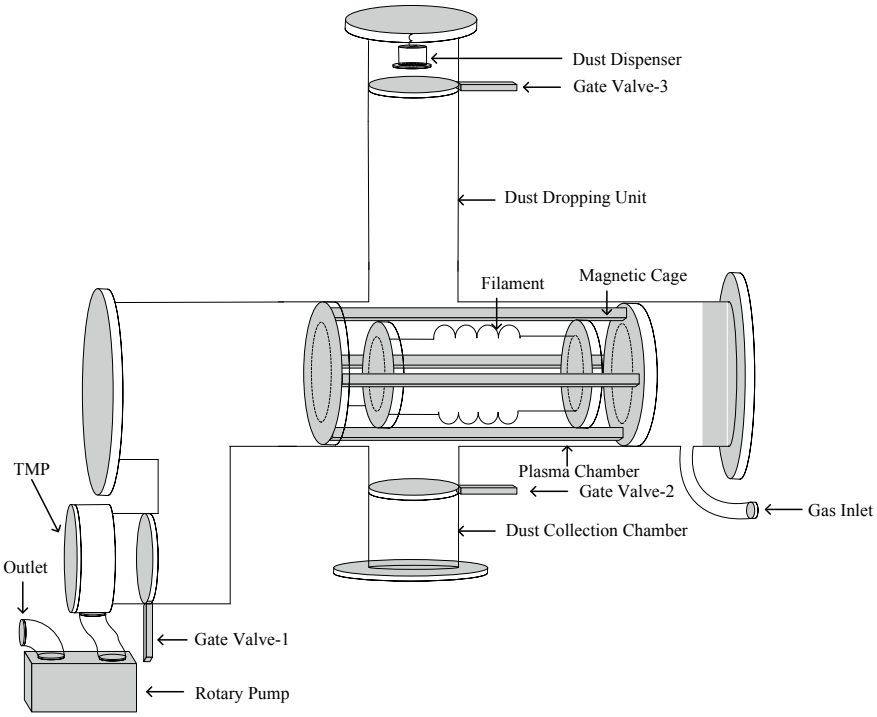

Fig. 28.1 Schematic of the experimental device

dusty plasma as well as for the production of negative hydrogen ions using cesium coated tungsten dust particles [3]. Since the experimental dusty plasma device is equipped with various kinds of instruments and subsystems, to acquire data, monitor and control different parameters, a PXI based DAQ&C is used. The data acquisition and control system is composed of a real time controller module (National Instruments™, PXIe-8840) and different input/output (IO) modules to meet the requirements. Some instruments have built-in measurement mechanism to monitor and control the parameters that can be accessed remotely from DAQ&C through proper communication interface. In some cases, parameters measured by sensors are fed to DAQ&C with developed signal conditioning circuit. Plasma diagnostics instruments are connected to DAQ&C through communication interfaces available to the instruments such as RS232, RS484, Ethernet etc. The whole system is controlled by a Real Time Controller in supervisory mode. User access is available at a host computer with the help of a properly developed GUI. Experimental data can be acquired in.csv format from controller to host computer.

28.3 Electro-Mechanical Dust Dispenser

The electro-mechanical dust dispenser has mainly two parts; suspended dust container and electro-mechanical striking unit. Schematic of the developed dust dispenser is shown in Fig. 28.2. A solenoid is used to activate the striker through the axial direction of the solenoid. The striker or the core is made of soft iron and aluminium road connected together. A suspension spring arrangement is made in such a way that soft iron part stay above the solenoid in absence of excitation current. On application of excitation current, the soft iron rod enters into the solenoid and the attached aluminium rod strikes dust container suspension support. The dust container is made of an aluminium cylinder attached with double layer 5 μm grid at the bottom. On top of the aluminium cylinder an arrangement is made to suspend the container with the help of two springs and guide rods. The fabricated dust dispenser is shown in Fig. 28.3.

28.4 Drive Circuit

The drive circuit consists of voltage regulator, feedback network and actuator driver. The circuit schematic is shown in Fig. 28.4. Drive circuit is powered by a 24 V, 10A power supply (Aplab, L3210). A transistor based series voltage regulator is designed to set voltage as per requirement such that amplitude of vibration can be controlled. The series voltage regulator is composed of a darlington pair of Q1 and Q2 (MJE13007) [4], error detector U1/2 (LM358) [5] and reference supply by U1/1 (LM358). Gain of U1/1 is represented by G and expressed by Eq. 28.1. G is set at 2.

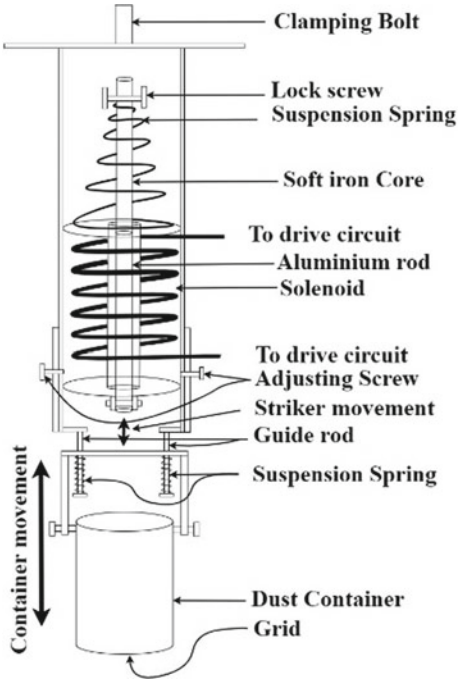

Fig. 28.2 Schematic of dust dispenser

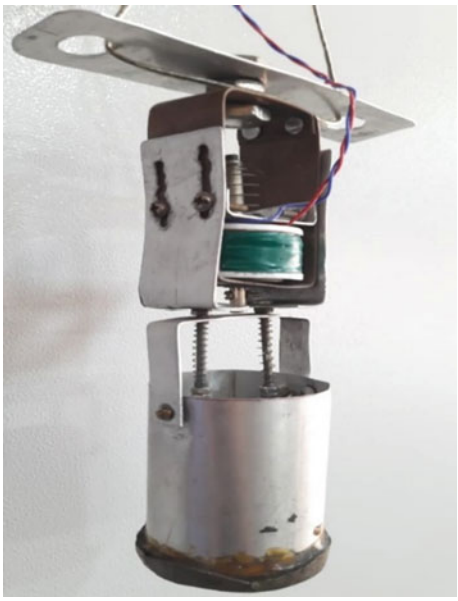

Fig. 28.3 Photograph of fabricated dust dispenser

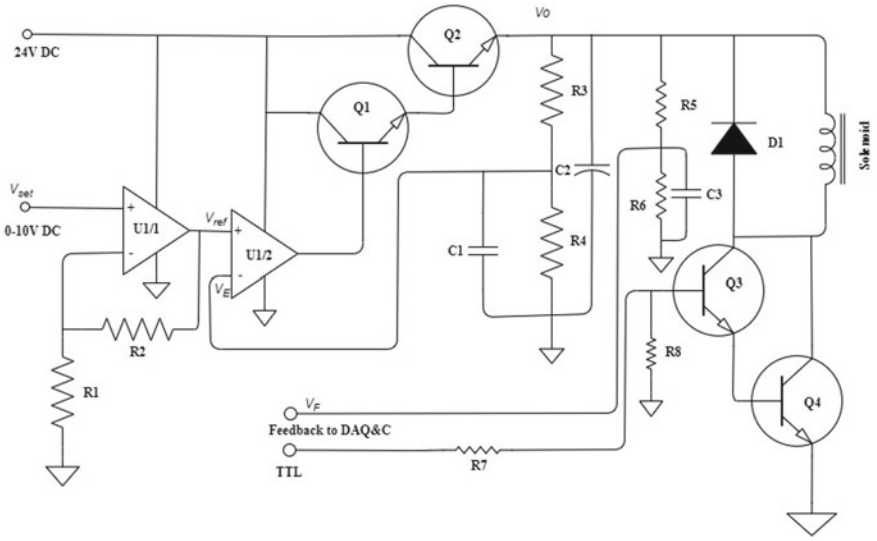

Fig. 28.4 Schematic of drive circuit

$$G = 1 + \frac{\text{R2}}{R1} \tag{28.1}$$

Error input voltage V_E is obtained from the output voltage of potential divider network composed of R3 and R4 as per the Eq. 28.2.

$$V_E = \frac{V_o}{R3 + R4} \times R4 \tag{28.2}$$

Capacitor C1 is used to decouple noise coming from solenoid during operation. On the other hand, capacitor C2 stabilizes the output voltage V_O.

Feedback voltage V_F to PXI system is obtained from the output voltage of another potential divider network composed of R5 and R6. Voltage at V_F is obtained from Eq. 28.3. C3 is used as decoupling capacitor.

$$V_F = \frac{V_o}{R5 + R6} \times R6 \tag{28.3}$$

Operating voltage is set by applying a suitable voltage from 0 to 10 V at *Vset* by PXI system. Feedback of the set voltage obtained from V_F is fed to the PXI system. Scaling is done in software.

Darlington pair composed of Q3 and Q4 (MJE13007) is used to drive the solenoid of dust dispenser. Darlington pair is excited by a TTL signal of appropriate frequency from PXI based DAQ&C system. Diode D1 is used as flywheel to supress back EMF produced by the solenoid during operation. The details of the components are given

Table 28.1 Components detail of drive circuit

Sl. No	Components	Part No./ type	Value
1	U1	LM358	–
2	Q1,Q2,Q3,Q4	MJE13007	–
3	C1, C3	Ceramic	0.1 μF
4	C2	Electrolytic	1000 μF
5	R1,R2,R3,R5	Carbon film, 0.25w	10kΩ
6	R4,R6	Carbon film, 0.25w	5 kΩ
7	R7	Carbon film, 0.25w	4.7 kΩ
8	R8	Carbon film, 0.25w	100kΩ

in Table 28.1. A TTL signal is from PXI system is used to drive the solenoid in required frequency.

28.5 GUI Development

To ensure proper operation and control of the whole system, algorithms have been developed and implemented on PXI controller. For user access and monitoring different parameters and instrument settings, a user interface is developed in the host PC using LabVIEW software. In Fig. 28.5, grounded tab of the developed GUI is shown. A close up of dust dispenser part is shown in Fig. 28.6. The dust dispenser has the provision to set operating voltage, vibrating frequency and predefined time duration for dust dispensing. Using START/STOP button dust dispensing can be initiated or terminated.

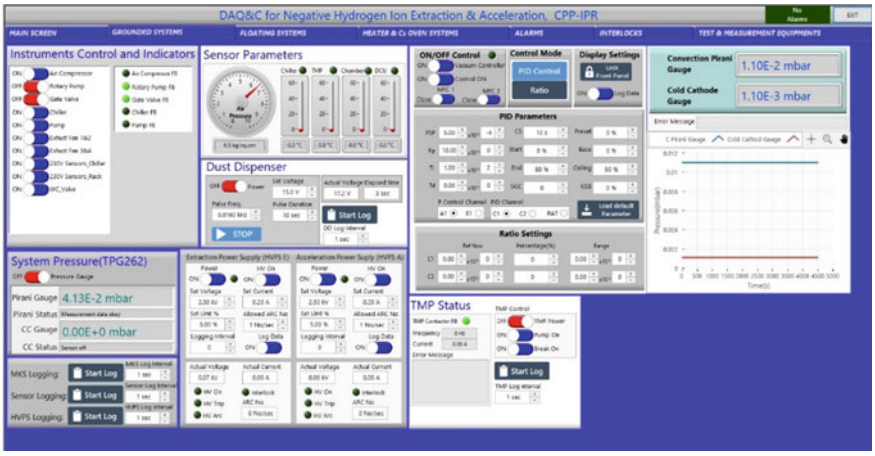

Fig. 28.5 Developed GUI for data acquisition and control

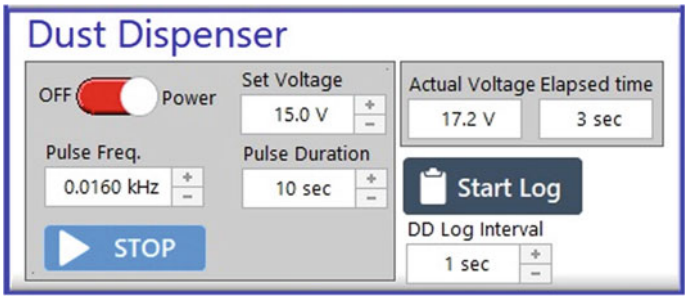

Fig. 28.6 Close up of dust dispenser control GUI part

28.6 Calibration and Testing

Before using the developed dust dispenser, it is necessary to calibrate the system and test its performance. The dust dispenser is calibrated using laser and photodiode arrangement. Calibration setup is shown in Fig. 28.7. A beam of wavelength 650 nm produced by a laser diode is used to illuminate tungsten (W) dust dropped from the dust container due to vibration. Intensity of the beam is controlled by a varying voltage source. Beam of the laser is spread out by a convex lens such that it uniformly falls on the entire sensing area of the used photodiode. The beam passes through the dropping dust column. As dust density changes, the amount of light also changes that falls on the photodiode sensing area and in turn the current through the photodiode. The change in current is measured by a multi-meter (RISH, multi18S) in current measurement mode. A 100kΩ resistor is used to protect the photodiode from overcurrent. A 20 V power supply is used to supply the current.

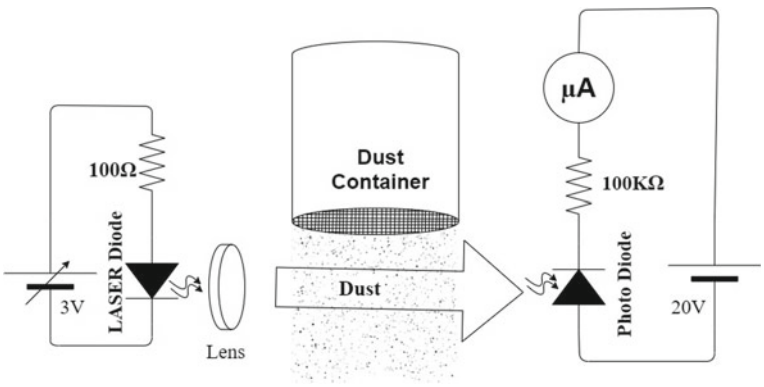

Fig. 28.7 Schematic of calibration setup

28.6.1 Dust Density Measurement

Dust density can be calculated using the formula shown in Eq. 28.4 [6].

$$I = I_0 e^{-\eta \pi a^2 l N_d} \tag{28.4}$$

where, I is the detector current with dust, I_0 is the detector current without dust, η is absorption coefficient, a is the radius of dust particle, l is the diameter of dust column, and N_d is the dust density. In our case, $\eta = 1$, $a = 3$ μm and $l = 5.24$ cm.

28.6.2 Frequency Response

The dust dispenser has been operated at 20 V and varying frequency from 10 to 30 Hz. Data is recorded and calculated the dust density using Eq. 28.4. Frequency versus dust density is plotted and shown in Fig. 28.8.

Average dust density is found to be $66.29 \times 10^5/\text{cm}^3$ in the frequency range of 10 to 30 Hz when operated in 20 V. Minimum and maximum dust densities in this range are $9.4 \times 10^5/\text{cm}^3$ and $1.06 \times 10^7/\text{cm}^3$. A minimum of $0.54 \times 10^5/\text{cm}^3$ and a maximum of $12.71 \times 10^5/\text{cm}^3$ standard deviations are observed in the dust density measurement.

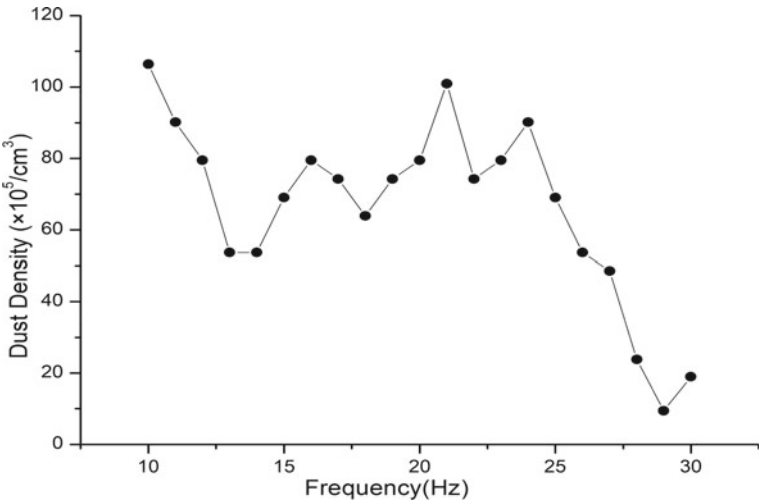

Fig. 28.8 Frequency versus dust density plot

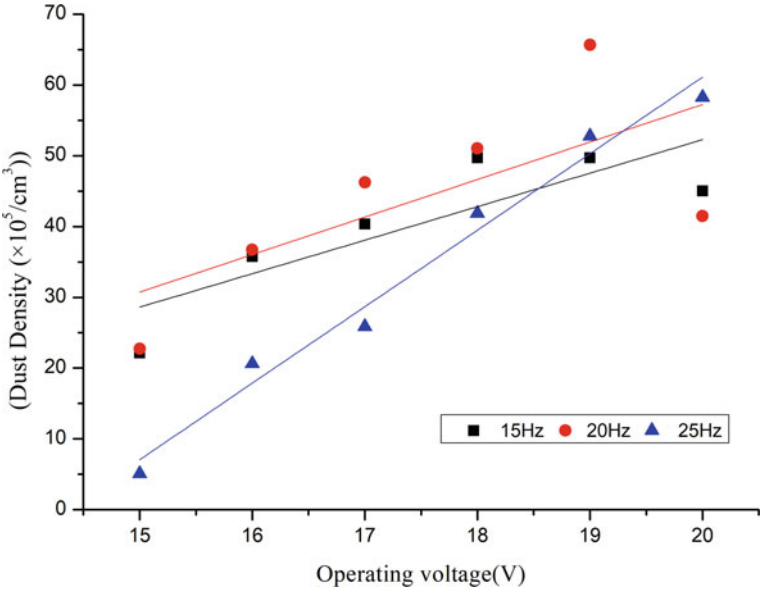

Fig. 28.9 Operating voltage versus dust density plot

28.6.3 Operating Voltage Response

The amplitude of vibration for the dust dispenser can be changed by setting different operating voltages keeping the operating frequency at a constant value. This results in variation of dust density. The dust dispenser has been tested at three different frequencies, 15, 20 and 25 Hz. The operating voltages have been changed from 15 to 20 V. Responses of the dust dispenser have been shown in Fig. 28.9.

Linear fit equations for the three frequencies, 15, 20 and 25 Hz are shown in Eqs. 28.5, 28.6 and 28.7, respectively, where y represents dust density and x represents applied operating voltage. The residual versus independent plot is shown in Fig. 28.10.

$$y = 4.73\text{x} - 42.30 \tag{28.5}$$

$$y = 5.30\text{x} - 48.69 \tag{28.6}$$

$$y = 10.81\text{x} - 155.09 \tag{28.7}$$

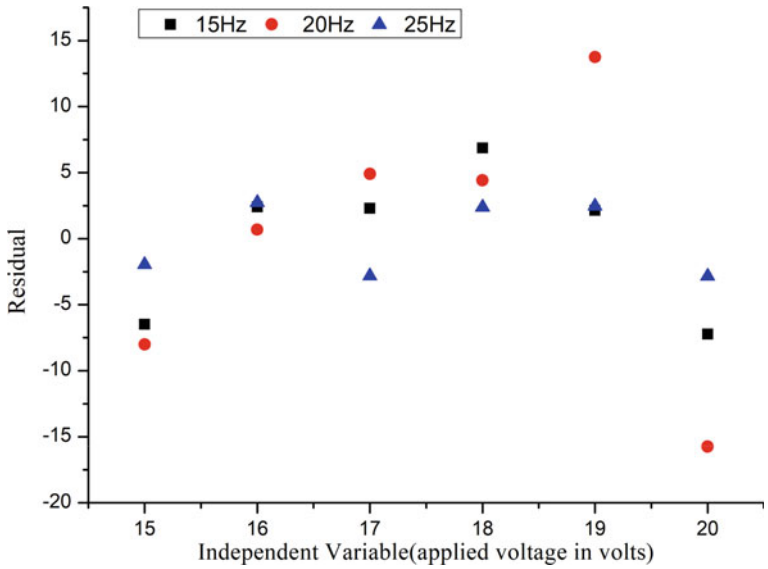

Fig. 28.10 Residual versus independent plot

28.7 Conclusions

An electro-mechanical dust dispenser is designed, developed and fabricated to use in dusty plasma experimental device. The density of dispensed dust can be controlled by controlling operating voltage and frequency. The dust dispenser is driven by a circuit that supplies operating voltage defined by PXI system in a specified frequency. A GUI is developed to control the developed dust dispenser as per user requirement. The developed system is calibrated using laser and photodiode arrangement. The dispenser can be operated in the frequency range of 10 to 30 Hz. An average of 66.29 $\times$ 10^5/cm^3 dust density was observed when the dust dispenser was operated in 20 V and 10–30 Hz frequency range. The observed minimum and maximum densities are 9.4 $\times$ 10^5/cm^3 and 1.06 $\times$ 10^7/cm^3 respectively. The dust dispenser is tested in three different frequencies and calibrated. Using calibration equations, the dust dispenser can be used as per the required dust density.

Acknowledgements The authors would like to thank Mr. G. D. Sarma and J. Barman for their helping hand in fabrication of the developed dust dispenser. A student trainee, Dhruba Jyoti Mudoi from Kaziranga University, Assam is also acknowledged for helping in data collection. Research scholars G. Sharma, R. Paul and K. Deka have been appreciated for their help in the work.

References

1. D.A. Mendis, Dust in cosmic plasma environments. Astrophys. Space Sci. **65**(1), 5–12 (1979). https://doi.org/10.1007/bf00643484
2. G.E. Morfill, A. Ivlev, Complex plasmas: an interdisciplinary research field. Rev. Mod. Phys. **81**(4), 1353–1404 (2009). https://doi.org/10.1103/RevModPhys.81.1353
3. B. Kakati, S.S. Kausik, M. Bandyopadhyay et al., Development of a novel surface assisted volume negative hydrogen ion source. Sci Rep **7**, 11078 (2017). https://doi.org/10.1038/s41598-017-10685-4
4. Datasheet of MJE13007. https://www.onsemi.com/pdf/datasheet/mje13007-d.pdf. Accessed 19 Mar 2021
5. Datasheet of LM358. https://www.ti.com/lit/ds/symlink/lm358-n.pdf?ts=1616104758153&ref_url=https%253A%252F%252Fwww.google.com%252F. Accessed 19 Mar 2021
6. Y. Nakamura, Experiments on ion-acoustic shock waves in a dusty plasma. Phys. Plasmas **9**, 440 (2002). https://doi.org/10.1063/1.1431974

Chapter 29
Radiation Exposure Due to Indoor Radon and Thoron in the Environs of Jowai Town, Meghalaya, India

A. Pyngrope and A. Saxena

Abstract Assessment of indoor activity levels of radon and thoron has been carried out in around 20 residential dwellings of Jowai town, Meghalaya, India. Passive integrated device—single-entry pin-hole dosimeter—based on solid-state nuclear track detectors (SSNTDs) has been used for the measurement methodology. Activity concentrations of measured radionuclides were found to vary appreciably amongst the studied dwellings. Overall, the activity levels were within the action level of 200–300 $Bq.m^{-3}$ as prescribed by International Commission on Radiological Protection (ICRP). The estimated inhalation dose due to radon and thoron was also found to be within the permissible limit of 3–10 $mSv.y^{-1}$.

29.1 Introduction

Radon is a naturally occurring radioactive gas that is ubiquitously present in the earth's atmosphere. In nature, radon mainly exists in three isotopic forms: ^{222}Rn (radon), ^{220}Rn (thoron) and ^{219}Rn (actinon). These radioisotopes originate from the decay series of ^{238}U, ^{232}Th and ^{235}U, respectively. Actinon is often neglected due to its shorter half-life and hence considered insignificant from the epidemiological point of view. Thoron also has a half-life of just 55.6 s, thus initially it was given less importance. But, later it is found that thoron's contribution to the overall exposure is notable [1]. Radium, the immediate parent of radon and thoron, is found in trace amounts in most of the commonly used building materials; this, in turn, can act as a significant source of indoor exposure. Besides, subsoil emanation beneath the floor is as well a potential contributor to indoor exposure [2, 3]. Apart from other radiation exposure, radon is considered to be one of the potential contributors to the overall exposure in a typical indoor environment and it is well documented that natural sources of radiation contribute about 82% of the total exposure dose to mankind, of which 52% is due to exposure to radon alone. The problem of exposure to radon and thoron in an indoor environment is considered so dire because on inhalation these

A. Pyngrope (✉) · A. Saxena
Department of Physics, North-Eastern Hill University, Shillong 793022, India

S. Sengupta et al. (eds.), *Selected Progresses in Modern Physics*, Springer Proceedings in Physics 265, https://doi.org/10.1007/978-981-16-5141-0_29

radionuclides can reach the lungs and cause irradiation of the soft epithelium tissues. Over time, it may cause cancer [4, 5].

The present study is carried out around the densely populated Jowai town, covering 20 residential dwellings, mainly concrete and semi-concrete structures, with an aim to investigate the difference in the indoor activity levels between these two types of dwelling. Further, the Jowai plateau is known to be composed of granites, sandstone, phyllite, limestones etc., which is one of the main reasons for choosing the study area, as trace amounts of primordial radionuclides are always present in such minerals, thereby becoming the potential radon/thoron emitters [6].

29.2 Materials and Methods

A new passive integrated instrument named 'pin-hole dosimeter' with single face entry, which is developed at Bhabha Atomic Research Centre, BARC, Mumbai, has been used for indoor measurement of radon and thoron. This dosimeter system consists of two chambers separated by a central disc of thickness 2 mm, and this disc contains four pin-holes of diameter 1 mm and length 2 mm, which basically act as thoron discriminator. At the entry a filter paper is fitted to trap the particulate radon and thoron progenies. Each chamber possesses a cylindrical shape of a common length of 4.1 cm and a radius of 3.1 cm. The dimension is so chosen to resonate with the sensitivity of the LR-115 detector. To attain a neutral electric field inside the chamber, metallic powders are coated inside, which helps in maintaining the uniformity in the deposition of progenies in the chamber volume [7] (Fig. 29.1).

Initially, LR-115 type-II film is fitted in both chambers of a pin-hole dosimeter. The dosimeter is then hanged at a height of 1.5 m above the floor and at least 10 cm away from the wall, to avoid possible disturbance during any household activity. The survey is for a period of three months. When the exposure period is due, detectors are retrieved and then subjected to chemical etching in 2.5 N NaOH solutions at a constant temperature of 60 C for about 90 ± 5 min. These films were then washed in running tap water and kept in a vacuum chamber for drying. The alpha tracks formed on the films are counted by using the standard spark counter at an operating voltage of 500 V prior to a pre-sparking voltage of 900 V [8].

Appropriate calibration factors have been used to obtain radon (C_r) and thoron (C_t) concentrations (in Bq.m^{-3}) from track densities recorded in both the filter and pin-hole compartments of the pin-hole dosimeter [7].

$$C_r = \frac{T_1 - B}{d.k_r} \tag{29.1}$$

$$C_t = \frac{T_2 - t_1}{d.k_t} \tag{29.2}$$

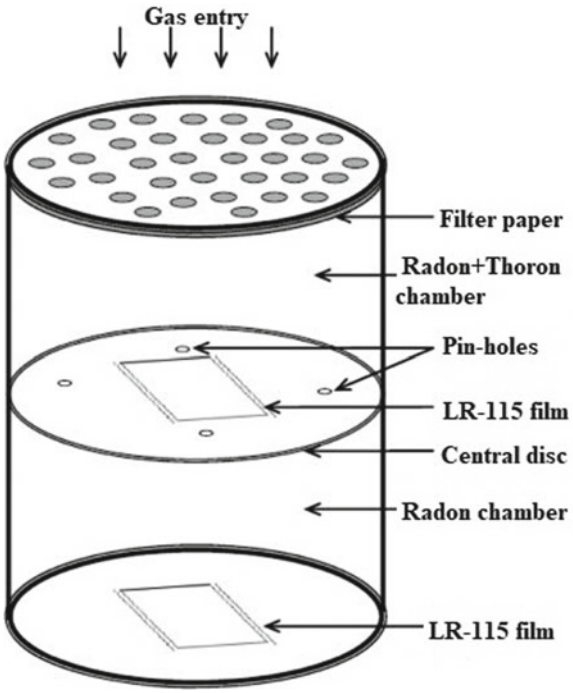

Fig. 29.1 Schematic diagram of a pin-hole dosimeter

where $k_r = 0.0170 \pm 0.002$ and $k_t = 0.010 \pm 0.001$ represent track density in 'radon' compartment and 'radon + thoron' compartment of the dosimeter, respectively, B is the background track density (~4 track cm^{-2}) on the LR-115 film which is usually subtracted from the observed track density, d represents the number of days of exposure, $k_r = 0.0170 \pm 0.002$ track.$cm^{-2}d^{-1}$(Bq.d.m^{-3})$^{-1}$ and $k_t = 0.010 \pm 0.001$ track.$cm^{-2}d^{-1}$(Bq.d.m^{-3})$^{-1}$ are the calibration factors for radon and thoron, respectively [7].

The inhalation dose due to radon and thoron is estimated using the following equation:

$$D(mSv) = 0.007\{(0.17 + 9F_r)C_r + (0.11 + 32F_t)C_t\} \tag{29.3}$$

where 0.17, 9, 0.11 and 40 {in unit of nSv (Bq.h.m^{-3})$^{-1}$} are the respective dose conversion factors of radon, radon progeny, thoron and thoron progeny. F_r and F_t are the respective radon and thoron equilibrium factors [3].

29.3 Results and Discussions

The indoor activity concentrations of radon and thoron together with the estimated inhalation dose and the respective GPS coordinates of the study's dwellings are given in Table 29.1. The average indoor activity concentrations of radon and thoron were found to be 39 ± 22 Bq.m^{-3} and 69 ± 55 Bq.m^{-3}, respectively, and the annual inhalation dose of the entire study region is estimated at 3 ± 1.6 mSv.y^{-1}. Figure 29.2 indicates appreciable variations of indoor activity of radon and thoron amongst the studied dwellings; this is attributed to few factors such as ventilation condition, the lifestyle of the inhabitants etc. It is also seen that the majority of the dwellings possessed indoor activity levels of both radon and thoron above the world average standard [9, 10]. Overall, the activity levels were within the action level of 200–300 Bq.m^{-3}, as prescribed by International Commission on Radiological Protection (ICRP) [11].

Figure 29.3 gives the box whisker plot of radon and thoron indoor activity in concrete and semi-concrete structures. From the plot, it is seen that concrete structure witnessed slightly higher indoor activity compared to semi-concrete, but the difference is not significant as seen from the t-test statistic (*p-value for radon is 0.06, p-value for thoron is 0.46*) [12], and this may be attributed to the typical design of concrete house structure, where in such house, floor, walls and ceiling are made of complete concrete, which enhances the process of radon/thoron emanation. Similarly, in the case of semi-concrete structures, the ceiling is made of either concrete or tin sheet, and the floor is usually of wood and the walls are concrete, so in such houses as well the contribution to the overall indoor activity is significant.

29.4 Conclusion

The indoor activity concentrations of radon and thoron have been measured in the environs of Jowai town, Meghalaya, India. It is observed that the values of measured radionuclides vary significantly amongst the studied dwellings, which is obvious from the high value of standard deviations of individual measurement. Fortunately, the overall activity levels were within the action level of 200–300 Bq.m^{-3}, as prescribed by International Commission on Radiological Protection (ICRP) [11]. The estimated inhalation dose due to these radionuclides was also found to be within the permissible limit of 3–10 mSv.y^{-1} [11]. With respect to house structure, it is seen that concrete witnessed a slightly higher indoor activity of both the radionuclides compared to semi-concrete; however, the difference is not significant as it is evident from the t-test statistic.

Table 29.1 Indoor activity concentrations of radon and thoron in concrete and semi-concrete types of dwelling of the study region, together with the estimated inhalation dose level, and their respective coordinate value

S. No.	GPS coordinate	House type	Radon conc. ($Bq.m^{-3}$)	Thoron conc. ($Bq.m^{-3}$)	Inhalation dose, D ($mSv.y^{-1}$)
1	N–25°27′ 80.91” E–92°11′ 38.77”	Semi-concrete	65 ± 6	21 ± 5	2.24
2	N–25°27′ 22.10” E–92°12′ 49.99”	Semi-concrete	36 ± 4	58 ± 7	2.34
3	N–25°27′ 24.73” E–92°13′ 22.27”	Concrete	26 ± 4	42 ± 6	1.69
4	N–25°26′ 01.95” E–92°11′ 25.08”	Semi-concrete	9 ± 2	23 ± 5	0.79
5	N–25°25′ 55.59” E–92°11′ 27.54”	Concrete	28 ± 4	81 ± 9	2.65
6	N–25°27′ 04.15” E–92°11′ 44.61”	Concrete	56 ± 6	58 ± 8	2.83
7	N–25°27′ 22.75” E–92°12′ 54.71”	Semi-concrete	37 ± 5	84 ± 9	2.94
8	N–25°27′ 25.79” E–92°12′ 57.39”	Concrete	8 ± 2	23 ± 5	0.78
9	N–25°26′ 20.34” E–92°11′ 49.70”	Semi-concrete	9 ± 2	71 ± 8	1.91
10	N–25°26′ 17.82” E–92°11′ 50.41”	Semi-concrete	43 ± 5	72 ± 8	2.83

(continued)

Table 29.1 (continued)

S. No.	GPS coordinate	House type	Radon conc. ($Bq.m^{-3}$)	Thoron conc. ($Bq.m^{-3}$)	Inhalation dose, D ($mSv.y^{-1}$)
11	N–25°25′ 57.73” E–92°11′ 47.08”	Concrete	60 ± 6	159 ± 12	5.30
12	N–25°27′ 10.61” E–92°12′ 02.57”	Concrete	32 ± 4	70 ± 8	2.48
13	N–25°27′ 00.93” E–92°11′ 39.50”	Concrete	70 ± 6	17 ± 4	2.27
14	N–25°27′ 08.36” E–92°11′ 50.32”	Semi-concrete	14 ± 3	79 ± 8	2.23
15	N–25°26′ 07.65” E–92°11′ 38.65”	Concrete	57 ± 6	12 ± 3	1.81
16	N–25°27′ 02.25” E–92°11′ 42.33”	Semi-concrete	30 ± 4	47 ± 6	1.90
17	N–25°27′ 02.81” E–92°11′ 40.29”	Concrete	87 ± 7	249 ± 15	8.08
18	N–25°26′ 15.60” E–92°11′ 44.59”	Semi-concrete	18 ± 3	21 ± 4	0.99
19	N–25°27′ 03.72” E–92°11′ 44.61”	Concrete	54 ± 5	63 ± 7	2.92
20	N–25°27′ 25.33” E–92°13′ 27.90”	Semi-concrete	36 ± 4	109 ± 10	3.51
Average (AM)			39	69	3
Standard deviation (SD)			22	55	1.6

[a]The uncertainty in the reported values is standard deviations.

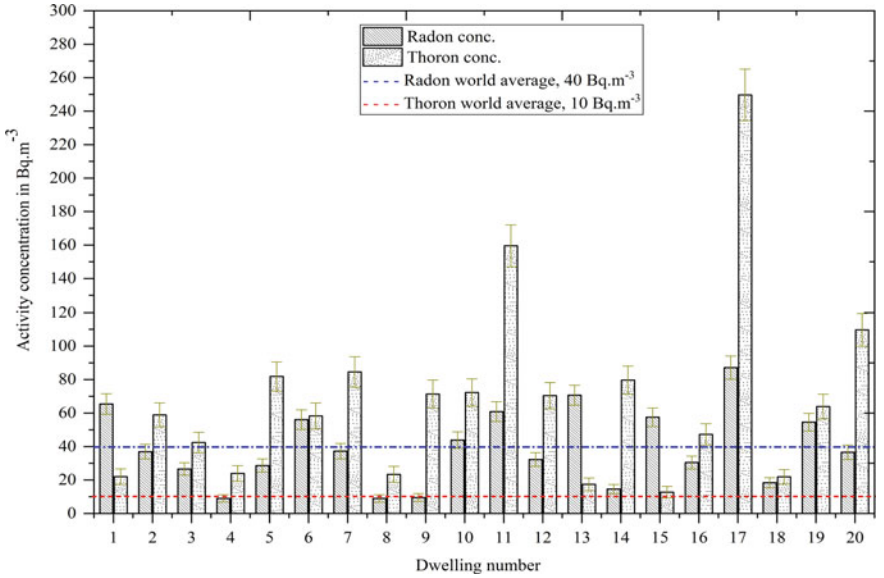

Fig. 29.2 Radon and thoron indoor activity concentrations in individual dwellings of the study region (with the demarcation of their respective world average values)

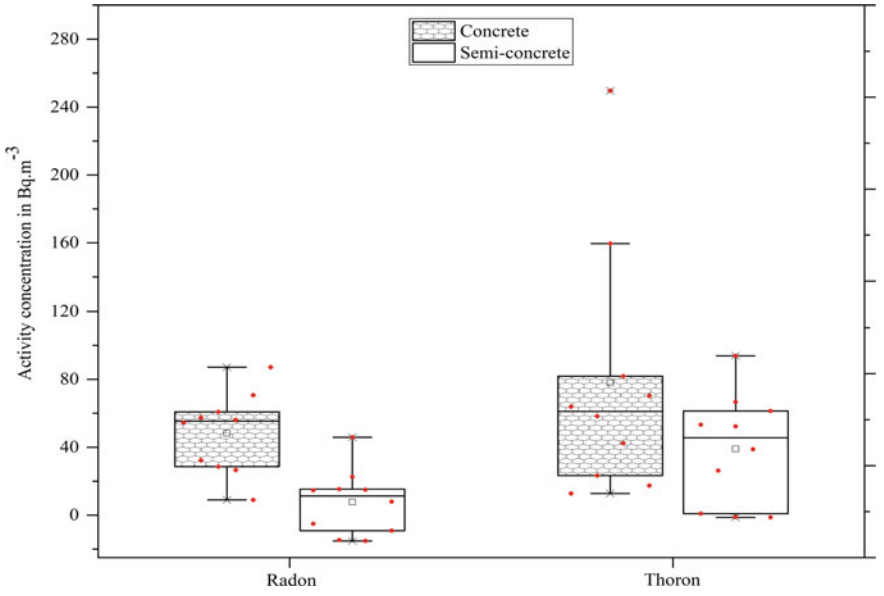

Fig. 29.3 Box-plot of indoor activity concentrations of radon and thoron in concrete and semi-concrete structures

Acknowledgements The authors are thankful to the Board of Research in Nuclear Science, BRNS-DAE for financial support in the form of a project.

References

1. W.W. Nazaroff, A.V. Nero, *Radon and Its Decay Products in Indoor Air*. (Wiley Inter Science Publication, 1988)
2. S.A Durrani, R. Illi¨c, *Radon Measurement By Etched Track Detectors.* (World Scientific Publishing co. Pte. Ltd, 1997)
3. UNSCEAR. United Nations Scientific Committee on the Effects of Atomic Radiation. *Sources and Effects Ionizing Radiation, Report to General Assembly With Scientific Annexes, Annex B, Exposure From Natural Sources of Radiation.* (United Nation, New York, 2000)
4. National Research Council. *Biological Effects of Ionizing Radiation, Health Effect of Radon and Other Internally Deposited Alpha Emitters: (Beir IV).* NRC Report. (National Academic Press, Washington DC, 1998)
5. World Health Organization. *WHO Handbook on Radon: A Public Health Prospective.* (2009)
6. www.westjaintiahills.gov.in
7. B.K. Sahoo, B.K. Sapra, S.D. Kanse, J.J. Gaware, Y.S. Mayya, A new pin hole discriminated $^{222}Rn/^{220}Rn$ passive measurement device with single entry face. Radiat. Meas. **58**, 52–60 (2013)
8. A. Pyngrope, A. Khardewsaw, Y. Sharma, D. Maibam, A. Saxena, B.K Sahoo, Study of indoor radon, thoron and their progeny in South-West Khasi Hills District of Meghalaya, India. Radiat. Prot. Dosim. **3**, 347–353 (2020)
9. UNSCEAR. United Nations Scientific Committee on the Effects of Atomic Radiation. *Sources and Effects Ionizing Radiation, Report to General Assembly With Scientific Annexes,* vol. 1. (United Nations, New York, 2008)
10. UNSCEAR. United Nations Scientific Committee on the Effects of Atomic Radiation. *Sources and Effect Ionizing Radiation*, *Report To General Assembly With Scientific Annexes*, *Annex E, Sources-to-Effects Assessment for Radon in Homes and Work-Places.* (United Nations, New York, 2006)
11. ICRP. International Commission on Radiological Protection. Radiological protection against radon exposure. Publication 126. Ann. ICRP (2014)
12. M.H. De Groot. *Probability and Statistics.* (Addison Wesley Publishing Company, 1975)

Chapter 30
Realization of Left-Right Symmetric Model by Discrete Flavor Symmetries

Bichitra Bijay Boruah and Mrinal Kumar Das

Abstract In this work, we have realized TeV-scale left-right symmetric model (LRSM), where type-I and type-II seesaw terms arise naturally using $A_4 \times Z_2$ discrete flavor symmetry. Within the model we have considered type-I dominant case to study neutrino phenomenology. Neutrinoless double beta decay (NDBD) is studied in the model by considering different contributions coming from extended particle content of the LRSM. We basically tried to find the leading order contributions to NDBD process in type-I dominance case in our work.

30.1 Left-Right Symmetric Model (LRSM) and Neutrino Mass

Left-right symmetric model (LRSM) [1, 4] has been extensively studied since 1970s by several groups. In LRSM, the fermions are assigned to the gauge group $\mathrm{SU(3)_c} \times \mathrm{SU(2)_L} \times \mathrm{SU(2)_R} \times \mathrm{U(1)_{B-L}}$ which is a very simple extension of the standard model gauge group where parity restoration is obtained at a high energy scale. The usual type-I and II seesaw terms arise naturally in LRSM. The RH neutrinos are a necessary part of LRSM which acquires a Majorana mass when the $SU(2)_R$ symmetry is broken at a scale v_R. Several other problems like parity violation of weak interaction, massless neutrinos, CP problems, hierarchy problems, etc. can also be addressed in the framework of LRSM. The seesaw scale is identified as the breaking of the $SU(2)_R$ symmetry. In this model, the electric charge generator is given by $Q = T_{3L} + T_{3R} + \frac{B-L}{2}$, where $\mathrm{T_{3L}}$ and $\mathrm{T_{3R}}$ are the generators of $\mathrm{SU(2)_L}$ and $\mathrm{SU(2)_R}$ and B-L being the baryon minus lepton number charge operator.

The Quarks are assigned with quantum numbers (3, 2, 1, 1/3) and (3, 1, 2, 1/3) and leptons with (1, 2, 1, −1) and (1, 1, 2, −1), respectively, under $\mathrm{SU(3)_c} \times \mathrm{SU(2)_L} \times \mathrm{SU(2)_R} \times \mathrm{U(1)_{B-L}}$. The Higgs sector in LRSM consists of a bi-doublet with quantum number Œ(1, 2, 2, 0) and the $SU(2)_{L,R}$ triplets, $\Delta_L(1, 2, 1, -1)$, $\Delta_R(1, 1, 2, -1)$.

B. B. Boruah (✉) · M. K. Das
Tezpur University, Tezpur 784028, Assam, India
e-mail: bijay@tezu.ernet.in

S. Sengupta et al. (eds.), *Selected Progresses in Modern Physics*, Springer Proceedings in Physics 265, https://doi.org/10.1007/978-981-16-5141-0_30

The Yukawa Lagrangian in the lepton sector is given by

$$\mathcal{L} = h_{ij}\overline{\Psi}_{L,i}\phi\Psi_{R,j} + \widetilde{h_{ij}}\overline{\Psi}_{L,i}\widetilde{\phi}\Psi_{R,j} + f_{L,ij}{\Psi_{L,i}}^{T}Ci\sigma_2\Delta_L\Psi_{L,j} + f_{R,ij}{\Psi_{R,i}}^{T}Ci\sigma_2\Delta_R\Psi_{R,j} + h.c. \quad (30.1)$$

where the family indices i, j are summed over, the indices $i, j = 1, 2, 3$ represents the three generations of fermions. $C = i\gamma_2\gamma_0$ is the charge conjugation operator, $\widetilde{\phi} = \tau_2\phi^*\tau_2$ and γ_μ are the Dirac matrices. Considering discrete parity symmetry, the Majorana Yukawa couplings $f_L = f_R$ (for left-right symmetry) give rise to Majorana neutrino mass after electroweak symmetry breaking when the triplet Higgs Δ_L and Δ_R acquire non-zero vacuum expectation value which leads to 6×6 neutrino mass matrix

$$M_\nu = \begin{bmatrix} M_{LL} & M_D \\ {M_D}^T & M_{RR} \end{bmatrix}, \quad (30.2)$$

where

$$M_D = \frac{1}{\sqrt{2}}(k_1 h + k_2\widetilde{h}), M_{LL} = \sqrt{2}v_L f_L, M_{RR} = \sqrt{2}v_R f_R, \quad (30.3)$$

where M_D, M_{LL}, and M_{RR} are the Dirac neutrino mass matrix, and left-handed and right-handed mass matrices, respectively. Assuming $M_L \ll M_D \ll M_R$, the light neutrino mass, generated within a type-I+II seesaws can be written as

$$M_\nu = {M_\nu}^I + {M_\nu}^{II}, \quad (30.4)$$

$$M_\nu = M_{LL} + M_D {M_{RR}}^{-1} {M_D}^T = \sqrt{2}v_L f_L + \frac{k^2}{\sqrt{2}v_R} h_D {f_R}^{-1} {h_D}^T, \quad (30.5)$$

where the first and second terms in Eq. (30.5) correspond to type-II seesaw and type-I seesaw mediated by RH neutrino, respectively. Here,

$$h_D = \frac{(k_1 h + k_2\widetilde{h})}{\sqrt{2}k}, k = \sqrt{|k_1|^2 + |k_2|^2}. \quad (30.6)$$

In the context of LRSM, both type-I and type-II seesaw terms can be written in terms of M_{RR} which arises naturally at a high energy scale as a result of spontaneous parity breaking. In LRSM, the Majorana Yukawa couplings f_L and f_R are same (i.e., $f_L = f_R$) and the VEV for left-handed triplet v_L can be written as

$$v_L = \frac{\gamma {M_W}^2}{v_R}. \quad (30.7)$$

Table 30.1 Fields and their respective transformations under the symmetry group of the model

Field	l_L	l_R	Φ	Δ_L	Δ_R	χ^l	χ^ν	ϵ
$SU(2)_L$	2	1	2	3	1	1	1	1
$SU(2)_R$	1	2	2	1	3	1	1	1
$U(1)_{B-L}$	-1	-1	0	2	2	0	0	0
A_4	3	3	1	1	1	3	3	1
Z_2	0	0	1	0	0	1	0	1

Thus, Eq. (30.5) can be written as

$$M_\nu = \gamma(\frac{M_W}{v_R})^2 M_{RR} + M_D {M_{RR}}^{-1} {M_D}^T. \tag{30.8}$$

30.2 A Left-Right Flavor Symmetric Model

In the present work, the symmetry realization of the structure of the mass matrices has been carried out using the discrete flavor symmetry A_4 [2, 5], which is a group of permutation of four objects, isomorphic to the symmetry group of a tetrahedron with an additional Z_2 symmetry. The particle content and the charge assignments are detailed in Table 30.1.

The Lagrangian of all Yukawa term can be written as

$$\begin{aligned}\mathcal{L}_Y = \bar{l}_L(Y_\epsilon\epsilon + Y_{l1}\chi^l + Y_{l2}\chi^l)\Phi l_R + \bar{l_L}(\tilde{Y}_\epsilon\epsilon + \tilde{Y}_{l1}\chi^l + \tilde{Y}_{l2}\chi^l)\tilde{\Phi} l_R \\ + \bar{l^c}_R(Y_R^0 + Y_R^\nu\chi^\nu)i\tau_2\Delta_R l_R + \bar{l^c}_L(Y_R^0 + Y_R^\nu\chi^\nu)i\tau_2\Delta_L l_L.\end{aligned} \tag{30.9}$$

30.2.1 Type-I Dominance

In case of type-I dominance scenario, the terms involving Δ_L are omitted since $\nu_l = 0$. Again, if we assume v_L is sufficiently small, then Dirac neutrino mass matrix M_D and charge lepton mass matrix M^l are given by

$$M_l = \nu_2 Y + \nu_1 \tilde{Y}, M_D = \nu_1 Y + \nu_2 \tilde{Y}, \tag{30.10}$$

where ν_1 and ν_2 are VEV of the Higgs bi-doublet and (Y ,$\tilde{Y}$) are Yukawa coupling which are given by

$$Y = Y_\epsilon + Y_{l1} + Y_{l2}, \tilde{Y} = \tilde{Y}_\epsilon + \tilde{Y_{l1}} + \tilde{Y_{l2}}. \tag{30.11}$$

In our work, we take the flavor alignment to be $\chi^l - (1, 0, 0)$, $\chi^\nu - (1, \omega, \omega^2)$. Now, this leads to diagonal charge lepton mass matrix given by

$$M_l = \begin{pmatrix} a+2b & 0 & 0 \\ 0 & a+(c-b) & 0 \\ 0 & 0 & a-(b+c) \end{pmatrix},$$

where $a = \nu_2 y_{l0} + \nu_1 \tilde{y_{l0}}$, $b = \nu_2 y_{l1} + \nu_1 \tilde{y_{l1}}$, and $c = \nu_2 y_{l2} + \nu_1 \tilde{y_{l2}}$.

Now, Dirac neutrino mass matrix (M_D) shares the same structure as charge lepton mass matrix (M_l) which can be further factorized into the form given below:

$$M_D = \lambda \begin{pmatrix} 1 & 0 & 0 \\ 0 & r_1 & 0 \\ 0 & 0 & r_2 \end{pmatrix},$$

where $\lambda = \nu_1 y_{l0} + \nu_2 \tilde{y_{l0}}$, $r_1 = \frac{\nu_1 y_{l1} + \nu_2 \tilde{y_{l1}}}{\lambda}$, and $r_2 = \frac{\nu_1 y_{l2} + \nu_2 \tilde{y_{l2}}}{\lambda}$.

The Majorana mass matrix is

$$M_R = a_R \begin{pmatrix} 2z+1 & -\omega^2 z & -\omega z \\ -\omega^2 z & 2\omega z & 1-z \\ -\omega z & 1-z & 2\omega^2 z \end{pmatrix},$$

where $a_R = \nu_R y_{R0}$ and $z = \frac{y_R}{y_{R0}}$. Now, the relevant mass generation formula for type-I dominance:

$$m_\nu = M_D^T M_R^{-1} M_D. \tag{30.12}$$

So, light neutrino mass matrix will be

$$m_\nu = \frac{m}{3z+1} \begin{pmatrix} z+1 & \omega z r_1 & \omega^2 z r_2 \\ \omega z r_1 & \omega^2 \frac{z(3z+2) r_2^2}{3z-1} & \frac{(z-3z^2+1) r_1 r_2}{1-3z} \\ \omega^2 z r_2 & \frac{(z-3z^2+1) r_1 r_2}{1-3z} & \frac{\omega z (3z+2) r_2^2}{3z-1} \end{pmatrix}.$$

30.3 Numerical Analysis and Results

We have constructed flavor symmetric model for type-I dominance and studied LNV (NDBD) [4] for standard as well as non-standard contributions for the effective mass as well as the half-life governing the decay process in the framework of LRSM. In standard model contribution to NDBD, the intermediate particles are the W_L^- bosons and light neutrinos. Effective mass governing this process is given by

$$\mathrm{m}_\circ^{\mathrm{eff}} = \mathrm{U}_{\mathrm{Li}}^2 \mathrm{m_i}, \tag{30.13}$$

where U_{Li} are the elements of the first row of the neutrino mixing matrix. U_{PMNS} is the diagonalizing matrix of the light neutrino mass matrix, m_ν, such that

$$m_\nu = U_{PMNS} M_\nu^{(diag)} {U_{PMNS}}^T, \tag{30.14}$$

where $M_\nu^{diag} = diag(m_1, m_2, m_3)$. In heavy right-handed neutrino contribution to NDBD, the mediator particles are the W_R^- bosons. We have also considered the contribution to NDBD from the triplet Higgs (Δ_R). Although the contribution of this can be suppressed if we invoke the constraints from LFV decays. We will discuss this contribution in certain conditions.

The contribution coming from right-handed current can be written as

$$m_N^{ee} = p^2 \frac{{M_{W_L}}^4}{{M_{W_R}}^4} \frac{{U_{Rei}}^* 2}{M_i}. \tag{30.15}$$

Here, $< p^2 >= m_e m_p \frac{M_N}{M_\cdot}$ is the typical momentum exchange of the process, where m_p and m_e are the mass of the proton and electron, respectively, and M_N is the NME corresponding to the RH neutrino exchange. We know that TeV-scale LRSM plays an important role in $0\nu\beta\beta$ decay. We have considered the values M_{W_R} = 10 TeV, M_{W_L} = 80 GeV, M_{Δ_R} ≈3TeV, the heavy RH neutrino ≈ TeV which are within the recent collider limits.

We discuss the impact of scalar triplet contribution in the limit, $M_{\Delta_R} = M_{heaviest}$. In this case, we can write down the contribution of scalar triplet (Δ_R) to the effective mass as

$$|m_{\Delta^{ee}}| = |p^2 \frac{{M_{W_L}}^4}{{M_{W_R}}^4} \frac{2M_N}{M_{\Delta_R}}|. \tag{30.16}$$

From Fig. 30.1, we can say that the effective mass of active neutrinos and new physics contribution coming from heavy neutrinos that we have obtained abides by

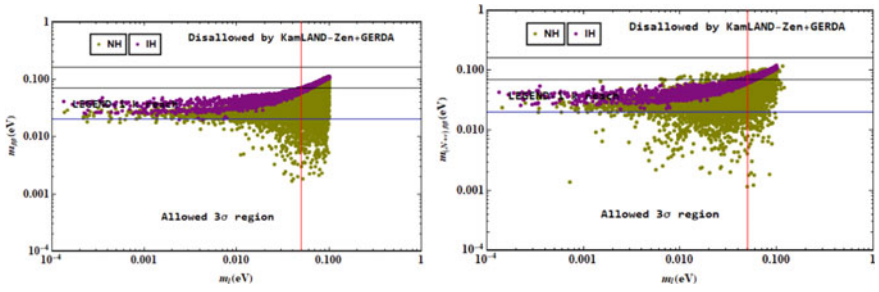

Fig. 30.1 The light neutrino contribution (left) and the total contribution (right) to neutrinoless double beta decay process considering new physics contribution coming from heavy neutrino, i.e., $|m_{N+\nu}{}^{eff}|$ for type-I considering both NH and IH cases. The black and the red solid lines represent the KamLAND-Zen bound on the effective mass and the Planck bound on the sum of the absolute neutrino mass, respectively. Blue color solid line represents the Legend-1k reach

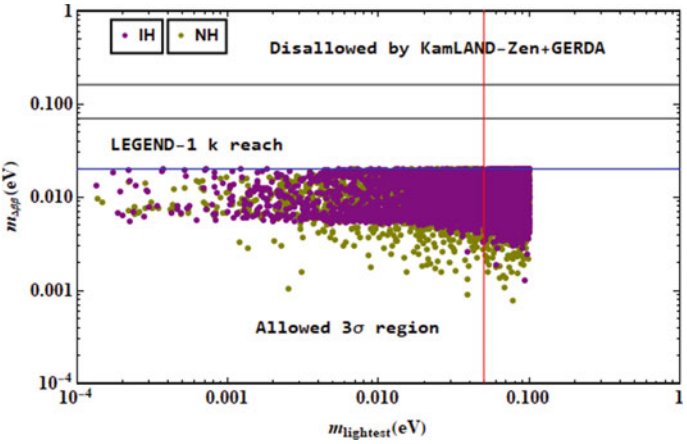

Fig. 30.2 The scalar triplet contribution to neutrinoless double beta decay process for type-I (left) and type-II (right) considering both NH and IH cases. The black and the red solid lines represent the KamLAND-Zen bound on the effective mass and the Planck bound on the sum of the absolute neutrino mass, respectively

the upper limit given by KamLAND-Zen experiment for both NH and IH. Also, it is seen that the lightest neutrino mass is of sub-eV which further implies to the summation of the neutrinos to obey the Planck limit, viz., $\sum_{k=1,2,3} m_k < 0.11$ eV. Although some of the points are excluded by Legend-1k reach. Again from Fig. 30.1, we can conclude that contribution coming from scalar triplet to the NDBD process lies within the experimental range.

30.4 Conclusion

We have limited our analysis to neutrinoless double beta decay in our flavor symmetric LRSM. In the standard light neutrino and total contribution considering new physics coming from heavy neutrino for type-I (NH/IH) dominance case shows results within the recent experimental bound for lightest mass varying from (0.00001–0.1) eV, respectively. Scalar triplet contributions for type-I (NH/IH) dominance are found to be 10^{-2} eV and 10^{-3} eV in the light neutrino mass range (0.0001–0.1) eV and (0.001–0.1) eV, respectively. It can be firmly concluded that the model is viable in light of the experiments undertaken to measure the effective neutrino mass.

References

1. G. Senjanovic, R.N. Mohapatra, Phys. Rev. D **12**, 1502 (1975). https://doi.org/10.1103/PhysRevD.12.1502
2. W. Rodejohann, Int. J. Mod. Phys. E **20**, 1833–1930 (2011) [arXiv:1106.1334 [hep-ph]]. https://doi.org/10.1142/S0218301311020186
3. K.S. Babu, S. Pakvasa, Neutrino Masses and Family Symmetry. Phys. Lett. B **172**, 360–362 (1986). https://doi.org/10.1016/0370-2693(86)90270-4
4. H. Borgohain, M.K. Das, Int. J. Theor. Phys. **56**(9), 2911–2934 (2017) [arXiv:1705.00922 [hep-ph]]. https://doi.org/10.1007/s10773-017-3458-8
5. W. Rodejohann, X.J. Xu, Eur. Phys. J. C. **76**(3), 138 (2016) [arXiv:1509.03265 [hep-ph]]. https://doi.org/10.1140/epjc/s10052-016-3992-1

Chapter 31
Relation Between the Variability of the Kilo-Hertz Quasi-Periodic Oscillations and the Low-Frequency Noise in $4U\,1608-52$

Soma Mandal

Abstract The neutron star low-mass X-ray binary $4U\,1608-52$ is known to show kHz QPOs as well as low-frequency noise. The energy dependence of the fractional r.m.s. amplitude of the kHz QPO reflects the underlying radiative mechanism responsible for the QPOs irrespective of their dynamical origin. In this work, we compute the energy dependence for 26 instances of kHz QPO observed by *RXTE*. We typically find as reported before that the r.m.s increases with energy in the slope of ~ 0.4. This indicates that the variation is in the hot thermal compotonization component and, in particular, the QPO is likely to be driven by variation in the thermal heating rate of the hot plasma. For the same data, we compute the energy-dependent r.m.s. variability of the low-frequency noise component by considering the light curves. In contrast to the behavior seen for the kHz QPO, the energy dependence is nearly flat, i.e., the r.m.s. is energy independent. This indicates that the driver here may be the soft photon source. Thus, the radiative mechanism driving the low-frequency noise and the high-frequency QPO is different in nature.

31.1 Introduction

Quasi-periodic oscillations (QPOs) are near-sinusoidal variability observed in both black hole and neutron star systems. QPOs appear as one or more relatively narrow peaks in the Fourier power density spectra. For neutron star systems, their frequencies are roughly between millihertz (mHz) and kilohertz (kHz) [1, 2]. Since kHz frequencies are of the same order as the orbital frequency close to the compact object, the phenomenon is associated with regions close to the surface of the neutron star. KHz QPOs are often seen in pairs and are named as the higher and the lower kHz QPOs. The frequencies of the kHz QPOs are strongly correlated with spectral and other timing properties [3–6]. Several authors have investigated the correlations between the upper and the lower kHz QPO frequencies [7–12] and these have been used to

S. Mandal (✉)
Department of Physics, Government Girls' General Degree College, 7, Mayurbhanj Road, Kolkata 700023, India

S. Sengupta et al. (eds.), *Selected Progresses in Modern Physics*, Springer Proceedings in Physics 265, https://doi.org/10.1007/978-981-16-5141-0_31

discriminate between various dynamical models proposed for the phenomena. Different models have been invoked to explain the physical origin of the kHz QPO. These include the relativistic precession model [13, 14], the MHD Alfvén wave oscillation model [15], the resonance model [16, 17], etc. But there is no universally accepted model that satisfactorily explains all the features of QPO signals and pinpoint a single mechanism. Lin et al. [18] studied the frequency relationship between the upper and the lower kHz QPOs by comparing the observations to some theoretical models. Each model has its own merits and demerits. The earlier proposed beat frequency [19, 20] and constant ratio models [16, 17, 21] were not supported by subsequent observations [10, 11].

All these models typically depend on the identification of the different frequencies as natural characteristic frequencies of the system and their strength or weakness depends on their ability to predict the correlations between different frequencies. While these dynamical models provide insight into the nature of the system, it is also important to understand the radiative mechanism responsible for the phenomenon.

Since some of the low-frequency QPO are observed to be correlated to the high-frequency ones, they may have a common origin and typically these properties are correlated with the spectral state inferred from color-color diagram [22].

Troyer et al. [23] performed a systematic spectral-timing analysis of kHz QPOs in the *RXTE* archive with a conclusion that while the production mechanism of kHz QPOs is the same for all populations of LMXBs, the emission mechanism of two types of kHz QPOs is different.

In addition to QPOs, low-frequency part of the power spectra is usually dominated by a broadband noise component, but it is not clear whether these are physically the same component or not [24].

Whatever their physical origin, the high frequency of these oscillations suggests that they probably originate in the innermost regions of these system and hence, in principle, could be used to probe and test effects of general relativity in the strong field limit. Moreover, a study of the temporal behavior of these systems, particularly QPO activity, could give new insight into the nature of these systems.

Clues to such underlying processes can also be obtained by studying the energy dependence of the QPO features like the amplitude and the phase lags. Variation of the r.m.s. and the time lag as a function of energy of this high-frequency oscillations can give crucial information regarding the size of the emitting region [25–27]. For the low-frequency case, there may be a causal connection between the spectral parameters [28]. Typically, the fractional r.m.s. amplitude increases with energy for neutron star low-mass X-ray binaries (LMXBs) [29]. It has also been reported that the fractional r.m.s. amplitude of kHz QPO increases with photon energy at lower energies and then saturates [2, 30]. Theoretical studies showed that an oscillating hot thermal corona may contribute to an overall increase of the r.m.s. amplitude with energy [31]. Kumar & Misra (2014) [26] developed a model to study the time lag due to the thermal compotonization. Their model predicted the shape of the r.m.s. as a function of energy as well as expected time lag as a function of energy. The observed energy-dependent features of the QPO are expected to depend primarily on the radiative mechanism and its coupling to the dynamic behavior of the system. The energy

dependence of the r.m.s. amplitude variability can be useful to probe the origin of the kHz QPO. Study of correlation between this high- and the low-frequency variabilities can put constraints on the origin of both the variability modes.

Here, in this work, we have carried out a systematic study of the energy dependence of the r.m.s. amplitude of kHz QPOs and low-frequency broadband noise observed in the X-ray emission of the neutron star LMXB $4U\,1608-52$, using archival data obtained with the *Rossi X-ray Timing Explorer* (*RXTE*). We have investigated the relationship between the energy dependence of the r.m.s. variability of both kHz QPOs and low-frequency broadband noise. We discussed whether this relationship displays features that could have a physical meaning in terms of the proposed QPO models.

$4U\,1608-52$ is a transient atoll source that shows outbursts with a waiting period varying between 80 days and several years [32]. G*ü*ver et al. [33] reported a distance of $5.8^{+2.0}_{-1.9}$ kpc and a NS mass of $M = 1.74 \pm 0.14 M_{\odot}$ with a radius of $R = 9.3 \pm 1.0$ km by studying the interstellar extinction toward the source. There are other estimates by using different methods [34, 35]. Low-frequency QPOs were discovered with the *Ginga* satellite [36] and kHz QPOs were discovered with *RXTE* [29, 37]. This is a well-studied source. Timing and spectral properties have been extensively studied by several authors [38–46]. Barret [44] and de Avellar et al. [47] showed that the energy and frequency dependence of the Fourier time lag and intrinsic coherence of the kHz QPOs with a hint of reverberation lag detected in AGN and stellar mass black hole. Cackett [48] showed that the observed lags in the lower kHz QPO of $4U\,1608-52$ cannot be explained only by reverberation.

31.2 Observations and Data Analysis

We have utilized the data from the *RXTE* archive for the neutron star system $4U\,1608-52$ taken by the Proportional Counter Array (PCA). $4U\,1608-52$ was observed 1145 times with the PCA during the lifetime of *RXTE*. We have taken data starting from the longest exposure time to ~ 3 kilosecond (ks) for our analysis. The analysis was limited to those observations taken in event modes, observations with no event mode data has been excluded from the dataset. In our dataset, we found several type-I X-ray bursts and we have excluded those dataset from our analysis.

We used the X-ray timing software GHATS[1] version 1.1.0 to generate power density spectra (PDS). We have extracted power density spectra for each event file and searched for QPOs. We have checked for all observations taken up to 3 ks exposure time. For 12 observations, a total of 26 event mode data, we have detected strong QPO signal. The lists of Observation IDs and the event files along with the start time of observation are given in Table 31.1.

[1] A package of General High Energy Aperiodic Timing Software developed by T. M. Belloni at INAF—Osservatorio Astronomico di Brera.

Table 31.1 Log of the observations of $4U\,1608-52$ used in this analysis

Sl. No.	Observation ID	Event file	Start time
1	10072-05-01-00	FS37-4153340-415408a	03/03/1996-19:18:24
2	10072-05-01-00	FS37-41549c0-4155836	03/03/1996-20:54:24
3	10072-05-01-00	FS37-4156040-4156772	03/03/1996-22:30:24
4	30062-02-01-000	FS37-7f315df-7f320aa	24/03/1998-15:37:03
5	30062-02-01-000	FS37-7f32b10-7f3390b	24/03/1998-17:07:28
6	30062-02-01-000	FS37-7f34190-7f34f8b	24/03/1998-18:43:28
7	30062-02-01-00	FS37-7f37030-7f37c8a	24/03/1998-22:02:24
8	30062-02-01-00	FS37-7f38a70-7f3930b	24/03/1998-23:54:24
9	30062-02-01-01	FS37-7f44f90-7f45a06	25/03/1998-13:55:28
10	30062-02-01-01	FS37-7f46610-7f473ce	25/03/1998-15:31:28
11	30062-02-01-01	FS37-7f47c90-7f48a4f	25/03/1998-17:07:28
12	30062-02-01-01	FS37-7f49310-7f49ab7	25/03/1998-18:43:28
13	30062-02-01-02	FS37-7f5a110-7f5abc3	26/03/1998-13:55:28
14	30062-02-01-02	FS37-7f5b790-7f5c54e	26/03/1998-15:31:28
15	30062-02-01-02	FS37-7f5ce10-7f5d503	26/03/1998-17:07:28
16	30062-01-01-00	FS37-7f6de19-7f6e51e	27/03/1998-12:28:09
17	30062-01-01-00	FS37-7f708d0-7f716cf	27/03/1998-15:30:24
18	30062-01-01-01	FS4f-7f84610-7f84f3a	28/03/1998-14:04:00
19	30062-01-01-02	FS4f-7f951d0-7f9584f	29/03/1998-09:06:24
20	30062-01-01-02	FS4f-7f96850-7f97072	29/03/1998-10:42:24
21	70059-01-20-00	FS4f-1054b8a0-1054c660	07/09/2002-03:43:28
22	70059-01-20-00	FS4f-1054cee0-1054dca4	07/09/2002-05:18:24
23	70059-03-01-00	FS4f-105b99b0-105ba1d9	12/09/2002-08:57:20
24	70059-03-02-07	FS4f-105f12c0-105f1d2c	15/09/2002-00:10:40
25	70059-03-02-07	FS4f-105f24f0-105f3370	15/09/2002-02:30:08
26	95334-01-03-04	FS4f-1e7addf0-1e7aebea	16/03/2010-14:52:53

This observation log lists the Serial no. of the science event file, Observation ID, Event File name, and start time of the observation dataset taken by *RXTE* PCA

We have taken these event files to compute the fractional r.m.s. amplitude at the lower kHz QPO frequency. We have taken standard products for background correction. For the low-frequency broadband noise, same dataset of event files was taken and a frequency range of 0.6–50 mHz has been taken into consideration to calculate the r.m.s. amplitude of low-frequency broadband noise. The energy dependence of the r.m.s. amplitude is plotted for some of the cases. We have fitted a linear function of these data and found the slope.

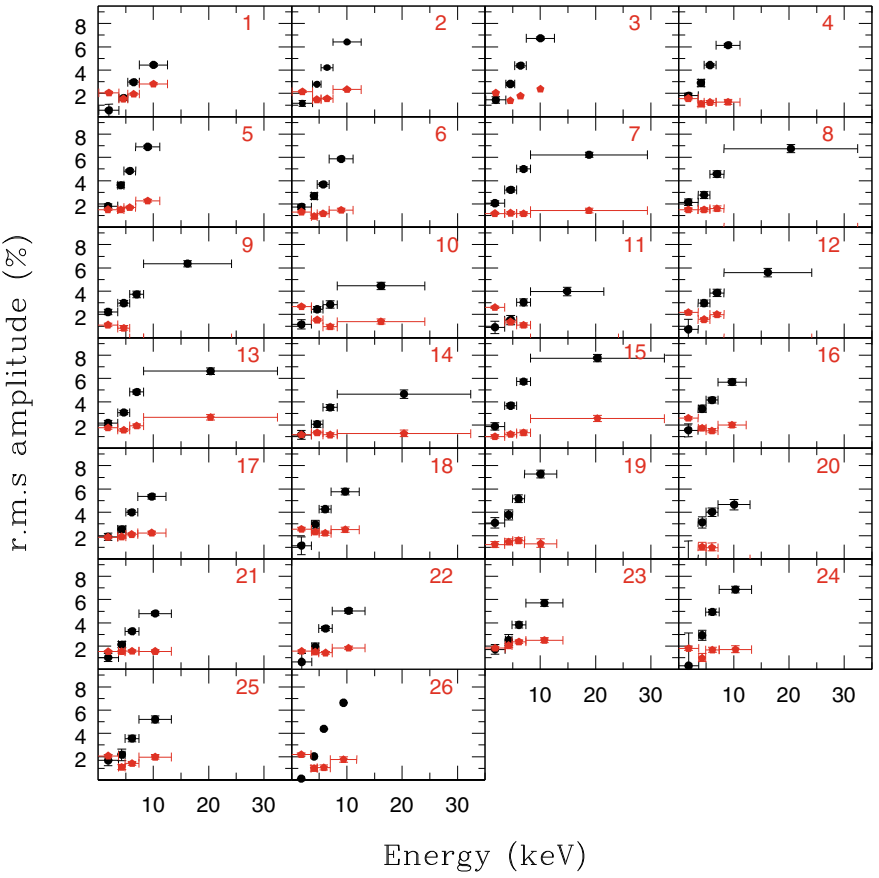

Fig. 31.1 Energy dependence of r.m.s. amplitude of the lower kHz QPO and the low-frequency broadband noise. The black points represent the r.m.s. amplitude for the lower kHz QPO and the red points represent the same for the low-frequency broadband noise (0.6–50 mHz)

31.3 Results and Discussions

Figure 31.1 represents the plot of the r.m.s. amplitude as a function of energy for the lower kHz QPO and the low-frequency broadband noise for some of the sampled observations considered for our analysis. We have found the slope of the r.m.s. versus energy plot fitted with a linear function and listed the parameters in Table 31.2. As a result, this relation can be described by a linear function. The slope is found to be ~ 0.4 for the lower kHz QPO. For the low-frequency broadband noise, we have estimated the slope with an average value ~ 0.05. The slope of the linear fit of the r.m.s. versus energy relation in the entire energy range 3–30 keV. We have also found that there is no correlation between the slope and the QPO frequency. In Fig. 31.2, we have plotted the slope of the energy dependence of r.m.s. variability with the

Table 31.2 Slope of the energy-dependent r.m.s. variability of kHz QPO and low-frequency broadband noise

Sl. No.	Frequency	Slope (Khz)	χ^2	Slope (LFN)	χ^2
1	848	0.495±0.073	4.724	0.236±0.005	0.066
2	832	0.658±0.036	2.427	0.161±0.039	3.77
3	832	0.710±0.044	1.904	0.181±0.014	0.243
4	760	0.588±0.103	3.105	0.027±0.024	0.142
5	808	0.657±0.029	0.437	0.162±0.017	0.250
6	768	0.663±0.013	0.059	0.105±0.017	0.162
7	648	0.185±0.112	33.51	0.016±0.007	0.199
8	652	0.225±0.087	9.95	−0.088±0.044	1.317
9	597	0.292±0.006	0.042	−0.068±0.047	1.962
10	566	0.174±0.0003	6.2e-05	−0.012±0.054	6.513
11	568	0.196±0.105	4.736	−0.119±0.001	0.001
12	613	0.222±0.034	0.780	−0.096±0.138	8.811
13	784	0.203±0.099	22.862	0.067±0.016	0.861
14	745	0.141±0.086	9.704	−0.006±0.017	0.803
15	791	0.233±0.120	25.69	0.086±0.005	0.075
16	736	0.424±0.003	0.002	0.055±0.070	1.772
17	776	0.467±0.116	4.146	0.059±0.021	0.413
18	776	0.487±0.083	1.109	0.038±0.040	0.597
19	672	0.582±0.057	0.417	−0.026±0.039	0.260
20	688	0.238±0.089	0.662	−0.180±0.059	0.347
21	656	0.405±0.059	1.731	0.003±0.007	0.059
22	688	0.434±0.113	4.339	0.060±0.037	1.468
23	800	0.449±0.066	0.833	0.062±0.038	0.767
24	776	0.561±0.148	4.037	0.085±0.102	2.037
25	808	0.449±0.084	1.081	0.141±0.010	0.052
26	800	0.721±0.162	3.348	0.154±0.042	0.483

This table lists the Serial No. of the science event file taken for the analysis, the frequency of the kHz QPO, the slope of energy versus r.m.s. amplitude of kHz QPO, and low-frequency broadband noise with error

serial no. of the event file. Black triangles represent the slope of r.m.s. versus energy plot for the lower kHz QPO; red rhombuses represent the same for low-frequency broadband noise of frequency range 0.6–50 mHz. It is also found that the slope for high frequency is always higher than the case of low-frequency noise. In case of kHz QPO, the r.m.s. amplitude increases with energy with slope of ~ 0.4. This implies that the phenomenon should be associated with the high-energy thermal compotonization component and not the soft blackbody one. If a fraction of the compotonized photons impinge back into the soft photon source and the system would show the energy dependence similar to what has been obtained in our analysis. This again indicates

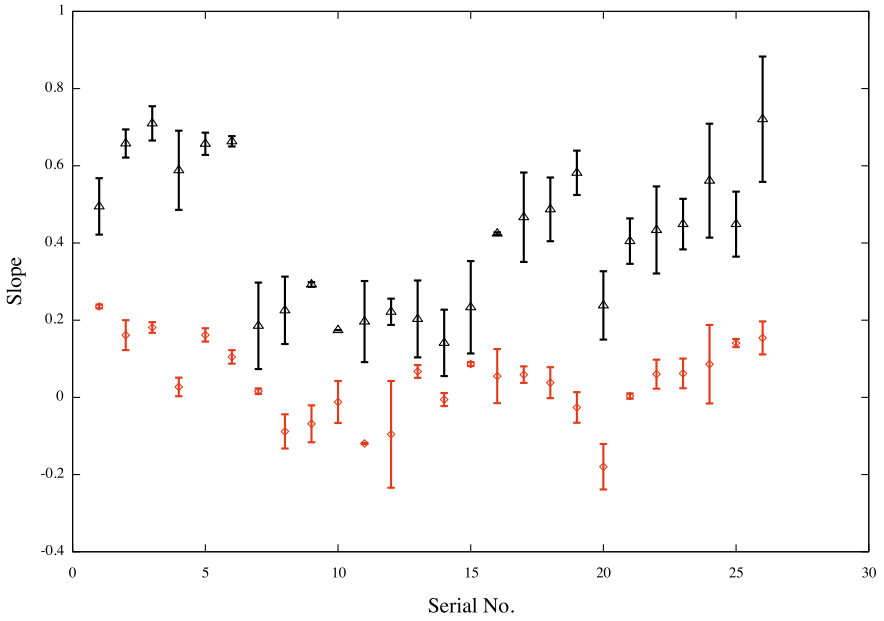

Fig. 31.2 Slope of the energy dependence of r.m.s. variability. Slope for kHz QPO is always higher than in the low-frequency broadband noise. Black triangles represent the slope of r.m.s. versus energy plot for the lower kHz QPO; red rhombuses represent the same for low-frequency broadband noise of frequency range 0.6–50 mHz

that the variation is in the hot thermal compotonization component and, in particular, the QPO is likely to be driven by variation in the thermal heating rate of the hot plasma. The energy-dependent r.m.s. variability of the low-frequency broadband noise is nearly flat, i.e., with slope ~ 0.05. This indicates that the driver here may be the soft photon source. Kumar & Misra [26] applied their model predictions to compare with the observed 850 Hz oscillation of $4U\,1608-52$ that is well described by such a model. We have studied the spectrum of the variability for the low-frequency broadband noise in the frequency range of 0.6 mHz–50 mHz. Our result also agrees well with their model predictions for the energy-dependent r.m.s. variability. Thus, the radiative mechanism driving the low-frequency broadband noise and the high-frequency QPO is different in nature. This is not the case where the QPO is simply a resonance at a particular high frequency which amplifies the underlying noise. Alternatively, if the QPO is a resonance, then the origin of the kHz QPO is different than the low-frequency broadband noise.

Acknowledgements This research has made use of data obtained from the High Energy Astrophysics Science Archive Research Center (HEASARC), provided by NASA's Goddard Space Flight Center. The author would like to thank IUCAA for visiting associateship. The research leading to this results has been funded by Department of Space, Government of India, under grant no. DS_2B-13013(2)/10/2020-Sec.2 and SERB research grant CRG/2019/001112.

References

1. M. van der Klis, Millisecond Oscillations in X-Ray Binaries. ARA&A **38**, 717 (2000). https://doi.org/10.1146/annurev.astro.38.1.717
2. M. van der Klis, Compact Stellar X-ray Sources, Cambridge University Press, p. 39 (2006)
3. E.C. Ford, M. van der Klis, Strong Correlation between Noise Features at Low Frequency and the KilohertzQuasi-Periodic Oscillations in the X-Ray Binary 4U 1728–34. ApJL **506**, L39 (1998). https://doi.org/10.1086/311638
4. D. Psaltis, T. Belloni, M. van der Klis, Correlations in Quasi-periodic Oscillation and Noise Frequencies among Neutron Star and Black Hole X-Ray Binaries. ApJ **520**, 262 (1999a). https://doi.org/10.1086/307436
5. T. Belloni, D. Psaltis, M.A. van der Klis, Unified Description of the Timing Features of Accreting X-Ray Binaries. ApJ **572**, 392 (2002). https://doi.org/10.1086/340290
6. S. van Straaten, M. van der Klis, R. Wijnands, Nuclear Physics B Proceedings Supplements **132**, 664 (2004)
7. D. Psaltis, M. Méndez, R. Wijnands et al., The Beat-Frequency Interpretation of Kilohertz Quasi-periodic Oscillations in Neutron Star Low-Mass X-Ray Binaries. ApJ **501**, L95 (1998). https://doi.org/10.1086/311455
8. D. Psaltis, R. Wijnands, J. Homan et al., On the Magnetospheric Beat-Frequency and Lense-Thirring Interpretations of the Horizontal-Branch Oscillation in the Z Sources. ApJ **520**, 763 (1999b). https://doi.org/10.1086/307460
9. M. Méndez, M. van der Klis, E.C. Ford, R. Wijnands, J. van Paradijs, Dependence of the Frequency of the Kilohertz Quasi-periodic Oscillationson X-Ray Count Rate and Colors in 4U 1608–52. ApJL **511**, L49 (1999). https://doi.org/10.1086/311836
10. T. Belloni, M. Méndez, J. Homan, The distribution of kHz QPO frequencies in bright low mass X-ray binaries. A&A **437**, 209 (2005). https://doi.org/10.1051/0004-6361:20041377
11. T. Belloni, M. Méndez, J. Homan, On the kHz QPO frequency correlations in bright neutron star X-ray binaries. MNRAS **376**, 1133 (2007). https://doi.org/10.1111/j.1365-2966.2007.11486.x
12. P. Peille, D. Barret, P. Uttley, The Spectral-timing Properties of Upper and Lower kHz QPOs. ApJ **811**, 109 (2015). https://doi.org/10.1088/0004-637X/811/2/109
13. L. Stella, M. Vietri, kHz Quasiperiodic Oscillations in Low-Mass X-Ray Binaries as Probes of General Relativity in the Strong-Field Regime. Phys. Rev. Lett. **82**, 17 (1999). https://doi.org/10.1103/PhysRevLett.82.17
14. L. Stella, M. Vietri, S. Morsink, Astrophysical Letters and Communications **38**, 57 (1999)
15. C. Zhang, The MHD Alfven wave oscillation model of kHz Quasi Periodic Oscillations of Accreting X-ray binaries. A&A **423**, 401 (2004). https://doi.org/10.1051/0004-6361:20035808
16. W. Kluźniak, M.A. Abramowicz, Strong-Field Gravity and Orbital Resonance in Black Holes and Neutron Stars–kHz Quasi-Periodic Oscillations (QPO). Acta Physica Polonica B. **32**, 3605 (2001)
17. M.A. Abramowicz, T. Bulik, M. Bursa, W. Kluźniak, Evidence for a 2:3 resonance in Sco X-1 kHz QPOs. A&A **404**, L21 (2003a). https://doi.org/10.1051/0004-6361:20030737
18. Lin, Y.-F., Boutelier, M., Barret, D., & Zhang, S.-N. Studying frequency relationships of kilohertz quasi-periodic oscillations for 4U 1636–53 and Sco X-1: observations confront theories. ApJ **726**, 74 (2011). https://doi.org/10.1088/0004-637x/726/2/74
19. M.C. Miller, F.K. Lamb, D. Psaltis, Sonic-Point Model of Kilohertz Quasi-periodic Brightness Oscillations in Low-Mass X-Ray Binaries. ApJ **508**, 791 (1998). https://doi.org/10.1086/306408
20. F.K. Lamb, M.C. Miller, Changing Frequency Separation of Kilohertz Quasi-periodic Oscillations in the Sonic-Point Beat-Frequency Model. ApJ **554**, 1210 (2001). https://doi.org/10.1086/323148
21. M.A. Abramowicz, V. Karas, W. Kluźniak, W.H. LEE, P. Rebusco, Non-Linear Resonance in Nearly Geodesic Motion in Low-Mass X-Ray Binaries. PASJ **55**, 467 (2003b). https://doi.org/10.1093/pasj/55.2.467

22. G. Hasinger, M. van der Klis, Two patterns of correlated X-ray timing and spectral behaviour in low-mass X-ray binaries. A&A **225**, 79 (1989)
23. J.S. Troyer, E.M. Cackett, P. Peille et al., A Systematic Spectral-timing Analysis of Kilohertz Quasi-periodic Oscillations in the Rossi X-Ray Timing Explorer Archive. ApJ **860**, 167 (2018). https://doi.org/10.3847/1538-4357/aac4a4
24. R. Wijnands, J. Homan, M. van der Klis, The Complex Phase-Lag Behavior of the 3–12 Hz Quasi-Periodic Oscillations during the Very High State of XTE J1550–564. ApJL **526**, L33 (1999). https://doi.org/10.1086/312365
25. H.C. Lee, R. Misra, R.E. Taam, A Compton Upscattering Model for Soft Lags in the Lower Kilohertz Quasi-periodic Oscillation in 4U 1608–52, ApJL **549**, L229 (2001). https://doi.org/10.1086/319171
26. N. Kumar, R. Misra, Energy dependent time delays of kHz oscillations due to thermal Comptonization. MNRAS **445**, 2818 (2014). https://doi.org/10.1093/mnras/stu1946
27. N. Kumar, R. Misra, Constraining the size of the Comptonizing medium by modelling the energy-dependent time lags of kHz QPOs of neutron star system. MNRAS **461**, 2580 (2016). https://doi.org/10.1093/mnras/stw1496
28. R. Misra, S. Mandal, Alternating Lags of QPO harmonics: A generic model and its application to the 67 mHz QPO of GRS 1915+105. ApJ **779**, 71 (2013). https://doi.org/10.1088/0004-637x/779/1/71
29. M. Berger, M. van der Klis, J. van Paradijs et al., Discovery of 800 Hz Quasi-periodic Oscillations in 4U 1608–52. ApJL **469**, L13 (1996). https://doi.org/10.1086/310256
30. M. Gilfanov, M. Revnivtsev, S. Molkov, Boundary layer, accretion disk and X-ray variability in the luminous LMXBs. A&A **410**, 217 (2003). https://doi.org/10.1051/0004-6361:20031141
31. C. Cabanac, G. Henri, P.-O. Petrucci, et al., Variability of X-ray binaries from an oscillating hot corona. MNRAS **404**, 738 (2010). https://doi.org/10.1111/j.1365-2966.2010.16340.x
32. J.C. Lochner, D. Roussel-Dupre, Recurrence Times and Periodicities in 4U 1608–52 as Observed by VELA 5B. ApJ **435**, 840 (1994). https://doi.org/10.1086/174863
33. T. Güver, F. Özel, A. Cabrera-Lavers, P. Wroblewski, The Distance, Mass, and Radius of the Neutron Star in 4U 1608–52. ApJ **712**, 964 (2010). https://doi.org/10.1088/0004-637X/712/2/964
34. D.K. Galloway, M.P. Muno, J.M. Hartman, D. Psaltis, D. Chakrabarty, Thermonuclear (Type I) X-Ray Bursts Observed by the Rossi X-Ray Timing Explorer. ApJS **179**, 360 (2008). https://doi.org/10.1086/592044
35. J. Poutanen, J. Nättilä, J.J.E. Kajava et al., The effect of accretion on the measurement of neutron star mass and radius in the low-mass X-ray binary 4U 1608–52. MNRAS **442**, 3777 (2014). https://doi.org/10.1093/mnras/stu1139
36. K. Yoshida, K. Mitsuda, K. Ebisawa et al., Low state properties of the low mass X-ray binaries X1608–52 onserved with Ginga. PASJ **45**, 605 (1993)
37. J. van Paradijs, W. Zhang, F. Marshall et al., U 1608–52. IAUC **6336**, 2 (1996)
38. M. Méndez, M. van der Klis, J. van Paradijs et al., Discovery of a Second Kilohertz Quasi-periodic Oscillation Peak in 4U 1608–52. ApJL **494**, L65 (1998). https://doi.org/10.1086/311162
39. M. Méndez, M. van der Klis, E.C. Ford, The Amplitude of the Kilohertz Quasi-periodic Oscillations in 4U 1728–34, 4U 1608–52, and Aquila X-1, as a Function of X-Ray Intensity. ApJ **561**, 1016 (2001). https://doi.org/10.1086/323486
40. M. Gierliński, C. Done, The X-ray spectrum of the atoll source 4U 1608–52. MNRAS **337**, 1373 (2002). https://doi.org/10.1046/j.1365-8711.2002.06009.x
41. D. Barret, J.-F. Olive, M.C. Miller, Drop of coherence of the lower kilo-Hz QPO in neutron stars: Is there a link with the innermost stable circular orbit? Astronomische Nachrichten **326**, 808 (2005a). https://doi.org/10.1002/asna.200510417
42. D. Barret, W. Kluźniak, J.F. Olive, S. Paltani, G.K. Skinner, On the high coherence of kHz quasi-periodic oscillations. MNRAS **357**, 1288 (2005b). https://doi.org/10.1111/j.1365-2966.2005.08734.x

43. D. Barret, J.-F. Olive, M.C. Miller, The coherence of kilohertz quasi-periodic oscillations in the X-rays from accreting neutron stars. MNRAS **370**, 1140 (2006). https://doi.org/10.1111/j.1365-2966.2006.10571.x
44. D. Barret, Soft lag in neutron star kHz quasi-periodic oscillations: evidence for reverberation? ApJ **770**, 9 (2013). https://doi.org/10.1088/0004-637x/770/1/9
45. Y.-J. Lei, S. Zhang, J.-L. Qu et al., The properties of cross-correlation and spectra of the low mass X-ray binary 4U 1608–52. AJ **147**, 67 (2014). https://doi.org/10.1088/0004-6256/147/3/67
46. M. Armas Padilla, Y. Ueda, T. Hori et al., Suzaku spectroscopy of the neutron star transient 4U 1608–52 during its outburst decay. MNRAS **467**, 290 (2017). https://doi.org/10.1093/mnras/stx020
47. M.G.B. de Avellar, M. Méndez, A. Sanna, J.E. Horvath, Time lags of the kilohertz quasi-periodic oscillations in the low-mass X-ray binaries 4U 1608–52 and 4U 1636–53. MNRAS **433**, 3453 (2013). https://doi.org/10.1093/mnras/stt1001
48. E.M. Cackett, Are the kHZ QPO lags in neutron star 4U 1608–52 due to reverberation? ApJ **826**, 103 (2016). https://doi.org/10.3847/0004-637x/826/2/103

Chapter 32
Review on Magnetism in Nanomaterials and Superparamagnetism

Bandana Gogoi and Upamanyu Das

Abstract Nanotechnology plays a prominent role in the fabrication of novel materials by controlling the structure of matter at the nanometric scale changing properties at a molecular level. The particles with nanodimensions change their material properties in a dramatic way showing uniqueness in behaviour with modified properties. In many ferromagnetic materials when the size is reduced to the nanoscale level, the magnetic properties enhance in a unique way, thus leading to a superparamagnetic state. The magnetic moment of the material randomly flips the direction of their magnetization, and the random orientations of magnetic spins inside the particles result in zero remanent magnetization and zero coercivity. An unusual change in the hysteresis loop shows the magnetization curve passing through the origin, showing the state of zero magnetization.

32.1 Introduction

At the nanoscopic dimension, the magnetic behaviours of magnetic nanomaterial show significant differences from those observed at bulk scale with the same chemical composition [1–3]. As the size is reduced material property gradually moves from the regime of bulk material behaviour to molecular-level material behaviour. Drastic changes in properties took place at the molecular level.

With the reduction of size, the basic magnetic properties or magnetism connected to different bulk ferro and anti-ferromagnetic material changes to develop in different modified ways. These changes may be shown to occur from the dimension of the material which becomes comparable to some of the basic fundamental characteristic lengths of one or more of various physical properties that are more relevant to the magnetic properties (e.g. the size of magnetic domains, exchange length etc.). With reduced size to nanoscale level, translation symmetry of the magnetic material breaks giving rise to specific sites with reduced coordination numbers, broken exchange and a higher proportion of atoms on the surface increasing surface effect. A high surface

B. Gogoi (✉) · U. Das
Rajiv Gandhi University, Doimukh, A.P, India

S. Sengupta et al. (eds.), *Selected Progresses in Modern Physics*, Springer Proceedings in Physics 265, https://doi.org/10.1007/978-981-16-5141-0_32

to volume ratio brings more close contact with the exterior system. The spin-wave spectrum of the nanometric material also tends to change and this change can be observed as spin-wave energy becomes comparable to the thermal energy which plays a prominent role in developing new magnetic properties [3–12].

Nanoscale magnetism has been basically studied to be developing from unpaired d-orbital electrons as well as the coupling effect of these electrons with nuclear spins. At nanosized dimension, the surface area gets more exposure to the exterior neighbouring system, as a result of which the material achieves higher modified functionalities like increased reactivity, higher catalytic action and decreased melting point due to surface effect. The surface energy increases with increased surface area and hence surface effect dominates over the other observed effects at nanosized dimension. This increased surface energy effect also helps in developing extraordinary magnetic behaviours in magnetic nanomaterials. Particle size plays a significant role in determining the basic material property of any material like magnetic, electrical, optical or electronic property. Therefore increasing interest has been developed to study magnetic nanomaterials in recent times due to their size-dependent properties [13, 14].

Figure 32.1 shows the typical hysteresis loop of any bulk ferromagnetic material. In order to observe the changes of magnetic properties of ferro or anti-ferromagnetic materials with particle size, the magnetic hysteresis curve of normal bulk ferromagnetic material needs to be understood. In normal ferromagnetic behaviour, the curve is observed to have a remanence and a coercive field, i.e. the line of magnetization curve does not pass through zero or origin.

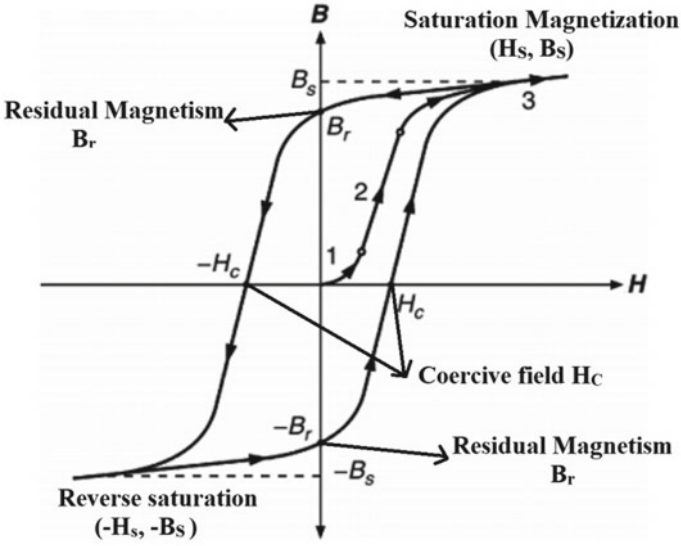

Fig. 32.1 Magnetization curve of ferromagnetic material in a bulk state

The development of uniqueness in the magnetic property of magnetic materials can be studied to be originated from the division of magnetic material into distinct and well-separated magnetic domains with magnetic moment alignment. The change in magnetic moment directions in magnetic domains may correspond to the total cancellation of the magnetic moment or may tend to minimize the total average magnetization to become nearly zero.

There are various interaction terms in a magnetic system that contribute to the total internal energy of a magnetic material and can be expressed as

$$E_{tot} = E_{ex} + E_A + E_{ms} + E_{ext} \tag{32.1}$$

Exchange interaction (E_{ex}) is responsible for the establishment of magnetic order in magnetic materials. This interaction arises from a quantum effect due to the indistinguishability of the electron.

$H = -2JS_iS_j$ where J is the exchange constant. S_i and S_j are spins.

Magnetostatic energy (E_{ms}) or dipolar energy is the measure of the magnetic energy of a magnetic sample because of its own magnetic field. This field is the demagnetizing field that arises from the divergence of magnetization.

Magnetic anisotropy (E_A) is crystallogenic in origin. The shape of the sample, the stress in the material and atomic segregation determine the value of magnetic anisotropy energy. The energy of a magnetically ordered sample depends on the relative direction of the magnetization and the structural axes; for example, a solid has an axis along which the energy is at a minimum. The anisotropy energy E_A is written as a function of the direction cosines $\alpha_{1,}\alpha_2$ and α_3 defined in relation to the axes of the crystal.

Uniaxial anisotropy is the approximation that in some samples anisotropy depends only on the angle θ between the magnetization and a given axis. The anisotropy energy per unit volume takes the form

$$E_A/V = K_1 sin^2\theta + K_2 sin^4\theta \tag{32.2}$$

where θ is the angle of magnetization with the single axis, and depending on the magnitude of anisotropy constants K_1 and K_2, the sample can have an easy axis or easy plan.

Magnetoelastic energy and magnetostriction is the elastic energy of a magnetic material that arises from the interaction between the magnetization and the strains. Magnetoelastic energy is the increase in the anisotropy energy of magnetic material when submitted to stress. Magnetostriction, the intrinsic property of magnetic material, is the coupling between magnetic and elastic energy, i.e. when subjected to magnetic field magnetic material changes shape [3, 14–16].

Exchange interaction is responsible for the ordering of atomic magnetic moments which causes the atomic magnetic moments to become parallel and showing magnetic ordering in ferromagnetic material. But the presence of other interactions such as anisotropy, dipolar, magnetoelastic etc. leads to the formation of magnetic domains,

where the magnetic moments are perfectly ordered [3]. As the size of the particle is reduced, the energy necessary to divide itself into magnetic domains is higher than the energy needed to remain as a single magnetic domain or monodomain [10, 17].

The size of the magnetic material has a great influence in determining its magnetic behaviour, e.g. a ferromagnetic material below a critical particle size (15 nm) can possess a single magnetic domain and can show paramagnetic behaviour above a characteristic temperature called blocking temperature (T_B). With the increase of the size of the magnet, the number of magnetic domains increases, and as a result, the number of domain walls also increases. During the whole process, there is a decrease in magnetostatic energy while there is an increase in the exchange and the anisotropy energies because of the more number of domain walls [8, 18]. This dependency of magnetic property on the size of the magnetic material can be illustrated by considering the coercivity of the magnet and the dependence of coercivity on the size of the magnet as shown in Fig. 32.2 [3, 16, 19].

For very small particles, with a diameter smaller than the critical diameter of superparamagnetism (D_{spm}), the particle shows unstable magnetization with flipping spin and it results in zero coercivity (H_c). For the diameter in the range between D_{spm} and the critical diameter of a single domain (D_{sd}), the magnetic moment shows stable nature and hence coercivity (H_c) does not become zero. Coercivity increases with the increase of single-domain diameter D_{sd} and after reaching the multidomain region with the increasing diameter, coercivity again decreases. Hence the magnet shows the maximum coercivity when the diameter is equal to the single-domain diameter, D_{sd} [8, 10, 20–22].

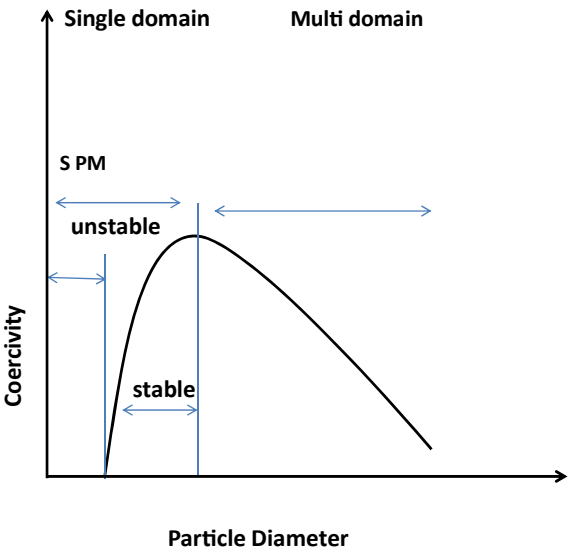

Fig. 32.2 Dependency of coercivity on the size of the particle diameter of magnetic nanomaterial

32.2 Basic Concept of Superparamagnetism

Superparamagnetism (SPM) is a type of magnetism that develops in small nanoparticles of ferromagnetic or anti-ferromagnetic materials which possess single-domain non-interacting magnetic moment grains. Nanosized material with a single magnetic domain can show superparamagnetic behaviour below T_B (blocking temperature) also when the size is sufficiently reduced below blocking volume (V_B), which is the maximum volume below which superparamagnetism starts at a particular temperature and that possibly arises due to spin-based momentum of the unpaired electrons present in the material [21–23].

The energetic stability of a single magnetic domain was theoretically predicted and established by Kittel in 1946 [24]. Magnetic nanoparticles generally show a preference along the direction where magnetic alignment takes place and are said to be anisotropic along these directions. Nanoparticles generally show uniaxial anisotropy, which means that there are two easy directions of magnetization pointing in opposite directions (antiparallel) and are separated by an energy barrier. For single-domain magnetic material, all the magnetic moments are aligned along the preferred anisotropy axis, therefore the free energy contribution from exchange and anisotropy becomes zero. Hence the magnetostatic energy becomes the only relevant energy term.

The critical diameter of the single domain (D_{sd}) of magnetic material has a close relationship with the anisotropy constant K. For identical saturation magnetization (M_s) single-domain diameter D_{sd} increases with domain wall energy, i.e. D_{sd} is proportional to the domain wall energy. When the size reduction of the particle is sufficiently large then thermal energy overcomes the anisotropy energy. At this stage of magnetization magnetic moment shows fluctuating nature rather than stable nature [8, 20, 21].

At a given temperature, as the size is reduced to a large extent, spin-wave energy modifies and becomes comparable to thermal energy in single-domain non-interacting magnetic grain or particle, and thermal energy becomes insufficient to overcome the spin–spin interaction and can lead to random orientations of magnetic spins inside the particles. The critical diameter D_{spm} is the maximum size below which the superparamagnetic behaviour starts at a particular temperature and the corresponding volume at which a particle goes from blocked to unblocked state is called blocking volume (V_B) [22, 23].

At blocking temperature (T_B), thermal energy overcomes the anisotropy barrier of nanoparticles. Above blocking temperature (T_B), thermal fluctuations dominate and magnetic moments are randomly orient. Nanoparticles with a uniaxial anisotropy randomly flip the direction of their magnetization and show a spontaneous reversal of magnetization when thermal fluctuation is sufficient enough to overcome the barrier potential that is supposed to arise from magneto crystalline in origin and due to magnetoelastic and shape anisotropy. It was Neel [25] who shows that above T_B a stable magnetization cannot be established due to thermal fluctuations acting on small particles, and as a result, the system shows *superparamagnetic* behaviour. The

typical time of average laps between two flips is called *Neel-relaxation time* τ_N. If τ_m is considered to be the measuring time of the magnetic effect of a particular nanomagnetic material for its observed magnetic behaviour, then the following observations can be made in a nanomagnetic material [25, 26].

If $\tau_m < \tau_N$, the material is in a blocked state and the magnetization flip does not take place.

If $\tau_m > \tau_N$, magnetic flip occurs and magnetic behaviour alters. The material shows superparamagnetism.

This shows that the observed magnetic behaviour in nanomagnetic material depends on measuring time τ_m. In most practical applications the measuring time τ_m is tried to keep constant. The transition between superparamagnetic and blocked state is used to study as a function of applied temperature.

The first and basic theory that describes the basic understanding of nanoparticle magnetism is the *Stoner-Wolfforth model* [14, 27]. In this model, each nanoparticle is considered as an ellipsoidal homogenous single-domain non-interacting grain. According to this theory, depending on the spin configuration nanoparticles may have a single domain, vortex or multidomain state. Nanoparticles in the smallest range of diameter do not behave as stable magnet but exhibit the phenomenon of superparamagnetism [3]. However, this model is suitable at $T = 0$ K and is applicable to nanoparticles with uniaxial anisotropy only. The large surface to volume ratio in nanoparticles enhances the magnetic moment and anisotropy [27].

32.2.1 BasicTheory

The energy expression for single-domain magnetic grain with uniaxial anisotropy in the presence of external magnetic field H can be expressed as the sum of magnetic anisotropy energy and Zeeman energies:

$$E = KV \sin^2 (\Phi - \theta) - \mu_0 M_s V H \cos \Phi \tag{32.3}$$

where V is the grain volume of the nanoparticle, K being the uniaxial anisotropy constant parameter and M_s is the saturation magnetization. All the three quantities, external magnetic field H, grain magnetization and magnetization easy axis lie in the same plane. Φ represents the angle between magnetization and magnetizing field and θ represents the angle between magnetization easy axis and magnetizing field [10, 17, 25, 28].

In absence of an external magnetic field, two equally energetically favourable directions exist. Both directions are parallel to the energetically favourable spontaneous magnetization direction also called magnetization easy axis for anisotropic magnetic material and there possess the energy barrier ΔE between them in KV. At temperatures higher enough, the thermal energy kT is capable of overcoming the

barrier potential and alteration of magnetization direction takes place. While in presence of an external magnetic field, the symmetry of the two magnetization easy axis directions breaks down. When magnetization direction is along the external magnetic field, domain energy of the nanoparticle grain decreases and therefore energy barrier for spin fluctuation becomes high. The reverse is the case when magnetization directs in opposite direction to an externally applied magnetic field, the energy barrier for spin fluctuation decreases and reversal of magnetization takes place spontaneously. So nanoparticles with uniaxial anisotropy flip the direction of their magnetization randomly and spontaneously. The thermally initiated fluctuations of the magnetization direction between the two easy axis directions are called *superparamagnetic (Neel) relaxation* and the typical expression for *Neel-relaxation time* τ_N can be expressed by the Neel-Brown expression as

$$\tau_N = \tau_0 exp\ (\Delta E\ /kT) \tag{32.4}$$

where τ_0 is the length of time and is the function of the characteristic of the material and usually lies between 10^{-12} s and 10^{-9} s. τ_0 depends weakly on temperature and various material parameters such as magnetic anisotropy constant, particle volume and saturation magnetization [10, 16, 17, 25, 28].

In this regard, a definition of blocking temperature T_B can be given as the temperature at which the relaxation time τ_N equals the experimental time τ_m or T_B can be defined as the temperature between the blocked and the superparamagnetic state [25, 28].

Equation (32.4) represents the connection between the time τ_N and the temperature *T*.

$$\text{At}\tau_N = \tau_m \quad T_B = \Delta E / kln\left(\tau_m / \tau_0\right), \tag{32.5}$$

A clear distinction between the two states can be expressed as

- The state is blocked when $\tau_m < < \tau_N or\ T < T_B$.
- The state becomes superparamagnetic when $\tau_m > > \tau_N or\ T > T_B$.

The first reveal of single-domain particle magnetization presented by *Stoner* and *Wohlfarth* [14] suggested the existence of high coercivity fields below T_B. The anisotropy energy arising from magnetocrystallogenic origin becomes comparable to thermal energy and the direction of the magnetic moment starts fluctuating spontaneously and goes through a rapid superparamagnetic relaxation. The supposed system of uniform non-interacting nanoparticles at $T > T_B$ overcomes barrier energy and the magnetic moments started flipping between the easy magnetization directions. At $T < T_B$, the magnetocrystalline-originated anisotropy energy barrier cannot be overcome by the thermal energy and the magnetic moment of each particle rotates from the field direction back to the nearest easy magnetization axis because of which non-zero coercivity results. The total magnetization decreases with increasing temperature as the nanoparticles and the corresponding easy magnetization directions are randomly

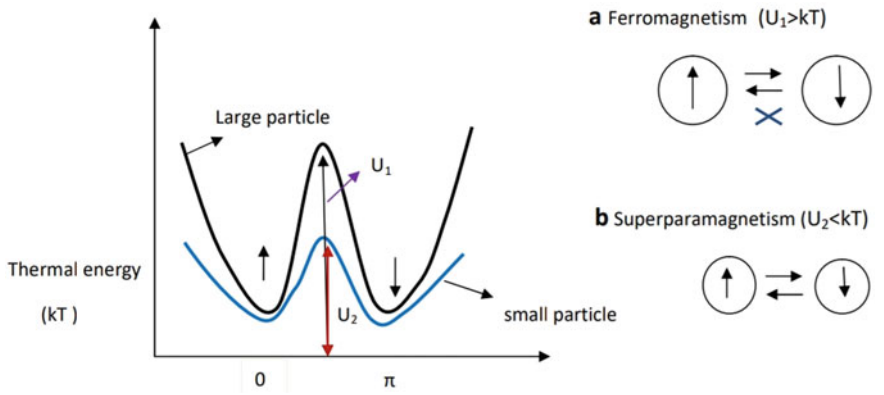

Fig. 32.3 Ferromagnetism in large and small magnetic particle,**a** large particle magnetism ($U_{1.} > kT$)**,** no spin flipping takes place, **b** small particle superparamagnetism ($U_{2.} < kT$), with spin flipping

oriented and the randomness increases with temperature [20, 21, 28]. Figure 32.3 shows the ferromagnetism in large particles and superparamagnetism in small nanoparticles.

32.3 Brief Discussions

The typical behaviour of large particle ferromagnetism and small particle ferromagnetism can be observed from the thermal energy transition curve. For two vectors spin directions (vector upward ↑ and vector downward ↓), if spin vector cannot move from one direction to other, there exist some net magnetization and the material shows ferromagnetism, i.e. when exchange energy $U_1 > kT$ vector spin cannot flip or re-orient. In the energy plot (thermal energy as a function of the orientation of the spin) if one spin magnetic moment vector lies in the first stability zone (minimum energy) and if it has to come to the next stability zone (with minimum energy) it has to overcome the energy barrier. The energy barrier is proportional to the grain particle volume (V). The energy barrier potential for a large particle is large. If the spin has to change its direction it has to overcome the large energy barrier. For a small-sized particle of nanodimension, this energy difference is much smaller; therefore, it is easy for the magnetic vector to change its direction crossing the potential barrier. At room temperature also the thermal energy is much greater than the exchange energy between the magnetic vectors [10, 28].

Hence for large particles, at room temperature, the thermal energy is much less than the energy required to cross the barrier, but this energy is sufficiently more than the energy required crossing the barrier in small particles changing the magnetic vector. Hence there is an automatic reversible change in the direction of magnetic vector or spin. At normal temperature also this spin flipping can take place in a

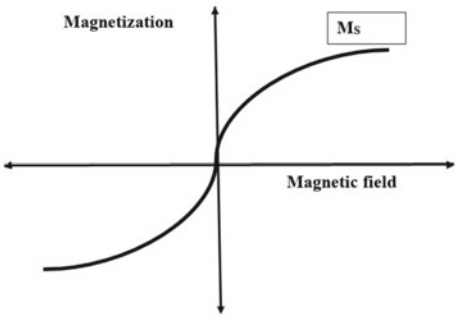

Fig. 32.4 Curve showing superparamagnetism with remanence $M_R = 0$ and $H_C = 0$

nanodimensional particle; hence both the possibilities of stable state are possible in the system. This spin flipping leads to the property of superparamagnetism in the nanosystem. Whenever the energy required or exchange energy U_2 is less than kT (thermal energy) then it can have spin fluctuation and it results in superparamagnetism. Figure 32.4 presents the typical behaviour of the superparamagnetism nature of magnetic nanoparticles, where the magnetization curve passes through the origin.

32.4 Conclusions

For large particle, the hysteresis loop possesses a particular area. When the particle size is reduced sufficiently (around 10–12 nm), these particles do not show the hysteresis loop but a plot that goes through the origin, which is like both remanence and coercive field are zero. This represents the typical paramagnetic behaviour. Although these particles are small they have several moments comprising ions or molecules. These moments are flipping among themselves and the resultant is a paramagnetic behaviour. This is one of the important aspects of the magnetic properties of nanostructures [29]. When the particle size is large it shows the hysteresis loop, but for the same material particle when the size is reduced to nanodimension it does not show hysteresis but passes through the origin with no remanence and coercive field, i.e. superparamagnetism is a function of the size of the particle.

References

1. D.J. Sellmyer, M. Zheng, R. Skomski, J. Phys.: Condens. Matter. **13**(25), R433 (2001)
2. J.P. Liu, E. Fullerton, O. Gutfleisch, D.J. Sellmyer, Springer Science +Business Media, LLC, (2009)
3. A.P. Guimaraes, *Principles of Nano Magnetism*, NanoScience and technology, ISBN 978–3–642–01481–9
4. C.Z. Wu, P. Yin, X. Zhu, C OuYang, Y Xie, J. Phys. Chem. B **110**(36), 17806 (2006)
5. D. Kim, N. Lee, M. Park, B.H. Kim, K. An, T. Hyeon, J. Am. Chem. Soc. **131**, 454 (2009)

6. C. Moya, A.M. Abdelgawad, N. Nambiar, S.A. Majetich, J. Phys. D: Appl. Phys. **50**(32), 325003 (2017)
7. M.V. Kovalenko, M.I. Bodnarchuk, R.T. Lechner, G. Hesser, F. Schaffler, W. Heiss, J. Am. Chem. Soc. **129**, 6352–6353 (2007)
8. C. Yang, Y.L. Hou, S. Gao, Chin. Phys. B **23**(5), 057505 (2014)
9. L.H. Zhang, J.J. Wu, H.B. Liao, Y.L. Hou, S. Gao, Chem. Commun. **454**, 378 (2009)
10. M. Knobel, W.C. Nunes, L.M. Socolovsky, E.D. Biasi, J.M. Vargas, J.C. Denardin, J. Nanosci. Nanotechnol. **8**(6), 2836–2857 (2008)
11. R.A. Lukaszew, *Hand Book of Nanomagnetism Application and Tools*, (Jenny Standford Publishing, 2015)
12. J. Shen, J. Kirscher, Surf. Sci. **500**, 300 (2002)
13. N.A. Spaldin, *Magnetic Materials Fundamentals and Device Applications,* (Cambridge University Press, New York, 2003), ISBN 0-521-81631-9
14. G. Schmid, (ed.), *Nanoparticles: From Theory to Application*, WILEY-VCH Verlag
15. GmbH & Co. KGaA, (2004)
16. M. Knobel, W.C. Nunes, A.L. Brandl, J.M. Vargas, L.M. Socolovsky, D. Zanchet, Phys. B: Condens. Matter **354**(1–4), 80–87 (2004)
17. J.M. Vargas, W.C. Nunes, L.M. Socolovsky, M. Knobel, D. Zanchet, Phys. Rev. B **72**(18), 184428 (2005)
18. B.D. Cullity (ed.), *Introduction to Magnetic Materials* (Addison-Wesley Publishing Co., Reading, Massachusetts, 1972)
19. G.C. Hadjipanayis, J. Magn. Magn. Mater. **200**, 373 (1999)
20. C.H. Chen, S.J. Knutson, Y. Shen, R.A. Wheeler, J.C. Horwath, P.N. Barnes, Appl. Phys. Lett. **99**, 012504 (2011)
21. D. Goll, A.E. Berkowitz, H.N. Bertram, Phys. Rev. B **18**, 184432 (2004)
22. C. Yang, J.J. Wu, Y.L. Hou, Chem. Commun. **47**, 5130 (2011)
23. J.L. Dorman, D. Fiorani, E. Trone, Adv. Chem. Phys. **98**, 283 (1997)
24. C. Bean, J.D. Livingston, J. Appl. Phys. **30**, 120S (1959)
25. C. Kittel, Phys. Rev. **70**, 965 (1946)
26. L. Neel, Ann. Geophys. **5**, 99 (1949)
27. W.C. Nunes, W.S.D. Folly, J.P. Sinnecker, M.A. Novak, Phys. Rev. B **70**, 014419 (2004)
28. E.C. Stoner, E.P. Wohlfarth, Philos. Trans. R. Soc. A **240**, 599 (1948)
29. W.C. Nunes, L.M. Socolovsky, J.C. Denardin, F. Cebollada, A.L. Brandl, M. Knobel, Phys. Rev. B **72**, 212413 (2005)

Chapter 33
Role of Laser Pre-pulse and Target Density Modification on the Acceleration of Protons from a Hydrogen Plasma Sphere

Ankita Bhagawati

Abstract In all the available high-power laser facilities, the intense main pulse is usually preceded by a pre-pulse of lower intensity which hits the target and ionizes it to form plasma. A 3D PIC simulation study is performed using a circularly polarized femtosecond main pulse interacting with a spherical hydrogen plasma. A finite time delay between the pre-pulse and the main pulse results in the plasma target to undergo expansion. The target density thus gets modified with a central peak density and gradually decreasing nearly isotropically towards the edges. The results are compared using a homogeneous density sphere in the absence of a pre-pulse and found that the interaction of the main pulse with an expanded target having a density gradient results in a stronger acceleration of protons along the laser propagation direction. The non-uniformity in the density favours the formation of shocks in the decreasing density gradient which eventually reflects protons to high velocities.

33.1 Introduction

The interaction of a high intensity laser pulse with a thin foiled target is known to result in the generation of intense and energetic ion beams of Mega-electron-volt energies. Such ions find relevance in a variety of inter-disciplinary fields, such as a fast ignitor in the inertial confinement of fusion fuel, as a source in hadron therapy of tumours and in the diagnosis of Warm Dense Matter. [1, 2]. In the case of a laser hitting the solid target, a significant amount of the laser energy is reflected, which proves detrimental to the generation of fast ions. This problem can greatly be avoided by using a near-critically dense target with density of the order of or slightly higher than the critical density, $n_c = \frac{m_e \omega^2}{4\pi e^2}$. Here, ω is the laser frequency, and m_e and e are the electronic mass and charge, respectively. Such targets absorb a large proportion of the incident energy [3]. These types of low-density targets are however difficult to manufacture experimentally, and manipulating the density requires extreme levels of precision. One way to produce such low-density targets is by letting a solid density

A. Bhagawati (✉)
Department of Physics, Tezpur University, Tezpur 784028, Assam, India

S. Sengupta et al. (eds.), *Selected Progresses in Modern Physics*, Springer Proceedings in Physics 265, https://doi.org/10.1007/978-981-16-5141-0_33

target to interact with a pre-pulse before the main pulse is incident on it. A pre-pulse of sufficient intensity will ionize the solid target and form plasma. The expansion of plasma leads to a drop in the average density of the target [4]. Producing a target of desired density will just require tuning the strength of the pre-pulse and the time delay between the pre-pulse and the main pulse. It is however worth mentioning that such targets will have density gradients inside it [4, 5]. The presence of pre-pulses in all the high-power laser facilities effectively makes the densities of the targets non-uniform to the main pulse. From a realistic point of view, it is therefore very important to study the dynamics of the ions using inhomogeneous density targets. The size and shape of the target has a major role to play in the interaction mechanisms and recently, microsphere targets have been used due to the lateral confinement provided by such targets and their ability to produce focused energetic beams [6–8].

In this article, a study is made on the role of the pre-pulse strength and the effect that the eventual modification of the target properties had on the acceleration of the protons. With a balanced fine-tuning of the laser and the target characteristics, it is possible to obtain high-energetic protons exiting out of the hydrogen plasma target. In Sect. 33.2, a description of the 3D-Particle-in-Cell simulation model is presented. The effect of the pre-pulse strength on the microsphere target and the subsequent influence on the dynamics of the energetic protons is also analysed in Sect. 33.2. In Sect. 33.3, a discussion is made on the shock-like acceleration process that is seen in some cases of the simulation. The reason behind the formation of these shocks and the factors on which its occurrence depends are further analysed.

33.2 Model Description and Effect of Laser Pre-pulse

For the simulations, a relativistic three-dimensional PIC code called Picpsi 3D is used. The simulation model is such that a high-intensity circularly polarized laser is interacted with a spherical hydrogen plasma target. A laser pulse with wavelength 1 μm and period 3.3 fs is allowed to propagate along the Z-axis. The laser intensity varies in a Gaussian manner both spatially and temporally, with a spatial FWHM of 10 μm and the laser pulse duration (temporal FWHM) of $\tau_L = 33$ fs. The critical density for 1 μm laser is $n_c = 1.1 \times 10^{21}\,\mathrm{cm}^{-3}$. Throughout this work, the peak intensity of the main pulse is fixed at $I_0 = 1.37 \times 10^{20}\,\mathrm{W/cm}^2$ corresponding to the normalized vector potential $a_0 = \dfrac{eE_0}{\sqrt{2}m_e\omega c} \approx 7$. To study the effect of the preceding low intensity pre-pulse, its peak intensity is varied. The simulation box is a cube of length, 20 μm with each side divided into 400 cells. The plasma target is placed at the centre (10 μm) of the box equidistant from its six walls. All the simulations are performed with 50 macro-particles per cell. The particles and fields vanish upon hitting the boundary walls of the box.

The hydrogen plasma target considered in the present work is a micron-sized sphere of solid density (density of solid hydrogen is $n_0 \simeq 6 \times 10^{22}\,\mathrm{cm}^{-3} \simeq 53 n_c$). This density is, however, maintained for the main laser pulse having $a_0 = 7$ only

when the laser system is free of any pre-pulse, which is realistically almost never true. In presence of a pre-pulse of lower intensity ($\tilde{a_0} < a_0$), the target density gets modified and a density gradient is formed. For a spherical plasma target (as in the present case), a sufficiently high intensity pre-pulse will ionize the solid hydrogen target and create a density variation such that the density is peaked at the centre of the sphere and dropping gradually towards the periphery. The drop in density from the centre is considered to be isotropic for simplicity.

The pre-pulse intensity is directly correlated with the central peak density (n_{peak}) and the delay time (Δt) between the pre-pulse and the main pulse using [4]

$$\tilde{a_0} = 4.7 \times 10^{-3} \sqrt{\frac{m_i}{m_e}} (\sigma - 1) \frac{R_0[\mu\text{m}]}{\Delta t[\text{ps}]} \tag{33.1}$$

Here, $\sigma = \dfrac{R}{R_0} = \left(\dfrac{n_0}{n_{\text{peak}}}\right)^{1/3}$ such that the radius of the target increases from R_0 to R as the density drops when a pre-pulse of normalized vector potential $\tilde{a_0}$ hits upon it. For these simulations, the peak of the main pulse interaction occurs at $\approx$188 fs which is assumed to be the time delay (Δt) between the pulses. By varying the pre-pulse intensity, therefore, the plasma target for the main pulse could be tuned to obtain the optimum accelerating condition of the protons. We varied $\tilde{a_0}$ from 0 to 2 and the corresponding values of the modified target radius and the central peak density is shown in Table 33.1.

Figure 33.1 shows the maximum proton energy obtained for different values of $\tilde{a_0}$. It is seen that $\tilde{a_0} = 0.5$ is the optimal energy case with maximum proton energy $\approx$36 MeV. It can be seen that the presence of the pre-pulse favours the generation of higher energetic protons when $\tilde{a_0} < 1$. Figure 33.2 shows the longitudinal proton momentum for four different strengths of the pre-pulse at different times. These phase space plots give the information about the dominant acceleration mechanisms that are participating after the interaction with the main pulse. It is seen that in the

Table 33.1 Variation of the modified target radius and the peak plasma density at the centre with the pre-pulse strength. The time delay between the pulses is 188 fs

Pre-pulse strength, $\tilde{a_0}$	Radius, R (μm)	Peak density (n_{peak}/n_c)
0	1.5 (R_0)	53 (solid H)
0.1	1.59	45.1
0.5	1.97	24
0.8	2.25	16.08
0.9	2.34	14.24
1	2.5	12
1.2	2.62	10.14
1.5	3.11	6.08
2	3.37	4.78

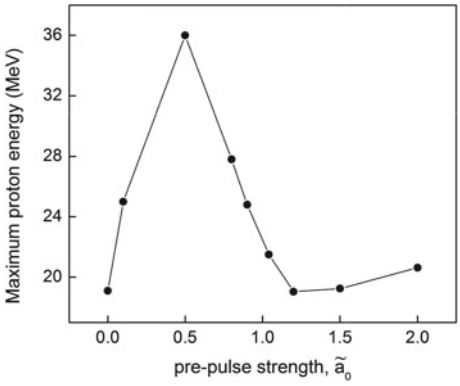

Fig. 33.1 The variation of maximum proton energy with the pre-pulse strength

no pre-pulse ($\tilde{a_0} = 0$) case (Fig. 33.2a), most of the protons gain momentum from the front side of the target. The sharp vacuum-target interface faced by the main pulse supports a strong density steepening at the front side of the target caused by the radiation pressure effect of the pulse. The laser propagation is stopped around the skin-depth and the plasma heating by the laser remains minimal. For the optimal energy case of $\tilde{a_0} = 0.5$ in Fig. 33.2b, the formation of a shock is visible in the downward density gradient ($Z > 10\,\mu$m) of the target. The protons reflected from the shock front gives an additional push to the expanding background protons and is the reason behind the production of high-energetic protons compared to the other cases. The shock formation is also seen in Fig. 33.2c for $\tilde{a_0} \simeq 1$. The maximum proton energy achieved in this case is however less in comparison the maximum energy obtained in the case with $\tilde{a_0} = 0.5$. When the pre-pulse strength is further increased to 1.5, the drop in the central density n_{peak} to $6.08n_c$ makes the target transparent to the main laser pulse and plasma expansion becomes the dominant mechanism. This is visible in Fig. 33.2d where the phase space displays a fairly uniform expansion of the target in both the forward and backward directions. With a further increase in the pre-pulse strength beyond this case, the maximum proton energy seems to slightly increase as seen from Fig. 33.1. This is because of a stronger expansion of the target before the laser main pulse hit upon it, rendering the target under-dense for the main pulse. As a result, the protons gain energy and are exploded in an isotropic manner.

33.3 Details of the Shock-Like Acceleration Mechanism

As discussed in the previous section, the formation of shock in the decreasing density region of the plasma has led to the production of high-energetic protons. The absorption of energy from the intense main laser pulse leads to the electrons attaining momentum and getting expelled from the central high density region of the plasma. This results in a strong anisotropic Coulomb repulsion among the left-over protons

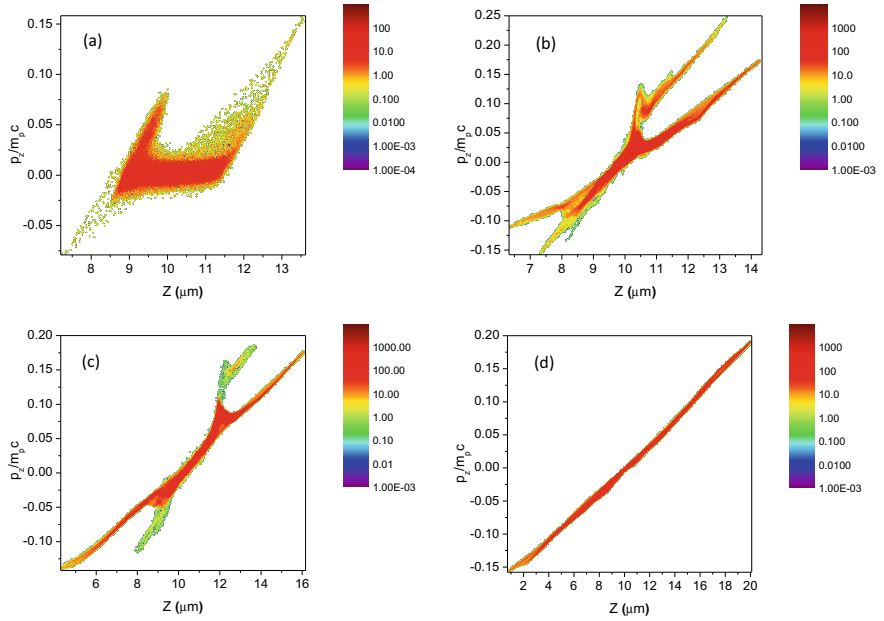

Fig. 33.2 The longitudinal proton momenta (p_z) along Z for four different cases with **a** $\tilde{a_0} = 0$, i.e. no pre-pulse at 246 fs, **b** $\tilde{a_0} = 0.5$ at 271.2 fs, **c** $\tilde{a_0} \simeq 1$ at 307 fs and **d** $\tilde{a_0} = 1.5$ at 388 fs. The colour axis represents the proton distribution in arbitrary units. The proton momentum is normalized by the product of proton mass and light velocity (m_pc)

in the centre of the target. The fast-moving protons from the inner regions eventually overrun the slow-moving protons at the outer region. This creates a density spike in the decreasing density gradient, and the wave-breaking results in the formation of a shock in this region [9–12]. The protons in the upstream region of this propagating shock will get reflected from the shock front to twice the shock velocity. The reflected protons are visible in the Fig. 33.2b, c, and these protons are expelled through the rear boundary of the target with the highest energies.

Figure 33.3 shows the temporal evolution of the peak value of the longitudinal electric field (E_z) (black-squares) and the maximum proton energy (blue-circles) for the two cases where shock formation takes place as seen in Fig. 33.2. In the first case $\tilde{a_0} = 0.5$ (Fig. 33.3a), apart from the principal maxima due to the laser field, there is another secondary maxima at around 270 fs. This peak is caused due to the shock formed by the overrunning among the protons. A similar secondary peak is seen in Fig. 33.3b for $\tilde{a_0} \simeq 1$, which signifies the formation of shock which was also implied from Fig. 33.2c. For this case, the shock-based peak emerges at a later stage ($\simeq$307 fs). Due to the low density in the central region compared to the previous case, the fast-moving inner protons take longer time to overcome the outer ions and as a result the shock formation is seen at around $Z \simeq 12.5\,\mu$m (from Fig. 33.2c). The reflection of protons from the shock front occurs for a shorter amount of time in this case and

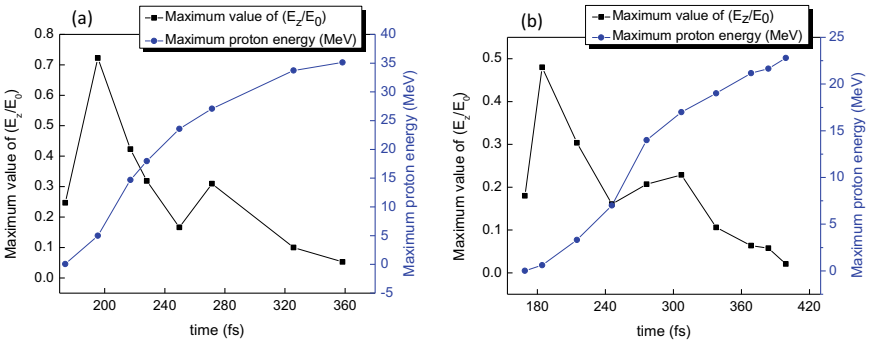

Fig. 33.3 The time evolution of the maximum longitudinal electric field (black squares) in the central Z-axis and the maximum proton energy (blue circles) for **a** $\tilde{a_0} = 0.5$ with $n_{\text{peak}} = 24n_c$, and **b** $\tilde{a_0} \simeq 1$ with $n_{\text{peak}} = 12n_c$. The electric field (E_Z) is normalized by the laser electric field E_0

as a result both the shock reflected proton number and the maximum proton energy remains low. On the contrary, the shock sustains for a longer amount of time in the case with $\tilde{a_0} = 0.5$ for which $n_{\text{peak}} \simeq 24n_c$, and the maximum proton energy as well as the proton number becomes high. The shock formation is not seen in the other two cases of Fig. 33.2. For the $\tilde{a_0} = 0$ case, the plasma density remains uniform for the main pulse. The protons attain a uniform expansion velocity and so overrunning of the protons does not take place which is the precursor of the shock formation for the other two cases. Again for the case with $\tilde{a_0} = 1.5$ and $n_{\text{peak}} = 6.08n_c$, the density gradient becomes too low for the inner protons to overtake the outer ions, and shock formation fails to occur.

33.4 Conclusion

3D PIC simulations were performed to observe the acceleration of protons from a micron-sized hydrogen sphere with a density gradient starting from the periphery and reaching a peak value at the target centre. The density gradient is created by hitting a uniform solid hydrogen sphere with a pre-pulse, before its interaction with the main laser pulse. The effect of various pre-pulse strengths has been studied and found that the presence of the pre-pulse (or the density gradient) helps in increasing the energy of the protons. The most efficient case of proton energy occurs for $\tilde{a_0} = 0.5$ where a two-stage acceleration process is seen. In the first stage, a strong Coulomb repulsion accelerates the protons. The presence of a decreasing density gradient induces a shock, which reflects upstream protons and accelerates them to high energies. This is the second stage of the acceleration. This process is crucially dependent on the density gradient and an optimum density gradient must be maintained by tuning the pre-pulse strength to attain highly energetic jets of protons for applications.

References

1. A. Macchi, M. Borghesi, M. Passoni, Rev. Mod. Phys. **85**, 751 (2013)
2. H. Daido, M. Nishiuchi, A.S. Pirozhkov, Rep. Prog. Phys. **75**, 056401 (2012)
3. A. Sgattoni, P. Londrillo, A. Macchi, M. Passoni, Phys. Rev. E **85**, 036405 (2012)
4. A.S. Novo, M. Kaluza, R. Fonseca, L. Silva, Sci. Rep. **6**, 29402 (2016)
5. A. Andreev, R. Sonobe, S. Kawata, S. Miyazaki, K. Sakai, K. Miyauchi, T. Kikuchi, K. Platonov, K. Nemoto, Plasma Phys. Control. Fusion **48**, 1605 (2006)
6. T. Kluge, W. Enghardt, S. Kraft, U. Schramm, K. Zeil, T. Cowan, M. Bussmann, Phys. Plasmas **17**, 123103 (2010)
7. T.M. Ostermayr, D. Haffa, P. Hilz, V. Pauw, K. Allinger, K.-U. Bamberg, P. Böhl, C. Bömer, P. Bolton, F. Deutschmann et al., Phys. Rev. E **94**, 033208 (2016)
8. P. Hilz, T. Ostermayr, A. Huebl, V. Bagnoud, B. Borm, M. Bussmann, M. Gallei, J. Gebhard, D. Haffa, J. Hartmann et al., Nat. Commun. **9**, 1 (2018)
9. E. d'Humières, P. Antici, M. Glesser, J. Boeker, F. Cardelli, S. Chen, J. Feugeas, F. Filippi, M. Gauthier, A. Levy et al., Plasma Phys. Control. Fusion **55**, 124025 (2013)
10. M. Gauthier, A. Levy, E. d'Humieres, M. Glesser, B. Albertazzi, C. Beaucourt, J. Breil, S. Chen, V. Dervieux, J. Feugeas et al., Phys. Plasmas **21**, 013102 (2014)
11. P. Antici, E. Boella, S. Chen, D. Andrews, M. Barberio, J. Böker, F. Cardelli, J. Feugeas, M. Glesser, P. Nicolaï et al., J. Sci. Rep. **7**, 1 (2017)
12. E. dHumières, V. Tikhonchuk, in *AIP Conference Proceedings*, Vol. 1299 (American Institute of Physics, 2010) pp. 704–709

Chapter 34
Searching the Limits on Heavy Majorana Mass Spectrum for Different Textures of Majorana Mass Matrices

Maibam Ricky Devi and Kalpana Bora

Abstract Seesaw mechanisms are used to generate the ultra-small mass of three active, observable neutrinos, in which three heavy right-handed Majorana neutrinos are needed. These three heavy Majorana neutrinos have so far remained undetected in the present-day collider experiments. The limits on this heavy neutrino mass spectrum can provide us interesting information on some other phenomenological aspects, such as the absolute mass scale of neutrinos and Leptogenesis, which remain unknown. In this work, we shall present a detailed analysis to measure the limits on the heavy Majorana masses for different textures of Dirac, Majorana and light neutrino mass matrices. We consider three zeroes texture of light neutrino mass matrix and a particular texture of Dirac mass matrix from which we can obtain heavy Majorana masses as well as the unknown neutrino oscillation parameters, viz., the lightest neutrino mass and the Dirac and Majorana CPV phases.

34.1 Introduction

We know that the light neutrino mass matrix can be evaluated as follows:

$$m_v = U_{PMNS}.M_{diag}.U_{PMNS}^T \tag{34.1}$$

where the U_{PMNS} mixing matrix can be parametrized as follows:

$$U_{\text{PMNS}} = \begin{pmatrix} c_{12}c_{13} & s_{12}c_{13} & s_{13}e^{-i\delta} \\ -s_{12}c_{23} - c_{12}s_{23}s_{13}e^{i\delta} & c_{12}c_{23} - s_{12}s_{23}s_{13}e^{i\delta} & s_{23}c_{13} \\ s_{12}s_{23} - c_{12}c_{23}s_{13}e^{i\delta} & -c_{12}s_{23} - s_{12}c_{23}s_{13}e^{i\delta} & c_{23}c_{13} \end{pmatrix} U_{\text{Maj}}\,, \tag{34.2}$$

M. R. Devi (✉) · K. Bora
Department of Physics, Gauhati University, Guwahati 781014, Assam, India
e-mail: kalpana@gauhati.ac.in

S. Sengupta et al. (eds.), *Selected Progresses in Modern Physics*, Springer Proceedings in Physics 265, https://doi.org/10.1007/978-981-16-5141-0_34

where $c_{ij} = \cos\theta_{ij}$, $s_{ij} = \sin\theta_{ij}$ and δ is the Dirac CP phase. The diagonal matrix with the Majorana CP phases α, β is given by $U_{\text{Maj}} = \text{diag}(1, e^{i\alpha}, e^{i(\beta+\delta)})$. Also from type-I seesaw we can find m_ν as follows:

$$m_\nu = M_D M_R^{-1} M_D^T. \tag{34.3}$$

We compare Eq. (34.1, 34.3) to find the limits of the Majorana masses for selective textures of the Majorana mass matrix as well as the Dirac and light neutrino mass matrix.

34.2 Majorana Mass Matrix as a 2 × 2 Symmetric Mass

For our work, first we assume a 2×2 Majorana mass matrix that requires a 3×2 Dirac matrix such that the light neutrino mass matrix turns out to be 3×3 after matrix multiplication. Suppose,

$$M_D = \begin{pmatrix} x_{11} & x_{12} \\ x_{21} & x_{22} \\ x_{31} & x_{32} \end{pmatrix}, \tag{34.4}$$

$$M_R = \begin{pmatrix} M_{11} & M_{12} \\ M_{21} & M_{22} \end{pmatrix}. \tag{34.5}$$

It is seen that after implementing type-I seesaw mechanism as given in Eq. (34.3) that *one of the eigenvalues of the light neutrino mass matrix is zero making its determinant zero too*. However, we already know that the neutrino mass matrix is not a singular matrix and is invertible. Thus, we disfavour this texture of 3×2 Dirac mass matrix.

34.3 Majorana Mass Matrix as a 3 × 3 Symmetric Mass

Next we take a 3×3 Majorana mass matrix such that the Dirac as well as the light neutrino mass matrices are a 3×3 matrix under a particular symmetry which we shall discuss in the later section. This is done in order to get the determinant as well as the three eigenvalues of the light neutrino mass matrix to be non-zero.

$$M_D = \begin{pmatrix} x_{11} & x_{12} & x_{13} \\ x_{21} & x_{22} & x_{23} \\ x_{31} & x_{32} & x_{33} \end{pmatrix}, \tag{34.6}$$

$$M_R = \begin{pmatrix} M_{11} & M_{12} & M_{13} \\ M_{21} & M_{22} & M_{23} \\ M_{31} & M_{32} & M_{33} \end{pmatrix}. \tag{34.7}$$

However, we know that the light neutrino mass matrix is a symmetric matrix, i.e. $m_\nu = m_\nu^T$. This can be possible only if both the Dirac as well as the Majorana mass matrices are symmetric too. Thus, we take a new texture of M_D and M_R such that $x_{ij} = x_{ji}$ and $M_{ij} = M_{ji}$ $(i, j = 1, 2, 3)$.

34.4 Numerical Analysis

As mentioned earlier in Eq. (34.1), we know that the light neutrino mass matrix can be obtained from the parametrized U_{PMNS} matrix and M_{diag}. We can re-write Eq. (34.1) as follows [1–3]

$$\Rightarrow m_\nu = V.U_{Maj}.M_{diag}.U_{Maj}^T.V^T \Rightarrow m_\nu = V.B.V^T, \tag{34.8}$$

where

$$B = \begin{pmatrix} m_1 & 0 & 0 \\ 0 & e^{2i\alpha}m_2 & 0 \\ 0 & 0 & e^{2i(\beta+\delta)}m_3 \end{pmatrix} = \begin{pmatrix} \lambda_1 & 0 & 0 \\ 0 & \lambda_2 & 0 \\ 0 & 0 & \lambda_3 \end{pmatrix}, \tag{34.9}$$

and

$$V = \begin{pmatrix} c_{12}c_{13} & s_{12}c_{13} & s_{13}e^{-i\delta} \\ -s_{12}c_{23} - c_{12}s_{23}s_{13}e^{i\delta} & c_{12}c_{23} - s_{12}s_{23}s_{13}e^{i\delta} & s_{23}c_{13} \\ s_{12}s_{23} - c_{12}c_{23}s_{13}e^{i\delta} & -c_{12}s_{23} - s_{12}c_{23}s_{13}e^{i\delta} & c_{23}c_{13} \end{pmatrix}, \tag{34.10}$$

where $\lambda_1 = m_1$, $\lambda_2 = e^{2i\alpha}m_2$ and $\lambda_3 = e^{2i(\beta+\delta)}m_3$. Now suppose we take the two-zero texture of the neutrino mass matrix of the form

$$m_\nu = \begin{pmatrix} 0 & 0 & \times \\ 0 & \times & \times \\ \times & \times & \times \end{pmatrix}. \tag{34.11}$$

This is one of the allowed two-zeroes texture of m_ν as discussed in ref [1]. By comparing Eqs. (34.8, 34.11), we get

$$\frac{\lambda_3}{\lambda_1} = e^{-2i\delta}\sec(\theta_{12})\sec^2(\theta_{13})\sec(\theta_{23})(\sin^2(\theta_{13})\cos(\theta_{12})\cos(\theta_{23}) - e^{i\delta}\sin(\theta_{12})\sin(\theta_{13})\sin(\theta_{23})) \tag{34.12}$$

$$\frac{\lambda_2}{\lambda_1} = \frac{2\sin^2(\theta_{12})\sin(\theta_{23}) - e^{-i\delta}\sin(2\theta_{12})\sin(\theta_{13})\cos t(\theta_{23})}{2\sin(\theta_{23})\cos^2(\theta_{12}) + e^{-i\delta}\sin(2\theta_{12})\sin(\theta_{13})\cos(\theta_{23})} \tag{34.13}$$

$$\frac{\lambda_2}{\lambda_3} = -\frac{e^{2i\delta}\sin(\theta_{12})\cos^2(\theta_{13})\cos(\theta_{23})}{\sin(\theta_{12})\sin^2(\theta_{13})(-\cos(\theta_{23})) - e^{i\delta}\sin(\theta_{23})\sin(\theta_{13})\cos(\theta_{12})} \tag{34.14}$$

where $\frac{\lambda_3}{\lambda_1} = \frac{e^{2i(\beta+\delta)}m_3}{m_1}$, $\frac{\lambda_2}{\lambda_1} = \frac{e^{2i\alpha}m_2}{m_1}$ and $\frac{\lambda_2}{\lambda_3} = \frac{e^{2i\alpha}m_2}{e^{2i(\beta+\delta)}m_3}$.

Since $|M_{ee}| = 0$ from the above texture, we can write

$$e^{2i\alpha}C_{13}^2 m_2 S_{12}^2 + C_{12}^2 C_{13}^2 m_1 + m_3 S_{13}^2 e^{2i(\beta+\delta)-2i\delta} = 0. \tag{34.15}$$

Now after multiplying both sides of Eq. (34.15) with $1/m_1$, we can substitute the values of $\frac{e^{2i\alpha}m_2}{m_1}$ and $\frac{e^{2i(\beta+\delta)}m_3}{m_1}$ from Eqs. (34.12, 34.13) into Eq. (34.15) to get the value of Dirac CPV phase, δ. Thus after computation we get the value of $\delta \sim (143.141 - 197.422)$. These values of Dirac CPV phase along with the values of mass squared differences from latest global fit values [4] can be substituted into Eqs. (34.12, 34.13, 34.14) to get the values of the Majorana phases within 3σ global fit values.

34.5 Results on the Limits of Majorana Masses

We take the textures of the Dirac, Majorana and the light neutrino mass matrices as shown below

$$m_\nu = \begin{pmatrix} a & b & c \\ b & d & e \\ c & e & f \end{pmatrix}, M_D = \begin{pmatrix} x_{11} & 0 & 0 \\ 0 & 0 & x_{23} \\ 0 & x_{32} & 0 \end{pmatrix}, M_R = \begin{pmatrix} M_{11} & M_{12} & M_{13} \\ M_{21} & M_{22} & M_{23} \\ M_{31} & M_{32} & M_{33} \end{pmatrix}. \tag{34.16}$$

Considering the above matrices as symmetric, we implement type-I seesaw mechanism and then compute the values of the Majorana mass matrix elements as follows:

$$M_{11} = \frac{x_{11}^2\left(e^2 - 1.df\right)}{-1.adf + ae^2 + b^2 f - 2.bce + c^2 d}, \tag{34.17}$$

$$M_{12} = M_{21} = \frac{x_{11}x_{32}(cd - 1.be)}{-1.adf + ae^2 + b^2 f - 2.bce + c^2 d}, \tag{34.18}$$

$$M_{13} = M_{31} = \frac{bfx_{11}x_{32} - 1.cex_{11}x_{32}}{-1.adf + ae^2 + b^2 f - 2.bce + c^2 d}, \tag{34.19}$$

$$M_{22} = \frac{x_{32}^2\left(b^2 - 1.ad\right)}{-1.adf + ae^2 + b^2 f - 2.bce + c^2 d}, \tag{34.20}$$

$$M_{23} = M_{32} = \frac{aex_{32}^2 - 1.bcx_{32}^2}{-1.adf + ae^2 + b^2 f - 2.bce + c^2 d}, \tag{34.21}$$

$$M_{33} = \frac{x_{32}^2\left(c^2 - 1.af\right)}{-1.adf + ae^2 + b^2 f - 2.bce + c^2 d}. \tag{34.22}$$

If we consider the light neutrino mass texture as given in Eq. (34.11), i.e. $a = b = 0$, then this put the constraint $M_{32}^2 = M_{22}M_{33}$ and $M_{22}M_{31} = M_{21}M_{32}$ as x_{11}, x_{32} are non-zero elements.

34.6 Summary

To summarize, in this work, we considered an ad-hoc texture of Dirac neutrino mass matrix and a two-zero texture of light neutrino mass matrix which induces correlation conditions between the unknown neutrino oscillation parameters $m_{lightest}$, δ_{CP} and Majorana phases α and β (as shown in Eqs. (34.12, 34.13, 34.14, 34.15). Taking the latest global fit values for the known parameters we can calculate the unknown neutrino parameters. After solving these relations, we obtained the Dirac CPV phase, δ in the range (143.141–197.422 Degrees) which falls within the 3σ range (128–359 Degrees). Next, we considered the textures as mentioned in Eq. (34.16) and implemented the type-I seesaw mechanism and compared it with Eq. (34.2), then computed the values of Majorana mass matrix elements. This analysis can be used to compute the limits of mass of heavy Majorana neutrinos for a particular texture of M_R obtained from the allowed two-zero texture of m_ν. This can also be done for other allowed textures of these matrices, and this work is in progress.

References

1. P.H. Frampton, S.L. Glashow, D. Marfatia, Phys. Lett. B. **536**, 79–82 (2002). arXiv:hep-ph/0201008 [hep-ph]. https://doi.org/10.1016/S0370-2693(02)01817-8
2. L. Lavoura, Phys. Lett. B. **609**, 317–322 (2005). arXiv:hep-ph/0411232 [hep-ph]. https://doi.org/10.1016/j.physletb.2005.01.047
3. Z.Z. Xing, Phys. Lett. B. **530**, 159–166 (2002). 10.1016/S0370-2693(02)01354–0 arXiv:hep-ph/0201151 [hep-ph]
4. P.F. de Salas, D.V. Forero, S. Gariazzo, P. Martínez-Miravé, O. Mena, C.A. Ternes, M.Tórtola, J.W.F. Valle, JHEP. **02**, 071 (2021). arXiv:2006.11237 [hep-ph]. https://doi.org/10.1007/JHEP02(2021)071

Chapter 35
Smartphone-Based Colorimetric Analyzer for Detection of Phosphate in Water

Priyanka Das, Biprav Chetry, and Pabitra Nath

Abstract This paper reports a low-cost, compact, field-portable smartphone-based colorimetric analyzer for the detection of phosphate concentration in water medium. A 3D printed cradle housing the required optical components is integrated with the built-in camera of the smartphone. Photographs of the reagent-treated test samples are captured by the camera phone; subsequently, the RGB color model of the images is converted to the HSV color model. Using an Android application, the RGB color model is converted to the HSV color model. For the quantification of phosphate, the V-channel value of HSV color space is co-related with the phosphate concentration. The obtained results are compared with the laboratory-grade standard spectrophotometer by measuring its absorbance at a specific wavelength. The designed smartphone sensing tool has the ability to measure phosphate concentration with a good accuracy (%bias < 1%) and precision (RSD < 2%). The sensing technique can be used as an alternative to the existing phosphate level detection sensors as it provides a fast and user-friendly analytical platform for in-field applications.

35.1 Introduction

Colorimetric analysis is a well-established technique of determining and analyzing the concentration of a chemical compound in a solution using a color reagent. It is a very useful method for the analysis of various kinds of nutrients, biomolecules [1], hazardous chemicals [2] and important parameters affecting the standard of an environmental entity. One of the important benefits of this method is that it provides a visual analysis of the sample which can roughly give us some idea about the concentration of an analyte present in that sample. However, visual analysis has poor accuracy and is subjected to the viewer's visual state and environmental conditions. In this regard, several laboratory-grade spectrophotometers have been developed to make use of the colorimetric principle but they are way too costly, complicated and bulky in nature. Also, to process and analyze the data from the spectrophotometers

P. Das (✉) · B. Chetry · P. Nath
Applied Photonics & Nano-Photonics Laboratory, Department of Physics, Tezpur University, Tezpur, Assam, India

S. Sengupta et al. (eds.), *Selected Progresses in Modern Physics*, Springer Proceedings in Physics 265, https://doi.org/10.1007/978-981-16-5141-0_35

a desktop computer system is required. All these factors related to the spectrophotometers give rise to a lot of hurdles for their utilization in resource-poor areas having financial instability.

To overcome these limitations, we have proposed here a sensing system utilizing the smartphone's camera as a sensing device for the colorimetric analysis of the sample solution. We have utilized the smartphone in this study due to the fact that nowadays smartphones have a lot of processing power and are also equipped with a lot of embedded features like Wi-Fi, gyroscope, accelerometer, ambient light sensor, superior high-resolution cameras, etc. Having a collection of such a large array of features a smartphone can truly act as a compact, portable, robust and low-cost optical sensing system and can be utilized for a wide range of sensing applications [3, 4] in resource-poor areas. Utilizing the built-in sensors and the superior software in smartphones, many research teams from around the globe have developed various systems for different sensing applications such as spectrometer [5, 6], pH sensor [7], phosphate detection in soil [8], protein and carbohydrate detection [9], fluoride detection [10], water turbidity and salinity measurement [11, 12], and many more.

In this work, we have developed a smartphone-based sensing system to detect the concentration of phosphorus available in various water bodies using a standard colorimetric method. The motivation behind selecting phosphorus as the analyte for estimation is that phosphorus is an integral part of the nutrients present in the aquatic ecosystem [13]. It is mainly present in water in the form of different phosphates. Phosphates are mainly present in aquatic animal bodies. The optimal concentration of phosphorus present in water is naturally in small amounts. But due to the rainfall, some amount of phosphorus may be swept from the agricultural lands into the nearby water bodies where phosphorus-containing fertilizers may be used [14]. Also, various human activities may also give rise to an increase in the level of phosphorus which can lead to a serious process of eutrophication. According to the World Health Organization, the permissible phosphate concentration limit in drinking water is 0.1 mg/l [15]. Also, the allowable phosphorus limits for natural and wastewater are 0.2 and 10 mg/l, respectively [16]. Hence monitoring of phosphorus level in water is very important in order to attain a balanced ecosystem.

35.2 Methodology

35.2.1 Design of the Experimental Setup

The schematic of the proposed smartphone sensor is shown in Fig. 35.1. A 3D printed cradle has been designed to house all the optical components together and printed out using ZW3D software. The setup consists of a white LED that has been powered by the phone's battery by using a USB OTG cable. The light emitted by the LED is collimated by using a plano-convex lens having a focal length of 11 mm. The collimated beam of light is diffused with a diffuser made up of nylon sheet having a

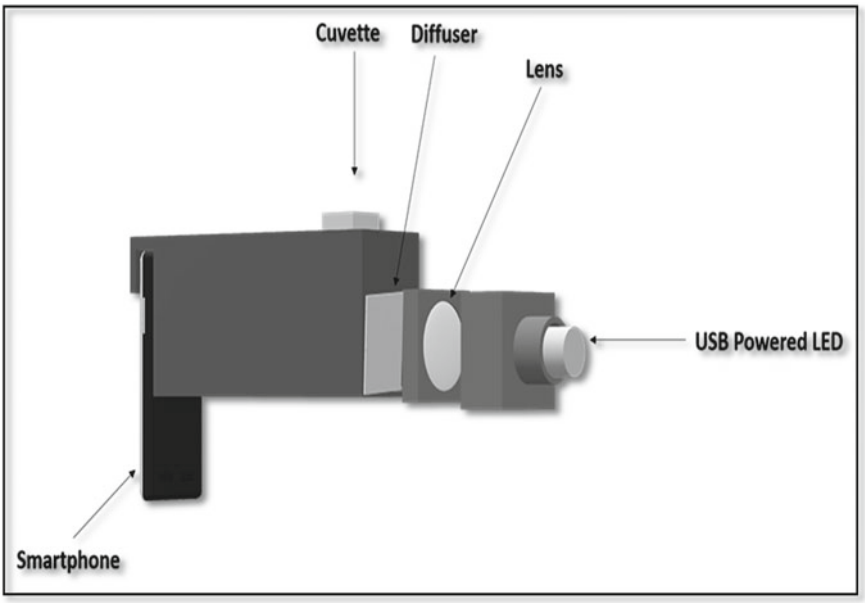

Fig. 35.1 Schematic diagram of the designed smartphone-based sensor

thickness of 5 mm and placed at a distance of 4 cm from the lens so that the light is uniformly illuminated on the sample. The sample solution is kept in a quartz cuvette which is then illuminated by the light coming from the nylon diffuser. The image of the illuminated cuvette is taken by the smartphone camera which is at a distance of 5 cm from the cuvette. The diffused light signal passes through the sample and subsequently the modulated light signal is received by the camera of the phone. The nylon sheet diffuser ensures that the bright spot of the LED gets reduced and the sample is uniformly illuminated. When there is no diffuser present the V value of the captured image of the sample is found to be saturated, and when the diffuser is present a fairly linear variation of V component with the change in the concentration of the sample is seen, which can be efficiently estimated by the use of this setup. The setup housing all the components is perfectly shielded to avoid any ambient light entering the unit and interfering with the image.

35.2.2 Reagents and Standard Sample Preparation

All the chemicals used in this work were of analytical grade and procured from Merck & Co. All the solutions were prepared in deionized water produced by a water purification system. The detection of phosphate is based on the standard ascorbic acid method where ammonium molybdate and potassium antimonyl tartrate react in an

acidic medium with orthophosphate to form a heteropoly acid—phosphomolybdic acid that is reduced to intensely colored molybdenum blue by ascorbic acid. Ten standard phosphate samples of concentration in the range of 0.1–1.0 mg/l with a step incremental value of 0.1 mg/l have been prepared for calibration of the designed sensor. For the colorimetric synthesis three reagents potassium antimonyl tartrate (dissolving 0.13715 g of potassium antimonyl tartrate in 50 ml of DI water), ammonium molybdate (dissolving 2 g of ammonium molybdate tetrahydrate in 50 ml DI water) and ascorbic acid solution (dissolving 0.88 g of ascorbic acid in 50 ml DI water) have been prepared. A 50 ml solution of combined reagent was prepared by mixing the reagents in the following proportions: 25 ml of 5N solution of H_2SO_4, 2.5 ml of potassium antimonyl tartrate solution, 7.5 ml of ammonium molybdate solution and 15 ml of ascorbic acid solution. After preparing all the reagents and standard solutions, 1.6 ml of the combined reagent was added to each of 10 ml of standard phosphate samples and allowed the samples to stand for at least 10 min. The samples slowly turned into light blue color depending on the phosphate concentration present in the samples. After about 10 min the sample was transferred to a cuvette and the images of the cuvette were captured by the smartphone sensor.

35.2.3 Android Application for Phosphate Analysis

In order to estimate phosphate concentration present in a medium directly within the phone itself, two freely available Android-based applications, 'RGB color detector' and 'stanXY' have been used for data acquisition and analysis. The V channel values of the photo images of the reagent-treated phosphate sample were obtained by using the RGB color detector application. In this application, the photo images of freshly prepared samples can be captured as well as images from the gallery of the phone can be loaded. After acquiring the V channel values of the respective phosphate samples, the observed sensor data were loaded in the stanXY application in order to generate the standard calibration graph and from the plotted calibration graph the phosphate concentration of an unknown sample can be estimated. The screenshots of the two used applications have been given in Fig. 35.2.

35.3 Results and Discussions

In the present work, the intensity of colored molybdenum blue has been measured by using a smartphone-based colorimetric analyzer. As suggested by the standard ascorbic acid method, the developed blue color in the samples becomes darker with the increase of phosphate concentration in the samples. The V channel values from the images of the samples of varying phosphate concentrations have been extracted for the colorimetric estimation of phosphate. From the obtained data, a calibration curve has been obtained between phosphate concentration and the V channel values

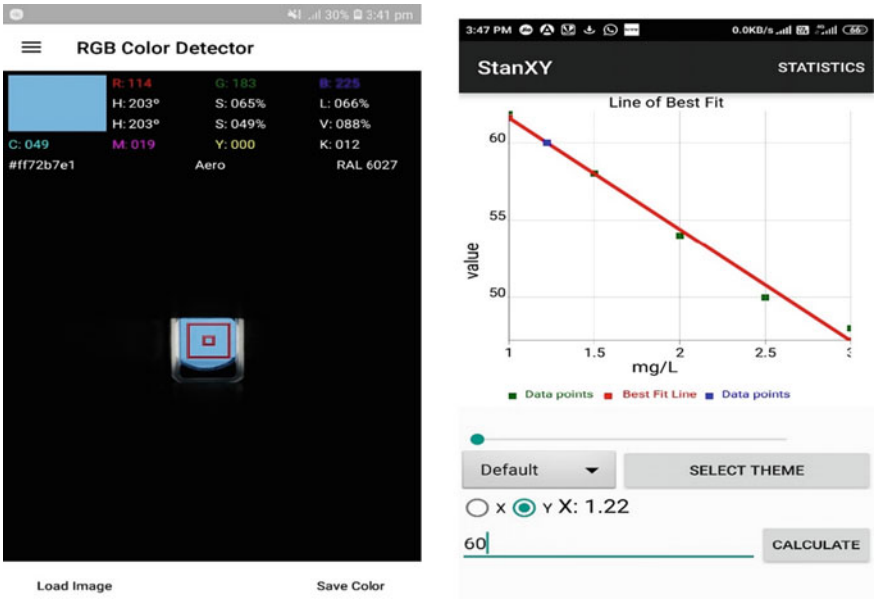

Fig. 35.2 Screenshots of the two used Android application

for the concentration range from 0.1 to 1 mg/l. Fig. 35.3 shows the calibration curve obtained with the designed smartphone sensor. From the calibration curve, it can be observed that the V channel values decrease linearly with the increase in phosphate concentration. The obtained data is in accordance with the general idea that the V value goes toward 1 when the image is brighter and it drops down toward 0 when the image gets darker. By doing the linear fitting with the data points we have obtained a good linear fitted curve having regression coefficients, $R^2 = 0.983$. From the linear fitted curve, the obtained calibration equation is given as

$$V\ channel - Value = (-\mathbf{0.15394})phosphate\ conc. + \mathbf{0.77867} \quad (35.1)$$

From the calibration equation, by putting the V channel value of the captured image we can determine the unknown phosphate concentration in a sample.

35.3.1 Spectrophotometric Analysis of the Standard Phosphate Samples

To test the accuracy of the designed smartphone-based optical setup for experimental investigation, the spectrophotometric analysis of the standard phosphate samples of

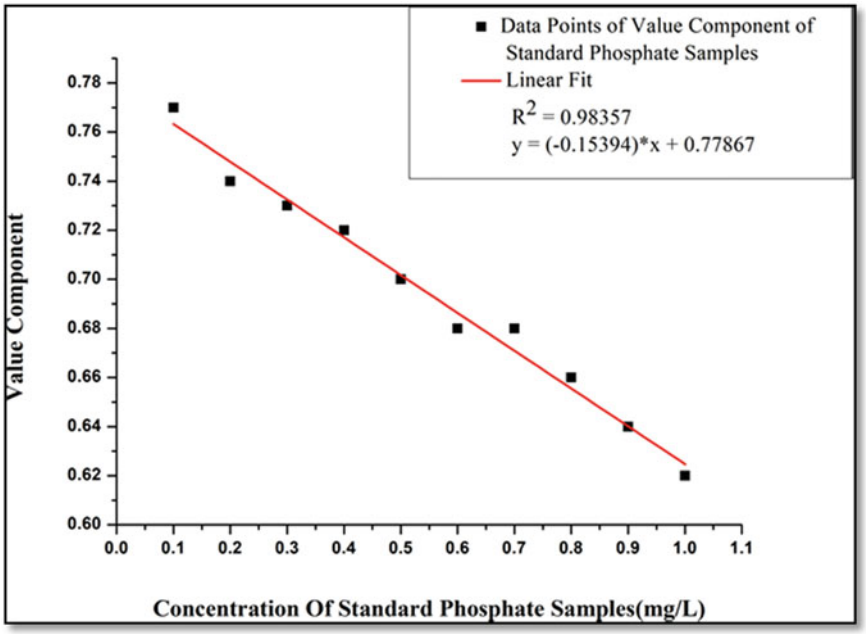

Fig. 35.3 Calibration curve showing the variation of V-channel of HSV color space obtained with the smartphone sensor within the limit 0.1–1 mg/l

varying concentrations was carried out using a standard laboratory-grade spectrophotometer (UV/Vis spectrophotometer). The peak absorption wavelength for different standard phosphate samples was observed to be at 880 nm. Figure 35.4 shows the variation of absorbance value with different phosphate concentrations. From the plot, it can be observed that the absorbance at the peak wavelength (880 nm) increases as the phosphate concentration in the samples increases. This variation of absorbance with concentration is in accordance with the Beer-Lambert law which states that the quantity of light absorbed by a substance dissolved in a transmitting medium is directly proportional to the concentration. For the prepared reagent-treated standard samples, as the phosphate concentration increases the developed blue color of the sample becomes darker and hence the absorbance of light increases with the sample concentration.

35.3.2 Sensor Characteristics

The sensitivity of a sensor gives us an idea of how efficiently a sensor can distinguish between two values relatively close to each other. The sensitivity of the designed

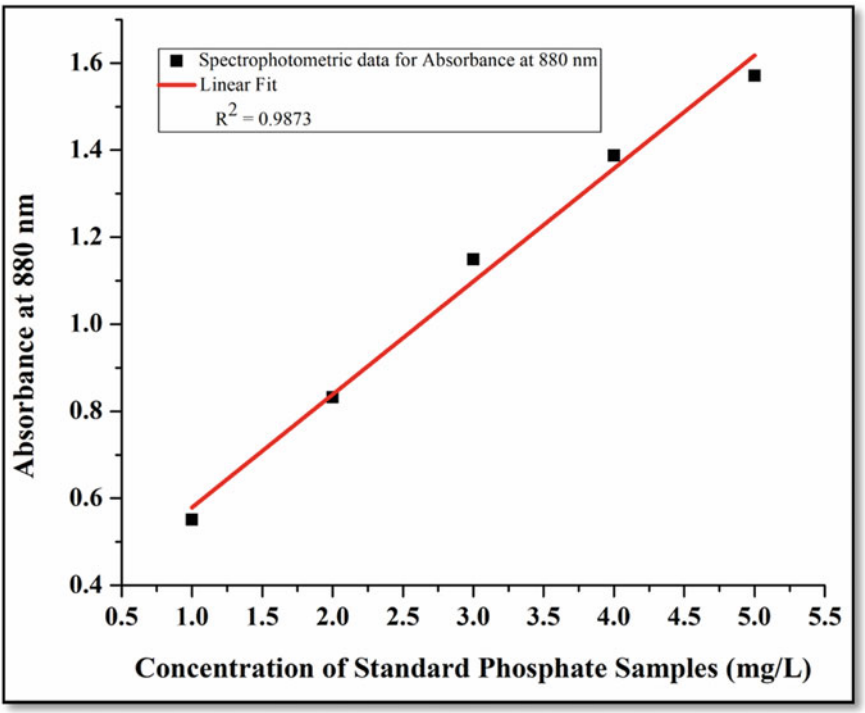

Fig. 35.4 Absorbance vs concentration plot of reagent-treated standard phosphate samples

system can be obtained from the slope of the linearly fitted calibration curve. The sensitivity of the designed sensor was found to be 0.15364 AU mg/l.

The accuracy and precision of the designed sensor have been evaluated by considering five standard phosphate samples with concentrations 0.5, 1, 1.5, 3, and 5 mg/l. The accuracy is expressed as % bias from the calculated mean phosphate concentration value as

$$\%bias = \frac{(Known\ phosphate\ conc. - Mean\ phosphate\ conc.)}{Known\ phosphate\ conc.} \times 100 \quad (35.2)$$

The precision is determined in terms of % residual standard deviations (% RSD) given as

$$\%RSD = \frac{Standard\ Deviation}{Mean} \times 100 \quad (35.3)$$

After calculating the %bias and %RSD of the five standard phosphate samples using the above formulas, the mean bias accuracy value was found to be 0.83%,

Table 35.1 Measured phosphate concentrations of field-collected water samples by spectrophotometer and designed smartphone-based sensing tool

Field-collected water samples	Designed sensor measurement (mg/L)	Spectrophotometer measurement (mg/L)
Tap water	0.018 ± 0.005	0.015 ± 0.001
Niribili lake water	0.049 ± 0.004	0.053 ± 0.001
Palmaiguli village water	0.089 ± 0.005	0.081 ± 0.003

while the mean RSD value was 1.75%. Both the values suggest a good accuracy and precision of the sensor while measuring the phosphate concentration.

35.3.3 Field-Collected Samples

The working of the designed sensor for the in-field applications has been evaluated. Different water samples have been collected from the Tezpur University nearby area, namely Niribili Pond in the campus, tap water from the campus and from a pond in Parmaiguli village in Napaam, Tezpur. Upon treating the field-collected water samples with the prepared combined reagent, the concentration of phosphate in the water samples has been determined by the designed smartphone-based sensor. The concentration of phosphate for the field-collected samples has been measured by using the proposed colorimetric analyzer, and the results were compared with the standard spectrophotometer as given in Table 35.1.

35.4 Conclusion

This study demonstrates the working of a smartphone-based sensing tool to determine the concentration of phosphate by image analysis technique. The proposed system offers advantages over a traditional sensing device mainly being low cost, compact and user-friendly and can be used in resource-poor areas. The designed setup is simple and easy to operate and can be adapted for any smartphone. The proposed setup can also be utilized for the detection and estimation of other environmentally hazardous elements such as arsenic, fluorine, etc. by treatment of the water samples containing such elements with suitable reagents. Moreover, using this simple setup one can also estimate the unknown quantity of numerous analytes in different environmental media in an easy and affordable manner.

References

1. D. Li, Y. Dong, B. Li, Y. Wu, K. Wang, S. Zhang, Colorimetric sensor array with unmodified noble metal nanoparticles for naked-eye detection of proteins and bacteria. Analyst **140**(22), 7672–7677 (2015)
2. L. Feng, C.J. Musto, J.W. Kemling, S.H. Lim, W. Zhong, K.S. Suslick, Colorimetric sensor array for determination and identification of toxic industrial chemicals. Anal. Chem. **82**(22), 9433–9440 (2010)
3. S.K. Vashist, E.M. Schneider, J.H. Luong, Commercial smartphone-based devices and smart applications for personalized healthcare monitoring and management. Diagnostics **4**(3), 104–128 (2014)
4. S.K. Vashist, O. Mudanyali, E.M. Schneider, R. Zengerle, A. Ozcan, Cellphone-based devices for bioanalytical sciences. Anal. Bioanal. Chem. **406**(14), 3263–3277 (2014)
5. A. Hossain, J. Canning, S. Ast, P.J. Rutledge, T.L. Yen, A. Jamalipour, Lab-in-a-phone: smartphone-based portable fluorometer for pH measurements of environmental water. IEEE Sens.S J. **15**(9), 5095–5102 (2014)
6. D. Jian, B. Wang, H. Huang, X. Meng, C. Liu, L. Xue, S. Wang, Sunlight based handheld smartphone spectrometer. Biosens.S Bioelectron. **143**, 111632 (2019)
7. P. Das, S. Paul, S.S. Bhattacharya, P. Nath, Smartphone-based spectrometric analyzer for accurate estimation of pH value in soil. IEEE Sens.S J. **21**(3), 2839–2845 (2020)
8. N. Moonrungsee, S. Pencharee, J. Jakmunee, Colorimetric analyzer based on mobile phone camera for determination of available phosphorus in soil. Talanta **136**, 204–209 (2015)
9. S. Dutta, G.P. Saikia, D.J. Sarma, K. Gupta, P. Das, P. Nath, Protein, enzyme and carbohydrate quantification using smartphone through colorimetric digitization technique. J. Biophotonics **10**(5), 623–633 (2017)
10. I. Hussain, K.U. Ahamad, P. Nath, Low-cost, robust, and field portable smartphone platform photometric sensor for fluoride level detection in drinking water. Anal. Chem. **89**(1), 767–775 (2017)
11. I. Hussain, K. Ahamad, P. Nath, Water turbidity sensing using a smartphone. RSC Adv. **6**(27), 22374–22382 (2016)
12. I. Hussain, M. Das, K.U. Ahamad, P. Nath, Water salinity detection using a smartphone. Sens.S Actuators B: Chem. **239**, 1042–1050 (2017)
13. American Public Health Association, American Water Works Association, Water Pollution Control Federation, & Water Environment Federation. *Standard Methods For The Examination Of Water And Wastewater,* vol. 2. (American Public Health Association, 1915)
14. M. Kumar, A. Puri, A review of permissible limits of drinking water. Indian J. Occup. Environ. Med. **16**(1), 40 (2012)
15. A.O. Fadiran, S.C. Dlamini, A. Mavuso, A comparative study of the phosphate levels in some surface and ground water bodies of Swaziland. Bull. Chem. Soc. Ethiop. **22**(2), 197–206 (2008)
16. A.L. Singh, A.K. Tripathi, A. Kumar, V.K. Singh, Nitrate and phosphate contamination in ground water of Varanasi. J. Ind. Res. Technol. **2**(1), 26–32 (2012)

Chapter 36
Structural, Morphological and Optical Properties of Titanium Dioxide Nanomaterials Prepared by Sol Gel Technique

Ansh Gupta, Deepak Kumar, Anupam Kumar, Jeeban P. Gewali, and Ankush Thakur

Abstract Titanium dioxide (TiO_2) nanoparticles have been successfully prepared by using titanium tetrachloride and ethanol as a starting reagent with the help of sol–gel technique to study insight behaviour of TiO_2 nanoparticles under an acidic environment. The prepared TiO_2 nanoparticles have been characterized for structural, morphological, and optical properties by using X-ray diffraction (XRD), Fourier transform infrared spectroscopy (FTIR), Field emission scanning electron microscopy (FESEM) and UV–vis spectroscopy (UV–vis). Structural analysis confirms the formation of crystalline nanoparticles, and line broadening technique has been employed to determine the crystallite size. FTIR reveals the lattice vibration in characteristic absorption frequency band. FESEM explores the surface morphology of synthesized nanoparticles, and UV–vis spectroscopy has been used to determine the optical band gap.

36.1 Introduction

In recent years, titanium dioxide extensively attracted the attention of researchers due to novel and unique properties. TiO_2 are often called Titania having structure stability and biocompatibility [1]. Unique physical, optical and structural properties lead Titania to be part of a variety of applications like photo-catalysis, solar-photovoltaic, ceramic material, filler, coating, pigment etc. UV screening properties and optical

A. Gupta (✉) · J. P. Gewali · A. Thakur
Department of Physics, School of Chemical Engineering and Physical Sciences, Lovely Professional University, Phagwara, Punjab 144411, India

D. Kumar
Department of Chemistry, School of Chemical Engineering and Physical Sciences, Lovely Professional University, Phagwara, Punjab 144411, India

A. Kumar
Department of Biotechnology, School of Bioengineering and Biosciences, Lovely Professional University, Phagwara, Punjab 144411, India

S. Sengupta et al. (eds.), *Selected Progresses in Modern Physics*, Springer Proceedings in Physics 265, https://doi.org/10.1007/978-981-16-5141-0_36

transparency in the visible spectrum make these particles suitable for cosmetics, resin and paint [2]. Currently, TiO_2 nanoparticles are used for its photocatalytic properties to improve the quality of materials for various applications such as in solar cells to produce e^- and hole pairs, extracting hydrogen gas from water by splitting water molecules etc. Titanium di-oxide exist in various polymorphs like anatase (tetragonal), rutile (tetragonal), brookite (orthorhombic), TiO_2 (B-Bronze), TiO_2 (H-Hollandite), TiO_2 (R-Ramsdellite), Akaogiite (baddeleyite) [3]. Only anatase, rutile and brookite are found in nature and remaining can be derived in laboratory. Anatase and rutile belong to $I4_1$ /amd and $P4_2$ /mnm space group [3]. TiO_2 anatase phase contains four formula unit in unit cell, and rutile contains two formulas per unit cell [4]. The calcinations at ~ 700°C leads to phase transformation from anatase to rutile occurred which is found to be irreversible process because rutile is highly stable phase of TiO_2. The calcination temperature depends on many factors such as synthesis, dopant (size and charge), atmosphere and oxygen defects. The substitution of dopant in TiO_2 affects the transition temperature, whereas doping of metal oxides with lower melting point (lower than TiO_2) promotes the phase transition [5, 6]. Cationic dopant has small ionic radii and low valence that help to accelerate transition to rutile due to increase in oxygen vacancy which definitely leads to instability in initial phase structure (anatase phase) [7, 8]. Thus, cationic dopant of valence less than four will promote transition and valence greater than four will inhibit transition. Similarly, anionic dopant is assumed to fill the oxygen vacancies and promotion or inhibition of phase transition will depend on its charge effects and size [8]. There are several methods that have been developed to incorporate the substitution in lattice such as hydrothermal method, solvo-thermal method, sol–gel method, chemical vapour deposition method, electro-deposition method, direct oxidation method, microwave method and sono-chemical method to enhance the properties for desired application [9]. Since 1971, sol–gel method has been opted for the production of multi component oxides due to low cost, ease of fabrication, mixing of ions at atomic level, and homogeneity of solution can be controlled easily. In present research work, TiO_2 has been synthesized and characterized for structural, morphological and optical properties.

36.2 Synthesis Procedure

In the synthesis of TiO_2, anhydrous titanium tetrachloride ($TiCl_4$) is added drop wise to absolute ethanol in the ratio 1:10 such that volume of total solution will be 20 ml. Mixing is done at room temperature under fume hood due to liberation of chlorine and HCl gas. This reaction is exothermic in nature, as a consequence the temperature of the solution increased during mixing. Allowing the solution to restore its temperature to room temperature and then measured the pH. The pH of solution is found to be highly acidic in nature. Now the solution is dried in a temperature range 60–70°C until gel is formed. Obtained TiO_2 was calcined for 2 h in furnace

at 500°C, and the same sample is further calcinated at 900°C (2 h). The obtained powder is kept in air tight bottle and subjected for further analysis.

Structural properties have been analysed with the help of X'Pert Pro diffractometer using Cu-K_α radiation to gather the information about physical parameters. IR-Prestige-21-FTIR-8400S, Shimadzu Corporation, has been employed to determine absorption characterization of prepared nanoparticles in Mid-IR range. Morphology has been analysed with the help of field emission scanning electron microscopy. Optical properties of the synthesized sample have been exposed using UV–vis spectroscopy. UV-1800, UV–vis scanning spectrophotometer designed under Shimadzu Corporation has been taken in to consideration for optical property analysis.

36.3 Results and Discussion

36.3.1 Structural Analysis

XRD is one of the important characterization techniques for qualitative analysis of synthesized nanoparticles with the help of Bragg's diffraction technique to study the presence of crystallographic planes. Figures 36.1 a, b represent diffraction pattern of sample calcinated at 500°C and 900°C, respectively. Structural analysis of the sample confirms the step formation of rutile phase from titanium tetrachloride ($TiCl_4$) and ethanol in acidic medium.

Figure 1a reveals the presence of diffraction planes (101), (004), (200), (105), (211), (204), (116) and (220) with sharp peak corresponding to diffraction angle at 25.30°, 37.87°, 48.03°, 53.98°, 55.05°, 62.73°, 68.87° and 70.27° confirms the presence of anatase phase in the crystal [10, 11]. Sharpness of the peaks with small Gaussian clearly indicates that synthesized TiO_2 nanoparticles are highly crystalline in nature and crystallite size falls in nanometer range. Peak's sharpness corresponding to (101), (004) and (200) miller indices or diffraction planes clearly indicates that arrangements of particles in a sample are highly periodic and maximum height of the peak corresponding (101) diffraction plane represents preferred crystal orientation whereas low intensity peaks corresponding to (204), (116) and (220) diffraction plane represent chaotic arrangement of particles in the sample for given diffraction planes [11].

Figure 1b depicts the diffraction pattern of TiO_2 nanoparticles calcinated at 900°C. Diffraction peaks at angles (2θ) 27.44°, 36.08°, 39.18°, 41.22°, 44.05°, 54.32°, 56.64°, 62.74°, 64.04° and 69.01° corresponding to (110), (101), (200), (111), (210), (211), (220), (002), (310) and (301) miller indices or diffraction planes strongly supports the complete phase transition of anatase phase into pure rutile phase having no trace of anatase phase and therefore rutile phase is highly thermodynamic stable phase in pure form. It has been observed that with increase in temperature, broadness in the peaks of anatase phase found to be decreased and a set of new sharp peak related to rutile phase at 900°C that indicates the crystallization of TiO_2 nanoparticles.

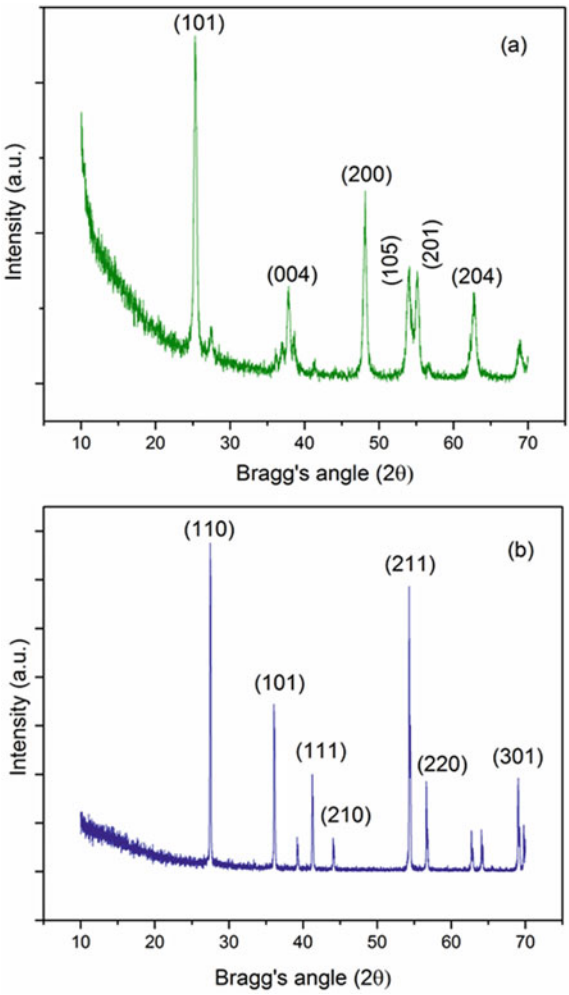

Fig. 36.1 **a** X-ray diffraction patterns of calcinated TiO_2 nanoparticles at 500°C **b** X-ray diffraction patterns of calcinated TiO_2 nanoparticles at 900°C

Crystallite size has been calculated by using Debye–Scherrer's formula:

$$D = \frac{k\lambda}{\beta \cos \theta} \tag{36.1}$$

where D is the crystallite size, λ is the wavelength of the X-ray used, k is usually taken as 0.89 and β is full width at half maxima. The calculated structural parameters are listed in Table 36.1.

Increment in particle size is due to the agglomeration of particles in a particular fashion to achieve periodicity and crystallinity in the sample. The least value of dislocation density evidently indicates that the arrangement of atoms in the lattice is

Table 36.1 Various structural parameters of undoped TiO_2 nanoparticles

Sample	Average crystallite size (D nm)	d-spacing (nm)	Lattice parameter (nm)	Unit cell structure	Dislocation density $\times 10^{-3}$ (nm^{-2})
500°C	20.11	0.351	a = b = 0.377 c = 0.949	Tetragonal	2.59
900°C	68.42	0.324	a = b = 0.458 c = 0.295	Tetragonal	0.27

uniform with minimal distortion in the structure. The structural analysis also confirms that the opted synthesis conditions are more favourable for the formation of rutile phase in acidic medium [12, 13].

36.3.2 Fourier Transform Infrared Spectroscopy Analysis

Fourier Transform Infrared spectroscopy is one of the basic characterizations to know the types of functional groups present in a synthesized sample by analysing the absorption of frequency in the infrared region. Absorption of frequency or wavelength depends on natural frequency with which molecules are vibrating at room temperature. Characterization of TiO_2 nanoparticles is done in the range of wave number 400–4000 cm^{-1} (Fig. 36.2 a, b). When different molecules are exposed to infrared radiations, they absorb different frequencies because the vibration frequencies of the molecules are differing from molecule to molecule. As a consequence, sharp dip is set up in the graph that represent the presence of molecule diversity in the sample. TiO_2 when calcined at temperature 500°C shows a peak at 1653.05 cm^{-1} which indicates that the presence of C = C bonds with absorption intensity about 93.43 ± 1.09 shows very less concentration of C = C bonds, and another peak is at 1273.06 cm^{-1} indicates that the presence of C-O bond with absorption intensity about 94.50 ± 1.09 also shows very less concentration of C-O bonds and peak absorbed at 447.5 cm^{-1} shows the formation of Ti–O bonds with absorption intensity about 65.94 ± 1.02 shows large concentration of Ti–O bonds in the given sample. Peaks observed at 509.22 cm^{-1} shows shift in anatase peaks towards rutile peak due to increase in temperature with O-Ti–O vibrations in a crystal. Peaks in the range of 2300 cm^{-1}—2400 cm^{-1} represents less concentration of O = C = O bonds and also no sharp peak is found in the range of 4000 cm^{-1}—2500 cm^{-1} indicates the absence of moisture of hydroxyl group which shows perfect synthesis of Titanium dioxide [14–17].

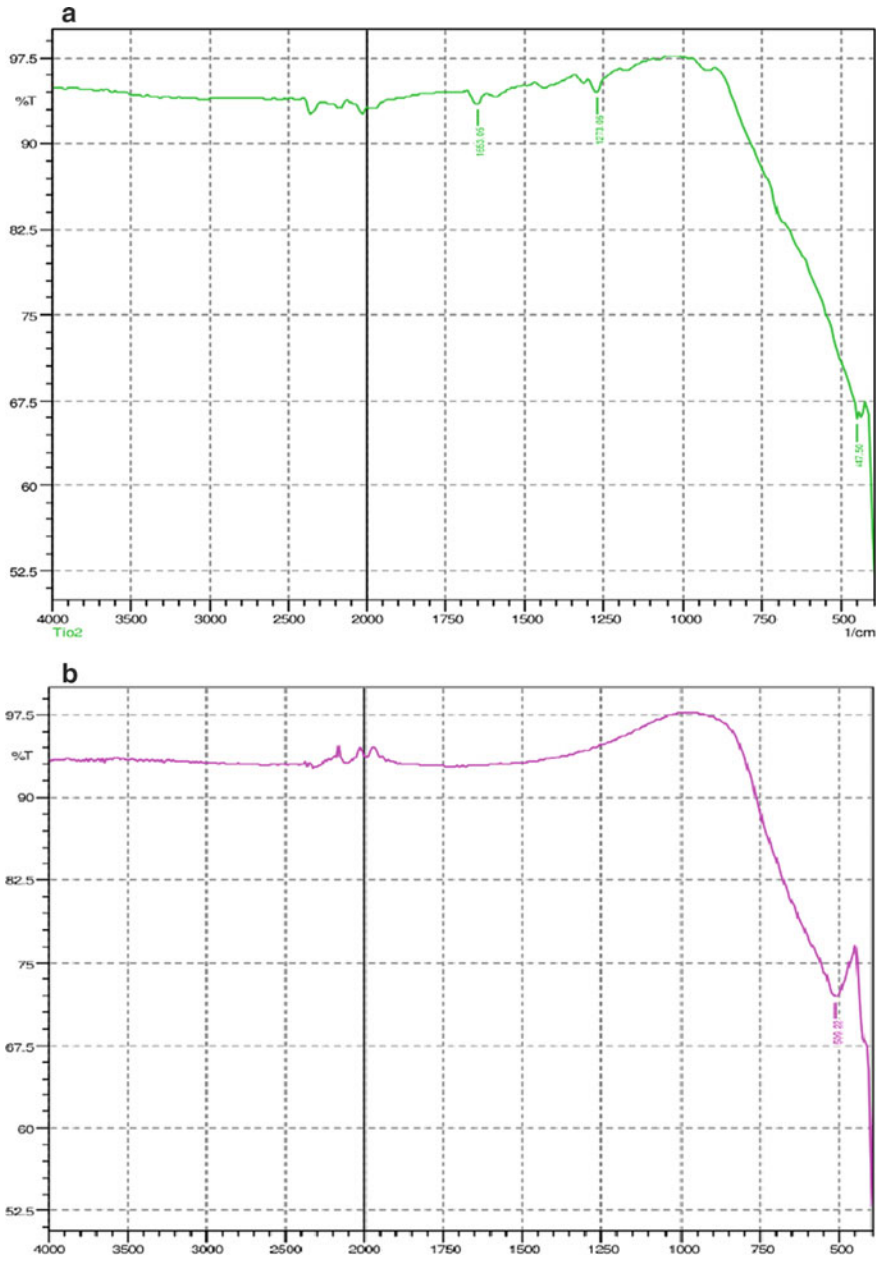

Fig. 36.2 **a** FTIR spectrum of calcinated TiO_2 nanoparticles at 500°C **b** FTIR spectrum of calcinated TiO_2 nanoparticles at 900°C

36.3.3 Morphological Analysis

FESEM is one of the most prominent characterization techniques to explore and understand the microstructures and surface morphology of synthesized material. Morphological analysis of calcinated nanoparticles has been shown in Figs. 36.3 a, b. Calcinations address a different anecdote that particles get agglomerated in non-uniform way with average particle size falls in the range of 20 nm to 40 nm having irregular shape for sample heat treated at 500°C. Moreover, as the calcinations increases to 900°C leads to aggregation of particles which is in the thermally stable phase of TiO_2 whose particle size falls in the range of 243 nm–1.14 μm and growth of rutile phase taken place on the behalf of anatase phase in the crystal. The reason associated with this agglomeration is nucleation of nanoparticles due to which increment in particle size is observed in anatase phase of TiO_2 nanoparticles [18, 19]. In other word, the appearance of larger grain size with the increase of calcination temperature may due to re-crystallization at higher temperature. This is because melting of smaller nanoparticles well below their melting points to form bigger particles.

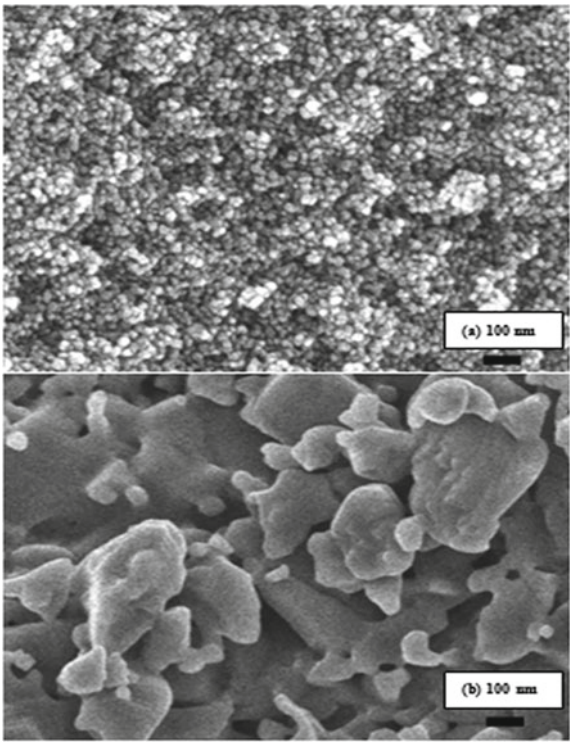

Fig. 36.3 FESEM micrograph of calcinated TiO_2 nanoparticles at different temperature (**a**) 500°C and (**b**) 900°C

36.3.4 Optical Analysis

UV–vis spectroscopy will give information about the energy band gap along with the type of transition associated with it. Transition among the energy band, i.e., conduction band and valence band, is either photon assisted or phonon assisted [20, 21]. This transition information gives an insight about the material energy band gap which is either direct band gap or indirect band gap. The dispersed phase of TiO_2 nanoparticles in ethanol is subjected in front of radiations that carry wavelengths in the range of 200–800 nm [22]. The band gaps of calcinated TiO_2 nanoparticles at 500°C and 900°C for duration of 2 h have shown in Figs. 36.4, 36.5. The band gap of synthesized particles is determined by using Kubelka–Munk function and Tauc plot [23]. The plot is extrapolated and made to cut the x-axis. The point at which the tangent to the curve cuts the x-axis gives the band gap for that sample. Nanoparticles of TiO_2 possess indirect band gap in anatase and rutile phase, and the assisted electronic transition is phonon based.

$$F\left(R'_{\infty}\right) = \frac{\left(1 - R'_{\infty}\right)^2}{2R'_{\infty}} \text{ (Kubelka - Munk Function)} \tag{36.2}$$

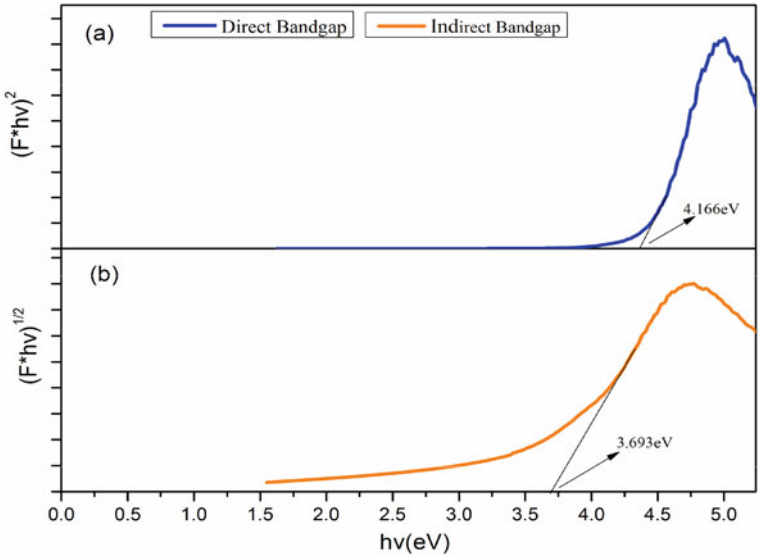

Fig. 36.4 UV–vis spectrograph of sample calcinated at 500°C for 2 h

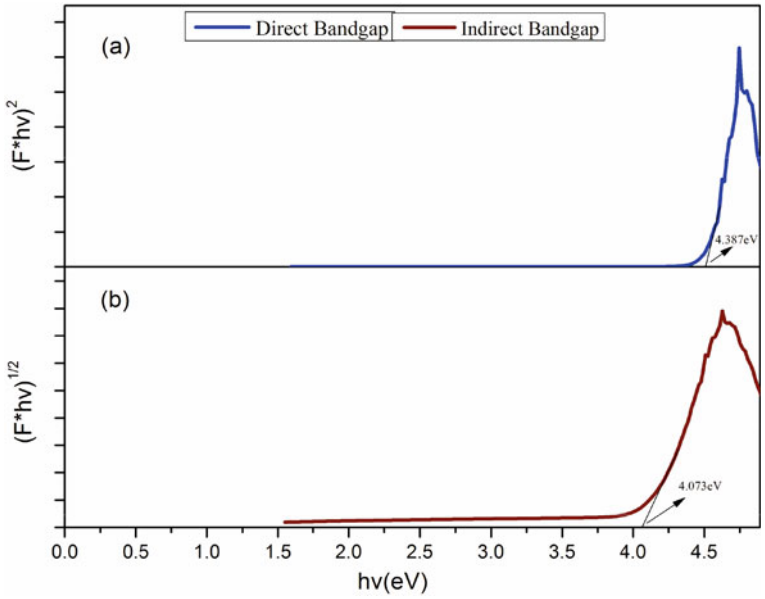

Fig. 36.5 UV–vis spectrograph of sample calcinated at 900°C for 2 h

36.4 Conclusion

TiO_2 nanoparticles are successfully prepared by using sol–gel technique in the presence of ethanol as a solvent. Prepared TiO_2 nanoparticles are characterized by using XRD, FTIR, SEM and UV–vis. X-ray diffraction analysis confirms the formation of crystalline nanoparticles with crystallite size in nanoscale. The diffraction pattern confirms the presence of both anatase and rutile phase at 500°C and 900°C with complete phase transition observed at 900°C. Mid-IR analysis of calcinated samples confirms the presence of stretching vibration of Ti–O indicating the presence of characteristic peaks position. Morphological analysis shows the development of globular shaped nanoparticles as well as aggregation of particles. The bandgap values obtained from the Tauc plot shows that the synthesized TiO_2 nanoparticles have indirect bandgap.

References

1. M.M. Byranvand, A.N. Kharat, L. Fatholahi, Z.M. Beiranvand, A review on synthesis of nano-TiO_2 via different methods. JNS Nanostructures **3**, 1–9 (2013)
2. X. Li, Z. Guo, T. He, The doping mechanism of Cr into TiO_2 and its influence on the photocatalytic performance. Phys. Chem. Chem. Phys. **15**, 20037–20045 (2013)

3. A.J. Haider, Z.N. Jameel, S.Y. Taha, Synthesis and characterization of TiO_2nanoparticles via sol-gel method by Pulse Laser Ablation. Eng. & Tech. Journal **33**, 761–771 (2015)
4. S. B. Deshpande, H. S. Potdar, Y. B. Khollam K. R. Patil, R. Pasricha, N. E. Jacob, "Room temperature synthesis of mesoporous aggregates of anatase TiO_2 nanoparticles", Materials Chemistry and Physics, **97** (2006) 207–212.
5. A. Kumar, G. pandey, "Different methods used for the synthesis of TiO_2based nanomaterials: A review", American Journal of Nano Research and Applications,**6** (2018) 1–10.
6. M.Kavitha, C.Gopinathan, P.PAndi, "Synthesis and characterization of TiO_2 nanopowders in hydrothermal and sol-gel method", International Journal of Advancements in Research & Technology, **2** (2013) 102–108
7. N. Khatun, Anita, P. Rajput, D. Bhattacharya, S.N. Jha, S. Biring, S. Sen, "Anatase to rutile phase transition promoted by vanadium substitution in TiO_2: a structural, vibrational and optoelectronic study", **43** (2017) 14128–14134.
8. D.A.H. Hanaor, C.C. Sorrell, Review of the anatase and rutile phase transformation. Journal Materials Science **46**, 855–874 (2011)
9. M.Z. Yahaya, M.A. Azam, M.A.M. Teridi, P.K. Singh, A.A. Mohamad, Recent Characterization of Sol-Gel Synthesized TiO_2 Nanoparticles. Recent applications in Sol-Gel synthesis **1**, 109–130 (2017)
10. M.M. Viana, V.F. Soares, N.D.S. Mohallem, Synthesis and characterization of TiO_2 nanoparticles. Ceram. Int. **36**, 2047–2053 (2010)
11. K. Thangavelu, R. Annamalai, D. Arulnandhi, Synthesis and characterization of nanosized TiO_2powder derived from a sol-gel process in acidic conditions. International Journal of Engineering Sciences & Emerging Technologies **4**, 90–95 (2016)
12. A. Karami, Synthesis of TiO_2 nano powder by the sol-gel method and its use as a photocatalyst. J. Iran. Chem. Soc. **7**, 154–160 (2010)
13. N. Venkatachalam, M. Palanichamy, V. Murugesan, Sol–gel preparation and characterization of nanosize TiO_2: Its photocatalytic performance. Mater. Chem. Phys. **104**, 454–459 (2007)
14. G. Nagaraju, T.N. Ravishankar, K. Manjunatha, S. Sarkar, H. Nagabhushana, R. Goncalves, J. Dupont, Ionothermal synthesis of TiO_2 nanoparticles: Photocatalytic hydrogen generation. Mater. Lett. **109**, 27–30 (2013)
15. Z. Wang, S. Liu, X. Cao, S. Wu, C. Liu, G. Li, W. Jiang, H. Wang, N. Wang, W. Ding, Preparation and characterization of TiO2 nanoparticles by two different precipitation methods. Ceram. Int. **46**, 15333–15341 (2020)
16. K. Sathiyan, R.B.-Ziv, O. Mendelson, T. Zidki, "Controllable Synthesis of TiO_2 Nanoparticles and Their Photocatalytic Activity in Dye Degradation", Materials Research Bulletin, **126** (2020), 110842.
17. N. Rathore, A. Kulshreshtha, R.K. Shukla, D. Sharma, "Study on morphological, structural and dielectric properties of sol-gel derived TiO_2 nanocrystals annealed at different temperatures", Physica B: Condensed Matter, **4526** (2019) 411969.
18. S. Mahshid, M. Askari, M.S. Ghamsari, Synthesis of TiO_2 nanoparticles by hydrolysis and peptization of titanium isopropoxide solution. J. Mater. Process. Technol. **189**, 296–300 (2007)
19. P. Praveen, G. Viruthagiri, S. Mugundan, N. Shanmugam, Structural, optical and morphological analyses of pristine titanium di-oxide nanoparticles—Synthesized via sol–gel route. SpectrochimicaActa Part A: Molecular and Biomolecular Spectroscopy **117**, 622–629 (2014)
20. S. Abbaspour, A. Nourbakhsh, R. Ebrahimi, H. Ghayour, K.J.D. Mackenzie, The effect of nanoparticles of reduced graphene oxide nanocomposites with zinc oxide under UV irradiation. Material Science & Engineering B **246**, 89–95 (2019)
21. S. Prasad, S.S. Kumar, V.P.M. Shajudheen, Synthesis, characterization and study of photocatalytic activity of TiO_2 nanoparticles. Materials Today: Proceedings **33**, 2286–2288 (2020)
22. K.T. Merin, K. Athira, T. Raguram, K.S. Rajni, Effect of Zinc concentration in TiO_2 nanoparticles synthesized by Sol-Gel technique for Photocatalytic Applications. Materials Today: Proceedings **33**, 2315–2320 (2020)
23. S. Valencia, J.M. Marin, G. Restrepo, Study of the Bandgap of Synthesized Titanium Dioxide Nanoparticules Using the Sol-Gel Method and a Hydrothermal Treatment. The Open Materials Science Journal **4**, 9–14 (2010)

Chapter 37
Structural, Spectral and Optical Properties of Lithium Sulphate Monohydrate L-Valine Semiorganic Crystal

Chandrashekhar M. Bhambere and N. G. Durge

Abstract L-Valine Lithium sulphate LV + LS crystal of considerably good size is a nonlinear optical semiorganic type material. It has been grown by slow evaporation solution technique at elevated temperature (40 °C). LV + LS crystal has enhanced crystallinity and is sufficiently good for SHG. To get high optical perfection, it is recrystallized by SEST at 40 °C, from supersaturated solution by stirring it for several hours. LV + LS with monoclinic crystal system is fairly suitable for NLO applications because of its wide optical transparency.

37.1 Introduction

Nonlinear optical materials play a central role in the evolution of modern optoelectronics technology and science [1]. In the development of nonlinear optics (NLO), purely organic second order nonlinear optical materials found practical applications in the fields of photonics, lasers, electro-optic switches, telecommunication, optoelectronic, frequency conversion and optical information storage devices [2]. Due to a non-centro symmetric structure most of the polar organic crystals shows excellent second order NLO properties. Although due to a lack of extended π electron delocalization, the purely inorganic materials have moderate optical nonlinearities, but they possess excellent mechanical strength, thermal stability, and transmittance. Hence, new class of semiorganic crystals was grown in order to combine the advantages of organic and inorganic materials and because of their interest, and stable physiochemical properties become important for device fabrication and applied research. [3–5].

L-valine is a dipolar amino acid, and it contains both an acidic group-a donor carboxylic (COOH) group and basic group-a proton acceptor (NH_2) group. So amino acid in solid state exists as zwitterions, which create hydrogen bonds, in the form

C. M. Bhambere (✉) · N. G. Durge
Department of Physics, S. S. and L. S. Patkar-Varde College, Goregaon west, Mumbai, Maharashtra 400062, India

S. Sengupta et al. (eds.), *Selected Progresses in Modern Physics*, Springer Proceedings in Physics 265, https://doi.org/10.1007/978-981-16-5141-0_37

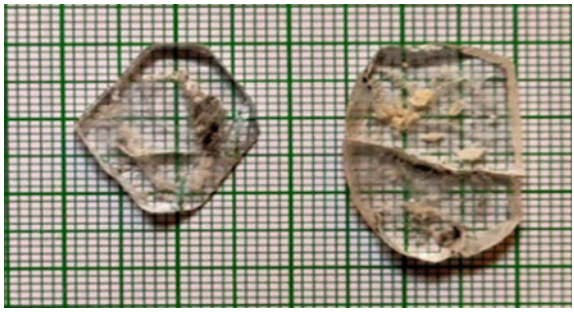

Fig. 37.1 Grown crystals of LV + LS

of N-H^+-O-C, which are used in the possible generation of non-centro-symmetric structures, which is a prerequisite for an effective SHG crystal [6].

This paper describes the synthesis of crystal structure of L-valine doped with lithium sulphate-monohydrate [LV + LSMH] at elevated temperature (40 °C) above room temperature. The grown crystal was characterized by powder XRD and is compared with Lithium Sulphate Monohydrate with amino acid (L-valine) grown at room temperature of 32 °C [7].

37.2 Material Synthesis and Crystal Growth

L-Valine [$C_5H_{11}NO_2$] and Lithium Sulphate-monohydrate $Li_2SO_4{\cdot}1H_2O$ (Loba Chemie), both of analytical grade, are used as the starting materials for synthesizing LM + LS. A solution was prepared by dissolving L-Valine and Lithium Sulphate-monohydrate in double distilled water and stirred continuously for eight hours and the solution was vacuum filtered by Whatman's filter paper to get homogeneous solution. The solution was kept for slow evaporation. at 40 °C temperature in PID controlled temperature bath for more than three weeks. The product was purified by recrystallization process. By continuous evaporation of the solvent, optically transparent and good quality crystals of LV + LS with dimensions of 30 × 15 × 3 mm^3 were obtained from the saturated mother solution over the period of 25 days. The photograph of the as grown crystal is shown in Fig. 37.1.

37.3 Characterizations

X-Ray Diffraction data of LV + LS was recorded on an X-ray diffractometer (Rigaku UltraX18, 18 kW, Germany, CuKα radiation of wavelength 1.5404 Å) in the range

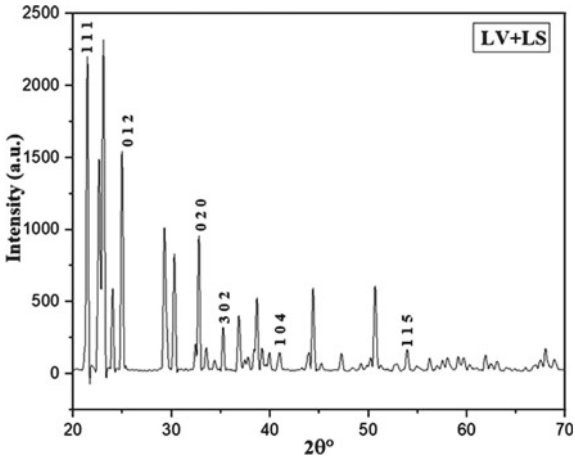

Fig. 37.2 Powder XRD pattern of LV + LS crystal

2θ = 20–70°. The grown crystals were subjected to FTIR spectroscopy to identify different functional groups of LV + LS. Optical transmission of grown crystals was measured by UV-Visible spectrometer (JASCO UV/VIS/NIR Spectrophotometer MODEL-670) in the spectral range 190–1400 nm. The grown crystal exhibits very excellent transmission range. The SHG efficiency was measured by using Kurtz and Perry powder method.

37.4 Results and Discussion

37.4.1 Crystal Structure

X-Ray Diffraction data of the LV + LS crystal was analysed using PowderX software (Fig. 37.2). It is found that the grown crystal belongs to monoclinic structure with non-centrosymmetric space group $P2_1$. The lattice parameters were determined Table 37.1. Crystallinity of the crystal material is found to be 68.07%.

Table 37.1 shows that there is increase in the volume of the unit cell of LV + LS grown at elevated constant temperature (40 °C) above room temperature compared with single crystal of LSM grown at room temperature (32 °C), and the crystal structure remained the same.

37.5 Optical Transmission Spectra

Optical transmittance is observed for 1.2 mm thin plates of and L-Valine Lithium sulphate. The transmittance spectrum is shown in Fig. 37.3, and spectral analysis

Table 37.1 Lattice parameters of LV + LS crystals grown at different temperatures

Lattice Parameters	LV + LS at 40 °C	L- Valine Doped LSM at 32 °C
a (Å)	10.4980	5.453
b (Å)	5.4660	4.846
c (Å)	9.5864	8.174
α (°)	90°	90°
β (°)	101.2958°	107.26
γ (°)	90°	90°
Volume ($Å^3$)	550.06	206.29
Space group	P_{21}	P_{21}
Crystal system	Monoclinic	Monoclinic

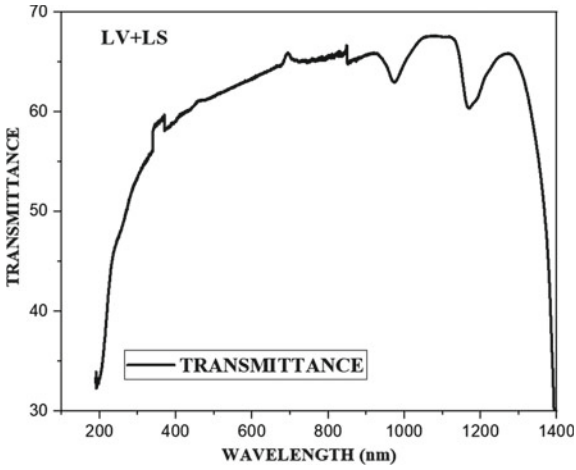

Fig. 37.3 UVVIS-NIR Transmission spectrum LV + LS crystal

shows that in the ultraviolet region the grown crystal has lower cut off wavelength around 252 nm. The UV-Visible spectral analysis shows that the crystal is transparent in the entire visible region. There is no prominent absorbance in the spectral range from 252 to 1150 nm; hence, the crystals grown at 40 °C are sufficiently good for SHG [8, 9]. Figure 37.4 shows absorbance spectrum of LV + LS.

The value of optical absorption coefficients (α) for a wavelength range 190–1400 nm was calculated using the relation.

$$\propto = \frac{2.303}{d} \log \frac{1}{T}$$

where 'T' is the transmittance and 'd' is the thickness of the crystal.

The transparent nature of the crystal in the visible region is the property which makes the material important for NLO applications. The value of band gap energy of the grown LV + LS crystal was estimated from the graph between photon energy (hυ)

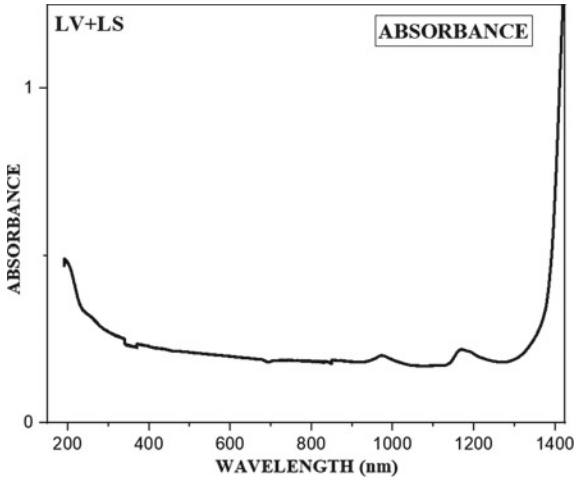

Fig. 37.4 UVVIS-NIR absorption spectrum LV + LS crystal

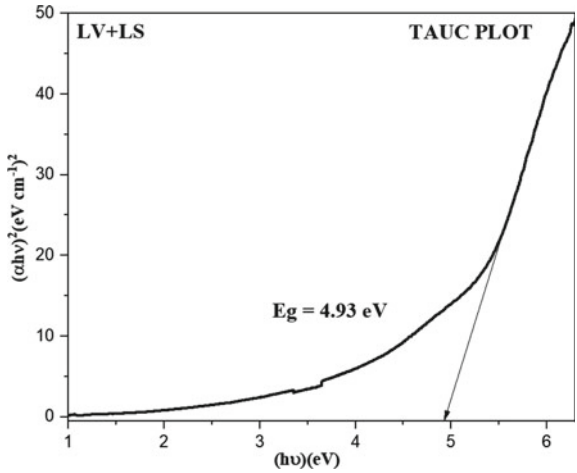

Fig. 37.5 Band gap of LV + LS crystal

and $(\alpha h\upsilon)^2$ by extrapolating the linear portion [10] of the curve to zero absorption (Fig. 37.5). The bandgap energy calculated is about 4.93 eV for the LV + LS crystal.

37.6 Determination of Optical Constants

The study of optical constants of a material is important for NLO applications. The optical band gap energy of the LV + LS crystal is found to be 4.93 eV. The relation between optical band energy **(E_g)** and the refractive index **(n)** of the crystal [11] is given by

$$E_g e^n = 36.3$$

The calculated refractive index is then used to determine the Reflectance **(R)** by applying the formula:

$$R = \left(\frac{n-1}{n+1}\right)^2$$

The calculated refractive index and the reflectance of LV + LS crystal are 1.996 and 0.110, respectively. The high value of the refractive index and low value of reflectance acknowledges that LV + LS crystal is more transparent to transmit light from 250 nm to above 800 nm [12]. The high transmission, low absorbance, low reflectance makes the material an important one for anti-reflection coating in solar thermal devices and nonlinear optical applications [13].

The electrical susceptibility (χ_c) was calculated using the following relation:

$$\chi_c = \varepsilon_r - 1$$

Or $\chi_c = n^2 - 1 \left(\because \varepsilon_r = n^2\right)$ Hence, $\chi_c = 2.9840$

Since electrical susceptibility is greater than 1, the material can be easily polarized when the incident light is more intense [12].

37.7 FTIR Studies

Functional groups that are present in L-valine and Lithium sulphate monohydrate- LV + LS crystal are identified by recording FTIR spectrum (ALPHA-II, Bruker, Japan) in the range between 4000 cm-1 to 400 cm-1. The resulting spectrum is shown in Fig. 37.6.

FTIR spectrum shows that the $SO4^-$ stretching bands are superimposed near 1098.60 cm^{-1}. The deformation bands observed at 1509 cm^{-1} is due to the protonated amino group $NH3^+$. An intense sharp peak at 1609.12 cm^{-1} is due to the bending vibration mode of H_2O. The sharp peak at 636.44 cm^{-1} indicates the presence of sulphate ion. The C-C deformation is observed at 715.45 cm^{-1}. The mode at 434.83 cm^{-1} indicates the vibrational mode δ (Li-O). The broad and weak spectra show the presence of H_2O molecule and O-H symmetric stretching at 3470.05 cm^{-1}.

FTIR assignments on the grown crystals are given in Table 37.2.

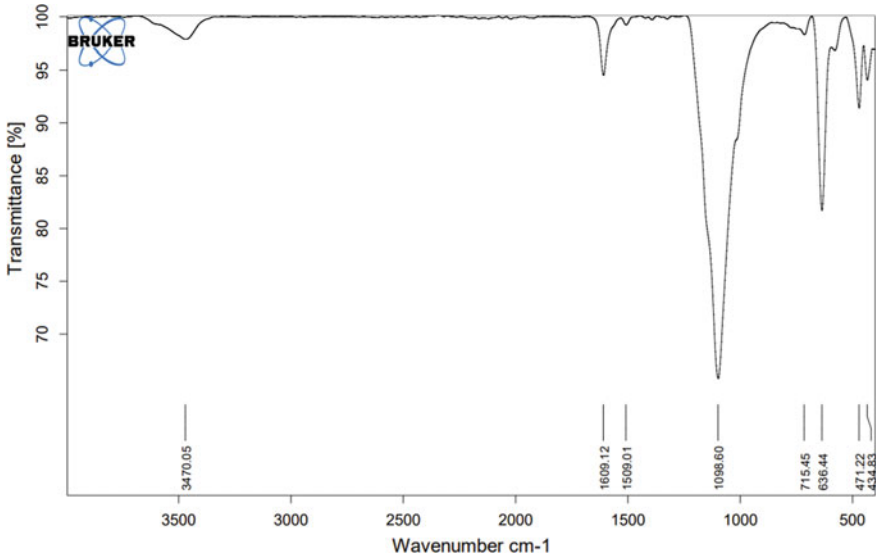

Fig. 37.6 FTIR spectrum LV + LS crystal

Table 37.2 Vibrational group assignment of LV + LS crystal

400 Wavenumber (cm^{-1})	Vibrational group
434.83	Vibrational mode of δ (Li-O)
636.44	Presence of Sulphate ion
715.45	C-C deformation
1098.60	S-O stretching
1509.01	NH_3 deformation
1609.12	Bending vibration mode of H_2O
3470.05	O-H stretching

37.8 SHG Measurements

The SHG conversion efficiency was measured by analogue setup of Kurtz and Perry powder method which consists of a: Quanta Ray Spectra Physics Model Q-switched mode locked Prolab 170 Nd:YAG laser beam of fundamental wavelength 1064 nm with an input power of 1.2 mJ and pulse width of 10 Hz was made to fall on the sample. The emission of green light ($\lambda = 532$ nm) confirms second harmonic signal generated from the LV + LS crystals and they have noncentrosymmetric crystal structure. The moderate SHG efficiency is due to lower polarizing ability of the material which was measured with digital storage oscilloscope.

37.9 Conclusions

A semi organic NLO crystal, LV + LS was successfully grown by SEST method at constant 40° C temperature. Powder XRD method reveals the crystalline nature (Crystallinity 68.07%) of the grown crystal, and it is found to be monoclinic. Various functional groups present in the crystal are confirmed by FTIR analysis. Analysis of UV-VIS-NIR spectrum reveals the wide transparency of the crystal. It has low UV cut off of 252 nm and good transmittance, and the band gap is found to be 4.93 eV. The transmission spectrum reveals that grown crystal have better transparency and have sufficient transmission in UV-Visible and IR region. The lower cut-off wavelength is found to be 252 nm. Crystal has good polarizability due to electrical susceptibility greater than one. Also the high refractive index and low reflectance confirm transparency of L-Valine Lithium sulphate and makes it suitable for SHG applications.

Acknowledgements The author sincerely thanks to Dr. Rajiv Bhatt and Dr. Gurvinderjit Singh (RRCAT- Indore, India) for XRD and UV measurement, CIF-Chemistry Department, (SPPU India) for FTIR and Prof. P. K. Das (IPC lab, IISC. Bengaluru, India) for SHG measurement.

References

1. H.S. Nalwa, *Handbook of Advanced Electronic and Photonic Materials and Devices* (Academic press, New York, 2001).
2. R.W. Boyd, *Non Linear Optics* (Academic Press, San Diego, 1992), p. 155.
3. P. Baskaran et al., Synthesis, growth and characterization of a nonlinear optical crystal: l-Leucinium perchlorate. Journal of Taibah University for Science **11**, 11–17 (2017).
4. R.A. Laudise, *The Growth of Single Crystals* (Prentice Hall, Eagle Wood Cliffs New Jersy, 1970).
5. R.A. Laudise, in: R. Ueda, J.B. Mullin (Eds.), Crystal growth and characterization, North–Holland publishing Co., 1975.
6. S. Ramalakshmi, K.A. Vijayalakshmi, "Growth And Characterization Of Semi-Organic Nlo Material: L Valine Potassium Nitrate And L-Valine Lithium Nitrate", (IOSR-JAP), 2278–4861.Volume 10, Issue 5 Ver. III (Sep.–Oct. 2018).
7. S. Bagavathi, C. Krishnan, P. Selvarajan, The Effect of L-Valine on the Growth and Characterization of Lithium Sulphate Monohydrate Single Crystals. Research & Reviews: Journal of Physics **8**(1), 92–103p (2019).
8. C. Sekar, R. Parimaladevi, Journal of Optoelectronics and Biomedical Materials, (2), 215–225, (2009).
9. P. Kumaresan, S. Murthy Babu P. M. Anbarsan. Thermal, dielectric studies on pure and amino acid (L-Glutamic acid, L-histidine, L-Valine) doped KDP single crystals" Optical Materials, 30 (2008).
10. R. Sankar, R. Muralidharan, C.M. Raghavan, R. Jayavel, Mater. Chem. Phys. **107**, 51–56 (2008).
11. R.R. Reddy, S. Anjaneyulu, Physica status solidi (b) **174**, 91 (1992).
12. P. Vasudevan, S. Sankar, D. Jayaraman, Bull. Korean Chem. Soc. **34**(1), 128 (2013).
13. F. Helen, G. Kanchana, Indian J. Pure Appl. Phys. **52**, 821 (2014).

Chapter 38
Study of Ion-Acoustic Waves in Two-Electron Temperature Plasma

G. Sharma, K. Deka, R. Paul, S. Adhikari, R. Moulick, S. S. Kausik, and B. K. Saikia

Abstract A plasma having two different electron energy groups is produced in a multi-dipole plasma device. An ion-acoustic (IA) wave is launched in the plasma to study its damping characteristics in the presence of two-electron groups. The electron temperatures and densities are varied to see their effects on the damping of the wave. An analytical treatment of wave damping is also carried out and the outcomes of the theoretical calculations have been compared with the experimental findings. It is observed that the presence of energetic electrons has a noteworthy contribution to the damping of IA waves.

38.1 Introduction

Plasmas having more than one electron group with different temperatures and densities are routinely found in laboratories. They are often termed as two-electron temperature plasmas in the literature. The presence of an energetic electron group brings notable changes in their properties where the density and temperature ratios of the electron groups play the crucial role [1–5]. Due to this reason, the study of wave propagation in such plasmas has been an exciting field of research for a long time. The propagation of ion-acoustic waves in two-temperature plasma has been studied by many researchers theoretically [6–9], but still it continues to be a potential area of research. In the theoretical studies, basically the nonlinear modulation of ion-acoustic waves is discussed based on various plasma models. Sharma and Buti [7] studied modulation properties of IA waves and found that their stability depends on the densities of hot and cold electron components. Rao and Shukla [2] reported that the presence of two-electron components introduces a new class of

G. Sharma · K. Deka · R. Paul · S. S. Kausik (✉) · B. K. Saikia
Centre of Plasma Physics, Institute for Plasma Research, Nazirakhat, Sonapur, Kamrup(M) 782402, Assam, India

S. Adhikari
Department of Physics, University of Oslo, P.O. Box 1048, Blindern, 0316 Oslo, Norway

R. Moulick
Department of Physics, Rangapara College, Rangapara, Sonitpur 784505, Assam, India

S. Sengupta et al. (eds.), *Selected Progresses in Modern Physics*, Springer Proceedings in Physics 265, https://doi.org/10.1007/978-981-16-5141-0_38

supersonic coupled Langmuir–ion-acoustic solitons. Verheest et al. [10] considered a kappa distribution of electrons and showed that such supersolitons have a parametric dependence which in turn has a strong kappa dependence. Lakhina et al. [11] has studied ion and electron acoustic solitary structures in space plasmas using the Sagdeev pseudopotential technique. Their model has applications in the auroral plasmas. All such theoretical studies provide a deep understanding of various aspects of IA waves in two-temperature plasmas. The first experiment of IA wave propagation in two-temperature plasma was performed by Jones et al. [12]. They have successfully demonstrated the theoretically predicted effect of second electron component on the phase velocity of the excited waves. In the present work, an attempt is made to study the damping characteristics of IA waves experimentally in a two-electron temperature plasma and compare the results with a theoretical model developed on the basis of the plasma fluid model. The paper is organized as follows. Section 38.2 gives a brief description of experimental arrangement, Sect. 38.3 contains the results of the experiment and the theoretical findings followed by the conclusion in Sect. 38.4.

38.2 Experimental Arrangement

The experiment is performed in a cylindrical stainless steel chamber of 100 cm length and 30 cm diameter (Fig. 38.1). Plasma is produced using a hot cathode discharge mechanism and full line cusp magnetic cages are used for plasma confinement. Cusp magnetic field geometry possesses the property of confining primary electrons due to which two-electron temperature plasma is obtained [13]. The detailed two-electron temperature plasma production mechanism will be published elsewhere. A stainless steel mesh grid of diameter 5 cm is used for exciting IA waves in the system. The excited wave is received by a planar probe of diameter 0.9 cm. The exciter and receiver are placed in the central region of the system where two-electron energy groups are present. A function generator is used for applying a sinusoidal perturbation in the plasma via the exciter. The detected wave of comparatively lower amplitude is observed in the oscilloscope.

38.3 Results and Discussion

The chamber is evacuated to a base pressure of 5×10^{-6} mbar. Hydrogen plasma is produced by maintaining a working pressure of 2×10^{-4} mbar. To measure the plasma parameters first, a cylindrical Langmuir probe is used. The electron temperature and density are changed by changing the discharge current while keeping the neutral pressure constant. The electron energy distribution function is plotted as shown in Fig. 38.2 which has an energetic tail confirming the presence of a hot electron group in the plasma. Now, an IA wave is excited in the system with a fre-

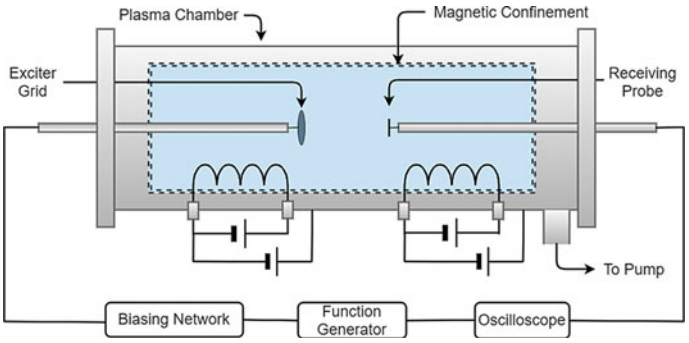

Fig. 38.1 Schematic of the experimental setup

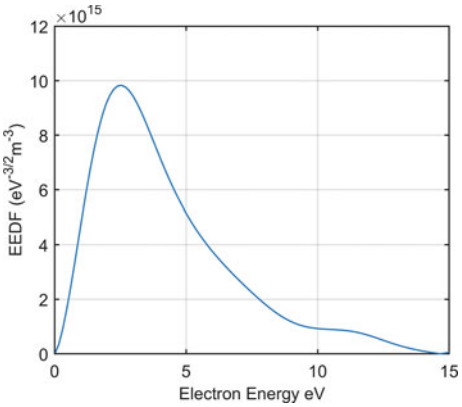

Fig. 38.2 Electron energy distribution function showing bi-Maxwellian nature of the plasma

quency of 50 kHz. To observe the effect of the hot component of electrons on the wave propagation, five regimes were selected where electron densities and temperatures were different. The cold electron temperature varies from 1.2 to 1.7 eV and the hot electron temperature is varied from 5 to 6 eV. The ratio of hot to cold electron temperature is defined as $\tau = T_h/T_c$ and the ratio of hot to cold electron density is defined as $\delta = n_h/n_c$. Figure 38.3 shows the amplitude of the received signal at various distances from the exciter for different τ and δ. It is seen that as δ decreases, i.e. the hot electron density decreases, the wave suffers more damping. The damping of the wave is believed to be due to collisions between the ions and the background gas. Later on, it has been also observed that the damping is not independent of wave frequency. Figure 38.4 shows how damping increases with the increase in the applied frequency. Due to the limitations of the experimental setup, the exciter to receiver distance cannot be increased to more than 10 cm. Still, from the trend of wave damping as seen in Fig. 38.3, it can be understood that the propagation distance of the pulse gradually decreases with the decrease of hot electron density.

To understand the physical reason of damping, an analytical expression for the dispersion relation has been derived using momentum equation for the ions, cold

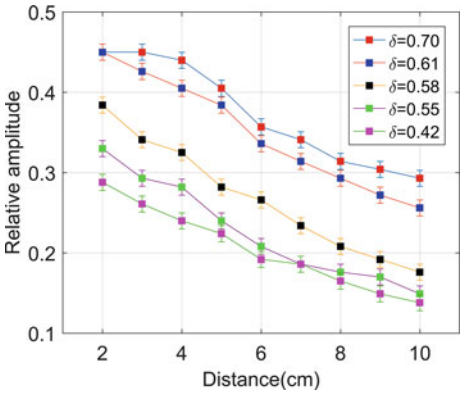

Fig. 38.3 Received signal amplitude at various distances from the exciter for different δ

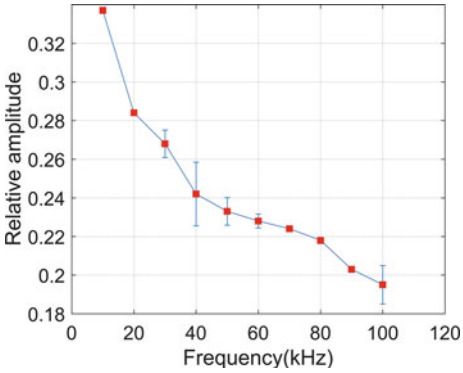

Fig. 38.4 Amplitude of the received signal for various frequencies of the wave

electrons and hot electrons (38.1, 38.2 and 38.3) followed by the continuity equations for each species (38.4, 38.5 and 38.6) and the Poisson equation (38.7), respectively.

$$m_i \frac{\partial v_i}{\partial t} = -e\nabla\phi - \frac{T_i}{n_{i0}}\nabla n_i - m_i \nu v_i \tag{38.1}$$

$$m_e \frac{\partial v_c}{\partial t} = e\nabla\phi - \frac{T_c}{n_{c0}}\nabla n_c \tag{38.2}$$

$$m_e \frac{\partial v_h}{\partial t} = e\nabla\phi - \frac{T_h}{n_{h0}}\nabla n_h \tag{38.3}$$

$$\frac{\partial n_{i1}}{\partial t} + \nabla.(n_{i0} v_i) = 0 \tag{38.4}$$

$$\frac{\partial n_{c1}}{\partial t} + \nabla.(n_{c0} v_c) = 0 \tag{38.5}$$

$$\frac{\partial n_{h1}}{\partial t} + \nabla.(n_{h0} v_h) = 0 \tag{38.6}$$

$$\nabla^2 \phi = -\frac{e}{\epsilon_0}(n_{i1} - n_{c1} - n_{h1}) \tag{38.7}$$

where n_{i0}, n_{c0} and n_{h0} are the equilibrium ion density, cold electron density and hot electron density, respectively, n_{i1}, n_{c1} and n_{h1} are the perturbed ion density, cold electron density and hot electron density, respectively, m_i is the ion mass, m_e is the electron mass and ν is the ion neutral collision frequency.

Assuming the perturbation proportional to $exp[i(\mathbf{k}.\mathbf{r} - \omega t)]$, the following dispersion relation has been obtained:

$$k^2 = \frac{1}{\lambda^2}\frac{\omega^2 + i\nu\omega}{\omega_{pi}^2} - \omega^2 - i\nu\omega \tag{38.8}$$

where

$$\frac{1}{\lambda^2} = \frac{1}{\lambda_{Dc}^2} + \frac{1}{\lambda_{Dh}^2}$$

The complex wave vector k can be written as $k = k_R + ik_I$. Then the wave can be represented as $e^{i(kr-\omega t)} = e^{-k_I r} e^{i(k_R r - \omega t)}$. The wave will experience damping for $k_I > 0$ [14]. Solving for (38.8) using $k = k_R + ik_I$, the following expressions for k_I and k_R has been obtained:

$$k_I = \frac{\omega\sqrt{\omega_{pi}^2 - \omega^2 - \nu^2}}{\sqrt{2\lambda^2\left[(\omega_{pi}^2 - \omega^2)^2 + \omega^2\nu^2\right]}} \sqrt{\left(1 + \frac{\nu^2\omega_{pi}^4}{\omega^2(\omega_{pi}^2 - \omega^2 - \nu^2)^2}\right)^{1/2} - 1} \tag{38.9}$$

$$k_R = \frac{\omega\nu\omega_{pi}^2}{2\lambda^2 k_I[(\omega_{pi}^2 - \omega^2)^2 + \omega^2\nu^2]} \tag{38.10}$$

In (38.9), except ν, the values of all other quantities are known. The value of ν has been estimated from the experiment using the following technique. Figure 38.5 shows experimentally observed values of k_I for different wave frequencies. While extrapolating the linear fitting curve, $k_I = 23.12\ \mathrm{m}^{-1}$ is obtained for zero frequency. This value corresponds to the collisional damping rate k_{coll}. Hence, using $k_{coll} = 23.12\ \mathrm{m}^{-1}$, an effective collision frequency has been drawn using the relation $\nu = 2v_p k_{coll} = 5.2 \times 10^5$ Hz [15]. Here, v_p is the phase velocity of the wave and it is measured to be $1.14 \times 10^4\ \mathrm{ms}^{-1}$. Therefore, with an ion density of the order of

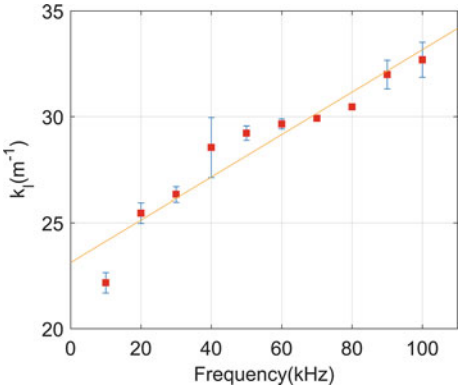

Fig. 38.5 Variation of k_I with respect to frequency of the applied signal

10^{17} m^{-3} and applied frequency of 50 kHz, (38.9) gives $k_I = 12.1$ m^{-1}. Similarly, using (38.10), the value of k_R is estimated to be 13.3 m^{-1}.

But, for 50 kHz signal, the experimentally observed average value for k_I is 20.87 m^{-1}. The experimental value is higher than that of the theoretically predicted one. A probable explanation behind the difference could be the presence of other damping sources like ion–ion collision and electron–ion collision which is not included in the theoretical model. Moreover, the dependence of damping on the frequency of the applied signal indicates that kinetic effects like Landau damping may be present in the system which cannot be described by the fluid theory.

38.4 Conclusion

In conclusion, the IA wave is excited in a two-electron temperature plasma. The wave suffers damping while propagating through plasma, and the amplitude of the damped signal is measured. It is observed that the presence of energetic electrons in plasma favors the propagation of ion-acoustic waves while cold electrons try to shield the disturbance thereby promoting damping of the wave. It is found that the analytical analysis carried out for the present model can only explain the experimental results up to a certain extent which includes the contribution from the collisions. The model is not fully adequate to answer all observations of the experiment since kinetic effects come into the picture. Hence, a kinetic treatment of the present problem may be more suitable in this regard which will be implemented in due course of time.

Acknowledgements The authors would like to thank Mr. G D Sarma, Dr. Nipan Das and Dr. Partha Saikia for their technical help and valuable ideas during the experiment.

References

1. A. Esfandyari-Kalejahi, H. Asgari, Ion-acoustic solitary excitations in a two-electron-temperature plasma with adiabatic warm ions: oblique modulation. Phys. Plasmas **12**, 102302 (2005)
2. N.N. Rao, P.K. Shukla, Coupled Langmuir and ion-acoustic waves in two-electron temperature plasmas. Phys. Plasmas **4**, 363 (1997)
3. S.S. Ghosh, A.N. Sekar Iyengar, Effect of cooler electrons on a compressive ion acoustic solitary wave in a warm ion plasma—forbidden regions, double layers, and supersolitons. Phys. Plasmas **21**, 082104 (2014)
4. A. Esfandyari-Kalejahi, I. Kourakis, M. Akbari-Moghanjoughi, Nonlinear modulation of ion-acoustic waves in two-electron-temperature plasmas. J. Plasma Phys. **76**, 169 (2010)
5. G. Sharma, S. Adhikari, R. Moulick, S.S. Kausik, B.K. Saikia, Effect of two temperature electrons in a collisional magnetized plasma sheath. Phys. Scr. **95**, 035605 (2020)
6. I. Kourakis, P.K. Shukla, Ion-acoustic waves in a two-electron-temperature plasma: oblique modulation and envelope excitations. J. Phys. A **36**, 47 (2003)
7. A.S. Sharma, B. Buti, Modulational instability of ion-acoustic-waves in two electron temperature plasmas. Pramana **10**, 629–637 (1978)
8. M. Tajiri, K. Nishihara, Solitons and shock waves in two-electron-temperature plasmas. J. Phys. Soc. Jpn. **54**, 572 (1985)
9. D. Dutta, S. Adhikari, R. Moulick, K.S. Goswami, Evolution of dust ion acoustic soliton in the presence of superthermal electrons. Phys. Scr. **94**, 125210 (2019)
10. F. Verheest, M.A. Hellberg, I. Kourakis, Ion-acoustic supersolitons in plasmas with two-temperature electrons: Boltzmann and kappa distributions. Phys. Plasmas **20**, 082309 (2013)
11. G.S. Lakhina, A.P. Kakad, S.V. Singh, F. Verheest, Ion- and electron-acoustic solitons in two-electron temperature space plasmas. Phys. Plasmas **15**, 062903 (2008)
12. W.D. Jones, A. Lee, S.M. Gleeman, H.J. Doucet, Propagation of ion-acoustic waves in a two-electron-temperature plasma. Phy. Rev. Lett. **35**, 1349 (1975)
13. M.K. Mishra, A. Phukan, Electron heating in a multi-dipole plasma by electrostatic plugging. J. Plasma Phys. **79**, 153–161 (2013)
14. J.A. Bittencourt, *Fundamentals of Plasma Physics* (Springer, Brazil, 2004)
15. R.J. Armstrong, W.J. Weber, J. Trulsen, Phys. Lett. **74A**, 5 (1979)

Chapter 39
Study of Plasma Sheath in the Presence of Dust Particles in an Inhomogeneous Magnetic Field

K. Deka, R. Paul, G. Sharma, S. Adhikari, R. Moulick, S. S. Kausik, and B. K. Saikia

Abstract In plasma processing devices, negatively charged dust particles appear as contaminants in etching, sputtering, and deposition processes. The dynamics of the dust particles at the edge region of the plasma plays an important role in such processes. The present study deals with a low-pressure plasma to investigate the effect of dust particles on the properties of plasma sheaths in the presence of a non-uniform magnetic field. A multi-fluid model is used to simulate the dynamics of electrons, ions, and dust particles. The governing equations for all the plasma species are solved numerically using the fourth-order Runge-Kutta (RK4) method. It has been observed that the presence of the dust particles significantly affects the plasma sheath parameters such as potential, electric field, particle density, and particle velocity. The present study is supposed to help in understanding the dynamics of negatively charged dust grains in the sheath. Therefore, the study may be helpful in the plasma processing of materials as well as in plasma wall interactions for various plasma-aided industrial applications

39.1 Introduction

The plasma sheath has prime importance in many plasma applications such as plasma-assisted material processing, fusion research, and in different types of plasma probes [1, 2]. The plasma sheath at the wall or probes is formed due to the large difference in the mobility of the electrons and ions present in the plasma. For the formation of the electrostatic sheath, the ions must enter the sheath with a velocity greater than the ion-acoustic speed. This condition is known as the Bohm criterion [3]. Dusty plasma can be defined as the mixture of electrons, ions, and charged particles having

K. Deka · R. Paul · G. Sharma · S. S. Kausik (✉) · B. K. Saikia
Centre of Plasma Physics, Institute for Plasma Research, Nazirakhat, Sonapur, Kamrup(M) 782402, Assam, India

S. Adhikari
Department of Physics, University of Oslo, PO Box 1048, Blindern, NO-0316 Oslo, Norway

R. Moulick
Department of Physics, Rangapara College, Rangapara, Sonitpur 784505, Assam, India

S. Sengupta et al. (eds.), *Selected Progresses in Modern Physics*, Springer Proceedings in Physics 265, https://doi.org/10.1007/978-981-16-5141-0_39

sizes in the range of micrometers to nanometers. The dust particles are commonly observed in most of the laboratory and space plasmas. Due to this, the study of plasma sheaths in the presence of dust particles has acquired significant attention among the researchers [4]. The behaviour of a plasma sheath is largely affected by the presence of dust particles near the wall [5]. Arnas et al. [6] experimentally showed the modification of the sheath in the presence of dust particles.

In recent times, the plasma sheath in the presence of dust and a magnetic field has been explored by many researchers [1, 4, 7, 8]. Pandey et al. [7] studied the dynamics of dust particles in the presence of a magnetic field. They found that the equilibrium and levitation of dust particles inside the sheath depend on collision frequency as well as on the magnetization. The structure of the plasma sheath in the presence of an oblique magnetic field and dust dynamics in the sheath has been studied by Davoudabadi et al. [9]. In the literature, a large number of studies can be found dealing with the properties of plasma sheath in the presence of dust particles and a uniform magnetic field. But no such studies of the dusty plasma sheath in the presence of an inhomogeneous magnetic field can be found. In this work, an attempt has been made to explore the properties of the plasma sheath in the presence of dust particles and an inhomogeneous magnetic field. For the rest of the paper, the inhomogeneous magnetic field has been represented by IHM for convenience.

The present study has been arranged into five sections. A brief introduction to the field is given in Sect. 39.1. In Sect. 39.2, the theoretical model and the governing equations are presented. In Sect. 39.3, the governing equations are normalized. In Sect. 39.4, the results of the study have been discussed. The conclusions of the study are made in Sect. 39.5.

39.2 Theoretical Model and Basic Equations

The inhomogeneous magnetic field that contains the gradient as well as the curvature term is given by [10]

$$B = B_0(1 + \alpha z)\hat{i} + (B_0\alpha x)\hat{k} \tag{39.1}$$

The first term of (39.1) is the gradient term and the second term is due to the curvature of the field. The dimension of the constant parameter α is the inverse of length.

For the present study, it is seen that the gradient term of the magnetic field dominates over the curvature term. The strength of the gradient term of the magnetic field is alone comparable with the strength of the total magnetic field. The field is parallel to the z-axis at the starting point of the simulation. The field gradually starts to align itself with the wall making a very small angle, the angle of inclination very slowly increases on moving from the bulk plasma towards the wall (at the wall, the field makes an angle $\theta < 19^0$). Further, if the study is confined in the region near the z-axis of the x-z plane, the angle of inclination becomes even more smaller. Due to this, the effect of the gradient term dominates over the curvature term on the properties

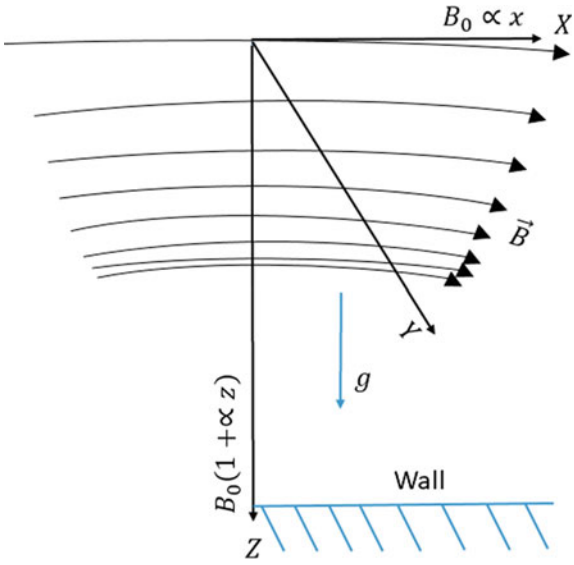

Fig. 39.1 Schematic diagram of the theoretical model

of the sheath. This enables us to reduce the $2D$ sheath problem to $1D$. Ebersohn et al. [11] also reduced the 2D plasma flow in a flux tube to 1D flow by considering the variation of the field only along the axis of the flux tube and the plasma properties are constant in the flux tube cross-section.

The effect of the external magnetic field on the properties of the sheath is determined by the term $q(\mathbf{v} \times \mathbf{B})$. For the $1D$ sheath formed along the z-axis, i.e. along the $x = 0$ line, the curvature term vanishes from the magnetic force term.

A low-pressure plasma consisting of positive ions, electrons, and dust grains has been considered for the present work. The sheath is perpendicular to the z-axis and the sheath parameters such as density, potential, velocity, and electric field vary along the z-axis. A schematic diagram for representing the theoretical model is shown by Fig. 39.1. All the three components of the plasma, i.e. positive ions, electrons, and dust particles are described by fluid equations.

The momentum equation for the singly charged cold ions is

$$m_i n_i v_{iz} \frac{d\mathbf{v_i}}{dz} = -n_i e \frac{\partial \phi}{\partial z}\hat{k} + n_i e(\mathbf{v_i} \times \mathbf{B}) - m_i n_i \mathbf{v_i} \nu_{in} \tag{39.2}$$

The momentum equation for the electrons is

$$m_e n_e v_{ez} \frac{d\mathbf{v_e}}{dz} = n_e e \frac{\partial \phi}{\partial z}\hat{k} - n_e e(\mathbf{v_e} \times \mathbf{B}) - T_e \frac{dn_e}{dz}\hat{k} \tag{39.3}$$

The momentum equation for the dust grains is

$$m_d n_d v_{dz} \frac{d\mathbf{v_d}}{dz} = -n_d q_d \frac{\partial \phi}{\partial z}\hat{k} + n_d q_d(\mathbf{v_d} \times \mathbf{B}) + m_d n_d g + n_d F_i \tag{39.4}$$

The continuity equations for the ions, electrons, and the dust particles are

$$\frac{\partial}{\partial z}(n_i v_{iz}) = \nu_{in} n_e - \nu_{id} n_d \tag{39.5}$$

$$\frac{\partial}{\partial z}(n_e v_{ez}) = \nu_{in} n_e - \nu_{id} n_d \tag{39.6}$$

$$\frac{\partial}{\partial z}(n_d v_{dz}) = 0 \tag{39.7}$$

In the above equations, ν_{ni}, ν_{in}, ν_{en}, ν_{id}, ν_{ed}, q_d, and F_i represent ionization frequency, ion-neutral collision frequency, attachment frequency of ions on the dust, attachment frequency of electrons on dust, charge on the dust grains and ion-drag force on the dust particles, respectively.

The ion-drag force F_i is the sum of collection drag force and Coulomb drag force [12–14]:

$$F_{collection} = \pi b_c^2 n_i m_i v_s \tilde{v}_i$$

$$F_{coulomb} = 2\pi b_0^2 n_i m_i v_s \tilde{v}_i \ln\left[\frac{b_0^2 + \lambda_{De}^2}{b_0^2 + b_c^2}\right]$$

where $\tilde{v}_i = v_i - v_d$ is the directed ion speed and $v_s = \sqrt{\left(\tilde{v}_i^2 + \frac{8T_i}{\pi m_i}\right)}$ is the total ion speed, i.e. the sum of directed and thermal speed. $b_0 = \frac{eq_d}{4\pi\epsilon_0 m_i v_s^2}$ is the impact radius for a 90° deflection. The direct collision impact parameter is given by

$$b_c = r_d\sqrt{1 - \frac{2b_0}{r_d}}$$

The governing equations for the ions, electrons, and dust particles are closed by Poisson's equation:

$$\frac{\partial^2 \phi}{\partial z^2} = -\frac{e}{\epsilon_0}(n_i - n_e + n_d q_d) \tag{39.8}$$

Here, ϵ_0 is the permittivity of free space.

The OML theory is used to determine the electron and ion currents to the dust grains. The electron and ion currents to the dust grains are given by [1, 15]

$$I_e = -\pi r_d^2 e \sqrt{\frac{8K_B T_e}{\pi m_e}} n_e \exp(y) \tag{39.9}$$

$$I_i = e\pi r_d^2 n_i v_i \left(1 - \frac{2K_B T_e y}{m_i v_i^2}\right) \tag{39.10}$$

for $y < 0$

$$I_e = -\pi r_d^2 e \sqrt{\frac{8K_B T_e}{\pi m_e}} n_e (1 + y) \tag{39.11}$$

$$I_i = e\pi r_d^2 n_i v_i \exp\left(\frac{2K_B T_e y}{m_i v_i^2}\right) \tag{39.12}$$

for $y \geq 0$ where $y = (\phi_d - \phi)/K_B T_e$ is the normalized potential difference between the dust and the plasma. In the charging equations, the ion velocity v_i has to be replaced with total ion velocity v_s. The value of y can be calculated from the equations given as follows:

$$\sqrt{\frac{8K_B T_e}{\pi m_e}} n_e \exp(y) = n_i v_s \left(1 - \frac{2K_B T_e y}{m_i v_s^2}\right) \tag{39.13}$$

for $y < 0$, and

$$\sqrt{\frac{8K_B T_e}{\pi m_e}} n_e (1 + y) = n_i v_s \exp\left(\frac{2K_B T_e y}{m_i v_s^2}\right) \tag{39.14}$$

for $y \geq 0$.

The OML theory for evaluating the charging current is valid only if the strength of the magnetic field B is less than the critical value B_{cr} determined from the equation [1]:

$$B_{cr}(kG) r_d(\mu m) = 41.37 \sqrt{\frac{T_e(eV)}{3(eV)}}$$

39.3 Normalized Equations

To carry out the numerical computation, the physical variables of the governing equations are normalized using the following variables:

$$u_i = \frac{v_{ix}}{c_s},\ v_i = \frac{v_{iy}}{c_s},\ w_i = \frac{v_{iz}}{c_s}$$

$$u_e = \frac{v_{ex}}{c_s},\ v_e = \frac{v_{ey}}{c_s},\ w_e = \frac{v_{ez}}{c_s}$$

$$u_d = \frac{v_{dx}}{c_s},\ v_d = \frac{v_{dy}}{c_s},\ w_d = \frac{v_{dz}}{c_s}$$

$$\eta = -\frac{e\phi}{kT_e},\ \xi = \frac{z}{L},\ L = \lambda_{ni} = \frac{c_s}{Z}$$

$$N_i = \frac{n_i}{n_{e0}}, \quad c_s = \sqrt{\frac{kT_e}{m_i}}, \quad N_e = \frac{n_e}{n_{e0}} \quad N_d = \frac{n_d}{n_{e0}}$$

After normalization, (39.2)–(39.7) take the form:

$$\frac{du_i}{d\xi} = -\left(\frac{L\nu_{in}}{c_s}\right)\left(\frac{u_i}{w_i}\right) \tag{39.15}$$

$$\frac{dv_i}{d\xi} = \gamma_i - \left(\frac{L\nu_{in}}{c_s}\right)\left(\frac{v_i}{w_i}\right) \tag{39.16}$$

$$\frac{dw_i}{d\xi} = \left(\frac{1}{w_i}\right)\left[\frac{\partial\eta}{\partial\xi} - \gamma_i v_i - \left(\frac{L\nu_{in}}{c_s}\right)w_i\right] \tag{39.17}$$

$$\frac{d\Gamma_i}{d\xi} = a_{ni}N_e - a_{id}N_d \tag{39.18}$$

$$\frac{du_e}{d\xi} = -\delta\left(\frac{u_e}{w_e}\right) \tag{39.19}$$

$$\frac{dv_e}{d\xi} = -\gamma_e - \delta\left(\frac{v_e}{w_e}\right) \tag{39.20}$$

$$\frac{dw_e}{d\xi} = -\left(\frac{w_e}{w_e^2 - \mu}\right)\left[\mu\frac{\partial\eta}{\partial\xi} - \gamma_e v_e + \delta w_e\right] + \left(\frac{\mu}{w_e^2 - \mu}\right)\left(\frac{a_{ni}N_e - a_{id}N_d}{N_e}\right) \tag{39.21}$$

$$\frac{d\Gamma_e}{d\xi} = a_{ni}N_e - a_{ed}N_d \tag{39.22}$$

$$\frac{du_d}{d\xi} = +\left(\frac{L}{m_d C_s^2}\right)F_{ix} \tag{39.23}$$

$$\frac{dv_d}{d\xi} = \left(\frac{q_d}{e}\right)\gamma_d + \left(\frac{L}{m_d C_s^2}\right)F_{iy} \tag{39.24}$$

$$\frac{dw_d}{d\xi} = \left(\frac{m_i}{m_d}\right)\left(\frac{q_d}{e}\right)\frac{\partial\eta}{\partial\xi} - \left(\frac{q_d}{e}\right)\gamma_d\left(\frac{v_d}{w_d}\right) + \left(\frac{Lg}{C_s^2}\right)\left(\frac{1}{w_d}\right) + \left(\frac{L}{m_d C_s^2}\right)F_{iz} \tag{39.25}$$

$$\frac{d\Gamma_d}{d\xi} = 0 \tag{39.26}$$

$$\gamma_i = \left(\frac{eB}{m_i Z}\right);\ \gamma_e = \left(\frac{eB}{m_e Z}\right);\ \gamma_d = \left(\frac{eB}{m_d Z}\right)$$

$$\delta = \left(\frac{L\nu_{en}}{c_s}\right);\ \mu = (m_i/m_e);$$

$$\Gamma_i = N_i w_i;\quad \Gamma_e = N_e w_e;\quad \Gamma_d = N_d w_d$$

where ν_{dn} is the dust neutral collision frequency.

$$\frac{d^2\eta}{d\xi^2} = a_0\left[N_i - N_e + \left(\frac{q_d}{e}\right)N_d\right] \tag{39.27}$$

$$where,\ a = \left(\frac{L}{\lambda_D}\right)^2$$

It can be shown that [16]

$$\frac{L\nu_{in}}{c_s} = K\sqrt{u_i^2 + v_i^2 + w_i^2}$$

where K is the collision parameter.

39.4 Results and Discussion

In the present work, the properties of the plasma sheath have been explored in the presence of dust particles and an inhomogeneous magnetic field. For this purpose, the normalized governing equations (39.15–39.27) of the sheath have been solved numerically using the Matlab routine ode45, which uses the fourth-order Runge-Kutta scheme for solving the differential equations.

To start the numerical simulation, the following parameters have been used $\eta \to 0$; $\frac{d\eta}{d\xi} \to 0$. The particle velocity $u_j \to 0$ and the particle density $N_j = 1$. The suffix j represents each species in the plasma.

Figure 39.2a,b shows that the z-component of the velocity of ions and dust particles decreases with the increase of the magnetic field strength B_0. The magnetic field always restricts the movement of charged particles perpendicular to the field direction. The strength of the magnetic field increases gradually towards the wall.

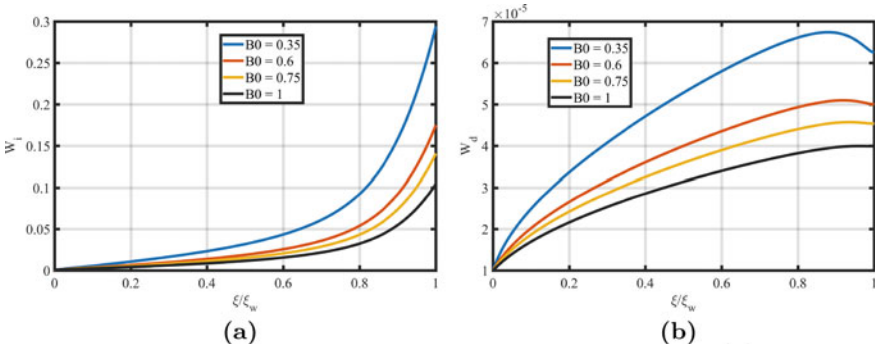

Fig. 39.2 **a** Variation of ion velocity w_i along the sheath for different magnetic field strengths B_0. **b** Variation of dust particle velocity w_d along the sheath for different magnetic field strengths B_0

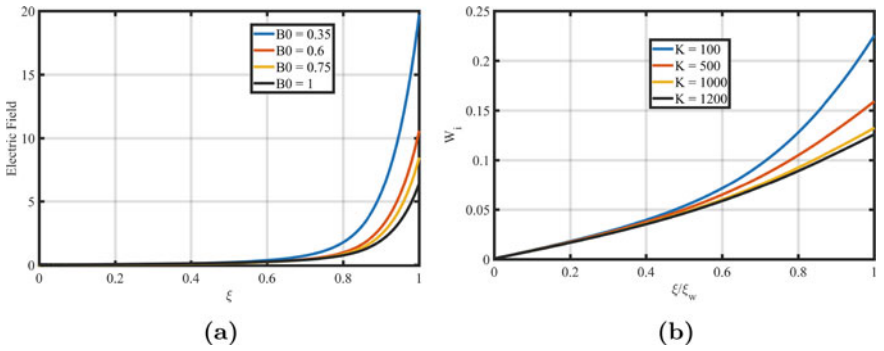

Fig. 39.3 **a** Evolution of electric field along the sheath for different magnetic field strengths B_0. **b** Variation of ion velocity along the sheath for different values of collision parameters K for $B_0 = 1T$

When B_0 is more, the strength of the magnetic field at each point of the space coordinate will be more. This reduces the movement of the ions and dust towards the wall, hence their velocity decreases.

Figure 39.3a depicts the evolution of electric field along the sheath for different magnetic field strengths B_0. It has been observed that the electric field decreases with the increase of the magnetic field strength. The Larmor radius of charged particle is given by $r_L = (mv_\perp/Bq)$. It has been seen that for the present study, the electron has the smallest Larmor radius among the charged species in the plasma. The Larmor radius of the charged particles decreases with the increase of the field strength, i.e. the charged particles are more strongly bounded by the field lines. The mobility of the charged particle perpendicular to the field direction decreases. Due to this, more and more electrons will accumulate on the dust grains, and hence the loss of electrons at the wall decreases. This reduces the space charge and the corresponding electric field.

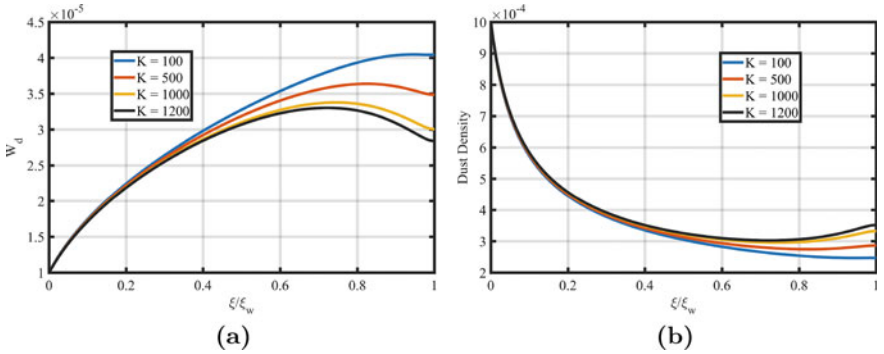

Fig. 39.4 **a** Velocity profiles of dust particles for different collision parameters K with $B_0 = 1T$. **b** Dust density variation along the sheath for different values of collision parameters K with $B_0 = 1T$

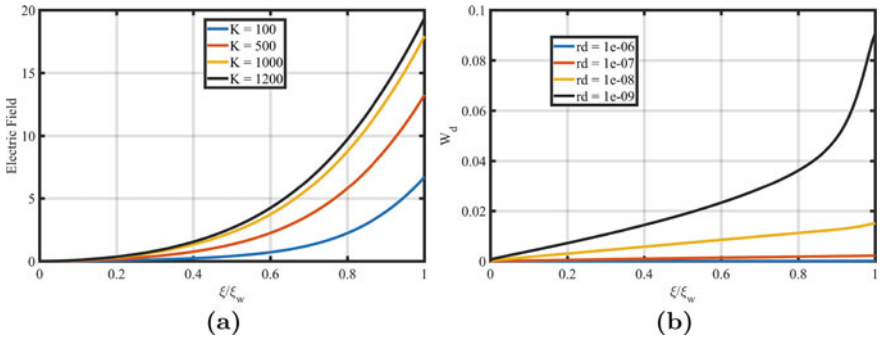

Fig. 39.5 **a** Evolution of electric field along the sheath for different values of collision parameters K with $B_0 = 1T$. **b** Variation of dust particle velocity along the sheath for different values of dust radii r_d with $B_0 = 1T$

Figures 39.3b and 39.4a show the variation of ion and dust particle velocity along the sheath length for different values of collision parameters K. It is seen that the velocity of ions and dust particles decreases with the increase of ion-neutral collision frequency. In an ion-neutral collision, the ions exchange their energy by colliding with the neutral background. With the increase of collision frequency, the energy lost by the ions is more and hence the ion velocity decreases. The ion-neutral collisions restrict the movement of the ions towards the wall. So, the wall becomes more negative with the increasing collision frequency. Due to this, the repulsive force between the negative wall and negatively charged dust particles increases, and consequently the dust velocity w_d decreases.

The dust density variation along the sheath for different values of collision parameter K is depicted by Fig. 39.4b. From (39.26), it is obvious that the flux of dust particles inside the sheath always remains constant. Figure 39.4a shows that the dust velocity decreases with the increase of collision parameter, therefore, to conserve

the dust flux in the sheath the dust density increases with the collision parameter as shown in Fig. 39.4b.

Figure 39.5a shows that the electric field increases with the increase of ion-neutral collision frequency. It has been observed that the electron density is independent of ion-neutral collision frequency. On the other hand, the ion-density increases with the increase of collision as more and more ions are deposited in space with collision. This causes the space charge to increase which in turn causes the electric field to increase.

Figure 39.5b describes the velocity variation of dust particles along the sheath length for different dust particle radii. It is seen that the velocity of dust particles increases with the decrease of dust radius. The accumulation of negative charge (electrons) on the dust grains decreases with the decrease of the dust size [17, 18], i.e. smaller size dust particles will be less negative. Due to this, the repulsive force between negative dust and negative wall decreases with the decrease of dust radius. Therefore, the dust velocity w_d increases with the decrease of dust radius.

39.5 Conclusions

In the present work, an attempt has been made to investigate the properties of plasma sheath in the presence of IHM and dust particles. From the study, the following observations can be made:

(i) In the presence of dust, it has been observed that the electric field decreases with the increase of magnetic field strength. The magnetic field restricts the movement of ions and electrons towards the wall, due to which the accumulation of electrons on the dust grain increases. This reduces the space charge and corresponding electric field.
(ii) As the magnetic field restricts the movement of the charged particle perpendicular to the field direction, therefore, the z-component of ion and dust particle velocity decreases with the increase of field strength.
(iii) The ion-neutral collision also tends to restrict the movement of ions towards the wall. It causes the z-component of ion velocity to decrease with the increase of collision frequency. From the study, it can be seen that ion-neutral collision and magnetic field have a similar effect on the ion dynamics.
(iv) With the increase of ion-neutral collision, the wall becomes more negative as it restricts the movement of ions. Therefore, the repulsive force on the dust particle increases with collision parameter K. As a result of this, velocity of the dust particles decreases with the increase of collision parameter.
(v) With the increase of ion-neutral collision, the space charge also increases. As a consequence, the electric field increases.
(vi) The z-component of dust particle velocity increases with the decrease of dust size. The net negative charge accumulated on the dust grain decreases with the decrease of dust size. Consequently, the repulsive force between the negative

wall and the dust particle decreases and so the dust velocity w_d increases with decreasing dust size.

The presence of IHM and dust particles modifies the properties of the plasma sheath. The magnetic field is always inhomogeneous in magnetic confinement devices like tokamak. The dynamics of dust particles play a very important role in the edge region of plasma-assisted material processing as well as in fusion devices like tokamak. Therefore, the study of a plasma sheath in the presence of IHM and dust particles may be helpful to understand the physics of plasma-assisted material processing as well as the edge region of tokamak devices.

References

1. G. Foroutan, H. Mehdipour, H. Zahed, Simulation study of the magnetized sheath of a dusty plasma. Phys. Plasmas **16**, 103703 (2009)
2. P.C. Stangeby, *The Plasma Boundary of Magnetic Fusion Devices* (Institute of Physics Publishing, Philadelphia, Pennsylvania, 2000), p. 224
3. K.-U. Riemann, The Bohm criterion and sheath formation. J. Phys. D Appl. Phys. **24**, 493 (1991)
4. S.F. Masoudi, G.R. Jafari, H.A. Shorakaee, Effect of dust-neutral collisions on the dust characteristics in a magnetized plasma sheath. Vacuum **83**, 1031 (2009)
5. H. Mehdipour, I. Denysenko, K. Ostrikov, Structure of the magnetized sheath of a dusty plasma. Phys. Plasmas **17**, 123708 (2010)
6. C. Arnas, M. Mikikian, G. Bachet, F. Doveil, Sheath modification in the presence of dust particles. Phys. Plasmas **7**, 4418 (2000)
7. B.P. Pandey, A. Samarian, S.V. Vladimirov, Dust in the magnetized sheath. Phys. Plasmas **14**, 093703 (2007)
8. I. Driouch, H. Chatei, M. El Bojaddaini, Numerical study of the sheath in magnetized dusty plasma with two-temperature electrons. J. Plasma Phys. **81** (2015)
9. M. Davoudabadi, F. Mashayek, Dust particle dynamics in magnetized plasma sheath. Phys. Plasmas **12**, 073505 (2005)
10. J.A. Bittencourt, *Fundamentals of Plasma Physics* (Springer, New York, 2004) (2018)
11. F.H. Ebersohn, J.P. Sheehan, A.D. Gallimore, J.V. Shebalin, J. Comput. Phys. **351**, 358–375 (2017)
12. M.S. Barnes, J.H. Keller, J.C. Forster, J.A. O'Neill, D.K. Coultas, Transport of dust particles in glow-discharge plasmas. PRL **68**, 313 (1992)
13. G. Foroutan, Fluid simulation of an electrostatic plasma sheath with two species of positive ions and charged nanoparticles. Phys. Plasmas **17**, 123711 (2010)
14. R. Moulick, K.S. Goswami, Sheath formation under collisional conditions in presence of dust. Phys. Plasmas **21**, 083702 (2014)
15. M. Davoudabadi, B. Rovagnati, F. Mashayek, Lateral motion of a dust particle in magnetized plasma sheath. IEEE Trans. Plasma Sci. **34**, 142 (2006)
16. R. Moulick, S. Adhikari, K.S. Goswami, Phys. Plasmas **26**, 043512 (2019)
17. C. Cui, J. Goree, Fluctuations of the charge on a dust grain in a plasma. IEEE Trans. Plasma Sci. **22**, 151 (1994)
18. J. Goree, Charging of particles in a plasma. Plasma Sci. Technol. **3**, 400 (1994)

Chapter 40
Study of Radiation Interactions in Makrofol-E and LR-115 Detectors Using SSNTD Technique

J. P. Gewali, P. Sheron, A. Thakur, and B. Jaishy

Abstract To understand nature has been the ultimate goal of the mankind in all the ages, various groups of scientist are working throughout the world to explore the hidden mysteries of the nature. Here we study the interaction of ionizing radiation with matter, in particular the organic and inorganic materials with a special focus on simple and effective technique of solid state nuclear track detector (SSNTD). Parameters like bulk etch rate, track etch rate, track length, range, and stopping power were measured for interaction of 11.56 meV/u ^{58}Ni and 11.6 meV/u ^{93}Nb in Makrofol-E detectors, which when compared with the available experimental result available in nuclear data tables from Hubert and Northcliff Schilling and theoretical result from SRIM, DEDXT programs the results are showing a close proximity. Thus proving its effectiveness to other detection technique.

40.1 Introduction

The ionizing radiation study has been in forefront since the discovery of X–ray by Roentgens in 1895, with its application not only in physical and chemical sciences but also in biological sciences. There is no field in modern physics and allied sciences where the ionization of radiation has no role to play. The basic property of ionizing radiation being its penetrating power, i.e., how it can pass through the matter with the degradation of energy and the disturbances created by it in the balance of electrical forces that hold the atoms and molecules together. But the most salient property of ionizing radiations is their great energy, which permits the physicist to deal with single atomic particles. Just as alpha particles (nuclei of helium) due to its high kinetic energy, it is individually detected. Thus the study of interaction of high energy radiation with matter basically have two aspects; what is the effect of radiation on the matter and what is the effect of a matter on radiation when it pass through it. High-speed particles in a sense permit exploration of the inner structure of matter. Their deflection during penetration provides a measure of the forces to

J. P. Gewali (✉) · P. Sheron · A. Thakur · B. Jaishy
Department of Physics, Lovely Professional University, Phagwara, Punjab 144411, India

S. Sengupta et al. (eds.), *Selected Progresses in Modern Physics*, Springer Proceedings in Physics 265, https://doi.org/10.1007/978-981-16-5141-0_40

which they are subjected in the interior of atoms and molecules. This we can understand from the experiment conducted by J J Thomson for electron penetration [1] and by Earnest Rutherford to determine structure of atomic nuclei [2]. The principle of interaction has been used to understand the arrangement of neutrons and protons in atomic nucleus also the structure of nuclear particle. This interaction technique has been used to understand different aspects of quantum theory of physics [3]. Also its effect on the human health due to both environmental and manmade radiation effects have motivated the researcher to work on this topic [4–6]. Upon entering any absorbing medium, the charged particle immediately interacts simultaneously with many electrons. In one such encounter, the electron feels an impulse from the attractive Coulomb force as the particle passes its vicinity. Depending on the proximity of the encounter, this impulse may be sufficient either to raise the electron to a higher-lying shell within the absorber atom (excitation) or to remove completely the electron from the atom (ionization). The energy that is transferred to the electron must come at the expense of the charged particle, and its velocity is therefore decreased as a result of the encounter [3, 7].

40.2 Interaction of Ionization Radiation with Matter

The interaction of each type of radiation with matter depends upon the mass and the charge (if any) of the radiation as well as upon its energy. Because high-energy neutrons have no electric charge, they interact feebly with atoms and therefore have great penetrating power. Eventually they give up their entire initial kinetic energy to the atomic nuclei that they happen to strike directly. In recoiling from these collisions, the atoms lose one or several of their orbital electrons and themselves become charged particles [3, 8, 9]. These energetic electrons, which again are electrically charged secondary particles, pursue their own paths through the medium, losing energy to it as would any electron of the same kinetic energy [9, 10].

40.3 Experimental Techniques for the Detection of Heavy Ions Interactions

A large number of detector systems have been developed over the time to study the interaction of charged particles with matter. This system tests the degrees to which the total initial energy, momentum, mass and charge of the system is balanced by quantities associated with the observed fragments and allows a reconstruction of the primary-event history. The detecting techniques are involved in the measurements.

The observation of the primary effects of ionizing radiation, the electrical counter invented by Rutherford and Hans Geiger in 1908, employs high voltages to break down the gas, once a passing particle has supplied an initial requirement of ions.

The most common variety, the Geiger counter, has applications ranging from refined physical experiment to uranium prospecting [1–3, 7].

The second basic method of detection rests upon the emission of light by excited molecules. When an isolated atom is excited, it must lose its excitation energy and return to its lowest energy state by emitting one or several photons [11].

Chemical reactions, engendered by both excitation and ionization, furnish a third important mode of observation and measurement. The blackening of photographic emulsion, a chemical effect that gave Wilhelm Conrad Roentgen the first clue to the existence of ionizing radiation, is still useful both for observing individual particles and for determining total amounts of radiation [12].

The improvement in the detectors has accompanied by the development of more versatile and reliable electronics measuring instruments, earlier where it was possible to record only a number of events in a certain detector, now it is quite common to record a complicated spectral data [10, 13]. With the compatibility between the digital computer technology and nuclear equipment many new technique of nuclear data processing has come up. Most advance detectors used today use the simple concept of ionization produced by the passage of charge particles. The principle behind the use of gas ionization detectors being the ions formed in a gas is exceedingly reactive; they often undergo chemical changes during the time required to collect them at an electrode.

Ionization chambers are widely employed to count energetic particles and to determine their individual energies [3, 8, 9].

All the technique discussed above requires a heavy instrumentation not feasible in laboratories as are not cost effective. Thus a simple and cost effective technique of SSNTDs has been developed which gives us good idea about the effect of radiation on detectors.

40.4 SSNTD Technique of Radiation Detection

The solid state nuclear track detection is simple, inexpensive compared to other techniques. The interactions will be registered as the tracks in SSNTD, and it in return gives the information about the charge/mass and velocity/energy of the fragments responsible for the creation of such tracks [14, 15]. On account of the above advantage of the SSNTD technique, it has been employed to study the behavior of the heavy ion interactions with the detectors. The material containing latent tracks if exposed to some chemically aggressive solution, and the chemical reactions would be more intensive along the latent tracks. Aqueous solutions of NaOH or KOH are the most frequently used chemical solutions. During the process, chemical solution etches the surface of the detector material, but with a faster rate in the damaged region. In this way, a ‘track’ of the particle is formed, which may be observed under an optical microscope. The technique based on the application of ‘Solid State Nuclear Track Detector’ (SSNTDs) has greatly expanded in range, scope and depth since its discovery in 1958 by Young [16]. In 1959, a rediscovery of Young’s work was

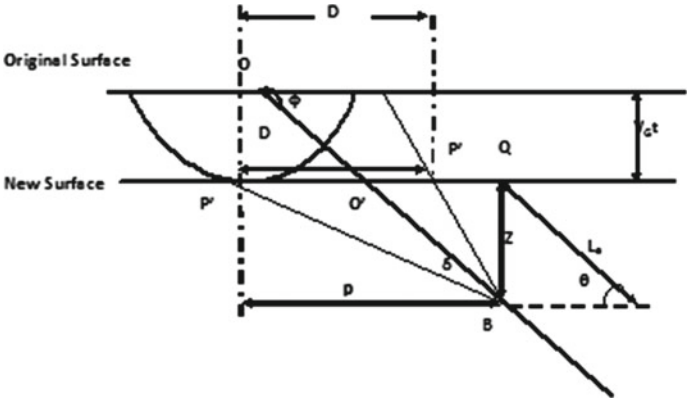

Fig. 40.1 The geometry of an inclined etched track [10]

done by Silk and Barnes in (1959) [17] by irradiating mica with fission fragments. In 1960 the team of R.L Fleischer, P.B Price and R.M walker [14] pioneered the extensive development of this method by transforming the radiation damage trails into permanent tracks. Later, many other workers developed such tracks in thin films of different insulating materials.

The track technique is based on the principle that an energetic charged particle passing through an insulating media creates submicroscopic damage trails in solid dielectrics. The damage regions forms the latent tracks which can be developed and fixed by suitable chemical etching technique. These permanent 'tracks' after etching can be observed under an optical microscope. The detail track geometry of which is discussed in Durrani and Bull 1987 [14] and is represented in Fig. 40.1.

40.5 Applications of SSNTD Technique

Nuclear track technology has been successfully employed in diverse fields like fusion-fission and particle evaporation, nuclear reaction, detection and identification of the synthesized element 104 (Rutherfordium). Fission track dating has been successfully applied to dating of geological, archeological, and cosmological samples. In the field of medicine, it has been used in filtering cancer cells from normal blood cells and in medical diagnostics. It has also been applied for uranium exploration, earthquake prediction, range and stopping power measurements and has found application in many more fields [14, 18–21].

We in this paper have calculated the various etching parameters using this technique for 11.56 meV/u $^{58}Ni^{14+}$ ion irradiated Makrofol-E detector.

(a) Bulk etch rate (V_G): The bulk etch rate V_G is the speed with which the undamaged regular material is dissolved out by an etchant. The track diameter method [14, 15, 22–24] has been used by us to measure V_G.

The bulk etch rate along the surface of the detector is given by

$$V_G = {}^{\Delta D}/_{2\Delta t}. \tag{40.1}$$

where ΔD represents the change in diameter of track with change in etching time Δt.

(b) Track etch rate (V_T): The track etch rate V_T is the rate at which the material is chemically etched along the damage trail of the particle trajectory, i.e., the rate at which the tip of the etched cone moves along the latent track during the etching process [25–27].

If Δl is changed in track length with the change in etching time Δt, then V_T is written as

$$V_T = {}^{\Delta l}/_{\Delta t}. \tag{40.2}$$

(c) True track length: The true track length (L) after any etching time (t) greater than complete etching time (T_C) is related to the measured projected length (l) by the following equations [28–31]

$$L = \frac{l}{cos\varnothing} + \frac{V_G t}{sin\varnothing} - V_G(t - T_C) \tag{40.3}$$

where $\varnothing$ is the incidence angle of ion, V_G is the bulk etch rate, t is the total etching time, and T_C is the time taken to etch the track completely. The second term is the surface etching correction factor, and the third term is over etching correction factor.

Table 40.1 shows the track length, track diameter, track etch rate, bulk etch rate calculated using the formulation above for 11.56 meV/u, ^{58}Ni irradiated Makrofol-E detectors etched at 6 N NaOH solution at 55 °C. It can be seen that the true track length calculated using Eq. (40.3) above matches quite well with the theoretical values of DEDXT [32] and SRIM [33] programs.

Other parameters like sensitivity of the detector, efficiency of detector, critical angle of irradiation, critical time of etching, activation energy, and the annealing study can be done through this technique as discussed detail in the literature [31].

Table 40.1 Etching parameters for 11.56 meV/u $^{58}Ni^{14+}$ ion irradiated Makrofol-E detector

Etching temp (°C)	Track etch rate (μm/hr)	Bulk etch rate (μm/hr)	Track diameter (μm)	True track length (μm)	Theoretical (DEDXT) (μm)	Theoretical (SRIM) (μm)
55	117.2 ± 1.4	0.63 ± 0.01	2.2 ± 0.6	176.9 ± 2.5	210.62	186.2

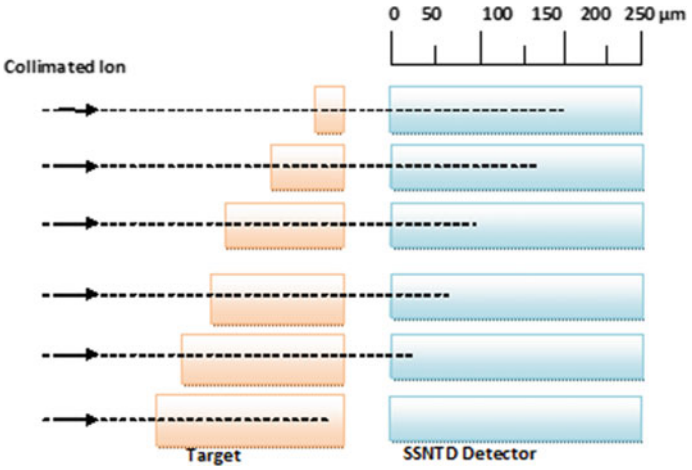

Fig. 40.2 A schematic diagram showing the basic idea of the measurement of range and stopping power [31]

40.6 Range and Stopping Power Measurements

Taking SSNTD as a tool range and stopping power of incident heavy ion can also be found out the schematic diagram showing the methodology to measure the range and stopping power using stacks of target and detector assembly is represented in Fig. 40.2. Using this technology, we have successfully measure the range and energy loss of heavy ion in target and detectors (both polycarbonate and glass) [31, 34–39].

40.7 Methodology

A collimated beam of a heavy ion ^{93}Nb is allowed to penetrate through the aluminum targets. For a given target thickness X, the energy loss can be calculated by the following expression:

$$E = E_i - E_X \tag{40.4}$$

where E_i and E_X are initial and transmitted energies, respectively, after passing through a target of effective thickness 'X', which is given by

$$X = X_2 - X_1 \tag{40.5}$$

where X_2 and X_1 are thickness of any two consecutive targets.

Hence the stopping power may be determined from the equation

$$\left(\frac{dE}{dX}\right)_{\overline{E},\overline{X}} = \frac{E_i - E_X}{X_2 - X_1} \tag{40.6}$$

where the mean value of energy $\overline{E}$ and target thickness $\overline{X}$ are obtained from $\overline{E} = (E_i + E_X)/2$ and $\overline{X} = (X_1 + X_2)/2$.

The mean range $R(E)$ can easily be obtained by extrapolating the energy loss curve to energy $E_X = 0$. From this value the mean ranges R(E) at energy E may be obtained from the equation

$$R(E) = R - X(E) \tag{40.7}$$

where $X(E)$ is the target thickness which reduces the ion energy from E_i to E and is obtained from the energy loss curve.

Table 40.2 lists the values of aluminum target thickness, measured track lengths in Makrofol-E of ^{93}Nb ions emerging out of Al targets, and corresponding ion energies obtained from the calibration curve. From these tabulated data, the mean range is obtained using Eq. (40.7). It has been found that mean range of 11.56 meV/u ^{93}Nb is 94 ± 3.2 μm. The ranges of ^{93}Nb in Al absorbers at several different energies are also obtained and are also presented in Table 40.2. The stopping power for ^{93}Nb in Al is calculated using Eq. (40.4), which is listed in Table 40.2. The experimental range and stopping power (energy loss) so calculated for of ^{93}Nb in aluminum found to be matching with the experimental data tables [40, 41] and theoretical programs [32, 33], thus validating the claim of higher efficiency of SSNTDs detectors.

Table 40.2 Values of aluminum target thickness, maximum etchable track length of ^{93}Nb in Makrofol-E detector, energy of the transmitted ion, ranges obtained in aluminum, and stopping power of ^{93}Nb in aluminum

Target Thickness (μm)	Track Length (μm)	Ion Energy (MeV/u)	Range (μm)	Stopping power (MeV mg^{-1} cm^2)
No Target	176.9 ± 2.5	11.6 ± 0.2	94 ± 3.2	–
64.6	147 ± 2.0	9.1 ± 0.2	71 ± 3.4	38.6
70.1	133 ± 2.1	8.1 ± 0.3	63 ± 3.6	39.6
72.9	128 ± 2.3	7.7 ± 0.3	59 ± 3.6	40.0
87.9	82 ± 2.1	4.6 ± 0.3	38 ± 3.7	43.5
94.9	66 ± 1.8	3.6 ± 0.3	28 ± 3.8	44.7
102.2	42 ± 1.7	2.2 ± 0.3	18 ± 3.8	46.6
106.5	29 ± 1.9	1.5 ± 0.2	11 ± 3.7	47.6

40.8 Detection of Environmental Radiation Using SSNTDs Technique

Also the SSNTDs technique has been used for detecting and measuring the radon, thoron concentration levels and of its decay products. As radon is being a large contributor to the radiation dose delivered to mankind from the environment which might leads to many health hazards, the study and measurement of its concentration has become a prime topic of research all over the world. During the study, track detectors which are composed of a plastic material are used to assess the tracks of the alpha particles (release during the decay of radon) and other radioactive materials. This exposure can be revealed later while etching the samples in the solution of NaOH. The track detectors that are mostly used are LR-115 (a thin film of colored cellulose nitrate on an inert backing), CR-39 (poly allyl diglycol carbonate, PADC), and some polycarbonate detectors [42].

Figure 40.3 shows the alpha tracks on LR115 type 2 detector etched in 6 N NaOH. The white spots are the alpha tracks which are to be counted by spark counter/optical microscope [43]. Counting that tracks using optical microscope or spark counter, we can find out how many alpha particles have hit the detector during particular period (we have taken 90 days), which is radioactive emission from radon with has half-life of only 3.8 days. Using this technique, we have installed LR-115 detectors at different sites in Chandigarh India and calculate the radon concentration of that region which is depicted in Fig. 40.4. Radon being a naturally occurring radioactive gas and one of the cause of lung cancer in the world, knowing the concentration of it and comparing with WHO/UNSCEAR effective dose limit, the risk it pose for

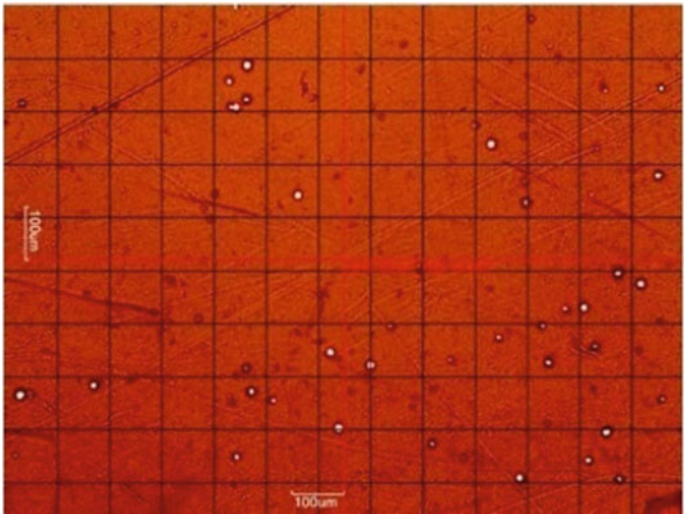

Fig. 40.3 Alpha tracks on LR115 type 2 detectors

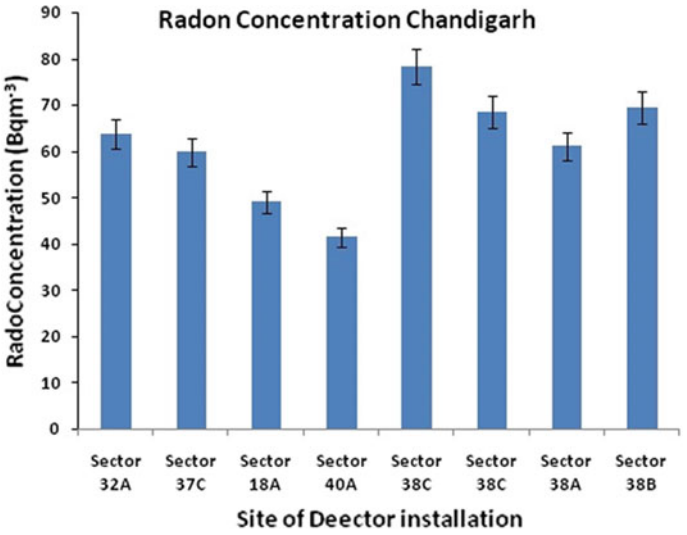

Fig. 40.4 Radon concentration in Chandigarh, India [43]

human being can be ascertained and can be minimized with certain precautions[4–6]. From the graph, it can be concluded that the average concentration of radon in the studied region lies between 40–80 Bq/m^3 though higher but is well below maximum exposure limit of 100 Bq/m^3 as recommended by WHO in 2009 [4]. Thus we can conclude in the studied area radon pose minimal threat to the health of the general population.

The technique also has been widely used to study the radon and thoron concentration in soil and water[44].

40.9 Conclusion

In this paper, we stressed on the SSNTDs technique for detecting and studying the effects of radiation in a matter (detector). The study shows this method is easier to perform and with less instrumentation, and the high efficiency results can be obtained compared to other detection technique which requires heavy instrumentations. Radon, thoron, and other radioactive decay detection using this methodology has helped to map the radiation content both indoor and outdoor environment thus serving purpose of mankind.

References

1. J.J. Thomson, Carriers of negative electricity, in *Nobel Lecture 1906* (Elsevier Publishing Company, Amsterdam, 1967)
2. K.S. Krane, *Introductory Nuclear Physics* (John Wiley & Sons, New York, U. S. A, 1988)
3. G.F. Knoll, *Radiation Detection and Measurement* (Wiley, University of Michigan, U.S.A, 2010)
4. UNSCEAR-2000 Sources and Effects of Ionizing Radiation. United Nations Scientific Committee on the Effect of Atomic Radiation, United Nations, New York (2000)
5. WHO Handbook on indoor radon: A public health perspective, World Health Organization (2009)
6. Monographs on the Evaluation of Carcinogenic Risks to Humans, Man Made Mineral Fibres and Radon. IARC Sci. Publ. **43**, 173 (1988)
7. P. Sigmund, *Stopping of Heavy Ions (A Theoretical Approach)* (Springer, 2004)
8. J. David, *Radiation Detection for Nuclear Physics Methods and Industrial Applications* (IOP publication, 2020)
9. G. Friedlander, J.W. Kennedy, E.S. Macias, J.M. Miller, *Nuclear and Radiochemistry* (Wiley, New York, 1981)
10. H. Freiesleben et al., Zeitschrift fur Physik A Atom and Nuclei (Z Physics A) **292**, 171–189 (1979)
11. A. Kamal, *Particle Physics* (Springer, New York, U. S. A, 2014)
12. O. Glasser, *W C Roentgen*, 2nd edn. (Springerfield IL, Thomas-Publisher, 1958)
13. P.A. Gottschalk et al., Two-, three-, and four-particle exit channels in the reaction (806 MeV) Kr+ U. Phys. Rev. **27**, 2703 (1983)
14. S.A. Durani, R.K. Bull, *Solid State Nuclear Track Detection, principal methods and applications* (Pergamon Press U K, 1987)
15. R.L. Fleischer et al., *Nuclear Tracks in Solids* (University of California Press, Berkeley, Principles and Applications, 1975)
16. D.A. Young, Etching of radiation damage in lithium fluoride. Nature **182**, 375 (1958)
17. E.C.H. Silk, R.S. Barnes, Examination of fission fragment tracks with an electron microscope. Philos. Mag. **4**, 970 (1959)
18. O.A. Bondarenko et al., Application of SSNTD for maintenance of radiation and nuclear safety of the Sarcophagus. Rad. Meas. **30**, 709 (1999)
19. S. Cecchini, L. Patrizii, Nuclear track detectors in astroparticle and nuclear physics. Rad. Meas. **43**, S144 (2008)
20. L.T. Chadderton, Nuclear tracks in solids: registration physics and the compound spike. Rad. Meas. **36**, 13 (2003)
21. P.B. Price, Advances in solid state nuclear track detectors. Nucl. Tracks Rad. Meas. **22**, 9 (1993)
22. H.I. Hasan, A.K. Hussein, R.B. Kheder, Angular response of nuclear track detector CR-39 for alpha particles with different energies. Concept Pure Appl. Sci. **1**, 22 (2013)
23. Matiullah, S.A. Durrani, Measurement of the etching characteristics of proton, fission-fragment and heavy-ion tracks in CR-39. Nucl. Tracks Rad. Meas. **15**, 203 (1988)
24. F. Pugliesi, V. Sciani, M.A. Stanojev, S. Pereira, R. Pugliesi, Digital system to characterize solid state nuclear track detectors. Braz. J. Phys. **37**, 446 (2007)
25. E.M. Awad, Direct determination of track etch rate and response of CR-39 to normalize incidence high-energy heavy ions. Rad. Meas. **33**, 855 (2001)
26. B. Dorschel et al., Variation of the track etch rate along the trajectories of light ions in CR-39. Rad. Meas. **35**, 177 (2002)
27. Dorschel et al., Measurement of the track etch rates along proton and alpha particle trajectories in CR-39 and calculation of the detection efficiency. Rad. Meas. **31**, 102 (1999)
28. K.K. Dwivedi, A. Saxena, Track lengths of heavy ions in CR-39 and ZnP-Glass detectors. Nucl. Tracks **12**, 241 (1986)
29. K.K. Dwivedi, S. Mukherji, Bulk and track etch rate studies with some solid dielectric track detectors. Nucl. Instr. Method **161**, 317 (1979)

30. K.K. Dwivedi, S. Mukherji, Heavy ion track length in solid dielectric track detectors. Nucl. Instr. Method **159**, 433 (1979)
31. J.P. Gewali, Studies on heavy ion electronic stopping power and thermal fading characteristics of nuclear tracks in solid state nuclear detectors, Ph. D. Thesis, North-Eastern Hill University, Shillong, India (2014)
32. K.K. Dwivedi, A Program for computation of heavy ion ranges, track lengths and energy-loss rate in elemental and complex media. Nucl. Tracks Radiat. Meas. **15**, 345 (1988)
33. J.F. Ziegler, M.D. Ziegler, J.P. Biersack, Nucl. Instr. Methods Phys. Res. Sect. B **268**, 1818 (2010)
34. A. Saxena, K.K. Dwivedi, E. Reichwein, G. Fiedler, Energy-loss measurement of ^{132}Xe in lead by a nuclear track technique. Nucl. Instr. Method Phys. Res. Sect. B **36**, 276 (1989)
35. A. Saxena, K.K. Dwivedi, G. Fiedler, Use of CR-39 detector in range and energy-loss measurement of 18.04 MeV/u ^{93}Nb in aluminium. Nucl. Tracks Rad. Meas. **15**, 327 (1988).
36. J.P. Gewali, Measurement of range and energy loss of heavy ion in ZnP glass, in *AIP in Proceedings of the Conference Proceedings*, vol. 2050, p. 020012 (2018)
37. J.P. Gewali, A. Saxena, Ranges of energetic 40 Ar in ZnP glass. J. Appl. Fundam. Sci. **1**(2), 187 (2015)
38. J.P. Gewali et al., Experimental range of energetic ^{238}U in tantalum. E. J. Mol. Clin. Med. **7**, 3493 (2020)
39. J.P. Gewali, A. Saxena, Range and maximum etchable track length of ^{93}Nb in CR39 detector. J. Phys. Conf. Ser. **1531**, 012040 (2020)
40. F. Hubert, R. Bimbot, H. Gauvin, Range and stopping power tables for 2.5–500 MeV/u heavy ions in solids. Atomic Data Nucl. Data Tables **46**, 1 (1990)
41. L.C. Northcliffe, R.F. Schilling, Range and stopping –power tables for heavy ions. Nucl. Data Tables. **A7**, 233 (1970)
42. S.A. Durani, R. Illi'c, *Radon Measurement by Etched Track Detectors* (World Scientific Publishing Co., Ltd, 1987)
43. J.P. Gewali et al, Radon concentration in Chandigarh India using LR-115 detector. J. Phys.: Conf. Ser. **1531**, 012039 (2020)
44. K.P. Eappen, Y.S. Mayya, Calibration factors for LR-115 (type-II) based radon thoron discriminating dosimeter. Rad. Meas. **38**, 5 (2004)

Chapter 41
Study of Structural, Electrical and Magnetic Properties of Nd-Ti Co-Doped $BiFeO_3$ Nanoparticles

Sanjay Godara

Abstract Single-phase BFO nanoparticles with compositions $Bi_{0.9}Nd_{0.1}FeO_3$ and $Bi_{0.9}Nd_{0.1}Fe_{0.95}Ti_{0.05}O_3$ have been synthesized by low temperature citric acid assisted auto-combustion route. Thereafter, effect of the co-substitutions on structural, electrical and magnetic properties of BFO has been investigated. X-ray diffraction revealed partial phase transformation from rhombohedral to orthorhombic for 10% Nd-substituted BFO, whereas Nd-Ti sample showed traces of pseudo-tetragonal symmetry. TEM micrographs confirmed nearly uniformly shaped particles with particle size under 50 nm. Resistivity of the co-doped sample increased remarkably and found to be $\rho_{dc} = 1.85 \times 10^{11}$ Ω-cm. Thus, Ti^{4+} ion reduced leakage current by suppressing oxygen vacancies. Ferroelectric nature has been improved on account of structural distortion induced by Nd-Ti ions as well as decreased leakage current. Also, dielectric behaviour improved significantly on doping. A broad peak nearby T_N in temperature-dependent dielectric confirmed magnetoelectric coupling for all the samples. The wasp-waisted type M-H loop was observed with improved weak ferromagnetism due to structural distortion induced by dopant ions and super-exchange like interaction between dopants and host ions. Therefore, co-doping of Nd and Ti ions considerably has enriched the electric and magnetic properties of BFO nanoparticles.

41.1 Introduction

Multiferroics are the materials having two or more ferroic parameters simultaneously. Magnetoelectrics are sub-class of multiferroic materials that exhibit ferroelectric and (anti)ferromagnetic orderings simultaneously. Due to coupled ferroic parameter in multiferroic, there is an extra degree of freedom which enhance their expedient applications in the field of low energy consuming and highly dense non-volatile memory devices, spintronics and sensors [1–3].

S. Godara (✉)
Department of Physics, MLV Government College, Bhilwara, Rajasthan 311001, India

S. Sengupta et al. (eds.), *Selected Progresses in Modern Physics*, Springer Proceedings in Physics 265, https://doi.org/10.1007/978-981-16-5141-0_41

Bismuth ferrite (BFO) is the representative room temperature multiferroic with perovskite structure (ABO_3 type) and possesses ferroelectric (T_C = 825 °C) and G-type antiferromagnetic (T_N = 370 °C) orderings [2]. However, BFO exhibits the weak magnetoelectric response at room temperature due to phase instability, high leakage current and weak magnetism, which limits its technological applications [4, 5]. Numerous ways like low-temperature synthesis, site engineering of BFO and formation of thin films are being employed to enhance its magnetoelectric properties [5, 6]. The doping/co-doping of rare-earth and transition metal ions have been found to improve electrical as well as magnetic properties of BFO [7–10].

In present study, partially substituted (10% Nd and 5% Ti) BFO nanoparticles with compositions $Bi_{0.9}Nd_{0.1}FeO_3$ and $Bi_{0.9}Nd_{0.1}Fe_{0.95}Ti_{0.05}O_3$ were synthesized by low temperature auto-combustion route. The effect of doping on multiferroic properties was studied with various characterization techniques.

41.2 Experimental Procedure

Nd and Ti co-doped BFO nanoparticles were synthesized by auto-combustion route using citric acid as complexing agent. For this, Bismuth nitrate, Ferric Nitrate, Neodymium nitrate and Titanium oxide were used as metal ions sources, which were dissolved in doubly distilled water as per stoichiometry of the sample and added some concentrated HNO_3. Solutions were maintained at 80 °C with vigorous stirring to homogenise it. Citric acid in 1:1 mol ratio with respect to each metal ions was added. As-obtained light brownish solution was dried on hot plate. Dried residue was powdered and further heated till combustion took place. Finally powder was sintered at 500 °C for 2 h to remove organic compounds and to get phase pure doped BFO NPs.

Structural (XRD: Rigaku Ultima IV; $\lambda = 1.5405$ Å), morphological (TEM: Tecnai 200 kV; FEI Company) and magnetic (VSM: JDAW-2000D) characterizations were carried on powder samples, whereas pelletized samples were used for ferroelectric (Marine India P-E loop tracer), Dielectric study (Agilent E 4980 A LCR meter) and Conductivity (Keithley 2400) studies.

41.3 Results and Discussion

41.3.1 XRD and TEM Analysis

Figure 41.1 c shows the XRD pattern of Nd and NdTi doped BFO Nanoparticles, where peaks are indexed according to hexagonal lattice system within space group R3c ((JCPDS card no.71–2494). The observed pattern confirms the single phase formation for the samples. The peaks (104) and (110) near $2\theta = 32°$ (Inset) are found

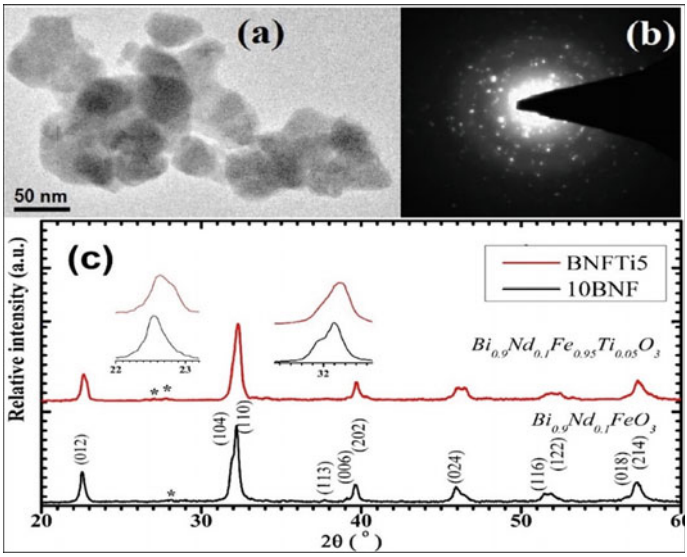

Fig. 41.1 **a** TEM micrograph, **b** SAED pattern and **c** Powder XRD pattern of BFO NPs

to be merged to a single peak for NdTi-BFO confirms partial phase transformation on Ti doping at Fe sites. This is a result of slight ionic radii difference between host ions (Fe^{3+} ~ 0.645 Å) and dopant ion (Ti^{4+} ~ 0.605 Å) [6].

Figure 41.1 a shows TEM image of Nd-BFO nanoparticles, which reveals nearly uniformly shaped particles with particle size under 50 nm. Bright spots on SAED confirms crystalline nature of NPs as expected.

41.3.2 Magnetic Study

Figures 41.2a, b show room temperature magnetization hysteresis (M-H) loops for Nd- and NdTi-doped BFO nanoparticles measured with the applied magnetic field up to 22 kOe. All the samples display well-developed M-H loop with non-zero remnant magnetization (M_r) and coercive field (H_C). Magnetic parameters for the samples are summarized in Table 41.1. For Nd-doped BFO, values of M_r and M_{max} have been enhanced significantly as compared to previous reports for undoped BFO, which may be resulted from magnetic activity of rare-earth ion Nd [3, 8]. However, no influence on magnetism was observed for partial substitution of non-magnetic ion Ti at the Fe-site.

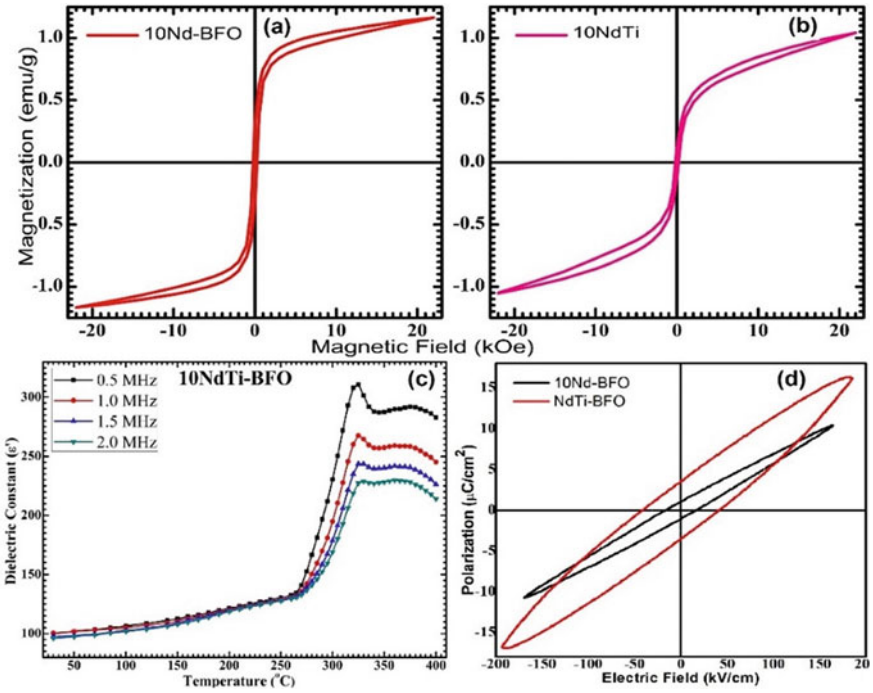

Fig. 41.2 Magnetic hysteresis loop for **a** 10Nd-BFO and **b** 10NdTi-BFO NPs, **c** Temperature dependent Dielectric constant and **d** P-E loops for co-doped BFO NPs

41.3.3 Dielectric Study

Figure 41.2c presents the temperature dependence of dielectric constant (ε') at various frequencies for NdTi-BFO nanoparticle sample. Dielectric constant increases gradually with raising temperature almost up to 250 °C. This may have resulted from thermally activated dipoles, as more and more dipoles participate toward polarization with increasing temperature and thus dielectric constant increases [6]. Afterwards, dielectric constant increases rapidly up to certain temperature where dielectric constant attains maximum value and then drops. This type of dielectric anomaly around antiferromagnetic-paramagnetic transition temperature (T_N) signifies strong coupling between magnetic and electric order parameters [5, 10].

41.3.4 Ferroelectric Study

Electric field dependent polarization (P-E) loops at frequency 50 Hz of Nd- and NdTi-doped BFO nanoparticles are presented in Fig. 41.2d. The values of remnant polarization (P_r), saturated polarization (P_s) and maximum applied field (E_m) of

Table 41.1 Magnetic and ferroelectric parameters for co-doped BFO NPs

	Magnetic parameters			Ferroelectric parameters			DC Resistivity
	$M_r(emu/g)$	M_{max} (emu/g)	$H_C(Oe)$	$P_r(\mu C/cm^2)$	$P_{max}(\mu C/cm^2)$	$E_{max}(kV/cm)$	$\rho_{dc}/10^9$ $(\Omega\text{-}cm)$
Nd-BFO	0.31	1.16	235	1.05	9.40	165	53.82
NdTi-BFO	0.11	1.05	170	3.50	14.30	185	184.5

respective samples are given in Table 41.1. For NdTi doped sample, lossy nature of P-E loop is reduced and strength to sustain maximum electric field is increased, due to decreased leakage current. Further, ferroelectric nature has also been improved in the NdTi co-doped sample on account of structural distortion induced by Ti ion [4].

41.4 Conclusion

In summary, Nd- and NdTi co-doped BFO nanoparticles were synthesized by low temperature citric acid assisted auto-combustion route, and their structural, electrical and magnetic properties were investigated. The XRD studies confirmed the partial phase transformation on doping from rhombohedral phase of pure BFO. The enhancement in ferromagnetic nature of the samples was observed due to Nd doping. The reduced leakage current was attributed to decreased oxygen vacancies due to Ti^{4+} ions and thus improved ferroelectricity were achieved in co-doped sample. Hence, co-substitution of rare-earth Nd and transition metal Ti stabilized the phase of BFO as well as enhanced multiferroic properties.

Acknowledgements I am thankful to Prof. Binay Kumar, Crystal Lab, Dept. of Physics & Astrophysics, University of Delhi, under the guidance of whom this piece of work was carried out for my Doctoral Research.

References

1. W. Eerenstein, N.D. Mathur, J.F. Scott, Multiferroic and magnetoelectric materials. Nature **442**, 759–765 (2006)
2. G. Catalan, J.F. Scott, Physics and applications of bismuth ferrite. Adv. Mater. **21**, 2463–2485 (2009)
3. S. Godara, N. Sinha, G. Ray, B. Kumar, Combined structural, electrical, magnetic and optical characterization of bismuth ferrite nanoparticles synthesized by auto-combustion route. *J. Asian Ceram. Soc.* **2**, (2014)
4. X. Qi, J. Dho, R. Tomov, M.G. Blamire, J.L. MacManus-Driscoll, Greatly reduced leakage current and conduction mechanism in aliovalent-ion-doped $BiFeO_3$. *Appl. Phys. Lett.* **86**, 062903 (2005)
5. V. Palkar, D. Kundaliya, S. Malik, S. Bhattacharya, Magnetoelectricity at room temperature in the $Bi_{0.9-x}Tb_xLa_{0.1}FeO_3$ system. Phys. Rev. B 69, 212102 (2004)
6. S. Godara, B. Kumar, Effect of Ba–Nb co-doping on the structural, dielectric, magnetic and ferroelectric properties of $BiFeO_3$ nanoparticles. Ceram. Int. **41**, 6912–6919 (2015)
7. A.I. Iorgu et al., Fast synthesis of rare-earth (Pr^{3+}, Sm^{3+}, $Eu^{3+}$and Gd^{3+}) doped bismuth ferrite powders with enhanced magnetic properties. J. Alloys Compd. **629**, 62–68 (2015)

8. N. Hernández, et al., Characterization and magnetic properties of $Nd_xBi_{1-x}Fe_{0.95}Co_{0.05}O_3$ nanopowders synthesized by combustion-derived method at low temperature. *J. Magn. Magn. Mater.* **377**, 466–471 (2015)
9. X.Y. Li, J.Q. Dai, T.F. Cao, X.W. Wang, Structure and physical properties of (Zn, Ti) co-doped BiFeO3 ceramics prepared using three different processes. Ceram. Int. **45**, 5015–5022 (2019)
10. A.T. Apostolov, I.N. Apostolova, J.M. Wesselinowa, Magnetic field effect on the dielectric properties of rare earth doped multiferroic BiFeO3. *J. Magn. Magn. Mater.* **513**, 167101 (2020)

Chapter 42
Frictional Effect of Neutrals Hall Current and Radiative Heat-Loss Functions on Thermal Instability of Two-Component Plasma

Sachin Kaothekar

Abstract The problem of neutral friction effects, Hall current and radiative heat-loss function on thermal instability of viscous two-component plasma has been explored including the consequences of finite electrical resistivity and thermal conductivity. A general dispersion relation is acquired taking the normal mode analysis technique having in account appropriate linearized perturbation equations of the difficulty, and a tailored thermal situation of instability is explored. It is clear that the thermal instability situation is amended because of the occurrence of radiative heat-loss function, thermal conductivity and neutral particle. The Hall current constraint influences only the longitudinal mode of propagation. Also, it is carried out that the situation of thermal instability is sovereign of the Hall current, magnetic field strength, finite electrical resistivity and viscosity of two-components, but depends on the radiative heat-loss function, thermal conductivity and neutral particle. From the graphs, it is seen that the temperature dependent heat-loss function, thermal conductivity and viscosity of two-components show stabilizing effect, while density dependent heat-loss function and finite electrical resistivity show destabilizing effect. The effect of neutral collision frequency is destabilizing in longitudinal mode. These results are helpful in understanding the structure formation in HI region.

42.1 Introduction

Astronomy and astrophysics are a vast, fascinating and evergreen field of research. In this direction, the process of birth of stars and formation of small and big structures in interstellar medium is an immense field of research, and the problem of the thermal instability of interstellar matter is of significant consequence in connection with proto-star and star formation in magnetic dust clouds. A detailed learning of thermal instability is given by Field [1], he explored the consequence of thermal instability in the configuration of solar prominences, condensation in planetary nebula and

S. Kaothekar (✉)
Department of Physics, Mahakal Institute of Technology & Management, Ujjain, M.P 456664, India

S. Sengupta et al. (eds.), *Selected Progresses in Modern Physics*, Springer Proceedings in Physics 265, https://doi.org/10.1007/978-981-16-5141-0_42

condensation of galaxies from the intergalactic medium. Hunter [2] has investigated the function of thermal instability in star configuration. Aggarwal and Talwar [3] have explored magnetothermal instability in a rotating gravitating fluid captivating radiative heat-loss function. Bora and Talwar [4] have investigated the magnetothermal instability with generalized Ohms law captivating the consequences of electrical resistivity, Hall current, electron inertia, thermal conductivity and radiative heat-loss function. Bode et al. [5] have explored magnetohydrodynamic thermal instability in cool inhomogeneous atmosphere. Ibanez [6] has investigated the sound and thermal waves in a fluid with an arbitrary heat-loss function. Burkert and Lin [7] have carried out the significance of thermal instability in the configuration of clumpy gas clouds, and they represented that the thermal instability can lead to the breakup of large clouds into cold dens clumps. Kim and Narayan [8] have explored the difficulty of thermal instability in clusters of galaxies with conduction taking the effects of radiative heat-loss function. Nejad-Asghar and Ghanbari [9] have studied the configuration of small-scale condensation in molecular clouds via thermal instability. Prajapati et al. [10] have investigated the self-gravitational instability of rotating viscous Hall plasma with arbitrary radiative heat-loss function and electron inertia. Kaothekar et al. [11] have explored the consequence of neutral collisions and radiative heat-loss functions on self-gravitational instability of viscous thermally conducting partially ionized plasma. Kaothekar [12] has investigated the difficulty of thermal instability of radiative plasma with finite electron inertia and finite Larmor radius corrections for structure formation. Jain et al. [13] have explored the consequence of FLR corrections on thermal instability of thermally conducting viscous plasma with Hall current and electron inertia. Kaothekar [14] has investigated the difficulty of star configuration via thermal instability of radiative thermally conducting viscous plasma with FLR corrections in ISM. Kaothekar et al. [15] have explored the Jeans instability of partially ionized self-gravitating viscous plasma with Hall effect FLR corrections and porosity. Kaothekar [16] has examined the difficulty of molecular cloud formation via thermal instability of finite resistive viscous radiating plasma with finite Larmor radius corrections. Golovnev et al. [17] have explored the difficulty of thermal instability in nano systems: molecular dynamic modelling. Recently, Sormani and Sobacchi [18] have studied the impact of rotation on the thermal instability of the stratified galactic atmospheres-II, the formation of high velocity clouds. More recently, Kempski and Quataert [19] have investigated the problem of thermal instability of halo gas heated by streaming cosmic rays. From the above discussed investigations, it is concluded that the thermal instability is important for the formation of astrophysical objects.

All the on top of studies in magneto-hydrodynamics are connected to the condition of fully ionized plasma. Pretty frequently, the plasma is not fully ionized and, in its place of it, plasma could be infused with neutral atoms. There are few areas of low temperature in the universe where a partially ionized plasma medium with neutral gas survives. Cases of such areas are chromospheres and photospheres of stars and HII regions of cool interstellar clouds. As a sensibly simple approximation for the interstellar gas, it may idealize it as a composite mixture of the hydromagnetic (ionized) component and neutral component, and due to this reason, two-component theory

is discussed. Thus, the two-component, i.e. hydromagnetic (ionized) and neutral, interacts with each other through mutual collisions. The magnetic field interacts only with the charged particles in the interstellar gas. The collisions (frictional) of plasma with neutral gas in the clouds are responsible for coupling of magnetic field to interstellar plasma clouds. In this direction, Mathis [20] has explored the problem of thermal instability in ionized gaseous plasma. Sharma and Sharma [21] have discussed the thermal instability of a partially ionized plasma. Sharma and Misra [22] have investigated the problem of thermal instability of a compressible and partially ionized plasma. Vandkurov [23] has explored thermal instability in two-component magnetized plasma. Sharma et al. [24] have examined the problem of Hall effect on thermal instability of rivlinericksen fluid. Lodato and Clarke [25] have discussed problem of massive planets in FU orionis discs: implications for thermal instability models. Fukue and Kamaya [26] have explored the problem of small structures via thermal instability of partially ionized plasma I condensation mode. Shadmehri et al. [27] have explored thermal instability in ionized plasma. Khesali [28] discussed the problem of thermal instability in a molecular cloud, including dust particles, Hall effect and ambipolar diffusion. Pensia et al. [29] have explored the problem of magnetothermal instability of rotating partially ionized Hall plasma flowing through porous medium. Recently, Kaothekar [30] has discussed thermal instability of partially ionized viscous plasma with Hall effect FLR corrections flowing through porous medium. More recently, Dudorov et al. [31] have explored the magnetic ionization thermal instability. Also in the above investigated problems of partially ionized plasma and two-component plasma Hall effect were not considered.

In totalling to this, the Hall current and electron inertia constraints are significant in the dynamics of interstellar matter, magnetic reconnection processes and in several other astrophysical situations. Tayler [32] has explored a simple hydromagnetic stability problem involving finite conductivity electron inertia and Hall effects. Kalra and Talwar [33] have studied magneto-gravitational instability of unbounded plasma with electron inertia and Hall effect. Sen and Chou [34] have explored the investigation of gravitational instability of plasma with Hall effect. Cothran et al. [35] have studied the role of the Hall term and electron inertia in the magnetic reconnection experiment of weakly collisional laboratory plasma. Shtemler et al. [36] have discussed the Hall instability of thin weakly ionized stratified Keplerian disc. Prajapati et al. [37] have explored the effects of Hall current, finite electron inertia and electrical conductivity on the self-gravitational instability of anisotropic pressure plasma using generalized polytrope laws. Shukla et al. [38] have studied the consequence of electron inertia on kinetic Alfven waves. Uberoi [39] has discussed the electron inertia consequences on the transverse gravitational instability incorporating the Hall current and rotation parameters. Kaothekar and Chhajlani [40] have explored the Jeans instability of self-gravitating partially ionized Hall plasma with radiative heat-loss functions and porosity. Kaothekar [41] has investigated the effect of Hall current and FLR corrections on thermal instability of radiative plasma for star formation in ISM. Recently, Sutar et al. [42] have explored the effect of electron inertia and electrical resistivity on Jeans instability of quantum plasma. More recently, Sutar et al. [43] have discussed the difficulty of involvement of the quantum

radiative effects on Jeans instability with electrical resistance and Hall current. Thus, it is clear that Hall current is the significant issue in conversation of self-gravitational instability and thermal instability.

From the on top of learning, it is clear that the Hall current radiative heat-loss function and neutral collision are the significant limitations to converse the thermal instability of plasma. Thus, in the nearby difficulty, we examine the consequences of neutral collisions, Hall current and radiative heat-loss function on the thermal instability of partially ionized, finitely conducting, viscous magnetized two-component plasma with the neutral pressure gradient and neutral viscosity. The on top of results are pertinent to dens molecular interstellar clouds and cometary plasma which includes a major fraction of neutral atoms.

42.2 Linearized Perturbation Equations and Dispersion Relation

Let us assume an infinite, homogeneous, viscous, thermally conducting and radiating composite fluid consisting of a finitely conducting ionized component of density ρ and neutral component of densityρ_n. The uniform magnetic field $\boldsymbol{B}(0, 0, B)$ work together only with conducting component and it gets combined with the bulk of the neutral gas through collisions of the two-components. The individual components by themselves, behave like continuum fluids. Assume the initial velocities of both the components zero. Let the pressure gradient of both the components be comparable. If $\delta p,\ \delta\rho,\ \boldsymbol{u}(u_x, u_y, u_z),\ b(b_x, b_y, b_z),\ \delta T,\ L$ are the respective perturbations in pressure, density, velocity, magnetic field, temperature and heat-loss function and let subscript n refer to neutral component of the gas, respectively, the linearized perturbation equations of the system are

$$\partial_t \boldsymbol{u} = -\frac{1}{\rho}\nabla\delta p + \frac{1}{4\pi\rho}(\nabla \times \boldsymbol{b}) \times \boldsymbol{B} + \upsilon_c(\boldsymbol{u}_n - \boldsymbol{u}) + \upsilon\nabla^2\boldsymbol{u}\,, \tag{42.1}$$

$$\partial_t \delta\rho = -\rho\,\nabla.u, \tag{42.2}$$

$$\frac{1}{\gamma-1}\,\partial_t\delta p - \left(\frac{\gamma}{\gamma-1}\right)\frac{p}{\rho}\partial_t\delta\rho + \rho\big[L_\rho\delta\rho + L_T\delta T\big] - \lambda\,\nabla^2\delta T = 0, \tag{42.3}$$

$$\frac{\delta p}{p} = \frac{\delta T}{T} + \frac{\delta\rho}{\rho}, \tag{42.4}$$

$$\partial_t b = \nabla \times (u \times B) + \eta\nabla^2 b - \frac{c}{4\pi Ne}[\nabla \times \{(\nabla \times b) \times B\}]\,, \tag{42.5}$$

$$\nabla.\,\boldsymbol{b} \;=\; 0, \tag{42.6}$$

$$\partial_t u_n = -\frac{1}{\rho_n}\nabla\delta p_n + \upsilon_n \nabla^2 u_n - \frac{\rho}{\rho_n}\upsilon_c(u_n - u), \tag{42.7}$$

$$\partial_t \delta\rho_n \;=\; -\rho_n \nabla . \boldsymbol{u}_n \tag{42.8}$$

$$\delta \mathrm{p}_n = \delta\rho_n c_n^2, \tag{42.9}$$

Where ρ, υ, η, υ_c, c, T, λ, γ, L_T, L_ρ, N, e are the density, kinematic viscosity, electrical resistivity, ion-neutral collision frequency, speed of the pressure perturbations, temperature, thermal conductivity, ratio of two specific heats, temperature dependent heat-loss function, density dependent heat-loss function, number density and charge of electron, respectively.

The variant in perturbation is taken as

$$\exp i(k_x x + k_z z + \sigma t), \tag{42.10}$$

Where σ is the frequency of harmonic disturbance and k_x, k_z are the components of the wave vector $\boldsymbol{k}$, in x, z directions so that

$$k^2 = k_x^2 + k_z^2, \tag{42.11}$$

Initiating the displacement vectors $\boldsymbol{\xi} = (\xi_x, \xi_y, \xi_z)$ and $\boldsymbol{\xi}_n = (\xi_{nx}, \xi_{ny}, \xi_{nz})$ such that

$$\boldsymbol{u} = \partial_t \xi, \quad \boldsymbol{u}_\mathrm{n} = \partial_t \boldsymbol{\xi}_n, \tag{42.12}$$

The components of Eq. (42.5) may be given as.

$$\begin{aligned} b_x &= \frac{iB}{d}k_z u_x - \frac{\Omega}{d}k_z^2 b_y, b_y = \frac{iB}{d}k_z u_y + \frac{\Omega}{d}(k_z^2 b_x - k_x k_z b_z), \\ b_z &= -\frac{iB}{d}k_x u_x + \frac{\Omega}{d}k_x k_z b_y, \end{aligned} \tag{42.13}$$

where $d = \eta k^2$, and $\Omega = \frac{cB}{4\pi Ne}$

Using Eqs. 42.2, 42.3, 42.4 and 42.13 for plasma components and Eqs. 42.7 and 42.8 for the neutral components along with Eqs. 42.9, 42.10, 42.11, 42.12, it may be written in the following algebraic equations for the amplitude components of Eqs. 42.1 and 42.7 as

$$\xi_x\left[\omega^2+\omega\left((1+\beta)\frac{V^2k^2d}{\left(d^2+\Omega^2k^2k_z^2\right)}+\Omega_i+\upsilon_c\right)+\frac{k_x^2}{k^2}\Omega_T^2\right]$$
$$-\xi_y\left[\frac{\omega V^2k^2(1+\beta)k_x^2\Omega}{\left(d^2+\Omega^2k^2k_z^2\right)}\right]-\xi_{nx}[\omega\upsilon_c]+\frac{k_xk_z}{k^2}\left[\Omega_T^2\xi_z\right]=0, \tag{42.14}$$

$$\xi_y\left[\omega^2+\omega\left((1+\beta)\frac{V^2dk_z^2}{\left(d^2+\Omega^2k^2k_z^2\right)}+\Omega_i+\upsilon_c\right)\right]$$
$$+\xi_x\left[\frac{\omega V^2k^2(1+\beta)k_z^2\Omega}{\left(d^2+\Omega^2k^2k_z^2\right)}\right]-\omega\upsilon_c\xi_{ny}=0, \tag{42.15}$$

$$\xi_z\left[\omega^2+\omega(\Omega_i+\upsilon_c)+\frac{k_z^2}{k^2}\Omega_T^2\right]-\xi_{nz}[\omega\upsilon_c]+\frac{k_xk_z}{k^2}\left[\Omega_T^2\xi_x\right]=0, \tag{42.16}$$

$$\xi_{nx}\left[\omega^2+\omega\left(\Omega_n+\frac{\upsilon_c}{\beta}\right)+\frac{k_x^2}{k^2}J_n^2\right]-\xi_x\left[\omega\frac{\upsilon_c}{\beta}\right]+\frac{k_xk_z}{k^2}\left[\xi_{nz}J_n^2\right]=0, \tag{42.17}$$

$$\xi_{ny}\left[\omega^2+\omega\left(\Omega_n+\frac{\upsilon_c}{\beta}\xi_y\right)\right]-\omega\frac{\upsilon_c}{\beta}\xi_y=0. \tag{42.18}$$

$$\xi_{nz}\left[\omega^2+\omega\left(\Omega_n+\frac{\upsilon_c}{\beta}\right)+\frac{k_z^2}{k^2}J_n^2\right]-\xi_z\left[\omega\frac{\upsilon_c}{\beta}\right]+\frac{k_xk_z}{k^2}\left[\xi_{nx}J_n^2\right]=0. \tag{42.19}$$

We have made the following substitutions:

$$V^2=\frac{B^2}{4\pi\rho_0},\quad \rho_0=\rho+\rho_n,\quad J^2=c^2k^2,\quad J_n^2=c_n^2k^2,$$
$$\Omega_T^2=\frac{\Omega_I^2+\omega J^2}{B_1+\omega},\quad \beta=\frac{\rho_n}{\rho},\quad \Omega_n=\upsilon_nk^2,\quad \Omega_i=\upsilon_ik^2,\quad \Omega_I^2=k^2A,$$
$$A=(\gamma-1)\left(TL_T-\rho L_\rho+\frac{\lambda k^2T}{\rho}\right),\quad B_1=(\gamma-1)\left(\frac{T\rho L_T}{p}+\frac{\lambda k^2T}{p}\right). \tag{42.20}$$

42.3 Dispersion Relation

The dispersion relation is obtained from the above six Eqs. (42.14, 42.15, 42.16, 42.17, 42.18, 42.19) for longitudinal direction to the magnetic field and conversed separately.

For wave propagation parallel to the magnetic field $\boldsymbol{k}$ $(0, 0, k)$, Eqs. (42.14, 42.15, 42.16, 42.17, 42.18, 42.19) have non-trivial solutions if the determinant of the

equations disappears.

$$\begin{bmatrix} I & -N & 0 & -\omega\upsilon_c & 0 & 0 \\ N & I & 0 & 0 & -\omega\upsilon_c & 0 \\ 0 & 0 & R & 0 & 0 & -D \\ -\omega\upsilon_c/\beta & 0 & 0 & Q & 0 & 0 \\ 0 & -\omega\upsilon_c/\beta & 0 & 0 & Q & 0 \\ 0 & 0 & -E & 0 & 0 & S \end{bmatrix} \begin{bmatrix} \xi_x \\ \xi_y \\ \xi_z \\ \xi_{nx} \\ \xi_{ny} \\ \xi_{nz} \end{bmatrix} = 0, \tag{42.21}$$

We have made the following assumptions:

$$I = M + \frac{\omega(1+\beta)V^2k^2d}{(d^2+\Omega^2k^4)}, \quad M = \omega^2 + \omega(\Omega_i + \upsilon_c), \quad Q = \omega^2 + \omega\left(\Omega_n + \frac{\upsilon_c}{\beta}\right),$$
$$R = \omega^2 + \omega(\Omega_i + \upsilon_c) + \Omega_T^2, \quad S = \omega^2 + \omega\left(\Omega_n + \frac{\upsilon_c}{\beta}\right) + J_n^2, \quad D = (\omega\upsilon_c),$$
$$E = \left(\omega\frac{\upsilon_c}{\beta}\right), \; F = R + \omega(1+\beta)\frac{V^2k^2}{d}, \quad N = \frac{\omega(1+\beta)\Omega V^2k^4}{(d^2+\Omega^2k^4)}. \tag{42.22}$$

The dispersion relation for longitudinal wave propagation from the determinant of matrix of Eq. (42.21) is given as

$$(RS - DE)\left[\left(IQ - \frac{\omega^2\upsilon_c^2}{\beta}\right)^2 + N^2Q^2\right] = 0, \tag{42.23}$$

The dispersion relation has two independent factors which may be independently discussed.

42.4 Discussion

42.4.1 Longitudinal Propagation

On equating the first term of Eq. (42.23) to zero, i.e. $(RS - DE) = 0$, on solving we get

$$\omega^5+\left\{\upsilon_c\left(1+\frac{1}{\beta}\right)+\upsilon_i k^2+\upsilon_n k^2+(\gamma-1)\left(\frac{T\rho L_T}{p}+\frac{\lambda k^2 T}{p}\right)\right\}\omega^4+\{(\gamma-1)$$
$$\times\left(\frac{T\rho L_T}{p}+\frac{\lambda k^2 T}{p}\right)\left[\upsilon_c\left(1+\frac{1}{\beta}\right)+\upsilon_i k^2\right]+\upsilon_i k^2\left[\upsilon_n k^2+\frac{\upsilon_c}{\beta}\right]+\upsilon_n k^2[(\gamma-1)$$
$$\times\left(\frac{T\rho L_T}{p}+\frac{\lambda k^2 T}{p}\right)+\upsilon_c\Bigg]+c^2k^2+c_n^2k^2\Bigg\}\omega^3+\left\{\upsilon_n k^2\left[(\gamma-1)\left(\frac{T\rho L_T}{p}+\frac{\lambda k^2 T}{p}\right)\upsilon_c\right.\right.$$
$$+(\gamma-1)\left(\frac{T\rho L_T}{p}+\frac{\lambda k^2 T}{p}\right)\upsilon_i k^2+c^2k^2\Bigg]+\upsilon_i k^2\left[(\gamma-1)\left(\frac{T\rho L_T}{p}+\frac{\lambda k^2 T}{p}\right)\frac{\upsilon_c}{\beta}+c_n^2k^2\right]$$
$$+\left(c^2k^2\right)\frac{\upsilon_c}{\beta}+k^2(\gamma-1)\left(TL_T-\rho L_\rho+\frac{\lambda k^2 T}{\rho}\right)+\left(c_n^2k^2\right)\left[(\gamma-1)\left(\frac{T\rho L_T}{p}+\frac{\lambda k^2 T}{p}\right)+\upsilon_c\right]\Bigg\}\omega^2$$
$$+\left\{\left(c_n^2k^2\right)\left[c^2k^2+(\gamma-1)\left(\frac{T\rho L_T}{p}+\frac{\lambda k^2 T}{p}\right)\upsilon_i k^2\right]+\upsilon_c(\gamma-1)\left(\frac{T\rho L_T}{p}+\frac{\lambda k^2 T}{p}\right)\right.$$
$$\times\left[c_n^2k^2\right]+\left[k^2(\gamma-1)\left(TL_T-\rho L_\rho+\frac{\lambda k^2 T}{\rho}\right)\right]\left[\upsilon_n k^2+\frac{\upsilon_c}{\beta}\right]\Bigg\}\omega$$
$$+k^2\left\{k^2(\gamma-1)\left(TL_T-\rho L_\rho+\frac{\lambda k^2 T}{\rho}\right)c_n^2\right\}=0. \tag{42.24}$$

The above (42.24) explains the dispersion relation for viscous two-component plasma having neutral collisions with thermal and radiative consequences. There is no consequence of magnetic field, Hall current and finite electrical conductivity of plasma in this case. The dispersion relation (42.24) may be confirmed with the previous known outcomes. In the absence of neutral particles (i.e.$\beta = 1,\ \upsilon_c = 0$), dispersion relation (42.24) reduces to the one obtained by Prajapati et al. [10] for non-gravitating medium. The condition of instability from constant term of (42.24) is given as

$$\left\{k^2\left(TL_T-\rho L_\rho+\frac{\lambda k^2 T}{\rho}\right)c_n^2\right\}<0, \tag{42.25}$$

The condition of instability (42.25) for thermal instability is in dependent of magnetic field strength, Hall current, finite electrical resistivity, density of neutral component of plasma and the condition is same as that obtained earlier by Field [1]. In the solar corona and the other astrophysical structures, the heat-loss function is the basic destabilizing mechanism forcing thermal instability that depends on temperature and density. These heat-loss functions decrease with temperature and increase with density, i.e. $L_T < 0$ and $L_\rho > 0$. In these types of conditions, a small temperature perturbation tends to raise naturally. In the case when we decrease the temperature, then, cooling increases due to the higher radiative losses. In the solar corona, as the local temperature decreases, the local pressure decreases, leading to the condensation of the cool plasma which radiates even faster because of an increase in density Bora and Talwar [4].

For pure plasma component, Eq. (42.24) reduces to

$$\omega^3 + \left[\upsilon_i k^2 + (\gamma - 1)\left(\frac{T\rho L_T}{p} + \frac{\lambda k^2 T}{p}\right)\right]\omega^2 + \left[\upsilon_i k^2(\gamma - 1)\left(\frac{T\rho L_T}{p} + \frac{\lambda k^2 T}{p}\right) + c^2 k^2\right]\omega + \left[k^2(\gamma - 1)\left(TL_T - \rho L_\rho + \frac{\lambda k^2 T}{\rho}\right)\right] = 0, \tag{42.26}$$

The condition of instability from constant term of Eq. (42.26) is given as

$$\left[k^2(\gamma - 1)\left(TL_T - \rho L_p + \frac{\lambda k^2 T}{\rho}\right)\right] < 0. \tag{42.27}$$

The above inequality is same as obtained by Bora and Talwar [4].

For non-viscous and collision-less (i.e. $\upsilon = \upsilon_n = \upsilon_c = 0$) two-component plasma, Eq. (42.24) gives the dispersion relation

$$\omega^5 + (\gamma - 1)\left(\frac{T\rho L_T}{p} + \frac{\lambda k^2 T}{p}\right)\omega^4 + \left\{k^2\left(c^2 + c_n^2\right)\right\}\omega^3 + \left\{k^2\left[(\gamma - 1)\left(TL_T - \rho L_\rho + \frac{\lambda k^2 T}{\rho}\right) + (\gamma - 1)\left(\frac{T\rho L_T}{p} + \frac{\lambda k^2 T}{p}\right)c_n^2\right]\right\}\omega^2 + \left\{k^2\left[k^2 c^2 c_n^2\right]\right\}\omega + k^2\left\{k^2(\gamma - 1)\left(TL_T - \rho L_\rho + \frac{\lambda k^2 T}{\rho}\right)c_n^2\right\} = 0. \tag{42.28}$$

The condition of instability gained from stable term of above Eq. (42.28) is similar as Eq. (42.25); hence viscosity and collisions of the two-components do not affect the condition of instability. However, they cause damping effect.

Now Eq. (42.24) can be written in the following form:

$$\omega^5+c_s\left\{\frac{\upsilon_c}{c_s}\left(1+\frac{1}{\beta}\right)+\frac{\upsilon_i}{c_s}k^2+\frac{\upsilon_n}{c_s}k^2+k_T+\frac{k^2}{k_\lambda}\right\}\omega^4$$
$$+c_s^2\left\{\left(k_T+\frac{k^2}{k_\lambda}\right)\left[\frac{\upsilon_c}{c_s}\left(1+\frac{1}{\beta}\right)+\frac{\upsilon_i}{c_s}k^2\right]\right.$$
$$\left.+\frac{\upsilon_i}{c_s}k^2\left[\frac{\upsilon_n}{c_s}k^2+\frac{\upsilon_c}{\beta\, c_s}\right]+\frac{\upsilon_n}{c_s}k^2\left(k_T+\frac{k^2}{k_\lambda}+\frac{\upsilon_c}{c_s}\right)+k^2\right\}\omega^3+c_s^3\left\{\frac{\upsilon_n}{c_s}k^2\left[\left(k_T+\frac{k^2}{k_\lambda}\right)\frac{\upsilon_c}{c_s}\right.\right.$$
$$\left.+\left(k_T+\frac{k^2}{k_\lambda}\right)\frac{\upsilon_i}{c_s}k^2+k^2\right]+\frac{\upsilon_i}{c_s}k^2\left[\left(k_T+\frac{k^2}{k_\lambda}\right)\frac{\upsilon_c}{\beta\, c_s}+k^2\right]+k^2\frac{\upsilon_c}{\beta\, c_s}+\frac{k^2}{\gamma}\left[k_T-k_\rho+\frac{k^2}{k_\lambda}\right]$$
$$\left.+k^2\left(k_T+\frac{k^2}{k_\lambda}\right)+\frac{\upsilon_c}{c_s}\right\}\omega^2$$
$$+c_s^4\left\{\left[k^2\left(k_T+\frac{k^2}{k_\lambda}\right)\frac{\upsilon_i}{c_s}k^2\right]+\frac{\upsilon_c}{c_s}k^2+\frac{k^2}{\gamma}\left[k_T-k_\rho+\frac{k^2}{k_\lambda}\right]\left[\frac{\upsilon_n}{c_s}k^2\frac{\upsilon_c}{\beta c_s}\right]\right\}\omega$$
$$+\frac{c_s^5k^4}{\gamma}\left[k_T-k_\rho+\frac{k^2}{k_\lambda}\right]=0. \tag{42.29}$$

We have used

$$k_\rho=\frac{(\gamma-1)\rho L_\rho}{Rc_sT},\quad k_T=\frac{(\gamma-1)L_T}{Rc_s},\quad k_\lambda=\frac{Rc_s\rho}{(\gamma-1)\lambda}, \tag{42.30}$$

To carry out the effect of viscosity, neutral collision frequency and radiative heat-loss functions on the growth rate of thermal instability, we solve Eq. (42.29) numerically. Therefore Eq. (42.29) can be represented in non-dimensional form with the help of following dimension-less quantities as given in Field [1]:

$$\omega^*=\frac{\omega}{k_\rho c_s},\quad \upsilon_i^*=\frac{\upsilon_i k_\rho}{c_s}k^2,\quad \upsilon_n^*=\frac{\upsilon_n k_\rho}{c_s}k^2,\quad \upsilon_c^*=\frac{\upsilon_c k_\rho}{c_s}\left(1+\frac{1}{\beta}\right),$$
$$k^*=\frac{k}{k_\rho},\quad k_\lambda^*=\frac{k_\rho}{k_\lambda},\quad k_T^*=\frac{k_T}{k_\rho}, \tag{42.31}$$

Using Eq. (42.31), we write Eq. (42.29) in non-dimensional form as

$$\omega^{*5} + \left\{\upsilon_c^* + \upsilon_i^* + \upsilon_n^* + k_T^* + k_\lambda^* k^{*2}\right\}\omega^{*4} + \left\{\left(k_T^* + k_\lambda^* k^{*2}\right)\left[\upsilon_c^* + \upsilon_i^*\right] + \upsilon_i^*\left(\upsilon_n^* + \upsilon_c^*\right) + \upsilon_n^*\left[k_T^* + k_\lambda^* k^{*2} + \upsilon_c^*\right] + k^{*2} + k^{*2}\right\}\omega^{*3} + \upsilon_n^* \times\left[\left(k_T^* + k_\lambda^* k^{*2}\right)\upsilon_c^* + \left(k_T^* + k_\lambda^* k^{*2}\right)\upsilon_i^* + k^{*2}\right] + k^{*2}\upsilon_c^* + \frac{k^{*2}}{\gamma} \times\left[k_T^* - 1 + k_\lambda^* k^{*2}\right] + k^{*2}\left(k_T^* + k_\lambda^* k^{*2} + \upsilon_c^*\right)\Big\}\omega^{*2} + \Big\{k^{*2}\left[k^{*2}\left(k_T^* + k_\lambda^* k^{*2}\right)\upsilon_i^*\right] + \upsilon_c^* k^{*2}\left[\frac{k^{*2}}{\gamma}\left(k_T^* - 1 + k_\lambda^* k^{*2}\right)\right]\left(\upsilon_n^* + \upsilon_c^*\right)\Big\}\omega^* + k^{*2}\left[\frac{k^{*2}}{\gamma}\left(k_T^* - 1 + k_\lambda^* k^{*2}\right)\right] = 0. \tag{42.32}$$

The numerical consequences of Eq. (42.32) have been represented in Figs. 42.1, 42.2, 42.3. In these figures, we have represented the dimensional-less growth rate (ω^*) against the dimensional-less wave number (k^*) for various values of density dependent heat-loss function, thermal conductivity, viscosity of both ionized component and neutral component of plasma.

Numerical calculations were performed to determine the roots of ω^* from dispersion relation (42.32), as a function of wave number k^* for several values of the different parameters involved, taking $\gamma = 5/3$. Out of the five modes, only one mode is unstable for which the calculations are presented in Figs. 42.1, 42.2, 42.3, where the growth rate is plotted against the wave number to show the dependence of the growth rate on the different physical parameters.

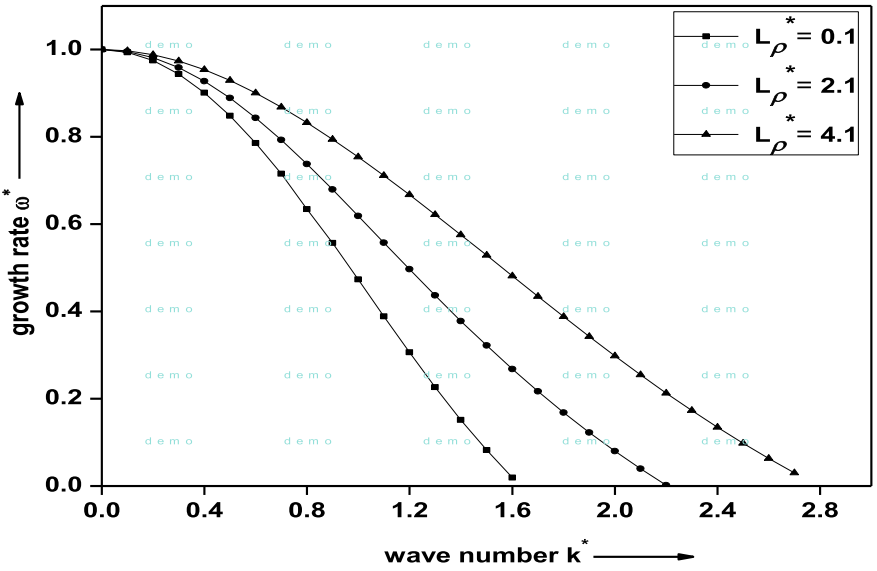

Fig. 42.1 Growth rate ω^* against wave number k^* for three values of parameter L_ρ^* keeping the other parameters fixed. $\left(C_0^{*2} = 1, \beta = 1, L_T^* = 1, \lambda^* = 1, \upsilon_i^* = 1, \upsilon_n^* = 1, \upsilon_c^* = 1, K_1^* = 1\right)$

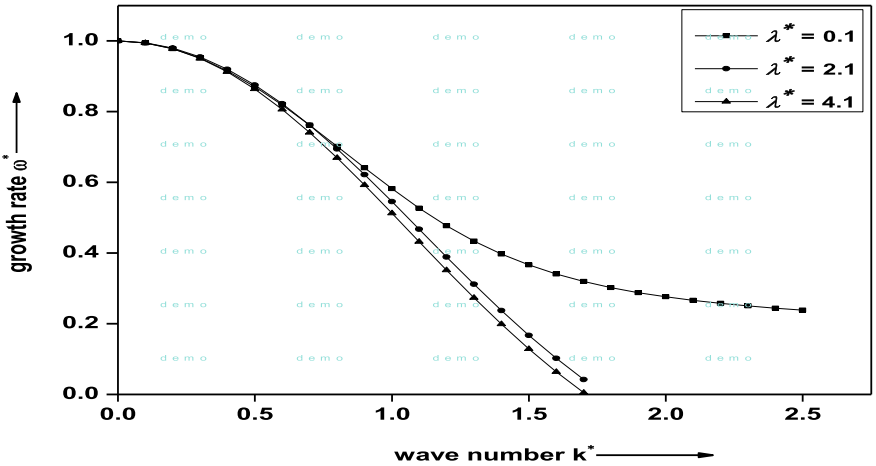

Fig. 42.2 Growth rate ω^* against wave number k^* for three values of parameter λ^* keeping the other parameters fixed. $\left(C_0^{*2}=1, \beta=1, L_\rho^*=1, \upsilon_c^*=1, \upsilon_i^*=1, \upsilon_n^*=1, L_T^*=1, K_1^*=1\right)$

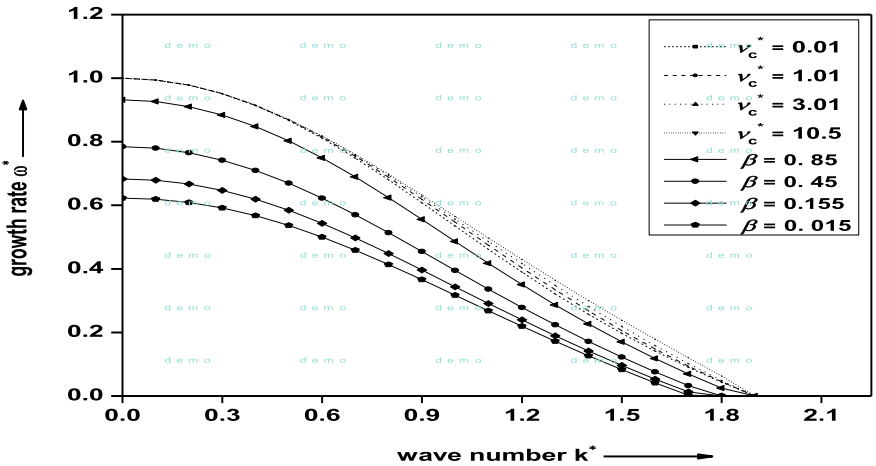

Fig. 42.3 Growth rate ω^* against wave number k^* for several values of parameters β and υ_c^* keeping the other parameters fixed. $\left(C_0^{*2}=1, \upsilon_n^*=1, L_\rho^*=1, \upsilon_i^*=1, L_T^*=1, \lambda^*=1, K_1^*=1\right)$

$$\beta = 1: \ (1)\ \upsilon_c^* = 0.0, \quad (2)\ \upsilon_c^* = 1.0, \quad (3)\ \upsilon_c^* = 3.0, \quad (4)\ \upsilon_c^* = 10.0,$$

$$\upsilon_c^* = 0: \ (5)\beta = 0.8, \quad (6)\ \beta = 0.4, \quad (7)\ \beta = 0.15, \quad (8)\beta = 0.01.$$

$$\upsilon_n^* = 0: \ (1)\upsilon_i^* = 0.0, \quad (2)\ \upsilon_i^* = 1.0, \quad (3)\ \upsilon_i^* = 4.0, \quad (4)\upsilon_i^* = 7.0,$$

$$\upsilon_i^* = \upsilon_n^* : \ (5)\, \upsilon_i^* = \upsilon_n^* = 1.0, \ \ (6)\, \upsilon_i^* = \upsilon_n^* = 2.0, \ \ (7)\, \upsilon_i^* = \upsilon_n^* = 4.0.$$

It is clear from Fig. 42.1 that the growth rate increases with increasing density dependent heat-loss function. Thus, the consequence of density dependent heat-loss function is destabilizing, whereas from Fig. 42.2, we conclude that growth rate decreases with increasing thermal conductivity. Thus, the impact of thermal conductivity is stabilizing. Figure 42.3 represents that the growth rate increases with increasing collision frequency. Thus, the consequence of collision frequency is destabilizing, one can also monitor from Fig. 42.3 that the growth rate increases with increasing density ratio β. The critical wave number also increases with increasing density ratio β. From Fig. 42.3, it is clear that the growth rate decreases with increase in viscosity of the charged component of plasma. Thus, the consequence of viscosity of charged component of plasma is stabilizing. If the viscosity of neutral component of the plasma is also taken into consideration together with the viscosity of the charged component of plasma, the damping rate increases effectively.

Thus, on top of the conversation, it is finished that the consequences of thermal conductivity, and viscosity of the two-component of the plasma have a stabilizing influence, whereas the density dependent heat-loss function and the collision frequency have a destabilizing influence on the thermal instability of two-component plasma. Hall current does not affect the instability.

On equating second factor of Eq. (42.24) to zero, i.e.
$\left[\left(IQ - \omega^2 \upsilon_c^2/\beta\right)^2 + N^2 Q^2\right] = 0$, on solving we get

$$\omega^4\left[X^2 + Y^2\right] = 0, \tag{42.33}$$

where

$$X = \omega^4 + \left\{\left[\upsilon_c\left(1 + \frac{1}{\beta}\right) + \upsilon_i k^2 + \upsilon_n k^2\right] + 2\,\eta\, k^2\right\}\omega^3 + \left\{\eta\, k^2\left[2\upsilon_c\left(1 + \frac{1}{\beta}\right)\right.\right.$$
$$+2\left[\upsilon_i k^2 + \upsilon_n k^2\right] + \left[\upsilon_n k^2 \upsilon_c + \upsilon_i k^2 \frac{\upsilon_c}{\beta}\right]$$
$$+\upsilon_i \upsilon_n k^4 + \eta^2 k^4 + \Omega^2 k^4 + (1+\beta) V^2 k^2\Big\}\omega^2 + \eta k^2$$
$$\times\left[2\left(\upsilon_i \upsilon_n k^4 + \upsilon_n k^2 \upsilon_c + \upsilon_i k^2 \frac{\upsilon_c}{\beta}\right)\right] + \left\{\eta^2 k^4\left[\upsilon_c\left(1 + \frac{1}{\beta}\right) + \upsilon_i k^2 + \upsilon_n k^2\right]\right.$$
$$+(1+\beta) V^2 k^2\left[\eta k^2 + \upsilon_n k^2 + \frac{\upsilon_c}{\beta}\right] + \Omega^2 k^4\left[\upsilon_c\left(1 + \frac{1}{\beta}\right) + \upsilon_i k^2 + \upsilon_n k^2\right]\Big\}\omega$$
$$+\left\{(\eta^2 k^4 + \Omega^2 k^4)\left[\upsilon_i \upsilon_n k^4 + \upsilon_n k^2 \upsilon_c + \upsilon_i k^2 \frac{\upsilon_c}{\beta}\right] + (1+\beta) V^2 k^2 \eta k^2\left[\frac{\upsilon_c}{\beta} + \upsilon_n k^2\right]\right\},$$
$$Y = \ (1+\beta)\,\Omega\, V^2 k^4\left[\omega + \upsilon_n k^2 + \frac{\upsilon_c}{\beta}\right].$$

The above Eq. (42.33) represents the dispersion relation for finitely conducting two-component viscous plasma including the effects of Hall current, magnetic field and neutral collisions. The Hall term included in both X and Y shows effect on the neutral component on plasma.

In the absence of viscosity, collision frequency, finite electrical resistivity and Hall current, Eq. (42.33) becomes

$$\omega^4 + 2\omega^2(1+\beta)V^2k^2 + (1+\beta)^2V^4k^4 = 0. \tag{42.34}$$

The roots of this equation are

$$\omega_{1,2}^2 = -(1+\beta)V^2k^2. \tag{42.35}$$

The above mode is Alfven mode modified due to density ratio of the two-components. This mode exists because of density ratio of the two-components and magnetic field. In absence of magnetic field or any one of the two-components, the above mode vanishes. Here, damping rate depends on the density ratio of the two-components and magnetic field.

If $\rho >> \rho_n$ then $\beta << 1$, so from Eq. (42.35), we get

$$\omega^2 + V^2k^2 = 0. \tag{42.36}$$

The above equation shows the stable Alfven mode in its simplest form.

42.5 Conclusion

Thus in the in attendance paper, the effects of collision frequency, Hall current, radiative heat-loss function, thermal conductivity, finite electrical resistivity and viscosity on the thermal instability of two-component plasma has been investigated. For the longitudinal wave propagation, stable modes are obtained. The instability conditions are obtained on the basis of thermal instability criterion. The value of the thermal instability is depending on radiative heat-loss functions, thermal conductivity and also depending on the ratio of sonic speeds, density of the two-components in some particular cases.

In the case of longitudinal wave propagation, we get two separate modes, one is the thermal mode having the effects of radiative heat-loss function, thermal conductivity, viscosity of ionized and neutral components, neutral collision frequency and ratio of neutral density to ion density. It is concluded that the condition of instability is unaffected by the presence of Hall current, finite electrical resistivity and viscosity. Another is a non-thermal Alfven mode modified by the presence of Hall current, viscosity of ionized and neutral components, finite electrical resistivity, neutral collision frequency and ratio of neutral density to ion density. From the curves, it is clear

that the density dependent heat-loss function and thermal conductivity shows mutually reverse effects on the growth rate of the instability. In other words, the density dependent heat-loss function has a destabilizing influence, while the thermal conductivity has a stabilizing role on the growth rate of the system. The collision frequency has a destabilizing influence on the growth rate of the instability. Also it is clear from the curves that the growth rate increases with increasing density ratio (β), this means that system becomes more and more unstable for higher values of the neutral density. The viscosity of ionized component of plasma has a stabilizing influence on the growth rate of the system. It is interesting to see that the damping rate increases effectively when we consider the viscosity of ionized component together with the viscosity of neutral component of plasma.

References

1. G.B. Field, Astrophys. J. **142**, 531–567 (1965)
2. J.H. Hunter, Mon. Not. R. Astron. Soc. **133**, 239–245 (1966)
3. M. Aggarwal, S. Talwar, P. Mon. Not. R. Astron. Soc. **146**, 235–242 (1969)
4. M.P. Bora, S.P. Talwar, Phys. Fluids B **5**(3), 950 (1993)
5. G. Bode, A. Ferrari, S. Massaglia, R. Rosner, G.S. Vaiana, Astrophys. J. **291**, 798–805 (1985)
6. M.H.S. Ibanez, Astrophys. J. **290**, 33–46 (1985)
7. A. Burkert, D.N.C. Lin, Astrophys. J. **537**, 270–282 (2000)
8. W. Kim, R. Narayan, Astrophys. J. **596**, 889–902 (2003)
9. M. Nejad-Asghar, J. Ghanbari, Mon. Not. Royal Astron. Soc. **345**, 1323–1328 (2003)
10. R.P. Prajapati, R.K. Pensia, S. Kaothekar, R.K. Chhajlani, Astrophys. Space Sci. **327**, 139–154 (2010)
11. S. Kaothekar, G.D. Soni, and R.K. Chhajlani, AIP Adv. **2**(042191), (1–18) (2012)
12. S. Kaothekar, J. Astrophys. Astron. **37**(23), (1–23) (2016)
13. S. Jain, P. Sharma, S. Kaothekar, R.K. Chhajlani, Astrophys, J. **829**, 122–138 (2016)
14. S. Kaothekar, R.K. Chhajlani, AIP Conf. Proc. **1536**, 1288–1289 (2016)
15. S. Kaothekar, J. Astrophys. Astr. **37**(23), (1–23) (2016)
16. S. Kaothekar, G.D. Soni, R.P. Prajapati, R.K. Chhajlani, Astrophys. Space Sci. **361**, 204 (2016)
17. I.F. Golovnev, E. Gogovneva, V.M. Fomin, AIP Conf. Proc. **1939**, 020038 (2018)
18. M.C. Sormani, E. Sobacchi, Mon. Not. Royal Astron. Soc. **486**, 215–226 (2019)
19. P. Kempski, E. Quataert, Mon. Not. Royal Astron. Soc. **493**, 1801–1817 (2020)
20. J.S. Mathis, Astrophys. J. **153**, 65–70 (1968)
21. R.C. Sharma, K.C. Sharma, Aust. J. Phys. **31**, 81–187 (1978)
22. R.C. Sharma, J.N. Misra, Z. Naturforsch, **41 a**, 729–732 (1986)
23. Yu.V. Vandkurov, Sov. Astron. Lett. **17**, 433–436 (1989)
24. R.C. Sharma, S. Sunil and Chand, Indian J. Pure appl. Math. **31**, 49–59 (2000)
25. G. Lodato, C.J. Clarke, Mon. Not. Royal Astron. Soc. **353**, 841–850 (2004)
26. T. Fukue, H. Kamaya, Astrophys. J. **669**, 363–377 (2007)
27. M. Shadmehri, M. Nejad-Asghar, A. Khesali, Astrophys. Space Sci. **326**, 83–90 (2010)
28. A.R. Khesali, S.M. Ghoreyshi, M. Nejad-Asghar, Mon. Not. Royal Astron. Soc. **420**, 2300–2306 (2012)
29. R.K. Pensia, V. Shrivastava, A.K. Patidar, Phys. Sci. Int. J. **8**, 1–21 (2015)
30. S. Kaothekar, J. Porous Media **21**, 679–699 (2018)
31. A.E. Dudorov, C.E. Stepanov, S.O. Fomin, S.A. Khaibrakhmanov, Mon. Not. Royal Astron. Soc. **487**, 942–951 (2019)
32. R.J.J. Tayler, Nucl. Energy, Part C Plasma Phys. **5**, 345–353 (1963)

33. G.L. Kalra, S.P. Talwar, Annales d'Astrophysique **27**, 102–103 (1964)
34. A.K. Sen, C.K. Chou, Can. J. Phys. **46**, 2553–2556 (1968)
35. C.D. Cothran, M. Landreman, M.R. Brown, W. Matthaeus, H. Geophys. Res. Lett. **32**, L03105 (2005)
36. Y.M. Shtemler, M. Mond, E. Viverts, Astrophys. J. **665**, 1371–1380 (2007)
37. R.P. Prajapati, A.K. Parihar, and R.K. Chhajlani, Phys. Plasmas **15**, 012107 (2008)
38. N. Shukla, P. Varma, M.S. Tiwari, Ind. J. Pure and Appl. Phys. **47**, 350–355 (2009)
39. C.J. Uberoi, Plasma Fusion Res. Series **8**, 823–825 (2009)
40. S. Kaothekar, Astrophys. Space Sci. **362**, 107 (2017)
41. S. Kaothekar, Astrophys. Space Sci. **365**, 80 (2020)
42. D. Sutar, R.K. Pensia, S. Sharma, V. Kumar, A. Patidar, AIP Conf. Proc. **2100**(020013), 1–4 (2019)
43. D. Sutar, G. Ahmed, R.K. Pensia, Radiat. Eff. Defects Solids (2020). https://doi.org/10.1080/10420150.2020.1817022
44. Please remove the extra figure 42.4 as it appears two times.

Chapter 43
Transport Coefficients of Dense Stellar Plasma in Strong Magnetic Field

Soma Mandal

Abstract Following an exact relativistic formalism (Ghosh et al. in Ann Phys 312, 398 (2004) [1]), we study the transport properties of dense stellar electron-proton plasma in a strong quantizing magnetic field. The transport coefficients, namely the coefficients of shear and bulk viscosities as well as thermal and electrical conductivities are obtained from the relativistic version of Boltzmann kinetic equation by linearizing the distribution function and using relaxation time approximation. The dependence of the kinetic coefficients on the strength of the magnetic field is discussed. The variation of these coefficients with magnetic fields are found to be insensitive for the field strengths $\leq 10^{17}$G beyond which decreases with magnetic field. As a consequence, in presence of ultra-strong magnetic field, the electron-proton plasma behaves like a superfluid insulator. Since the electrical conductivity of the medium becomes extremely low (almost zero) in presence of ultra-strong magnetic field, the magnetic field at the core region must, therefore, decay very quickly. Hence, strong magnetic field can not exist at the core of magnetars.

43.1 Introduction

The study of the transport properties of hot and dense matter has sharply been increased in the context of heavy ion collision physics. Knowledge of various transport coefficients is also required in astrophysical problems such as for the description of various phenomena in supernova and neutron stars [2, 3]. It is, therefore, worthwhile that these transport coefficients be understood and derived rigorously within a microscopic theory.

There have been a lot of attempts to estimate the transport coefficients involving different approximation schemes, e.g., relaxation time approximation [4–6], Green-Kubo formalism [7], Chapman-Enskog formalism [8], weak coupling QCD [9] etc. Method for the calculation of transport coefficients were probed in description of

S. Mandal (✉)
Department of Physics, Government Girls' General Degree College, 7, Mayurbhanj Road, Kolkata 700023, India

S. Sengupta et al. (eds.), *Selected Progresses in Modern Physics*, Springer Proceedings in Physics 265, https://doi.org/10.1007/978-981-16-5141-0_43

non-relativistic classical gases [10], liquid and gases [11], relativistic gases [12], cold atomic gases [13], Fermi liquid [14].

The discovery of magnetars opened a new window in the study of the effect of a strong magnetic field on dense stellar plasma. The surface magnetic fields are observed to be $\sim 10^{15}$G. Then it is quite possible that the field strength at the core region may go up to 10^{18}G [15, 16]. If the magnetic fields are really so strong, in particular at the core region, they have an impact on most of the important physical properties and the physical processes of such stellar objects. The elementary processes, in particular, the weak and the electromagnetic processes taking place at the core region of a neutron star are strongly affected by such ultra-strong magnetic field. Further, the rates of the electromagnetic processes in presence of a strong quantizing magnetic field should modify significantly the transport properties of dense stellar matter, in particular for electron gas present at the core region of the neutron stars [17–19]. Since the cooling of neutron stars are mainly controlled by neutrino/anti-neutrino emissions, the strong magnetic field should affect the thermal history of strongly magnetized neutron stars [20, 21]. Further, the electrical conductivity of neutron star matter which directly controls the evolution of neutron star magnetic field will also change significantly.

Here we study the effect of strong quantizing magnetic field on the transport properties of dense stellar electron-proton plasma. We developed a relativistic formalism of Landau theory of Fermi liquid for dense neutron star matter in the presence of strong quantizing magnetic field with $\sigma - \omega$ meson exchange [1]. Following the formalism [1], which is to obtain two-body scattering matrix for a wide range of magnetic field strengths we compute the transport coefficients from the relativistic version of Boltzmann kinetic equation by linearizing the distribution function and using relaxation time approximation. We also obtain the relaxation time from the rates of standard electromagnetic processes taking place inside the electron-proton plasma and make necessary modification in the rate calculation due to the presence of strong quantizing magnetic field. The formalism we have developed to obtain rates of electromagnetic processes or the relaxation time is also applicable to evaluate neutrino emissivity and mean free path in presence of a strong quantizing magnetic field.

In this work, we have incorporated the quantum mechanical effect of a strong magnetic field on dense stellar plasma. In our formalism, therefore, the matter is treated as a dense Landau diamagnetic system, the transverse part of charged particle momentum gets quantized, which decreases in magnitude with the increase of magnetic field strength and in the extreme case, it vanishes. As a result, the system effectively becomes one-dimensional in nature in the momentum space, and from the symmetry of the problem all the kinetic coefficients should vanish. The system, therefore, behaves like a charge neutral superfluid.

In presence of strong quantizing magnetic field, the momentum space volume element becomes

$$\frac{d^3p}{(2\pi)^3} = \frac{dp_x dp_y dp_z}{(2\pi)^3} = \frac{eB_m}{4\pi^2}\sum_{\nu=0}^{\infty}(2-\delta_{\nu 0})dp_z \tag{43.1}$$

(we have assumed $\hbar = c = k_b = 1$) where we have chosen the gauge $A^\mu \equiv (0, 0, xB_m, 0)$, so that the constant magnetic field B_m is along the z-direction. We have considered the simplest possible picture of neutron star matter with $n - p - e$ out of thermodynamic equilibrium and the neutrinos are assumed to be non-degenerate. The baryonic components are interacting via $\sigma - \omega - \rho$ meson exchange type mean field and the electrons are assumed to be freely moving particles.

We shall first calculate the transport coefficients of electron gas. Then the transport coefficients for proton matter could be obtained just by replacing mass, chemical potential etc. of electrons by protons and taking into account the proper modification in presence of $\sigma - \omega - \rho$ meson exchange type mean field [22]. Spinor solutions for electrons in presence of strong quantizing magnetic fields are then given by

$$\Psi^{(\uparrow)(e)} = \frac{1}{\sqrt{L_y L_z}}\frac{\exp(-i\varepsilon_\nu^{(e)}t + ip_y y + ip_z z)}{[2\varepsilon_\nu^{(e)}(\varepsilon_\nu^{(e)} + m_e)]^{1/2}} \times \begin{pmatrix} (\varepsilon_\nu^{(e)} + m_e) I_{\nu;p_y}(x) \\ 0 \\ p_z I_{\nu;p_y}(x) \\ -i(2\nu e B_m)^{1/2} I_{\nu-1;p_y}(x) \end{pmatrix} \tag{43.2}$$

and

$$\Psi^{(\downarrow)(e)} = \frac{1}{\sqrt{L_y L_z}}\frac{\exp(-i\varepsilon_\nu^{(e)}t + ip_y y + ip_z z)}{[2\varepsilon_\nu^{(e)}(\varepsilon_\nu^{(e)} + m_e)]^{1/2}} \times \begin{pmatrix} 0 \\ (\varepsilon_\nu^{(e)} + m_e) I_{\nu-1;p_y}(x) \\ i(2\nu e B_m)^{1/2} I_{\nu;p_y}(x) \\ -p_z I_{\nu-1;p_y}(x) \end{pmatrix} \tag{43.3}$$

where $\uparrow$ and $\downarrow$ represent up and down spin states respectively,

$$I_{\nu;p_y}(x) = \left(\frac{eB_m}{\pi}\right)^{1/4} \frac{1}{\sqrt{\nu!}\,2^{\nu/2}} \times \exp\left[-\frac{1}{2}eB_m\left(x - \frac{p_y}{eB_m}\right)^2\right] H_\nu\left[\sqrt{eB_m}\left(x - \frac{p_y}{eB_m}\right)\right], \tag{43.4}$$

where H_ν is the νth order Hermite polynomial and

$$\varepsilon_\nu^e = \sqrt{(p_z^2 + m_e^2 + 2e\nu B_m)}$$

is the energy eigen value with $\nu = 0, 1, 2, \ldots$, the Landau quantum numbers. We consider the usual spinor solutions for neutron. We have not considered the negative energy spinor solutions, because the temperature of the system is much less than the electron chemical potential. We have studied the variation of transport coefficients in presence of strong quantizing magnetic field to overcome the problem on the mechanical stability and hence the existence of magnetars. We aimed to show whether the electrical conductivity which directly controls the evolution of neutron star magnetic field, becomes sufficiently small in presence of ultra-strong magnetic field.

Following de Groot [12], we have developed the relativistic version of the Boltzmann kinetic equation for fermions in presence of a strong quantizing magnetic field. We have obtained the expressions for transport coefficients. The effect of magnetic field on the transport coefficients has been studied and finally, we have discussed the importance of our results.

43.2 Boltzmann Equation

The relativistic version of Boltzmann transport equation is given by [12]

$$p_\mu \partial^\mu f + eF^{\mu\nu} p_\nu \frac{\partial f}{\partial p^\mu} + \Gamma^\mu_{\nu\lambda} p^\nu p^\lambda \frac{\partial f}{\partial p^\mu} = C \tag{43.5}$$

where the second and the third terms are due to electromagnetic and gravitational interactions respectively and C is the collision term. The curvature term is neglected here.

We make the relaxation time approximation to obtain transport coefficients namely the shear and bulk viscosity coefficients, heat conductivity and electrical conductivity of dense electron gas, given by

$$C = -\frac{p_0}{\tau}\left(f(x, p) - f^0(p)\right) \tag{43.6}$$

where

$$f(x, p) = f^{(0)}(p)\left(1 + \chi(x, p)\right) \tag{43.7}$$

Here f^0 is the (local) equilibrium distribution (Fermi distribution) function, given by.

$$f^{(0)}(p) = \frac{1}{\exp \beta(\epsilon_\nu - \mu_e) + 1} \tag{43.8}$$

and τ is the relaxation time. We write the four derivative as the sum of a space like part and a time like part, given by $\partial^\mu = u^\mu D + \nabla^\mu$ with u^μ the hydrodynamic velocity, $D = u^\mu \partial_\mu$ is the convective time derivative and $\nabla^\mu = \Delta^{\mu\nu}\partial_\nu$ is

the gradient operator, with $\Delta^{\mu\nu} = g^{\mu\nu} - u^{\mu}u^{\nu}$ some kind of projection operator, $g^{\mu\nu} = \mathrm{diag}(1, -1, -1, -1)$ the metric tensor. From particle current conservation $\partial_{\mu}N^{\mu} = 0$, where $N^{\mu} = nu^{\mu}$, we get the equation of continuity which is given by $Dn = -n\nabla_{\mu}u^{\mu}$. Here n is the equilibrium no. density. And from the energy-momentum conservation $\partial_{\mu}T^{\mu\nu} = 0$, where $T^{\mu\nu} = \epsilon u^{\mu}u^{\nu} - P\nabla^{\mu\nu}$,we get the eqn. of motion $Du^{\mu} = \frac{1}{nh}\nabla^{\mu}P$. Here ϵ is the energy density and P is the kinetic pressure. Similarly we get the eqn. of motion $C_v DT = -F(T)\nabla_{\mu}u^{\mu}$. This is energy equation where $h = (\epsilon + P)/n$, the enthalpy per particle.

We obtain the perturbative part χ, given by

$$\begin{aligned}\frac{Tp^0}{\tau}\chi = {} & QX\left(1 - f^{(0)}\right) - \left(p^{\mu}u_{\mu} - h\right)p_{\nu}X_q{}^{\nu}\left(1 - f^{(0)}\right) \\ & + p^{\mu}p^{\nu}X^0_{\mu\nu}\left(1 - f^{(0)}\right) + e\left[\frac{p_{\mu}u^{\mu}}{h} + 1\right]p_{\nu}E^{\nu}(1 - f^{(0)}) \qquad (43.9)\end{aligned}$$

where

$$X = -\nabla^{\mu}u_{\mu} \qquad (43.10)$$

is the driving force for bulk viscosity

$$X^{\mu}_q = \nabla^{\mu}T - \frac{T}{nh}\nabla^{\mu}P \qquad (43.11)$$

is the driving force for heat conduction,

$$X^{0\mu\nu} = \nabla^{\mu}u^{\nu} - \frac{1}{3}\Delta^{\mu\nu}\nabla_{\sigma}u^{\sigma} \qquad (43.12)$$

is the driving force for shear viscosity and E^{ν} is the driving force for electric current (E^{ν} for $\nu = i = 1, 2, 3$ are the components of electric field vector). The quantity Q is given by

$$\begin{aligned}Q = {} & -\frac{1}{3}\Delta^{\mu\nu}p_{\mu}p_{\nu} + (p^{\mu}u_{\mu})^2\frac{F(T)}{T}(1 - \gamma) \\ & + \left(T^2(1 - \gamma)\frac{F(T)}{T}\frac{\partial}{\partial T}\left(\frac{\mu}{T}\right) - n\frac{\partial\mu}{\partial n}\right)p^{\mu}u_{\mu} \qquad (43.13)\end{aligned}$$

where $F(T) = P(T)/n(T)$, $P(T)$ and $n(T)$ are the equilibrium local kinetic pressure and number density and $\gamma = C_p/C_v$ the ratio of specific heats at constant pressure and constant volume respectively. For a non-relativistic Boltzmann gas $F(T) = T$, where T is the local temperature of the system.

Now from the definition, the heat flow four current is given by

$$I_q^{\mu} = \frac{eB_m}{4\pi^2}\sum_{\nu}(2-\delta_{\nu 0})\int_{-\infty}^{+\infty}\frac{dp_z}{p_0}\,(p^{\nu}u_{\nu}-h)\,p^{\mu}f(x,p)$$
$$= I_q^{(0)\mu} + I_q^{(1)\mu} \tag{43.14}$$

In the equilibrium contribution, the first term is identically zero. So the irreversible term can be written as

$$I_q^{(1)\mu} = I_q^{\mu}$$
$$= \frac{eB_m}{4\pi^2}\sum_{\nu}(2-\delta_{nu0})\int_{-\infty}^{+\infty}\frac{dp_z}{p_0}p^{\mu}(p^{\nu}u_{\nu}-h)$$
$$f^{(0)}(p)\chi(x,p) \tag{43.15}$$

Again using the definition

$$I_q{}^{\mu} = \lambda^{\mu\nu}X_{q\nu}, \tag{43.16}$$

we have the heat conductivity coefficient

$$\lambda = \frac{1}{3}\Delta^{\mu\nu}\lambda_{\mu\nu}$$
$$= -\frac{1}{3T^2}\frac{eB_m}{4\pi^2}\sum_{\nu}(2-\delta_{\nu 0})\int_{-\infty}^{+\infty}\frac{dp_z}{p_0^2}\tau$$
$$(p^{\sigma}u_{\sigma}-h)^2 f^{(0)}(1-f^{(0)})\Delta^{\mu\nu}p_{\mu}p_{\nu} \tag{43.17}$$

The energy-momentum tensor is given by

$$T^{\mu\nu} = \frac{eB_m}{4\pi^2}\sum_{\nu}(2-\delta_{\nu 0})\int_{-\infty}^{+\infty}\frac{dp_z}{p_0}p^{\mu}p^{\nu}f(x,p) \tag{43.18}$$

We can write $T^{\mu\nu}$ as $T^{\mu\nu} = T^{(0)\mu\nu} + T^{(1)\mu\nu}$. The equilibrium value is given by

$$T^{(0)\mu\nu} = \frac{eB_m}{4\pi^2}\sum_{\nu}(2-\delta_{\nu 0})\int_{-\infty}^{+\infty}\frac{dp_z}{p_0}p^{\mu}p^{\nu}f^{(0)}(p)$$

and the non-equilibrium part

$$T^{(1)\mu\nu} = T^{\mu\nu}$$
$$= \frac{eB_m}{4\pi^2}\sum_{\nu}(2-\delta_{\nu 0})\int_{-\infty}^{+\infty}\frac{dp_z}{p_0}p^{\mu}p^{\nu}\chi(x,p)f^{(0)}(p)$$

Let us now consider a model assuming a flow of electron gas with cylindrical symmetry. Considering $\mu = r$, $\nu = z$, we have

$$T^{(1)rz} = -\eta_s \frac{du_z}{dr} \tag{43.19}$$

Hence the shear viscosity coefficient is given by

$$\eta_s = \frac{eB_m}{4\pi^2 T} \sum_{\nu} (2 - \delta_{\nu 0}) \int_{-\infty}^{+\infty} \frac{dp_z}{p_0^2} (p^r p^z)^2 f^{(0)} (1 - f^{(0)}) \tau \tag{43.20}$$

where $p_r = (2\nu e B_m)^{1/2}$ is the transverse component of electron momentum.

We next consider the pressure tensor to obtain an expression for bulk viscosity coefficient, given by

$$\Pi^{\mu\nu} = \Delta^{\mu}_{\sigma} T^{\sigma\tau} \Delta^{\nu}_{\tau} + P \Delta^{\mu\nu} \tag{43.21}$$

where the reversible part

$$\Pi^{(0)\mu\nu} = 0 \tag{43.22}$$

and the non-equilibrium part

$$\begin{aligned} \Pi^{(1)\mu\nu} &= \Delta^{\mu}_{\sigma} T^{\sigma\tau(1)} \Delta^{\nu}_{\tau} \\ &= \frac{eB_m}{4\pi^2} \sum_{\nu} (2 - \delta_{\nu 0}) \int_{-\infty}^{+\infty} \frac{dp_z}{p_0} \\ &\quad \Delta^{\mu}_{\sigma} \Delta^{\nu}_{\tau} p^{\sigma} p^{\tau} \chi(x, p) f^{(0)}(p) \end{aligned} \tag{43.23}$$

Now, we have the traceless part of pressure tensor

$$\begin{aligned} \Pi &= -\frac{1}{3} \Pi^{\mu}_{\mu} \\ &= -\frac{1}{3} \frac{eB_m}{4\pi^2} \sum_{\nu} (2 - \delta_{\nu 0}) \\ &\quad \int_{-\infty}^{+\infty} \frac{dp_z}{p_0} \Delta_{\sigma\mu} \Delta^{\mu}_{\tau} p^{\sigma} p^{\tau} f^{(0)}(p) \chi(x, p) \\ &= \eta_v \nabla_{\mu} u^{\mu} \end{aligned} \tag{43.24}$$

Hence we have the bulk viscosity coefficient

$$\eta_v = \frac{1}{3T} \frac{eB_m}{4\pi^2} \sum_{\nu} (2 - \delta_{\nu 0}) \int_{-\infty}^{+\infty} \frac{dp_z}{p_0^2} \Delta_{\tau\sigma} p^{\tau} p^{\sigma} \tau Q (1 - f^{(0)}) f^{(0)} \tag{43.25}$$

We shall now calculate the the electrical conductivity for electron gas. The electric four current is given by

$$j^{\mu}(x) = \frac{eB_m}{4\pi^2} \sum_{\nu} (2 - \delta_{\nu 0}) \int_{-\infty}^{+\infty} \frac{dp_z}{p_0} p^{\mu} f(x, p) \tag{43.26}$$

The reversible part $j^{\mu(0)} = 0$ and the non-equilibrium part is given by

$$\begin{aligned} j^{\mu(1)} &= j^{\mu} \\ &= \frac{eB_m}{4\pi^2} \sum_{\nu} (2 - \delta_{\nu 0}) \int_{-\infty}^{+\infty} \frac{dp_z}{p_0} p^{\mu} f^{(0)} \chi(x, p) \end{aligned}$$

Then using the covariant form of Ohm's law

$$j^{\mu} = \sigma^{\mu\nu} E_{\nu} \tag{43.27}$$

the electrical conductivity tensor is given by

$$\begin{aligned} \sigma^{\mu\nu} = \frac{e^2}{T} \frac{eB_m}{4\pi^2} \sum_{\nu} (2 - \delta_{\nu 0}) \int_{-\infty}^{+\infty} \tau \frac{dp_z}{p_0^2} p^{\mu} p^{\nu} \left(\frac{p^{\alpha} u_{\alpha}}{h} + 1 \right) \\ f^{(0)}(1 - f^{(0)}) \end{aligned} \tag{43.28}$$

The zz-component of electrical conductivity is given by

$$\begin{aligned} \sigma^{zz} = \frac{e^2}{T} \frac{eB_m}{4\pi^2} \sum_{\nu} (2 - \delta_{\nu 0}) \int_{-\infty}^{+\infty} dp_z \frac{\tau}{p_0^2} p_z^2 \left(1 + \frac{p^{\alpha} u_{\alpha}}{h} \right) \\ f^{(0)}(1 - f^{(0)}) \end{aligned} \tag{43.29}$$

The $\perp\perp$-component of electrical conductivity is given by

$$\begin{aligned} \sigma^{\perp\perp} = \frac{e^2}{T} \frac{eB_m}{4\pi^2} \sum_{\nu} (2 - \delta_{\nu 0}) (2\nu e B_m) \int_{-\infty}^{+\infty} dp_z \frac{\tau}{p_0^2} \\ \left(1 + \frac{p^{\alpha} u_{\alpha}}{h} \right) f^{(0)}(1 - f^{(0)}) \end{aligned} \tag{43.30}$$

and finally the $\perp z$-component of electrical conductivity is given by

$$\begin{aligned} \sigma^{\perp z} &= \sigma^{z\perp} \\ &= \frac{e^2}{T} \frac{eB_m}{4\pi^2} \sum_{\nu} (2 - \delta_{\nu 0}) (2\nu e B_m)^{1/2} \int_{-\infty}^{+\infty} dp_z \frac{\tau p_z}{p_0^2} \\ &\quad \left(1 + \frac{p^{\alpha} u_{\alpha}}{h} \right) f^{(0)}(1 - f^{(0)}) \end{aligned} \tag{43.31}$$

From 43.30 and 43.31 it is quite obvious that just like the shear viscosity coefficient, both $\sigma^{\perp\perp}$ and $\sigma^{\perp z}$ components of electrical conductivity vanish for $\nu_{\max} = 0$, i.e., in the ultra-strong magnetic field limit. This is of course not at all evident for η_v, λ and σ^{zz}.

43.3 Rate of Electromagnetic Processes

Now to obtain the numerical values of all these transport coefficients, or their variations with the strength of magnetic field we have to know the relaxation time τ, given by

$$\frac{1}{\tau} = \sum_i W_i \tag{43.32}$$

where W_i is the rate of ith electromagnetic process and the sum is over all possible electromagnetic processes taking place involving the electrons.

Therefore, to obtain the relaxation time we evaluate the rates of the basic electromagnetic processes, given by $e + e \rightarrow e + e$, and $e + p \rightarrow e + p$. Now in the case of $e - e$- scattering it is necessary to consider both direct and exchange processes, whereas in the case of $e - p$ scattering only the direct term contributes.

Numerically we have estimated the rate of the $e - e$ and $e - p$ scattering process and we also obtain relaxation time by using 43.32 and finally evaluate the kinetic coefficients from 43.17, 43.20, 43.25, 43.29, 43.30, 43.31 for different values of magnetic fields B_m, temperature T and matter density n_B. The variation of kinetic coefficients with magnetic field strength is shown in Fig. 43.1.

43.4 Conclusions and Discussions

From Fig. 43.1 it is seen that the kinetic coefficients are almost independent of magnetic field for moderate strengths ($< 10^{17}G$), but all of them decrease rapidly for magnetic field strength beyond $10^{17}G$. And all the three components of electrical conductivity go to almost zero in presence of an ultra strong magnetic field ($> 10^{17}G$). Therefore, at ultra-strong magnetic field, the matter (electron or proton matter) behaves like a neutral superfluid.

We have noticed that the electrical conductivity of the medium becomes extremely small in presence of ultra-strong magnetic field ($\geq 10^{17}$G). The magnetic field at the core region of a magnetar must, therefore, decay very rapidly (time scale $\sim$ a few mins.) and becomes moderate or low enough. As a consequence, there will be in principle no problem with the existence of magnetars with very low or moderate core magnetic field.

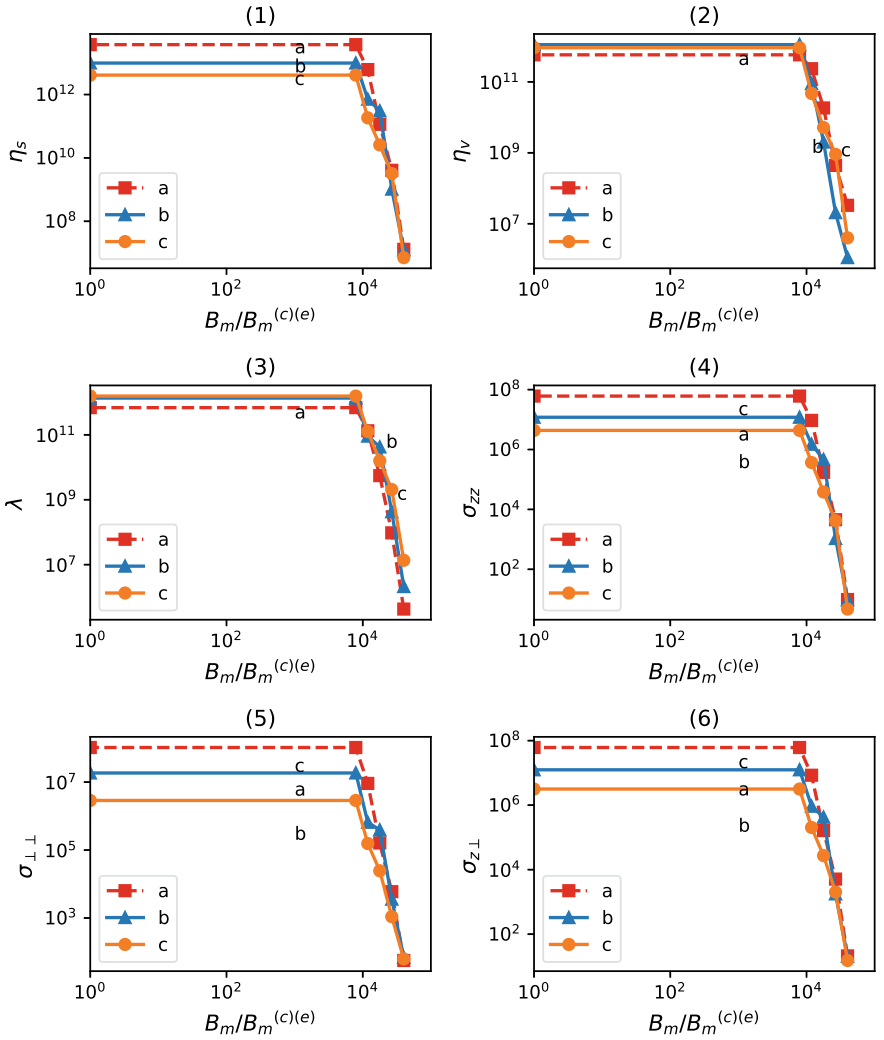

Fig. 43.1 Variation of kinetic coefficients with magnetic field B_m. (1) : Shear viscosity coefficient η_s vs. $B_m/B_m{}^{(c)(e)}$, (2) : Bulk viscosity coefficient η_v versus $B_m/B_m{}^{(c)(e)}$, (3) : Heat conductivity coefficient λ versus $B_m/B_m{}^{(c)(e)}$, (4) : zz component of electrical conductivity coefficient σ_{zz} vs. $B_m/B_m{}^{(c)(e)}$, (5) : $\perp\perp$ component of electrical conductivity coefficient $\sigma_{\perp\perp}$ vs. $B_m/B_m{}^{(c)(e)}$, (5) : $z\perp$ component of electrical conductivity coefficient $\sigma_{z\perp}$ vs. $B_m/B_m{}^{(c)(e)}$. $B_m{}^{(c)(e)}$ is the critical value of the magnetic field strength for the electron. Curve (a): $T = 5$MeV and $n_B = 5n_0$, Curve (b): $T = 15$MeV and $n_B = 5n_0$ and Curve (c): $T = 30$MeV and $n_B = 5n_0$

Acknowledgements The research leading to these results has been funded by the Department of Space, Government of India, under grant no. DS_2B-13013(2)/10/2020-Sec.2 and SERB research grant CRG/2019/001112. The author acknowledges IUCAA for the visiting associateship.

References

1. S. Ghosh, S. Mandal, S. Chakrabarty, Ann. Phys. **312**, 398 (2004)
2. T.A. Thompson, E. Quataert, A. Burrows, ApJ **620**, 861 (2005)
3. H. Heiselberg, C.J. Pethick, Phys. Rev. D **48**, 2916 (1993)
4. C. Sasaki, K. Redlich, Phys, Rev. C **79**, 055207 (2009)
5. G. Kadam, H. Mishra, L. Thakur, Phys. Rev. D **98**, 114001 (2018)
6. P. Deb, G.P. Kadam, H. Mishra, Phys. Rev. D **94**, 094002 (2016)
7. S. Plumari, A. Puglisi, F. Scardina, V. Greco, Phys. Rev. C **86**, 054902 (2012)
8. A. Wiranata, M. Prakash, Phys. Rev. C **85**, 054908 (2012)
9. P. Arnold, G.D. Moore, L.G. Yaffe, J. High Energy Phys. 001 (2000); 030 (2003);051 (2003)
10. S. Chapman,T.G. Cowling, *The Mathematical Theory of Non-uniform Gases*, 3rd edn. (Cambridge University Press, 1970)
11. S.R. Elliott, *Physics of Amorphous Materials* (Longman Group Ltd., London, 1983)
12. S.R. de Groot, W.A. van Leeuwen, C.G. van Weert, *Relativistic Kinetic Theory* (North Holland, Amsterdam, 1980)
13. T. Schäfer, D. Teaney, Rep. Prog. Phys. **72**, 126001 (2009); G. Rupak, T. Schäfer, Phys. Rev. A **76**, 053607 (2007)
14. G. Baym, C. Pethick, *The Physics of Liquid and Solid Helium* (Wiley, Part II, 1978)
15. D. Bandopadhyaya, S. Chakrabarty, P. Dey, S. Pal, Phys. Rev. D **58**, 121301 (1998)
16. S. Chakrabarty, D. Bandopadhyay, S. Pal, Phys. Rev. Lett. **78**, 2898 (1997); D. Bandopadhyay, S. Chakrabarty, S. Pal, Phys. Rev. Lett. **79**, 2176 (1997)
17. D.G. Yaklovlev, D.A. Shalybkov, Astrophys. Space Sci. **176**, 171 (1991)
18. D.G. Yaklovlev, D.A. Shalybkov, Astrophys. Space Sci. **176**, 191 (1991)
19. D.G. Yaklovlev, D.A. Shalybkov, Sov. Astron. Lett **16**, 86 (1990)
20. D.G. Yakolev, A.D. Kaminker, O.Y. Gnedin, P. Haensel, Phys. Rep. **354**, 1 (2001) (and references therein)
21. V.G. Bezchastnov, P. Haensel, Phys. Rev. D **54**, 3706 (1996); D.A. Baiko, D.G. Yakolev, Astron. Astrophys. **342**, 192 (1999)
22. S. Chakrabarty, D. Bandyopadhyay, S. Pal, Phys. Rev. Lett **78**, 2898 (1997); D. Bandyopadhyay, S. Chakrabarty, S. Pal, Phys. Rev. Lett. **79**, 2176 (1997)

Chapter 44
Variation of High and Low Energetic Electron Densities Across a Magnetic Filter in a Hot Cathode Discharge

Jocelyn Sangma and Monojit Chakraborty

Abstract In hot cathode discharges, at a pressure (equal to or more than) 10^{-4} mbar, two electron temperature groups are found to exist. In our experiment, a magnetic filter acts as an electron cooler which divides the whole chamber into two regions: Source and Target. Plasma produced in the source region diffuses towards the target region. The density of high energetic and low energetic electron groups is calculated at different experimental parameters, and a comparative study has been carried out. By changing the plasma production conditions, the density of high energetic electrons and low energetic electrons is observed in the target side. In spite of the use of the magnetic filter, high energetic electrons were still found in the target region, though their density is lower than that of the low energetic electrons. With an increase of working pressure, the density of both high and low energetic electron groups decreased, but as the filament current is increased, there is a significant increase in the density of the two electron groups. On the other hand, with increase in discharge voltage, the density of low energetic electrons increases while the density of high energetic electrons decreases slightly.

44.1 Introduction

The formation of distinct electron energy groups has been observed in low-temperature plasma and is found to be similar to that of the solar wind, which has three groups: Core, Strahl, and Halo [1]. Experimentally, different electron temperature groups have also been observed in helicon plasma [2] as well as in magnetron sputtering plasma [3]. In the double plasma device, when the space potential became almost equal to the filament potential, two-electron temperature was found by Yamazumi and Ikezawa [4]. Mishra et al. reported the control of high (primary)

J. Sangma (✉) · M. Chakraborty
Centre of Plasma Physics-Institute for Plasma Research, Tepesia Sonapur, Assam, Kamrup (M) 782402, India

M. Chakraborty
e-mail: monojit@cppipr.res.in

S. Sengupta et al. (eds.), *Selected Progresses in Modern Physics*, Springer Proceedings in Physics 265, https://doi.org/10.1007/978-981-16-5141-0_44

as well as low (plasma) electron temperature groups. They stated that the primary electrons have maximum energy up to the applied discharge voltage, while the temperature of the plasma electrons depends on the rate of collision [5].

Control of electron temperature is an area of great interest for various researchers as this allows methods to control various processes like material processing and plasma processing, finds application in fusion devices and also to perform basic plasma studies.

The two-electron temperature groups are important in the production of negative ions by volume production technique, where the high energetic electron groups are responsible for vibrationally exciting the molecule and the low energetic electron group is essential for the production of negative ions by dissociative attachment with the vibrationally excited molecule [6]. However, the high energetic electron group is also responsible for the destruction of negative ions by electron detachment [6]. And so, filters made up of magnets or grids are used as electron coolers [7], by restricting the flow of high energetic electrons from diffusing through the magnets or grids and only allowing low energetic electrons to diffuse through, such that the whole plasma volume is divided into two regions, the source region with a combination of low energetic and high energetic electrons and target region containing low energetic electrons.

In our work, magnets are used as a filter and its effect on the two electron temperature is observed. Various parameters such as working pressure, filament current and discharge voltage are varied, and its effect is observed on the two-electron temperature densities. Section 2 describes the experimental setup; Sect. 3 is the description of the experimental results, and Sect. 4 gives the conclusion of the manuscript.

44.2 Experimental Setup and Procedure

The Double Plasma Device of CPP-IPR consists of a cylindrical device of length 1.2 m and diameter 0.3 m as shown in Fig. 44.1a. Two multipole magnetic cages, which are made up of 14 magnetic channels, are placed inside the chamber each of length 0.32 m and diameter 0.25 m (Fig. 44.1b). A detailed description of the experimental setup is given in the references [8–10]. Two magnetic channels placed at a distance of 15 cm with each other, between the two magnetic cages, act as the magnetic filter (MF) (Fig. 44.2). The surface field strength of the magnetic channels which act as filter are of (~) 110 G each. A planar Langmuir probe of diameter ~3 $\times$ 10^{-3} m is used to collect the data from the source and target regions, and analysis is done using Hiden ESPsoft.

From the classical theory of diffusion, the cross field diffusion co-efficient is given as [9],

$$D_{\perp} = \frac{kT_e m_e \nu}{e^2 B^2}, \tag{44.1}$$

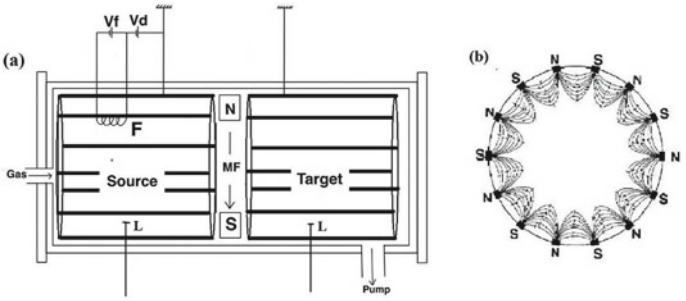

Fig. 44.1 **a** Schematic diagram of the double plasma device. The source and target regions have multipole magnetic cages. Here, L is the planar Langmuir probe, F is the filament, V_f and V_d are the filament and discharge voltage applied between the multipole cage of the source and the filaments. MF is the magnetic filter. **b** The cross-sectional view of the magnetic cage

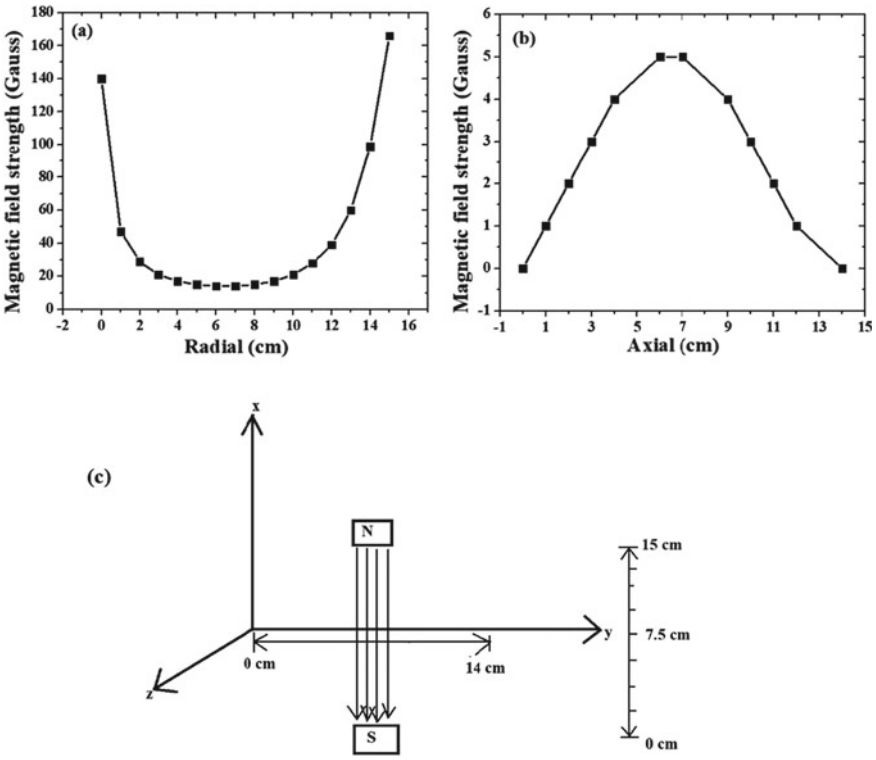

Fig. 44.2 The magnetic field strength of the magnetic filter when **a** measured radially from one channel to the other along the x-axis and **b** measured axially at the radial distance of 7.5 cm from a point where the field strength is zero (0 cm) along the y-axis, up to the point where the field strength is zero again (14 cm) **c** is the schematic diagram of the magnetic filter with its axes

where, m_e is the mass of an electron, k is Boltzmann's constant, ν is the collision frequency and T_e is the electron temperature.

Also [9],

$$\nu = n_e K T_e^{-3/2}, \tag{44.2}$$

where K is a constant $\approx 2 \times 10^{-6} Z \ln \Lambda$ such that Z is the charged state of the ion and $\ln\Lambda$ ~10 is the Coulomb logarithm.

Using Eqs. (44.1) and (44.2):

$$D_\perp = \frac{K m_e k T_e^{-1/2} n_e}{e^2 B^2}. \tag{44.3}$$

Equation (44.3) shows that as the temperature and magnetic field strength is increased, the cross field diffusion of electrons decreases.

By subtracting the ion current from the total probe current [11] and by using the semi-log plot method, the temperature of the two electron groups is calculated. The electron temperature calculated in the plot above the floating potential gives the low energetic electron temperature (T_{le}), while below the floating potential is the high energetic electron temperature (T_{he}) [12].

Using the method by Yamazumi and Ikezawa [4], the density of both high energetic and low energetic electrons are measured:

$$N_{he} = \frac{4 I_{heS}}{\left(eA\sqrt{\frac{8kT_{he}}{\pi m}} \right)}, \tag{44.4}$$

$$N_{le} = \frac{4 I_{leS}}{\left(eA\sqrt{\frac{8kT_{le}}{\pi m}} \right)}, \tag{44.5}$$

where N_{he} and N_{le} are the densities of high energetic and low energetic electrons, I_{heS} and I_{leS} are the ion saturation current of high energetic and low energetic electrons, A is the probe area, and T_{he} and T_{le} are the temperatures of high and low energetic electrons.

44.3 Experimental Results and Discussions

44.3.1 Source Versus Target with Variation of Working Pressure

Figure 44.3 shows the temperature and density of high and low energetic electron groups in both source and target regions as the working pressure is gradually increased from 10^{-4} mbar to 10^{-3} mbar for discharge voltage 50 V and filament current 24.5 A. It can be observed that both temperature and density of the two groups in the target region is lower than that in the source region because of the presence of the magnetic filter.

With the increase in working pressure, the temperature of both the groups in source and target regions gradually started to decrease as can be seen in Fig. 44.3a. In the target region, because of the magnetic filter, most of the high energetic electrons are restricted from diffusing towards the target region, and hence we observe a decrease in the temperature of both the high and low energetic groups. In the source side, as the working pressure is increased, the temperature of high energetic electrons gradually decreases from ~9 eV to 6 eV. Across the magnetic filter, this electron group further decreases from ~7.7 eV to 3 eV. The decrease in the temperature due to the filter in the target region is observed even in the case of the low energetic electrons. In the source region, with the increase in working pressure, the temperature decreases from ~2.5 eV to 1.1 eV and in the target region, the temperature decreased further from ~2 eV to 0.7 eV.

Since the number density of neutral particles increases with the increase in working pressure, the ionization rate also increases, which leads to the increase in the density of the low energetic electrons ~4.2×10^{15} m^{-3} to ~1×10^{16} m^{-3} as observed in Fig. 44.3b. This is because low energetic electrons are produced as a result of ionizing collisions between the neutral particles and the high energetic electrons [5, 13]. On the other hand, for the high energetic electrons which are attributed to the primary electrons [13], no change is observed as the working pressure is varied, since the filament current is kept constant.

As the high energetic electrons undergo various collisional process with the neutral particles, it loses its energy and so a decrease in temperature for the high energetic electrons is observed as the working pressure is gradually increased. Also, as the density of low energetic electron group increased as working pressure was increased, its temperature started to decrease.

However, in the target region, with increase in working pressure, the density of both the high and low energetic electrons decreased from ~2.1×10^{13} m^{-3} to 4.8×10^{12} m^{-3} (N_{he}) and from ~2.2×10^{15} m^{-3} to 5.4×10^{14} m^{-3} (N_{le}) (Fig. 44.3b). Most of the high energetic electrons are restricted by the filter from diffusing towards the target region as seen from Fig. 44.3a, and the electrons (~7.7 eV and below) that manage to escape towards the target region further loses their energy to the neutral particles in the target region via elastic collision. This leads to the decrease

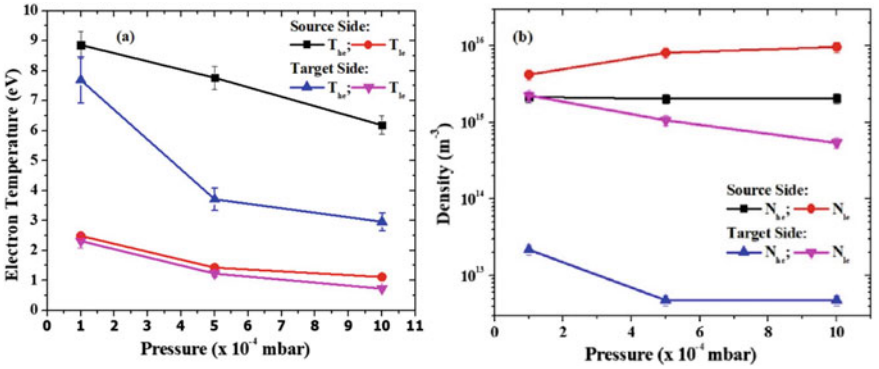

Fig. 44.3 Comparison of source and target side parameters at discharge voltage 50 V and filament current 24.5 A where **a** is electron temperature of high and low energetic electron groups as working pressure is varied and **b** is the density of high and low energetic electron groups as working pressure is varied

in ionization at the target region and hence the density of the low energetic electron group also starts to decrease.

44.3.2 Variation with Discharge Voltage in the Target Region

Figure 44.4 shows that the variation of temperature and density of high and low energetic electrons as the discharge voltage is increased from 50 to 80 V, for filament current 24.5 A and working pressure 10^{-3} mbar in the Target region. It is observed that as the discharge voltage is gradually increased, temperature of high energetic electrons gradually increased from ~3 eV to 5 eV, while there was little or almost no change in the temperature of the low energetic electron group (~0.72 eV to 0.9 e V).

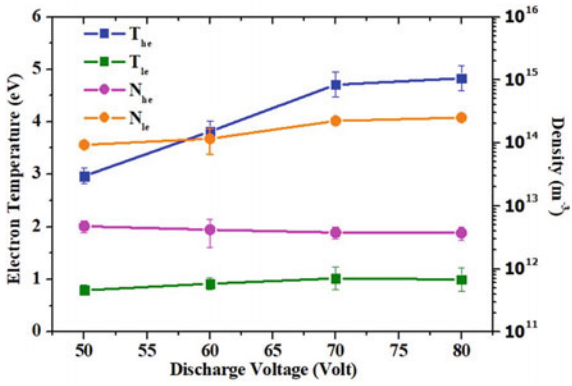

Fig. 44.4 Effect of increase in discharge voltage on the temperature and density of high and low energetic electron groups for working pressure 10^{-3} mbar and filament current 24.5 A in the Target region

On the other hand, the density of low energetic electrons increased from ~9.2×10^{13} m^{-3} to 2.5×10^{14} m^{-3}, while very slight decrease in the density of high energetic electrons was observed (~5×10^{12} m^{-3} to 3.7×10^{12} m^{-3}).

With increase in the discharge voltage, the primary electrons in the source side get highly energized and their energy is maximum up to the applied discharge voltage [5]. Hence the temperature of high energetic electrons increases as the discharge voltage is increased. This leads to an increase in electron flux from the source towards the target side, resulting in the increase in ionization rate in the target region [5, 13]. This increase in the ionization rate in the target side leads to the increase in the density of low energetic electrons as the discharge voltage is increased. Hence, an increase in the density of low energetic electrons is observed in the target region. On the other hand, the density of high energetic electrons in the target side decreases slightly due to the ionization process with the neutral particles.

44.3.3 Variation with Filament Current in the Target Region

In Fig. 44.5, the filament current is increased from 24.5 A to 25.5 A at fixed discharge voltage of 50 V and working pressure 10^{-3} mbar and its effect on the temperature of high and low energetic groups and also on its density are observed in the target side. It has been observed that the temperature of high energetic electrons gradually increases, while there was little to no increase in the temperature of the low energetic electrons (~0.7 eV to 0.86 eV). On the other hand, the density of both the high and low energetic electron groups started to increase as the filament current increased.

As the filament current is increased, more primary electrons are emitted from the filament in the source region and hence more energetic electrons are able to escape towards the target region through the magnetic filter from the source side. Therefore, we see an increase in the density of high energetic electrons from ~4.8×10^{12} m^{-3} to 1.6×10^{13} m^{-3}. With increase in the density of the high energetic electrons in both the source and target region, the ionization rate also increases in both the regions. This

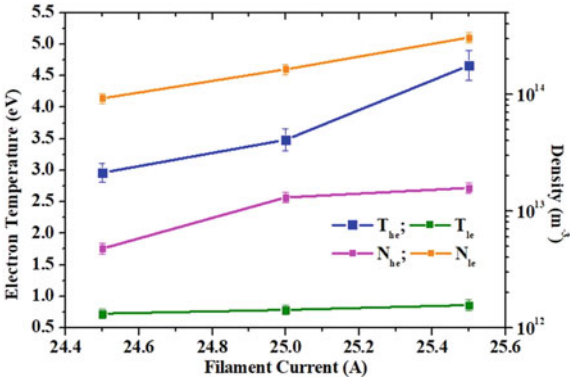

Fig. 44.5 Effect of increase in filament current on the temperature and density of two-electron groups at discharge voltage 50 V and working pressure 10^{-3} mbar in the Target region

increase in ionization rate of high energetic electrons with that of neutral particles has led to the slight increase in the density of the low energetic electrons in the target side as well from ~9.2×10^{13} m^{-3} to 3.1×10^{14} m^{-3}.

44.4 Conclusion

It has been observed that experimental parameters like working pressure, discharge voltage and filament current affects the temperature and density of the high and low energetic electron groups. It was found that the magnetic filter restricted the flow of high energetic electrons from diffusing towards the target region and hence the temperature in the target region was quite low than the temperature in the source region. However, this also affected the density of the electron groups which was found to be lower than that in the source side.

By changing the various parameters, like working pressure, it was found that even though the density of low energetic electrons increased slightly in the source side, an opposite trend was observed in the target region for both the electron groups. This is due to electrons in the source side losing their energy to the neutral particles via collisions. When the discharge voltage was gradually increased, the temperature of the high energetic electrons increased since they start to acquire very high kinetic energy [13], leading to the increase in the ionization rate and so the density of low energetic electrons start to gradually increase. On the other hand, as the filament current was gradually increased, the density of the high energetic electrons in the target side started to increase as more primary electrons emitted from the filament in the source side resulted in more high energetic electrons escaping towards the target side. This increase in the density of high energetic electrons in the target side led to the increase in ionization rate and so the density of low energetic electrons also started to increase.

The control of the temperature of both the high and low energetic electron groups is important to create a suitable environment for the production of negative ions. The electron temperature in the target region should not be high so that the negative ions are not destroyed by electron detachment [6, 7]. Also, while lowering the electron temperature in the target region, it must be noted that it should not lower the density of the low energetic electrons which assists in production of negative ion by dissociative attachment in volume production technique [7].

References

1. V. Kolobov, V. Godyak, Electron kinetics in low-temperature plasmas. Phys. Plasmas **26**, 060601 (2019)
2. B.B. Sahu, A. Ganguli, R.D. Tarey, Warm electrons are responsible for helicon plasma production. Plasma Sources Sci. Technol **23**, 065050 (2014)

3. T.E. Sheridan, M.J. Goeckner, J. Goree, Observation of two-temperature electrons in a sputtering magnetron plasma. J. Vac. Sci. Technol. A **9**(3), (1991)
4. T. Yamazumi, S. Ikezawa, Control of the Two-Electron-Temperature Plasma Parameter in a DP Device. Jpn. J. Appl. Phys. **29**, 1807 (1990)
5. M.K. Mishra, A. Phukan, M. Chakraborty, K.S. Goswami, Role of high energetic electrons in controlling diffused plasma parameters in a double plasma device. Phys. Lett. A **365**, 135–139 (2007)
6. M. Bacal, Volume production of hydrogen negative ions**.** Nuclear Instruments and Methods in Physics Research B37/38, 28–32 (1989)
7. M. Bacal, M. Wada, Negative hydrogen ion production mechanisms. Appl. Phys. Rev. **2**, 021305 (2015)
8. P. Hazarika, M. Chakraborty, B.K. Das, M. Bandyopadhyay, A technique to control cross-field diffusion of plasma across a transverse magnetic field. Phys. Plasmas **23**, 122105 (2016)
9. B.K. Das, A study of Plasma Dynamics across a magnetic Filter Field in a Double Plasma Device. PhD Thesis (Guahati University Dept. of physics, Assam, India) (2014)
10. B.K. Das, P. Hazarika, M. Chakraborty, M. Bandyopadhyay, Improvement of charged particles transport across a transverse magnetic filter field by electrostatic trapping of magnetized electrons. Phys. Plasmas **21**, 072118 (2014)
11. M. Oertl, A. Skoelv, Primary Electron diagnostics with a Langmuir Probe in a discharge Plasma. Proceedings of the International Conference on Plasma Physics, Lausanne, Switzerland, 331 (1984)
12. M.K. Mishra, A. Phukan, Electron heating in a multi-dipole plasma by electrostatic plugging. J. Plasma Physics **79**(2), 153–161 (2013)
13. M.K. Mishra, A. Phukan, M. Chakraborty, Effect of discharge voltage on bi-Maxwellian electrons in the diffusion plasma region of a double plasma device. J. Plasma Physics **79**(5), 913–920 (2013)